

P-ISSN :- 2415-4806
E-ISSN :- 2523-2401
DOI :10.22317/JNUC



J.N.U.C.



Especial Issue Proceedings The Third International Scientific Conference for Renewable Energy
Applied Research / Southern Technical University From 14th - 15th March , 2018

Journal of Al-Nisour University College

Bi-annual Scientific Journal Published
by
Al-Nisour University College

Vol. : 6

Year: 2018

Especial Issue Proceedings

**The Third International Scientific
Conference for Renewable Energy
Applied Research /Southern Technical
University**

From 14th - 15th March, 2018

Bi- annual Scientific Journal

Published by

Al-Nisour University College

P – ISSN: 2415 - 4826

E- ISSN: 2523 – 2401

DOI: 10.22317. JNUC

Special Issue Proceedings



J.N.U.C.

Bi-annual Scientific Journal Published
by Al-Nisour University College



Vol.: 6 Year : 2018

Editor in chief

Asst. Prof. Dr. Abed J. Kadhum

Editorial manager

Asst. Prof. Dr. Jasim M. Salman

Editorial board

- Prof. Dr. Bassam A. Mohammed
- Prof. Dr. Nidham S. Hameed
- Asst. Prof. Dr. Othman H. Salman
- Asst. Prof. Dr. Abdulridha J. Jasim
- Asst. Prof. Dr. Zuhair I. Abdaljabar
- Asst. Prof. Dr. Alaauldeen M. Kareem
- Asst. Prof. Dr. Khalid S. Al-Mhadwi
- Asst. Inst. Dr. Maki M. Abedulhassan

Advisory board

- Prof. Dr. Zafra M. Lerman, Ph.D., FRSC, President, Malta Conferences Foundation - USA .
- Prof. Dr. Mariam Balban, Rome University, Italy .
- Prof. Dr. Bassim H. Hmeed, University of Science Malaysia / Malaysia.
- Prof. Dr. Adel Sharif Al-Hussani , Surrey University / England.
- Prof. Dr. Mudhafar S . Al-Zuhiri , Technical South University / Iraq.
- Prof. Dr. Fared M. Abid Al-Attar , Technical Middle University/ Iraq.
- Prof. Dr. Abdalwahab R. Hamed, Al-Zarqa University/ Jordan .
- Prof. Dr. Usama S. Abdulrazzak, Middle Technical University / Iraq .
- Prof. Dr. Zuhair N. Hamed, Middle Technical University / Iraq .

Special Issue Proceedings



J.N.U.C.

Bi-annual Scientific Journal Published
by Al-Nisour University College



Vol.: 6 Year : 2018

Copy Editor (English)

Prof. Dr. Nidham S. Hameed / Al-Nisour University College

Copy Editor (Arabic)

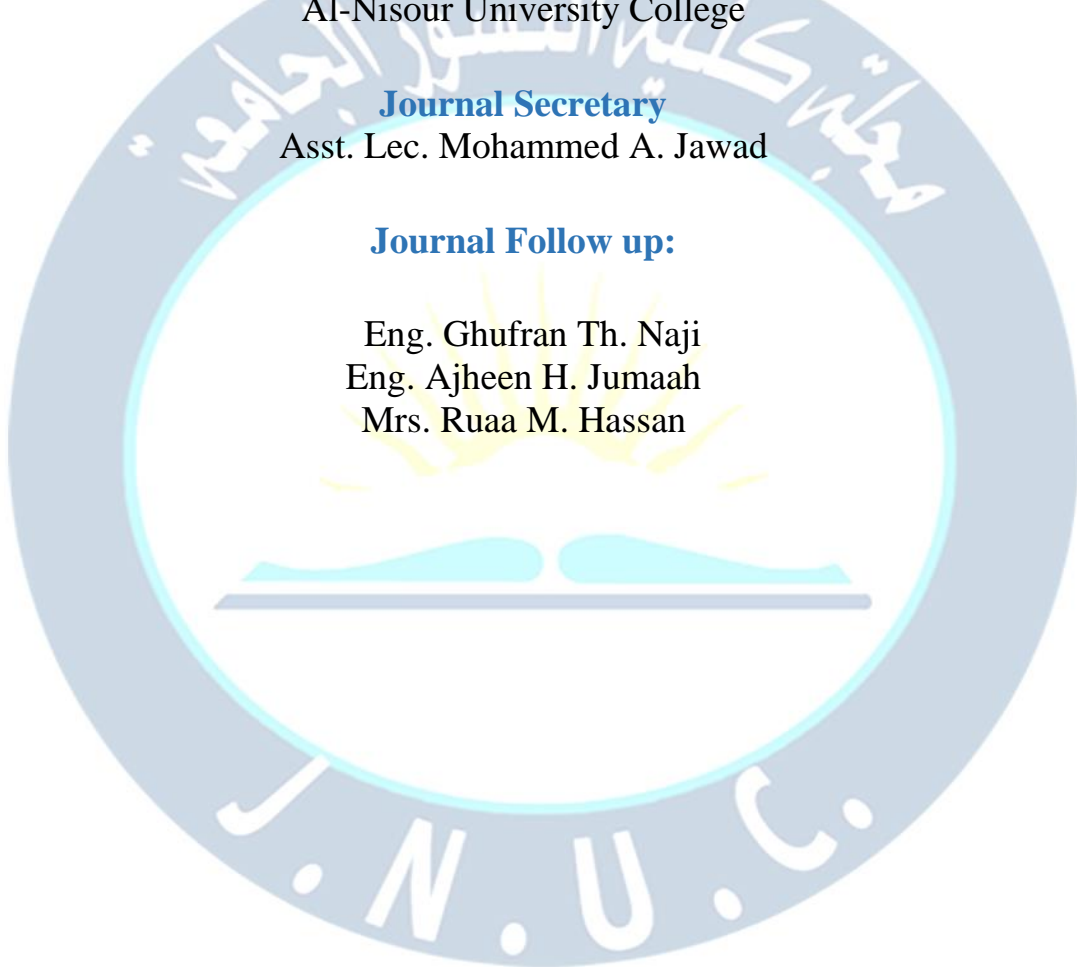
Asst.Inst. Dr. Shamem Radhi Abed
Al-Nisour University College

Journal Secretary

Asst. Lec. Mohammed A. Jawad

Journal Follow up:

Eng. Ghufran Th. Naji
Eng. Ajheen H. Jumaah
Mrs. Ruaa M. Hassan

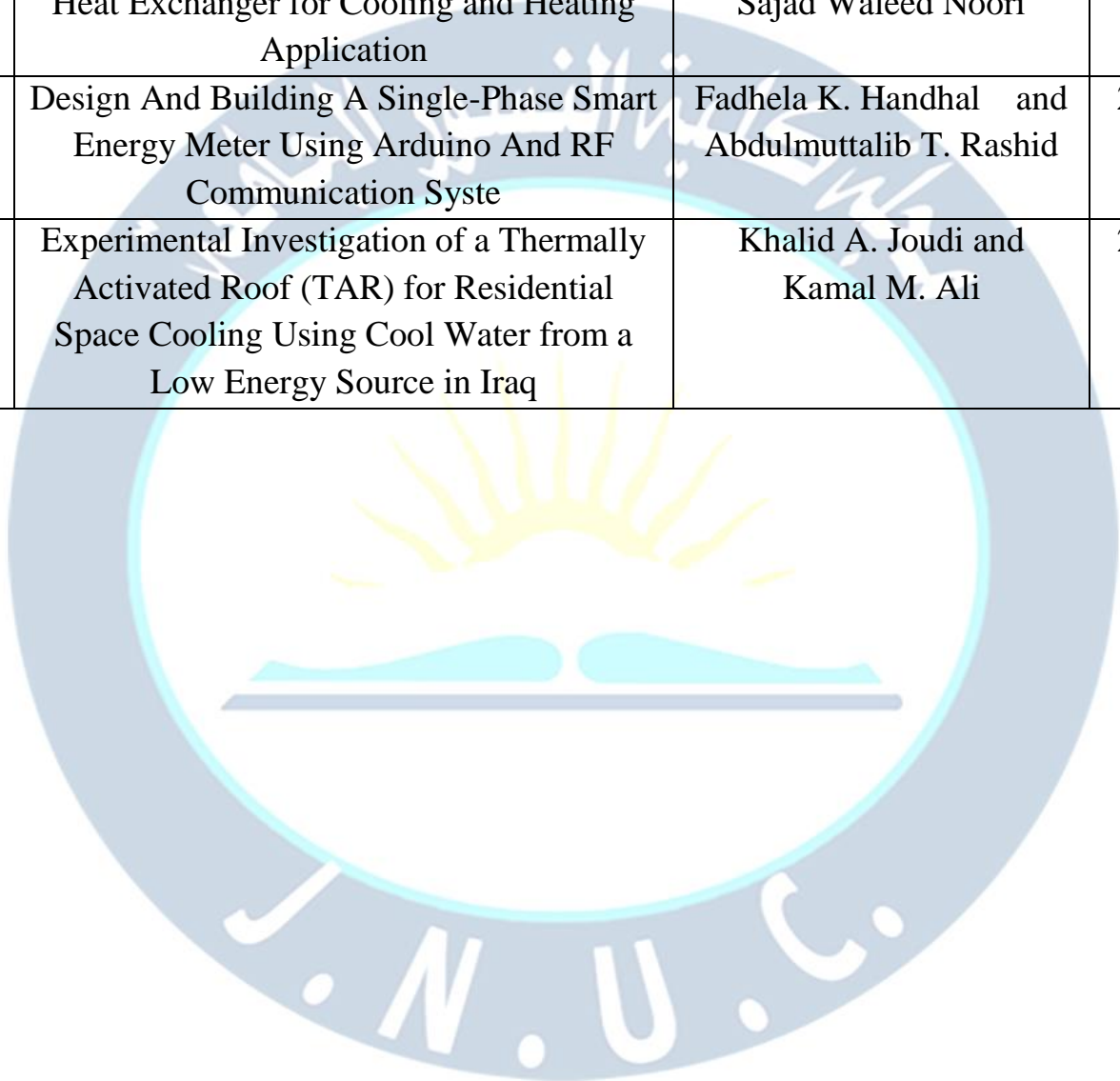


List of Content

| No | Title of the Paper | Authers | Page |
|-----------|---|--|-------------|
| 1 | Three-Dimensional Numerical Simulation of Heat Transfer Characteristics in Cooling Systems Using Phase Change Materials in the Rectangular Containers | Ahmed K. Alaharaa and Ali S. Falihb | 1 |
| 2 | Design and Implementation of P&O and FLC Maximum Power Point Tracking Algorithms Based on PLC for a PV System | Ahmed Sadeq Hunaish and Jawad Radhi Mohmood | 14 |
| 3 | CFD Investigation of Turbulent Mixed Convection Heat Transfer in a Tringular Cavity | Saadoon F. Dakhil , Falah A. Assi and Rasha N. laubi | 22 |
| 4 | Faults Investigation in Renewable Energy Sources Penetrated Distribution Feeders Based on the Theory of Wavelets and Artificial Intelligence | Sara J. Authafa and Khalid M. Abdul-Hassan | 35 |
| 5 | Electricity Production by Microbial Fuel Cell | Doaa Faisal Ghazi and Alaa A. Saleh | 45 |
| 6 | Design Consideration of a Remote Area Power Supply System Utilizing SolarDiesel Energies | Abdul-kareem Khamis Hassan land Hiba Abdulkareem Khamis | 50 |
| 7 | Design and Implementation a prototype of a Smart Prepaid Power System Based on IOT | Ikraam Kassim Abid and Ali Fadhil Marhoon | 55 |
| 8 | Design and Implementation of Load Balancing System for a Smart Home | Abdulmuttalib T. Rashid and Mofeed T. Rashid | 65 |
| 9 | State Feedback Control based Genetic Algorithms of a Modified Cuk Convertor | Nashwan Saleh Sultan | 72 |
| 10 | Investigation the Performance of Solar Water Pump | Ali K. Al-Sayyab, Akeel M.Ali and Mohammed A. Abdulwahid | 80 |
| 11 | Regeneration Energy Using Electromagnetic Actuator with Nonlinear Active Suspension System | Ammar A. Aldair, Eman Badee Alsaedee and Turki Y. Abdalla3 | 87 |

| | | | |
|----|---|---|-----|
| 12 | Numerical Investigation of The Effect of Gaseous and Diesel Fuel Under Dual and Tri-mode on The Combustion and Exhaust Emissions in a CI Engine | Hayder A. Alrazen, Saadoon F. Albahadili and K.A.Ahmed | 103 |
| 13 | Power Quality Improvement for Grid-connected Solar Plant Using Intelligent Decision Support System | Dr. Ali Hadi Abdulwaid1, Diyah Kammel Sharry and Mohammed Al-Mumin3 | 112 |
| 14 | Evaluation Of An Off-grid Photovoltaic Technology For Household Application In Iraq | Mohammed.H.R.Alktrane and Qudama Al- Yasiri | 118 |
| 15 | Effect The Change of Absorber Length on Thermal Performance of Parabolic Dish Solar Collector | Ahmed. W. Hamed, Ali. A.F.Al-Hamadani and Mahmmud aziz muhammed | 124 |
| 16 | Evaluation the effect of wastewater conductivity on the final stable voltage applied to electrocoagulation reactor | Forat Yasir AlJaberi and Wadood T. Mohammed | 133 |
| 17 | Experimental Study the Effect of Ambient Temperature on the Performance of Photovoltaic System Work with MPPT Charge Controller in Technical Engineering College of Najaf | Dhafer Manea Hachim Al- Hasnaw | 140 |
| 18 | Effects of substrate temperature on optical constants of CdS thin films produced by a thermal vacuum evaporation technique for solar cells application | Salah Abdul-Jabbar Jassim and A.M. Abdulwahab | 149 |
| 19 | Synthesis and enhancement efficiency of organic solar cell device | Abdullah A. Hussein, Rajaa M. Abdullah and Abdullwahab A. Sultan | 156 |
| 20 | A Probabilistic Finite State Machine based Residential Environment for Obligation Agent Development | Wasan A. Jwad and Kasim A. Al-Salim | 164 |
| 21 | Simulation of Wind-Diesel Hybrid Power System for Fuel and Energy Department Building | Bahiya Abdulla Jabbar and Hiba Abdulkareem Khamis | 172 |

| | | | |
|----|--|---|-----|
| 22 | Effect of location and direct solar radiation on the performance of electric power transformer | Rafid M. Hannun, Salmaan H.Hammadi and Mohammed H. Khalaf | 177 |
| 23 | A Novel Dual Injection Strategy to Improve the Performance of Ethanol Small Spark Ignition Engine | Nizar F.O. Al-Muhsen and Guang Hong | 184 |
| 24 | Numerical Investigation of Earth to Air Heat Exchanger for Cooling and Heating Application | Mushtaq Ismael Hasan and Sajad Waleed Noori | 193 |
| 25 | Design And Building A Single-Phase Smart Energy Meter Using Arduino And RF Communication Syste | Fadhela K. Handhal and Abdulmuttalib T. Rashid | 204 |
| 26 | Experimental Investigation of a Thermally Activated Roof (TAR) for Residential Space Cooling Using Cool Water from a Low Energy Source in Iraq | Khalid A. Joudi and Kamal M. Ali | 212 |



Three-Dimensional Numerical Simulation of Heat Transfer Characteristics in Cooling Systems Using Phase Change Materials in the Rectangular Containers

Ahmed K. Alahara^a,

^a Civil Engineering Department, College of Engineering, Misan University, Iraq

Ali S. Falih^b

^b Mechanical Engineering Department, College of Engineering, Basrah University, Iraq

1. Introduction

Abstract: In this study a full numerical simulation is made to simulate the 3-D phase change process and developing flow in the latent cool thermal energy storage system (LCTES) to investigate its thermal performance. The Navier-Stokes equations of the flow are solved for laminar, 3-D, steady state, incompressible, and no slip conditions; while the energy equation of the heat transfer fluid is solved for unsteady state condition. The heat conduction in the phase change material (PCM) (paraffinic hydrocarbon) and the solid partitions are considered as unsteady 3-D heat conduction problem using the effective heat capacity method for PCM. The governing equations are discretized using finite-volume method (explicit method)-upwind differencing scheme. These equations are solved using SIMPLE algorithm method on staggered grid with FORTRAN code to obtain the velocities distribution, and then the energy equations for the fluid and the periphery domain (solid and PCM) are solved simultaneously in the separately program as second step. A detailed parametric investigation is performed, including effects of Reynolds number (Re), Stefan number (Ste), aspect ratio (α_c) and container height (H_p) on the performance of the LCTES system. From the obtained results, it was found that Re , Ste , α_c and H_p play an important role during solidification process and has a strong effect on performance of the LCTES system.

Keywords: PCM, LCTES system, Heat capacity method

Corresponding author: Tel: +9647709000655

E-mail: dr.ahmed_alshara@uomisan.edu.iq (Ahmed Alshara)

As the demand for refrigeration and air conditioning has been increased during the last decades, the cool storage systems can be used to the economic advantage over conventional cooling systems. Cool storage system using PCMs can be used for peak load shifting if they are installed in the building materials or in conventional active space cooling system to improve the overall thermal efficiency as well as to reduce the peak cooling electrical load. Storage of energy in suitable form and its conversion to the required form is a present day challenge to the technologists. LHSU using the PCMs is a better engineering option for such problems. This is because of their inherent high storage capacity and their nearly isothermal performance during the charging and discharging processes. Thermal energy storage has recently attracted increasing interest related to thermal applications such as: Refrigeration and air conditioning, Thermal storage of solar energy and Passive storage in bioclimatic building...etc [1].

Successful utilization of PCM and HTF depends on developing means of containment. A survey of previously published papers dealing with LHTES reveals that three geometries commonly employed as PCM containers [2, 3]. One of them is the rectangular or slab container; two modes of rectangular container are shown in Fig. 1-a and Fig. 1-b. The second geometry is the cylindrical container; three modes of cylindrical PCM container configurations are shown in Fig. 1-c. The final geometry is spherical container (grains) as shown in Fig. 1-d.

One of the most practical reasons for the use of CTES is to implement an extra cooling load without altering existing air conditioning systems. These systems (CTES systems) can be installed and run in conjunction with existing air conditioning systems or installed as individual part and depending on the cool night storage to help alleviate any extra cooling loads that may be required during particularly hot days.

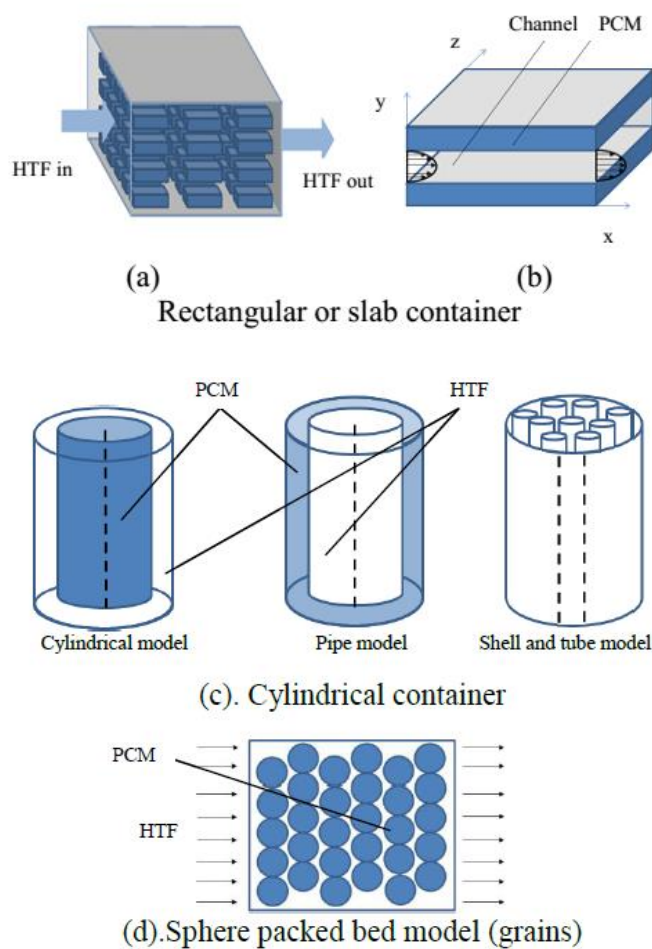


Fig. 1. Classification of commonly used PCM containers

As a widely used PCM, paraffin waxes possess attractive characteristics: large latent heat capacity, little or no supercooling, chemical stability and non-corrosive characteristics [4], for this reasons; **Zohoor and Moosavi 2010 [5]** proposed a hybrid system of storing solar energy which can be considered an intelligent storage system. The results showed that the use of such system can improve the capability of energy gathering comparing to the individual water storage tank during the cold months of the year.

Understanding the heat transfer behavior during phase change in storage system is extremely important for the design of efficient storage systems. Solutions to phase change problems include analytical, experimental and numerical using one-dimensional, two-dimensional or three dimensional models to solve energy formulated equation [6]. In light of this, **Zhang and Faghri 1996 [7]** studied numerically the heat transfer enhancement in the LHTEs system by using an externally finned tube. The melting in the PCMs and heat conduction in the tube wall and fins are described by a temperature transforming model (effective heat capacity method) coupled to the heat transfer from transfer fluid and solved by a finite difference method (Implicit Method). Their results showed that the initial subcooling has almost no effect on the melting front on the

two sides of the transverse fins. Also, the molten volume fraction can be significantly increased by increasing the heights of fins.

Fang and Li 2002 [8] presented the details of a mathematical model that is used to predict the charging performance of ice storage for stacked rectangular capsules. The numerical results showed that the time required for the charging process of ice storage will increase when the coolant flow rate decreases.

Shatikian 2004 [9] numerically studied the processes of melting and solidification of PCM (Rubitherm RT25 with melting temperature of 23-25°C). The storage unit is a rectangular box which bottom is a hot or a cold wall with parallel partitions are attached to this wall. Between the partitions, there is PCM. Transient two-dimensional numerical simulations were performed using the Fluent 6.0 software and based on the enthalpy method. Results showed that, the higher difference between the temperature of the bottom and the melting point of the PCM, the more rapid is the melt fraction growth.

Numerical and experimental model developed by **Bony and Citherlet in 2007 [10]** to simulate heat transfer in PCMs plunged in water tank storage. The temperature evolution inside the PCM during the charging and

discharging cycle has been monitored with thermocouples placed inside a PCM module (paraffin). The time evolution of these temperatures has been compared with the simulation. The comparison between monitored data and simulation results has shown a good agreement.

Rathod and Banerjee 2011 [11] numerically investigated in 3-D to analyze the performance of latent heat storage units employing PCM. Results showed that for the same mass of PCM and surface area of heat transfer, cylindrical shell container takes the least time for freezing the PCM.

Takeda et al. 2004 [12] developed an experimental ventilation system that features direct heat exchange between ventilation air and granules containing a phase change material (PCM). They proposed to install some thermal storage capacity in ventilation ducts. It will then be possible to use cool night air to remove thermal energy from the storage material so it can be used for cooling during the day. **Fang et al. 2014 [13]**, performed an experimental assessment on the thermal energy storage performance of a novel family of paraffin-based composite phase change materials (PCMs) filled with hexagonal boron nitride (h-BN) nanosheets. They noted that clearly exhibited acceleration of both melting and solidification heat transfer rates, afforded by the increased thermal conductivity of the composite PCMs. Finally, **Hasan et al. 2016 [14]** tested a phase change material (PCM) contained in an insulated concrete block in extremely hot weather in the United Arab Emirates (UAE) to evaluate its cooling performance. They found that at the best case, a temperature drop of 8.5% and a time lag of 2.6 h were achieved in peak indoor temperature, rendering a reduction of 44% in the heat gain.

The aims of the present study are: make a full numerical simulation to simulate the 3-D phase change process and developing flow in the CTES system to investigate its thermal performance, and study the effect of the Re , Ste , α_c and H_p on the heat transfer characteristics.

2. Theoretical Analysis

The physical model which is studied as shown in the schematic, Fig. 2-a which represents the flow of HTF in rectangular channel with PCM fills the rectangular container above it and horizontal plate-type conducting partition between them. They consist a storage unit, system constructed from the number of these storage units with vertical plate-type conducting partitions between them. This model of LCTES system is developed here to obtain a complete description for heat transfer and hydrodynamics characteristics of this system.

Based on the symmetry of the system and since all the channels are receive the same mass flow rate at the inlet and heat flow across the boundaries, the computational domain can be restricted to the unit volume including one - half HTF channel, one - half horizontal and vertical partition and one - half PCM container, as shown in Fig. 2-b.

To solve this problem, the following assumptions are necessary:

- (1) The thermophysical properties of the PCM, solid and HTF are independent of temperature, but the properties of the PCM can be different in the solid and liquid phases.
- (2) The freezing of the PCM occurs at a range of phase change temperature from $(T_{pm} + \Delta T_p)$ to $(T_{pm} - \Delta T_p)$.
- (3) The PCM is homogeneous and isotropic.
- (4) The PCM is initially in liquid phase at initial temperature greater than melting temperature.
- (5) The heat transfer in the PCM is controlled only by conduction.
- (6) The flow of HTF is three dimensional, incompressible, laminar, no slip and steady state velocities with variable temperature with time.
- (7) The energy dissipation of HTF is negligible.
- (8) The pressure gradient of HTF flow is in axial direction only.

Now, based on the previous assumption, the system of equations governs the velocity and temperature fields of HTF inside the channel are written as follows:

Continuity equation

$$u \frac{\partial u}{\partial x} + v \frac{\partial v}{\partial y} + w \frac{\partial w}{\partial z} = 0 \quad (1)$$

x-momentum equation

$$u \frac{\partial u}{\partial x} + v \frac{\partial u}{\partial y} + w \frac{\partial u}{\partial z} = -\frac{1}{\rho_f} \frac{dp}{dx} + \frac{\mu_f}{\rho_f} \left(\frac{\partial^2 u}{\partial x^2} + \frac{\partial^2 u}{\partial y^2} + \frac{\partial^2 u}{\partial z^2} \right) \quad (2)$$

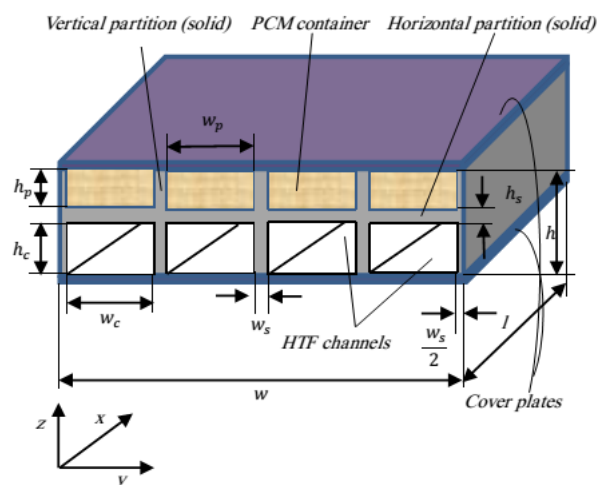


Fig. 2-a Physical model.

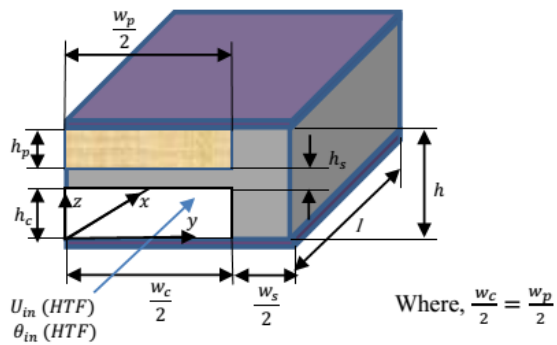


Fig. 2-b Computational model.

y-momentum equation

$$u \frac{\partial v}{\partial x} + v \frac{\partial v}{\partial y} + w \frac{\partial v}{\partial z} = \frac{\mu_f}{\rho_f} \left(\frac{\partial^2 v}{\partial x^2} + \frac{\partial^2 v}{\partial y^2} + \frac{\partial^2 v}{\partial z^2} \right) \quad (3)$$

z-momentum equation

$$u \frac{\partial w}{\partial x} + v \frac{\partial w}{\partial y} + w \frac{\partial w}{\partial z} = \frac{\mu_f}{\rho_f} \left(\frac{\partial^2 w}{\partial x^2} + \frac{\partial^2 w}{\partial y^2} + \frac{\partial^2 w}{\partial z^2} \right) \quad (4)$$

energy equation

$$\frac{\partial T_f}{\partial t} + u \frac{\partial T_f}{\partial x} + v \frac{\partial T_f}{\partial y} + w \frac{\partial T_f}{\partial z} = \frac{k_f}{c_f} \left(\frac{\partial^2 T_f}{\partial x^2} + \frac{\partial^2 T_f}{\partial y^2} + \frac{\partial^2 T_f}{\partial z^2} \right) \quad (5)$$

Also, the suitable and simplified governing energy equation for three dimensional, unsteady state heat transfer in the solid without heat generation is shown below:

$$\frac{\partial T_s}{\partial t} = \frac{k_s}{c_s} \left(\frac{\partial^2 T_s}{\partial x^2} + \frac{\partial^2 T_s}{\partial y^2} + \frac{\partial^2 T_s}{\partial z^2} \right) \quad (6)$$

And finally, the PCM has three states in the heat storing/releasing process, i.e. solid state, liquid state and solid-liquid coexistence state, a unified control equation in the whole region (including solid state, liquid state and solid-liquid coexistence state) is expressed mathematically according to "effective heat capacity model" for three dimensional, unsteady state heat transfer in the PCM without heat generation and the advective movements in the inner of the liquid are disregarded as follow [15]:

$$\frac{\partial T_p}{\partial t} = \frac{k_p}{c_p} \left(\frac{\partial^2 T_p}{\partial x^2} + \frac{\partial^2 T_p}{\partial y^2} + \frac{\partial^2 T_p}{\partial z^2} \right) \quad (7)$$

Effective heat capacity model introduces the concept of effective or equivalent heat capacity in the whole phase transition temperature interval.

The pending parameters, such as the equivalent heat capacity c_p and the thermal conductivity k_p are considered as a function of the nodal temperature, which transforms the phase change problem into the conductive problem of variable thermal properties. When the specific heat in solid state and liquid state are considered to be constant; the density is constant, equivalent heat capacity c_p and thermal conductivity k_p are shown as [15]:

$$c_p = \begin{cases} c_{ps} & (\text{solid}) \\ \rho_p h_{fg} + \frac{c_{ps} + c_{pl}}{2} & T_{pm} - \Delta T_p \leq T_p \leq T_{pm} + \Delta T_p \\ c_{pl} & (\text{liquid}) \end{cases} \quad (8)$$

$$k_p = \begin{cases} k_{ps} & (\text{solid}) \\ k_{ps} + \frac{k_{pl} - k_{ps}}{2 \Delta T_p} [T_p - (T_{pm} - \Delta T_p)] & T_{pm} - \Delta T_p \leq T_p \leq T_{pm} + \Delta T_p \\ k_{pl} & (\text{liquid}) \end{cases} \quad (9)$$

This model assumes that the freezing process occurs over a range of phase change temperatures from $(T_{pm} + \Delta T_p)$ to $(T_{pm} - \Delta T_p)$, but it also can be successfully used to simulate the freezing process occurring at a single temperature by taking a small range of phase change temperature $2\Delta T_p$ [7].

The initial and boundary conditions can be written as following (for all domains, including HTF, solid and PCM):

A. Initial condition:

$$T_i(t=0) = T_{ini} \quad \text{for} \quad 0 \leq x \leq l, 0 \leq y \leq \left(\frac{w_c}{2} + \frac{w_s}{2}\right), 0 \leq z \leq h$$

Where, i represent either f , s or p refer to the HTF, solid and PCM respectively.

B. Boundary conditions:

❖ At the channel inlet:

$$\left. \begin{aligned} u &= u_{in}, v, w = 0 \\ p &= p_{in} \\ T_f &= T_{in} \end{aligned} \right\} \text{at } x=0 \text{ for } 0 \leq y \leq \frac{w_c}{2}, 0 \leq z \leq h_c$$

❖ At the channel outlet:

$$\left. \begin{aligned} \frac{\partial u}{\partial x} = \frac{\partial v}{\partial x} = \frac{\partial w}{\partial x} &= 0 \\ \frac{\partial T_f}{\partial x} &= 0 \end{aligned} \right\} \text{at } x=l \text{ for } 0 \leq y \leq \frac{w_c}{2}, 0 \leq z \leq h_c$$

❖ At the Symmetry planes:

$$\frac{\partial u}{\partial y} = \frac{\partial v}{\partial y} = \frac{\partial w}{\partial y} = 0 \quad \text{at } y=0 \quad \text{for} \quad 0 \leq x \leq l, 0 \leq z \leq h_c$$

$$\frac{\partial T_i}{\partial y} = 0 \quad \text{at } y=0 \quad \text{and} \quad y = \frac{w_c}{2} + \frac{w_s}{2} \quad \text{for} \quad 0 \leq x \leq l,$$

$$0 \leq z \leq h$$

❖ At the Insulated surfaces:

$$\frac{\partial T_i}{\partial x} = 0 \quad \text{at } x=0 \text{ and for } 0 \leq y \leq \left(\frac{w_c}{2} + \frac{w_s}{2}\right), h_c \leq z \leq h$$

$$\frac{w_c}{2} \leq y \leq \left(\frac{w_c}{2} + \frac{w_s}{2}\right), \quad 0 \leq z \leq h_c$$

$$u = v = w = 0 \quad \text{at} \quad z = 0 \quad \text{for} \quad 0 \leq x \leq l, \quad 0 \leq y \leq \frac{w_c}{2}$$

$$\frac{\partial T_f}{\partial z} = 0 \quad \text{at} \quad z = 0 \quad \text{and} \quad z = h \quad \text{for} \quad 0 \leq x \leq l,$$

$$0 \leq y \leq \left(\frac{w_c}{2} + \frac{w_s}{2}\right)$$

❖ Fluid-solid interfaces:

$$\left. \begin{aligned} u = v = w = 0 \\ -k_f \frac{\partial T_f}{\partial y} = -k_s \frac{\partial T_s}{\partial y} \end{aligned} \right\} \text{at } y = \frac{w_c}{2} \quad \text{for } 0 \leq x \leq l, \quad 0 \leq z \leq h_c$$

And

$$\left. \begin{aligned} u = v = w = 0 \\ -k_f \frac{\partial T_f}{\partial z} = -k_s \frac{\partial T_s}{\partial z} \end{aligned} \right\} \text{at } z = h_c \quad \text{for } 0 \leq x \leq l,$$

$$0 \leq y \leq \frac{w_c}{2}$$

❖ PCM-solid interfaces:

$$-k_p \frac{\partial T_p}{\partial y} = -k_s \frac{\partial T_s}{\partial y} \quad \text{at} \quad y = \frac{w_p}{2} \quad \text{for} \quad 0 \leq x \leq l,$$

$$(h_c + h_s) \leq z \leq h$$

And

$$-k_p \frac{\partial T_p}{\partial z} = -k_s \frac{\partial T_s}{\partial z} \quad \text{at} \quad z = h_c + h_s \quad \text{for} \quad 0 \leq x \leq l,$$

$$0 \leq y \leq \frac{w_p}{2}$$

To convert the above governing equations with the initial and boundary conditions into dimensionless form, the following dimensionless parameters are used:

$$U = \frac{u}{u_{in}} \quad V = \frac{v}{u_{in}} \quad W = \frac{w}{u_{in}} \quad P = \frac{P}{\rho_f u_{in}^2}$$

$$X = \frac{x}{D_h} \quad Y = \frac{y}{D_h} \quad Z = \frac{z}{D_h} \quad Fo = \frac{\alpha_{ps} t}{D_h^2}$$

$$C = \frac{c}{c_{ps}} \quad K = \frac{k}{k_{ps}} \quad \theta = \frac{T - T_{in}}{T_{pm} - T_{in}} \quad \Delta\theta_p = \frac{\Delta T_p}{T_{pm} - T_{in}}$$

$$Ste = \frac{c_{ps} (T_{pm} - T_{in})}{\rho_p h_{fg}} \quad Re = \frac{\rho_f u_{in} D_h}{\mu_f}$$

Using the above dimensionless form of temperature, velocity and parameters of the problem, the equations (1)–(9) can be written as:

Continuity equation

$$\frac{\partial U}{\partial X} + \frac{\partial V}{\partial Y} + \frac{\partial W}{\partial Z} = 0 \quad (10)$$

x-momentum equation

$$U \frac{\partial U}{\partial X} + V \frac{\partial U}{\partial Y} + W \frac{\partial U}{\partial Z} = -\frac{dP}{dX} + \frac{1}{Re} \left(\frac{\partial^2 U}{\partial X^2} + \frac{\partial^2 U}{\partial Y^2} + \frac{\partial^2 U}{\partial Z^2} \right) \quad (11)$$

y-momentum equation

$$U \frac{\partial V}{\partial X} + V \frac{\partial V}{\partial Y} + W \frac{\partial V}{\partial Z} = \frac{1}{Re} \left(\frac{\partial^2 V}{\partial X^2} + \frac{\partial^2 V}{\partial Y^2} + \frac{\partial^2 V}{\partial Z^2} \right) \quad (12)$$

z-momentum equation

$$U \frac{\partial W}{\partial X} + V \frac{\partial W}{\partial Y} + W \frac{\partial W}{\partial Z} = \frac{1}{Re} \left(\frac{\partial^2 W}{\partial X^2} + \frac{\partial^2 W}{\partial Y^2} + \frac{\partial^2 W}{\partial Z^2} \right) \quad (13)$$

Energy equation for HTF

$$\frac{\alpha_r}{Pe} \frac{\partial \theta_f}{\partial Fo} + U \frac{\partial \theta_f}{\partial X} + V \frac{\partial \theta_f}{\partial Y} + W \frac{\partial \theta_f}{\partial Z} = \frac{1}{Pe} \left(\frac{\partial^2 \theta_f}{\partial X^2} + \frac{\partial^2 \theta_f}{\partial Y^2} + \frac{\partial^2 \theta_f}{\partial Z^2} \right) \quad (14)$$

$$\text{Where, } \alpha_r = \frac{\alpha_{ps}}{\alpha_f}, \quad Pe = Re Pr, \quad Pr = \frac{\mu_f c_{pf}}{k_f} \quad \text{and}$$

$$Fo = \frac{\alpha_{ps} t}{D_h^2}$$

Energy equation for solid

$$\frac{\partial \theta_s}{\partial Fo} = \frac{K_s}{C_s} \left(\frac{\partial^2 \theta_s}{\partial X^2} + \frac{\partial^2 \theta_s}{\partial Y^2} + \frac{\partial^2 \theta_s}{\partial Z^2} \right) \quad (15)$$

Energy equation for PCM

$$\frac{\partial \theta_p}{\partial Fo} = \frac{K_p}{C_p} \left(\frac{\partial^2 \theta_p}{\partial X^2} + \frac{\partial^2 \theta_p}{\partial Y^2} + \frac{\partial^2 \theta_p}{\partial Z^2} \right) \quad (16)$$

Where,

$$C_p = \begin{cases} 1 & \theta_p < 1 - \Delta\theta_p \\ \frac{1}{2 Ste \Delta\theta_p} + \frac{1 + C_{pl}}{2} & 1 - \Delta\theta_p \leq \theta_p \leq 1 + \Delta\theta_p \\ C_{pl} & \theta_p > 1 + \Delta\theta_p \end{cases} \quad (17)$$

$$K_p = \begin{cases} 1 & \theta_p < 1 - \Delta\theta_p \\ 1 + \frac{K_{pl} - 1}{2 \Delta\theta_p} [\theta_p - (1 - \Delta\theta_p)] & 1 - \Delta\theta_p \leq \theta_p \leq 1 + \Delta\theta_p \\ K_{pl} & \theta_p > 1 + \Delta\theta_p \end{cases} \quad (18)$$

Also, the initial and boundary conditions can be written in the dimensionless form as following:

A. Initial condition:

$$\theta_i (Fo=0) = \theta_{mi} \quad \text{for} \quad 0 \leq X \leq L, \quad 0 \leq Y \leq \left(\frac{W_c}{2} + \frac{W_s}{2}\right), \quad 0 \leq Z \leq H$$

B. Boundary conditions:

❖ At the channel inlet:

$$\left. \begin{aligned} U = 1, V, W = 0 \\ P_m = \frac{P_m}{\rho_f u_{in}^2} \\ \theta_f = 0 \end{aligned} \right\} \text{at } X=0 \quad \text{for} \quad 0 \leq Y \leq \frac{W_c}{2}, \quad 0 \leq Z \leq H_c$$

❖ At the channel outlet:

$$\left. \begin{aligned} \frac{\partial U}{\partial X} = \frac{\partial V}{\partial X} = \frac{\partial W}{\partial X} = 0 \\ \frac{\partial \theta_f}{\partial X} = 0 \end{aligned} \right\} \text{at } X=L \quad \text{for } 0 \leq Y \leq \frac{W_c}{2},$$

$$0 \leq Z \leq H_c$$

❖ At the Symmetry planes:

$$\frac{\partial U}{\partial Y} = \frac{\partial V}{\partial Y} = \frac{\partial W}{\partial Y} = 0 \quad \text{at } Y=0 \quad \text{for } 0 \leq X \leq L,$$

$$0 \leq Z \leq H_c$$

$$\frac{\partial \theta_i}{\partial Y} = 0 \quad \text{at } Y=0 \text{ and } Y = \frac{W_c}{2} + \frac{W_s}{2} \quad \text{for } 0 \leq X \leq L,$$

$$0 \leq Z \leq H$$

❖ At the Insulated surfaces:

$$\frac{\partial \theta_i}{\partial X} = 0 \quad \text{at } X=0 \text{ and } X=L \quad \text{for } 0 \leq Y \leq \left(\frac{W_c}{2} + \frac{W_s}{2}\right),$$

$$H_c \leq Z \leq H$$

$$\frac{W_c}{2} \leq Y \leq \left(\frac{W_c}{2} + \frac{W_s}{2}\right), 0 \leq Z \leq H_c$$

$$U = V = W = 0 \quad \text{at } Z=0 \quad \text{for } 0 \leq X \leq L, 0 \leq Y \leq \frac{W_c}{2}$$

$$\frac{\partial \theta_i}{\partial Z} = 0 \quad \text{at } Z=0 \text{ and } Z=H \quad \text{for } 0 \leq X \leq L,$$

$$0 \leq Y \leq \left(\frac{W_c}{2} + \frac{W_s}{2}\right)$$

❖ Fluid-solid interfaces:

$$\left. \begin{aligned} U = V = W = 0 \\ -K_f \frac{\partial \theta_f}{\partial Y} = -K_s \frac{\partial \theta_s}{\partial Y} \end{aligned} \right\} \text{at } Y = \frac{W_c}{2} \quad \text{for } 0 \leq X \leq L,$$

$$0 \leq Z \leq H_c$$

And

$$\left. \begin{aligned} U = V = W = 0 \\ -K_f \frac{\partial \theta_f}{\partial Z} = -K_s \frac{\partial \theta_s}{\partial Z} \end{aligned} \right\} \text{at } Z = H_c \quad \text{for } 0 \leq X \leq L,$$

$$0 \leq Y \leq \frac{W_c}{2}$$

❖ PCM-solid interfaces:

$$-K_p \frac{\partial \theta_p}{\partial Y} = -K_s \frac{\partial \theta_s}{\partial Y} \quad \text{at } Y = \frac{W_p}{2} \quad \text{for } 0 \leq X \leq L$$

$$, (H_c + H_s) \leq Z \leq H$$

And

$$-K_p \frac{\partial \theta_p}{\partial Z} = -K_s \frac{\partial \theta_s}{\partial Z} \quad \text{at } Z = H_c + H_s$$

$$\text{for } 0 \leq X \leq L, 0 \leq Y \leq \frac{W_p}{2}$$

By solving the governing equations, the discretization equations for the velocity, pressure and temperature fields can be obtained. The governing equations are solved numerically using the finite volume method (Upwind scheme) by explicit difference for time and forward difference for dimension [16]. All discretization equations, except energy equations, are solved by using the SIMPLE (Semi-Implicit Method for Pressure-Linked Equations) algorithm method. A computer program of the operation is built in FORTRAN Language. From the obtained pressure, velocity and temperature distributions, respectively, one can determine solid fraction, solid front, accumulative cool energy storage and axial variation of the average Nusselt number.

Solid fraction computes the fraction of the cells which are in solid state, and solid front is the location of interface between solid and liquid phases in the solid-liquid coexistence state. This solid fraction, β , is defined to vary between $\beta = 0$ if $\theta_p > 1 + \Delta\theta_p$ (liquid state) and $\beta = 1$ if $\theta_p < 1 - \Delta\theta_p$ (solid state). Any cells which have a temperature range of $(1 - \Delta\theta_p) \leq \theta_p \leq (1 + \Delta\theta_p)$ (solid-liquid coexistence state) will have a solid fraction between 0 and 1 and the solid fraction will depend on the amount of latent heat released. Also, solid front can be specified based on temperature range for the each nodal in 3-D.

The solid fraction for the total volume of PCM can be estimated as following:

$$\beta_{total}^n = \frac{\sum_{(I,J,K)} dV_n}{V_p} \times 100\% \quad (19)$$

Where dV_n is the solid volume of the PCM in the one node and V_p is the total volume for the PCM.

For a typical run, the amount of cool energy storage consists of latent heat of phase change process and sensible heat of both solid and liquid phases. Thus, the total storage energy becomes [17]:

$$e_{total} = \sum_{(I,J,K)} (e_{sensible,liquid} + e_{latent} + e_{sensible,solid}) \quad (20)$$

Where,

$$e_{sensible,liquid} = v_N c_{pl} (T_{pi} - T_{pl}) \quad \text{for } T_p > T_{pm} + \Delta T_p$$

$$e_{latent} = \rho_p v_N h_{fg} \beta_{total}^n \quad \text{for } T_{pm} - \Delta T_p \leq T_p \leq T_{pm} + \Delta T_p$$

$$e_{sensible,solid} = v_N c_{ps} ((T_{pm} - \Delta T_p) - T_{ps}) \quad \text{for } T_p < T_{pm} - \Delta T_p$$

Where, v_N : node volume, m^3

Charging of a node involves either a decrease in the liquid temperature ($e_{sensible,liquid}$), or a phase change with an increase in solid fraction (e_{latent}), or a decrease in the solid

temperature ($e_{sensible,solid}$) or a combination of first two consecutive processes, or all three processes.

Finally, The axial variation of the average Nusselt number, $Nu(x)$, can be calculated from [17]:

$$Nu(x) = \frac{\overline{q_s''(x)} D_h}{k_f (\overline{T_w(x)} - \overline{T_b(x)})} \quad (21)$$

The fluid bulk temperature and average temperature of the channel surface can be evaluated as the following [18]:

$$\overline{T_b(x)} = \frac{\int_0^y \int_0^z c_f u T_f dy dz}{\int_0^y \int_0^z c_f u dy dz} \quad (22)$$

Where, $c_f = \rho_f c_{pf}$

The fluid bulk temperature may also be expressed in terms of non-dimensional variables as:

$$\overline{\theta_b(X)} = \frac{\int_0^Y \int_0^Z C_f U \theta_f dY dZ}{\int_0^Y \int_0^Z C_f U dY dZ} \quad (23)$$

Where, $C_f = \frac{c_f}{c_{ps}}$

The channel surface temperature is assumed to be equal to the sum of local channel surface temperatures averaged on the heated perimeter of the channel,

$$\overline{T_w(x)} = \frac{1}{(y+z)} \left(\int_0^z T_s(x, y = \frac{w_c}{2}, z) dz + \int_0^y T_s(x, y, z = h_c) dy \right) \quad (24)$$

Equation (24) can also be non-dimensionalized to obtain the non-dimensional average channel surface temperature as:

$$\overline{\theta_w(X)} = \frac{1}{(Y+Z)} \left(\int_0^Z \theta_s(X, Y = \frac{W_c}{2}, Z) dZ + \int_0^Y \theta_s(X, Y, Z = H_c) dY \right) \quad (25)$$

Also, the average heat flux at the solid-fluid interface is defined:

$$\overline{q_s''(x)} = \frac{-1}{(y+z)} \left(\int_0^z k_s \frac{\partial T_s}{\partial y} \Big|_{y=\frac{w_c}{2}} dz + \int_0^y k_s \frac{\partial T_s}{\partial z} \Big|_{z=h_c} dy \right) \quad (26)$$

Equation (26) can be written in the following dimensionless form as:

$$\overline{Q_s''(X)} = \frac{-1}{(Y+Z)} \left(\int_0^Z K_s \frac{\partial \theta_s}{\partial Y} \Big|_{Y=\frac{W_c}{2}} dZ + \int_0^Y K_s \frac{\partial \theta_s}{\partial Z} \Big|_{Z=H_c} dY \right) \quad (27)$$

Where,

$$\overline{Q_s''(X)} = \frac{\overline{q_s''(X)} D_h}{k_{ps} (T_{pm} - T_{in})}$$

3. Criterion of the Stability

In this study the computational program divided into two segments, the first program used to finding the HTF flow variables distribution (including pressure and velocities) in the steady state flow inside the channel, in this program the accuracy of an iterative solution (iterative solution based on SIMPLE algorithm method) depends on "Convergence Criterion".

Here, the convergence of a solution variable ϕ is defined as the form [18]:

$$\frac{|\phi_n - \phi_{n-1}|}{|\phi_n|} \leq \varepsilon \quad (28)$$

Where ϕ represents any dependent variable, namely u, v and w, and n is number of iteration.

A value of $\varepsilon = 1 \times 10^{-5}$ was selected for the present study.

The second program is used to finding the transient temperature distribution for all domain (including HTF, solid and PCM).

For stability in the second program, all coefficients must be positive in the discretized energy equations [19]. The size of the network chosen affects the accuracy of the estimated derivatives and, therefore, the accuracy of the result. In general, the smaller the intervals ΔX , ΔY , ΔZ and ΔFo , the more accurate is the result. However, in the transient explicit method, these intervals may not be chosen in a completely arbitrary manner, therefore, ΔFo can be determined as follow:-

To solve the equation (14) must be:

$$\theta_{jp}^{n+1} = A_p \theta_{jp}^n + \frac{Pe \Delta Fo}{\alpha_r \Delta V} (A_w \theta_{jw}^n + A_E \theta_{je}^n + A_S \theta_{js}^n + A_N \theta_{jn}^n + A_B \theta_{jb}^n + A_T \theta_{jt}^n) \quad (29)$$

$$A_p = 1 - \frac{Pe \Delta Fo}{\alpha_r \Delta V} (A_w + A_E + A_S + A_N + A_B + A_T + \Delta F) \geq 0 \quad (30)$$

Where,

A: algebraic coefficient

$$\Delta F = F_e - F_w + F_n - F_s + F_t - F_b$$

F = (U, V, or W) * Normal area on the control volume face

$$\Delta Fo \leq \frac{1}{\frac{Pe}{\alpha_r \Delta V} (A_w + A_E + A_S + A_N + A_B + A_T + \Delta F)} \quad (31)$$

And by using the same procedure for the final form of discretized energy equation for the solid and the PCM one can be obtained the minimum ΔFo .

The strongly explicit solver that requires considerably less computational time step and after determine the results of ΔFo by using the above procedure, it can be concluded that the value ΔFo in eq.(31) is the smallest one, therefore, can be used in all the discretize finite volume equations.

4. Results and Discussions

The results of a numerical heat transfer analysis on the encapsulated PCM based CTES are presented in this section. When creating control volume domains for numerical procedures, one of the most important keys to the accuracy of the results is the grid size independence. Many cases considered, but from checking the results it can be decided that, the best case is carried out for a grid size of (60×48×100) nodes in the (x,y,z) directions respectively for the computational model shown in the Fig. 2-b and the governing equations were solved based on these grid, with a very small of ΔFo (ΔFo ≈ 4.86E-007). The thermophysical properties of PCM [12] and carbon steel [20] are given in Table 1. Air is used as HTF as the system corresponds to that one used for domestic cooling applications with ambient temperature lower than the melting temperature of PCM. The identified design and operating parameters are listed in Table 2.

Before charging into the results, a model validation must be performed to ensure the model is a viable simulation of real processes. The verification is made by comprising the results of Shatikian 2004 [9] (enthalpy model) numerically with the results of present numerical model (effective heat capacity model) for the solidification process under the following conditions: The initial temperature of the whole system was 27°C, i.e. the PCM was slightly overheated. At t=0, the temperature of the bottom was changed to 6 °C, while the ambient air above the unit was 27 °C and kept constant through the entire process.

Table1. Thermo physical properties of PCM,solid and HTF.

| Material Property | PCM (Paraffinic hydrocarbon) | | Solid (Carbon steel) | HTF (Air) |
|-------------------------------|---------------------------------|--------|-------------------------|--------------|
| | solid | liquid | | |
| ρ (kg / m ³) | 1360 | 1360 | 7854 | 1.2 |
| c_p (J / kg.K) | 1210 | 1220 | 434 | 1006 |
| k (W / m.K) | 0.13 | 0.129 | 60.5 | 0.0272 |
| h_{fg} (J / kg) | 41900 | | — | — |
| $T_{pm} - \Delta T_p$ (°C) | 23.5 lower | | — | — |
| $T_{pm} + \Delta T_p$ (°C) | 24.9 upper | | — | — |

Table2. Design and operating parameters.

| Parameter | Value |
|--|----------------|
| Length, L | 90 |
| Horizontal partition thickness, H _s | 0.05 |
| Vertical partition thickness, W _s | 0.036×2 |
| Aspect ratio of the channel, α _c | 2.0 |
| Height of PCM Container, H _p | 0.363 |
| Width of PCM Container, W _p | 0.75×2 |
| Reynolds number, Re | 300 |
| Stefan number, Ste (T _{in} °C) | 0.4 (10.35 °C) |
| Dimensionless initial temperature, (θ _{ini}) | 1.5 (31.13 °C) |

Fig. 3 shows the comparison of the temperature at the plane of symmetry of the PCM at various distances from the base at time 1800 second obtained by the present model and Shatikian [9], under the previous conditions. From this figure the agreement is good and the maximum percentage error was 0.251%

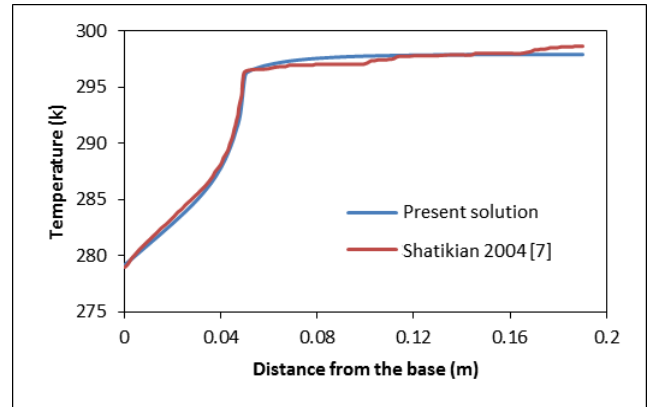


Fig. 3 Comparison between the results of present model and the numerical results of Shatikian [9].

In order to demonstrate the validity of the present work, another comparison is made with numerical results of Rathod and Banerjee 2011 [11].

Fig. 4 shows the variation of the PCM temperature with time at the center of rectangular container obtained by the present model and Rathod and Banerjee [11]. From these results it can be seen that, the agreement between results of present model and results of Rathod and Banerjee [11] is acceptable and the maximum percentage error was 4.3%.

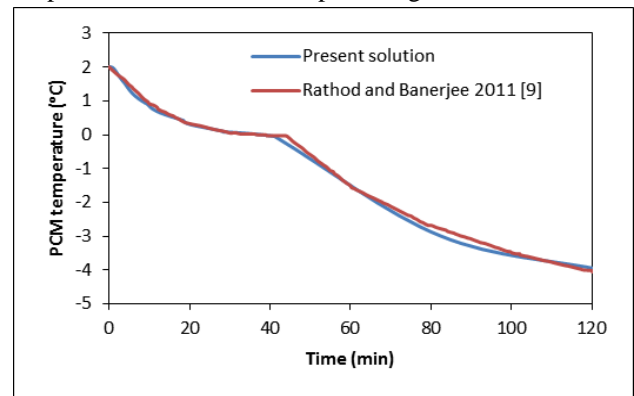


Fig. 4 Comparison of the temperature-time history obtained from the numerical program and the numerical results of Rathod and Banerjee [11].

Preliminary Study

The preliminary study served as a basis for the detailed study performed later. For this reason, its results are discussed here. The dimensions and values of parameters used in this section are the same as listed in table 2.

Fig. 5 shows the distribution of the dimensionless central axial u-velocity with dimensionless axial distance for different values of Reynolds number. From this figure it can be seen that, the flow is developing and the central velocity increased in flow direction until reach its maximum value in the fully developed region. The figure shows that Reynolds number have considerable effect on the developing of the flow and the length of entrance region which increased with increasing Re.

Fig. 6 shows the dimensionless temperature distribution of PCM at the center section of the storage rectangular container with three different axial locations as indicated in this figure i.e., the PCM near the inlet ($\theta_{p,inlet}$) at the middle ($\theta_{p,middel}$) and near the outlet ($\theta_{p,outlet}$) of the storage container. At the beginning the drop in temperature of the liquid PCM is very high due to the higher heat transfer rate that exists between the HTF and liquid PCM as the temperature difference between the PCM and the HTF was very high. With time, the PCM changes its phase with the dimensionless temperature remaining within the phase change range (1.05–0.95). In this period the PCM reaches the freezing state, solidification process begins. The cool energy is stored by freezing the PCM at a very small range of dimensionless temperature. Part of the PCM is in the liquid state and part in the solid state. However, at the final stage of solidification, $\theta_{p,inlet}$ becomes lower than the freezing temperature range first as the subcooled PCM, while $\theta_{p,middel}$ and $\theta_{p,outlet}$ are still in solidification temperature range. Finally, all temperatures are decreasing until they reach the steady state after very long time.

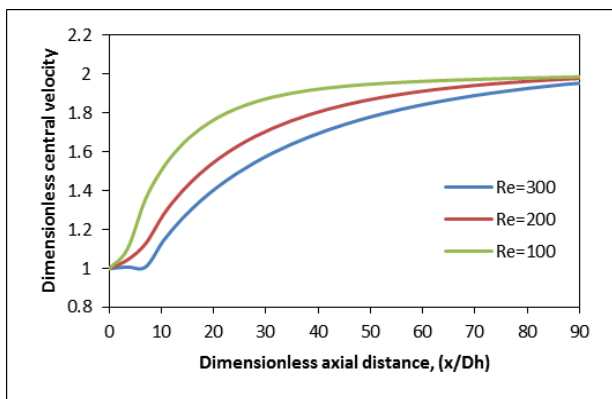


Fig. 5 Dimensionless centerline velocity profiles of the HTF.

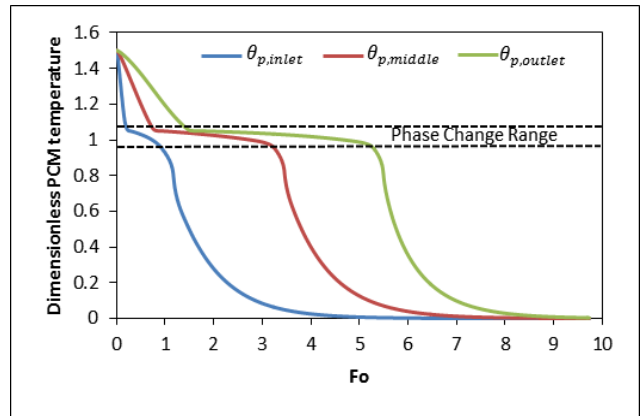


Fig. 6 Variation of Dimensionless temperature of the PCM with Dimensionless time at the center sections of the container.

Fig. 7 shows the solid fraction distribution of the PCM as function of dimensionless time and axial position. It is appeared from Fig. 7 that solidification process near the outlet of the container is slower than near the inlet of the container. This is due to the temperature difference between the PCM and HTF near the outlet of storage container is smaller than near the inlet of storage container.

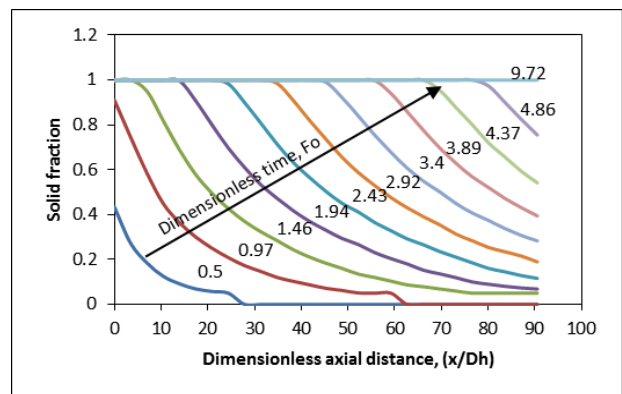


Fig. 7 Solid fraction distribution of the PCM as a function of dimensionless time

Detailed Study

The geometrical and heat transfer parameters such as (Re), (Ste), (α_c) and (H_p) have an observable effect on the characteristics of the system. In this section, the effect of each parameter on the system performance is discussed with constant other parameters as indicated in table 2.

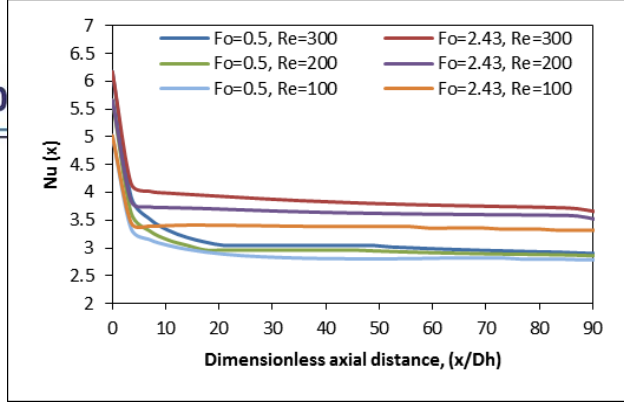


Fig. 8 indicates the longitudinal variation of the local Nusselt number for HTF with dimensionless axial distance at different dimensionless times for different Reynolds numbers. It can be seen that the Nu has high value at the entrance region (initial part of channel), due to the development of boundary layer and then decreases towards fully developed flow. Also, It's clear that, the local Nusselt number increases with time, as mentioned in [7], this is because the PCM enter phase change process and release its latent heat content where this causes high heat transfer in this period. Also, Nu increases with Re because increase the mass flow rate with increasing Re which leads to increase the heat transfer rate.

Fig. 8 Effect of Reynolds number on local Nusselt number.

Fig. 9 shows the effect of Reynolds numbers on the time-wise variation of dimensionless HTF outlet bulk temperature. It can be seen that for any Reynolds number, there is continual drop in dimensionless HTF outlet bulk temperature as the time progresses. As can be seen, the dimensionless HTF outlet bulk temperature decreases when the Re increases. This is because, when the Re increases, the amount of fluid increase and then the heat convection of HTF increased. Though there is a sudden drop in the initial period of solidification where the sensible cooling for the liquid PCM is predominant, in the later period, where the whole surface of the PCM is at the solidification dimensionless temperature range, the dimensionless HTF outlet bulk temperature decreases gradually and finally approaches the dimensionless inlet temperature at the end of process.

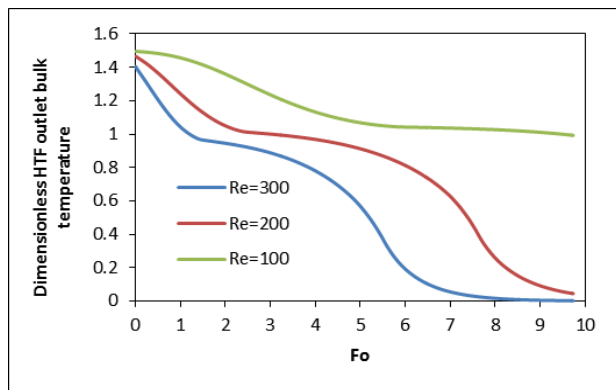


Fig. 9 Effect of Reynolds number on the dimensionless HTF outlet bulk temperature.

Fig. 10 shows the effect of the Reynolds number on the solid fraction. The figure shows that solid fraction is increased with increasing Reynolds number, this due to increase of the heat transfer at the inner surface of the channel which increases the solidified PCM amount.

Fig. 11 shows the dimensionless temperature variation and phase change process with time at center of the end section of the CTES container under effect of Stefan numbers. It is clear that, the variation of Stefan number does not have any effect on the dimensionless temperature profiles of the PCM during the sensible cooling of liquid phase for the PCM whereas the effect is quite large in the later part of the storage process. It can be seen that the dimensionless solidification time significantly decreases with increment of Stefan number. This due to increase the driving temperature gradient for heat transfer, i.e. the temperature difference between phase change temperature and inlet HTF temperature ($T_{pm} - T_{in}$).

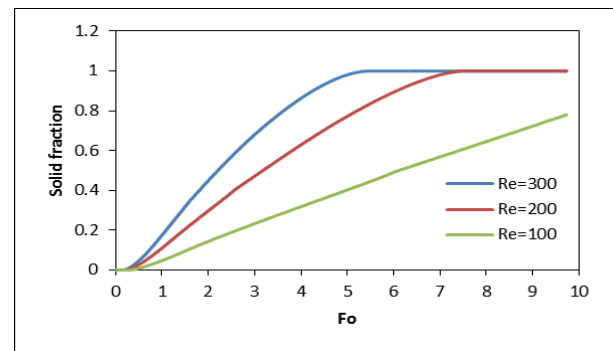


Fig.10 Effect of Reynolds number on the solid fraction.

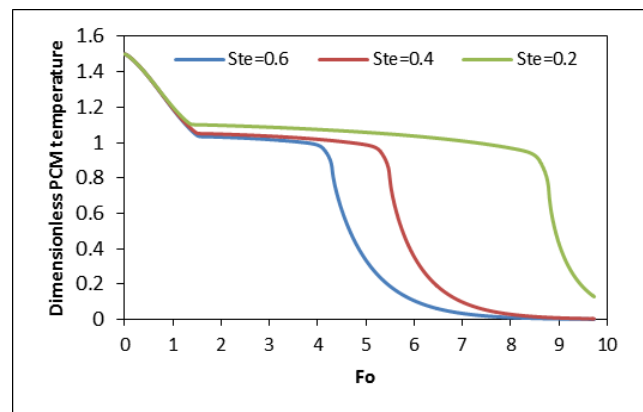


Fig.11 Effect of Stefan number on the dimensionless PCM temperature.

Fig. 12 shows the effect of Stefan number on the dimensionless solid front in 3-D. As can be seen that, the advancement of the solid front can be accelerated by increasing the Stefan number. Higher Stefan number reflects the decreased HTF inlet temperature, hence, the heat transfer rate increases with the increase of Stefan number.

Fig.13 represents the calculated cumulative cool energy storage, as a function of dimensionless time for different values of aspect ratio with the same mass of PCM inside the container and constant hydraulic diameter (D_h) of HTF channel. It can be seen from the figure that as the aspect ratio decreases (therefore both channel perimeter and channel cross-sectional area decreases and vice versa, also width of the container decreases while its height is increased) the instantaneous cool energy storage slightly decreases too. This due to the reduced surface area for the heat transfer, and this causes the slow heat recovery process.

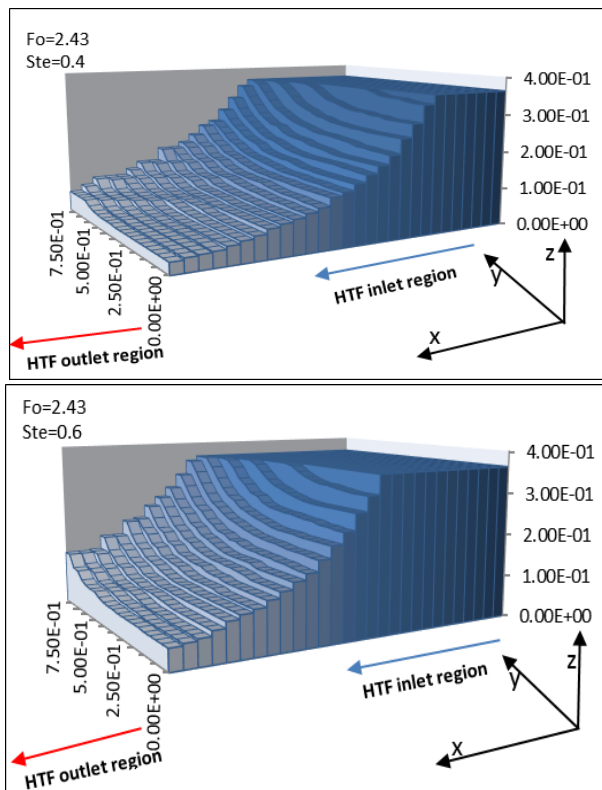


Fig.12 Effect of Stefan number on the solid front in 3-D.

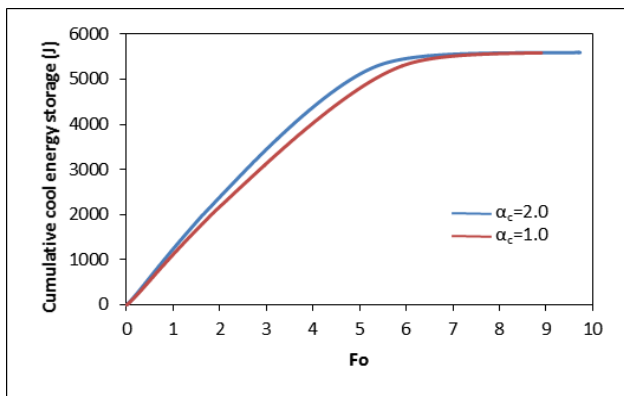


Fig.13 Effect of aspect ratio on the cumulative cool energy storage.

Fig.14 shows the effect of dimensionless container height of the PCM on the solid fraction. It can be seen that the solid fraction can be significantly increased if dimensionless

container height of the PCM is decreased, because decrement of the container height means decrement of system volume and so, volume of the PCM.

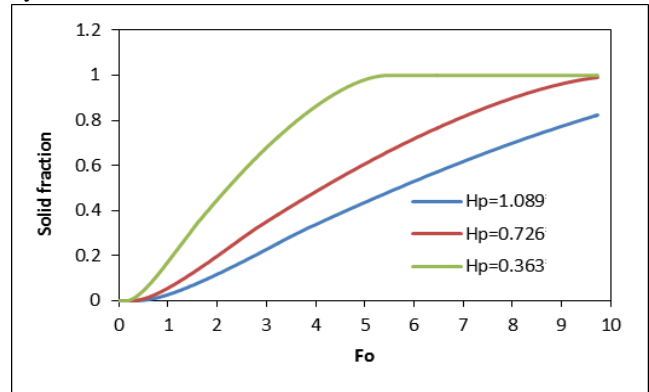


Fig.14 Effect of container height on the solid fraction.

5. Conclusions

A theoretical three-dimensional model based on the effective heat capacity formulation, for solving phase change problem in the PCM, and explicit finite volume method is used to predict the performance of the CTES system.

According to the results obtained in this work, the following main conclusions can be specified:

1. Reynolds number plays a significant role on the heat transfer and hydrodynamics characteristics. Where the time required for completion of charging process decreases with increase in Re number.
2. The time required for completion of charging increases with decrease in the Ste number. The Ste number is mainly related to storage capacity.
3. As the aspect ratio decreased, the charging time increased.
4. The solidification process can be accelerated but with lower storage capacity for the unit at lower container height.
5. Cold storage with PCM could be a very useful component of ventilation system in buildings since it uses cold from the environment. But from the analysis it can be seen that such a system could be only an addition to the conventional cooling systems and not an individual part.

6. REFERENCES

[1] **Regin A. F., Solanki S.C. and Saini J.S.**, "Heat transfer characteristics of thermal energy storage system using PCM capsules: A review", *Renewable and Sustainable Energy Reviews*, Vol. 12, pp. 2438–2458, 2008.

[2] **Nasiru I. Ibrahim, Fahad A. Al-Sulaiman, Saidur Rahman, Bekir S. Yilbas, Ahmet Z. Sahin**, "Heat transfer enhancement of phase change materials for

- thermal energy storage applications: A critical review' *Renewable and Sustainable Energy Reviews* 74, pp.26–50, 2017.
- [3] P.Pradeep Castro, P.Karthick Selvam, C.Suthan 'Review On The Design Of Pcm Based Thermal Energy Storage Systems' *Imperial Journal of Interdisciplinary Research (IJIR)* Vol.2, Issue-2 , 2016
- [4] **Liu C. and Groulx D.**, "Thermal performance of phase change materials in a cylindrical latent heat energy storage system", *The Fourth Annual Mechanical Engineering Research Conference, Dalhousie University*, 2011.
- [5] **Zohoor H. and Moosavi Z. M.**, "Increase in solar thermal energy storage by using a hybrid energy storage system", *International Journal of Mathematical, Physical and Engineering Sciences* 4:1, 2010.
- [6] **Agyenim F., Hewitt N., Eames P. and Smyth M.**, "A review of materials, heat transfer and phase change problem formulation for latent heat thermal storage systems (LHTESS)", *Renewable and Sustainable Energy Reviews*, Vol. 14, pp. 615-628, 2010.
- [7] **Zhang Y. and Faghri A.**, "Heat transfer enhancement in latent heat thermal energy storage system by using an external finned tube", *Journal of Enhanced Heat Transfer*, Vol.3, No.2, pp.119-127, 1996.
- [8] **Fang G.Y. and Li H.**, "Study on dynamic charging performance of ice storage for stacked rectangular capsules", *International Journal on Architectural Science*, Vol. 2, No. 4, pp.135-142, 2002.
- [9] **Shatikian V.**, "Melting and solidification of a phase change material with internal fins", M. sc., Thesis, Ben-Gurion University of the Negev, Faculty of Engineering Sciences, Department of Mechanical Engineering, 2004.
- [10] **Bony J., Citherlet S.**, "Numerical model and experimental validation of heat storage with phase change materials", *Energy and Buildings*, Vol. 39, pp. 1065–1072, 2007.
- [11] **Rathod M. K. and Banerjee J.**, "Numerical investigation on latent heat storage unit of different configurations", *World Academy of Science, Engineering and Technology* pp.75, 2011.
- [12] **Takeda S., Nagano K., Mochida T. and Shimakura K.**, "Development of a ventilation system utilizing thermal energy storage for granules containing phase change material", *Solar Energy*, Vol. 77, pp. 329–338, 2004.
- [13] Xin Fang, Li-Wu Fan, Qing Ding, Xiao-Li Yao, Yu-Yue Wu Jian-Feng Hou, Xiao Wang, Zi-Tao Yu, Guan-Hua Cheng Ya-Cai Hu, "Thermal energy storage performance of paraffin-based composite phase change materials filled with hexagonal boron nitride nanosheets", *Energy Conversion and Management* Vol. 80, pp.103–109, 2014.
- [14] Ahmad Hasan , Khaled A. Al-Sallal, Hamza Alnoman, Yasir Rashid and Shaimaa Abdelbaqi, 'Effect of Phase Change Materials (PCMs) Integrated into a Concrete Block on Heat Gain Prevention in a Hot Climate', *Sustainability* Vol. 8, 1009, 2016.
- [15] **Chen C., Guo H., Liu Y., Yue H. and Wang C.**, "A new kind of phase change material (PCM) for energy-storing wallboard", *Energy and Buildings*, Vol. 40, pp. 882–890, 2008.
- [16] **Versteeg H. K. and Malalasekera W.**, "An introduction to computational fluid dynamics-the finite-volume method", Longman, 1995.
- [17] **Acar M. A.**, "Study of finned tube thermal energy storage systems", M. sc. Thesis, Mechanical Engineering Department, Graduate School of Natural and Applied Sciences of Dokuz Eylül University, 2003.
- [18] **Wisam Habas Khudheyer**, "Three-dimensional numerical simulation of heat transfer and slip-flow in microchannel heat sinks", M. sc. Thesis, Mechanical engineering Department, College of Engineering, Basrah University, 2010.
- [19] **Mohammed Hussein Hadi**, "Enhancement of heat transfer in PCM storage systems", M. sc. Thesis, Mechanical engineering Department, College of Engineering, Basrah University, 2010.
- [20] **Incropera R.P., Dewitt D.P.**, "Fundamentals of heat and mass transfer", 2nd Edition, John Wiley & Sons, 1985.

NOMENCLATURE

English Symbols

| | |
|-----------|--|
| A_{sec} | Flow area, $w_c h_c$, (m^2) |
| c | Heat capacity, ρc_p ($J/m^3.K$) |
| c_p | Specific heat ($J/kg.K$) |
| D_h | Hydraulic diameter, $4 A_{sec} / Per$ (m) |
| e | Energy stored (J) |
| h_{fg} | Latent heat of solidification for the PCM (J/kg) |
| h | System height (m) |
| h_c | Channel height (m) |
| h_p | PCM container height (m) |
| h_f | Local Heat transfer coefficient of HTF ($W/m^2.K$) |
| k | Thermal conductivity ($W/m.K$) |
| l | Channel length (m) |
| m | Mass (kg) |
| p | Pressure (N/m^2) |
| Per | Channel Perimeter, $2(w_c + h_c)$ (m) |
| P_{in} | Inlet Pressure (N/m^2) |
| q'' | Heat flux (W/m^2) |
| q_s'' | Heat flux at the solid-fluid interface (W/m^2) |
| T | Temperature (K) |
| t | Time (s) |
| u | Velocity in x-direction (m/s) |
| v_N | Node Volume (m^3) |
| v | Velocity in y-direction (m/s) |
| w | Velocity in z-direction (m/s) |
| w_c | Channel width (m) |
| w_p | PCM container width (m) |
| w_s | Solid width (m) |
| x, y, z | Cartesian coordinates (m) |
| C | Dimensionless heat capacity, c/c_{ps} |
| Fo | Fourier number, $\alpha_{ps} t / D_h^2$ |
| H | Dimensionless system height, h/D_h |
| H_c | Dimensionless channel height, h_c/D_h |
| H_p | Dimensionless PCM container height, h_p/D_h |
| K | Dimensionless thermal conductivity, k/k_{ps} |
| L | Dimensionless channel length, l/D_h |
| Nu | Local Nusselt number, $h_f D_h / k_f$ |
| P | Dimensionless pressure, $p / \rho_f u_{in}^2$ |
| Pe | Peclet number, $Re Pr$ |
| Pr | Prandtl number, $\mu_f c_{pf} / k_f$ |
| Q_s'' | Dimensionless heat flux at the solid-fluid interface, $q_s / (k_{ps} (T_{pm} - T_{in}))$ |
| Re | Reynolds number, $\rho_f u_{in} D_h / \mu_f$ |
| Ste | Stefan number, $c_{ps} (T_{pm} - T_{in}) / \rho_p h_{fg}$ |
| U | Dimensionless Velocity in x-direction, u/u_{in} |
| V | Dimensionless Velocity in y-direction, v/u_{in} |
| W | Dimensionless Velocity in z-direction, w/u_{in} |

| | |
|-----------|--|
| W_c | Dimensionless Channel width, w_c / D_h |
| W_p | Dimensionless PCM container width, w_p / D_h |
| W_s | Dimensionless Solid width, w_s / D_h |
| X, Y, Z | Dimensionless Cartesian coordinates, $(x, y, z) / D_h$ |

Greek symbols

| | |
|-------------------|---|
| μ | Dynamic viscosity ($N.s/m^2$) |
| ρ | Density (kg/m^3) |
| α | Thermal diffusivity, k/c (m^2/s) |
| α_c | Aspect ratio, W_c / H_c |
| α_r | Thermal diffusivity ratio, α_{ps} / α_f |
| ε | Convergence criterion |
| β | Solid fraction |
| $2\Delta T_p$ | Phase-change temperature range (K) |
| θ | Dimensionless temperature, $(T - T_{in}) / (T_{pm} - T_{in})$ |
| $2\Delta\theta_p$ | Dimensionless Phase-change temperature range, $2\Delta T_p / (T_{pm} - T_{in})$ |

Subscript

| | |
|--------------------|---|
| E, W, N, S, T, B | east, west, north, south, top and bottom neighboring control volume faces in the east, west, north, south |
| e, w, n, s, t, b | control volume faces in the east, west, north, south |
| P | Central node |
| b | bulk |
| f | Heat transfer fluid |
| ini | Initial condition |
| in | Inlet |
| p | Phase change material |
| ps | Solid phase of the Phase change material |
| pl | Liquid phase of the Phase change material |
| pm | Phase change point of the Phase change material |
| s | Solid |
| w | Channel surface |

Superscript

| | |
|-------|-------------------|
| n | Current time step |
| $n+1$ | Next time step |
| — | Average value |

Abbreviations

| | |
|-------|------------------------------------|
| CTES | Cool thermal energy storage |
| HTF | Heat transfer fluid |
| LHTES | Latent heat thermal energy storage |
| LHSU | Latent heat storage unit |
| LCTES | Latent cool thermal energy storage |
| PCM | Phase change material |
| PCMs | Phase change materials |

Design and Implementation of P&O and FLC Maximum Power Point Tracking Algorithms Based on PLC for a PV System

Ahmed Sadeq Hunaish & Dr. Jawad Radhi Mohmood

Basra Oil Company

Ministry of Oil

Basra, Iraq

alibadyahmed@yahoo.com

Department of Electrical Engineering

University of Basra

Basra, Iraq

alali.jhana@uobasrah.edu.iq

Abstract: In this paper, the maximum power point tracking techniques (P&O and FLC) are implemented by using Siemens PLC (SIMATIC S71215) to increase the energy generation efficiency of the photovoltaic energy. The maximum power point tracking system has been designed and experimentally implemented. The system consists of photovoltaic modules, boost converter, and DC load. The proposed maximum power point tracking techniques are Perturb and Observe (P&O) and fuzzy logic controller (FLC) have been realized and experimentally tested. The results show that these techniques tracked the MPP efficiently under rapidly irradiation change and suddenly load change as well as a sunny day (without clouds). Considering the daily collected power, the P&O technique is more efficient than FLC technique (the daily collected power by using P&O is 189.66W for 16.6Ω load and 190.76W for 25Ω load and by using FLC is 187.6W for 16.6Ω load and 184.24W for 25Ω load while the direct loading power is 113.04W for 16.6Ω and 69.421W for 25Ω resistive load).

Index Terms— Programmable logic controller (PLC); maximum power point tracking (MPPT); continuous current mode (CCM), irradiation level (G), perturb and observe (P&O), fuzzy logic controller (FLC).

I. INTRODUCTION

The electrical energy is the reason of economic growth and it is essential to the sustainability of the modern economy [1]. The future growth of the economy depends on the continuation of energy sources. These sources must be readily available, obtained, easily accessible, and Eco-friendly. In general, the surveys show that fossil-fuel energy sources are going into decay. Moreover, they are not environmental friendly due to greenhouse gas emissions and other pollutants. Nuclear energy has a great establishment cost along with a number of safety concerns. Also for people living in rural locations, the access to national grid is not always possible. In such areas, most of the times the nearest electric utility is far and the cost of accessing to the grid is very expensive.

For overcoming this dilemma an alternative energy sources should be adopted. The photovoltaic source is one of the most encouraging one because it is characterized by being free environmental friendly, do not need fuel, has no moving parts to wear out, can be integrated with other renewable energy sources and it is available almost everywhere.

PV power sources have low generation efficiency less than 17% [2] and the output power of the PV varies with the

weather conditions [3]. Moreover, the current-voltage characteristics are nonlinear and depend on the diversity of intensity of irradiation (G) and temperature (T) [4]. With this variation, there are several I-V curves, on these curves; there are unified points on the I-V curves which represent maximum power points (MPPs). In the maximum power point, the PV array operates with maximum efficiency and supplies the available maximum power to the load. The MPP is unknown but can be founded by calculation or by

some searching algorithms which vary the duty ratio of the switching device of DC/DC converter according to the PV voltage and current. Therefore Maximum Power Point Tracking (MPPT) techniques are required to force the PV array to operate at the MPP all the time.

In an endeavor to enhance productivity, research works are being done in maximum power point tracking (MPPT) and they are differing in the control technique, the type of controllers, and the kind of DC/DC converter used. Several techniques are adopted for maximum power point tracking search: fuzzy set theory has been implemented by using 16 bit single chip 80C196KI3 microcontroller [3], incremental conductance method has been implemented by using the PIC16F873 microcontroller [5], injecting a small signal sinusoidal perturbation into the switching frequency and comparing the ac component and the average value of the panel terminal voltage [6], an analytical model for the performance of PV modules to be used in distributed power generation [7], P&O and incremental conductance are implemented by using MATLAB simulation [8], P & O method are used to develop and verify in simulation for water pumping system [9], FLC algorithm for MPPT was implemented with the embedded microcontroller [10], P&O implementation technique on the basis of system stability [11], design and implementation of FLC with FPGA technology for MPPT [12], a P&O method MPPT charge controller are implemented to FPGA. [13], and Adaptive Neuro- Fuzzy “ANFIS” and fuzzy logic controller were implemented in the MATLAB/Simulink [14].

Many of the above MPPT techniques are implemented by using different types of microcontrollers, electronic circuits, simulation, or FPGA. In this paper, P&O and FLC techniques have been implemented using Programmable Logic controller (CPU 6ES7215-1AG31-0XB0).

II. PHOTOVOLTAIC ENERGY SYSTEM

The photovoltaic system consists of three main parts. The first is the energy capturing one represented by the photovoltaic panel. The second is the matching stage represented by the DC/DC power converter (boost converter). The third is the controller which is responsible to match the load with the energy source through the DC/DC converter switching. Fig.1 demonstrates the block diagram of the solar energy system adopted in this paper. In this system, the energy source is 240 W PV panel (2 modules type PS P644120 each one is 120W) and Table I shows the PV panel parameters. The control functions have been assigned to Siemens PLC (6ES7215-1AG31-0XB0).

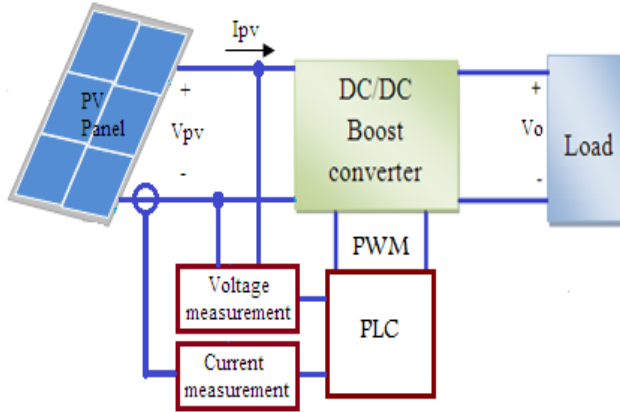


Fig.1 The block diagram of a standalone PV system

Fig.2 shows the basic electric circuit components of the boost converter. The selection of inductor (L) affects the operation mode of the boost converter. Small value of (L) causes discontinues current mode (DCCM) of operation while large value of (L) ensure continuous current mode of operation (CCM). The critical value of the inductor that maintains continuous mode can be defined as [15]:

$$L_{crt} = \frac{R \times D \times (1 - D)^2}{2f_s} \quad (1)$$

Where, L_{crt} is the critical value of the inductor, f_s is the switching frequency (Hz), D is the duty ratio, and R is the load resistance (Ω).

The voltage gain is defined as [15]:

$$\frac{V_o}{V_{in}} = \frac{1}{1 - D} \quad (2)$$

From Eq.2, duty ratio (D) is:

$$D = 1 - \frac{V_o}{V_{in}} \quad (3)$$

TABLE I
Electrical characteristics of PS P644120 PV module ($G=1000\text{W/m}^2$ and $T=25^\circ\text{C}$).

| | |
|-------------------------------------|---------------------------|
| Maximum Power (P_{max}) | 120W \pm 3% |
| Voltage at P_{max} (V_{max}) | 22.5V |
| Current at P_{max} (I_{max}) | 5.34A |
| Open circuit voltage (V_{oc}) | 28.1V |
| Short circuit current (I_{sc}) | 5.72A |
| Temperature coefficient of I_{sc} | 0.055 %/ $^\circ\text{C}$ |
| Temperature coefficient of V_{oc} | 0.33V%/ $^\circ\text{C}$ |

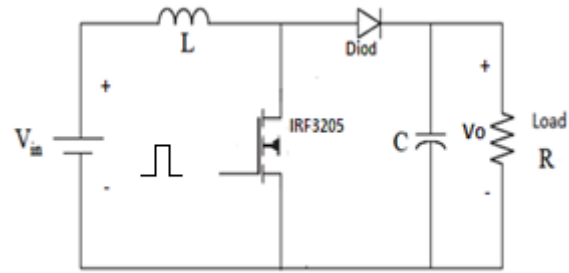


Fig.2 Power circuit of the boost converter

For the system under consideration, the used frequency (f_s) is 20 kHz, the load resistance is 25 Ω , and the maximum expected duty ratio is 0.6. According to these data and Eq.1, the critical value of the inductor is:

$L_{crt} = 0.06$ mH. To insure continuous current mode operation, $L = 1.2$ mH

While Capacitor value affects the ripple of the output voltage (V_o), to maintain an acceptable ripple value (ΔV), approximate expression for the required capacitance can be defined as [15]:

$$C_{min} = \frac{V_o \times D}{f_s \times \Delta V_o \times R} \quad (4)$$

Where, C_{min} is the minimum value of the capacitor.

To achieve the acceptable output voltage ripple, C has been selected to be 8 times C_{min} and this equals to 2200 μF .

III. IMAXIMUM POWER POINT TRACKING METHODS

As the irradiation and temperature vary along the day and seasonally (or monthly), PV maximum power (P_{max}) varies during changes in these conditions, so the maximum power point (P_{max}) must continuously be tracked. To achieve this target two of tracking techniques have been developed and they were:

- Perturb and Observe (P&O)
- Fuzzy Logic Control (FLC)

A. Perturb and Observe

In P&O method, the MPPT algorithm is based on the calculation of the PV output power and the power change by sampling both the PV current and voltage. The tracker operates by periodically incrementing or decrementing the solar array voltage. As shown in Fig.3, if a given

perturbation leads to an increase or decrease in the output power of the PV, then the subsequent perturbation is generated in the same direction. So, the duty cycle of the DC chopper is changed and the process is repeated until the maximum power point being reached [15].

The problem of oscillation about the maximum power point is a major issue. If ΔV has low value, the MPPT is slower, but it has small oscillations around the MPP [16]. ΔV is function of ΔD ; therefore also the perturb ΔD play significant role in power oscillation reduction and must be selected carefully to increase the MPPT efficiency. ΔD has been experimentally selected through using trial and error method.

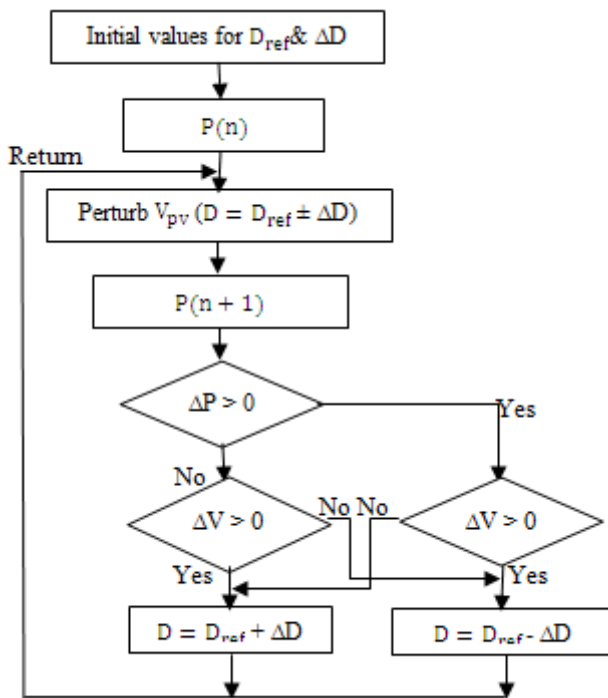


Fig. 3 The P&O flow chart [8]. Where $\Delta P = (P(n) - P(n-1))$ and $P(n)$, $P(n-1)$, $P(n+1)$ are the PV output power at the instants n , $n-1$, $n+1$ respectively, D_{ref} is the reference duty ratio; ΔD is the incremental duty ratio

The system behavior has been experimentally tested for three values of incremental duty ratio (ΔD) as shown in Fig.4. Fig.4 (a) states that for, $\Delta D=0.035$, the power oscillates between 184.2W and 189W with 0.685sec startup time, Fig.4 (b) shows that, for $\Delta D=0.03$, the power oscillation is between 185.4W and 189W with 0.935sec startup time, while Fig.4 (c) shows that, for $\Delta D=0.02$, the power oscillates between 196.3W and 198.1W with 2.3sec startup time. These results emphases that the decreasing in the incremental duty ratio leads to an increase in the startup time (decrease the dynamic efficiency) and decrease the power oscillation (increase the static efficiency).

B. The Proposed FLC Technique

The output power of the PV panel is function of the PV voltage (V_{pv}) and current (I_{pv}) as following:

$$P_{pv} = V_{pv} \times I_{pv} \quad (5)$$

The maximum power harvesting is achieved when [17]:

$$\frac{dP_{pv}}{dV_{pv}} = V \frac{dI_{pv}}{dV_{pv}} + I_{pv} = 0 \quad (6)$$

In this research work ($\frac{dP_{pv}}{dV_{pv}} = V \frac{dI_{pv}}{dV_{pv}} + I_{pv} = 0$) has been used as an error ($e(n)$) and its change ($\Delta e(n)$) is:

$$\Delta e(n) = e(n) - e(n-1) \quad (7)$$

The proposed FLC structure adopted here is two inputs and one output Mamdani FLC. In this system the first input is the error (Eq.6) and the second is the change in error (Eq.7).

Fig.5 represents the used FLC structure. The two inputs have the same triangle membership functions (N, Z, and P) as shown in Fig.6, while the output membership functions (NB, NS, Z, PS, and PB) are single tone as illustrated in Fig.7. Table II states the proposed rules.

With this FLC, there are three parameters (K_1 , K_2 , and K_3) affect on the system output response. These are the scaling factors of the error, change in error and the change in the duty ratio (ΔD) respectively. These parameters are experimentally adjusted by using trial and error method to get good performance.

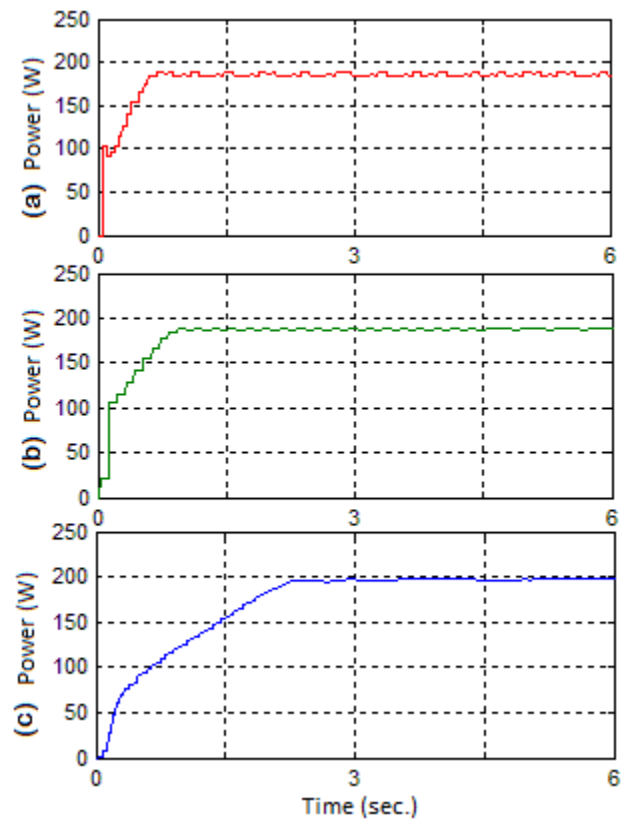


Fig.4 incremental duty ratio (ΔD) effect on the PV power response under P&O technique, (a) $\Delta D=0.035$, (b) $\Delta D=0.03$ and (c) $\Delta D=0.02$

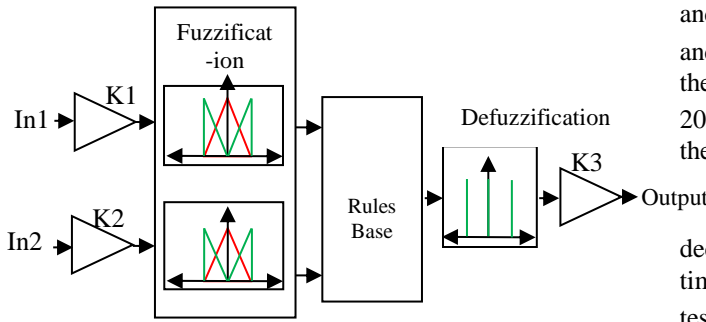


Fig. 5 FLC structure

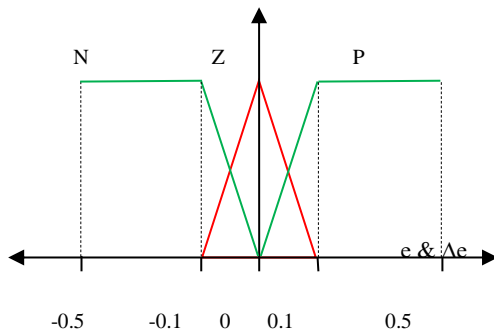


Fig. 6 Membership function for the inputs

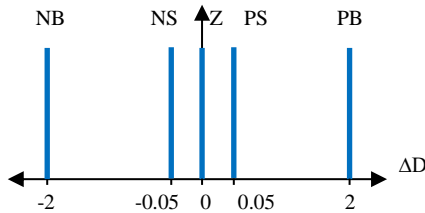


Fig.7 Output membership function of the FLC

TABLE II
Rules of the duty change ΔD

| | | | |
|----------------|----|----|----|
| Δe \ e | N | Z | P |
| N | Z | PS | PB |
| Z | NS | Z | PS |
| P | NB | NS | Z |

Fig.8 and Fig.9 show the effect of these parameters on the system performance.

In Fig.8 K_3 has been kept constant ($K_3=0.05$) whereas K_1 and K_2 are varied with sampling time $T_s=50\text{msec}$. From this figure, for $K_1 = K_2 = 3.7$, the startup time is 0.24sec and the generated PV power swing between 162W and 202.6W. When $K_1 = K_2 = 3.5$, the startup time is 0.36sec and the generated PV power swing between 181.5W and 203W, while for $K_1 = K_2 = 3$, the startup time is 1.6sec and the generated PV power swing between 201.7W and 203.6W.

In Fig.9, K_1 and K_2 has been kept constant ($K_1=K_2=3$) while K_3 has been changed with sampling time $T_s=50\text{msec}$.

From this figure, for $K_3=0.06$, the startup time is 0.38sec and the generated PV power oscillation is between 189W and 206.7W. At $K_3 = 0.07$, the startup time is 1.42sec and the generated PV power is oscillated from 179 W to 201.5W, while for $K_3 = 0.05$ the startup time is 1.6sec and the generated PV power swing between 201.7W and W.

From the obtained test results, it is clear that the decreasing in K_1, K_2 and K_3 leads to increase the startup time and decrease the power oscillation. According to this test, the selected values were $K_1 = K_2 = 3$ and $K_3 = 0.05$ with sampling time $T_s = 50\text{msec}$.

The P&O and FLC maximum power point searching techniques are implemented by using PLC (6ES7215-1AG31-0XB0) and tested on the system. When the system startup, the duty ratio (D) is set to initial value and applied to MOSFET gate. The new value of D is determined by the control program FLC where PV voltage and current (V_{pv} and I_{pv}) are measured with sample time 50msec.

For P&O method tests, $\Delta D = 0.02$ has been selected to satisfy low power oscillation, under this value, the system exposes good responses under sunny day, load change, and rapid change in the irradiation as shown in the following Fig. 12, 14, and 16.

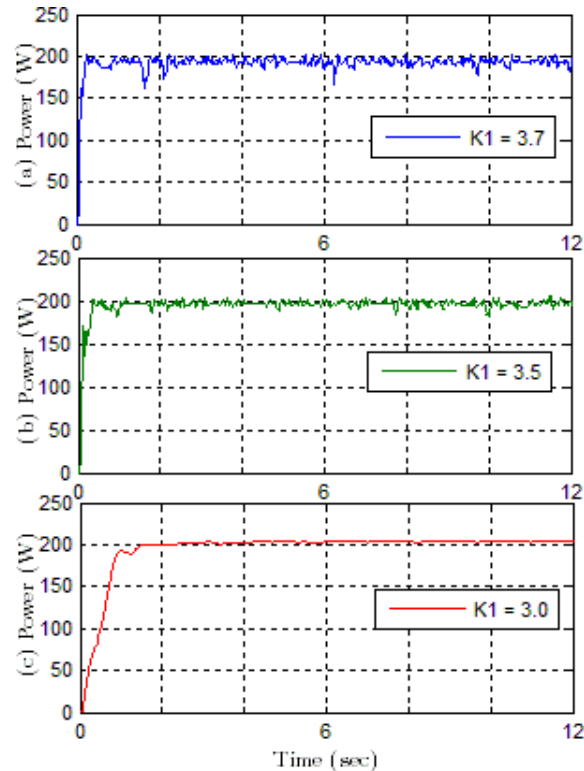


Fig.8 K_1 and K_2 (where $K_1 = K_2$) effect on the MPPT under FLC method with $K_3 = 0.05$

IV. EXPERIMENTAL RESULTS

Fig.10 (a) gives the PV panel output power during a sunny day on 28th of June under P&O technique at 12.10 PM. The measured irradiation density was approximately

1050 W/m². 25Ω load has been used in this test. Fig.10 (b, c) show the generated voltage and current by the PV panel for the same conditions. From Fig.10 (a), the measured startup time was 2.1sec.

Fig.11 states the startup response with 25Ω load under FLC on the 28th at 12.15 PM. Fig.11 (a) shows the delivered power from the PV panel where the measured irradiation was approximately 1065 W/m². The measured startup time is 0.972sec. Fig.11 (b, c) illustrate the voltage and current responses for the same load.

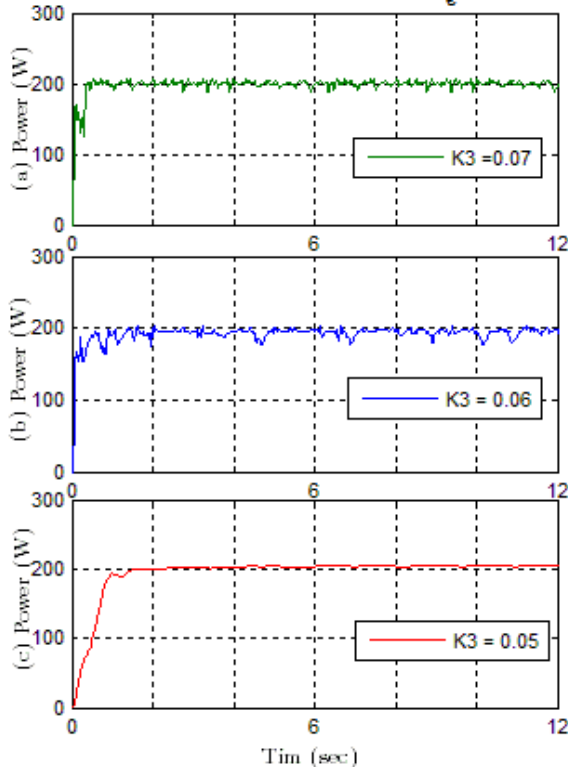


Fig.9 K₃ effect on the MPPT under FLC method for constant K₁ and K₂ (K₁=K₂=3)

For the developed FLC tests, the selected parameters were: K₁=K₂=3, and K₃=0.05 as stated in Fig. 8 and 9.

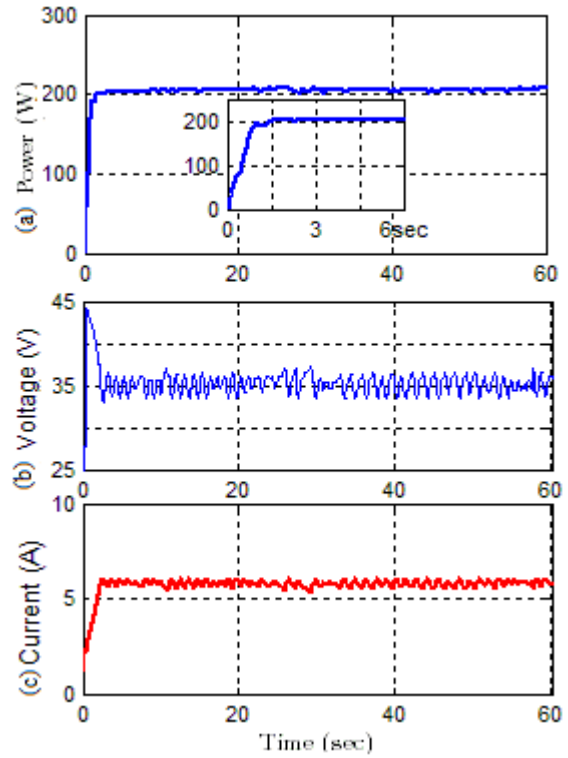


Fig.10 Startup response of P&O method: (a) power curve, (b) voltage & current curves on

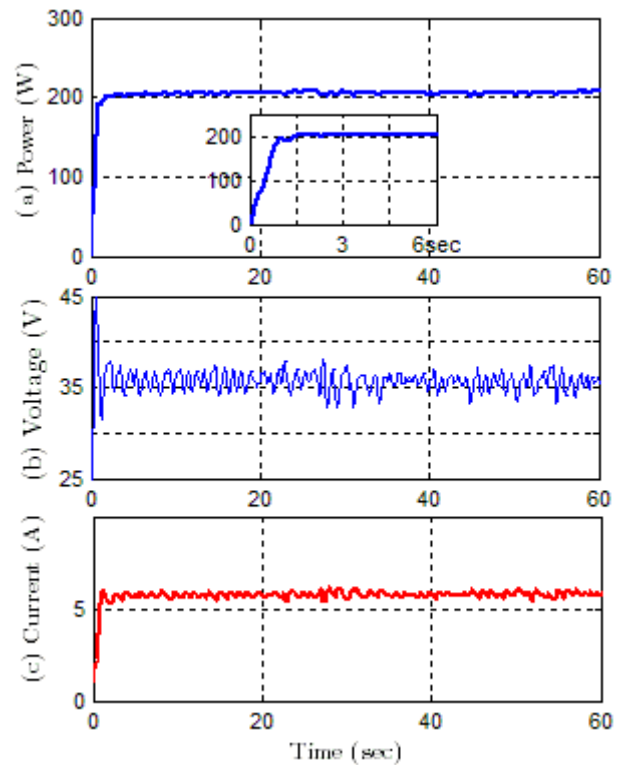


Fig.11 Startup response of FLC method: (a) power curve, (b) voltage & current curves on

From Fig. 10 and Fig. 11, one can note that the startup time of the output power of the photovoltaic panel by using FLC technique (0.972 sec.) is better than that of the P&O technique (2.1 sec.), while the ripple in the output power curve of the photovoltaic panel by using P&O technique (at the worst case is 2.6 W) technique is better than that of the FLC technique (at the worst case is 2.9 W) and this mean

the introduced output average power by using P&O technique is more than that of the FLC technique.

As shown in Fig.12, the system had been tested under P&O technique with load step change (suddenly change) from 25Ω to 16.6Ω to 25Ω on the 1st of July at 12.00 PM. Fig.12 (a) shows the generated power from the PV panel where the measured irradiation was approximately 1035 W/m². The system can quickly get the previous power point approximately with time about 0.55 sec and 0.86sec for the two load changes. Fig.12 (b) gives the voltage and current responses for the same load step change.

Fig.13 states the system behavior under FLC with step load change from 25Ω to 16.6Ω to 25Ω. In Fig.13 the first sudden load change is from 25Ω to 16.6Ω and the second is from 16.6Ω to 25Ω, the system gets the previous power point approximately during 2.9sec for the first case and 2.01sec for the second one. Fig.13 (b) shows the voltage and current responses for the two cases.

Fig.14 (a) shows the delivered power from the PV panel under P&O. For the rapid irradiation change the system can get the new power point during a period equals approximately to 8.25sec for the sudden irradiation change from 910 W/m² to 595W/m², and 9sec for the rapid irradiation change from 595W/m² to 910W/m². Fig.14 (b) gives the voltage and current curves for the same irradiation levels.

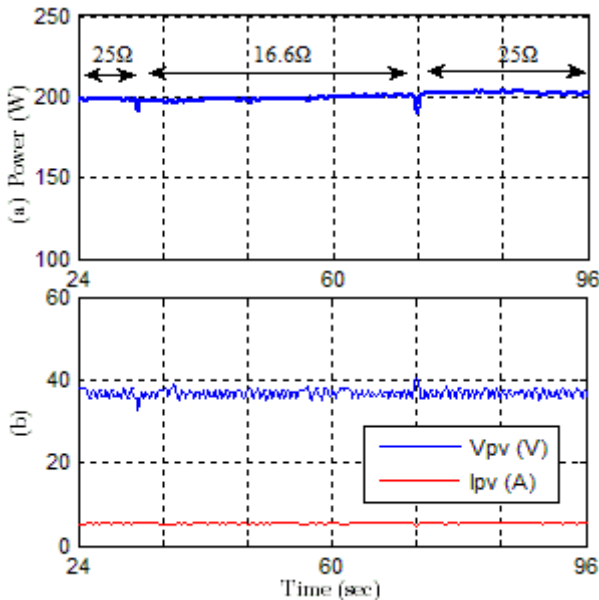


Fig.12 Load change response of P&O: (a) power curve, (b) voltage & current curves on

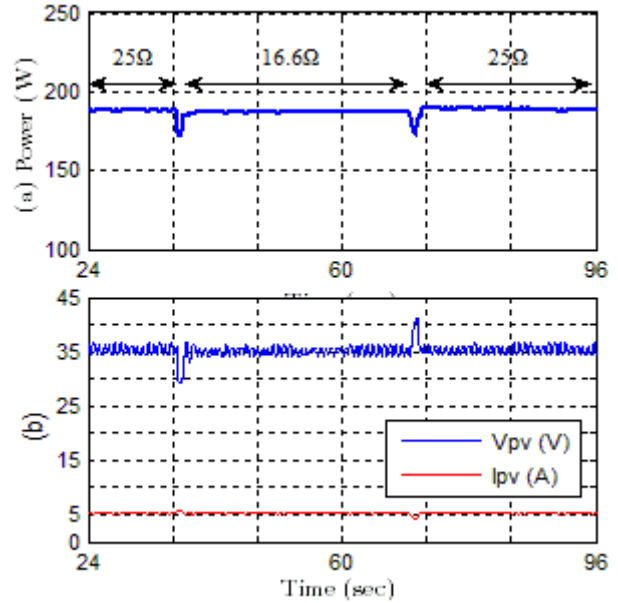


Fig.13 Load change response of FLC method: (a) power curve, (b) voltage & current curves

Fig.15 (a) shows the PV output power response when the irradiation has been changed rapidly. The irradiation has been changed at the first case from 863 W/m² to 557W/m² and at the second from 557W/m² to 863 W/m² as shown in Fig.15(a). The test has been done on the 19th of July at 2.20 PM. Fig.15 (b) represents the generated PV voltage and current curves of the PV panel for the same irradiation levels.

V. THE MPPT TECHNIQUES EFFICIENCY

From the obtained results, the MPPT methods maintain the operating point at the maximum power point for different ambient conditions as possible. To state the effect of the MPPT, the harvested power has been measured with and without these techniques, the power measures have been took each hour over one day (from 8AM to 5PM) and then determine the average power for one day for each case as tabulated in tables III and IV and, also sketched as shown in Fig. 16 and 17.

The daily collected power (average) techniques efficiency (%η) is equal to the difference between the collected power by using MPPT technique and the collected power without using MPPT technique divided by the collected power without using MPPT technique during one day (Eq.8 as listed in Table III and IV.

$$\% \eta = \frac{P_{MPPT} - P_d}{P_d} * 100\% \quad (8)$$

Where, P_{MPPT} the collected power by using MPPT technique during one day and P_d is the collected power without using MPPT technique during one day.

From tables III and IV the collected power during one day (from 8AM to 5 PM) are:

1. With P&O, the collected power equal 189.66W for 16.6 Ω and 190.76W for 25Ω.
2. With FLC, the collected power equal 187.6W for 16.6 Ω and 184.24W for 25Ω.

3. Without any maximum power point tracking technique (direct loaded), the collected power is 113.04W for 16.6 Ω and 69.421W for 25 Ω.

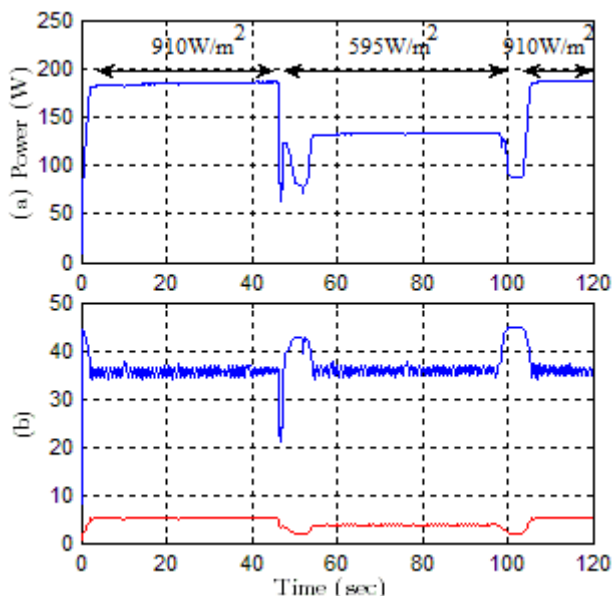


Fig.14 Radiation change response of P&O method: (a) power curve, (b) voltage & current curves for three levels

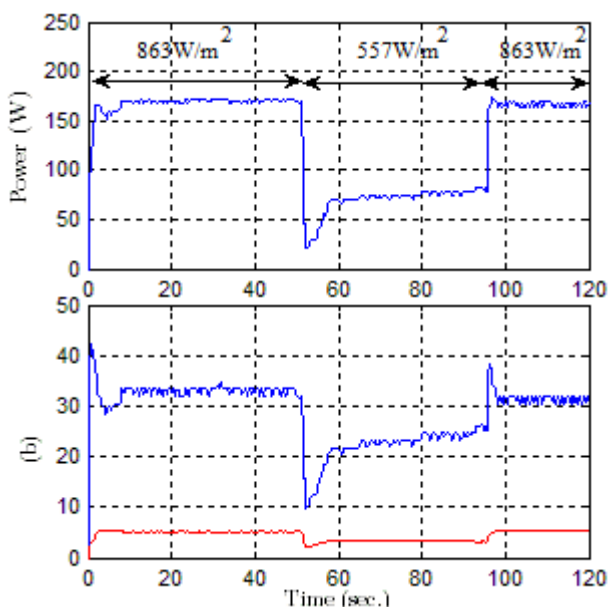


Fig.15 Radiation change response of FLC method: (a) power curve, (b) voltage & current curves for three levels

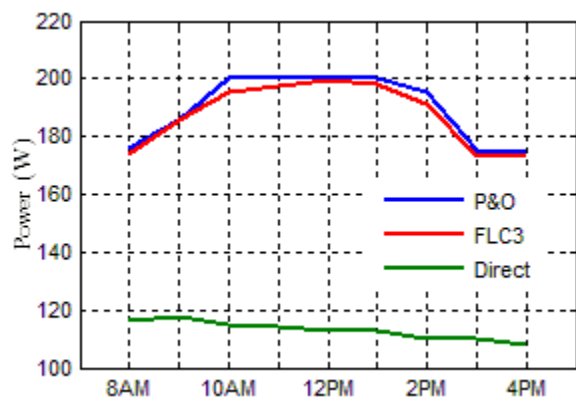


Fig.16 Daily power by using P&O, FLC, and direct loading methods with 16.6Ω

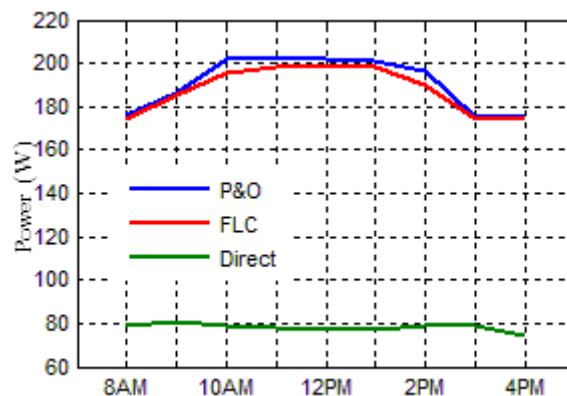


Fig.17 Daily power by using P&O, FLC, and direct loading methods with 25Ω

Table III
Daily collected power by using resistive load 16.6Ω

| | Power (W) | | |
|---------|-----------|-------|--------|
| | P&O | FLC | Direct |
| Average | 189.66 | 187.6 | 113.04 |

Table IV
Daily collected power by using resistive load 25Ω

| | Power (W) | | |
|---------|-----------|--------|--------|
| | P&O | FLC | Direct |
| Average | 190.76 | 184.24 | 69.421 |

From above, daily collected power techniques of P&O method increased the daily collected power by 67.8% and 174.78% over that of the direct loading for 16.6Ω and 25Ω resistive load respectively, while FLC method will have a daily power about 65.96% and 165.4% more than that of the direct loading for 16.6Ω and 25Ω resistive load respectively.

From the previous results, these maximum power point tracking techniques efficiently increase the daily collected power (the power harvested by the PV panel during one day) as compared to the direct connected load to the PV panel; also the daily collected power under P&O technique is more efficient than that of FLC technique.

VI. CONCLUSION

In this paper, two MPPT techniques have been implemented by using programmable logic controller. In MPPT tests, P&O, and FLC are selected to be implemented by using PLC because of their effectiveness in extracting maximum power.

The experimental test results show that the two approaches improve the energy harvesting efficiency but the P&O better than FLC. In this context, the P&O technique shows better efficiency than that of the FLC one but the startup time of P&O is greater than that of FLC. From the point of view of memory occupation and execution time, P&O takes low execution time and occupies low memory as compared to the FLC based approach.



REFERENCES

- [1] S.Gomathy, S.Saravanan, and S. Thangavel, "Design and Implementation of Maximum Power Point Tracking (MPPT) Algorithm for a Standalone PV System", vol. 3, pp. 1-7, 2012.
- [2] R. Roshan, Y. Yadav, Umashankar S, Vijayakumar D, and Kothari D , "Modeling and Simulation of Incremental Conductance MPPT Algorithm Based Solar Photo Voltaic System using CUK Converter," in Nagercoil, India, 2013 Energy Efficient Technologies for Sustainability, International Conf. pp. 584-589.
- [3] Ch. Won, D. Kim, S. Kim, W. Kim, and H. Kim," A New Maximum Power Point Tracker of Photovoltaic Arrays Using Fuzzy Controller," in Taiwan, 1994 IEEE Power Electronics Specialists Conf., pp. 396-403.
- [4] S. Jain and V. Agarwal, "A New Algorithm for Rapid Tracking of Approximate Maximum Power Point in Photovoltaic Systems," IEEE Power Electronic Letters, vol. 2, no. 1, pp. 16-19, 2004.
- [5] Th. Nguyen," Solar Panel Maximum Power Point Tracker", Ph.D. dissertation, Dept. of Computer Science & Elect. Eng, University of Queensland., 2001.
- [6] K. Tse, M. Ho, S. Chung and S. Y., "A Novel Maximum Power Point Tracker for PV Panels Using Switching Frequency Modulation", IEEE Trans. Power Electronics, vol. 17, no. 6, pp 980-989, 2002.
- [7] E. Ortiz-Rivera and F. Peng, "Analytical model for a photovoltaic module using the electrical characteristics provided by the manufacturer data sheet," 2005, 36th IEEE Power Electronics Specialists Conf., pp.2087-2091.
- [8] A. Oi," Design and Simulation of Photovoltaic Water Pumping System", M. Sc dissertation, California Polytechnic State University, 2005.
- [9] A. Durgadevi, S. Arulselvi and S. Natarajan," Study and Implementation of Maximum Power Point Tracking (MPPT) Algorithm for Photovoltaic Systems", in CA, USA, Electrical Energy Systems (ICEES), 2011 1st International Conf., pp. 240-245.
- [10] Md. Hossain, Sh. Khan, Md. Shafiulla and M. Hossain, "Design and Implementation of MPPT Controlled Grid Connected Photovoltaic System," In Malaysia, 2011 IEEE Computers & Informatics (ISCI), IEEE Symposium, pp. 284-289.
- [11] M. Elgendy, B. Zahawi and D. Atkinson, "Assessment of Perturb and Observe MPPT Algorithm Implementation Techniques for PV Pumping Applications," IEEE Trans. Sustainable Energy, vol. 3, no. 1, pp. 21-33, Jan. 2012.
- [12] B. Hamed and M. El-Moghany, " Fuzzy Controller Design Using FPGA for Photovoltaic Maximum Power Point Tracking," (IJARAI) International Journal of Advanced Research in Artificial Intelligence, vol. 1, no. 3, pp. 14-21, 2012.
- [13] T. Saini, D. Raveendhra, and P. Thakur, "Stability Analysis of FPGA Based Perturb and Observe Method MPPT Charge Controller for Solar PV System," in india, 2013, Engineering and Systems (SCES), Students Conf., pp 1-5.
- [14] B. Tarek, D. said and M. Benbouzid, "Maximum Power Point Tracking Control for Photovoltaic System Using Adaptive Neuro-Fuzzy," in Monaco, 2013, IEEE, Ecological Vehicles and Renewable Energies, 2013 8th International Conf. and Exhibition , pp. 1-7.
- [15] S. Kolsi, H. Samet, and M. Amar, "Design Analysis of DC-DC Converter Connected to a Photovoltaic Generator and Controlled by MPPT for Optimal Energy Transfer throughout a Clear Day," Journal of Power and Energy Engineering, vol. 2, pp. 27-34, 2014.
- [16] G. Azevedo, MC. Cavalcanti, K. Oliveira, F. A. Neves, Z. Lins, "Evaluation of maximum power point tracking methods for grid connected photovoltaic systems," in Greece, 2008, IEEE Power Electronics Specialists Conf. pp. 1456-1462.
- [17] G. Hsieh, H. Hsieh, C. Tsai, and C. Wang "Photovoltaic Power-Increment-Aided Incremental-Conductance MPPT With Two-Phased Tracking" IEEE Transactions on Power Electronics, vol. 28, no. 6, pp. 2895 – 2911, 2013.



CFD Investigation of Turbulent Mixed Convection Heat Transfer in a Tringular Cavity

Saadoon F. Dakhil₁

Falah A. Assi₂

Rasha N. laubi₃

1,3 Basra Technical Engineering Colege.Southern Technical College.

2 Basra Engineering College.Basra University.

Abstract- Mixed convection in a triangular enclosures having an adiabatic rotational solid cylinder inserted at the center of cavity has been studied numerically. Three-dimensional steady-state continuity, momentum and energy equations along with the boussinesq approximation were solved by finite volume method with a commercial available software ANSYS FLUENT 15. The bottom wall of the enclosure was supplied with constant heat flux \dot{q} , while the left and right inclined walls of the cavity were exposed to environmental temperature T_{∞} . The governing equations subject to suitable boundary conditions and standard $k-\omega$ turbulent model were examined with the PRSITO scheme. Results present both streamlines, temperature distribution counter and Nusselt numbers at constant $Ra = 2 \times 10^9$, for the variant parameters such cylinder rotation $\omega = (26.18, 52.36 \text{ and } 62.83)$ rad/s clockwise and cavity inclination angle $\phi = (0, 30, 60 \text{ and } 90)$ degree at the same direction. The results show that both flow field and temperature distributions are high affected by combined both cylinder rotation and inclination angle. So high rate of convection heat transfer was indicated at lower angular velocity. Symmetric heat transfer at horizontal base was indicated, while the inclination angle high effected on the heat transfer from the inclined two walls.

keyword: turbulent flow, natural convection, inclination angle, equilateral triangle, finite volume.

1. General introduction

Mixed convection in closed enclosures has been widely studied both experimentally and numerically due to the great scientific interest in many responses to energy-related applications. Heat transfer through attics of building, thermal insulation of building, solar collectors, nuclear reactors, furnaces and fire control in buildings, refrigeration in electronic components. Fluids, such as air, in the absence of external forces like fans or exterior wind, move due to density variations in their bulk. A. Rincón et al showed new correlations for laminar and turbulent regimes in enclosures with natural convection of $10^3 \leq Ra \leq 5 \times 10^{11}$ and an aspect ratio of $0.5 \leq H/L \leq 2$. These correlations are oriented to build enclosures and implemented in thermal building simulation programs [1]. Mixed convection was analyzed at closed cavity with computational fluid dynamics field by Seyed [2]. He examined test cases were of tall cavities with different angles of inclination whose two opposite long sides are differentially heated. Also he used the turbulence diffusivity to denote the mixing of momentum, mass and thermal energy by the turbulence eddies. The inclined cavity with angle of 5 degrees between its tall walls and the horizontal, so that the upper wall is hot and lower wall is cold ($Ra = 4.16 \times 10^8$).

Ercan Erturkthe[3] studied incompressible 2-D driven cavity flow at high Reynolds numbers numerically. It was conducted at high Reynolds numbers, when the incompressible driven cavity flow is

considered as two-dimensional and also steady state, then the considered flow is a fictitious flow. Mathematically, it is always possible to obtain a steady solution of a fictitious flow at the limiting case when Re goes to infinity. The flow behavior and heat transfer in closed cavity with different shapes are discussed by many researchers [4-6] were investigated. Natural convection inside a two-dimensional rectangular cavity with a triangular roof having an adiabatic solid strip inserted at a middle of the cavity

is studied numerically using a finite volume method. The Computational Fluid dynamics (CFD) solution commercial package ANSYS FLUENT 14.0 is used for the numerical simulation purpose. Anderson et-al[7] performed experimentally and theoretically study on natural convection heat transfer in an isosceles triangular enclosure with Gr range of 10^7 to 10^9 . They proved that at higher temperature gradients and higher degree of turbulence heat transfer, and also the buoyancy gradients were higher. Baïri[8] presented experiment and theoretical study of natural convection in tilted square cavity with different value of Ra and angle of inclination (α) of the cavity. Thier result showed that for small or moderate inclination angles ($0 \leq \alpha \leq 45$) at increase of Ra produces an increase of the maximum flow velocity. At angle of inclination goes up to 60 degree the influent of Ra starts to be perceptible. Dipak Sen et-al [9] worked numerically to compute laminar natural convection in a right-angled triangular cavity

filled with air. The side wall is considered as hot wall compare to the bottom wall while the hypotenuse of the triangular enclosure was kept thermally insulated. They examined that the vortex flow of the fluid is cumulative with higher Rayleigh number which indicates the rate of heat transfer is enhancing between hot wall and fluid with increasing Ra.

Yingchun [10] studied theoretically heat transfer in air cavities using four eddy viscosity turbulence models. 2-D closed cavities with differentially heated walls opposite each other and other one 3-D open ended tall cavity with one side is heated and adiabatic for all the others were investigated. The CFD simulation results for the two 2D cases were compared with their corresponding experimental measurements and it was found that the k omega turbulence model offered the best solution among the turbulence models tested. Natural convection laminar flow in a square cavity when two adjacent walls of the enclosure are insulated and the other two were kept at different temperatures, had been investigated numerically by Aminossadati and Ghasemi[11]. They examined a two-dimensional and square enclosure the various angles of inclination. At low Ra, both the flow field and Nusselt number did not show significant changes with the inclination angle. The result showed that as the inclination angle has risen, the average temperature in the enclosure started to increase until it reached its maximum and then decreased. However, on the present work the problem of turbulent natural convection heat transfers in equilateral triangular enclosure with an adiabatic cylinder was examined. Also the flow and heat convection is studied. conducted at high Reynolds numbers, when the incompressible driven cavity flow is

considered as two-dimensional and also steady state, then the considered flow is a fictitious flow. Mathematically, it is always possible to obtain a steady solution of a fictitious flow at the limiting case when Re goes to infinity.

and it was found that the k omega turbulence model offered the best solution among the turbulence models tested. Natural convection laminar flow in a square cavity when two adjacent walls of the enclosure are insulated and the other two were kept at different temperatures.

2-Problem definition and governing equations

In the present study, model consists of 3-D triangular enclosure having a solid cylinder (D=5cm) located in center of this enclosure. Bottom wall length equal (30cm) while the high is(22.5cm) for three different situations of the enclosure (horizontal $\phi=0$, titled with $\phi=30$ and $\phi=60$ vertical situations $\phi=90$).The two inclined wall are exposed to environmental temperature while the cavity's base was kept at constant heat flux(\dot{q})and both the other side walls of cavity and the cylinder were kept at adiabatic boundary condition. There are some assumptions was taken into account during this study as follows: -

i-Boussinesq approximation has been employed where all physical properties of the fluid are constant except the density in the buoyancy term depends on temperature.

ii-The fluid is Newtonian (i.e. exhibits a linear relationship between the shear stress and the velocity gradient) and that there is no internal heat source.

iii-The flow is steady, turbulent and three-dimensional flows inside the cavity and radiation is neglected.

3-Governing equation

The mass, momentum and energy conservation equations solved during the simulation for turbulent natural convection inside the domain can be written as[12]:-

Continuity

$$\frac{\partial(\rho u_i)}{\partial x_i} = 0 \quad \dots\dots(1)$$

For Momentum,

$$\frac{\partial(\rho u_j u_i)}{\partial x_j} = -\frac{\partial P}{\partial x_i} + \frac{\partial}{\partial x_j} \left(\mu \left[\frac{\partial u_i}{\partial x_j} + \frac{\partial u_j}{\partial x_i} \right] - \overline{\rho u_i u_j} \right) + B_{Ti} \quad \dots\dots(2)$$

B_{Ti} is the buoyancy term = $g_i(\rho - \rho_o)$

$$(\rho - \rho_o) \approx -\rho_o g_i \beta (T - T_o) \quad \dots\dots(3)$$

for incompressible flows is expressed by

$$\frac{\partial(\rho u_j T)}{\partial x_j} = \frac{\partial}{\partial x_j} \left[\frac{\mu}{Pr} \frac{\partial T}{\partial x_j} - \overline{\rho u_j T} \right] \quad \dots\dots(4)$$

$$Ra = \frac{g \beta q'' H^4}{k \nu \alpha} \quad \dots\dots(5)$$

4-Boundary condition.

The simulation domain for the cavity with boundary condition are showed in Fig.(1) Bottom wall of the domain is supplied with constant heat flux boundary condition ,the two inclined walls are exposed to T_∞ convection boundary condition and the rest left and right walls are thermally insulated. The solid cylinder which construct at the center of enclosure is also considered adiabatic wall .near horizontal and

inclined walls for velocity components, no slip boundary condition is applied as follow :-

1. no slip condition is applied at all enclosure boundary, i.e., $u=v=w=0$
2. the base of cavity at $x=0-30, z=0-75$ and $y=0$ is supplied with uniform heat flux $\dot{q}=\text{constant}$
3. the two inclined walls are exposed to environmental temperature where convection = conduction
4. the left and right cross face of cavity as well as the solid cylinder are considered adiabatic, i.e.,

$$\frac{dT}{dz} = 0 \text{ for left and right walls}$$

$$\frac{dT}{dr} = 0 \text{ for solid cylinder}$$

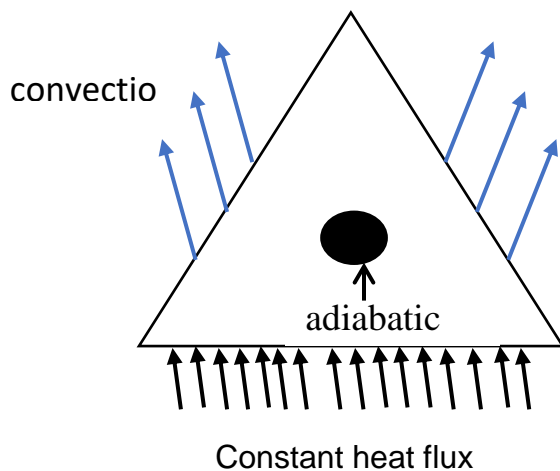


Fig. 1 Schematic diagram of Computation Triangular cavity boundary conditions

5-Numerical method .

To solve and analyze problems that involve fluid flows and heat transfer numerically the commercial software package ANSYS15 is used. Model includes the control volume generation to discussed the governing equations

with the specified boundary conditions. After the domain has been divided into discrete control volumes forming a computational grid or mesh, the governing equations are integrated over the individual control volumes forming surface integrals using Gauss' divergence theorem. The COUPLED algorithm has been employed to achieved the coupling between pressure and velocity with the PRESTO scheme for the pressure correction equation and the cell-face values of pressure could be obtained from simple arithmetic averaging of centroid values. The advantages of the PRESTO scheme for pressure interpolation are available for all meshes in FLUENT. Under relaxation factors of 0.3 for pressure, 0.8 for momentum and 1.0 for energy were used for convergence of all the considered variables. Tetrahedral elements were used for the entire computational domain. The diffusion terms are discretized by the second order differencing scheme and convective term is discretized with the second order upwind scheme. The solution convergence criteria were set to 10^{-6} for both continuity, Naive stock equations and 10^{-8} for energy

6-Results & Discussion.

In this section it will discuss the variation of the temperature distribution and streamlines contours in the cavity by varying the inclination angle and cylinder rotation. The effect of tilted angle in mixed turbulent convection heat transfer in the equilateral triangular enclosure filled with air has been investigated. Results

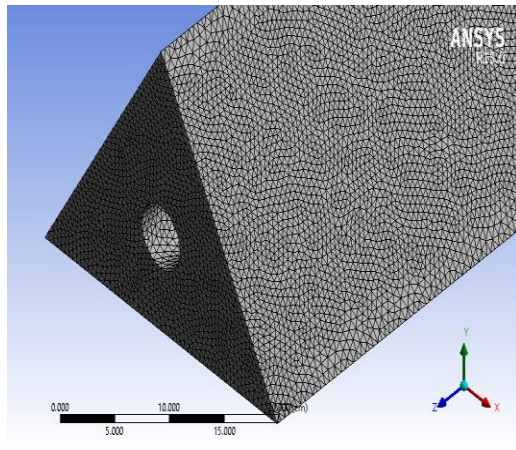


Fig. 2 Three dimensional triangular cavity meshing

were performed for $\phi=30^\circ$, 60° , 90° and the horizontal one, while the angular velocity ranging from 26.83 to 62.83 rad/s. This study can be divided into two separate parts. The first part is discussing the effect of different inclination angle while the second part discuss the effect of increasing angular velocity .

Fig 3. Shows the temperature contours for $Ra=2*10^9$, $\omega=52.36$ rad/s clockwise direction and $\phi = (0^\circ, 30^\circ, 60^\circ$ and $90^\circ)$ respectively It is observed from this figure that at zero inclination angle the thermal boundary layer in left side was more expanded than the right side this behavior due to rotating direction which in clockwise , however, at this rang of Rayleigh number and for tilted situation with $\phi = 30$ and 60 , it is observed from temperature contours that the growth of thermal boundary was approximate equally over entire cavity. That means equivalent two effects which are gravity effect and rotating effect so that the thermal boundary layer will be equal ,but with

more turbulent occur at $\phi = 60$.the last case is with $\phi = 90^\circ$ where uniform temperature distribution occur at vertical situation and thermal boundary layer concentrated near the hot wall.,.

Fig 4.Presents the streamlines at $Ra=2*10^9$, $\omega=52.36$ rad/s and various inclination angle. From this figure, For zero inclination angle $\phi=0^\circ$ there are distinguishing profile where a small vortex is formed above the solid cylinder of the cavity and located at mid-way from two inclined cold surface and large vortex occupied most lower space from cavity . At $\phi = 30$ and 60 it can be see that the vortex flow of the fluid is cumulative at the left side of cavity . The vortex formation along the cavity is maximized and extrude above and down bottom of cylinder at vertical situation with $\phi = 90^\circ$

Fig 5. show the effect of angular velocity with constant angle at $\phi = 0^\circ$ and 90° respectively. It can be observed that the curves of Nu_{local} decreases from the edge toward the midpoint to its minimum value at $x=15$ cm than increased at the same range from midpoint toward the other edge to its maximum value as showed in figure 5 for upper part. The different between this two curves was occur at mid plan. It is interestingly noticed that at zero inclination all velocity curves have the similar profile while at vertical situation $\phi = 90^\circ$ local Nu at high angular velocity take opposite profile compare with that at $\phi = 0^\circ$

Fig 6. Shows the Local Nu along X axis near the base plane, the effect of inclination angle at constant $\omega=52.36$ rad/s and various inclination angle, $\phi = 0^\circ$ and 30° as with performance explain above for first part from figure 5 where local Nusselt decrease to minimum value at middle -X plane the increase at terminate edge. The other two case for the same ω are with $\phi = 60^\circ$ and 90° have a special behavior where at $\phi = 60^\circ$ the curve of local Nusselt number start from a specified value which less than the starting value for other case than increasing to maximum peak at approximate $x=12$ cm and complete with decreasing to its minimum just before the terminate edge usually at $X=20$ cm. The last case from figure 6 is with $\phi = 90^\circ$ at this inclination angle the Nusselt Number curve take opposite form with compare to $\phi = 0^\circ$ or 30° because the position of solid cylinder relative to vertical hot wall give the minimum temperate gradient between hot and cold walls which cause the maximum Na_{local}

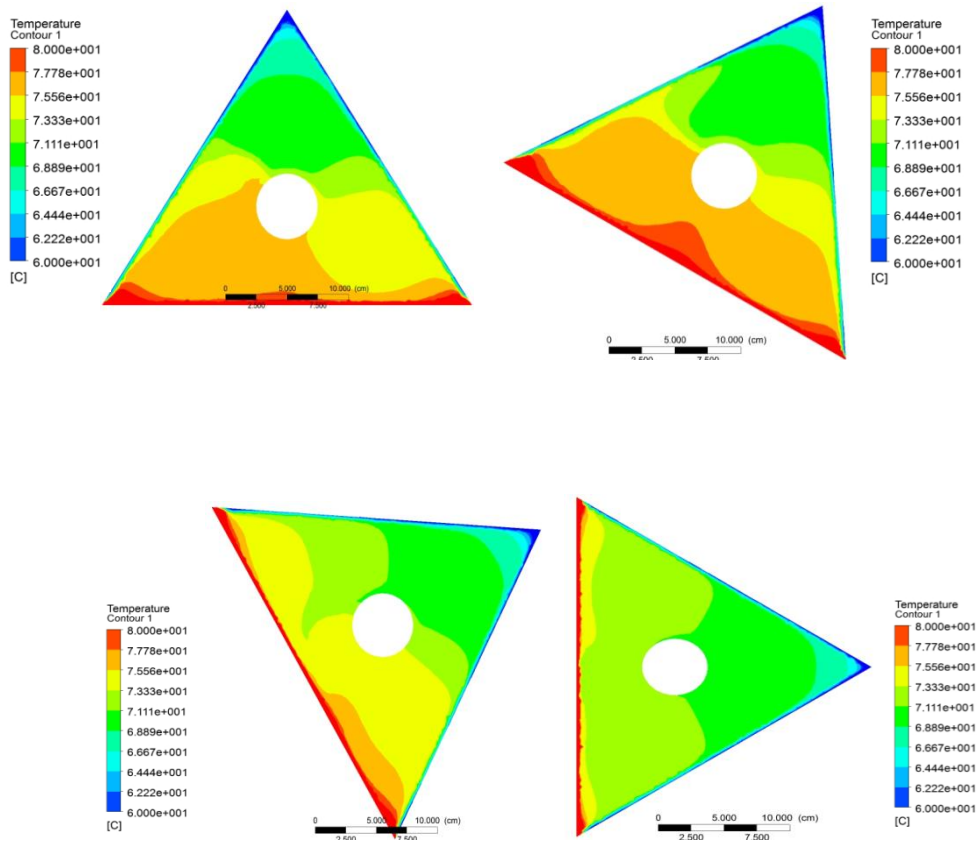


Fig. 3 Temperature counter for $Ra=2*10^{10}$, $\omega=52.36$ rad/s and inclined angle $\phi= (0^\circ,30^\circ,60^\circ$ and $90^\circ)$ restrictively

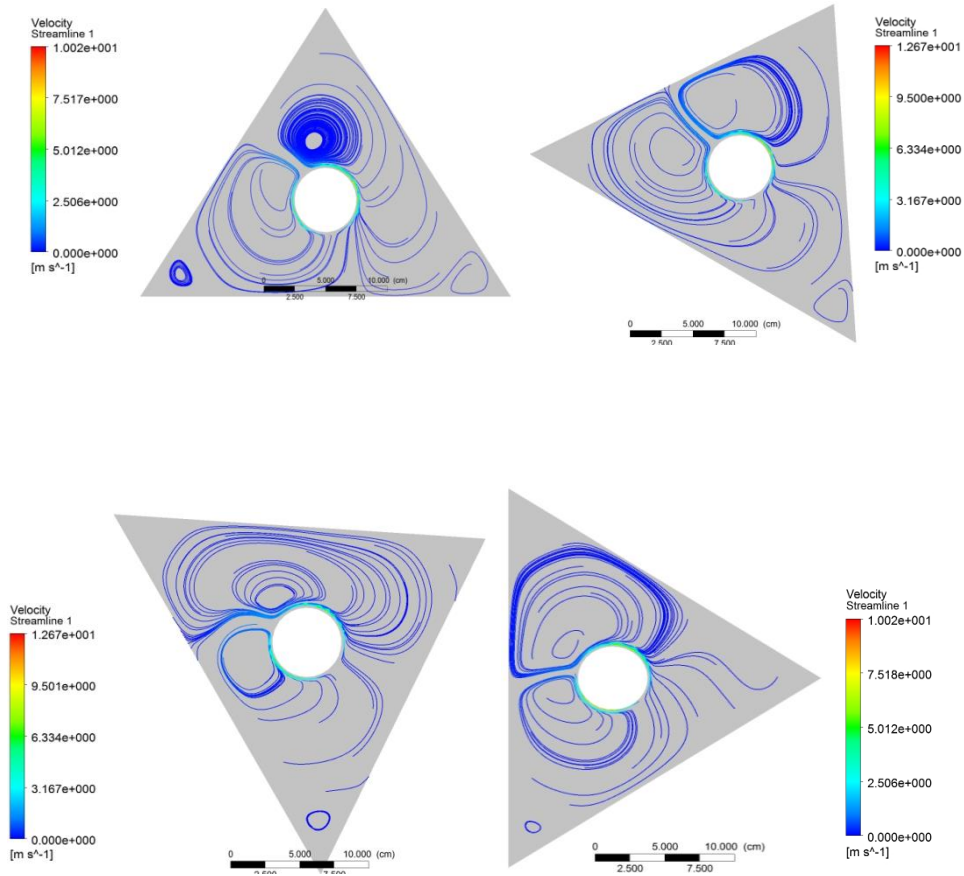


Fig. 4 Velocity Streamline counter for $Ra=2*10^{10}$, $\omega=52.36$ rad/s and $\phi= (0^\circ, 30^\circ, 60^\circ$ and $90^\circ)$ restrictively

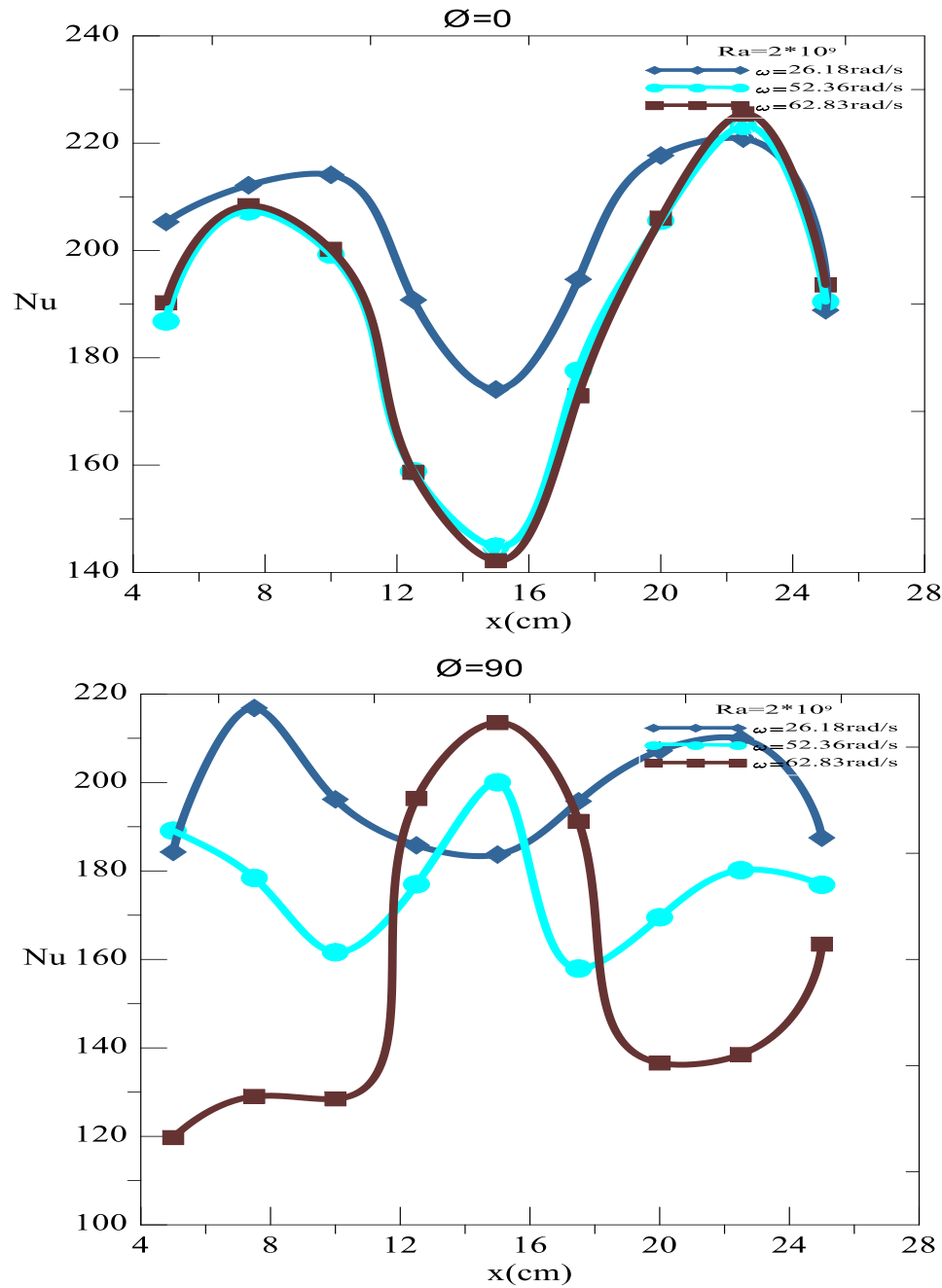


Fig 5. local Nu along bottom wall at $Ra=2 \times 10^{10}$, with different ω rad/s and two inclined angle $\phi=0^\circ$ and $\phi=90^\circ$ respectively

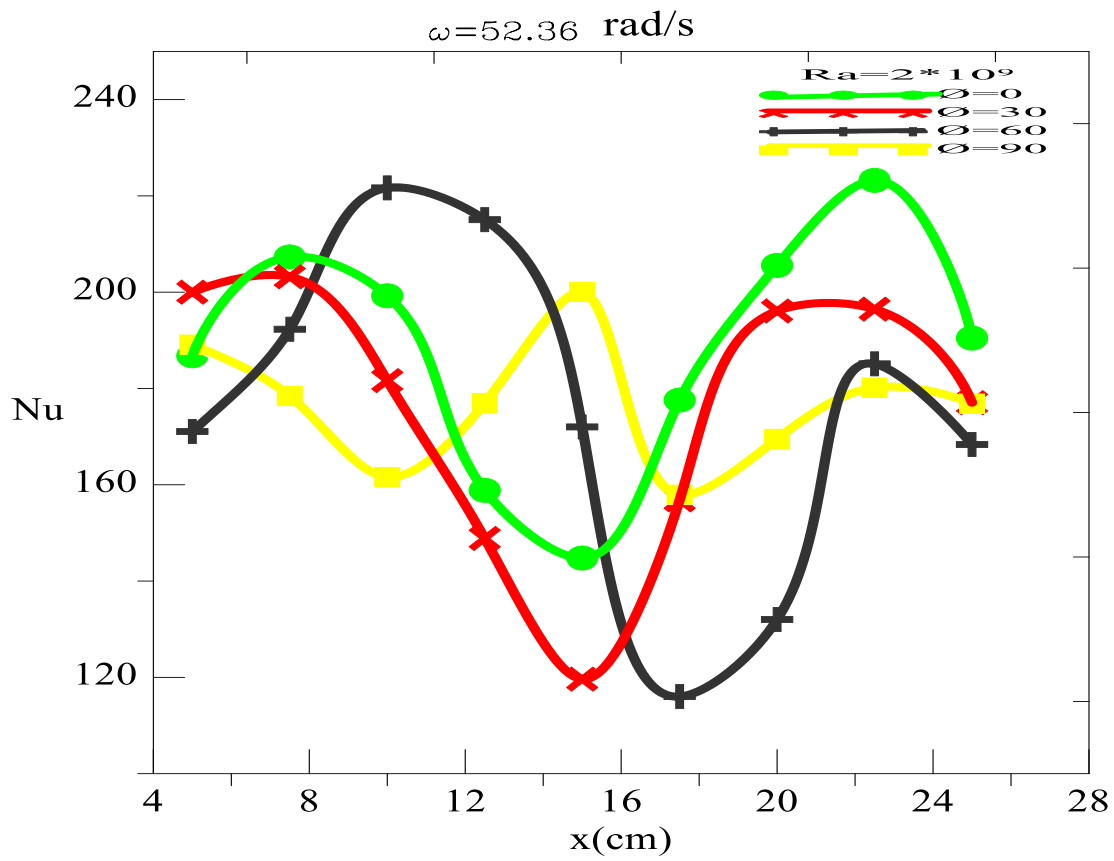


Fig 6. Local Nu along bottom wall at $Ra=2*10^{10}$, $\omega=52.36 \text{ rad/s}$ for inclined angle $\phi= (0^\circ ,30^\circ,60^\circ \text{ and } 90^\circ)$



7-Conclutions:

A numerical study has been carried out for a modified triangular enclosure with rotary solid cylinder at the center observe the influence of the inclined angle and cylinder rotation on the turbulent air flow and heat transfer. Some of the important outcomes of the present investigation are as follows:

Based on the data from the simulations, the following conclusions were obtained;

- 1) It found that the local Nusselt number for horizontal and vertical cavity take a opposite form at all local point
- 2) The thermal boundary layer is thinner than the velocity boundary layer (Figures 5 and 6). This means, fluid temperature within the enclosure increases, not by flowing from isothermal wall into the bulk of the air, but by natural turbulent transport mechanism. Hence, convective heat transfer is more significant than conduction and air flow in this enclosure .
- 3) Nusselt number enjoys maximum value under the two situations: $\phi = 60^\circ$ with low ω and at $\phi = 0^\circ$ with high ω while the minimum value for Nu occur at $\phi = 30^\circ$.

- 4) At zero inclination angle $\phi = 0^\circ$ and high angular velocity, high rate of heat transfer through the right wall than the left wall.

8-Refrences.

- 1- A. Rincón, F.J. Sánchez de , E. Chacón & J. Sánchez "New natural convection heat transfer correlations in enclosures for building performance" simulation Engineering Applications of Computational Fluid Mechanics, UK Limited, VOL. 11, NO. 1, 340–356, trading as Taylor & Francis, 21 Mar 2017.
- 2- Seyed A.Omranian" The Computation of Turbulent Natural Convection flows" PhD thesis ,Manchester, United Kingdom, 2011
- 3- Ercan Erturk " Discussions On Driven Cavity Flow" International Journal for Numerical Methods in Fluids ,Vol 60: pp 275-294
- 4- Ahmed K.Hussini, Sachindra K. R Rout, Farshid F , Ramesh C, Mohammed H." NATURAL CONVECTION IN A TRIANGULAR TOP WALL ENCLOSURE WITH A SOLID STRIP"ournal of Engineering Science and Technology
Vol. 10, No.10 (2015) 1326 – 1341, October 2015



- 5- Syeda H. Tasnim, Michael R. Collins"Suppressing natural convection in a differentially heated square cavity with an arc shaped baffle "International Communications in Heat and Mass Transfer 32 (2005) 94–106, Ontario, Canada
- 6- Md. Mustafizur Rahman, Md. Elias and M. A. Alim" MIXED CONVECTION FLOW IN A RECTANGULAR VENTILATED CAVITY WITH A HEAT CONDUCTING SQUARE CYLINDER AT THE CENTER"ARPJN Journal of Engineering and Applied Sciences. VOL. 4, NO. 5, JULY 2009
- 7- T.N. Anderson¹ , M. Duke and J.K. Carson" Experimental determination of natural convection heat transfer coefficients in an attic shaped enclosure"
- 8- A. Barri " Experimental and numerical investigation of natural convection in tilted square air filled enclosures." Energy Conversion and Management 49 (2008)771–782, September 2007
- 9- Manoj Kr. Triveni, Dipak Sen, RajSekhar Panua" NUMERICAL ANALYSIS OF NATURAL CONVECTION IN A RIGHTANGLED 10- TRIANGULAR ENCLOSURE" Frontiers in Heat and Mass Transfer (FHMT),
- 11- M.Aminossadati and B.Ghasemi" THE EFFECTS OF ORIENTATION OF AN INCLINED ENCLOSURE ON LAMINAR NATURAL CONVECTION"Heat and Technology Vol. 23, No. 2, 2005. Shahrekord, Iran
- 12- Thamer Khalif Salem"THE INFLUENCE OF INCLINATION ANGLE ON NATURAL CONVECTION IN A RECTANGULAR ENCLOSURE " Nutural and Applied Sciences,Academic Research InternationalVol 4,No.2, March 2013.
- 13- Shia-Hui Peng , Lars Davidson , Sture Holmberg "The Two-Equation Turbulence k- ω Model Applied to Recirculating Ventilation Flows" Msc Thesis , CHALMER UNIVERSITY OF TECHNOLOGY

List of symbols.

- K turbulent kinetic energy
- g Acceleration due to gravity, m/sec
- k Fluid thermal conductivity, W / m. °C
- L Characteristic length, m
- Nu Average Nusselt number
- g Acceleration due to gravity
- Gr Grashoffe number
- Pr Prandtl number



q'' Heat flux per unit area, W/m^2

Ra Rayleigh number

Ri Richardson number

T_c temperatures of the cold inclined wall

Greek Symbols

α, α^* model constants

β, β^* model constants

μ molecular viscosity

μ_t turbulent eddy viscosity

ν kinematic molecular viscosity

ν_t kinematic turbulent viscosity

ρ density of air

σ_k, σ_ω model constants

ω specific dissipation rate

Faults Investigation in Renewable Energy Sources Penetrated Distribution Feeders Based on the Theory of Wavelets and Artificial Intelligence

Sara J. Authafa & Khalid M. Abdul-Hassan

Power and Machines Dept. College of Engineering Basra, Iraq

saraauthafa7@gmail.com khmh7447@gmail.com

Abstract- In this paper, a protection scheme for distribution feeders having a number of renewable energy distributed generation is proposed. The scheme is based on utilizing the wavelet transform as a measurement signals features extraction tool in order to facilitate decision making in an accurate and fast manner. Two decision making systems have been introduced; the first is responsible for the detection and faults, the second is responsible for the classification of their types. The two schemes work together for the diagnosis of short circuit (shunt faults) which constitute the dominant type of faults in power systems. The switching transient events provided by some components in the distribution system such as the power factor correcting capacitor banks, the main feeder, laterals, or sections en route energization events can contaminate the measurement signals waveforms. This will affect successful faults diagnosis; therefore, such events has to be taken into account in order to for the protection scheme to work reliably and securely without the nuisance of false detections. Efforts has been made to reduce the protection scheme requirements and the response time without affecting the accuracy of fault detection and classification schemes predictions. All the simulations and signals analysis are performed through Matlab R2016b environment. The results are satisfactory in a way that the proposed scheme can be utilized as a part of digital relaying protection functionality dedicated for distribution systems having a number of distributed generation connected as main feeder source supportive supplements or in an islanded mode.

Index Terms—Distribution Feeders, Distributed Generation, DWT, Fuzzy, Fault classification, Fault detection, IEEE 123, Protection, Renewable Energy Resources, Wavelets.

I. INTRODUCTION

The newly growing publicity requirements of more as well as cleaner and self-sustaining types of electrical energy sources led to the introduction of new fields of research. Such fields rely on the utilization of solar, wind, bioenergy, tidal, geothermal energy sources instead of the old air pollutant ones that depend on fossil fuel combustion like oil, coal, and natural gas. The introduction of such fields impose new concerns about the effects of their penetration on the ancient electrical networks having their own designed protection schemes. Many research papers has been introduced regarding the involvement of the newly evolved computing and signal processing techniques in constructing the underlying schemes for power systems intelligent electronic devices functionalities. Protection techniques dedicated for conventional power systems can be studied for the applicability to the unconventional distributed generation (DG) penetrated systems. References [1,3]

introduce individual and combined detection and classification schemes for the traditional power systems. Reference [1] proposed a single phase to ground fault detection scheme based on the discrete wavelet transform (DWT) features extraction from current signals. Current signatures extraction with the help of DWT is also introduced in [2]; in which, a fuzzy inference system (FIS) is implemented as a decision maker to indicate fault types. A detection and classification of faults approach based on voltages and currents measurements as input quantities as well as neural networks as decision makers are introduced in [3]. The accuracy of the results for the last approach could be improved greatly if the wavelet transform is employed as a pre-processing tool before the application to the decision making system.

References [4]-[6] studied faults detection techniques regarding renewable energy sources penetrated power systems. Reference [4] introduces a continuous assessment, detection, and classification of faults protection scheme that has adaptability to the different operating conditions of the DGs connected in an islanded mode. A wavelet analysis has been introduced by [5] in order to detect islanding as well as faults disturbances in IEEE 14 bus distribution feeder. The results show the superiority of wavelet transform based techniques in detecting the disturbances over the old utilized techniques. A multi-agent, communication, automation, and control based protection scheme has been proposed in [6]. The scheme is based on exploiting the capability of information exchange between intelligent power system devices as well as the ability to analyze fault signatures for the purpose of faults classification and location. For the sake of faults features extraction, the wavelet transform has been also introduced for the analysis.

In this paper, a detection and classification of faults protection scheme for a distribution feeder having a number of connected DGs is introduced. Current signals measurements near the main substation of the main feeder are utilized and analyzed with the help of DWT to extract useful features. The features are then manipulated and fed to the decision making systems to indicate faults presence or absence and investigative their types. A trip signal is sent once a fault is detected to isolate power sources pending faulted feeder section repair.

II. WAVELET TRANSFORM

The wavelet transformation is a specific signal processing technique that evolved as an improvement of the previously

applied Fourier transformation tool. It utilizes certain functions of specific characteristics and shape called the wavelets to reveal aspects like sharp changes, trends, breakdown points that the sine wave which is the basis function of the Fourier transform cannot analyze accurately. The differences between the two transforms are shown in Fig. 1. Although the most recent developments of Fourier transform such as the short time Fourier transform (STFT) can be set to reveal such aspects; the fixed resolution related to this transform is regarded as a drawback. This is due to the affectedness of the accuracy of the signal analysis in the time and frequency domains by one another in such a way that good accuracy in time means poor frequency accuracy and vice versa. Wavelet transform has overcome this difficulty by introducing the multi resolution analysis (MRA); by which, the analyzed signal can be represented in both time and frequency with high accuracy. The MRA can be realized through a number of high and low pass filters specific to a certain wavelet function called as the mother wavelet. The discretized signal will enter such filters, convolved with their related transfer functions to get the wavelet coefficients, then downsampled by 2 to sustain fixed length signal representation at each stage of decomposition as shown in Fig. 2. Where, $f(n)$: is the discretized signal to be analyzed, $h(n)$, $g(n)$: represent the low and high pass filters transfer functions respectively. cA : Approximation coefficients, cD : Detail coefficients.

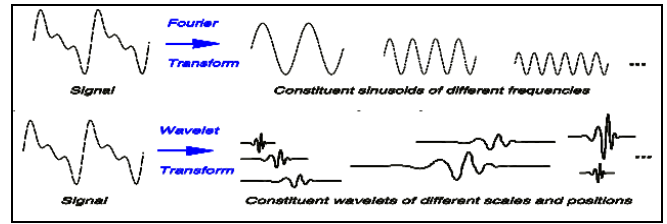


Fig. 1. The difference between Fourier and wavelet transform

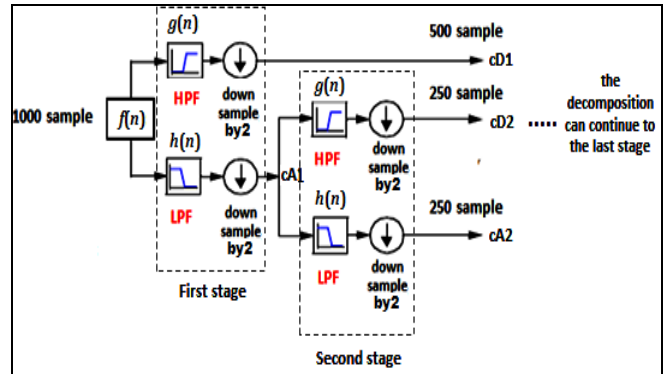


Fig. 2. The MRA on the input signal

Where, $f(n)$: the discretized signal to be analyzed, $h(n)$, $g(n)$: represents the low and high pass filters transfer functions respectively, cA : Approximation coefficients, cD : Detail coefficients.

The mathematical representation of the MRA processes is given in (1) and (2).

$$cA(n)^j = \sum_k A(n)^{j-1} h(2k - n) \quad (1)$$

$$cD(n)^j = \sum_k A(n)^{j-1} g(2k - n) \quad (2)$$

Where, cA^j : the approximation coefficients at the certain level j , $j \geq 1$. A^{j-1} is the approximation coefficients at a previous level. When $j=1$, this implies the first stage decomposition and that A^{j-1} is the original signal $f(n)$. cD^j : the detail coefficients at the level j .

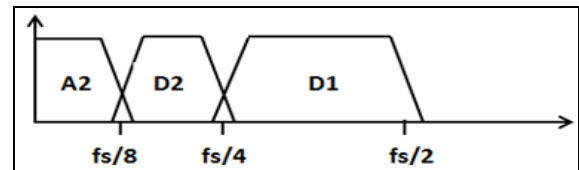


Fig. 3. Frequency band division by the DWT

Where, A_i : approximations, D_i : details, i : specific stage, f_s : the sampling frequency that satisfies Nyquist's sampling criteria.

III. SYSTEM MODEL

The MRA analysis will also act on the frequency spectrum of the analyzed signal; by which, the first stage of decomposition will divide the signal spectrum into two halves, low and high bands. The second stage will divide the low frequency divided bandwidth by the first stage into other two halves and so on as shown in Fig. 3. This form of analysis is called the discrete wavelet transform (DWT) which is different from another type of analysis called the wavelet packet transform (WPT) into which, the high frequency bands are also filtered through a set of low and high pass filters. Since the DWT is a powerful features extraction tool utilized widely in the field of digital protection relaying, it is chosen for the analysis. The advantages provided by such transform over the WPT is the less amount of decomposition stages provided that less down sampling and convolution processes are implemented on the analyzed signal. As a result, the DWT will be faster as compared with the WPT due to the less computational burden provided by the DWT related schemes which means faster detection and isolation of faults.

In order to simulate a reliable distribution feeder model with the ability to handle the idea of distributed generation, the IEEE 123 bus distribution feeder is chosen. This feeder has many specifications regarding the low voltage level distributed sources of energy, the presence of many switches that provide many paths of power flow, and having a number of the power factor improving capacitor banks to solve for the voltage drop problems in such feeder. The data required to build the system are provided in [7]-[8]. The current measurements required to analyze system conditions are taken only at the main supply point of the feeder near the main substation. All the signals analysis and the protection scheme construction and testing are performed through MATLAB R2016b environment. In which, the SimPowerSystems toolbox is used to build and simulate the model, the Wavelet toolbox is used to analyze signals, and the Fuzzy logic toolbox is used to build the fault type indicating FIS. The distribution feeder system topology is shown in in Fig. 4.

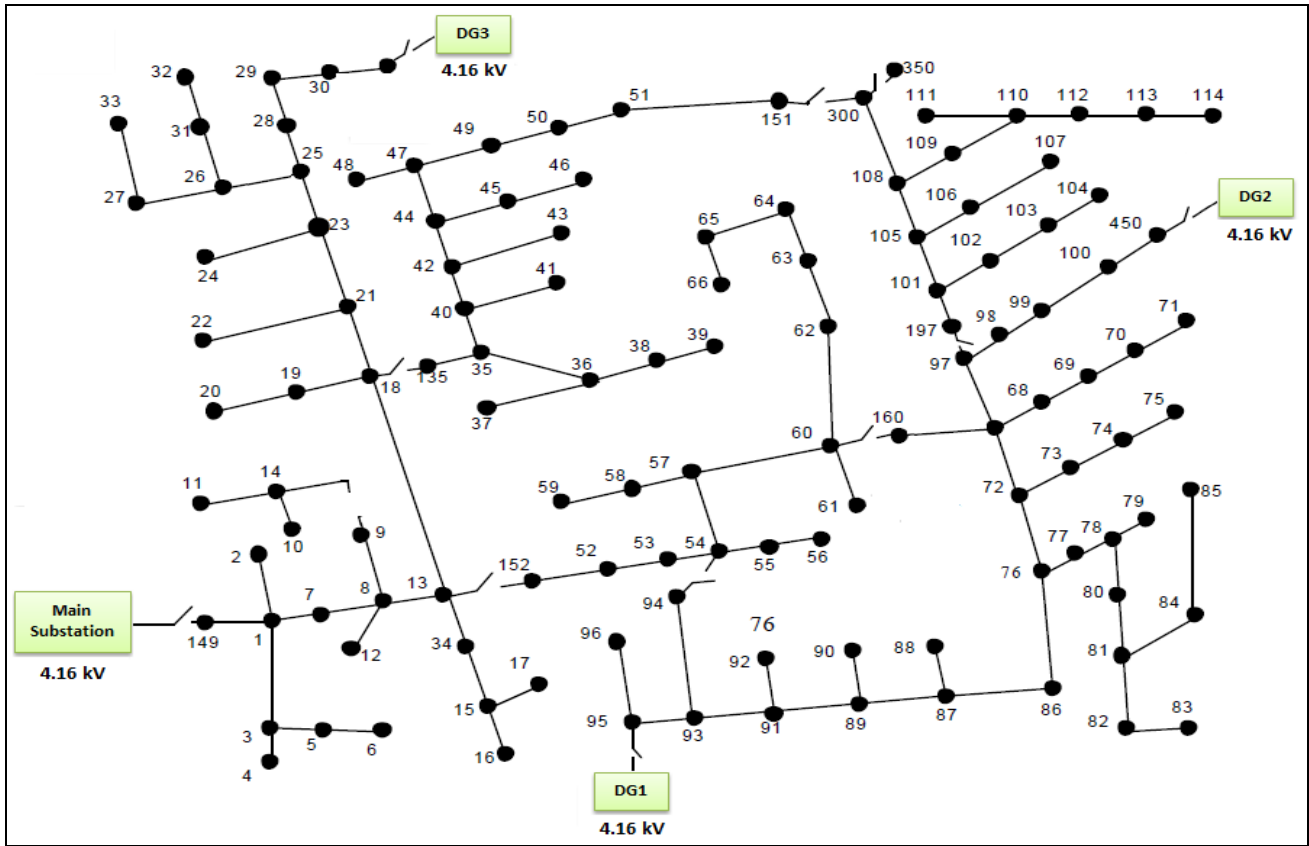


Fig. 4 The IEEE 123 distribution feeder topology

IV. THE PROTECTION SCHEME

A large number of tests is conducted in order for the protection scheme to be built and verified. The underlying requirements for building such scheme are based on the following:

A. Signal Processing

The signal processing requirements for the system are abbreviated in the following table:

TABLE I
SIGNAL PROCESSING REQUIREMENTS FOR THE PROTECTION SCHEME

| | |
|-----------------------------|--|
| Sampling frequency | 12.8 kHz |
| Frame size | 64 samples |
| Frames processing technique | Successive frames will acquire one new sample at a time, in the same way of leaving one sample behind. This will provide major improvements in the speed of the detection of faults |
| The DWT features utilized | The first stage approximations and details related to the Daubechies mother wavelet of the order 2 (Db2) for the detection of faults scheme, and the first stage details only related to the Haar mother wavelet for the classification of fault types scheme. The DWT FIR filters related to the Db2 and Haar mother wavelets are shown in figs. 5 & 6. |
| DWT features representation | Through Parseval's energy formula as given in (3): $E = \sum_{i=1}^N S_i ^2 \quad (3)$ |

Where, N : window length, S_i : individual samples of signal S

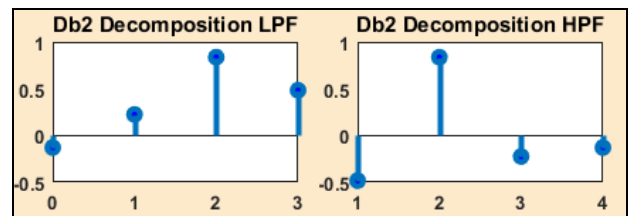


Fig. 5 The set of FIR filters dedicated for the analysis that related to the mother wavelet Db2

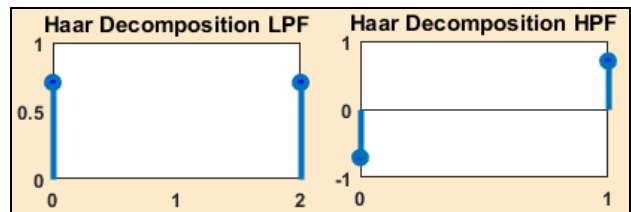


Fig. 6 The set of FIR filters dedicated for the analysis that related to the mother wavelet Haar

B. DWT Analysis Results Assessment

Through performing the DWT analysis on discretized phase and zero sequence current signals, it is found that:

- a) The high frequency components of signals can be extracted through the detail features. At steady

state, these features will have small values as compared to faulty state.

small amount of time to reveal faulty signals sharp changes.

- c) There will certain healthy state transients that can cause the detail features to exhibit high magnitudes approaching or exceeding those related to faulty state. Such transients are found to be the result of the switching events of certain feeder sections, energy sources, or power factor correcting capacitor banks energization.
- d) The approximation features will not be affected by the mentioned switching transients or the affectedness will be so small in a way that it cannot be distinguished.
- e) The approximation features will also exhibit high values after faults initiation; however, they will require more time to reveal faulty trends. This is due to the low frequency dependency of such features on that of analyzed signals.

After conducting the mentioned analysis, it can be concluded that utilizing the details in representing signals faulty trends will produce fast scheme. However, it can be affected by the healthy state transients; therefore, utilizing both details and approximations will provide reliable and

secure detection functionality. Reliable means being sensitive to all fault types being designed for, and secure means not falsely detecting non faulty conditions [9]. Table II reveal the detail and approximation features energy represented variations (ecA and ecD respectively) for an analysed phase (a) current samples with the help of first stage Db2 mother wavelet analysis for different system states. Fig. 6 reveals the sharp rise in detail coefficients at the instant of fault initiation and the smooth rise of approximation coefficients at the same instant.

TABLE II

DWT COEFFICIENTS VARIATIONS DURING SOME OF SYSTEM STATES TAKEN FOR A QUARTER OF CYCLE POST DISTURBANCE OF CURRENT SIGNALS ANALYSIS UTILIZING THE DB2 MOTHER WAVELET

| Healthy State | | Faulty State | |
|------------------------------------|----------|------------------------|------------------------|
| ecA | ecD | ecA | ecD |
| Steady State | | | |
| 1.2468*10 ⁷ | 0.8961 | 2.9972*10 ⁸ | 2.3982*10 ⁶ |
| Capacitor Energization | | | |
| 1.2788*10 ⁷ | 109.6620 | 3.0107*10 ⁸ | 10.8167 |
| Feeder Section Energization | | | |
| 1.7206e*10 ⁷ | 746.6291 | 2.9881*10 ⁸ | 35.0114 |

- b) The detail features are exhibiting high values at the moment of faults initiation and they occupy

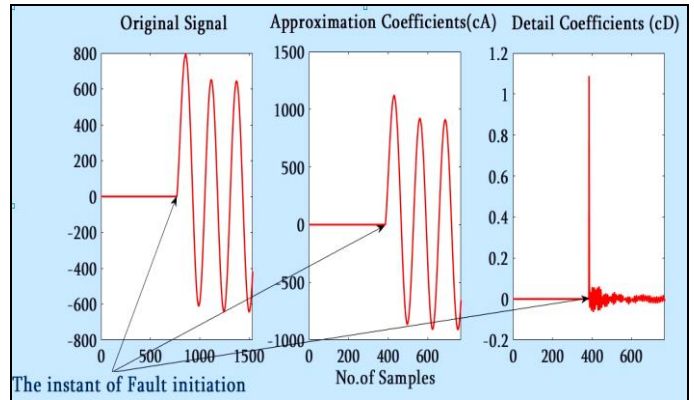


Fig. 7 Details and approximation variations before and after the faulty state for six cycles of phase (a) current signal analysis

C. Protection Scheme Construction

The proposed protection scheme for the simulated distribution system consists of two stages, which are:

1) The Detection of Faults Stage:

Since the detection of faults has to be done as fast as possible, there must be reductions in the calculations performed on the analyzed signals in addition to picking the suitable processing and analysis features. This will lead to fast system response and therefore, fast tripping action. As such, it is found that utilizing one signal instead of the three phase and zero sequence current signals analysis for the sake of detection of faults will provide major reduction in the number of DWT decompositions. This is done through analyzing a certain function provided in (4), [10]. The shape of which through healthy and faulty states associated with the DWT analysis coefficients are shown in Fig. 8.

$$f[n] = (a[n]^2 + b[n]^2 + c[n]^2)^{1/2} \quad (4)$$

Where *a*: phase (a) current samples, *b*: phase (b) current samples, *c*: phase (c) current samples.

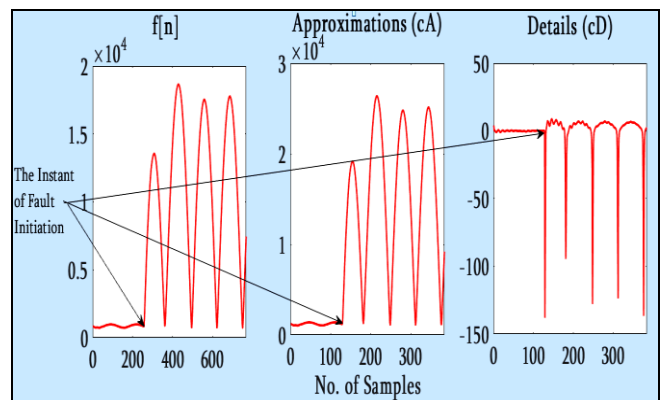


Fig. 7 Details and approximations variations before and after the faulty state for three cycles of analysis

Besides the previously mentioned benefits for the detection scheme, this function has also the advantages of concentrating the faults transients. The concentration will help in further fastening the detection by utilizing the detail components of DWT analysis of such signal. Due to the affectedness of the detail components also by the switching transient events as mentioned in the signals analysis section, the detection stage is built based on two thresholds utilizing the detail and approximation features of such function as shown in flow chart of Fig. 8. The values for the two thresholds are chosen based on the energy of coefficients calculations given in Table II for the given system states and other faulty states simulated at different locations on the feeder system. The dependability in operating the detection scheme is taken into account when choosing the thresholds provided that all faults experienced must be detected successfully. The security in decisions such that no healthy state is falsely indicated as a faulty state is also taken into consideration.

Threshold 1 = 3.277×10^8
 Threshold 2 = 32

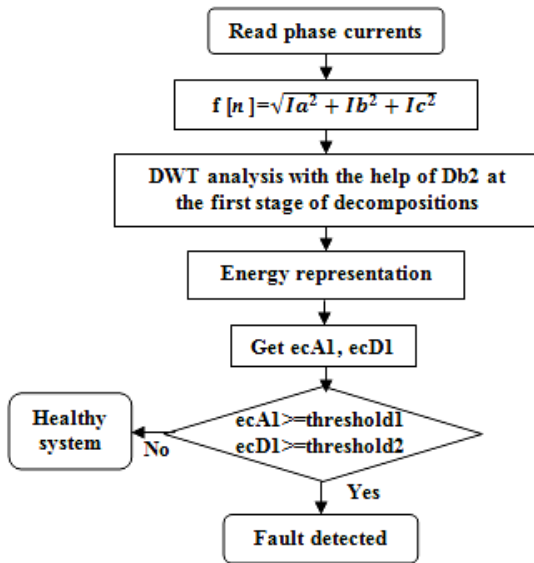


Fig. 8. Fault Detection flow chart

2) The Classification of Faults Stage:

After the detection and isolation of faults are employed, the captured three phase current signals are analyzed and manipulated in order to be entered for the fault type decision indicating scheme. In order to reveal and distinguish between faulty and healthy phases as fast and accurate as possible, the three phase and zero sequence current samples high frequency components are extracted with the help of DWT. Those components (the details) will then be represented by the energy formula and normalized by the highest energy value. The results are found to represent fuzzy variables; therefore, a Mamdani based FIS fault type indicating scheme is built and tested.

The manipulations performed on the current signals are shown in Fig. 9. The FIS specifications and rules are shown in Table III, and Fig. 10 respectively.

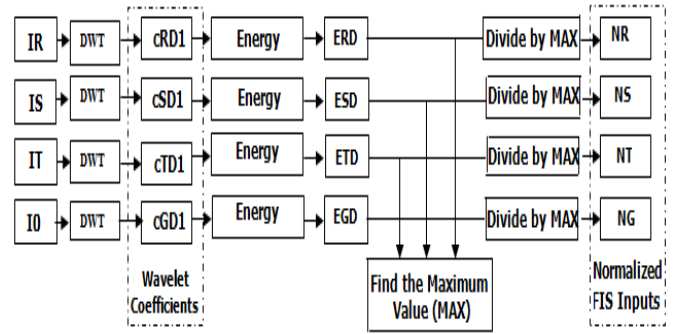


Fig. 9. FIS inputs pre-processing

TABLE III
 THE SPECIFICATIONS OF THE FIS

| Input Variables | Membership function Type | No. of membership functions | Names | Range | Parameters |
|------------------|--------------------------|-----------------------------|-----------------|------------|------------------------|
| Na, Nb, Nc | Trapezoidal | 2 | Zero | 0-0.3 | 0,0,0.25,0.3 |
| | | | One | 0.25-1 | 0.25,0.3,1,1 |
| Ng | Trapezoidal | 2 | Zero | 0-0.0013 | 0,0,0.001,0.0013 |
| | | | One | 0.001-0.15 | 0.001,0.0013,0.15,0.15 |
| Output Variables | Mf. Type | No. of Membership functions | Names | Range | Parameters |
| Fault Type | Triangular | 10 | A-G | 0-1.5 | 0, 1, 1.5 |
| | | | B-G | 1.5-2.5 | 1.5, 1, 2.5 |
| | | | C-G | 2.5-3.5 | 2.5, 2, 3.5 |
| | | | AB-G | 3.5-4.5 | 3.5, 4, 4.5 |
| | | | AC-G | 4.5-5.5 | 4.5, 5, 5.5 |
| | | | BC-G | 5.5-6.5 | 5.5, 6, 6.5 |
| | | | AB | 6.5-7.5 | 6.5, 7, 7.5 |
| | | | AC | 7.5-8.5 | 7.5, 8, 8.5 |
| | | | BC | 8.5-9.5 | 8.5, 9, 9.5 |
| A-B-C | 0-1.5 | 0, 1, 1.5 | | | |
| AND Method | Implication | Aggregation | Defuzzification | | |
| Min | Min | Max | Centroid | | |

| |
|--|
| 1. If (Na is one) and (Nb is zero) and (Nc is zero) and (Ng is one) then (Fault Type is a_g) (1) |
| 2. If (Na is zero) and (Nb is one) and (Nc is zero) and (Ng is one) then (Fault Type is b_g) (1) |
| 3. If (Na is zero) and (Nb is zero) and (Nc is one) and (Ng is one) then (Fault Type is c_g) (1) |
| 4. If (Na is one) and (Nb is one) and (Nc is zero) and (Ng is one) then (Fault Type is a_b_g) (1) |
| 5. If (Na is one) and (Nb is zero) and (Nc is one) and (Ng is one) then (Fault Type is a_c_g) (1) |
| 6. If (Na is zero) and (Nb is one) and (Nc is one) and (Ng is one) then (Fault Type is b_c_g) (1) |
| 7. If (Na is one) and (Nb is one) and (Nc is zero) and (Ng is zero) then (Fault Type is a_b) (1) |
| 8. If (Na is one) and (Nb is zero) and (Nc is one) and (Ng is zero) then (Fault Type is a_c) (1) |
| 9. If (Na is zero) and (Nb is one) and (Nc is one) and (Ng is zero) then (Fault Type is b_c) (1) |
| 10. If (Na is one) and (Nb is one) and (Nc is one) and (Ng is zero) then (Fault Type is a_b_c) (1) |

Fig. 10 FIS rules

I. TEST RESULTS

The results of the employment of the proposed protection scheme are introduced in this section. Many test cases are performed regarding healthy state switching transient events and different fault types simulated on different sections of the feeder. In case of a fault detection, a popping up message will appear indicating the system

status and the type of fault as soon as the fault is detected. The various current waveforms and the tripping signals status for healthy and faulty conditions will be shown in the following sections. The popped up messages and the FIS rules firing functions are associated with the faulty state test cases. All the events are performed at the 3rd cycle of operation, i.e. at the time 0.05 sec.

A. Main Feeder Energization Event with DGs Offline

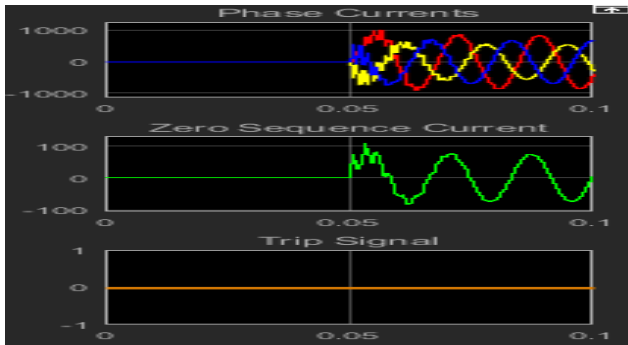


Fig. 11 Main feeder energization with DGs offline

B. Main Feeder Energization Event with DGs Online

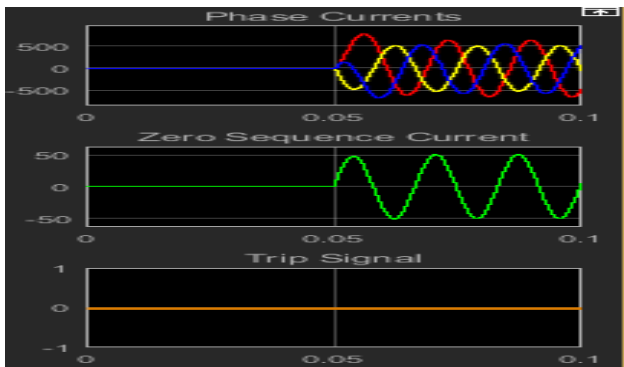


Fig. 12 Main feeder energization with DGs online

C. 13-152 & 135-18 Feeder Sections Energization with DGs Offline

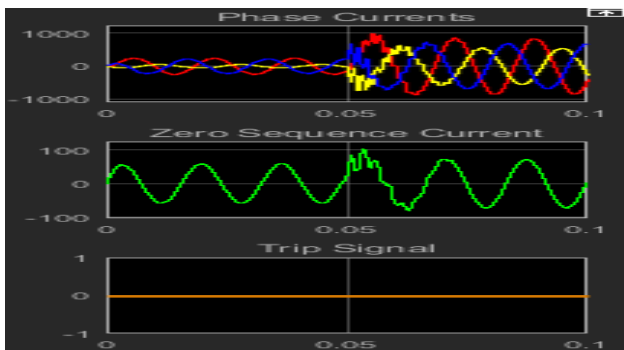


Fig. 13 Certain feeder sections energization with DGs offline

D. 13-152 & 135-18 Feeder Sections Energization with DGs Online

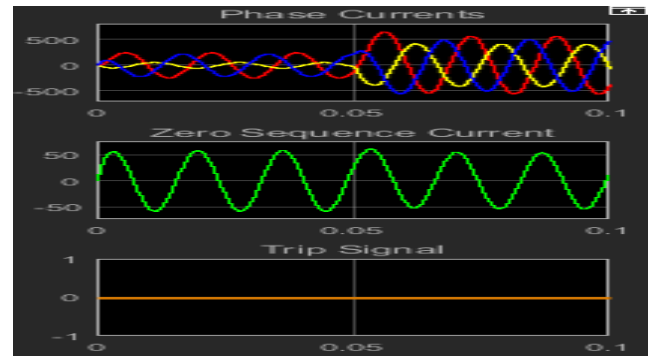


Fig. 14 Certain feeder sections energization with the DGs online

E. Node 83 Capacitor Bank Energization Event with DGs Offline

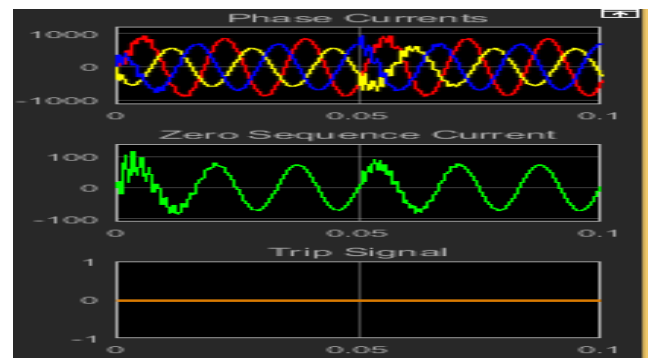


Fig. 15 Power factor improving capacitor bank energization with the DGs offline

F. Node 83 Capacitor Bank Energization Event with DGs Online

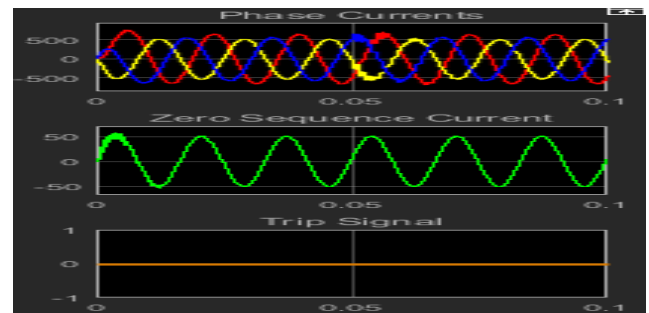
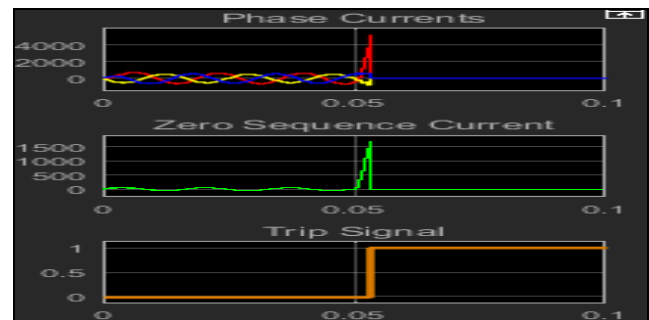


Fig. 16 Power factor improving capacitor bank energization with the DGs online

G. A single Line to Ground Fault involving Phase (a) at Node 52 with DGs Online



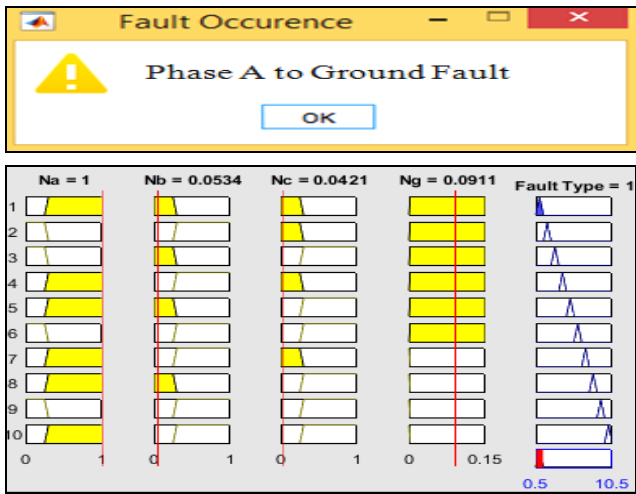


Fig. 17 Phase (a) to ground fault at node 52, the waveforms, trip signal, system status message, and FIS rules firing diagram

H. A single Line to Ground Fault involving Phase (b) at Node 42 with DGs Online

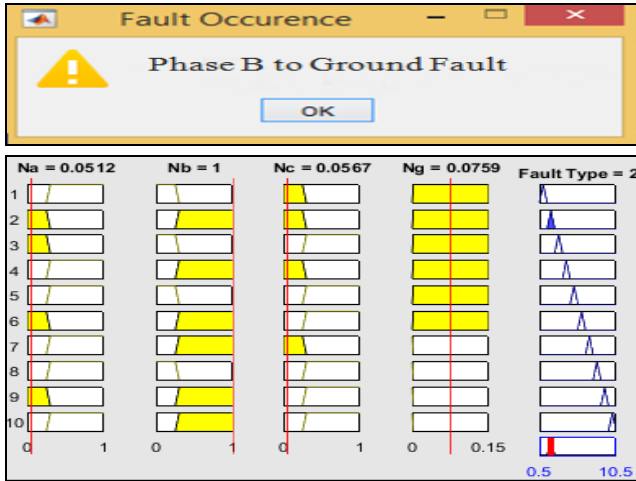
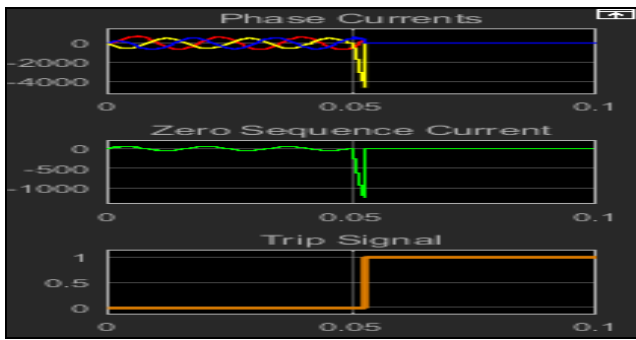


Fig. 18 Phase (b) to ground fault at node 42, the waveforms, trip signal, system status message, and FIS rules firing diagram

I. A single Line to Ground Fault involving Phase (c) at Node 51 with DGs Online

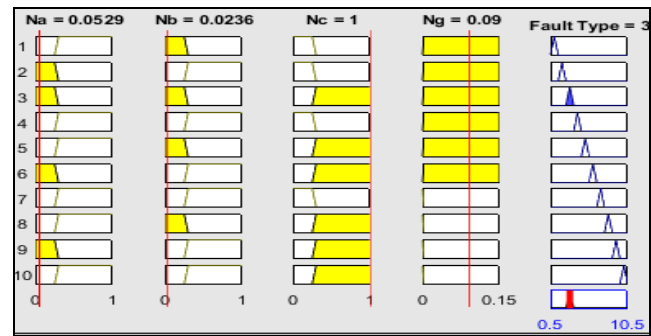
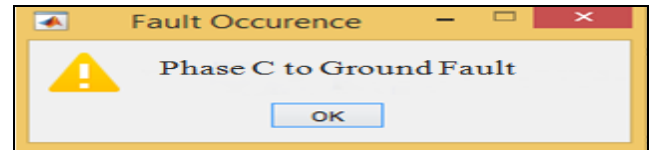
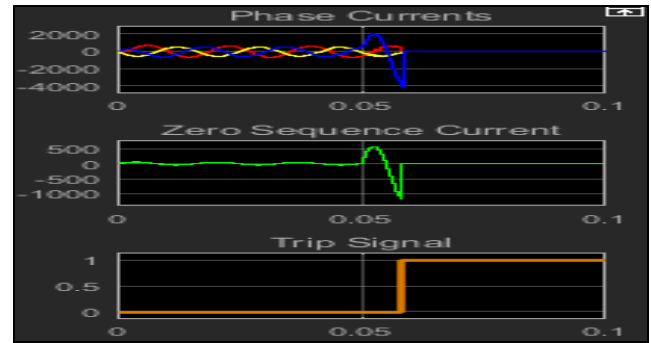
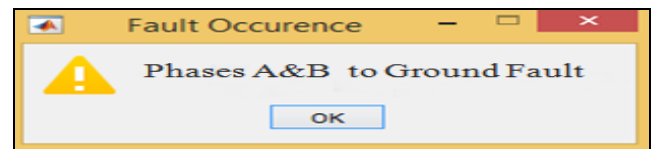
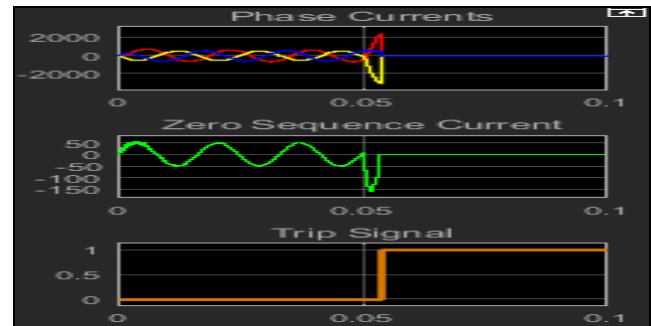


Fig. 19 Phase (c) to ground fault at node 51, the waveforms, trip signal, system status message, and FIS rules firing diagram

J. A Double Line to Ground Fault Involving Phases (a & b) at Node 66 with DGs Online



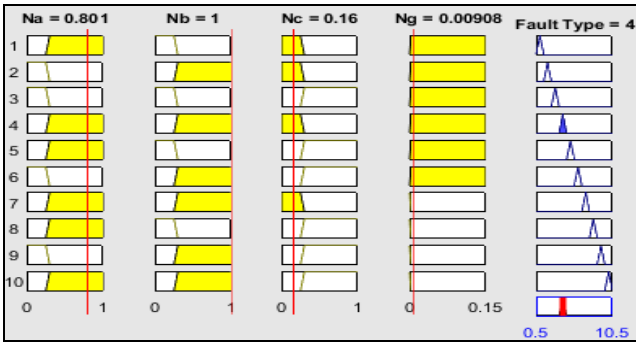


Fig. 20 Phases (a & b) to ground fault at node 66, the waveforms, trip signal, system status message, and FIS rules firing diagram

K. A Double Line to Ground Fault Involving Phases (a & c) at Node 101 with DGs Online

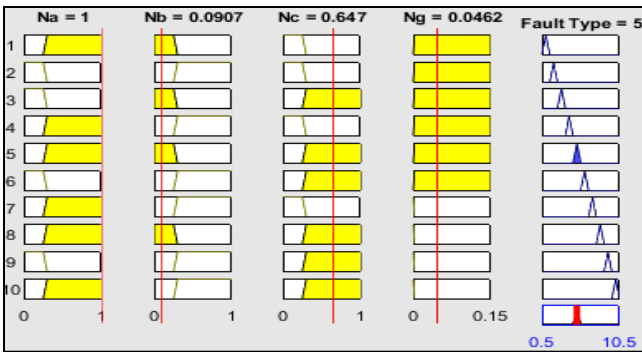
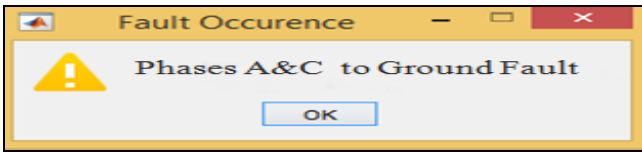
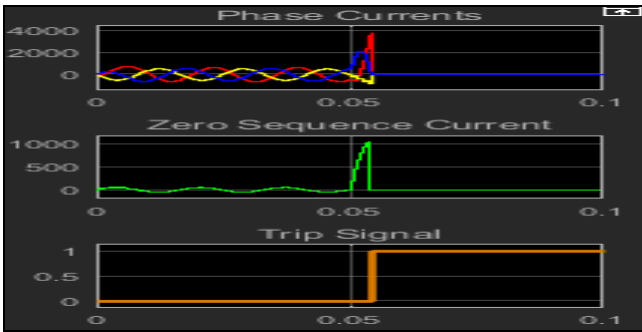


Fig. 21 Phases (a & c) to ground fault at node 101, the waveforms, trip signal, system status message, and FIS rules firing diagram

L. A Double Line to Ground Fault Involving Phases (b & c) at Node 72 with DGs Online

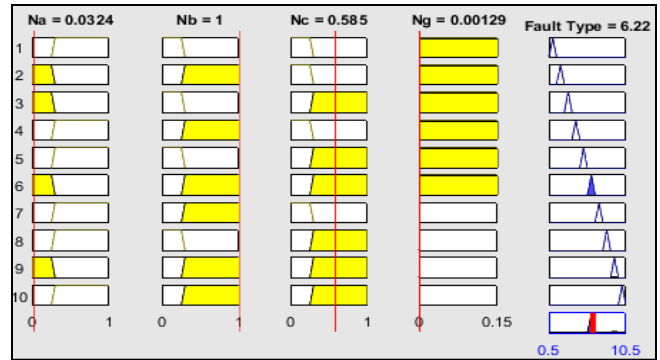
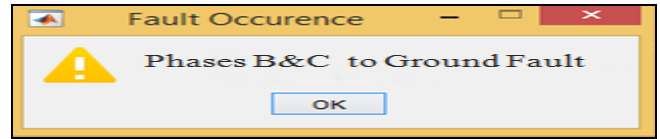
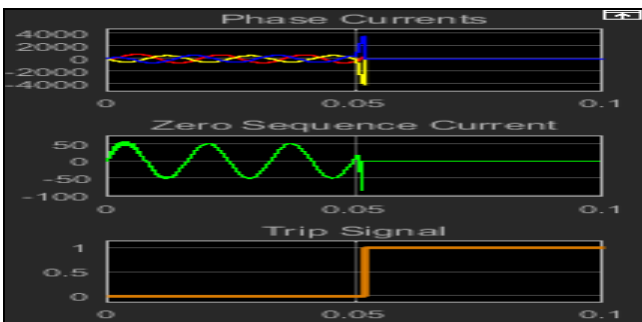


Fig. 22 Phases (b & c) to ground fault at node 72, the waveforms, trip signal, system status message, and FIS rules firing diagram

M. A Double Line Fault Involving Phases (a & b) at Node 79 with DGs Online

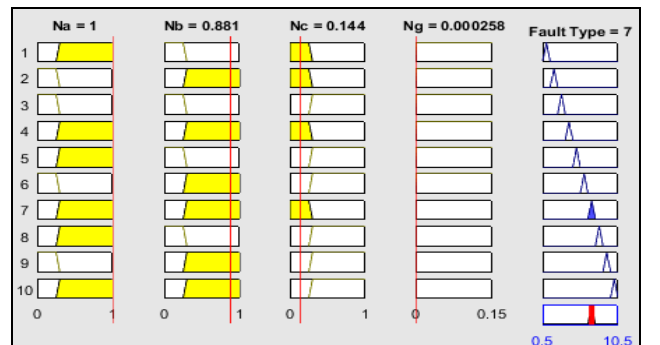
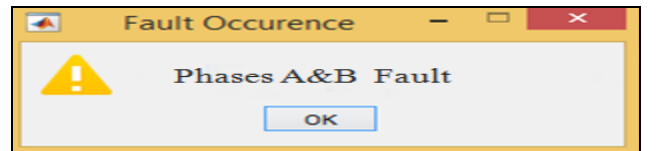
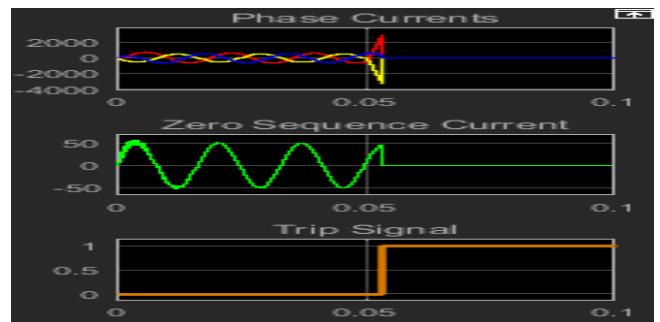


Fig. 23 Phases (a & b) fault at node 79, the waveforms, trip signal, system status message, and FIS rules firing diagram

N. A Double Line Fault Involving Phases (a & c) at Node 86 with DGs Online

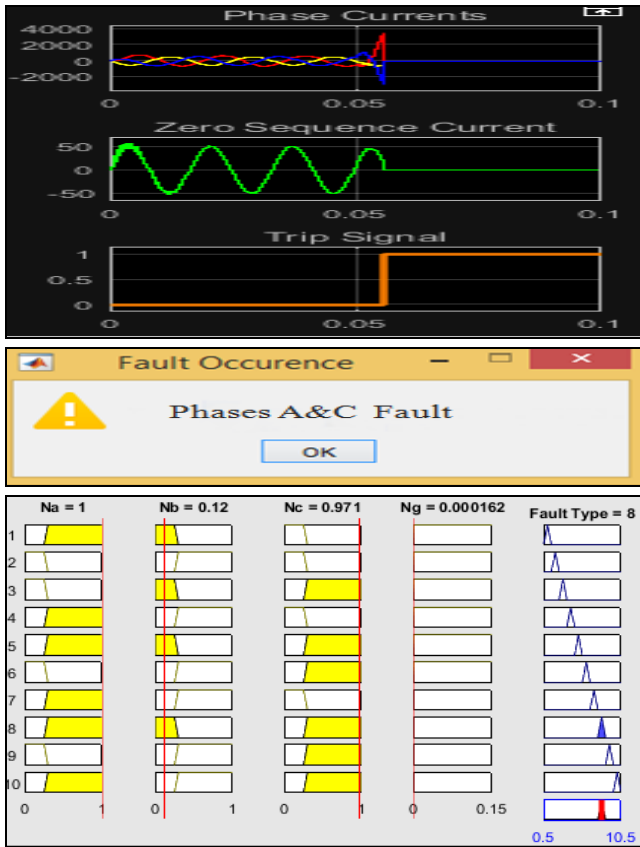


Fig. 24 Phases (a & c) fault at node 86, the waveforms, trip signal, system status message, and FIS rules firing diagram

O. A Double Line Fault Involving Phases (b & c) at Node 81 with DGs Online

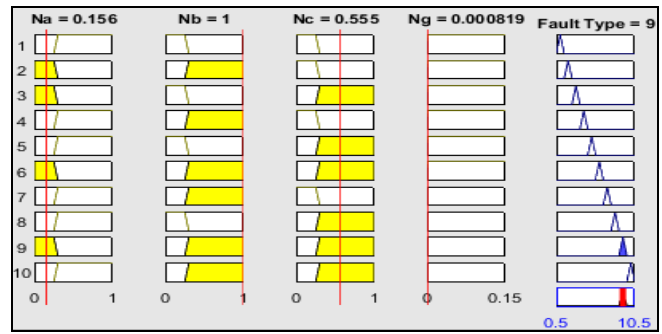
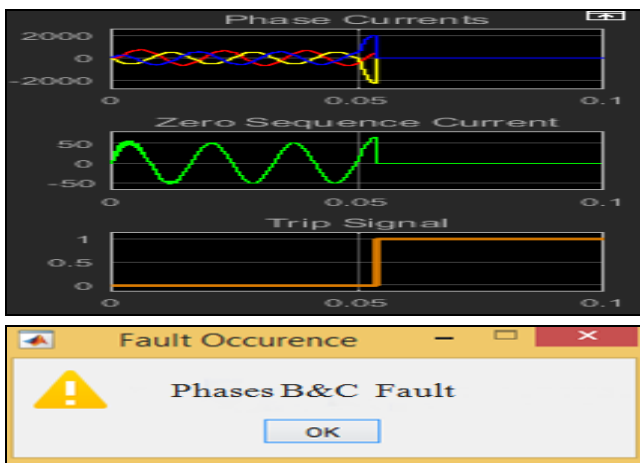


Fig. 25 Phases (b & c) fault at node 81, the waveforms, trip signal, system status message, and FIS rules firing diagram

P. A Three Phase Fault at Node 61 with DGs Online

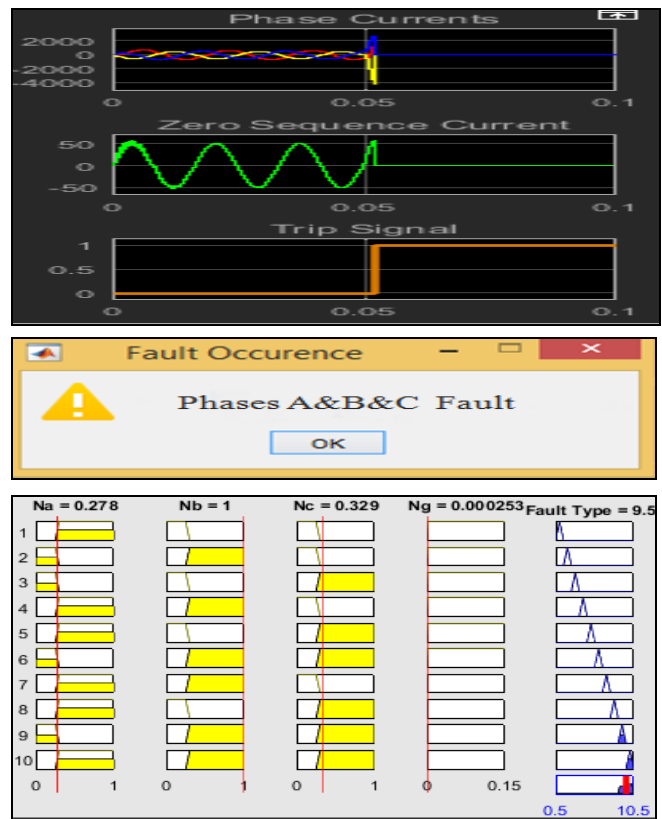


Fig. 26 A three phase fault at node 61, the waveforms, trip signal, system status message, and FIS rules firing diagram

The previously shown results of different fault type cases simulated at different fault locations for a feeder system having the DGs connected (online), could also be attained without having them connected (offline). In case of operating the DGs in an (islanding mode), i.e. operating the DGs alone without having the main feeder supply connected; there will be the same results if for one or each DG penetration point (common coupling with the main feeder circuit) there exists a monitoring and protection facility that perform the same protection functions provided by the proposed scheme. Such application may require additional automation and control resources between the main feeder substation intelligent electronic devices and those related to the DGs in order to manage between the different protection units in case of main supply existence or absence.



II. CONCLUSIONS

Test results of the proposed scheme has shown satisfactory results from the point of view of power system relaying requirements [9]. The first two important characteristics of any protection relaying scheme is that to accomplish the reliability and security during implementation. The scheme has proven high reliability in detection such that all tested faults has been investigated properly. The scheme also works securely in a manner that no healthy state case has been falsely diagnosed as a faulty state. Another important task of the protection relaying scheme, is the ability to diagnose and make a decision in a small amount of time. Response time of the order of few milliseconds is the most preferable in order to isolate faults and reduce their severity to human beings and power system equipment. This is in most times hard to be accomplished because of the reverse relationship between certainty of relaying decision and response time [9]. With the introduction of advanced signal processing techniques involving the wavelet transformation tool, major improvements of the speed of fault diagnosis has been experienced. The utilization of the powerful capability of this transform to extract the high frequency signals features through the detail components has given such improvements. Therefore, exploiting detail components of current signals in capturing useful fault features has provided faults detection and isolation process in about less than a quarter of cycle in most cases.

The advantages provided by the proposed scheme can be utilized as part of an online digital relaying functionality dedicated for a distribution system having a number of connected renewable energy resources en route.

III. REFERENCES

- [1] Rodrigo Hartstein Salim, Karen Rezende Caino De Oliveira, and Arturo Suman Bretas, "Fault detection in primary distribution systems using wavelets," in Proc. 2007 Power Systems Transients Int. Conf. (IPST'07).
- [2] Majid Jamil, Rajveer Singh, and Sanjeev Kumar Saharma, " Fault identification in electrical power distribution system using combined discrete wavelet transform and fuzzy logic," Journal of Electrical Systems and Information Technology, vol. 2, pp. 257-267, September 2015.
- [3] Ankit Jain and Beulah Moses, "Soft computing based fault detection & classification for transmission lines," in Proc. 2016 Electrical, Electronics, and Optimization Techniques (ICEEOT) Int. Conf., pp. 4061-4064.
- [4] Sushil Thale, Vivek Agarwal, and Sheetal Gore, "Adaptive protection scheme with fault detection, classification and isolation features for off-grid distributed generation system," in Proc. 2012 IEEE Power Electronics, Drives and Energy Systems Int. Conf.
- [5] Prakash K. Ray, B. K. Panigrahi, P. K. Rout, Asit Mohanty, and Harishchandra Dubey, "Fault detection in IEEE 14-Bus power system with DG penetration using wavelet transform," in Proc. 2016 Advancement of computer communication & electrical technology Int. Conf., pp. 221-225.
- [6] A. El-Zonkoly, "Fault diagnosis in distribution networks with distributed generation," Smart Grid and Renewable Energy, Vol. 2, pp. 1-11, 2011.
- [7] W. H. Kersting, "Radial distribution test feeders," in Proc. 2001 IEEE Engineering Society Winter Meeting.
- [8] Distribution Test Feeder Working Group. (2013, Aug.). Distribution test feeders. IEEE PES Power & Energy Society. [Online]. Available: <https://www.ewh.ieee.org/soc/pes/dsacom/testfeeders/feeder123.zip>.
- [9] Stanley H. Horowitz and Arun G. Phadke, Power system relaying, 3rd Ed., England: Wiley, 2008, p. 7-10.
- [10] M. A. Kafiey, "A Wavelet Packet Transform Based on-Line Technique for the Protection of Three-phase Interior Permanent Magnet Motors," M.S. thesis, Memorial University of Newfoundland, St. John's, Canada, May 2006.

Electricity Production by Microbial Fuel Cell

Doaa Faisal Ghazi & Alaa A. Saleh

Environment and Pollution Engineering Dept. Technical College of Basra

Iraq, Basra, Alasmaee Aljadede

doaa.faisal@stu.edu.iq

Iraq, Basra, Hay Almohandesin

alaa.alsaedi.71@gmail.com

Abstract- Microbial fuel cell (MFC) is a new technology discovered to be a new way of utilizing renewable energy sources. MFC is a bio-electrochemical device that converts the chemical energy in the organic materials to electrical energy through microbial catalysis at the anode under anaerobic conditions, and reduces the electron acceptor, which is most preferentially oxygen, at the cathode. Due to the rapid development in the MFC-based technology, MFC power production has increased by several orders of magnitude and extended into a variety of areas.

The microbial fuel cells are designed for the purpose of electricity generation using various waste samples. The designed microbial fuel cells consist of two chambers, zinc electrode (Anode), copper electrode (Cathode), air pump, water, sludge and salt bridge. Waste samples are collected from various locations to set up microbial fuel cells with the aid of salt bridge. This is passed on the presence of *Shewanella Putrefaciens* bacteria, *Sulfate Reducing* bacteria and algae. The produced voltage is measured by multimeter.

In this research, the results indicated that the voltage generation is very high at the beginning of the microbial fuel cell operation then it started to reduce gradually with the time. It is observed that the extent of voltage generation in the presence of *Sulfate Reducing* bacteria is higher than the voltage generation in the presence of *Shewanella Putrefaciens* bacteria and algae. The highest voltage generation produced from the microbial fuel cell in the presence of *Sulfate Reducing* bacteria is 3.0 V.

Lastly to conclude, microbial fuel cell essentially is a way of renewable energy that emitted by bacteria activity and need to take a further attention, research and development.

Keywords— algae; electricity generation; microbial fuel cell; oxidation; reduction; *Shewanella Putrefaciens* bacteria; *Sulfate Reducing* bacteria.

الخلاصة- تعتبر خلية الوقود الميكروبية من التقنيات الجديدة والتي تعتمد على طرق حديثة في استخدام مصادر الطاقة البديلة. خلية الوقود الميكروبية هي جهاز حيوي كهروكيميائي تحول الطاقة الكيميائية في المادة العضوية إلى طاقة كهربائية من خلال التحفيز الميكروبي عند القطب الموجب (الأنود) تحت ظروف غير هوائية واختزال المستقبل الأليكتروني عند القطب السالب (الكاثود).

تم تصميم خلية الوقود الميكروبية من حوضين يربطهما جسر ملحي. الحوض الأول لخلية الوقود الميكروبي يحتوي على القطب الموجب (الخاصين). أما الحوض الثاني يحتوي على القطب السالب (النحاس). إضافة إلى ذلك، تحتوي الخلية على مضخة هواء العينات المستخدمة بالخلية أخذت من عدة مصادر لمياه الصرف الصحي. استخدم في هذه الدراسة بكتريا شوانيلا بوتريفاسيانز، البكتريا المختزلة للكبريت والطحالب. وتم قياس فولتية الخلية باستخدام جهاز (الملمتيمتر). أوضحت النتائج إنتاج عالي جداً للفولتية في بداية عمل الخلية وبعدها تبدأ الفولتية بالتناقص تدريجياً بمرور الوقت. كما لوحظ أن إنتاج الفولتية في الخلايا الحاوية على البكتريا المختزلة للكبريت أعلى من الفولتية الناتجة من الخلايا الحاوية على بكتريا شوانيلا بوتريفاسيانز والطحالب. حيث أوضحت النتائج أنه أعلى قيمة للفولتية المتولدة تم الحصول عليها بوجود البكتريا المختزلة للكبريت كانت 3.0 فولت.

وأخيراً، أكدت نتائج البحث أهمية خلية الوقود الميكروبية في إنتاج الطاقة المتجددة

والتي تعتمد على فعالية البكتريا. كما أكدت على أن هذه الخلايا تحتاج الى مزيد من البحث والتطوير.
الكلمات المفتاحية- الاختزال، الأوكسدة، بكتريا شوانيلا بوتريفاسيانز، البكتريا المختزلة للكبريت، خلية وقود ميكروبية، طحالب.

I. INTRODUCTION

These days our society is continuously in search of sustainable, renewable, and alternative energy sources. Solar cells, wind mills, and microbial fuel cells (MFCs) may also be a part of the picture [1]. In order to decrease the pollution and find an eco-friendly energy source, it is suggested to use the microbial fuel cells.

Microbial fuel cell is a great technology to convert organic waste materials into electrical energy. MFC is a microbial electrochemical device that oxidizes the organic or inorganic matter using microorganisms and provides the resulting electrons to an electrode, thus generating electric current [2, 3]. Microbial fuel cell has several advantages of high efficiency, low energy consumption, clean and environmental protection, as well as electricity generation. It is considered an important wastewater treatment process and a new green power generation technology. Microbial fuel cell represents one of the most efficient and carbon neutral energy sources [4, 5].

Microbial fuel cells have several uses in domestic wastewater treatment, desalination plants, hydrogen production, remote sensing, and pollution remediation. Also, microbial fuel cells can be used as a remote power source [6]. It reported that microbial fuel cells can generate power densities as much as 1kW/m³ of reactor volume [7].

The most important parameter in the design of the microbial fuel cell is that choosing an active inoculum. The most common sources of electro active microorganisms have been domestic wastewater, activated and anaerobic sludge, and marine sediments. Also, there are several alternative sources that could be used for this purpose such as heat treated soils, garden compost, manure, rumen, marine sediment, wastewater, and fresh water sediment [8]. Electricity could be obtained from the hydrolysis and fermentation of algae using microbial fuel cells [9].

There are two different types of the fuel cells that use bacteria to generate the electricity. These fuel cells are classified as: biofuel cells which produce the electricity from the addition of mediators and microbial fuel cells that do not require the addition of mediator. The full process of microbial fuel cell design requires the removal of electrons from some source of organic matter (oxidation), and gives those electrons to an object that will accept them (reduction),

such as oxygen or nitrate. This method could be done using bacterium already present in the wastewater as catalysts to generate the electricity while simultaneously treating wastewater or by adding the bacteria directly to the wastewater [10].

Microbial fuel cell design mainly consists of various parts such as an anode and cathode chambers, a proton exchange membrane (PEM) and an electrical circuit, as shown in Fig.1 below.

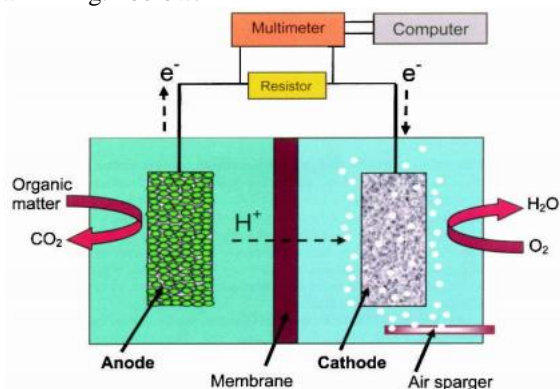


Fig.1 Graphical Representation of Microbial Fuel Cell

The anode and cathode electrodes of the microbial fuel cell are connecting to each other by a copper wire and a membrane to allow the excess protons to transfer from the anode chamber to the cathode chamber or to allow the proton to pass from the cathode chamber to the anode chamber [11]. The anode chamber contains mixed or pure microorganisms which used to accelerate the decomposition of the organic matter into electrons and protons. Electrical generation occurs through the reduction of oxygen or another chemical at the cathode chamber [7]. The fact that bacteria can oxidize the substrates to produce electricity makes the MFCs an ideal solution for wastewater treatment and domestic energy production [12].

The aim of this research is to make an electrical fuel cells by construct a working two-chamber microbial fuel cell using swamp water, discharge and industrial wastewater, water with algae, and oil waste to express voltage generated from the cells as a continuous function of time. Also, the research aims to study the efficiency of using both of *Shewanella putrefaciens* bacteria and *Sulfate Reducing* bacteria in the voltage generation.

II. MATERIALS AND METHODS

A. Samples collection

To set up the microbial fuel cell, different types of samples (Swamp water, discharge and industrial wastewater, oil waste, and water with algae) were collected from different places of Basra city (Technical College of Basra, Petrochemical Factory of Basra, and Yassin Krebut). For the better efficiency of microbial fuel cell, it is necessary that there should be sufficient amount of organic load in the wastewater so as to degrade it by using microorganisms in the MFC unit.

B. Bacteria Used in the Experiment:

In this research, the electricigens and its activity have important influence on the power generation capacity and organic matter degradation ability of MFC system. The electricigens are microorganisms that have the ability to convert renewable biomass and organic detritus into electricity without consume the fuel wasting energy in heat form [13].

Two kinds of microorganisms used in the microbial fuel cells in this research, which are *Shewanella Putrefaciens* bacteria and *Sulfate Reducing* bacteria. These are electrochemically active microorganisms. They can supply energy by drawing electrons directly from an external source, using external structure called "Nano cables" that can also use to supply electrons to an external object [13].

In the anode chamber, *Shewanella Putrefaciens* was used as biocatalyst. Colonies of *Shewanella Putrefaciens* bacteria were grown on the agar at 35 C° for 48 h. Each of these colonies was incubated in 100 mL conical flasks and shake continuously on a shaker with 180 RPM for at least 48 h under aerobic conditions. 25 mL of the culture was used as inoculum for the MFCs.

For *Sulfate Reducing* bacteria, SO_4^{2-} was used as the electron acceptor at the cathode chamber. The bacteria was activated and inoculated in the anaerobic medium, which mainly contained sodium lactate SO_4^{2-} in 37 C° and culture 5 days. Then the biofilm was formed. The reason that activated *Sulfate Reducing* bacteria inoculated in the anode chamber including anaerobic medium was to make *Sulfate Reducing* bacteria attach to the surface of the anode.

C. Salt Bridge and proton exchange membrane Preparation

The separator of the anode and the cathode compartment in the microbial fuel cell is called a proton exchange membrane (CEM). In this experiment, the salt bridge was used instead of CEM. The salt bridge was prepared by the saturation of 5 g of agar in 150 ml of boiling water solution. Sodium chloride (NaCl) was added to the agar and water mixture while the mixture is still hot. Short section of plastic pipe used for the salt bridge preparation. One end of the plastic pipe sealed and the salt mixture added before it begins to get thick. After a while, the agar/salt mixture started to cool and solidify.

D. Electrodes Assembly:

In microbial fuel cells, the anode represents the negative part of the cell, while the cathode is the positive terminal. The electrodes materials are must be nonconductive, biocompatible, and chemically stable in the solution [14]. The oxidation and the release of electrons happen in the anode chamber, while all cathodes are terminals which undergo reduction. In this experiment, zinc metal was used as anode electrode with dimensions of 5.5 cm in length and 5 cm in width. Copper metal was used as cathode electrode with the dimensions of 5 cm in length and 5 cm in width. The copper wire connected to piece of zinc and copper plate. In the anode chamber, the copper wire was passed

through a hole in the chamber lid and sealed with epoxy. Cathode chamber does not necessarily need a lid.

E. MFC Assembly:

To construct the microbial fuel cell, two plastic containers with 17 cm length, 22.5 cm width, 12 cm height, and 5 liters capacity. Each of these containers has sealable lid and connected with an external circuit and fish tank air pump with plastic tubing. External circuit is completed with a copper wire. Salt bridge also connected between the two chambers and sealed with epoxy to prevent the leakage of the containers as shown in Fig.2.

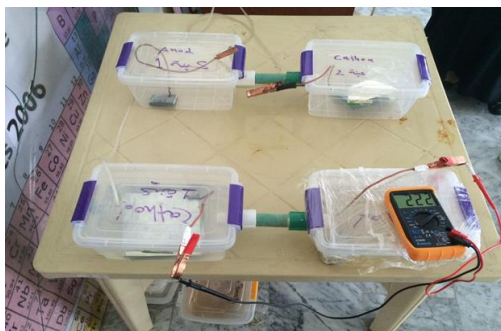


Fig.2 Simple Microbial Fuel Cell

Different wastewater samples and two kinds of microorganisms (*Shewanell Putrefaciens* bacteria, *Sulfate reducing* bacteria) were used in this research and added to the anode chamber. Salt water used as a conductive solution and added to the cathode chamber. Cathode electrode inserted into the cathode chamber and the anode electrodes inserted into anode chamber. A digital multimeter (type DT860D) was used to measure the voltage in volt generated in the MFC unit.

II. RESULTS AND DISCUSSION

The experiments conducted using MCF were performed at room temperature (25 C°). The results in this research showed that electricity could be generated using different wastes include: swamp water, industrial wastewater, discharged wastewater in river, water with algae, and oil waste samples. The effect of type of waste on voltage generation was observed through Fig.3 to Fig.8. All MFCs were continuously monitored during the experiment and readings were taken after each 24 hrs.

The initial voltage generated using swamp water recorded 2 V, as shown in Fig.3. The rate of electric voltage production experienced a rapid increase at the beginning from the start of MFC operation to the 24 hrs. This is because the exoelectrogenes in the swamp water are capable of forming a biofilm for electron transfer to the surface of the electrode. At more efficient rate, it has very few bacteria to extract the electrons rapidly from the organic matter.

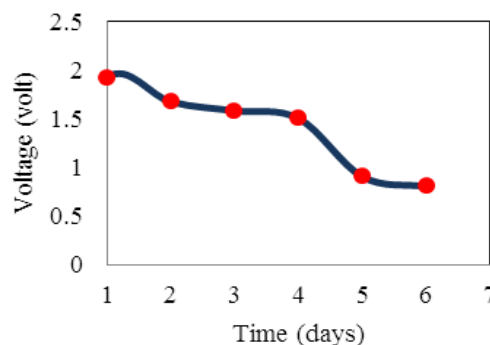


Fig.3 Voltage Generation from Swamp Water

The voltage generation from wastewater sample in the presence of *Sulfate-Reducing* bacteria summarized in Fig.4. The results showed that the rate of voltage generation was high at the first two days of the microbial fuel cell operation. Experimental data indicated that voltage generation was decreased with time from 3.0 V at day 1 to 1.4 V at day 14. The factor that explains the decrease in the voltage reading is the thickness of the biofilm formed on the electrode surface. The biofilm can produce more current when the biofilm thickness is at an intermediate level. If the biofilm is very thick, the electrons should travel very far to get to the anode. In contrast, if the biofilm is very thin [15].

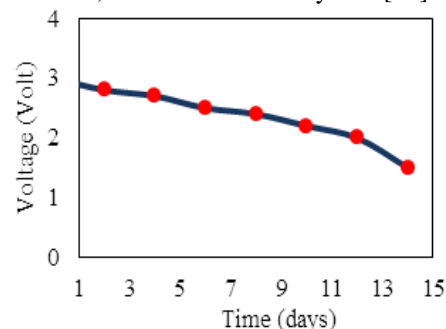


Fig4. Voltage Generation from Wastewater Sample with Sulfate-Reducing Bacteria

Fig.5 & Fig.6 below show the electrical production from the MFCs that contain discharge wastewater and industrial wastewater in the presence of *Shewanella putrefaciens* bacteria. The initial voltage recorded by an MFC that use discharge wastewater in river is 0.83 V and final voltages of 0.78 V, as shown in Fig.5. The success of specific MFC applications in wastewater depends on the concentration and biodegradability of the organic matter in the wastewater. The voltage generation as shown in Fig.6, decreased in the presence of industrial wastewater. The decrease in electric voltage may also occur due to inactive microorganisms and low electron transfer from the microorganisms to the electrode [16].

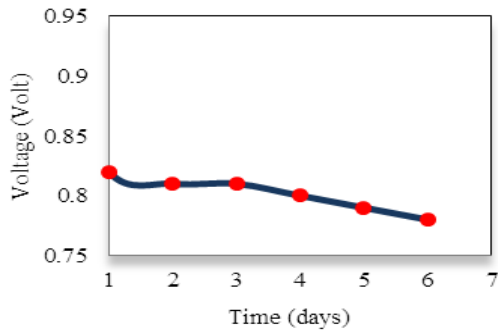


Fig.5 Voltage Generation from Discharge Wastewater with *Shewanella Putrefaciens* bacteria

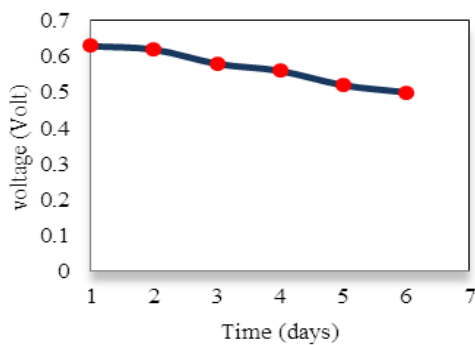


Fig.6 Voltage Generation from Industrial Wastewater with *Shewanella Putrefaciens* Bacteria

The results in Fig.5 and Fig.6 show that there was low electricity generation in the presence of *Shewanella Putrefaciens* than the electricity production from using industrial wastewater in the presence of *Sulfate Reducing* bacteria. In comparison with the results in Fig.4, the voltage generation was much higher in the presence of *Sulfate Reducing* bacteria than the voltage production using *Shewanella Putrefaciens* bacteria in the microbial fuel cell. It shows that the electricity production was very high at the beginning then it started to decrease gradually in the discharge and industrial wastewater. This explains the lower energy of bacteria to convert generate power from the biomass.

For the discharge wastewater in Fig.7, electrical growth was found for algae. Thus pure culture of algae sample was used to produce electricity in the MFC. The results indicated that pure culture produced stable and good power. Water sample with algae produced 1.3 V at day 1 whereas it decreased gradually to about 0.3 V at day 11. It might be due to the participating of algae in photosynthesis in higher rate of fast growing and converting maximum amounts of energy [9].

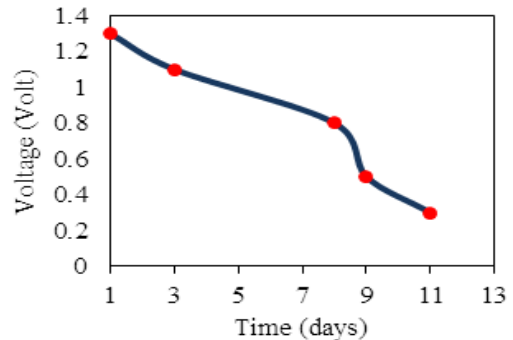


Fig.7 Voltage Generation from Discharge Wastewater with Algae

The voltage generation from oil waste was higher than the voltage generation from all wastewater samples with *Shewanella putrefaciens* bacteria and algae in this study. Fig.8 below shows that the voltage generation from oil waste was 2.15 V at the beginning of the microbial fuel cell operation. This is because the oil wastewater containing sufficient chemical oxygen demands which could be used as a substrate for electricity generation in the reactor of the MFC [17].

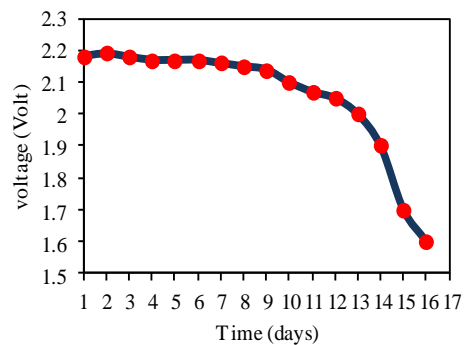


Fig.8 Voltage Generation from Oil Waste

III. CONCLUSION

Microbial fuel cells represent a promising, novel, cost effective, environ-benign technology for sustainable energy production. This study suggests that not only microorganisms, algae can also produce the electricity in same efficiently with the Microbial fuel cells.

Electrical generation can be achieved by coupling wastes with the microbial conversion of organics to electricity in the MFC system. The results showed that both individually and in combinations, swamp water, wastewater with bacteria, water with algae, and oil waste can be used in microbial fuel cells to generate electricity.

Sulfate Reducing bacteria and *Shewanella Putrefaciens* were used as active microorganisms to enhance the work of microbial fuel cell to generate the voltage. It is observed that the increase of voltage generation in the presence of *Sulfate Reducing* bacteria was much higher than the voltage generation produced in the presence of *Shewanella Putrefaciens* Bacteria and algae. The highest result for microbial fuel cell with the presence of *Sulfate Reducing* bacteria was 3.0 V.



Results showed that water containing algae and oil waste can also generate voltage. The voltage generation in the presence of algae in the water was lower than the electricity production gained from the wastewater sample containing Sulfate Reducing bacteria. As well as, the voltage generation from discharge wastewater was higher than the generation of voltage from industrial wastewater.

All the results in this study showed that voltage generated from various wastes in the microbial fuel cell decreased linearly with respect to the time and the decrease in all of the cases was very highly steep. The decrease in the voltage generation in the microbial fuel cell depends on the inactive microorganisms and low electron transfer from the microorganisms to the electrode. It is concluded that bioelectricity can be produced from wastewater samples and it also controls the water pollution problem.

IV. REFERENCES

- [1] J. Li, "An Experimental Study of Microbial Fuel Cells for Electricity Generating: Performance Characterization and Capacity Improvement", *Journal of Sustainable Bioenergy Systems*, vol. 03, no. 03, pp. 171-178, 2013.
- [2] B. Logan and J. Regan, "Microbial Fuel Cells—Challenges and Applications", *Environmental Science & Technology*, vol. 40, no. 17, pp. 5172-5180, 2006.
- [3] D. Pant, G. Van Bogaert, L. Diels and K. Vanbroekhoven, "A review of the substrates used in microbial fuel cells (MFCs) for sustainable energy production", *Bioresource Technology*, vol. 101, no. 6, pp. 1533-1543, 2010.
- [4] E. HaoYu, S. Cheng, K. Scott and B. Logan, "Microbial fuel cell performance with non-Pt cathode catalysts", *Journal of Power Sources*, vol. 171, no. 2, pp. 275-281, 2007.
- [5] C. Salgado, "microbial fuel cells powered by geobacter sulfurreducens", *Basic Biotech*, vol. 5, 5:1, 2009.
- [6] H. Luo, G. Xu, Y. Lu, G. Liu, R. Zhang, X. Li, X. Zheng and M. Yu, "Electricity generation in a microbial fuel cell using yogurt wastewater under alkaline conditions", *RSC Advances*, vol. 7, no. 52, pp. 32826-32832, 2017.
- [7] B. Logan, "Scaling up microbial fuel cells and other bioelectrochemical systems", *Applied Microbiology and Biotechnology*, vol. 85, no. 6, pp. 1665-1671, 2009.
- [8] B. Cercado-Quezada, M. Delia and A. Bergel, "Testing various food-industry wastes for electricity production in microbial fuel cell", *Bioresource Technology*, vol. 101, no. 8, pp. 2748-2754, 2010.
- [9] D. Merina Paul, "Bioelectricity production using algae in microbial fuel cell", *Department of Industrial Biotechnology*, vol. 7, no. 11, pp. 8-10, 2015.
- [10] O. Duduyemi, O. Shoewu, A. Yussouff and R. Hunyibo, "Evaluation of Electricity Generation from Animal Based Wastes In A Microbial Fuel Cell", *International Journal of Scientific & Technology Research*, vol. 4, no. 4, April 2015.
- [11] L. Aino-Maija and S. Mira "Bioelectricity Production from Simulated Mining and Forest Industry wastewaters in Microbial Fuel Cells", *Tampere University of Technology*, 2016.
- [12] K. Schwartz, " Microbial fuel cells: Design elements and application of a novel renewable energy sources", *Basic biotech.ells. Enzyme and Microbial Technology*, 47, PP. 179-188, 2007.
- [13] L. Fan and S. Xue, "Overview on Electricigens for Microbial Fuel Cell", *The Open Biotechnology Journal*, vol. 10, no. 1, pp. 398-406, 2016.
- [14] K. Guo, D. J. Hassett, T. Gu, "Microbial Fuel Cells: Electricity Generation from Organic Wastes by Microbes," Chapter 9 in *Microbial Biotechnology: Energy and Environment* edited by R. Arora, ISBN 978-1845939564, pp. 162-189, CAB International, Oxon, United Kingdom. (2012).
- [15] N. Syazana Natasya Hisham, S. MD Zain, S. Jusoh, N. Anuar, F. Suja, A. Ismail and N. Ezlin Ahmad Basri, "Microbial Fuel Cells Using Different Types of Wastewater for Electricity Generation and Simultaneously Removed Pollutants", *Journal of Engineering Science and Technology*, vol. 8, no. 3, pp. 316 - 325, 2013.
- [16] G. Liliana, *Microbial Fuel Cells for Wastewater Treatment, Waste Water - Treatment and Reutilization, InTech open Access Publisher*, DOI: 10.5772/15546, (2011).
- [17] D. Majumder, J. Maity, M. Tseng, V. Nimje, H. Chen, C. Chen, Y. Chang, T. Yang and C. Chen, "Electricity Generation and Wastewater Treatment of Oil Refinery in Microbial Fuel Cells Using Pseudomonas putida", *International Journal of Molecular Sciences*, vol. 15, no. 9, pp. 16772-16786, 2014.

Design Consideration of a Remote Area Power Supply System Utilizing Solar-Diesel Energies

Abdul-kareem Khamis Hassan¹& Hiba Abdulkareem Khamis²

1)Computer Engineering Department
BasrahUniversity
Basrah, Iraq

kareemkhamis@yahoo.com

2)Power Engineering Department
South Technician College of Engineering Basrah, Iraq
hibakareem84@yahoo.com

Abstract-

An economic feasibility study and a complete design procedure of a hybrid system consists of photovoltaic (PV) panels and a diesel generator as a backup power source has been implemented in this paper.

The proposed system was designed in a rural site in Basrah region, southern area of Iraq. It is found that electrifying small home using this system is very beneficial and competitive with other types of conventional sources as it decreases both operating costs and pollutant emissions.

Index: Photovoltaic, Solar Energy, Diesel generator, Off grid

I.INTRODUCTION

Two types of technologies are widely used in the generation of power, the first and the oldest one was the classical power generation using fossil fuel, whereas the second one is the renewable energy technologies where they have rapidly improved due to the increasing efficiency of power generation and to reducing in their costs. The other factor that make the using of the renewable technologies very important is the fact that the transmission and distribution of energy generated from fossil fuels in remote areas was very difficult and expensive, while producing renewable energy locally can offer a suitable source [1]. The solar energy is infinite, site-dependent, non-polluting, and high potential source for backup energy production, it's widely used nowadays [2].

The main suitable option for supplying electrical energy for remote areas is the diesel generator (DG) because of their compact design and high specific power, but the main drawback of using this system is the operational cost which is influenced by load profiles which are affected by the economic condition [3].

The photovoltaic system can be installed and customized in a very short time, as well as the diesel generators, which are not cost effective systems, mainly in remote areas. [4] This is so called hybrid system which combines the low initial cost of diesel generator with a high initial cost of PV system. [5]

This combination of PV– diesel system is economically feasible in many applications for supplying electric energy in remote areas where the electric utility is not available. Taking into account that PV-Diesel system has greater reliability for electricity production than a PV-only system or diesel-only system. [6]

The main advantages of renewable energy technologies are, offer clean, sustainable, green and reliable power generation as well as low operating and maintenance cost of power supply [7].

The photovoltaic systems can be installed in rural areas independent of electricity network. Many systems are built in Cambodia, Latin America, Iran, Kyrgyzstan and China as well as Maltese islands, Republic of Botswana, Bangladesh , South Africa, and Brazil [8].

The main reason of using hybrid system or the combination of different energy resources are to allow the improvement of the overall system efficiency, reliability of the power supply and to reduce the energy storage requirements compared to the systems comprising only one renewable energy source [9].

The hybrid renewable energy system such as PV system with diesel generator offers several advantages which include reduction in operating cost by decreasing operating time of the generator, reduction of environmental pollution and lower maintenance costs [9].

There are some researches that illustrate the importance of using hybrid (solar- diesel) in order to support the grid power and minimize the cost of power. Such as, Wei Zhou [11]demonstrated by comparing the predictions with the field measured data. Using photovoltaic system only . The results demonstrate an acceptable accuracy of the model for modeling PV array outputs under various environmental conditions.

Yousif El Tous [12] represented a universal and flexible model for sizing and selecting hybrid off grid Photovoltaic and Wind energy system, the main goal of their research is to develop a comprehensive model with the automatic sizing and selection of the optimum size of Wind PV and battery banks, the system depends on the electrical load to be

supplied, the wind and PV resources and the needed backup time.

As shown at the previous studies Wei Zhou deals with photovoltaic power only, where it will be weak source for supplying power to loads, Yousif El Tous using photovoltaic –wind energy sources that wind energy is not useful energy source for this region while wind speed is almost low.

In this research, electric energy was supplied using photovoltaic- diesel energy sources to a remote area in Basrah, southern region of Iraq, since the solar radiation is good and the fuel was available. Modeling and experimental studies in the literature concluded that hybrid solar/diesel systems have a clear advantage over conventional stand-alone diesel system for remote areas electric energy. It was proven to reduce fuel consumption, operation and maintenance costs whilst maintaining the required quality of service. Using the essential input data, the generator and PV output powers and fuel consumption were accurately predicted and validated using experimental data.

I. PROBLEM MOELLING

A. Photovoltaic system

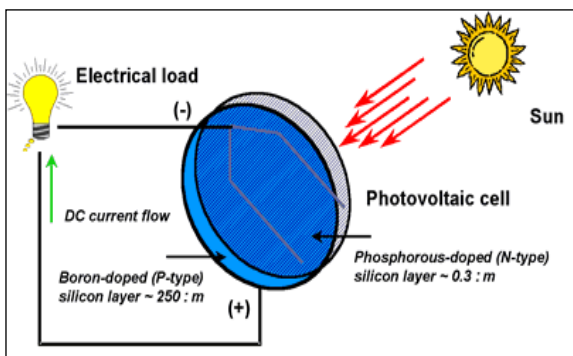


Fig. 1 generation of electricity from solar cell

Figure1 shows the generation of electricity from solar cell. PV arrays are built up with combined series/parallel combinations of PV solar cells, which are usually represented by a simplified equivalent circuit model such as the one given in Fig. 2.

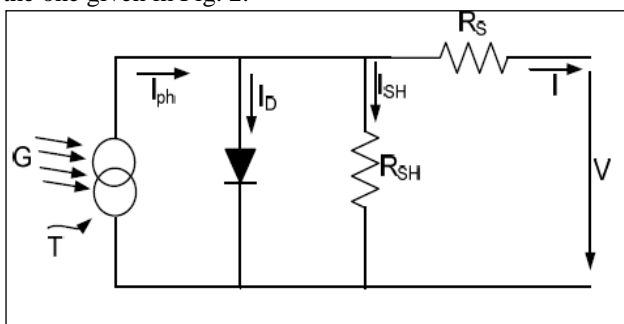


Fig. 2 Simplified-equivalent circuit of photovoltaic cell.

Photo current I_{ph} is directly proportional to solar radiation G . Temperature T and photo current I_{ph} have a linear relationship.[11]

Power output from the PV array can be obtained by using the equation:

$$P_{pv}(t) = I_{ns}(t) \times A \times E_{ff}(pv) \quad (1)$$

Where $I_{ns}(t)$ is isolation data at time t (kw/ m²), A is the area of single PV panel (m²), $E_{ff}(pv)$ is overall efficiency of the PV panels and dc/dc converters.

B. Diesel Generation system

The diesel generator shown in Fig. 3 is generally composed of a synchronous generator coupled to a diesel engine. The frequency of the alternating output current is maintained by a speed regulator. The regulator operates by adjusting the flow of fuel to keep the engine speed and the speed of the generator constant. In the case of high solar radiation, the machine functions as a synchronous generator and provides reactive energy [9].

The fuel consumption of DG unit is related with the rated power and its generated power. The fuel cost is calculated for a year as follows:[9]

$$AFC = C_f \sum_{t=1}^{Tend} F(t)$$

Where AFC is the annual fuel cost of DG , $F(t)$ is the hourly fuel consumption (I.D. /hour), based on load characteristic of the diesel generators [10].This parameter is calculated as follows:

$$F(t) = (0.246 \times P_{DG}(t) + 0.08415 \times P_R)$$

where; P_R is the rated power of diesel generators in kW, $P_{DG}(t)$ is the power generated by diesel generators in kW and C_f is the fuel cost per liter in 1.28 I. D.

Diesel engines are more efficient internal combustion engines. The speed of rotation of such generator depends on the amount of injected fuel and the load applied to the engine crankshaft. The diesel engine is a nonlinear system. It presents delays, which makes it difficult to control. Diesel engines are equipped with cruise control: mechanical, electromechanical or electronic. It carries out the automatic control of the speed of the diesel engine by adjusting the fuel injection depending on the load. It acts on the acceleration mechanism [9].

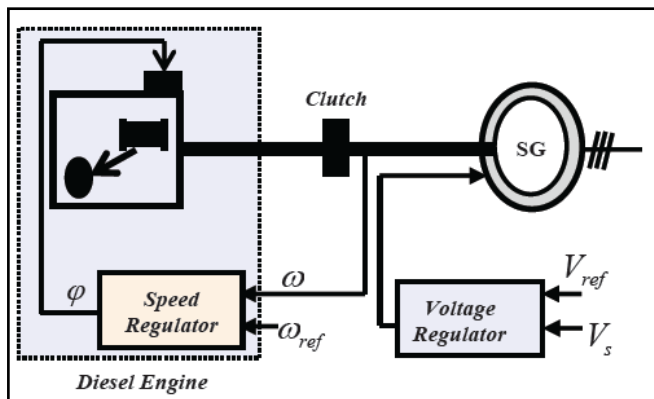


Fig. 3 The structure of diesel generator

C. Modeling of solar-diesel system

The system configuration of PV-Diesel system in this research is shown in Fig.4. PV model follows $I-V$ characteristic. The input variables of this model are solar radiation as shown in Fig.5, and cell temperature of PV panel.

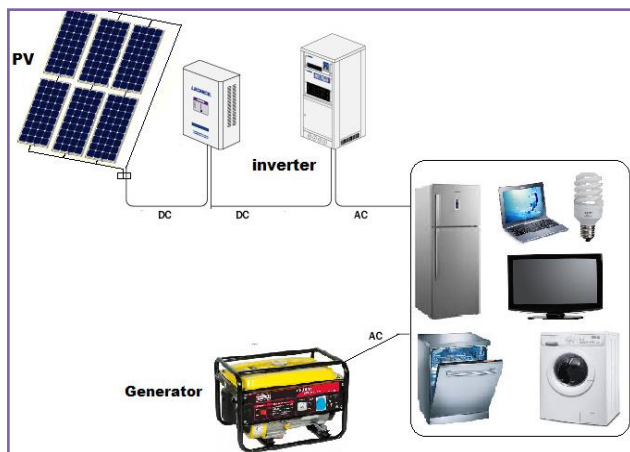


Fig. 4 Scheme of Hybrid power system

II. CONTROL STRATEGIES

The solar radiation for a week in Basrah/Iraq are measured in January as shown in Fig.5. The proposed loads maintained in this research listed in table 1. The control strategy that has been applied for this research is shown in the flowchart that shown in Fig.6 which explain the steps that must be taken in order to turn-on the loads with the availability of solar radiation, and in maximum load demand it should be supported the system by turn-on the diesel engine .

According to the real data that calculated for week at basrah region, Fig.5 shows the solar radiation that will used to generate power from PV system.

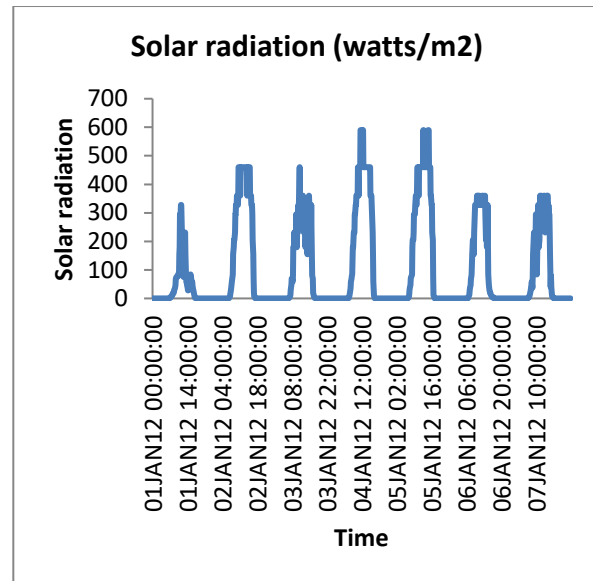


Fig. 5 Weekly solar radiation data

TABLE I
THE PROPOSED LOADS WITH THEIR POWER

| Load name | Load power (w) |
|-----------------------|----------------|
| Electric Iron | 1000 |
| 100 Incandescent Lamp | 60 |
| Air Conditioner | 2500 |
| Fluorescent Lamp | 60 |
| Fluorescent Lamp | 100 |
| Refrigerator | 400 |
| Cooking Range | 1500 |
| Air Cooler | 250 |
| Freezer | 250 |
| Color TV | 80 |
| Satellite Receiver | 25 |

The proposed loads are typed at excel sheet and the program was designed using visual basic program using the hybrid (solar- diesel) power energy sources . The turn-on , turn-off operation for these loads will be done according to the strategy that shown in flowchart at fig.6.

Where according to the existence of solar radiation and using diesel engine as buck-up source these loads will operate taking into account a factor that was added to this program deal with the fuel cost for diesel generator. The increasing and decreasing the value of this factor will affect on the loads implementation , all these procedures will appear at Fig.7.

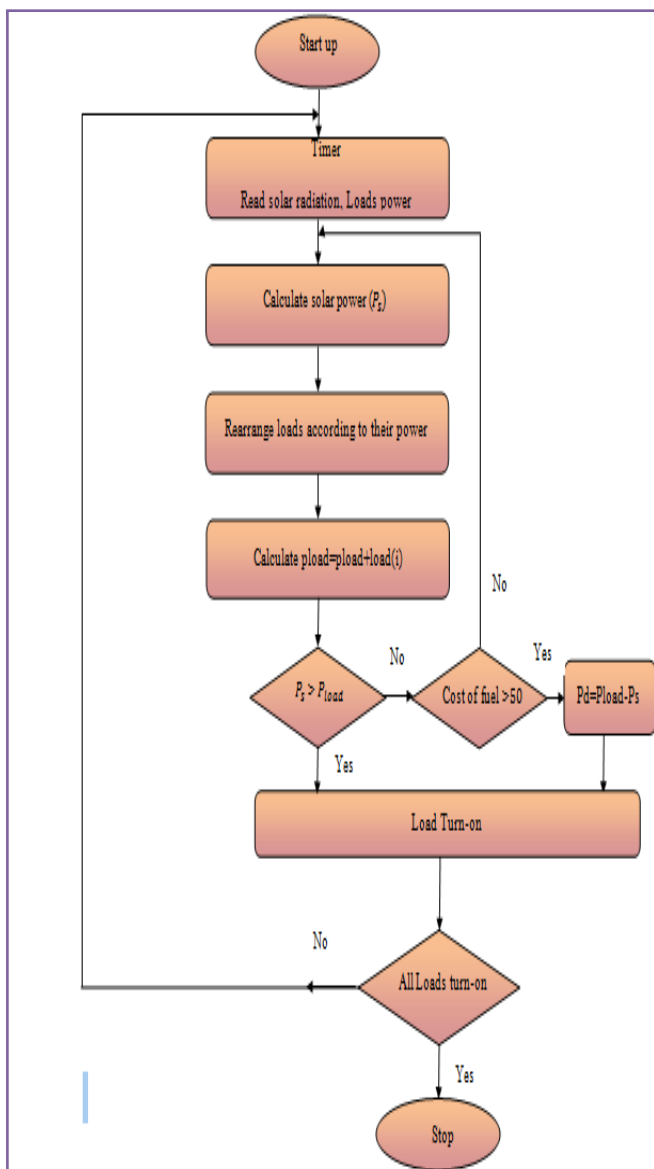


Fig. 6 Flow chart of the control strategy

III. RESULTS AND DISCUSSION

Figure 7 (a, b, and c) denotes the loads turn-on depending on solar energy only, it appears that not all loads will be turn-on since the solar power is low according to the loads power. Fig 7 (d) shows the operation of loads will increase according to the raising of the value of the factor that deals with cost of fuel as the scroll bar that shown in this figure, that's mean the diesel turn-on and then all loads turn-on.

The operation depend on the solar radiation and the cost of diesel fuel. The program having factor which represent the value of cost (I.D) which limit the turn-on for loads depending on its value. If the customer pay more money for fuel then will get more loads turn-on if the payment reduce the program immediately return back to solar energy with turn-off some loads.



a



b



c



d

Fig. 7 loads turn-on using solar-diesel power system(a, b, c and d)

IV. CONCLUSION



This research represented an option of supplying a remote area in Basrah, southern region in Iraq using Sola-Diesel hybrid systems. It has been shown that areal data calculated for solar radiation with proposed loads profile taken as a case study. Even though the region have an excellent solar radiation the optimal system configurations obtained through simulation in visual program which prefer using all PV power until the need for diesel in order to decrease the atmosphere pollution. Due to the continued reduction in PV module prices, PV could also be a major component in the hybrid systems in the area. Though the leveled cost of electricity from the hybrid systems demonstrated in this study is highly comparable to the subsidized electricity price in the country; it is significantly lower than a diesel only electricity supply. This advantages by using this hybrid system are decreasing the indoor pollution, encouraging small scale productive activities and reducing burden on the country's economy by replacing using a lot of fuel. This scheme can be modified using addition of another renewable energy sources like wind, geothermal or batteries as backup system and for any season and any place (village, building, ..., etc).

V. REFERENCES

- [1]Yasar Demirel, "Energy Production, Conversion, Storage, Conservation, and coupling" ,Springer London Heidelberg New York, 2012.
- [2] Godefrey Boyle,"Renewable Energy Power for a sustainable future" second edition
- [3] P. Arun, R. Banerjee, S. Bandyopadhyay, 'Optimum sizing of battery-integrated diesel generator for remote electrification through design-space approach,' *Energy*, vol. 33, 2008.
- [4] S.H. El-Hefnawi, "Photovoltaic Diesel-Generator Hybrid Power System Sizing", *Renewable Energy*, Vol. 13, No. 1, pp. 33-40, 1998.
- [5] Abd El-Shafy A. Nafeh, "Proposed Technique for Optimally Sizing a PV/Diesel Hybrid System", *International Conference on Renewable Energies and Power Quality Granada (Spain)*, Vol.1, No.8, 2010.
- [6] M. Ashari, C.V. Nayar, W.W.L. Keerthipala, "Optimum operation strategy and economic analysis of a photovoltaic-diesel-battery mains hybrid uninterruptible power supply," *Renewable energy*, vol. 22, 2001
- [7] Kareem K.Jasim, Mahdi A. Abdul-Hussain "Optimization of Hybrid PV/Diesel Power System for Remote Telecom Station" *International Journal of Application or Innovation in Engineering & Management*, Vol.5, pp.39-46, 2016.
- [8] Saban Yilmaz , Hasan Riza Ozcalik, Mustafa Aksu, Celebi Karapinar "Dynamic Simulation of a PV-Diesel-Battery Hybrid Plant for Off Grid Electricity Supply " *Energy* Vol. 75 ,pp. 381 – 387,2015.
- [9] Salima Meziane a, Omar Feddaoui a and Riad Toufouti "Modeling and simulation of hybrid wind-diesel power generation system" *International Journal of Renewable Energy*, Vol. 8, No. 2, July - December 2013
- [10] H. Suryoatmojo, A. A. Elbaset, F. A. Pamuji, D. C. Riawan, Nursalim, M. Abdillah " Optimal Sizing and Control Strategy of Hybrid PV-Diesel-Battery Systems for Isolated Island" *Momona Ethiopian Journal of Science (MEJS)*, Vol 5, No.2, pp62-80, 2013
- [11] Wei Zhou a, Hongxing Yang a, Zhaohong Fang " A novel model for photovoltaic array performance prediction" *Applied Energy* Vol. 84, pp 1187–1198 ,2007
- [12]Yousif El Tous, Sandro Abdel Hafith "Photovoltaic / Wind Hybrid off Grid simulation model using Matlab simulink.", *International Journal of Latest Research in Science and Technology* ,Vol. 3, pp 167-173 , 2014



Design and Implementation a prototype of a Smart Prepaid Power System Based on IOT

Ikraam Kassim Abid & Ali Fadhil Marhoon
 Computer Sciences Electric Engeneering
 Basra University Basra University
 Basra-Iraq Basra- Iraq
Ikraam_Kassim@yahoo.com ali_marhoon2003@Email

Abstract- Internet of Things (IoT) is a concept refers to a communication between a computers, devices and sensors in less human entry. The idea in this paper is to design and implement a Smart prepaid power System (SPPs) as a smart prototype for electric prepaid management having a wireless communication facility based IOT applications. The proposed system is implemented in this work by designing three sub systems : electricity providing server system , smart meter system , and a mobile application system are communicated with each other by using GSM and Internet technology .A matching protocol is proposed for transmitting the data between these sub systems. The main goal of the designed system is to control and manage the electricity supplying between the consumer and the electricity providing server to prepaying the amount of the consumed energy for sending a request to the electricity provider server using the proposed mobile application to recharging the balance, manage the smart meter operations, and to help the consumer controlling and monitoring the activation of his premises (home or a facility) appliances using the smart phone.

Index Terms-IOT, smart meter, electricity billing , prepaid meter billing, IOT applications

I. INTRODUCTION

High automated and secured systems are presented in many internet of thing applications including electricity distribution and billing. In Iraq traditionally, information of energy consumed is collected from customers' meter by electric provider employees who visit the customers' premises periodically, the cost of the consumed power is paid by the consumers manually .When the consumer fails to pay the required amount in time, their premises electricity is cut-off until payment is made. This method of measuring power consumption suffers from many problems including a delay in the money which must be paid to the electric provider organization, the customers might be out of home during the visits of meter readers , required efforts for bill reading, the required number of the employers to collect and distribute all the bills of the large number of the consumers, so the readings made by the human operators are prone to errors. The proposed idea is a (Smart Prepaid Power System (SPPs) is introduced an attempt to overcome these problems using prepayment of the amount of energy using a smart metering system, which is from the consumer's point of view , encourages

the user to economize the power consumption n. In addition, it controls and monitors the power consumption values. Many studies and efforts have been made to control the consumption of electricity between the consumer and the energy provider.

In 2013 Anmar Arif et al. published a development of a GSM and ZigBee based smart meter. This meter can measure the energy and send the information to the service provider, who can store this information and notify the consumer through SMS messages or through the internet[1]. In 2014 Atheena Charly et al. designed a hardware model to provide an efficient management of electrical energy in homes, which checks the electricity consumption and control the electric energy which used with the demand response technique, the operation of the low priority appliances can be implemented in a predefined interval at off peak times using through ZigBee communication communicated with utility through (GSM) [2]. In 2016 Swati Arote et al. proposed a system presents a total electronic of three phase four the wire energy meter , All the power measurements are taken in the digital domain. These readings are transmitted to the mobile of user via wireless GSM technology. User can have the updates of electric energy consumption data on his mobile[3].

II. THE PROPOSED SYSTEM

The proposed system design is made up by design and implements three main units or sub systems:

1. Electric provider server system (EPSs)
2. Smart Meter system (SMs).
3. Smart Meter Mobile Application (SM. app.).

The communication among these sub systems is based on the internet and GSM technology using a proposed matching protocol.

Fig (1) shows the general structure of the proposed system. And the work flow among the different sub systems and all the activities of the proposed system are clarified in Fig (2).

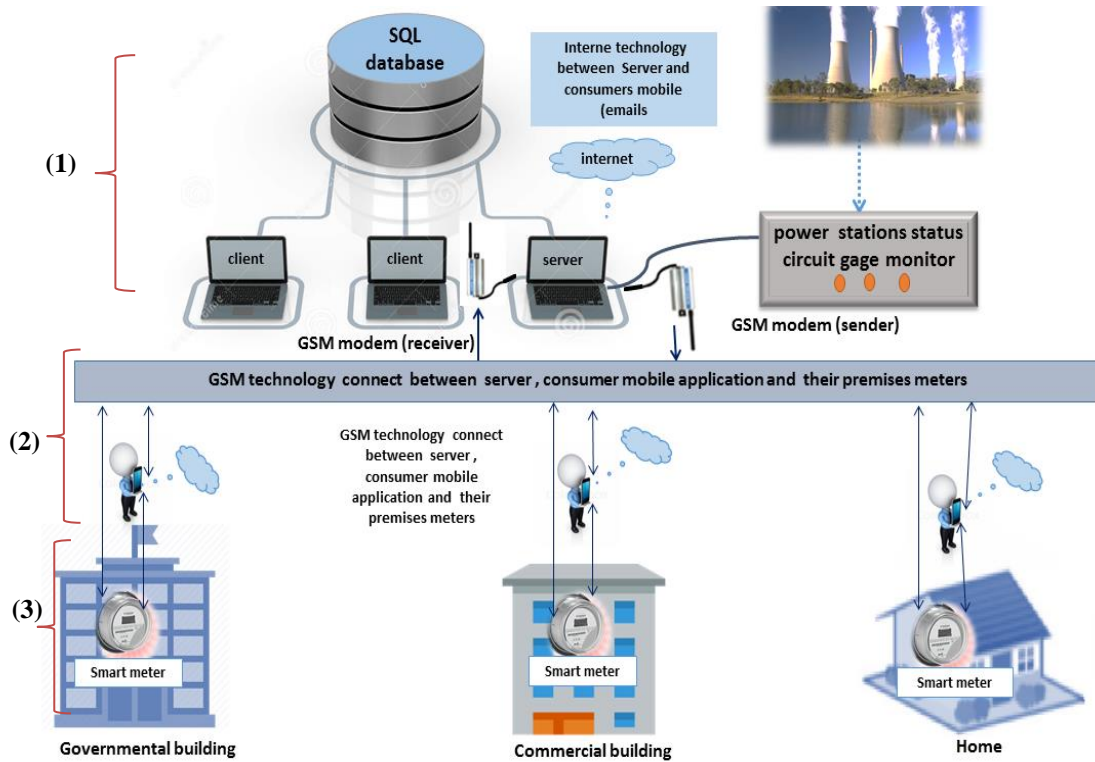


Fig.1 The general Structure of the proposed system

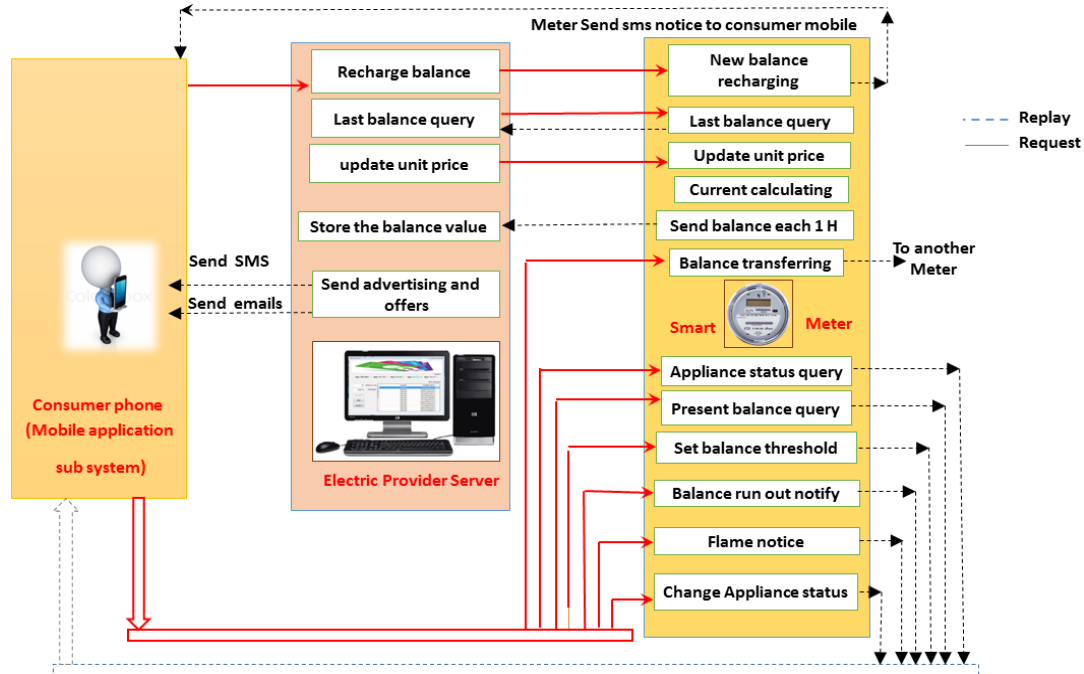


Fig.2 The proposed system units and servers need for communication protocols to allow the devices and servers to communicate with each other. In this paper , the main communication tool is the GSM , utilized SMS messages to control the operations of the overall the

The Internet of Things consist of many devices interconnected with each other to do one or many operations ; To connect all these sub systems together are

system. So, there is a need to accommodate such utility to be suitable for such application. Hence, matching protocol is proposed, the idea of such protocol is developed from the standard ZigBee protocol with some modifications to be suitable with our application. Fig (3) shows the proposed protocol packet (PMP) format :

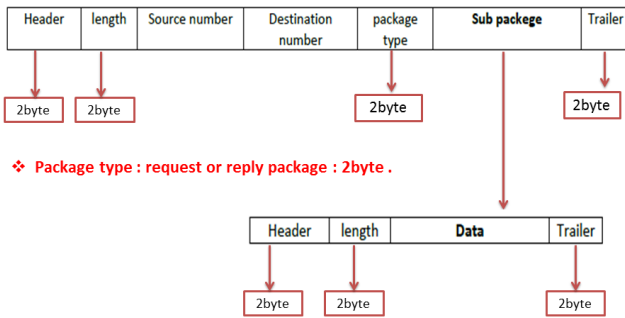


Fig 3.The proposed matching Protocol Structure (PMP)

Table (1) describe the header and trailer of each sub system and Table (2) shows some of the sub packages structure.

Table(1) : The header and trailer of each sub system

| The sub system | The header |
|--------------------|------------|
| Smart meter | SM |
| Server system | PM |
| Mobile application | MP |

Table(2) : Some of the sub packages structure.

| The sub package type | Header |
|-----------------------------|--------|
| Balance recharging | Nb |
| backup balance 1 H | Bt |
| Unit price notification | uN |
| Last recharging query reply | BQ |
| Meter activation message | mt |

Where :

- Header: is the start of package.
 - Tailer : the end of package .
- Each one of the header and tailer is a two characters , these characters are different for each subsystem to allow the other subsystems to recognize the subsystem source to determine the required decision for the packet process.
- Length : is the length of the data package: that means it is refer to the total length of the data in the packet.
 - Packet type: is two characters to recognize the packet whether it is a request or a replay.
 - Sub package : the format of the sub packet is:
 - Header and tailer : two characters.
 - Length : 2byte is the total length of the sub data packet.

- Data : the transmitted data , for example : the balance value which required to be topped up, Balance code , appliances states ... etc.

each operation has different header and tailer characters used to recognize the data which the sub packet contains.

In the following section a detailed descriptions of the sub systems operations is presented.

III. ELECTRIC PROVIDING SERVER SUB SYSTEM (EPSs.)

Block (1) of Fig (1) describes the Electric provider sub system (Eps) which consists of three units: electric provider server system unit , GSM unit, and the power stations status circuit. Electric provider server system unit programmed using (C#), whereas SQL server for database, and GSM AT commands are used to up the program with GSM unit (GSM modem).

One the other hand , power stations status circuit is designed based on the Arduino UNO (AT 2560) microcontroller to simulate the practical power status via three potentiometer resistor to represent the power drawn from each power station.

This circuit is attached to the server system via USB cable to inform it about the power which drawn from each station. Accordingly , the server contain a display window as shown in Fig (4) to display the acquired information to the administrator in order to enable him to increase or decrease the unit price to maintain the power consumption with in allowable limit. Fig (5) shows the window which help the system administrator to update the unit price value , where the system capsulate it in a packet before sending it to meters, where he can send a deferent value for each meter type or the same value for all meters if he choose all option from the shown drop box.

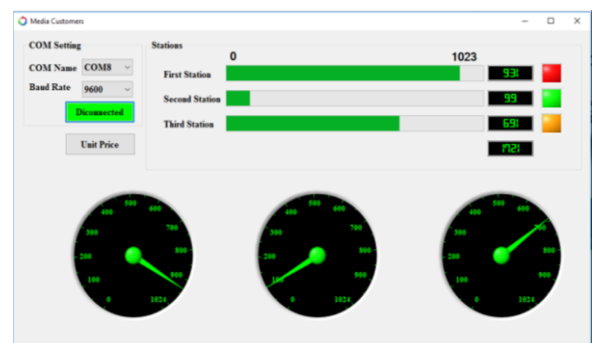


Fig 4. The power consumption station value as shown on EPS system



Fig 5. Updating the unit price window

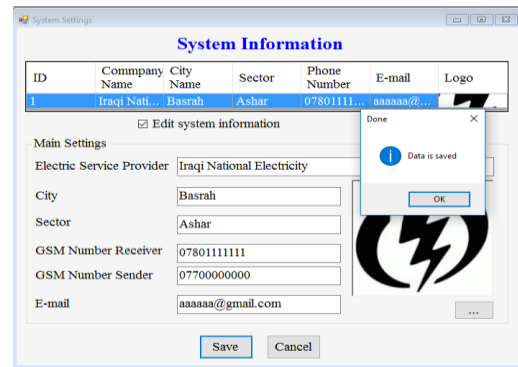


Fig 6. (b) system initialization, GSM ports

A. EPS initialization:

The (EPS) needs to initialization settings before operation , settings include : ports settings, system settings ,server settings , and specify the Users and admins of the system.

The following is a short description of each setting .

1. *The port setting:* to choose the ports of the GSM modems (sender modem and receiver modem) ,and power station status circuit .
2. *The system settings :* system settings include: ID, name ,sector, sever modem number, email ,and logo. This setting is very important to fix because the system used these setting in message packing , data transformation , and report printing.
3. *The server setting:* used to set the server name and the way to log in to the server either by windows authentication or SQL server authentication . SQL server authentication name and password of the server.
4. *Users and admins:* to save the users and administrators of the system by specify Unique username, password and tasks for each one. Figure (6) show the port and system setting window .

B. EPS Tasks:

The main responsibilities of EPS sub system are:

1. Store and manage the information of all the consumers.
2. In the server database, the system administrator enrolls each new meter in the database then fix the meter setting by sending some of the enrolled information to meter through USB cable to the meter microcontroller, these information include: meter number, server number, consumer number, password. Fig (7) shows the window of the meter enrolling and setting in server system.



Fig 7. meter enrolling (a) add new meter

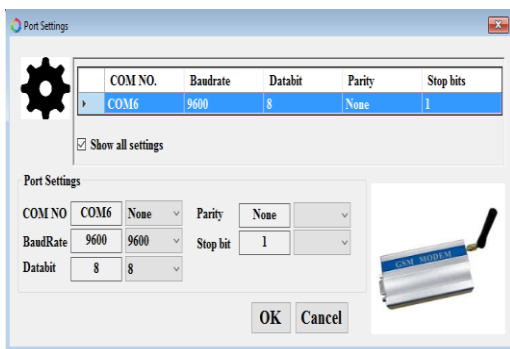


Fig 6. (a) system initialization , port setting



Fig 7. (b) meter setting

3. Manage the accounts of the administrator and other users and specify the permissions of each user.

4. Generate, store, manage the electricity balance cards codes in the server database as shown in Fig(8).
5. The presented work proposed five balance categories of the cards in Iraqi dinar, they are(50,000,100,000, 250,000,500,000,1000,000) IQD as shown in the top of the window.

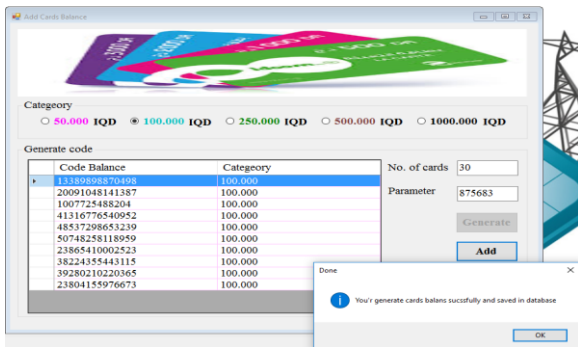


Fig 8. Balance card code recharging window in the proposed EPS system

6. Receive and processing the recharge balance requests and replay on it, two methods are designed for recharging process:
 - a. *Direct recharging*: in this method , the consumer can recharge his meter directly from (EPS) by enter the card code into the server via available clients, as shown in Fig (9) .
 - b. *Via mobile application*: in this method , the consumer can recharge his meter by sending the card code via the propped mobile application to the server using GSM .

when the consumer send the balance card code to the electricity provider server (EPS) by the proposed mobile application , EPS check if the balance card code is valid and send the balance amount to the consumer's meter if the card code available. After the meter received the balance amount packet, the meter saves the recharging information including: date, time ,card code and balance class, to save the rights of the consumer and provider if any error occurs. The server can ask the meter about the last recharging information to check if some defect occurred in the card code recharging , by comparing the meter reply information with the stored recharging information for this meter in the server database. It will check the packet, and add the new balance to the remainder balance of the meter to use it in the calculation equation to calculate the consumed balance and display it an LCD display, the meter also send a notification SMS to the consumer about the present balance after new recharging.

7. Update the unit price value for the consumers' meter in the server database by sending the new unite price to the meters using the GSM technology, and save this

unit price (value, date, time) in the server database. The presented work classifies buildings into three types: homes, commercial estate and governmental estate. The electricity provider system have a permission to determine different or equal unit price for each meter type. Therefore the system gives the service provider the possibility of contributing to encourage the consumer to rationalize electricity consumption by increase/decrease the price of the unit, with changing the seasons of the year or consumption peak times.

8. The System administrator can send a request about the last balance query to any desired meter, to query about the last recharging information .
9. Send an offers and advertising messages as SMS or emails to the consumer mobile or emails .
10. Activate/deactivate any specified meter by sending a request packet.
11. Monitor the power consumption stations as shown in Fig (4).

IV. SMART METER SYSTEM (SMS):

Smart meter is an electronic device that record electrical energy consumption in a unit of time. Fig (10) shows the block diagram of hardware design of smart meter which is controlled by the Arduino microcontroller. The other peripheral that attached to the microcontroller are used as a sensor and actuator in addition to the smart meter sub hardware design in this work is the modular approach where the overall design was first broken down into a functional block diagrams, with each block in Fig (9) representing a section of the circuit that carries out a specific function.

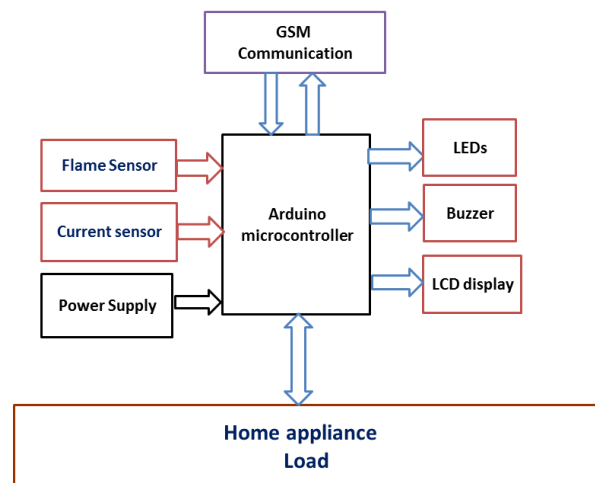


Fig 10. The block diagram of hardware design of smart meter

A. Smart Meter Initialization:

Each meter must be set before installing it in any building to be ready to work. Meter settings step is described in the first point of EPS task paragraph.

B. Smart Meter Tasks:

The smart meter in the proposed system designed to do many tasks beside the task of calculating the cost of consumed power , these tasks include :

1. Calculate the current that the premises appliance consumed each one minutes, update the unit price value in the meter , and display the required information on LCD.
2. Send the remainder balance value each one hour to EPS system.
3. Check and respond to any received request from the consumer mobile application or from the electricity provider server system, the type of the request will be illustrated in the following tasks.
4. Switch off the consumer premise appliance sequentially based on the programed priority of the appliance when the balance close to the given threshold value , this means that the meter switches off all the consumer premise appliance if the balance run out.
5. Notify the consumer if the balance is close to the threshold value and if the balance is run out.
6. Perform and replay to any consumer messages as : the remainder balance, a premise status, change the premise status and change the meter balance threshold value query.
7. Perform and reply to ESPs messages as a new balance, recharge, change unit price value and the last balance query.
8. Save the last balance information (card code ,class value, date, time) .
9. The meter is equipped with a flame sensor for securing.
10. The meter give a permission to the consumer to transfer balance amount to any other meter when the consumer request that by using the proposed mobile application.

C. Smart Meter Design

Hardware and software tools were utilized to design the proposed smart meter in this work, Arduino C language were used to program the microcontroller, The hardware components of smart meter design are: Arduino microcontroller, SIM900A GSM shield, LCD Display, current sensor, flame sensor, relays, buzzer and LED.

Fig (11) details the wire connection between the meter hardware components.

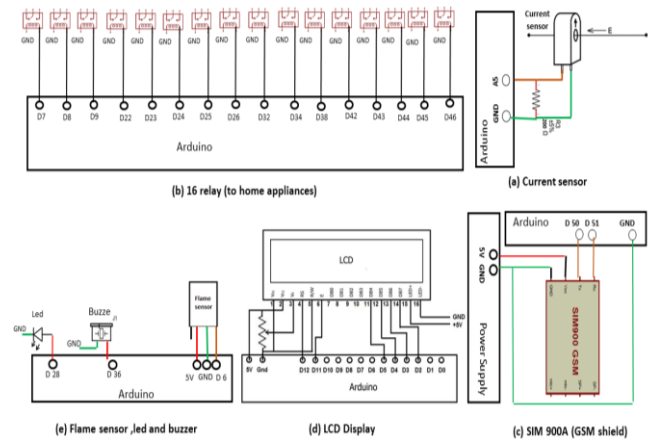


Fig 11. Wire connection of hardware component of the proposed smart meter

The benefits of use each one of the meter components are:

1. Arduino mega: are used to control on the meter components activities.
2. GSM shield : for data transmitting.
3. 4x16 LCD display: to show the necessary information for consumer , as the remaining balance, unit price , power , the amount of the consumed balance at the last minute.
4. Current sensor to detect the energy consumption.
5. Flame sensor : to protect the appliance from fire .
6. Led & buzzer : for alarm purposes.
7. 16 relays : to switch on/off the premises appliances, Fig (12) shows a sample of relay connection with the meter microcontroller and appliance .
8. Power supply : to supply the microcontroller and GSM shield with a power.

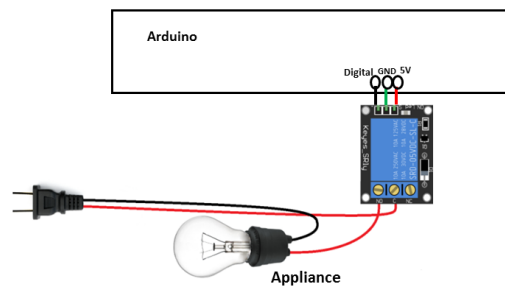


Fig 12.: A sample of the relay connection with the Arduino and appliance

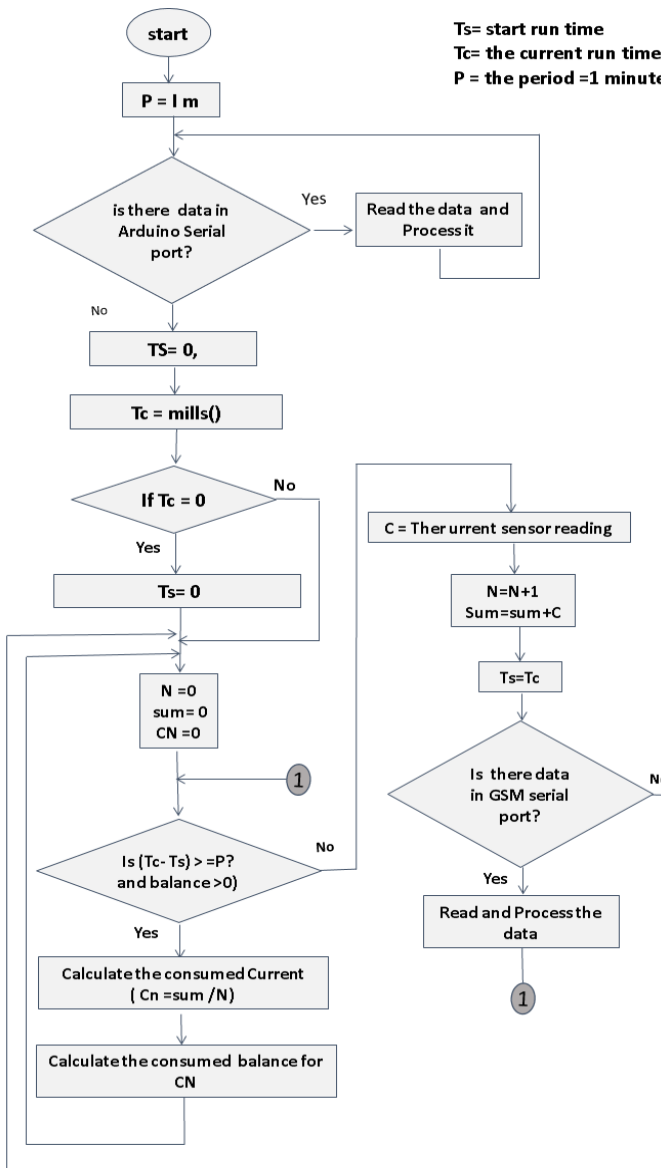


Fig 13. Show the sequence of the meter operations.

D. Meter Operations

After the setting and installing steps, the meter will be ready to work. installing steps refer to setup the meter in the consumers' premises by connecting the appliance of the premise in the specified ports of the meter (with meter relays) and connecting the main current wire which supplies the premises to the wire connected to the current sensor in the meter. Fig (13) show the meter sequences of operations.

The main steps (operations) in Fig (13) are : the current calculation step and Cn calculation balance step, in the Cn balance calculation process, the meter program reads the current sensor value periodically each 1 minute to:

1. calculate the consumed power.
2. calculate the consumed balance.

3. calculate the remaining balance in meter .
4. update these values on LCD.
5. And starting to switch off/on premises appliance if the balance reaches to a threshold value.

In this work the voltage value is assumed (220) and the power factor is (1) .The measured current is alternative, and the sensor is calibrated to measure a max of 100A AC. 100A is the RMS value of the maximum current the sensor can handle.

The following steps details the steps which are used to calculate the current value :

1. At first that needs to extract the measurable max peak-current.

$$i(\text{measured}) = \sqrt{2} * i(\text{rms_current}) = 1.414 * 100A = 141.4 A$$

2. The current at the output of the sensor is defined by its number of turns (here is 2000)

$$i(\text{sensor}) = i(\text{measured}) / nb_turns = 141.1A / 2000 = 0.0707A$$

3. As the current is alternative around 0 and to maximize measurement resolution, the max voltage at burden resistance should be :

$$\text{Max accepted voltage} / 2 = 2.5V.$$

4. Now we are going to compute the better Burden resistor value

$$R(\text{burden}) = U(\text{sensor}) / I(\text{sensor}) = 2.5V / 0.0707A = 35.4\Omega$$

5. EmonLib library are used to convert the raw data from analog input into a nice useful values.

$$\begin{aligned} \text{calibration_value} &= (i(\text{measured}) / i(\text{sensor})) / R(\text{burden}) \\ \text{calibration_value} &= (141.4 A / 0.0707A) / 33\Omega \\ \text{calibration_value} &= 2000/35\Omega = 60 \end{aligned}$$

6. 1480 is the number of sample used to compute a value. Now the power is calculated by :

$$\text{Power} = Irms * 220 . (\text{power in watt})$$

Where Irms is the calculated current by use the EmonLib and calibration .

The result value which resulted from the experiments are checked with a ampere meter .The program collect the results since 1 minute and increase N index after each detection operating , and if the time reached to 1 minute , the summation of the of the calculation current values divided on N (Cn) using: sum=sum/n , and the program will calculate the consumed balance at for this Cn , the program will do the following main steps:

- Subtract the consumed balance for this current from the remainder balance.

$$\text{Consumed balance} = p (\text{kw in minute}) * \text{unit price}.$$

New balance= remaining balance – consumed balance.

- Update the necessary data to show it on the LCD display.
- Check the balance with threshold value or if balance finishing to switch on/off the required appliances.

The home appliances will switched off automatically if the balance be less than the threshold value.

The Smart Mobile Application Sub system (SM app.):

V. THE SMART MOBILE APPLICATION SUB SYSTEM (SM APP.)

in this work is an Android application designed using MIT inventor2 app to design the interfaces , and TinyDB database to store and return the necessary data.

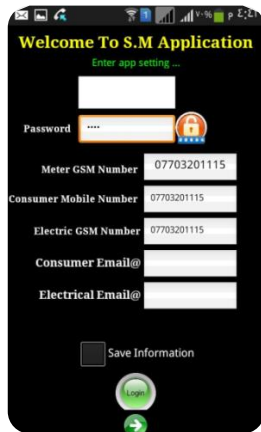


Fig 14. The mobile application setting Screen

A. Mobile application initializations:

The application must be set before using it , these setting involve: consumer mobile sim card number, meter GSM sim card number, Electric provider GSM modem sim card number, consumer Email and Electric provider email as shown in Fig(14).

The consumer can change the meter password by press key icon which shown on the right of the password field in the setting screen. The application proposed two way to change the password , the first way : by enter the previous password with the new as shown in the top part of the setting screen in Fig (15). And the second way by asking the meter to send a password setting code , in the case , when the consumer was forget the current password.



Fig 15. Changing the password screen

All these information are saved in TinyDB database to avoid the data losing when the mobile shutdown. These setting must be set by the consumer to activate the SMs app, this settings must be the same setting which enrolled in the electric provider server database because the system based on to check the transmitting packages based on the proposed matching protocol.

The application built a package for each function that is requested from the consumer to be understood for the other subsystems. The Electric provider server and smart meter of consumer , also the mobile application is unpacking each message it received from other sub systems , to extract the interesting data and show it in an easy way to the consumer.

The proposed mobile application use the consumer mobile, meter GSM and Electric provider GSM modem sim card numbers that given in setting information to pack , unpack, and check the transmitting system packages .

B. The Mobile Application Design :

Fig (16) show the main screen of the application which contain five icons, Each icon is used to select a specific task .

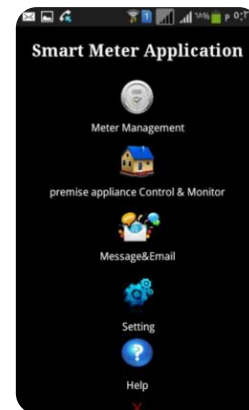


Figure (16) : Main screen of the proposed mobile application

C. The Meter Management Screen :

This screen helps the consumer to :
 recharging balance: the consumer write the balance card code in the specified textbox and press send , the application will send it after packing to EPSs using the application settings and matching protocol. recharging Screen as shown in Fig (17:A) .

- *Updating threshold value*: consumer enter the threshold value and the application will send it as a package to the meter, the meter depends on threshold to notify the consumer about the amount of the balance

expiration in the meter from meter management Screen as shown in Fig (17:A).

- *Transferring balance* : in this option the consumer enter the balance amount to be transformed to another meter via entering its number with the meter password as in Fig(17:A).

2. premises' appliance monitoring and controlling Screen

This screen helps the consumer to :

- *Check meter balance*: the consumer can check the remaining balance in his meter by sending check balance query, the application packing the request and send it to the meter, and when the meter answer , the application will unpack , check, and display the balance value to consumer and save it in a database. This option use home appliance control and monitoring screen as shown in Fig (17:B).

- *Control and monitor appliance* : the consumer can use the application to check The appliance status, and change appliance status, control and monitor the premises appliances by sending appliance status query or change appliance status request to meter. As shown Fig (17:B) .

3. *Message &Email Screen* : consumer can read the notification or advertising SMS which incoming from consumer meter or EP server in special inbox. Also it helps the consumer to send an email to EP server mail .

4. *Setting Screen* : the setting entire option is very important to the application. This option described in details in mobile application initializations paragraph.

5. *Help screen* : this screen help the consumer to read some instructions to Clarification about the usage of the application .

The presented mobile application is communicate with the Smart meter and Electric provider server by GSM technology based on SMS message . Also the proposed application do the following:

- Display the last unit price value that received from the meter and the last balance query replay constantly in home appliance control and monitoring Screen.
- Save all the incoming alarm , offer or notice SMS from ESPs GSM modem number or meter GSM number. as shown in Fig(17:C) .
- Also this application enable the consumer to send Email to EPSs from send email option Screen as shown in Fig (17:C).

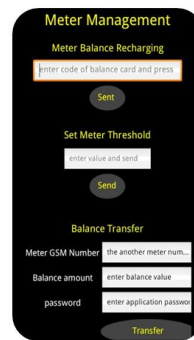


Figure (17:A)
Meter management Screen



Figure (17:B)
Home appliance control and monitor Screen



Figure (17:C)
SMS Inbox &Email sending Screen

VI. RESULT

In addition to all the details of the proposed system and its tasks, this work is distinguished from other previous works by combining the prepayment of electricity cost and the possibility of control and monitor the consumer's appliance status . Also the communication way is the GSM technology only. Moreover , the system gave Solutions for possible routes such as recharging errors Also the proposed protocol can be developed to a more complex way to increase the security .

VII. CONCLUSION

This paper proposes a design of Smart prepaid power system using GSM technology .The designed system helps to get rid of the difficulties which are resulted from the traditional energy billing , by using an intelligent electricity preparing system .This is achieved by a secured SMS among the composed subsystems. Consequentially the system gives consumer the possibility to control their home devices in easy way, the consumed electricity balance amount is calculated by a smart meter .Current sensor is used to measure the total current consumption as analog input to calculate the balance based on the entire unit price value .The electricity provider have the ability to change of the unit price value at any time by sending the new value to the smart meters. Also the system gives the consumer the possibility to monitor and control their premises appliance in an easy way .As a result this work will contribute So that shorten the large number of required staff that supposed to collect , calculate and process the electricity bills in the traditional way , this also will prevent possible error in the system component's . Concisely, the proposed system solve many problems of the traditional way to collect the electricity bills by shorten the time, efforts, human entry and error prone .

REFERENCES



- [1] A. Anmar, A. Muhannad, A. Nawaf, A. Essam, K. Yasin, M. Nazar, Experimental Study and Design of Smart Energy Meter for the Smart Grid, In Conference Record - IEEE Instrumentation and Measurement Technology, 2013.
- [2] CH. Atheena, R. Janardhanan and S. Ashok, Development of Inbuilt Energy Management Controller for Smart meter, IEEE, 2014.
- [3] A. Swati, N.M. Gourang, K. Arti, Design and Implementation of Smart Three Phase Energy Meter, International Conference on Smart Grid and Clean Energy Technologies 2016.
- [4] A. Olawuni and M. Omotayo, Design of SMS Prepaid Energy Meter for a Cashless Economy with Recharge Option and Bypass, AJER, e-ISSN: 2320-0847 p-ISSN: 2320-0936 Volume-5, Issue-6, pp-74-78, 2016.
- [5] K. Yasin, K. Ersan, A Low Cost Smart Metering System Design for Smart Grid Applications, International Conference - 8th Edition Electronics (IEEE), Computers and Artificial Intelligence, 30 June -02 July, 2016, Ploiesti, ROMANIA.
- [6] Q. Julius, O. B. Kwame, A Retrofit Design Science Methodology for Smart Metering Design in Developing Countries, International Conference on Computational Science and Its Applications, 15th, 2015.
- [7] R. Hariharan, Design of controlling the smart meter to equalize the power and demand based on virtual instrumentation, International Conference on Power, Energy and Control (ICPEC), 2013.
- Applications, (IJCA), 2012.
- [8] Dwijen Rudrapal, Smita Das, Goutam Pal, "SMS Based Load Shedding Period Control System", International Journal Of Computer Applications (0975 - 8887), Volume 29- No.7, September 2011.
- [9] Herman Chung-Hwa Rao, Di-Fa Chang, Yi-Bing Lin, "ISMS: An Integration Platform For Short Message Service And IP Networks", 0890-8044/01/\$10.00 2001 IEEE, March/April 2001.
- [10] Simon So, "The Development Of A SMS-Based Teaching And Learning System", Journal Of Educational Technology Development And Exchange (JETDE), Volume 2, No. 1, October, 2009.
- [11] N. Mavrikakis, I. Androulidakis, D. Pylarinos, K. Siderakis, "A Labview Based Leakage Current Monitoring System For HV Insulators", Journal Of Engineering Science And Technology Review, 1 December 2015.
- [12] Dragan Mlakic, Srete Nikolovski, Emir Alibasic, "Designing Automatic Meter Reading System Using Open Source Hardware And Software", International Journal Of Electrical And Computer Engineering (IJECE), Vol. 7, No. 6, December 2017.
- [13] Donald Wilcher, "Learn Electronics With Arduino", President And Publisher: Paul Manning, 2012.
- [14] M.C. Juan Antonio Arízaga, Dr. Jorge De La Calleja, Ing. Roberto Hernández, Dr. Antonio Benitez, "Automatic Control For Laboratory Sterilization Process Based On Arduino Hardware", Researchgate, 978-1-61284-1325-5/12/\$26.00 ©2012 IEEE, February 2012.
- [15] Maya Zayats, Bilha Willner, Itamar Willner, "Design Of Amperometric Biosensors And Biofuel Cells By The Reconstitution Of Electrically Contacted Enzyme Electrodes", WILEY-VCH Verlag GmbH & Co. KGaA, Weinheim, Electroanalysis 20, No. 6, 583 - 601, 2008.
- [16] Andi Adriansyah, Akhmad Wahyu Dani, "Design Of Small Smart Home System Based On Arduino", The 7th - Electrical Power, Electronics, Communications, Controls, And Informatics International Seminar, 2014.
- [17] Xiaohui Qu, Siu Chung Wong, Chi K. Tse, "Color Control System For RGB LED Light Sources Using Junction Temperature Measurement", The 33rd Annual Conference Of The IEEE Industrial Electronics Society (IECON), Nov. 5-8, 2007.

Design and Implementation of Load Balancing System for a Smart Home

Abdulmuttalib T. Rashid¹ & Mofeed T. Rashid²

Electrical Engineering Department

University of Basrah / Basrah, Iraq

abdturky@gmail.com¹ mofid76@gmail.com²

Abstract— The electrical energy measurement, controlling, monitoring and saving for homes are today have a great interested in the field of research. In this paper, a new management system is designed and constructed in order to perform measurement, controlling, monitoring, and saving the electrical energy. A three phase load balance system has been designed for home smart meter. The principal work of this system is based on measure the current of the three-phase lines, and then adjusts the distributed current by replacing the load of some power outlets. The energy measured by this system can be arranged in a time schedule to produce a monitoring platform with graphical user interface (GUI). This GUI displays the real-time power information to give an idea about the amount of consumed energy and also can be used for a smart meter system.

Keywords—Monitoring system; Load balance; Smart meter; Contactors.

I. INTRODUCTION

Currently, consumption of electrical energy is the most common problem in smart home and building environments which the amount of electrical energy consumed by each device in real time is unknown. Accordingly, the monitoring of electrical energy consumption data of electrical equipment is becoming progressively important. In recent field of research, the design of efficient electrical management system for homes or buildings is an active subject.

Electrical energy management system is the combination of technologies and services through home networking for an intelligent living environment. Smart power outlets are considered as the most commonly used electrical devices in modern home environments. They could measure consumption of electrical energy and control the operation of the electrical equipment. The intelligent power outlets have recently appeared as a new form for home energy management that can control electrical equipment and produce secure electrical environment [1-3].

Many researchers have contributed in the development of electrical energy meters. The first generation of these meters were electromechanical meters and then evolved to emulate the most accurate measurements, less expensive and safe which represented by electronic meters. Then the researchers developed the methods of the transmitting data to the main

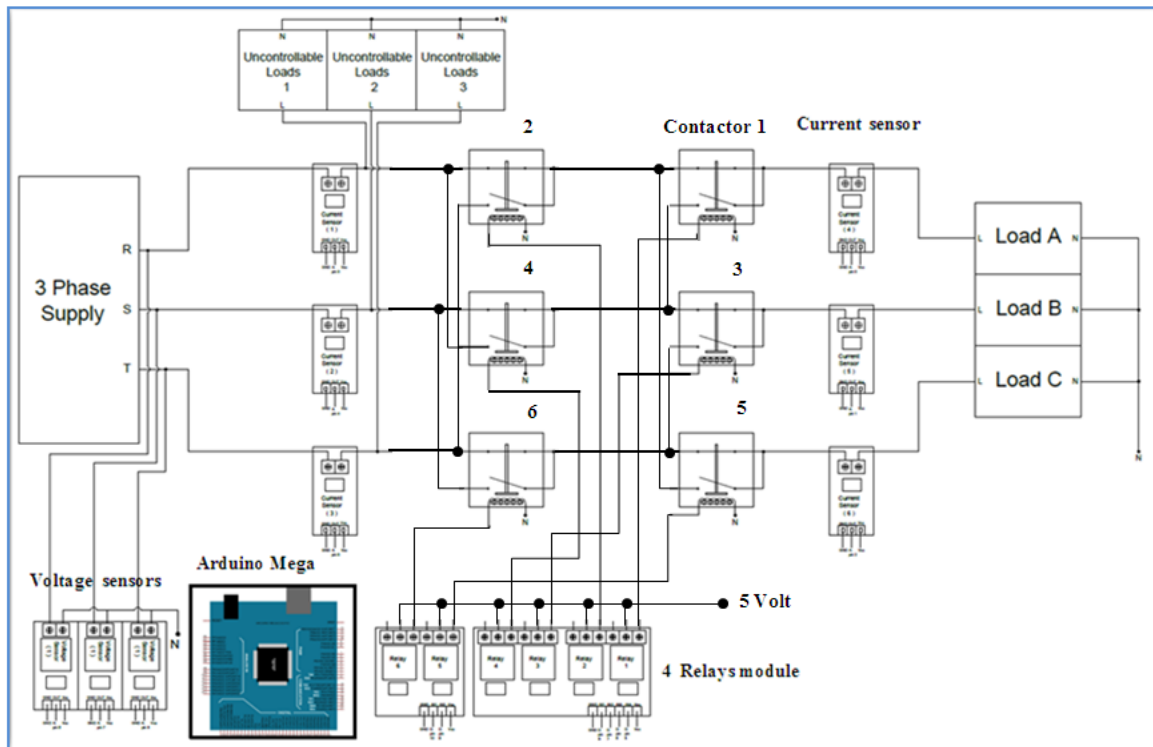
monitoring and control unit, which were use wiring for data transmission and then evolved into wireless communication systems [4-6].

Electrical energy management system can be addressed as one of the developments in the electrical energy meters. An intelligent technique to detect any new devices installed in a smart environment is presented [7]. This technique capable to monitor and identify any load, but it is unable to accumulate power data. A smart home with a ZigBee-based power socket is constructed [8]. The weakness of this system is appearing in the measuring of the electrical energy consumption. Another system with a ZigBee-based smart power outlet network is proposed for gathering power consumption data [9, 10]. This system not has any protection in an emergency. A method that based on the ZigBee communication and infrared remote control is proposed to perform active control for reducing standby power using sensor information, but it lacks to overload protection and detection [11]. A ZigBee-based monitoring system with self-protection is constructed [12]. This system is equipped each power socket with an energy metering integrated circuit IC to compute power parameters from the socket. It produces a higher device costs and more complex circuit structure. In addition, they just focused on two sockets protection in a branch.

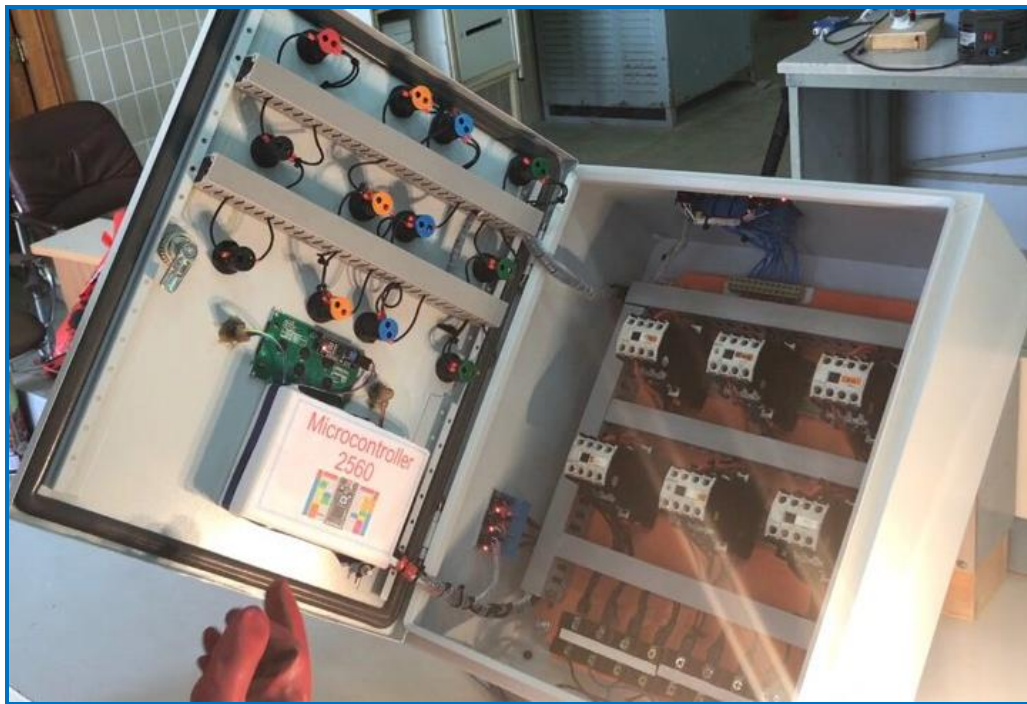
In this paper, the electrical energy management method has been designed and implemented to control, monitor, and save the electrical energy. A three-phase load balance system is constructed by replacing the loads of some power sockets while the energy measuring system gives an idea about the amount of consumed electrical energy. Finally, the proposed comprehensive system can be represented as a three phase load balance smart meter.

II. SYSTEM ARCHITECTURE AND OPERATION

Load balance, power monitoring and controlling can be achieved by three-phase power management system (TPPMS). This section presents the architecture of TPPMS realization. Fig. 1 (a) shows the circuit diagram of TPPMS for one home while the realization of load balance system is shown in Fig. 1 (b). The following subsections describe the measuring module; the monitoring and the load balance modules where all installed in the main home breaker.



(a)

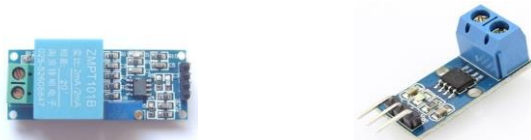


(b)

Fig.1. The three phase load balance system (a) The circuit diagram (b) The realization of three phase load balance system

A. The measuring module

The measuring module works as a three-phase metering circuit. The electrical power meter is designed to sense and measure the consumed electrical energy in home to provide a balance load for the three-phase supply and monitor the current, voltage and electrical power per hour. The design and implementation of the three-phase energy metering circuit is achieved by using an Atmega2560 microcontroller circuit. Three ZMPT101B voltage sensors are used in this module to measure the voltage of each phase of the three-phase supply as shown in Fig.2 (a). The current passes at each phase in this module is measured by using the ACS712 Fully Integrated, Hall Effect-Based Linear Current Sensor IC as shown in Fig.2 (b). This sensor has a copper conduction path. The current passes through this path produce a magnetic field that converts by the Hall IC into a proportional voltage.



a. The ZMPT101B voltage sensor. b. The ACS712 current sensor.

Fig.2. Voltage and current sensors.

Six current sensors are used in this system. Three of these sensors are connected directly to the three-phase supply to measure the total three-phase supply currents. The other three current sensors are connected across the three controllable loads to measure the three-phase current drawn by these loads. The controllable loads have the ability to change their connections to the three-phase supply. The difference between the supply currents and the controllable load currents represent the currents drawn by the uncontrollable loads. By knowing the currents drawn by the uncontrollable loads we can rearrange the connection of the controllable loads in a manner that gives the best balance to the three-phase supply currents. The electrical energy measurement in this module depends on the reading of both the current and voltage sensors. The real power is computed by taken the sum of the instantaneous values of current and voltage for several times and divide it by the number of these times [13].

$$W = \frac{1}{N} \sum_{j=1}^N v_j i_j \quad (1)$$

Where v_j and i_j represent the instantaneous voltage and current at j time respectively. N is the number of period. Since the sampling rate of the voltage is V_{rms} and the sampling rate of the current is I_{rms} then the real power is computed by the following equation:

$$W = v_{rms} i_{rms} pf \quad (2)$$

Where pf is the power factor. v_{rms} and i_{rms} are computed from the following equations:

$$v_{rms} = \sqrt{\sum_{j=1}^N \frac{v_j^2}{N}} \quad (3)$$

$$i_{rms} = \sqrt{\sum_{j=1}^N \frac{i_j^2}{N}} \quad (4)$$

B. The monitoring module

The monitoring module could monitor the current, voltage, power factor and electrical energy that consumed at each phase in main home breaker. The data which collected by the monitoring and control module are necessary to work of other modules and can be used to implement a smart meter system. The periodically monitoring of electrical energy consumed in home helps the customer to control and save the electrical energy. The HD44780 LCD has been used for the monitoring module which displays the information in 4 rows with 20 characters for each row.

C. The load balance module

The three phase load balance system is characterized by a three-phase balancing unit that represents the important part because it contributes in the load balancing of the three phase supply in order to reduce the probability of damages. This module can detect any device connected to the power outlet and then this module replaces the connection of this outlet to a suitable phase that satisfy the best balance among phases which, several contactors have been used for replacement process. If all homes in distribution station have the same balance system then this process make the load is balance which leads to prevent the phase fault, and also helps to use most of the electrical energy that generated by main station. Six relays (see Fig. 3) and six contactors are used in this module to swap three controllable loads (load A, load B and load C) among the supply phases as shown in Fig. 1. The relay boards are used as complete electrical isolation between the control signal and the controlled circuits.



(a) Two channels

(b) Four channels.

Fig. 3. The relay modules.

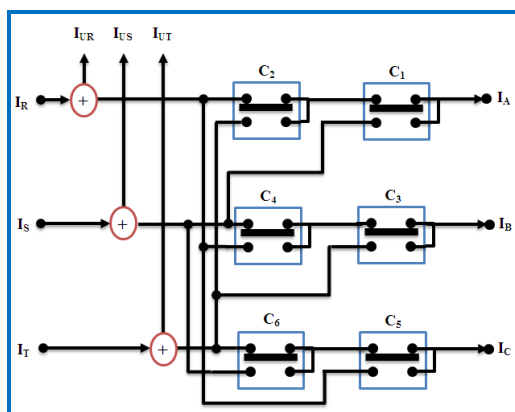
A contactor is an electrical control switch used for switching an electrical power circuit, similar to a relay except with higher current ratings. The contactor has four components (see Fig. 4 (a)): The contacts are the current carrying part of the contactor. This includes power contacts and auxiliary contact. The coil provides the driving force to close the contacts.

Auxiliary Block this is for additional auxiliary contacts. Unlike general-purpose relays, contactors are designed to be directly connected to high-current load devices.

Fig. 4 (b), shows the block diagram for contactors (C_1 , C_2 , C_3 , C_4 , C_5 and C_6), where each two contactors are used to swap one of the controllable loads (A, B and C) among the three supply phases. The implementation of contactors board is shown in Fig. 4 (c).



(a)



(b)



(c)

Fig. 4. The contactors board. (a) The contactor (b) The block diagram (c) The contactors circuit implementation.

D. The load balance algorithm

This section describes the algorithm for measuring current, voltage, power factor, and electrical energy consumed by each

phase. Also, this algorithm used to control the balancing of the three phase supply currents. The steps for investigation this algorithm is as follows:

1. Measuring the total current of each phase of the three phase supply I_R , I_S , and I_T . Assume load A is connected to phase R, load B is connected to phase S and load C is connected to phase T.
2. Measuring the voltage of each phase of the three phase supply V_R , V_S , and V_T .
3. Measuring the current of each the three controllable loads I_A , I_B , and I_C .
4. Calculating the currents of the uncontrollable loads.

$$\left. \begin{aligned} I_{UR} &= I_R - I_A \\ I_{US} &= I_S - I_B \\ I_{UT} &= I_T - I_C \end{aligned} \right\} \quad (5)$$

5. Construct the second column in table 1 which represents the connectivity between the supply phases and the controllable loads. This connectivity depends on all the predicated status of the contactors which shown in the first column.
6. Construct the index values (third column) according to the following equation.

$$Index = i + 4j + 16k \quad (6)$$

Where the variable i , j and k represent the status of contactors in load A, B and C. Values of these variable for each load are:

(0) for contactors status ($C_2, C_4, C_6 = \text{OFF}$, $C_1, C_3, C_5 = \text{OFF}$)

(1) for contactors status ($C_2, C_4, C_6 = \text{OFF}$, $C_1, C_3, C_5 = \text{ON}$)

(2) for contactors status ($C_2, C_4, C_6 = \text{ON}$, $C_1, C_3, C_5 = \text{OFF}$).

7. The total current of each phase at each row is computed in fourth column according to the contactors status in first column and the index value (third column). When any contactor is OFF then it represents by logic 0 else it represents by logic 1 as shown in first column in table 1. For each value of index the total currents for all phase are computed as follows:

$$\left. \begin{aligned} I_R(index) &= I_{UR} + \text{NOT}(C_1)\text{NOT}(C_2)I_A + C_4I_B + C_5I_C \\ I_S(index) &= I_{US} + C_1I_A + \text{NOT}(C_3)\text{NOT}(C_4)I_B + C_6I_C \\ I_T(index) &= I_{UT} + C_2I_A + C_3I_B + \text{NOT}(C_5)\text{NOT}(C_6)I_C \end{aligned} \right\} \quad (7)$$

8. For each index value compute the maximum and minimum values for the total currents.

$$Max(index) = \text{Max}(I_R(index), I_S(index), I_T(index)) \quad (8)$$

$$Min(index) = \text{Min}(I_R(index), I_S(index), I_T(index)) \quad (9)$$

9. For each index value compute the deviation D which represents the difference between maximum and minimum values.

$$D(\text{index}) = \text{Max}(\text{index}) - \text{Min}(\text{index}) \quad (10)$$

10. The minimum value from the deviation column in table 1 means the best case for balancing. The full balance is occurs when this value of deviation equal to zero.

Table 1. List all the contactors status to choose the best load balances.

| Contactors status | | | | | | Connectivity | | | Index | Total currents | | | Deviation |
|-------------------|----------------|----------------|----------------|----------------|----------------|--------------|-----|-----|-------|---|---|---|-----------|
| C ₆ | C ₅ | C ₄ | C ₃ | C ₂ | C ₁ | C | B | A | | I _T | I _S | I _R | |
| 0 | 0 | 0 | 0 | 0 | 0 | T→C | S→B | R→A | 0 | I _{UT} +I _C | I _{US} +I _B | I _{UR} +I _A | D(0) |
| 0 | 0 | 0 | 0 | 0 | 1 | T→C | S→B | S→A | 1 | I _{UT} +I _C | I _{US} + I _B +I _A | I _{UR} | D(1) |
| 0 | 0 | 0 | 0 | 1 | 0 | T→C | S→B | T→A | 2 | I _{UT} + I _C + I _A | I _{US} + I _B | I _{UR} | D(2) |
| 0 | 0 | 0 | 1 | 0 | 0 | T→C | T→B | R→A | 4 | I _{UT} +I _C + I _B | I _{US} | I _{UR} + I _A | D(4) |
| 0 | 0 | 0 | 1 | 0 | 1 | T→C | T→B | S→A | 5 | I _{UT} +I _C + I _B | I _{US} +I _A | I _{UR} | D(5) |
| 0 | 0 | 0 | 1 | 1 | 0 | T→C | T→B | T→A | 6 | I _{UT} +I _C +I _B +I _A | I _{US} | I _{UR} | D(6) |
| 0 | 0 | 1 | 0 | 0 | 0 | T→C | R→B | R→A | 8 | I _{UT} +I _C | I _{US} | I _{UR} +I _B + I _A | D(8) |
| 0 | 0 | 1 | 0 | 0 | 1 | T→C | R→B | S→A | 9 | I _{UT} +I _C | I _{US} +I _A | I _{UR} +I _B | D(9) |
| 0 | 0 | 1 | 0 | 1 | 0 | T→C | R→B | T→A | 10 | I _{UT} +I _C + I _A | I _{US} | I _{UR} +I _B | D(10) |
| 0 | 1 | 0 | 0 | 0 | 0 | R→C | S→B | R→A | 16 | I _{UT} | I _{US} + I _B | I _{UR} +I _C +I _A | D(16) |
| 0 | 1 | 0 | 0 | 0 | 1 | R→C | S→B | S→A | 17 | I _{UT} | I _{US} +I _B +I _A | I _{UR} +I _C | D(17) |
| 0 | 1 | 0 | 0 | 1 | 0 | R→C | S→B | T→A | 18 | I _{UT} + I _A | I _{US} + I _B | I _{UR} +I _C | D(18) |
| 0 | 1 | 0 | 1 | 0 | 0 | R→C | T→B | R→A | 20 | I _{UT} + I _B | I _{US} | I _{UR} +I _C +I _A | D(20) |
| 0 | 1 | 0 | 1 | 0 | 1 | R→C | T→B | S→A | 21 | I _{UT} + I _B | I _{US} +I _A | I _{UR} +I _C | D(21) |
| 0 | 1 | 0 | 1 | 1 | 0 | R→C | T→B | T→A | 22 | I _{UT} +I _B + I _A | I _{US} | I _{UR} +I _C | D(22) |
| 0 | 1 | 1 | 0 | 0 | 0 | R→C | R→B | R→A | 24 | I _{UT} | I _{US} | I _{UR} +I _C +I _B +I _A | D(24) |
| 0 | 1 | 1 | 0 | 0 | 1 | R→C | R→B | S→A | 25 | I _{UT} | I _{US} +I _A | I _{UR} +I _C +I _B | D(25) |
| 0 | 1 | 1 | 0 | 1 | 0 | R→C | R→B | T→A | 26 | I _{UT} + I _A | I _{US} | I _{UR} +I _C +I _B | D(26) |
| 1 | 0 | 0 | 0 | 0 | 0 | S→C | S→B | R→A | 32 | I _{UT} | I _{US} + I _C + I _B | I _{UR} +I _A | D(32) |
| 1 | 0 | 0 | 0 | 0 | 1 | S→C | S→B | S→A | 33 | I _{UT} | I _{US} +I _C +I _B +I _A | I _{UR} | D(33) |
| 1 | 0 | 0 | 0 | 1 | 0 | S→C | S→B | T→A | 34 | I _{UT} + I _A | I _{US} + I _C + I _B | I _{UR} | D(34) |
| 1 | 0 | 0 | 1 | 0 | 0 | S→C | T→B | R→A | 36 | I _{UT} + I _B | I _{US} + I _C | I _{UR} +I _A | D(36) |
| 1 | 0 | 0 | 1 | 0 | 1 | S→C | T→B | S→A | 37 | I _{UT} + I _B | I _{US} +I _C +I _A | I _{UR} | D(37) |
| 1 | 0 | 0 | 1 | 1 | 0 | S→C | T→B | T→A | 38 | I _{UT} + I _B + I _A | I _{US} + I _C | I _{UR} | D(38) |
| 1 | 0 | 1 | 0 | 0 | 0 | S→C | R→B | R→A | 40 | I _{UT} | I _{US} + I _C | I _{UR} +I _B +I _A | D(40) |
| 1 | 0 | 1 | 0 | 0 | 1 | S→C | R→B | S→A | 41 | I _{UT} | I _{US} + I _C +I _A | I _{UR} +I _B | D(41) |
| 1 | 0 | 1 | 0 | 1 | 0 | S→C | R→B | T→A | 42 | I _{UT} + I _A | I _{US} +I _C | I _{UR} +I _B | D(42) |

Table 2. Comparison the current reading of our system with the clamp meter.

| Clamp meter (Amp.) | ACS712 Current Sensor (Amp.) |
|--------------------|------------------------------|
| 0.81 | 0.821 |
| 1.64 | 1.643 |
| 3.25 | 3.227 |
| 6.4 | 6.436 |

III. EXPERIMENTAL RESULTS

Two experiments are implemented to test the performance and accuracy of the load balance and monitoring system. The first experiment (see Fig. 5) is used to test the accuracy of the load balance system with respect to the laboratory reading. The experiment is repeated for different loads and the results recorded in three tables. The table 2 is for measuring the currents with respect to (Fluke 325) clamp meter which has 2% accuracy. The table 3 is to compare the voltage reading with respect to the (Fluke 83V) Industrial Multi-meter which has $\pm(0.5\% + 2)$ accuracy. The table 4 is to compare the power factor and consumed power for different values of loads with respect to the (Fluke) wattmeter has $\pm(0.5\% + 2)$ accuracy. All the results show that the designed system produces good accuracy with respect to the laboratory reading.

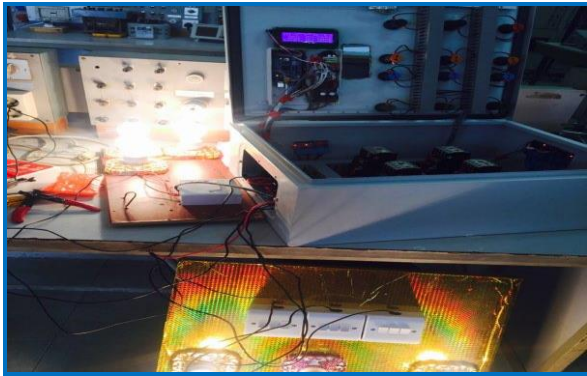


Fig. 5. The measuring of the currents, the voltages, the power and the power factor.

Table 3. Comparison the voltage reading of our system with the voltmeter.

| | Voltmeter (V) | AC Voltage sensor (V) |
|---------|---------------|-----------------------|
| Phase 1 | 219.5 | 220 |
| Phase 2 | 218.7 | 218 |
| Phase 3 | 219.9 | 219.5 |

Table 4. Comparison the power reading of our system and the Wattmeter.

| Wattmeter reading | | Smart meter | |
|----------------------|--------------|----------------------|--------------|
| Power / phase (Watt) | Power factor | Power / phase (Watt) | Power factor |
| 95 | 0.952 | 94.05 | 0.95 |
| 190.2 | 0.951 | 188 | 0.948 |
| 376.02 | 0.947 | 357.1 | 0.944 |

The second experiment (see Fig. 6) is to test the performance of the designed balance system with respect to number of controllable loads. That is mean, the experiment is repeated for different number of contactors since each controllable load needs two contactors for swapping among supply phases. Fig. 7 shows that as the number of controllable loads increases the currents balancing among supply phases also increase. From this figure we found that five controllable loads give about 90% currents balancing accuracy and 100% accuracy needs more than five controllable loads. The increasing of the controllable loads leads to increase the cost because the numbers of contactors also increase.

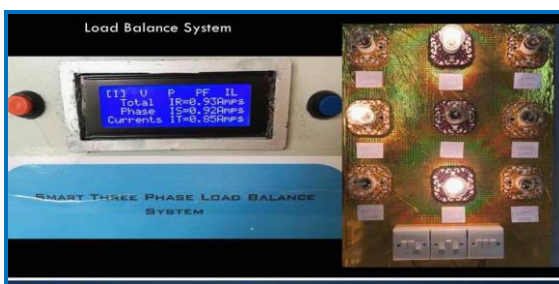


Fig. 6. The performance analysis for different number of controllable loads.

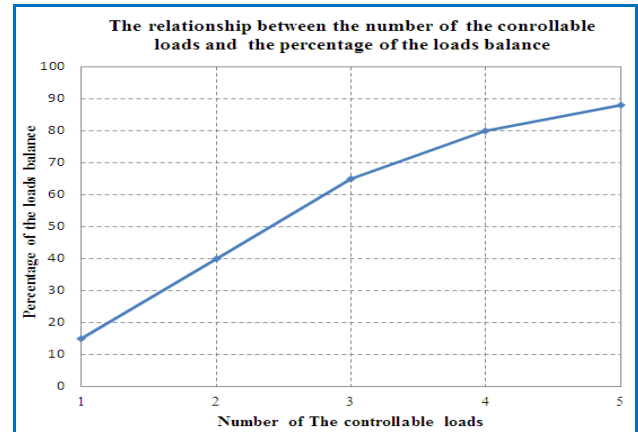


Fig. 7. The percentage of loads balance with respect to the number of the controllable loads.

IV. CONCLUSIONS

In this paper a proposed system for measuring, balancing and monitoring the three-phase supply in smart meter is introduced. This system has a good accuracy with respect to the laboratory reading when measuring the three-phase currents, voltages, powers and power factor. This system investigates the load balancing with a good percentage when used three controllable loads. The measuring system helps the user to take an idea about the amount of kilowatt hours consumed by customer that helps to take a right decision to minimize the using of electrical energy and also, it is useful in design a smart meter for each home. The designed system has the feature to use the local wire for each power socket in main electricity circuit. This means we not need to use a wireless system to transfer the measuring data to main control system.

This system can be scalable to balance the loads on the reign power transformer by applying it on all the homes connected to this power transformer. This process helps to reduce the occurrences of phase fault and helps to balance the loads on the main power station.

V. ACKNOWLEDGMENT

The authors gratefully acknowledge the fourth year students (Mohammed Q. Abdul Jalil, Marwan k. jabbar, Safaa A. Tabaan, and Anwer M. Hameed) in the college of Engineering for their grateful support.

REFERENCES

- [1] Y. Hiranaka, Y. Sato, T. Taketa, and S. Miura, "Smart power outlets with cross-layer communication," in Proceedings of the 13th International Conference on Advanced Communication Technology (ICACT '11), pp. 1388–1393, Phoenix Park, The Republic of Korea, February 2011.
- [2] T. Noma and Y. Ookuma, "Power and safety management of electrical appliances in a smart power distribution system," in Proceedings of the IEEE International Conference on Consumer Electronics (ICCE '11), pp. 511–512, Las Vegas, Nev, USA, January 2011.
- [3] A.Heller and C. Orthmann, "Wireless technologies for the construction sector—requirements, energy and cost efficiencies," Energy and Buildings, vol. 73, no. 4, pp. 212–216, 2014.



- [4] Mofeed T. Rashid, "Design and Implementation of Smart Electrical Power Meter System," Iraq J. Electrical and Electronic Engineering, Vol.10, No.1, pp. 1-14, 2014.
- [5] J. Byun, B. Jeon, J. Noh, Y. Kim, and S. Park, "An intelligent self-adjusting sensor for smart home services based on ZigBee communications," IEEE Transactions on Consumer Electronics, vol. 58, no. 3, pp. 794–802, 2012.
- [6] D.-M. Han and J.-H. Lim, "Smart home energy management system using IEEE 802.15.4 and zigbee," IEEE Transactions on Consumer Electronics, vol. 56, no. 3, pp. 1403–1410, 2010.
- [7] A. Elzabadani, A. Helal, B. Abdulrazak, and E. Jansen, "Self-sensing spaces: smart plugs for smart environments," in Proceedings of the 3rd International Conference on Smart Nomes and Health Telematics, pp. 91–98, Magog, Canada, July 2005.
- [8] G. Song, F. Ding, W. Zhang, and A. Song, "A wireless power outlet system for smart homes," IEEE Transactions on Consumer Electronics, vol. 54, no. 4, pp. 1688–1691, 2008.
- [9] Mofeed T. Rashid, "Design and Implementation of Wireless Electric Power Meter Based on XBee Model", Iraqi Journal for computer and informatics (IJCI), Vol. 1, No. 1, pp. 15-19, 2014.
- [10] K. Abe, H. Mineno, and T. Mizuno, "Development and evaluation of smart tap type Home Energy Management System using sensor networks," in Proceedings of the IEEE Consumer Communications and Networking Conference (CCNC '11), pp. 1050–1054, Las Vegas, Nev, USA, January 2011.
- [11] J. Han, C.-S. Choi, and I. Lee, "More efficient home energy management system based on ZigBee communication and infrared remote controls," IEEE Transactions on Consumer Electronics, vol. 57, no. 1, pp. 85–89, 2011.
- [12] L.-C. Huang, H.-C. Chang, C.-C. Chen, and C.-C. Kuo, "A ZigBee-based monitoring and protection system for building electrical safety," Energy and Buildings, vol. 43, no. 6, pp. 1418–1426, 2011.
- [13] G. n. Stenbakken, "High-Accuracy Sampling Wattmeter", IEEE Transaction on Instrumentation and Measurement. VOL. 41. NO.6,1992.

State Feedback Control based Genetic Algorithms of a Modified Cuk Converter

Nashwan Saleh Sultan

Electrical Power Technology Engineering

Technical Engineering College / Mosul, Northern Technical University

Mosul, Iraq

Sultan_nashwan@yahoo.com

Abstract- The present work that includes a genetic algorithm technique programed as intelligent controller. It designed to control the output voltage response of the modified DC-DC Cuk converter. The modified Cuk DC-DC converter examined and studied. Changes involve coupling the two coils around one mutual core. A exact classical of converter is represented and derived using differential equations and state space representation, then a national feedback method designed and controlled for the modified DC-DC Cuk converter using a decimal coded genetic algorithm with a modified selection method. The open and closed loop output voltage responses have been analyzed, and studied; it shows a great improvement in the output performance.

I. INTRODUCTION

Switching Mode Power Supplies (SMPSs) get more interest and importance with the technologic advance all over the world.^[1] They can be classified into a few basic types such as buck, boost, and Cuk converters,^[2] in addition to that, many various types were derived from the basic types. These modifications produce more efficiency over the basic types, or suffice specific requirements of certain operational circumstances.^[3]

Evolutionary algorithms ,on the other hand, have been occupied a considerable portion of the researches in many fields of science.^[4] Since 1975 when (*John Holland*) proposed the idea of simulating the operators of the Darwinian evolution computationally to reproduce a group of possible solutions for a certain problem from a random generated group. Then evaluates these solution throughout the consecutive generations in order to obtain the best (*optimal*) solution for the problem ^[5] . The improvement performance of modified Cuk converter based on practical swarm optimization ^[6] . The present work tries to design a feedback controller for the Cuk convertor to improve its performance using genetic algorithm.

II. SYSTEM DESCRIPTION:

The modified dc-dc Cuk converter is one of the numerous prospered modified converters, that have been completed to the usual Cuk DC-DC convertor. This has been finished by winding the dual coils of the DC-DC convertor about a sole core with the tall joint among these coils as exposed in figure (1).

This modified has completed to attain several advantages finished the mutual DC-DC Cuk convertor, such as the skill to diminish the wave current to zero, if good turn ratio and link constant chosen. Also, the adapted DC-DCCuk convertor produced a converter with a lower weight, lower cost, and smaller size.

The study of a system in the control process, which created three chief difficulties, which can be observed in scheme dynamics, structure documentation or modeling, and scheme control. Since adapted DC-DC Cuk convertor covers a four energy storing fundamentals (C_1 , C_2 , L_1 , L_2), so; the system dynamics are stated by a fourth command state space depiction.

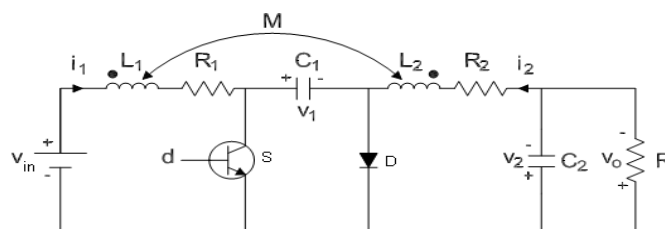


Fig. 1. The Modified dc-dc Cuk Converter Circuit

The converter works with two modes to produce complete dc level output conversion .^[6]:

Mode 1: Afterward the switch is ON, as in figure (2.a):

The capacitor (C_1) emotional by the electrical foundation when the switch twisted ON, the current complete (L_1) rises

equivalently with the duty cycle ratio of the power switch. The diode can be opposite prejudiced, and the capacitor (C1) can be missed its charge done two directions; through the locked switch to its load and (C₂), and finished (L₂) formerly (L₁) by the joint core.

Mode 2: After the switch is turn OFF, as in figure (2.b): The diode can be advanced biased and the first capacitor (C₁) can be recharged done the electrical source, the made voltage complete the mutual core and first inductor (L₁).

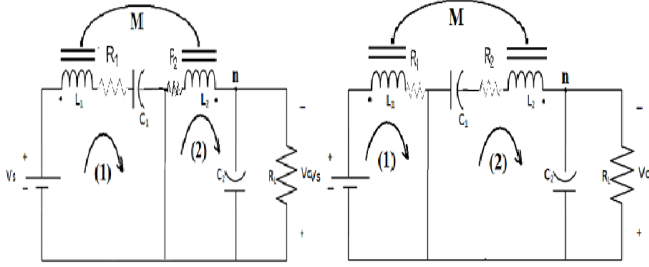


Fig. 2. a. Mode 1 (switch on) b. Mode 2 (switch off)

The circuit mathematical classical and the current track are the similar into the together inductors, and formerly one will use the arithmetical sum to direct the relative of the inductances, as tracks:

$$V_{L1} = L_1 \frac{di_1}{dt} + M \frac{di_2}{dt} \quad (1)$$

$$V_{L2} = M \frac{di_1}{dt} + L_2 \frac{di_2}{dt} \quad (2)$$

The Solving of these instantaneous equations, which can get:

$$\frac{di_1}{dt} = \frac{L_2}{L_1 L_2 - M^2} V_{L1} + \frac{-M}{L_1 L_2 - M^2} V_{L2} \quad (3)$$

$$\frac{di_2}{dt} = \frac{-M}{L_1 L_2 - M^2} V_{L1} + \frac{L_1}{L_1 L_2 - M^2} V_{L2} \quad (4)$$

The overall mathematical model of the representation system that analyzed in the difference calculations for the double methods, as shadows:

Mode 1: Smearing Kirchhoff law of the corresponding studied circuit of this style, exposed in figure (2.a), and by ignoring the voltage diagonally the switch, single will get:

$$V_{L1} = V_{in} - i_1 R_1 \quad (5)$$

$$V_{L2} = V_1 - V_2 - i_2 R_2 \quad (6)$$

By substituting, these tow equations (5) and (6) in (3) and (4):

$$\frac{di_1}{dt} = \frac{M}{\rho} V_2 + \frac{-M}{\rho} V_1 + \frac{MR_2}{\rho} i_2 + \frac{-L_2 R_1}{\rho} i_1 + \frac{L_2}{\rho} V_{in} \quad (7)$$

$$\frac{di_2}{dt} = \frac{-L_1}{\rho} V_2 + \frac{L_1}{\rho} V_1 + \frac{-L_1 R_2}{\rho} i_2 + \frac{MR_1}{\rho} i_1 + \frac{-M}{\rho} V_{in} \quad (8)$$

$$\text{As: } \rho = L_1 L_2 - M^2$$

While:

$$-i_{L2} = C_1 \frac{dv_{c1}}{dt} \quad (9)$$

$$\frac{dv_{c1}}{dt} = -\frac{1}{C_1} i_{L2} \quad (10)$$

Then, by applying Kirchhoff current law at node (n) :

$$i_{c2} = i_{L2} - I_o \quad (11)$$

$$i_{c2} = C_2 \cdot \frac{dv_{c2}}{dt} \quad (12)$$

$$I_o = \frac{v_{c2}}{R_L} \quad (13)$$

$$\frac{dv_{c2}}{dt} = \frac{1}{C_2} i_{c2} \quad (14)$$

$$\frac{dv_{c2}}{dt} = \frac{1}{C_2} i_{L2} - \frac{1}{C_2 R_L} v_{c2} \quad (15)$$

The output system matrix characterized by the relative

$$V_o = V_{c2} \quad (16)$$

Mode 2: Smearing Kirchhoff voltage rule for the corresponding circuit of this style, shown in figure (2.b), and by ignoring the voltage through the switch, one will grow:

$$V_{L1} = V_{in} - i_1 R_1 - V_1 \quad (17)$$

$$V_{L2} = -V_2 - i_2 R_2 \quad (18)$$

By substituting these two equations in (3) and (4):

$$\frac{di_1}{dt} = \frac{M}{\rho} V_2 + \frac{-L_2}{\rho} V_1 + \frac{MR_2}{\rho} i_2 + \frac{-L_2 R_1}{\rho} i_1 + \frac{L_2}{\rho} V_{in} \quad (19)$$

$$\frac{di_2}{dt} = \frac{-L_1}{\rho} V_2 + \frac{M}{\rho} V_1 + \frac{-L_1 R_2}{\rho} i_2 + \frac{MR_1}{\rho} i_1 + \frac{-M}{\rho} V_{in} \quad (20)$$

For the mode 1, the symbol of the voltages through the each inductor will be created by the next equations:

$$i_{L1} = C_1 \cdot \frac{dv_{c1}}{dt} \quad (21)$$

$$(22) \quad \frac{dv_{c1}}{dt} = \frac{1}{C_1} i_{L1}$$



$$(23) \frac{dv_{c2}}{dt} = \frac{1}{C_2} i_{L2} - \frac{1}{C_2 R_L} v_{c2}$$

The output voltage is expressed by the same equation (16):

So as to mark the overall state space accurate classical for the complete modified DC-DC Cuk converter scheme, lease the state variable as shown:

$$x = \begin{bmatrix} x_1 \\ x_2 \\ x_3 \\ x_4 \end{bmatrix} = \begin{bmatrix} i_{L1} \\ i_{L2} \\ v_{C1} \\ v_{C2} \end{bmatrix}$$

$$x_1 = i_{L1}$$

$$x_2 = i_{L2}$$

$$x_3 = v_{C1}$$

$$x_4 = v_{C2}$$

Using the normal method of the state space symbol [7]:

$$x' = Ax + Bu \quad (24)$$

$$y = Cx + Du \quad (25)$$

$$B_{off} = B_{on} = \begin{bmatrix} \frac{L_2}{L_1 L_2 - M^2} \\ \frac{M}{L_1 L_2 - M^2} \\ 0 \\ 0 \end{bmatrix}$$

$$A_{on} = \begin{bmatrix} -\frac{L_1 R_1}{L_1 L_2 - M^2} & \frac{MR_1}{L_1 L_2 - M^2} & -\frac{M}{L_1 L_2 - M^2} & \frac{M}{L_1 L_2 - M^2} \\ \frac{MR_1}{L_1 L_2 - M^2} & -\frac{L_1 R_1}{L_1 L_2 - M^2} & \frac{L_1}{L_1 L_2 - M^2} & -\frac{L_1}{L_1 L_2 - M^2} \\ 0 & -\frac{1}{C_1} & 0 & 0 \\ 0 & \frac{1}{C_2} & 0 & -\frac{1}{R_2 C_2} \end{bmatrix}$$

$$A_{off} = \begin{bmatrix} -\frac{L_1 R_1}{L_1 L_2 - M^2} & \frac{MR_1}{L_1 L_2 - M^2} & -\frac{L_2}{L_1 L_2 - M^2} & \frac{M}{L_1 L_2 - M^2} \\ \frac{MR_1}{L_1 L_2 - M^2} & -\frac{L_1 R_1}{L_1 L_2 - M^2} & \frac{M}{L_1 L_2 - M^2} & -\frac{L_1}{L_1 L_2 - M^2} \\ -\frac{1}{C_1} & 0 & 0 & 0 \\ 0 & \frac{1}{C_2} & 0 & -\frac{1}{R_2 C_2} \end{bmatrix}$$

$$C_{off} = C_{on} = [0 \quad 0 \quad 0 \quad 1]$$

So as to get the circuit matrix (A) of the modified converter, (A_{on}) is increased by the joining dated (the switch is ON), and (A_{off}) is increased by the stoppage period (the switch is Off), then summation the two matrices to find the overall modified Cuk converter system matrix,^[8] and as follows:

$$D_{off} = 1 - D_{on} \quad (26)$$

$$A = A_1 * D_{on} + A_2 * D_{off} \quad (27)$$

$$A = \begin{bmatrix} \frac{L_2 R_1}{L_1 L_2 - M^2} & \frac{MR_2}{L_1 L_2 - M^2} & \frac{-\text{Don}M + L_2 + Ds L_2}{L_1 L_2 - M^2} & \frac{M}{L_1 L_2 - M^2} \\ \frac{MR_1}{L_1 L_2 - M^2} & \frac{L_1 R_2}{L_1 L_2 - M^2} & \frac{\text{Don} L_1 + M \cdot \text{Don}M}{L_1 L_2 - M^2} & \frac{L_1}{L_1 L_2 - M^2} \\ \frac{1 \cdot \text{Don}}{C_1} & \frac{-\text{Don}}{C_1} & 0 & 0 \\ 0 & \frac{1}{C_2} & 0 & -\frac{1}{R_2 C_2} \end{bmatrix}$$

III. GENETIC ALGORITHM

Genetic algorithm is searching technique that used as a general purpose, which used successfully for more types of computation application and optimal system problems. It proposed by John Holland, 1975 up to date. It follows by its operators the values of growth future by Darwin. Genetic algorithm smears selection, crossover, and mutation machinists with the aim of result the finest solution to a difficult. [9]

1. Initial population: A random initial population of 50 individual, decimally encoded, has been used, each single individual with four genes, representing the produce four state feedback gains, (each individual gene represents a possible state feedback gain). The initial population forms a matrix of (50*4) dimensions. [10]

A programming method for scaling the initial choice of the random individuals from the period (0 to 1) to any other period has been proposed. Most of the running cases were started with an initial population of values within the space (-10) to (20).

2. Fitness function [1] (objective function): The code of discovery the integral absolute error (IAE) as a presentation table has been offered to frontrunner the search of the genetic algorithm, and seeming to lessen this error in the choice and recombination of the together individuals through every the generations.

$$IAE_{Min} = \int_0^T |e(t)| dt = \frac{1}{N} \sum_{k=1}^N abs(e_k) \quad (28)$$

Where: N = number of samples.

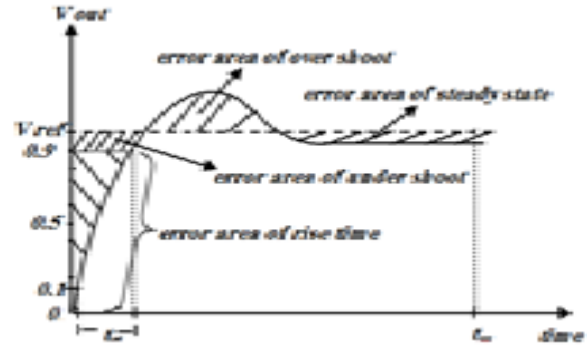


Fig.3. the step response components of the fitness function

3. Selection: A selection technique used in this algorithm that called the modified roulette selection method, which mixed of the both selection methods of the weighted random selection [11] and the elitism selection methods, produced by Kenneth De Jong 1975. [12] The purpose of using a hybrid selection technique is approach to : 1) overcome the drawbacks of the roulette wheel [13] (the wheel may stop at the divider of the worst possibility more than one time), 2) to overcome the drawback of using the selectiveness criteria with a very high selectiveness rate (steady state GA) which is the slow overshooting to notice and explore new search areas. So, the selection method which was used keeps the best 20% individuals as elite, and fee them forward to the next generation without any changing, and applied the roulette wheel selection on the remaining 80% of the population. [14]

4. Crossover[15-18]: Because of the chosen individuals were decimally encoded, the "Arithmetic Crossover method" that used to recombine the individuals and form those of the next

| Parameter | Value | Parameter | Value |
|------------------------------------|--------|--------------------------------------|---------------------|
| Vs : Source voltage | 12 V | R ₁ : Inductance resistor | 0.01 Ω |
| Vref : Reference Voltage | 12V | R ₂ : Inductance resistor | 0.01 Ω |
| L ₁ : First Inductance | 18mH | C ₁ : First Capacitance | 200μF |
| L ₂ : Second Inductance | 18 mH | C ₂ : Second Capacitance | 470μF |
| M : Mutual Inductance | -1.6mH | R _L : Resistor Load | 2 Ω 10 Ω 45 Ω |

produced generation (offspring), and as follows:

$$\text{Offspring 1} = a * \text{Parent 1} + (1 - a) * \text{Parent 2} \quad (29)$$

$$\text{Offspring 2} = (1 - a) * \text{Parent1} + a * \text{Parent 2} \quad (30)$$

Whereas the factor number selected randomly at each coupling. Also, the matrix establishing the initial population was divided vertically into two matrices, each of (50*2) dimensions, and made the crossover worker separately for each matrix, and then connecting the two matrices after the

crossover operation. This technique can be used in order to simplify the ability of choosing the limits of the initial population values for the similar mechanisms separately. Because that the effect of the similar components is significantly similar, that we chose to started each two alike components from their proper search space. Many crossover rates were tried, and the main rate used was 100% of the recombined individuals, (there was an elite of 20%).

5. Mutation: The mathematics mutation used in this algorithm. Also because of the decimal encoding of the each individuals, and produced as shown:

$$\text{Mutated Individual 1} = \text{Mutated Individual 1} + a \quad (31)$$

$$\text{Mutated Individual 2} = \text{Mutated Individual 1} - b \quad (32)$$

Whereas (a) and (b) are the random generated values.

Many rates of mutation were tested in the algorithm, and finally the rate of (3.5 %) was used. It noticed that the many higher mutation rates produced not useful performances.

6. Stopping criteria: it is containing a multi-condition stop criteria, which has been used in the genetic algorithm, and presented as shown below.

a. End if at doing three of the next four borders:

(1) Steady state error (Ess)=0.

(2) Highest over shoot (P.O.SH) <1%. (3) Settling time (Ts) <0.001 in the second (4) Rise time (Tr) <0.0009 in the second

b. Finish if the state did not happen, later effecting a exact amount of generations.

IV. SIMULATION RESULTS

The dc-dc modified Cuk converter parameters have been represented as shown in table (2). The converter state space parameters and the genetic algorithm with the limitation criteria such as rising time, settling time, peak over shoot and steady state error. The step responses of the modified DC-DC Cuk converter at the factors when three changed loads are exposed in the figures (4).

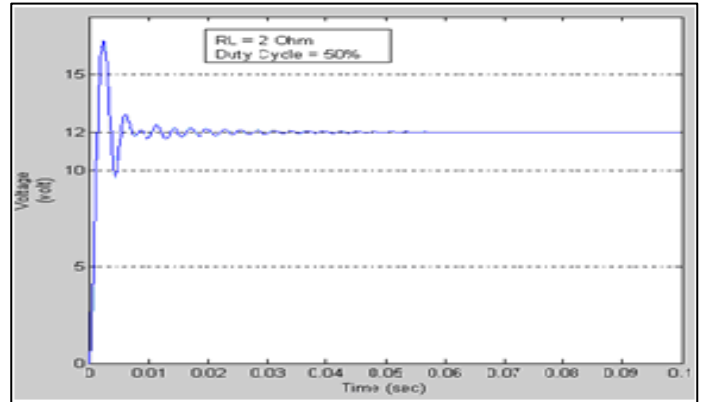


Fig 4.a

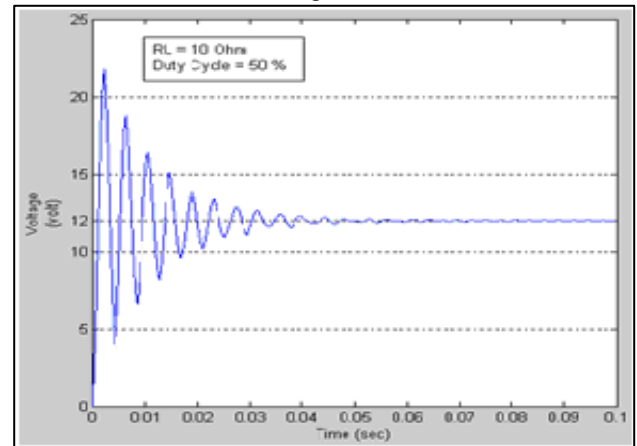


Fig 4.b

| Table 1. Genetic algorithm parameters | |
|--|--------|
| Parameters | Values |
| Number of string (population) | 50 |
| Number of Generations | 50 |
| Probability of Crossover (P _c) | 1.0 |
| Probability of Mutation (P _m) | 0.01 |

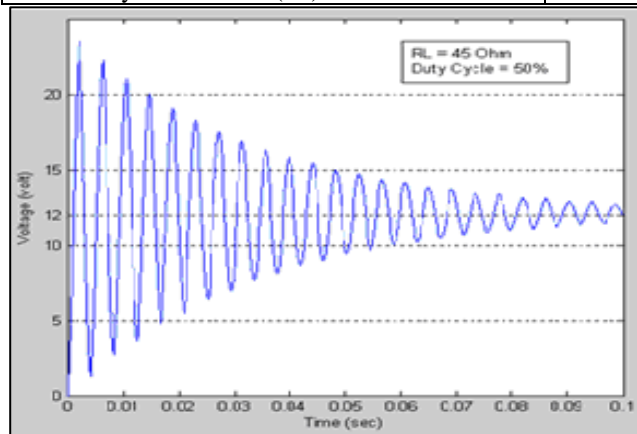


Fig 4.c

Figure (4) The output open loop voltage responses at: a.

RL=2Ω, b.10Ω and c. RL=45 Ω

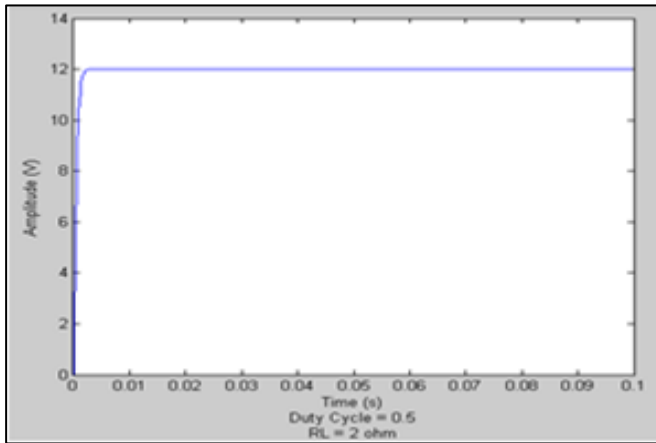


Fig 5. a

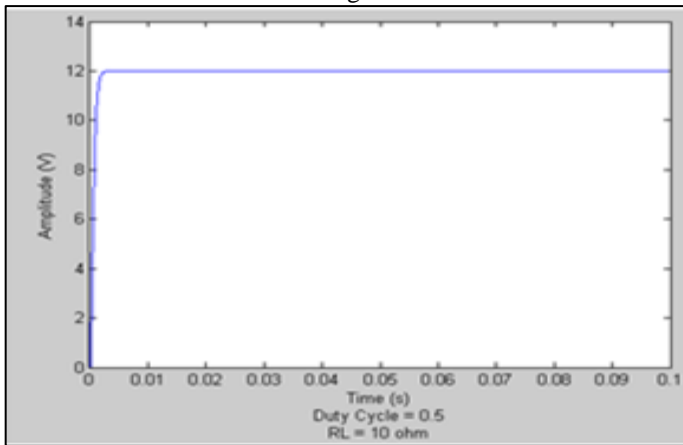


Fig 5. b

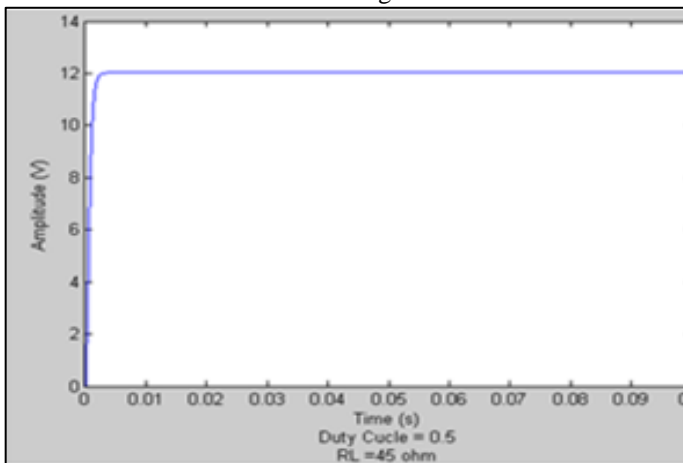


Fig 5.c

Figure (5) the output open loop voltage responses at a. RL=2Ω, b.10Ω and c. RL=45 Ω

The system responses with the designed genetic algorithm controller for the converter whose elements are registered in table (2) and whose open loop responses are exposed in the figure (4), and close loop converter responses are exposed in the figures (5).

The results shown in the figures (4) and (5) show that:

1. All the results taken with the state feedback controller (closed-loop) are better than the results of the open-loop system without controller.
2. The effect of the load variation on the response of the system is very small or eliminated because of the controller.
3. The passed time by the decimal coded genetic algorithm is too short compare with the open loop system response.

From the open and close loop output, converter voltage responses, which produce the output response limitation parameters, depend on the resistive load value.

Table 3 The combative results of the modified Cuk converter circuit when $RL=10\Omega$

| Design system | Steady state error (e_{ss})[%] | Peak Over shoot (p.o.s) [%] | Settling time (t_{ss}) [s] | Rising time (t_r) [s] |
|---|---------------------------------------|--------------------------------|--------------------------------|------------------------------|
| Open loop system at duty cycle of converter=50% | 2.8 | 83.33 | 0.052 | 0.0018 |
| Close loop system with Hybrid GA controller | 0 | 0 | 0.0019 | 0.0017 |

V. CONCLUSION

A calculated symbol for the modified DC-DC Cuk convertor was studied, analysis and controlled. The modified Cuk converter elements is operation as energy storage where are used to give a fourth order mathematical model representation. The mutual inductance does not increase the order of the system. The open loop circuit responses were taken with a three different resistance loads. The open loop response performance was study and produces bad properties of the transient response specifications (peak overshoot, rising, settling time and steady state error). A state feedback studied and designed using genetic algorithms technique to improve the output response performance of the system. The genetic algorithm is required (4*1) input matrix, whose individuals contain four genes at each in order to find an optimal solution of (1*4) values representing the state feedback gains.

The decimal coded of a genetic algorithm with a hybrid selection criterion that used for optimal choose of the state space feedback controller gains for the system. Crossbreeding the best choice with the roulette choice process joined the genetic algorithm with a better stability, by evading the algorithm from the drawback of behind the decent solution through the generations due to replicating. Extra testing and validation for the application of the genetic algorithm controller with the electric Cuk converter voltage given in this object. The simulation results formed that the genetic algorithm controller method prospered to advance the reply of the system for the studied range of the working conditions. The response standards presented a excessive stability at the dissimilar resistive load. The active of the load need was lost and removed by by means of the future controller. Lastly, the future algorithm controller did not leftover a extended time for creating the numerous solutions. In the current paper we compared the output circuit results and the reference results

REFERENCES

- [1] S. S. S. Ali "Optimal Fuzzy Controller Design For (Cuk) Converter Circuit Using Genetic Algorithm", M.Sc Thesis, University of Technology, Department of Electrical Engineering, Mosul University , Mosul-Iraq, 2008.
- [2] M.Rashid ,“Power Electronics Circuits ,Devices and Applications”, 3rd Edition ,Electrical and Engineering, University of West Florida 2004.
- [3] P.C. SEN, “Modern Power Electronics”, S. Chand & Company LTD., India, 2004.
- [4] S.N.Sivanandam & S.N.Deepa, "Introduction to Genetic Algorithms", PSG College of Technology Coimbatore - 641 004 TN, India, Springer-Verlag Berlin Heidelberg, 2008.
- [5] Holland, J. H. "Adaptation in Natural and Artificial Systems". University of Michigan Press.1975 (Second edition: MIT Press, 1992.).
- [6] A.H.Ahmed & K. Mezher . “Modified Cuk Converter Optimal Controller Design using particle Swarm Optimization ". 2nd conference ,engineering college University of Mosul, Mosul-Iraq. 2013.
- [7] K. Ogata, “Modern Control Engineering”, Fourth Edition, Prentice-Hall, Inc, New jersey,2002.
- [8] S. Chonsatidjamroen, et al."Dynamic Model of a Buck Convertor with a Sliding Mode Control", World Academy of Science, Engineering & Technology60, 2011.
- [9] MMelanie "An Introduction to Genetic Algorithms", Massachusetts Institute of Technology • London,England,5th printing, 1999
- [10] David E. Goldberg, "Real-coded Genetic Algorithms, Virtual Alphabets, and Blocking", University of Illinois, Urbana , USA, 1991.
- [11] Randy L. Haupt & Sue Ellen Haupt "Practical Genetic Algorithms", Second Edition, John Wiley & Sons, Inc. 2004.
- [12] K. A. De Jong, "An Analysis of the Behavior of a Class of Genetic Adaptive Systems". Ph.D. thesis, University of Michigan, 1975.
- [13] Mitchell Melanie "An Introduction to Genetic Algorithms", Massachusetts Institute of Technology • London, England, A Bradford Book, The MIT Press. Fifth printing, 1999.
- [14] E. S. Gopi, "Algorithm Collections for Digital Signal Processing Applications Using Matlab", National Institute of Technology, Tiruchi, India, Springer, P.O. Box 17, 3300 AA Dordrecht, The Netherlands, 2007.
- [15] N. Hammerman and R. Goldberg, "Algorithms to Improve the Convergence of a Genetic Algorithm with a Finite State Machine Genome", Computer Science Department ,Graduate Center and Queens College of CUNY, CRC Press LLC, 1991.
- [16] D. E. Goldberg, "Genetic Algorithms in Search, Optimization & Machine Learning" , Addison-Wesley, Reading, MA, 1989.
- [17] “Genetic Algorithms and Direct Search Toolbox User’s Guide” The Math Works, Inc.,2004.



- [18] Zbigniew Michalewicz "Genetic Algorithms + Data Structures = Evolution Programs", Department of Computer Science, University of North Carolina, Charlotte, NC 28223, USA. Third, Revised and Extended Edition, 1996.



Investigation the Performance of Solar Water Pump

Ali K. Al-Sayyab
 Thermal Mechanical Engineering
 Southern Technical University
 Iraq-Basra
 ali.alsayyab@stu.edu.iq

Akeel M. Ali
 Thermal Mechanical Engineering
 Southern Technical University
 Iraq-Basra
 akeel@stu.edu.iq

Mohammed A. Abdulwahid
 Thermal Mechanical Engineering
 Southern Technical University
 Iraq-Basra
 mohw2016@stu.edu.iq

Abstract- This study presents the theoretical modeling of solar water pumps, which can be useful work at the Sun days. The solar water pump it is a thermally driven pump which raised the water form the deep well by evaporating the Ethanol at the solar collector (parabolic heater), which in turn pumps the water to the top without any mechanical work. The model focuses to determine the optimum configuration geometries of the system. The pumping capacity of the water based on the amount of the evaporated Ethanol in solar heater based on previous study, the supply capacity examined of Ethanol vapor ranged of 2 L/min to 8 L/min in two steps. The results show that at the inner diameter of (10, 12, 14 mm) the length of the lift tube pump obtained (4 to 27 m), with hydrostatic head is (0.5, 1, 1.5 and 2 m), while the pumping capacity of the tube will be decreased and that leads to decrease in the elevation of the mixture. The pumping efficiency obtained by (0.02 to 0.12) of the lift, tube is varying with the mixer diameter.

Keywords: pollution, solar water pump, parabolic water heater, two-phase flow, lift tube.

I. INTRODUCTION

In the last period, the water releases into the Tigris and Euphrates rivers are decreased; this means the level of the river in the estuary will reduce. That which leads to reducing the required water for irrigation so the decline of green areas in the southern regions of Iraq. In these regions, the farmers resorted to the using of geothermal water by drilling the water wells. The deep of the well ranged from 10 to 15 m which that required a pump to lift the water. These towns are so far away from the national grid. Therefore, the population in these towns are trying to use another source, like the use of diesel generators, which that required maintenance of the generators, they will produce air pollutants (carbon dioxide). There are many sources of green energy as alternative energy source like wind energy and solar energy. The southern of Iraq has solar radiation intensity ($13 \text{ MJ m}^{-2} \text{ day}^{-1}$ to $27 \text{ MJ m}^{-2} \text{ day}^{-1}$) [1]. Solar cells are one of the most widely used as renewable energy resources. Solar cells are one of the equipment that used to collect electricity from solar energy. But, these cells have low efficiency, high manufacturing cost and low generation capacity. Many studies have been conducted on the use of direct and indirect solar energy. Bhave [2] performs a study for using photovoltaic cell to operate water pumping systems. The study concluded that the replacing traditional and diesel pumps with solar pumps for low and medium head pumping applications but the costs are very high. In addition, the solar water pumping systems are more suitable

for drinking water and minor irrigation requirements due to their cost and size factors considerations. Sumathy [3] carried out an experimental work to study the performance of solar water pump operate on solar collector of exposed area 1 m^2 , with different discharge heads, namely 6, 8 and 10 m. The study show that pump was perform 23 cycles at 6 m head, where perform only 17 and 12 cycles at discharge head of 8 and 10 m, respectively. The efficiencies varied from (0.12 to 0.14%) depending on the discharge head. Natthaphon et al. [4] used solar water pump instead of electrical one for solar water heater. The pump was powered by the steam produced from a flat plate collector. The study shows that the required solar energy input values are equal to or greater than 580, 600, and 630 W/m^2 to discharge heads of 1, 1.5, and 2 m respectively. It was found that water circulation within the system ranged between 12 and 59 lit/day. The mean pump efficiency is about 0.0014–0.0019%. Shahidul et al. [5] carried out an experimental study for using solar energy as source to drive water pump. The study uses photovoltaic cell as solar energy to electric convertor with dc motor, the study shows the discharge capacity was found in the range of 35-58 lit/min. M. Benganem et al. [6] investing the performance of water pump operating by electric from photovoltaic cell array located in Madienah city, with different head of pumping named (50 m, 60 m, 70 m and 80 m). The study shows that, the head with 50 m is optimum for low solar radiation in the afternoon and for efficient performance the head of 80 m which is recommended. Ahmad et al. [7] used the generated electric power from photovoltaic cells to operate water pump. The Power system is constructed utilizing the total of 32 solar panels consists of four branches with 8 solar panels in the series configuration for each branch. The study shows that the power system produces about 3200 Wp, which operates two submersible pumps with water flow rate is about 0.4 – 0.9 lit/s. M. Aghamohammadi et al. [8] study the performance of solar water pump by using system consist from two cycles, the collector cycle, and a Rankine cycle. In Rankine cycle R114 is used as a secondary fluid in a binary cycle engine. Flat plate collectors are employed to pump water by hydraulic transmission. The study shows that the temperature and flow rate of the collector is not constant so the pumped water from well, and the average working hours and flow rate of the system are 4-6 hours and $20 \text{ m}^3 / \text{day}$. The overall efficiency of the cycle is 2.804%. Rohini kumar et al. [9] performed an experimental study of predicted the performance of solar water pump working in principle of thermo-siphon circulation of low boiling point liquid. In study used ethyl ether as working substance. The performance of solar water pump has been analyzed for three different delivery heads 3, 4 and 5 m. The artificial neural network model has been applied successfully to

predict the performance of the system at different working conditions. The study shows that the pump is found to be capable of operating 7 cycles per day the number of cycles per day is less the overall efficiency of the pump obtained ($0.14 \times 10^{-2} \%$), where the maximum water delivered by day is 35 liter. A light of literature, the water pump can be operated mainly by any of the following three principles; the first by electricity obtained from Photovoltaic cells; second pump driven by turbine operating with steam or an organic vapour generated using solar flat plate collectors or concentrators. The third an unconventional pump in which the vapour of a low boiling point liquid generated through solar collector provides the motive power for lifting water, while condensation of the vapour and the subsequent decrease in pressure provides for suction. The using photovoltaic cell required a high cost of the system; also there are many operation and maintenance problems because of the number of stages involved in the conversion of solar energy to hydraulic work. In the second method, the present cost of the solar cells makes the system uneconomical. The third method appears to be an attractive proposition.

Proposed Cycle Description

The solar water pump system is a dependable water supply pump system based on renewable energy sources, such as solar and wind energy. This system incorporates as submersible lift tube pump, which is very bendable as to its energy supply and performance. It can be combined and adapted to any need according to the conditions on the installation site.

The system components are

- Solar collector heater.
- Ethanol Liquid-Vapor reservoir.
- Mixer.
- Lift tube pump.
- Separator.
- Heat exchanger.
- Conducted pipes.

The parabolic solar collector heater generated (4 L/min and 6 L/min) of Ethanol vapor. This vapor supplied at point (1) through supply pipe with the check valve at near the end of the pipe, due to prevent the water liquid flow back in the supply pipe. The supply Ethanol vapor pipe entrance at the bottom of the well inside mixer at point (2), inside the mixer the homogenous flow of water liquid and Ethanol vapor will be supplied by the buoyancy effect to bush this mixture through the lift tube point (3), as shown in (Fig. 1). The flow of this mixture becomes as a two-phase flow. The aim of this pump used to pump water liquid, not to inject Ethanol vapor, therefore, the slug two-phase flow is recommended to obtain this flow. Moreover, inside lift tube pump the mixture of Ethanol vapor and water liquid is supposed not dissolve in each other. Because, the used Ethanol is absolute, thus leads to non-interactive between Ethanol vapor and water liquid. The water liquid and Ethanol vapor are raised in lift tube then they enter the separator. The Ethanol vapor will be separated from the water liquid in the separator. The water liquid will flow at point (4) and enters the pipe of the heat exchanger. But the Ethanol vapor enters the heat exchanger at point (6) from outside of the pipe. The Ethanol vapor condensates in the heat exchanger due to the heat recovery of the Ethanol vapor and the water liquid. The water continuous flow to the supply point (5), while the Ethanol liquid flows to the reservoir at point (7). It again flows to the solar collector heater to repeat the cycle.

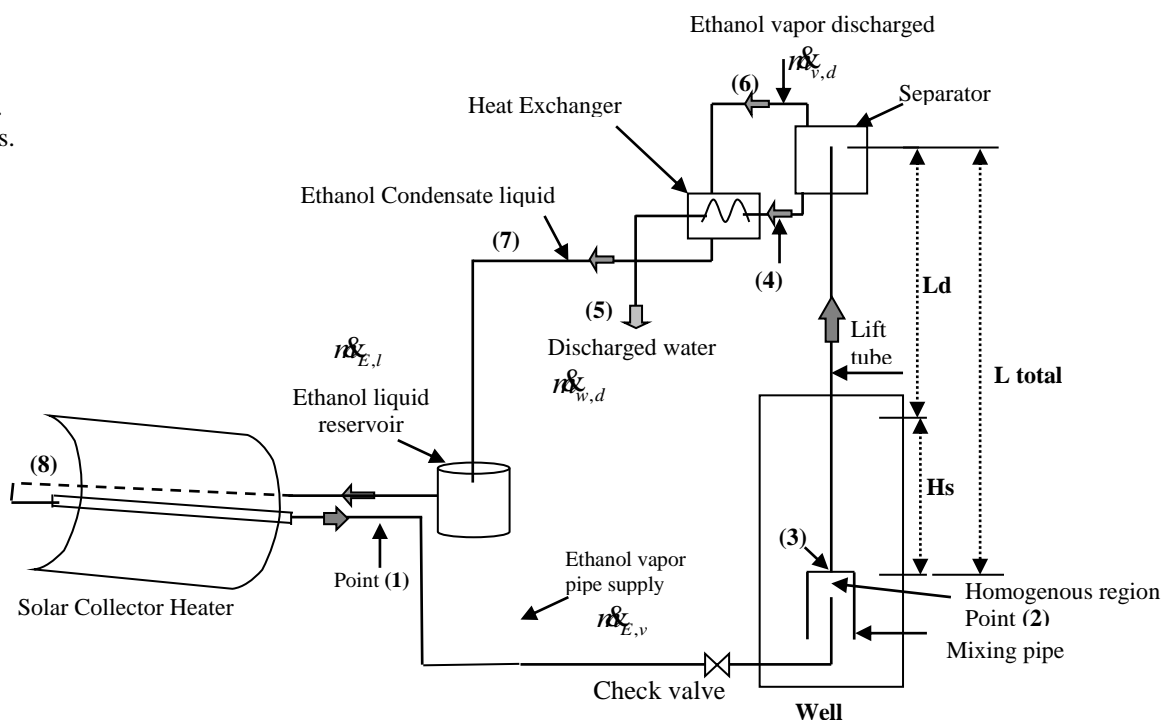


Fig. 1. A solar water pump cycle



Model Analysis

1- Lift Pump Configuration Modeling

The optimum capacity of the lift pump or its ability to pump an amount of liquid per unit gas input is a function of its physical geometry, cycle pressure difference, and the fluid mixture properties that it carries. Many researchers were proved theoretically and experimentally [10] and [11], that the intermittent of slug flow provides the maximum liquid circulation rate. Hence, the lift pump is modeled of intermittent of slug flow so that the basic governing equations are the conservation of mass, momentum, and energy written.

The following assumptions have been made for the analysis:-

- Steady state, one dimensional and incompressible flow.
- Minor frictional losses in the conduction pipes and inside the lift tube have been considered insignificant.
- The solution does not oscillate between Ethanol and Water inside the lift pump.
- The Ethanol is evaporated uniformly in the solar collector.
- No heat loss along the lift tube (adiabatic flow).
- Constant vapor quality along the lift tube.

The Ethanol vapor is generated at the solar collector, this vapor directs to the mixing pipe that exists in the well through the supply Ethanol vapor pipe. There is a check valve in that pipe allows flow in one direction and automatically prevents backflow (reverse flow) when fluid in the line reverses direction. At the mixing pipe, the water mixes with Ethanol vapor. At point 2 the mixture is homogenous. The gas-liquid mixture enters the lift tube at point 3; the mixture rises up through the lift tube direct to the separator.

Refer to Fig. (1), point 1 represents the Ethanol vapor flow rate ($\dot{m}_{E,v}$) to the lift tube at the velocity of V_1 .

$$\dot{m}_{E,v} = \rho_{E,v} A V_1 \quad 1$$

Where, A is the tube cross section area (m^2) and $\rho_{E,v}$ is the Ethanol vapor density.

Applying Bernoulli's equation between the bottom of the well at the mixing region which the hydrostatic head pressure (H_s) and pressure (p_s) at point 1, neglecting friction pressure drop, (for constant pipe diameter the fluid velocity remains constant), and yields[13]:

$$P_1 = p_s + \rho_w g H_s - \rho_{E,v} \frac{V_1^2}{2} \quad 2$$

Where: H_s is the hydrostatic pressure head of water in the well (m), ρ_w is the water density.

The conservation of mass between points 1 and 2 is applied (at the control volume to which heat is applied). Assuming that the mixture exits this control volume at the two phase flow velocity (V_2)[13]:

$$V_2 = V_1 \frac{V_h}{V_w} \quad 3$$

$$V_h = V_w + x(V_{E,v} - V_w) \quad 4$$

where, $v_{E,v}$, v_w and v_h are the specific volumes of Ethanol vapor, water liquid and the homogeneous mixture, respectively. x is the dryness fraction that is defined as the mass ratio of the vapor phase m_w to the total mixture (liquid mass flow rate \dot{m}_w and the vapor mass flow rate $\dot{m}_{E,v}$)

$$x = \frac{\dot{m}_{E,v}}{\dot{m}_{E,v} + \dot{m}_w} \quad 5$$

So, the total fluid flow rate (\dot{m}_{total}) in the lift tube is;

$$\dot{m}_{total} = \dot{m}_{E,v} + \dot{m}_w \quad 6$$

Applying the continuity equation and the conservation of momentum from point 1 to 2, and neglecting the friction losses in the small region yields[13]:

$$P_1 - P_2 = \rho_{TP} V_1 (V_2 - V_1) \quad 7$$

Substituting equations (2) and (3) in equation (7) and rearranging gives;

$$P_2 = P_{atmo} + \rho_w g H_s - \rho_{E,v} \frac{V_1^2}{2} - \rho_w V_1^2 \left(\frac{V_h}{V_w} - 1 \right) \quad 8$$

Next, the conservation of momentum is applied to the lift tube.

$$P_3 = P_{atmo} + \left(f_{TP} \frac{\rho_{TP} V_2^2}{2} \frac{4L}{d} + \frac{W}{A} \right) \quad 9$$

Where, the friction factor f_{TP} of two-phase of mixture flows in the lift tube[13]:

$$f_{TP} = \frac{64}{\text{Re}_{TP}} \quad 10$$

$$\text{Re}_{TP} = \frac{\rho_{TP} V_2 d}{\mu_{TP}} \quad 11$$

Where, ρ_{TP} is two-phase fluid density, and μ_{TP} is two phase fluid viscosity.

The weight of fluid in the lift tube (W), is the sum weight of the water liquid and Ethanol vapor in this tube, which can be calculated on the basis of two-phase mixture flow as:

$$W = L_{tube} g A \rho_{TP} \quad 10$$

Where, L_{tube} is the length of lift tube.

It is assumed that the total cross section area of the tube is partially occupied by the Ethanol vapor $A_{E,v}$ and by water liquid A_w , such that:

$$A = A_{E,v} + A_w \quad 11$$

The void fraction is ε (the ratio between the average cross-sectional area occupied by the gas to the total cross-sectional area of the pipe);

$$\varepsilon = \frac{A_{E,v}}{A} \quad 12$$

$$A_w = A(1 - \varepsilon) \quad 13$$

$$\frac{A_{E,v}}{A_w} = \frac{\left(\frac{\nabla_{E,v}}{V_{E,v}}\right)}{\left(\frac{\nabla_w}{V_w}\right)} \quad 14$$

Where, $\nabla_{E,v}$ and ∇_w are the volume flow rate of gas phase and liquid phase respectively.

$$\nabla_w = \frac{\dot{m}_w}{\rho_w} \quad 15$$

$$\nabla_{E,v} = \frac{\dot{m}_{E,v}}{\rho_{E,v}} \quad 16$$

And $V_{E,v}$, V_w are the velocities of the Ethanol vapor and water liquid respectively.

Using the definition of the void fraction and the gas to liquid velocity ratio ($S = \frac{V_{E,v}}{V_w}$), equation (14) can be rearranged to be as:

$$\frac{\varepsilon}{1 - \varepsilon} = \frac{\nabla_{E,v}}{\nabla_w \cdot S} \quad 17$$

Or;

$$\varepsilon = \frac{\nabla_{E,v}}{\nabla_{E,v} + \nabla_w \cdot S} \quad 18$$

The value for S was recommended by [12] to be between 1.5 and 2.5. The performance is not very sensitive to change in S , the maximum flow rate increases by only 12 percent when S is decreased from 2 to 1.5. Many researchers [9] and [10], used $S=2.5$, so this value of S is used in this study.

The two-phase density ρ_{TP} can be found from the density definition applied to the lift tube: [11] and [13]

$$\rho_{TP} = \rho_{E,v} \varepsilon + \rho_w (1 - \varepsilon) \quad 19$$

and the two-phase viscosity is μ_{TP} :

$$\mu_{TP} = \varepsilon_h \mu_{E,v} + \mu_w (1 - \varepsilon_h) (1 + 2.5 \varepsilon_h) \quad 20$$

Where, the homogeneous void fraction ε_h is:

$$\varepsilon_h = \frac{X}{X + \frac{\rho_w}{\rho_{E,v}} (1 - X)} \quad 21$$

To operate the lift tube pump that dependent on the Ethanol vapor and water, it needs to study the behavior of water lift pump and ($P_{Sap} = P_{atmo}$). The following equation is modeled to determine the length of lift tube:-

$$L_{tube} = \frac{V_1^2 \rho_{E,v}}{2g \rho_w} \left[2 \frac{v_h}{v_w} - 1 \right] H_s + \left[\frac{\rho_{TP}}{\rho_w} \frac{4f_{TP}}{d_{tube}} \frac{V_2^2}{2g} + 1 \right] H_s \quad 22$$

2- Mass and Energy Balance

Refer to the Fig. 1, the mass flow rate of Ethanol vapor pipe supplied $\dot{m}_{E,v}$ from the solar collector at point 1 is:

$$\dot{m}_{E,v} = \rho_{E,v} A_{SP} V_1 \quad 23$$

where, A_{SP} is the supply pipe cross section area.

Then, the Ethanol vapor is supplied to the well at the bottom of lift tube through the mixing chamber and it is considered as a homogeneous region at point 2 as:

$$\dot{m}_w = \rho_w A_{MC} V_2 \quad 24$$

Where, A_{MC} is the mixing chamber cross section area.

The mixture of the water liquid and the Ethanol vapor are entering together to the lift tube, the mass flow rate of the mixture is

$$\dot{m}_3 = \dot{m}_{E,v} + \dot{m}_w \quad 25$$

The total mass flow rate at point 3 is the two-phase flow of the Ethanol vapor and the water liquid, there is a small amount of the Ethanol vapor that may be condensed with



water. Thus, the slip value and the void fraction in Eq. (18) is used to calculate as:

$$\dot{m}_3 = \rho_{TP} A_{LT} V_3 \tag{26}$$

where, A_{LT} is the cross-section area of the lift tube.

The lift tube is work like as a pump, which has the ability to rise up and lifting the water liquid along the lift tube using the principles of the bouncy effects. Many literatures present the efficiency of the lift tube pump [14]

$$\eta = \frac{\rho_w g \nabla_w (L_{LT} - H_s)}{P_{atmo} \nabla_{E,v} Ln \frac{P_{in}}{P_{atmo}}} \tag{27}$$

where, P_{atmo} and P_{in} is the atmospheric pressure and Ethanol vapor input pressure respectively.

At the top of lift tube pump, the separator was placed to separate the water liquid from the Ethanol vapor.

The heat exchanger is used to recover heat from the water liquid to condensate the Ethanol vapor at point (7). Heat exchanger effectiveness is defined as the ratio of the actual heat transfer to the maximum possible heat transfer for inlet conditions, accordingly the heat exchanger effectiveness ($E=0.7$) and can be written the relation as:

$$E = \frac{\dot{m}_{E,v} C_{p_{E,v}} (T_6 - T_7)}{\dot{m}_w C_{p_w} (T_4 - T_5)} \tag{28}$$

Where, $C_{p_{E,v}}$ and C_{p_w} is the specific heats of the Ethanol vapor and the water liquid respectively.

The outlets of the heat exchanger are the supply water and liquid Ethanol. The liquid Ethanol is continued flow and deposited it in the Ethanol liquid reservoir at point (7). While the Ethanol liquid flow by gravity to the solar collector to evaporate it again.

Results and Discussion

The results of this study show the water flow rate as a function of Ethanol vapor has been generated in the solar collector heater. Otherwise, many of the geometries of the pipes and tubes were examined theoretically to determine

| Ethanol vapor generated $\nabla_{E,vap}$ (L/min) | Inner diameter of the pipe supply of Ethanol vapor (cm) | Inner pipe diameter of the mixer (cm) | Inner diameter of the lift tube pump (cm) |
|--|---|---------------------------------------|---|
| 2 | 1.2 | 0.5 | 1 |
| 4 | 1.4 | 1 | 1.2 |
| 6 | 1.6 | 1.2 | 1.4 |
| 8 | - | 1.4 | - |
| - | - | 1.6 | - |

the optimum geometries of the system. Table (1) shows all the parameters have been examined.

Table 1 the examined geometric parameters of the system

Comparison with previous work

The water lift pump is widely used in recent days. Especially, when the applicant trying to lift water from the depth well in the up direction. Moreover, in these days, this application type is used a solar energy or geothermal energy is more suitable. In order to examine the results of the present work proposed model compared with experimental data obtained from Natthaphon et al. (2008). Fig. 2 shows this comparison at the different hydrostatic head (H_s) of 1, 1.5, and 2 m with pumping efficiency at d_{lift} of 0.01 m, and d_{supp} , of 0.012 m. The figure clearly shows the maximum pumping efficiency of the present work is more developed than of the Natthaphon et al. (2008) for the same parameters.

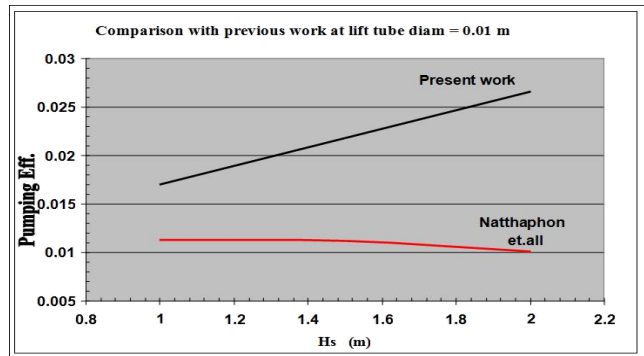


Fig. 2 Comparison between the present proposed model and the work of Natthaphon et.all (2008).

Performance modeling of geometric parameters

The model simulated to predict the water flow rate as a function of Ethanol vapor flow rate. The geometric parameters of (total lift tube pump length L_{total} , the inner diameter of supply pipe d_{supp} , the inner diameter of the mixer d_{mix} , the inner diameter of lift tube pump d_{lift} , and hydrostatic head H_s). Fig. 3 shows the variation of the total length of lift tube with a hydrostatic head at a different the inner diameter of the lift tube pump. The Fig. 3 clearly shows that at increasing the H_s at a given the inner diameter of d_{lift} , the L_{total} will be given more elevation of pumping mixture (i.e. water liquid with Ethanol vapor). When the inner diameter of the lift tube pump increases, the pumping capacity of the tube will be decreased and that leads to decrease in the elevation of the mixture.

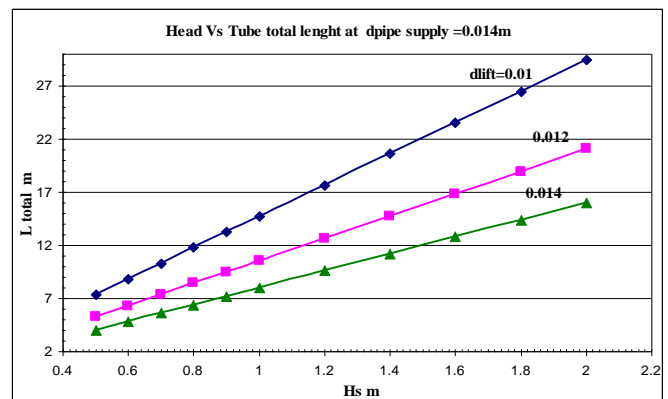


Fig. 3 Variation of the total lift tube length with different hydrostatic head of water.

Fig 4 shows the variation of elevation of the lift tube pump with a different lift tube pump inner diameter for H_s of 2 m, supply pipe diameter of 0.014 m and the mixer diameter of 0.12 m. Again, as the increasing in the lift tube diameter the elevation of the lift tube will decrease, due to require a higher amount of the Ethanol vapor, the frictional pressure drop is lowering with inner diameter. It will decrease with increased in the tube diameter and also the amount of the mixture lifted seen decreased too, that because of the amount of the Ethanol vapor should be supplied with greater value when the lift tube becomes bigger.

The Fig. 4 also, shows the variation of the water supplied mass flow rate at a different lift tube diameter. Of course, when the lift tube diameter increases, the mass flow rate of the pump water will be increased too.

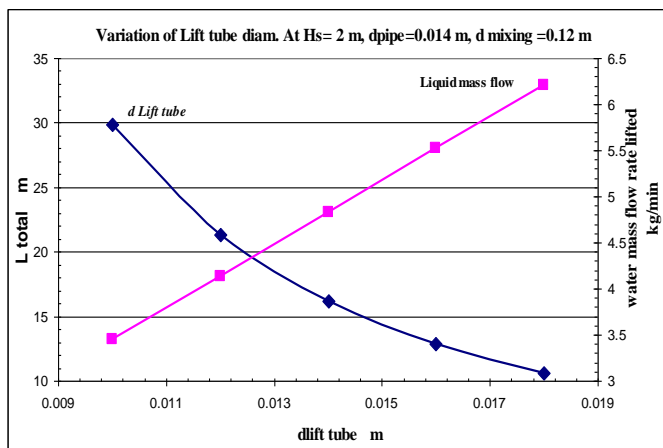


Fig. 4 Variation of the total lifts tube length at a different lift tube diameter and pump water capacity.

For more evidence of the geometric parameters affected, Fig. 5 shows the affected of the different diameters of the mixer (i.e. the region that mixed the Ethanol vapor with water at the depth well). In this region, the Ethanol vapor is mixed with water at the bottom of the lift tube pump, this mixture is modeled as a homogenous region, and the control action will be predetermined of the flow as a slug flow through across the lift tube. Moreover, the Fig shows the variation of the height of the lift tube pump it is affected directly with the increase in diameter of the mixer, due to the acclamation of the Ethanol vapor acting like a piston to push up more water. The Fig. also shows the pumping efficiency of the lift tube with variations in mixer diameter. The main reason for decreasing the pumping efficiency is revealed to require more amount of Ethanol vapor to increase the water pumping capacity.

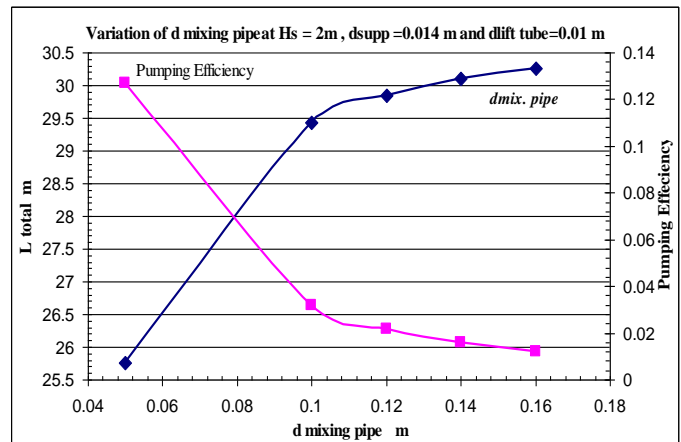


Fig. 5 Variation of the total lifts tube length at a different mixer diameter and pump efficiency.

Conclusions

From the present study, the following concluding remarks as:

1. The length of the lift tube pumps directly affected by the diameter of the supply pipe of Ethanol vapor, the diameter of the mixer and hydrostatic head.
2. The more mass flow rate of supply water required a large amount of the Ethanol vapor supply.
3. The proposed cycle gives a good agreement with the evidence that shown in a result, which leads to use in a practical range of the operation of solar water pumping mechanism in a desert area.
4. The optimum tube configuration geometers for hydrostatic head of 2 m, the inner diameter of lift tube is 0.012 m, with a mixer diameter of 0.12 m, while the diameter of Ethanol vapor supple pie is 0.014 m, the maximum length of the tube is approximately 22 m.
5. The solar water pump with lift tube diameter of 0.12 m is suitable to operate for water well of depth less than 20 m to get 1.5 tons of water pumping capacity per six-hour operation.

REFERENCES

- [1] I. Ahmad, N. Al-Hamadani And K. Ibrahim, Solar Radiation Maps For Iraq, Solar Energy, Vol. 31, No. 1, pp. 29-4, 1983.
- [2] A.G. Bhawe, Potential for solar water-pumping systems in India, Applied Energy, vol.48, pp:197-200, 1994.
- [3] K. Sumathy, Experimental studies on a solar thermal water pump, Applied Thermal Engineering Vol.19, pp: 449-459, 1999.
- [4] Natthaphon Roonprasang, Pichai Namprakai, Naris Pratinthong Experimental studies of a new solar water heater system using a solar water pump. Energy, Vol. 33 pp: 639-646, 2008.



- [5] Shahidul I. Khan, Md. Mizanur R. Sarkar, and Md. Quamrul Islam, design and analysis of a low cost solar water pump for irrigation in Bangladesh, Journal of Mechanical Engineering, Vol. ME 43, No. 2, December 2013.
- [6] M. Benghanem, K.O. Daffallah, S.N. Alamri, A. A. Joraid, Effect of pumping head on solar water pumping system Energy Conversion and Management 77,2014, pp.334–339.
- [7] Ahmad Agus Setiawana, Didik Hari Purwantoa, Didit Setyo Pamujia, Nurul Huda Development of a Solar Water Pumping System in Karsts Rural Area Tepus, Gunungkidul through Student Community Services. Energy Procedia vol.47, pp: 7 – 14, 2014.
- [8] M. Aghamohammadi, J. Zarinchang and M. Yaghoubi. Performance of a Solar Water Pump in Southern Part of Iran; Proceedings of Sharjah Solar Energy Conference, Sharjah, United Arab Emirates, 19-22 Feb. 2001.
- [9] Rohini kumar Bandaru, Chandrasekharan Muraleedharan, Performance Prediction of Solar Thermal Water Pump using Artificial Neural Networks, Int. J. of Thermal & Environmental Engineering, Vol. 15, No. 1 1-8, 2017.
- [10] Delano, A.D., "Design Analysis of the Einstein Refrigeration Cycle", PhD Dissertation, Georgia Institute of Technology, 1998.
- [11] White, S.J, "Bubble Pump Design And Performance" M.Sc. Thesis, Georgia Institute of Technology, 2001.
- [12] Stenning, A. and Martin, C., " An analytical and Experimental Study of Air-lift Pump Performance", ASME Journal of Engineering for Power pp.106-110, 1968.
- [13] Schaefer, Laura A. , " Single Pressure Absorption Heat Pump Analysis" PhD Thesis, Georgia Institute of Technology, 2000.
- [14] S.Z. Kassab, H.A. Kandil, H.A.Warda and W.H.Ahmed , " Air-Lift pumps characteristics under two-phase flow conditions" , Inter. Jour. Of Heat and Fluid Flow, 30, pp. 88-98, 2009.

Nomenclature

| Symbol | Definition | unit |
|---------------|------------------------------|--------------------------------------|
| \dot{m} | mass flow rate | kg .sec ⁻¹ |
| A | cross section area | m ² |
| V | velocity | m.sce ⁻¹ |
| P | pressure | kpa |
| H | head | m |
| v | specific volume | m ³ .kg ⁻¹ |
| d | inner diameter | m |
| L | lift tube length | m |
| LT | total length | m |
| W | weight | N |
| Re | Reynolds number | |
| S | slip ratio | |
| T | temperature | °C |
| F | friction factor | |
| E | heat exchanger effectiveness | |
| X | dryness fraction | |
| CP | specific heat | |
| ρ | density | kj.kg ⁻¹ .K ⁻¹ |
| ρ_{TP} | Two Phase density | kg.m ⁻³ |
| ρ_L | Liquid density | kg.m ⁻³ |
| μ | viscosity | N.sec.m ⁻² |
| ε | void reaction | |
| ∇ | volume flow rate | m ³ .sec ⁻¹ |
| η | efficiency | |

Regeneration Energy Using Electromagnetic Actuator with Nonlinear Active Suspension System

Ammar A. Aldair¹ & Eman Badee Alsaedee² & Turki Y. Abdalla³

College of Engineering / University of Basrah, Iraq

Mmr.ali2@googlemail.com¹, eman.badee24@gmail.com², Protryounis@yahoo.com³

Abstract- This paper presents a modeling and control of the nonlinear full vehicle active suspension system with passenger seat utilizing Fuzzy Model Reference Learning Control (FMRLC) technique. The main objective of designing the controller is to improve the performance of suspension system, while the aim of suspension system in automobiles is to isolate the road disturbance experienced by the tires from being transmitted to the passengers. The effects of the nonlinearities forces which are come from damper, spring and actuator have been taken into account. Therefore, the forces between the body of the vehicle and tires are generated using nonlinear active suspension system. When a vehicle is driving on a bumpy road, plus driver's acceleration and deceleration operations, there will be a shock between the sprung mass and the unsprung mass. This part of the mechanical power is normally converted into heat power by a damper and is dissipated in a natural way. If the wasted energy can be reclaimed in a proper way, the overall energy consumption demand for the vehicle can be reduced. In this paper, electromagnetic actuator with nonlinear active suspension system has been used to reduce the full consumption and to decrease the harmful emission to protect the environment.

Index Terms—Electromagnetic actuator, Fuzzy model reference learning control (FMRLC), eight degrees of freedom vehicle model, non-linear active suspensions.

INTRODUCTION

Recently, the researchers have carried out research to reduce the fuel consumption required for the vehicle and decrease the harmful emission to protect the environment. In this direction, it has been considered that the energy used to be wasted as heat energy dissipated by the dampers can be recovered by a suitable energy regenerative device. In fact, there are several types of energy regenerative suspension designs already under investigation such as: hydraulic storage suspension [1], battery coil induction suspension [2], rack and

pinion suspension[3], ball screw suspension [4] and linear motion suspension[5].

In the recent years, worldwide attempts concentrated on vehicle vibration control and energy regeneration, theoretical and experimental progresses [6-9] have been achieved. In order to improve the performance of vehicle suspension systems, the developments achieved in power electronics, permanent magnet materials and microelectronic systems enable the possibility of actual implementation of electromagnetic actuators [10]. In the reference [11], the authors investigated the idea of an energy regeneration of active suspension systems in petrol-electric hybrid vehicles. A hybrid energy storage system, which consists of electrochemical batteries and super-capacitors, is proposed. In Reference[12], a new hydraulic electromagnetic energy regenerative suspension design is proposed and a comparison is made with the other two energy regenerative suspension designs based on their structural and working principles, and an evaluation using the fuzzy comprehensive judgment is made. A retrofit regenerative shock absorber is designed that is characterized and tested to recover the vibration energy within a compact space in an efficient way [13].

Vehicles are complex mechanical systems with many degrees of freedom and they may incorporate linear or nonlinear springs and various types of damping characteristic. The primary function of a vehicle suspension system is to isolating passengers and the chassis from the roughness of the road to provide a more comfortable ride and to increasing the road handling. In the other words, very important role of the suspension system is the riding control [14, 15].

Several engineers and researchers in the automotive industry field devoted particular attention to discuss the problem of vehicle suspension control in order to develop the characteristics of both ride comfort and driving safety. The developing on suspension system is start from passive suspension to intelligent suspension. The intelligent or active suspension system includes control strategies, sensor technology and actuator and so on are adding in



parallel with passive components. By using this arrangement, the significant achievements in vehicle response can be carried out, where the suspension systems are became controllable systems [16, 17].

There are many types of actuators can be connected in parallel with the passive elements such as: hydraulic actuator, magneto-rheological actuator or pneumatic actuator, in this work the hydraulic actuators are used. The actuators supply additional forces to the suspension system in order to eliminate the vibrations come from rough roads, these forces are determined by a feedback control law utilizing data from sensors that are attached to vehicle [18].

Due to fast developments in the control technology, electronically controlled suspension has gained more interest to improve the riding requirements. Many types of controller systems such as adaptive control, LQR, LQG, H_∞ control are developed for vehicle suspensions model with active components to obtain more comfortable riding for passengers and guarantee road handling for the vehicle [14,15].

One of the most important control systems is the fuzzy logic control that has been developed rapidly in the last years as the effective alternatives to some conventional control. It has shown success in many control strategies and engineering applications in particular when the ability to describe the system model mathematically becomes more difficult or even impossible due to highly nonlinear, time variant and ill-defined processes. Mathematical model of a system is required for controlling the conventional controller. While, the fuzzy logic based control theory is a rule based system hence it does not require a mathematical model. Therefore, fuzzy logic controller has an advantage over classical controllers [19,21].

Despite of this success, there are some significant drawbacks of this approach, especially in the design of fuzzy controllers, due to the fuzzy controller unlike traditional controllers where it have several effective parameters that can be adjustable. While, there is no systematic process or general rules to tune these parameters, so the designing task is not easy and relying on the quality of the human expert. In other word, it needs specialist knowledge and consumes much time to adjust the control parameters. Also, it is often hard to justify the choices for many parameters in the fuzzy controller (e.g., the membership functions, rules, and scaling gains) [22, 24].

Moreover, the dynamics of most of plants is changing in time, therefore, reason the classical controllers with fixed parameters will be unreliable and thus the system performance is affected

seriously. In these cases, using of an adaptive controller is needed. To overcome the drawbacks of traditional fuzzy control system, some researchers over the last two decades, proposed adaptive algorithms to design the fuzzy system with optimal parameters. A significant class of adaptive controllers based on fuzzy logic approach is represented by self-organizing, self-structuring or self-learning controllers [25, 26].

In 1979, the first self-organizing fuzzy controller was developed by Mamdani and Procyk, where the work of Mamdani and his colleagues on fuzzy logic control was incited by Zadeh's work. Then the work of Procyk and Mamdani on the linguistic self-organizing controller has been further elaborated by many authors, especially by Yamazaki in 1982 and Shao in 1988. Unfortunately, those works did not become successful because the controllers are designed with difficulty for tracking reference signals different from step signals. This algorithm was later modified and extended by Layne and Passino (1992) and Layne and Passino (1993) to what it is called Fuzzy Model Reference Learning Control (FMRLC). This method developed by synthesizing several basic ideas from fuzzy set and control theory, conventional adaptive control, and self-organizing control. The main idea of this algorithm is based on model reference adaptive control (MRAC) [Astrom and Wittenmark (2008)]. In 2006; Kovai and Bogdan have described other self-learning or adaptive fuzzy control methods [27, 28].

In this paper, the mathematical model for full vehicle nonlinear active suspension systems with 8 degrees of freedom included a passenger seat with hydraulic actuators has been derived to take into account all the motions of the vehicle and the nonlinearity behaviors of active suspension system and hydraulic actuators. To improve the performance of the vehicle suspension system with FLC and to eliminating the previous fuzzy control drawback a self-learning control algorithm is presented, this algorithm employs a reference model to provide closed-loop performance feedback for synthesizing and tuning a fuzzy controller's knowledge, a reference model with the desired performance demonstrates of how the designer would like the controlled system to behave. Consequently, this algorithm is referred to as a "fuzzy model reference learning controller" (FMRLC). The performance of vehicle with FMRLC is compared with passive system by implement computer simulations through the MATLAB and SIMULINK toolbox. The consumption energy by each suspension has been calculated.

II MATHEMATICAL MODEL FOR FULL VEHICLE NONLINEAR ACTIVE SUSPENSION SYSTEM WITH PASSENGER SEAT

A full vehicle model with eight degrees of freedom (8DOF) is considered for analysis to investigate the problem of balancing riding comfort and road handling, where a passenger seat is included in the vehicle model to predict the response of the passenger due to a road disturbance as shown in Figure(1). A number of researchers deal with the suspension models as linear system by ignoring the nonlinearities behavior of suspension systems in order to simplify models. But on the other hand, the results become more realistic when take into account the effects of nonlinearities behavior of suspension systems such as dry friction on dampers and springs. Therefore, in this work, the effects of the nonlinearities forces which are came from damper, spring and actuator have been taken into account.

The full vehicle nonlinear active suspension system with a passenger seat model used in this study

is shown in Figure (1), consisting of passenger seat, sprung mass (M_s) referring to the part of the car that is supported on springs and unsprung mass (M_{us}) which refers to the mass of wheel assembly or in the other word the unsprung mass is total mass of the components under the suspension system. The tires have been replaced with their equivalent stiffness and damping. The tires are modeled by linear springs in parallel with linear dampers, while the suspension systems and passenger seat consists the nonlinear hydraulic actuators which are connected in parallel with nonlinear springs and nonlinear dampers. The spring in model of the tire and suspension system has stiffness coefficient labeled as k_{ti} , k_{si} respectively, and the damper has damping coefficient labeled as c_{ti} , c_{si} .

In order to control vehicle body motions, the vehicle model sprung mass is considered to have 3DOF. These are three types of motions: bounce motion, pitch motion and roll motion, while passenger seat and four unsprung mass have 1DOF

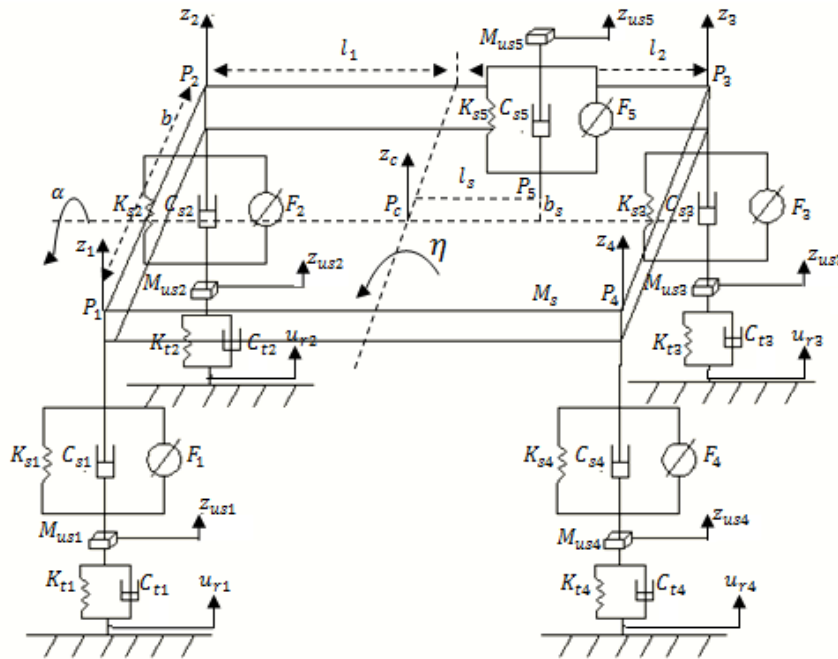


Fig 1: Full vehicle model with 8-DOF

for each. Based on the Newton's third law of motion the differential equations of the full vehicle nonlinear active suspension system can be obtained as explain below.

The heave motion of sprung mass can be written as follows

$$M_s \ddot{z}_c = - \sum_{i=1}^5 F_{ksi} - \sum_{i=1}^5 F_{csi} + \sum_{i=1}^5 F_i \quad (1)$$

Where:

F_{ksi} are the nonlinear forces of i^{th} spring

F_{csi} are the nonlinear forces of i^{th} damper

F_i is the applied nonlinear force between the sprung mass and unsprung masses which is generated from i^{th} hydraulic actuator. Those nonlinear forces can be written as

$$F_{ksi} = K_{si}(z_{si} - z_{usi}) + \zeta K_{si}(z_{si} - z_{usi})^3 \quad (2)$$

$$F_{csi} = C_{si}(z_{si} - z_{usi}) + \zeta C_{si}(z_{si} - z_{usi})^2 \text{sgn}(z_{si} - z_{usi}) \quad (3)$$

$$F_i = F_{hi} - F_{fi} \quad (4)$$



Where:

z_{usi} are the vertical displacements of unsprung masses

ζ is the empirical operator

F_{hi} is the i^{th} nonlinear hydraulic real force

F_{fi} is the i^{th} nonlinear frictional force

The force F_{hi} that generated by the i^{th} hydraulic actuators can be written as

$$F_{hi} = A_p P_{Li} \quad (5)$$

Where P_{Li} the pressure across the i^{th} actuator's piston or the load pressure, can be written this pressure equation in term of spool valve displacement x_{vi} as bellow

$$\dot{P}_{Li} = -\beta P_{Li} - \sigma A_p \dot{x}_{vi} + \frac{\sigma C_d \omega x_{vi}}{\sqrt{\rho}} (P_{si} - \text{sgn}(x_{vi}) P_{Li}) \quad (6)$$

Where x_{pi} is the difference between the vertical displacement of i^{th} corner of sprung mass z_{si} and the vertical displacement of corresponding i^{th} unsprung mass z_{usi} , i.e. $x_{pi} = z_{si} - z_{usi}$.

The actuator friction represents the friction associated with mechanical surfaces rubbing together, bearing friction, viscous friction, and so. This frictional force is found to be of significant magnitude and cannot be neglected. Therefore, the net force provided by the actuator is the different between the hydraulic force and the frictional force. Frictional forces are modeled with an approximation of Signum function [17]. Therefore, the mathematical model of friction forces can be written as:

$$F_{fi} = \begin{cases} \mu \text{sgn}(\dot{x}_{pi}) & \text{for } |\dot{x}_{pi}| \geq 0.01 \\ \mu \sin\left(\frac{\pi \dot{x}_{pi}}{0.02}\right) & \text{for } |\dot{x}_{pi}| < 0.01 \end{cases} \quad (7)$$

Where μ is the empirical operator

Then the rolling motions of the sprung mass can be given as

$$J_x \ddot{\alpha} = ((F_{ks1} - F_{ks2} - F_{ks3} + F_{ks4}) \frac{b}{2} + b_s F_{ks5} + ((F_{cs1} - F_{cs2} - F_{cs3} + F_{cs4}) \frac{b}{2} + b_s F_{cs5}) + ((F_3 - F_1 + F_2 - F_4) \frac{b}{2} - b_s F_5) + T_x \quad (8)$$

Where:

J_x is the roll moment of inertia about x-axis.

T_x is the cornering torque.

The pitching motion of sprung mass can be written as

$$J_y \ddot{\eta} = (F_{ks3} + F_{ks4}) l_2 - (F_{ks1} + F_{ks2}) l_1 + l_s F_{ks5} + (F_{cs3} + F_{cs4}) l_2 - (F_{cs1} + F_{cs2}) l_1 + l_s F_{cs5} + (F_1 + F_2) l_1 - (F_3 + F_4) l_2 - l_s F_5 + T_y \quad (9)$$

Where:

J_y is the pitch moment of inertia about y-axis.

T_y is the braking torque.

While the heave motion of unsprung masses can be governed by the following equation

$$M_{usi} \ddot{z}_{usi} = -k_{ti}(z_{usi} - u_{ri}) - c_{ti}(\dot{z}_{usi} - \dot{u}_{ri}) + F_{ksi} + F_{csi} - F_i \quad (10)$$

Where u_{ri} is the road input.

III FUZZY MODEL REFERENCE LEARNING CONTROL (FMRLC)

The FMRLC is a novel learning control technique was first proposed by Mamdani in 1989. The FMRLC is based on combining two control technologies: the Fuzzy Logic Control (FLC) and the Model Reference Adaptive Control (MRAC) scheme that guarantees stability with satisfactory performance for non-linear systems. It goes one step beyond direct fuzzy control since it has the ability to modifying the performance of the closed loop system [29, 30].

The FMRLC utilizes the learning mechanism that observes data from a fuzzy control system, characterizes its current performance, and automatically synthesizes and/or adjusts the fuzzy controller so that some given performance objectives are met. These performance objectives are characterized via the reference model shown in Figure (2). In an analogous manner to conventional MRAC where conventional controllers are adjusted, the learning mechanism seeks to adjust the fuzzy controllers so that the closed loop system (the map from $r(kT)$ to $y(kT)$) acts like a pre-specified reference model (the map from $r(kT)$ to $y_m(kT)$). For a much more detailed each component of the FMRLC will describe in the following subsection [31, 32].

The fuzzy controller

The major components of the direct fuzzy controller are the fuzzification, inference mechanism and defuzzification. As illustrate in Figure (2), the fuzzy controller has two inputs and one output, most often the inputs to the fuzzy controller are generated by some linear function of the plant output $y(kT)$ and reference input $r(kT)$. So the inputs to the fuzzy controller are represented by the error $e(kT)$ and the change of error $c(kT)$ as which are given in Eqs.(11) and (12) respectively [10].

$$e(kT) = r(kT) - y(kT) \quad (11)$$

$$c(kT) = \frac{e(kT) - e(kT-1)}{T} \quad (12)$$

The control signal input into the plant (the output of the fuzzy controller) is $u(kT)$. The signals error, change in error and controller output are scaled using the scaling gains g_e , g_c and g_u respectively.

The knowledge-base for the fuzzy controller associated with the plant input is generated from IF-THEN control rules of the form:

$R_q: IF \tilde{e} \text{ is } \tilde{E}_q^j \text{ and } \tilde{c} \text{ is } \tilde{C}_q^l \text{ Then } \tilde{u} \text{ is } \tilde{U}_q^r$

where \tilde{e} and \tilde{c} denote the linguistic variables associated with controller inputs $e(kT)$ and $c(kT)$ respectively, \tilde{u} denote the linguistic variables associated with controller output $u(kT)$, R_q denote the q^{th} rule of the fuzzy controller and $\tilde{E}_q^j, \tilde{C}_q^l$ and \tilde{U}_q^r denote the j^{th}, l^{th} and r^{th} linguistic values of the q^{th} rule associated with \tilde{e}, \tilde{c} and \tilde{u} respectively [19].

In this work, the triangular shape membership functions have been used for both input and output linguistic values. The fuzzy controller's rule base can be initialized by either setting all centers of the output membership functions to zero or providing an initial guess as to how the controller should act. The Center Average (CA) defuzzification method has been applied to compute the output of the fuzzy controller.

The reference model

The reference model provides a capability for quantifying the desired performance of the close feedback loop. It can take any type of dynamical system such as linear or non-linear, time-invariant or time-variant, discrete or continuous time etc. The reference model characterizes design criteria should be given, such as stability, rise time, overshoot, settling time, etc. [20].

The input to the reference model is the reference input $r(kT)$, the desired performance of the controlled plant is achieved if the error between reference model output ($y_m(kT)$) and plant output $y(kT)$ remains very small for all time. If the performance is achieved ($y_e(kT) \approx 0$) then the learning mechanism will not make significant modifications to the fuzzy controller. On the other hand if $y_e(kT)$ is big, the desired performance is not met and the learning mechanism must modify the parameters of the fuzzy controller [32].

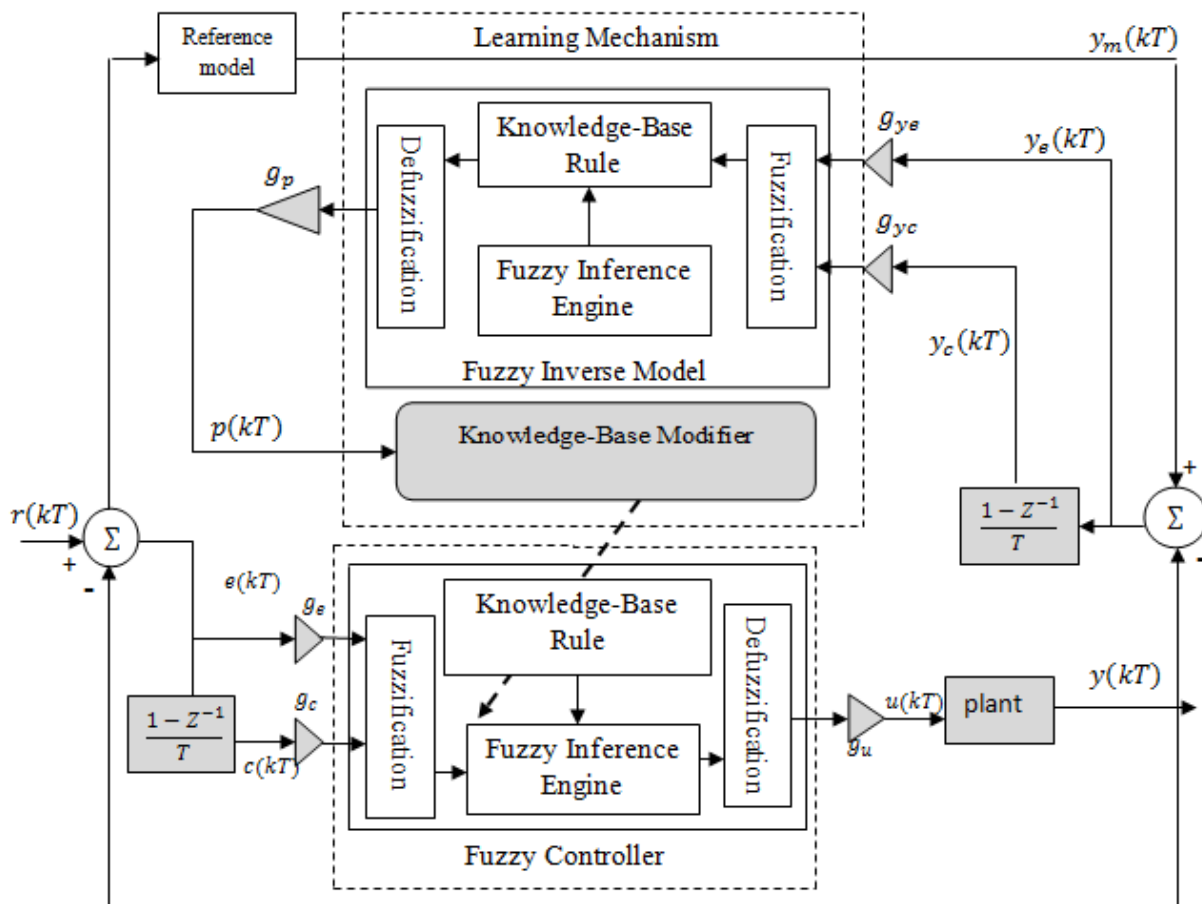


Fig 2: Architecture of the FMRLC



c. The learning mechanism

As previously mentioned, the main advantage of learning mechanism is to modifying the knowledge base of the direct fuzzy controller, so that the closed-loop system become like the reference model behaves by providing small value of $y_e(kT)$. These knowledge base modifications are made based on observing data from the controlled plant, the reference model, and the fuzzy controller [9].

The learning mechanism consists of two parts: a fuzzy inverse model and a knowledge base modifier. The fuzzy inverse model produces the suitable outputs $p(kT)$ to press the error $y_e(kT)$ to be zero. The knowledge base modifier performs the function of modifying the fuzzy controller's rule-base to apply the needed changes in the process inputs [10]. These parts are explained in details as follows:

- The fuzzy inverse model

The fuzzy inverse model is a direct fuzzy logic system which performs the function mapping of $y_e(kT)$ and possibly functions of $y_e(kT)$ such as the rate of error ($y_c(kT) = \frac{1}{T}(y_e(kT) - y_e(kT - T))$) or the plant operating conditions, to the relative changes in the plant inputs $p(kT)$ that are necessary to force the process output $y(kT)$ to be as close as possible to model reference output $y_m(kT)$ (i.e., to force $y_e(kT)$ to zero) [32, 33].

As shown in Figure (2), the fuzzy inverse model similar to the fuzzy controller where contains normalizing scaling factors, namely g_{y_e} , g_{y_c} and y_p for each universe of discourse. Selection of the normalizing gains can impact the overall performance of the system [19]. The knowledgebase form for the fuzzy inverse model can be written as

$$R_v: \text{If } \tilde{y}_e \text{ is } \tilde{Y}_{e,v}^j \text{ and } \tilde{y}_c \text{ is } \tilde{Y}_{c,v}^l \text{ Then } \tilde{p} \text{ is } \tilde{P}_v^r$$

Where \tilde{y}_e and \tilde{y}_c denote the fuzzy set for the error and change in error $y_e(kT)$ and $y_c(kT)$, respectively associated with plant output. The variable \tilde{p} denotes the linguistic variables describing the necessary change in the process input, associated with fuzzy inverse model output $p(kT)$. R_v denoted the v^{th} rule of the fuzzy inverse model; $\tilde{Y}_{e,v}^j$, $\tilde{Y}_{c,v}^l$ and \tilde{P}_v^r denoted the j^{th} , l^{th} and r^{th} linguistic values of the v^{th} rule associated with \tilde{y}_e , \tilde{y}_c and \tilde{p} , respectively [32].

As with the fuzzy controller, the membership functions utilize for normalized input universes of discourse. Any membership function shapes can be assumed. In this work, a symmetric triangular membership functions have been utilized.

It is important to note that the development of the fuzzy inverse model does not depend on the existence and specification of the mathematical model of the plant or its inverse. The fuzzy inverse

model should not be confused with the mathematical model of the inverse of the plant that is sometimes used in the fixed control (i.e. the non-adaptive control) [32, 33].

- The Knowledge-Base Modifier

The knowledge base modifier gives the information about the necessary changes in the input, which are represented by $p(kT)$, to force the error $y_e(kT)$ to zero. The knowledge base modifier changes the rule-base of the fuzzy controller so that the previously applied control action will be modified by the amount $p(kT)$ [32].

Therefore consider that the previously computed control action is $u(kT)$ which contribute to the present good or bad system performance. Note that $e(kT - T)$ and $c(kT - T)$ would have been the processed error and the change in error respectively at time $(kT - T)$. Likewise, $u(kT - T)$ would have been the controller output at that time. In order to force the fuzzy controller to produce small error, the fuzzy controller's knowledgebase should be modifying to produce a desired output $u(kT - T) + p(kT)$ [33].

Assume that a symmetric output membership functions are utilized for the fuzzy controller, where c_m denote the center value of the output membership functions associated with \tilde{B}_q^r . Knowledgebase modification is performed by shifting centers of the membership functions (c_m) of the output linguistic value \tilde{B}_q^r which are associated with the fuzzy controller rules that contributed to the previous control action $u(kT - T)$ [9].

To modify the centers of the output membership functions, the following two stages should perform:

1. The active set of rules for the fuzzy controller at time $(kT - T)$ is first determined ($\mu_i(e(kT - k), c(kT - T)) > 0$); those rules set can be characterized by indices of the input membership functions of each rule that is on. Since all possible combinations of rules have been used, so one output membership function for each possible rule will be on [12].
2. the centers of the output membership functions, which were found in the active set of rules determined earlier, are modified by using the following equation

$$c_m(kT) = c_m(kT - T) + p(kT) \quad (13)$$

Where $c_m(kT)$ represents the center of the m^{th} output membership function at the time kT . The centers of the output membership functions that are not in the active set of rules will not be update. This ensures that only those rules that actually contributed to the current output $y(kT)$ are modified [34].

This kind of learning is very useful since it does not need to entire rule base in order to be adjusted for every time step, just those rules that have been applied to the present statuses will be updated and stored. So, when the process encounter familiar operating conditions it does not required re-adapt again, where the controller will actually know how to cope with the process. This represents a feature for this type of controller due to its rid from the time consuming at re-learning.

IV. MATHEMATICAL MODEL OF THE ELECTROMAGNETIC ACTUATOR:

The electromagnetic actuator consists of a permanent-magnet DC motor with ball screw and a nut. Figure 3 shows the prototype of the electromagnetic actuator (copy from article [35]).



Figure 3 Electromagnetic Actuator

The electromagnetic actuator converts the vibration energy into electrical energy through the rotation of the DC motor and stores it in the battery. Therefore, the generated electrical energy can contribute to run the electrical pumps of the hydraulic actuators.

The DC motor can operate here in the electromotor mode or generator mode. In general, the power of the motor (P_e) can be represented as:

$$P_e = \frac{4\pi\Phi}{P_H} vI \quad (14)$$

where Φ is the flux linkage; P_H is the lead of the ball-screw, v is the relative velocity; and I is the electric current flow through the motor's coils.

If the demand power is positive, the motor that operates in the electromotor mode and the current flows from the battery into the positive terminal of the motor and the energy of battery will be consumed. On the other hand, if the power is negative, the motor operates inversely and the current flows to the positive electrode of the battery and the motor charges the battery as a generator with reclaimed energy from vibration of the vehicle.

The torque of the DC motor (T_e) can be written as:

$$T_e = C_e I \quad (15)$$

where the equivalent torque constant C_e can be expressed as:

$$C_e = 2\Phi \quad (16)$$

There are two types of forces which can be generated by using an electromagnetic actuator. The first force is called damping force (F_m) which comes from the mechanism friction and inertia. The second force is called the vertical force F_a . The total force generated by the electromagnetic mechanism can be written as:

$$F_c = F_m + F_a = C_m(z'_{sl} - z'_{ust}) + \left(\frac{2\Phi \cos\phi}{r}\right)I \quad (17)$$

where r is the effective radius for force conversion.

V. SIMULATION AND RESULTS

In this section, the simulation results for the full vehicle nonlinear active suspension systems including passenger seat with hydraulic actuators are presented. The performance of the fuzzy logic controllers that which designed based on the FMRLC algorithm, in this approach the centers of the output membership functions of the fuzzy logic controller are modify. The MATLAB/SIMULINK program package has been utilized to simulate the FRMLC with the controlled system as illustrate in Figure (4). As shown in this Figure the inputs of the fuzzy inverse model are the error and change of error, the output is an adaptation factor $p(kT)$ that which utilized by the rule base modifier to adapted the center of the output MFs of fuzzy controller. For these inputs and output, 7 fuzzy sets are defined with triangular form MFs which are equally distributed on the properly universe of discourse. For simplicity the fuzzy inverse model is selected as the same structure of standard fuzzy controller (the same membership function, rule base, inference engine, fuzzification and defuzzification).The reference model has been chosen to be a unity block.

Each inputs and output of the fuzzy control have seven membership functions linked with seven linguistic values are defined as: NB negative big, NM negative medium, NS negative small, ZE zero, and PS positive small, PM positive medium and PB positive big. These MFs are selected to be symmetric triangular in shape because they are widely used and convenient. The input membership functions are equally distributed on the normalized input universe of discourse, while the distributed of output MFs on the output universe of discourse are initialized randomly.

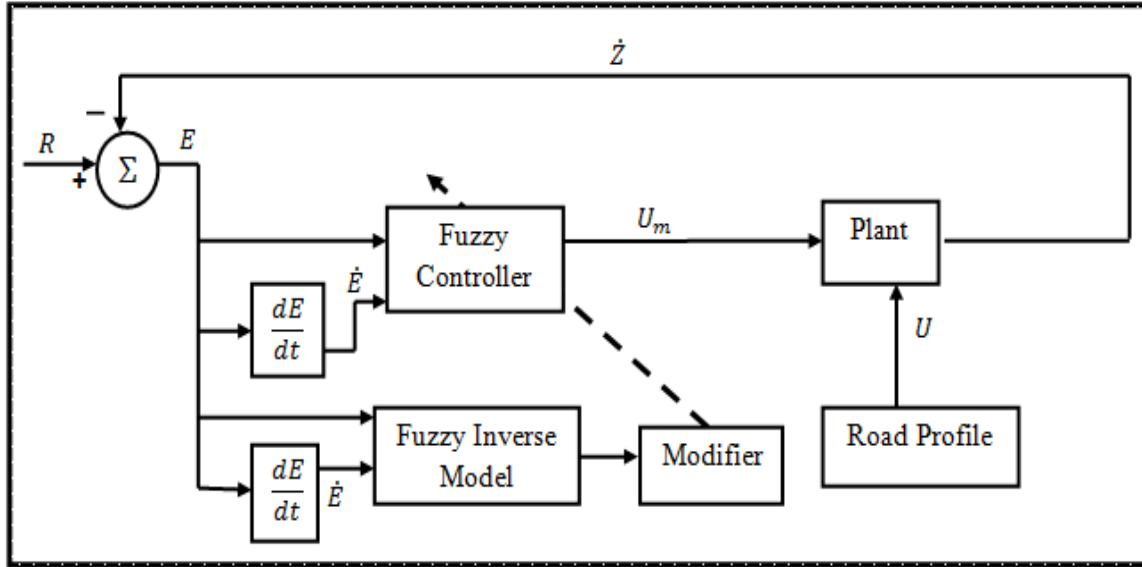


Fig 4: Fuzzy model reference learning control with plant

The fuzzy controller rules table, which is given in Table(1),are represented linguistic values of IF-THEN of rules, the total numbers of rules are $7 \times 7 = 49$ which are designed heuristically based on the knowledge of the controlled system.

Table 1
The rule base for the fuzzy control

| u_m | | \dot{e} | | | | | | |
|-------|----|-----------|----|----|----|----|----|----|
| | | NB | NM | NS | Z | PS | PM | PB |
| e | NB | NM | NS | NS | NS | Z | PS | PM |
| | NM | NM | NM | NM | NS | PS | PM | PM |
| | NS | NB | NM | NM | NS | PM | PB | PB |
| | Z | NB | NB | NM | Z | PM | PB | PB |
| | PS | NB | NB | NM | PS | PM | PM | PB |
| | PM | NM | NM | NS | PS | PM | PM | PM |
| | PB | NM | NS | Z | PS | PS | PS | PM |

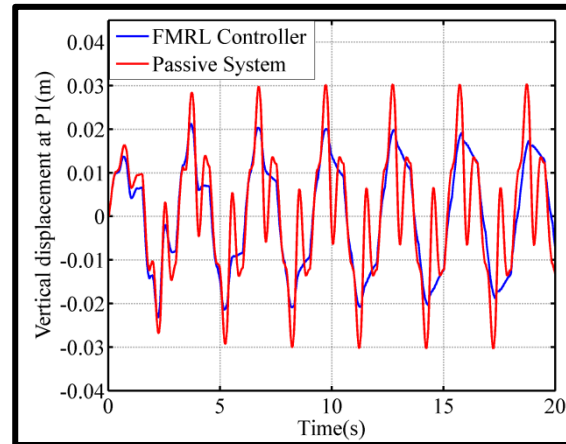
Then the COG defuzzification method and the inference mechanism in the FRMLC case are utilized to obtain the crisp output this output represent the controller output or the input of the controlled system. For simplicity the fuzzy inverse model is selected as the same structure of standard fuzzy controller (the same membership function, rule base, inference engine, fuzzification and defuzzification).The reference model has been chosen to be a unity block.

After training phase, the optimal values of the centers (c_m) of output MFs of the five fuzzy controllers that obtained from using the FMRLC are given in Table (2) and, where the initial values are zeros.

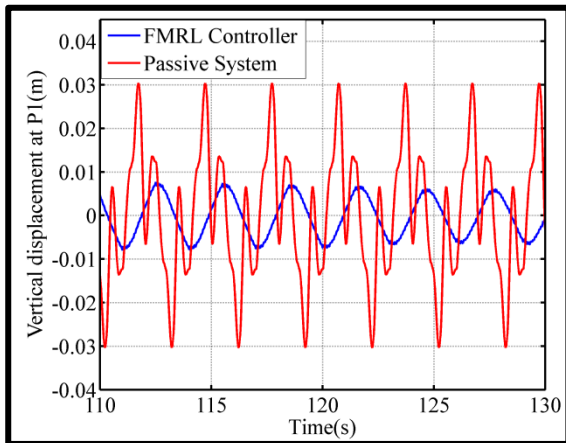
Table 2
Optimal solutions of each FMRLC

| c_1 | c_2 | c_3 | c_4 | c_5 | c_6 | c_7 |
|-------|----------|-----------|---------|----------|---------|-------|
| 0 | -36.4143 | -404.1287 | -0.0371 | 404.0915 | 36.3772 | 0 |

The vertical displacement for the each corner of the vehicle body, passenger seat and vehicle center, that obtained during training phase with FMRLC approach are shown in Figures(5-10).

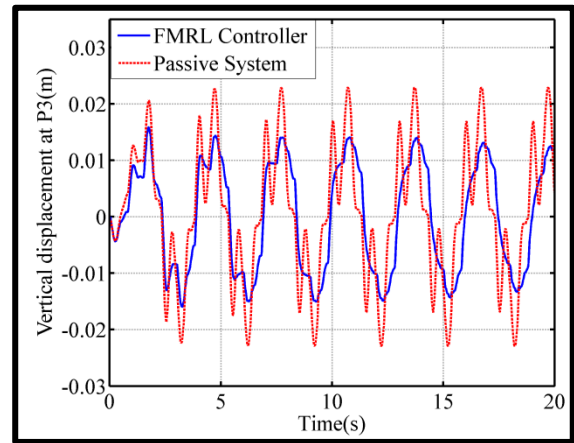


(a)

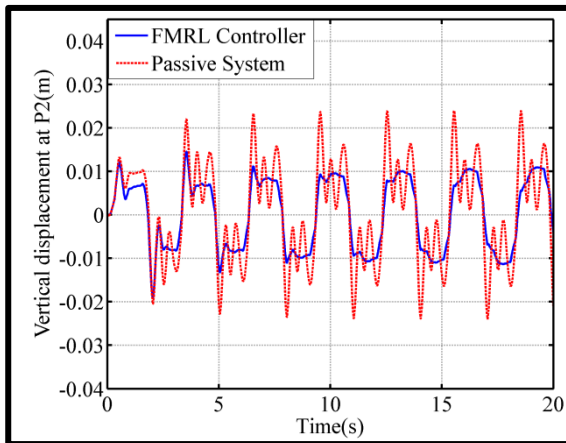


(b)

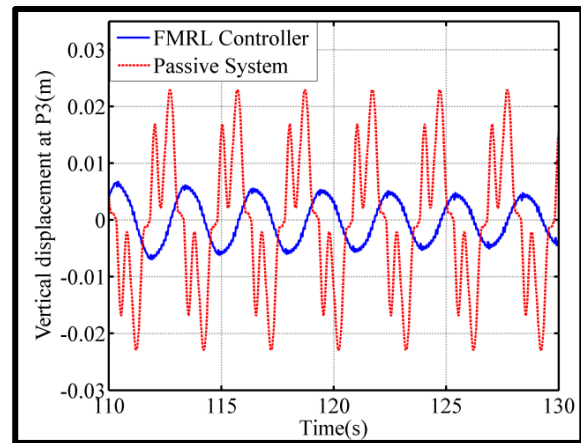
Fig 5: Vertical displacement at P1 for (a) first 7 training periods, (b) last 7 training periods



(a)

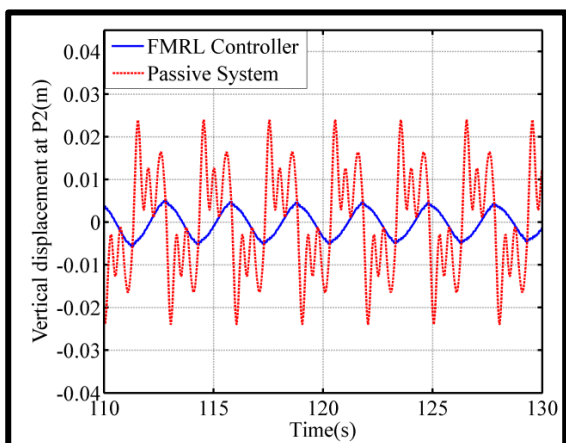


(a)



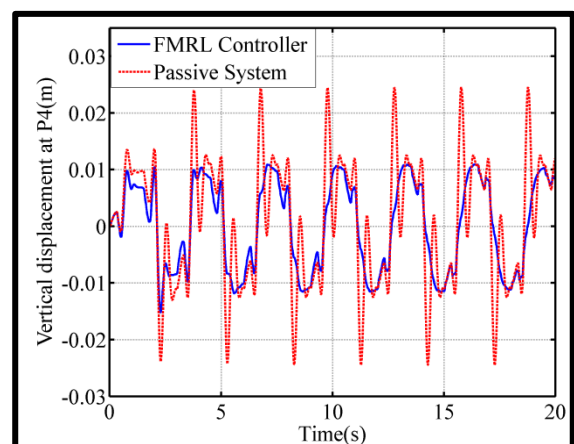
(b)

Fig 7: Vertical displacement at P3 for (a) first 7 training periods, (b) last 7 training periods

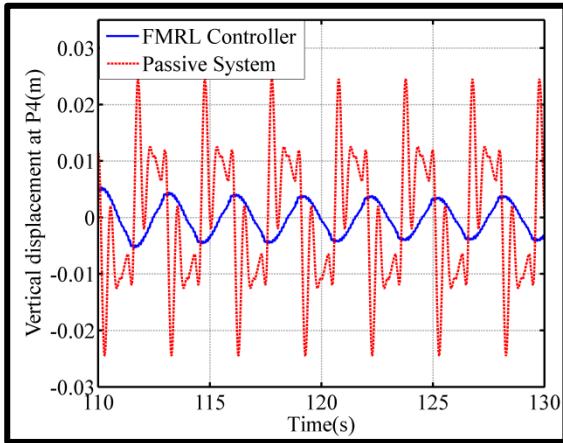


(b)

Fig 6: Vertical displacement at P2 for (a) first 7 training periods, (b) last 7 training periods

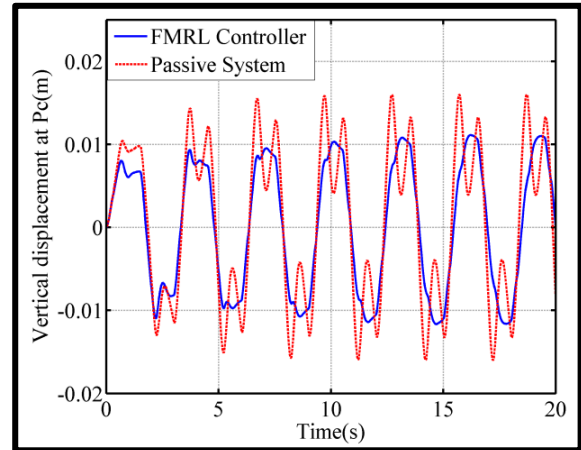


(a)

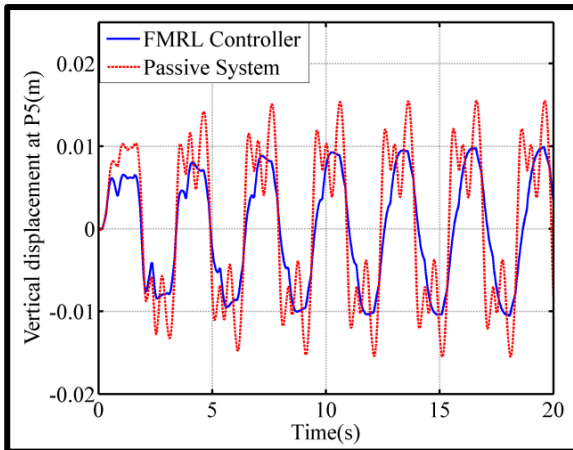


(b)

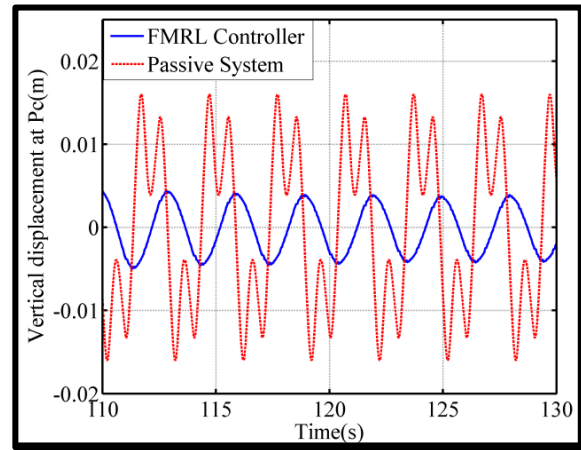
Fig 8: Vertical displacement at P4 for (a) first 7 training periods, (b) last 7 training periods



(a)

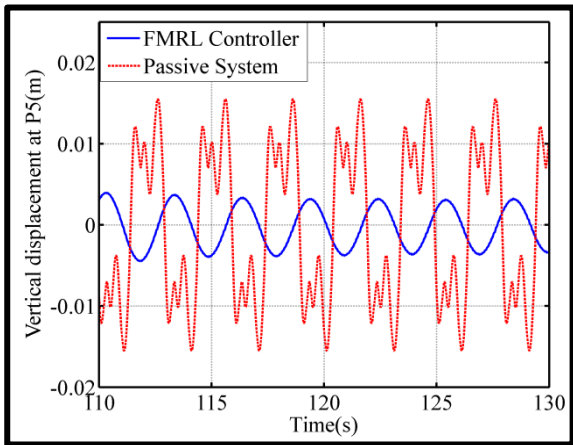


(a)



(b)

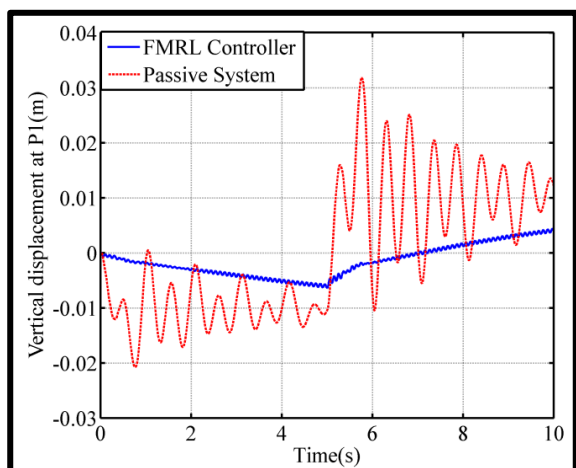
Fig 10: Vertical displacement at Pc for (a) first 7 training periods, (b) last 7 training periods



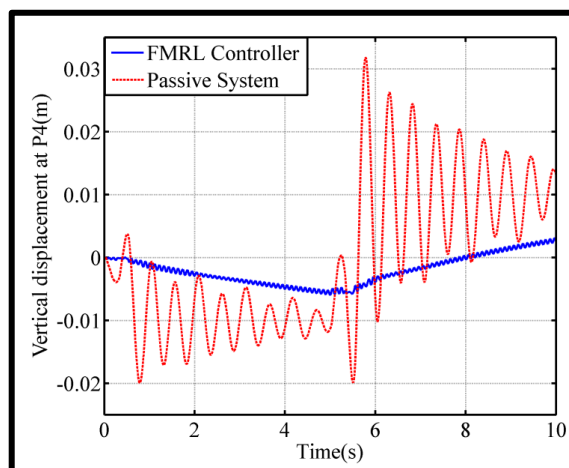
(b)

Figure 9: Vertical displacement at P5 for (a) first 7 training periods, (b) last 7 training periods

In order to evaluate the efficient of the proposed controller method the optimal values for the center output MFs must be examined. Figures(11-12) illustrate a comparison between the outputs of controlled system with FMRLC and corresponding outputs of the passive system also, in this status, the square input has been provided as a road profile with a range [-0.01 0.01] meters.

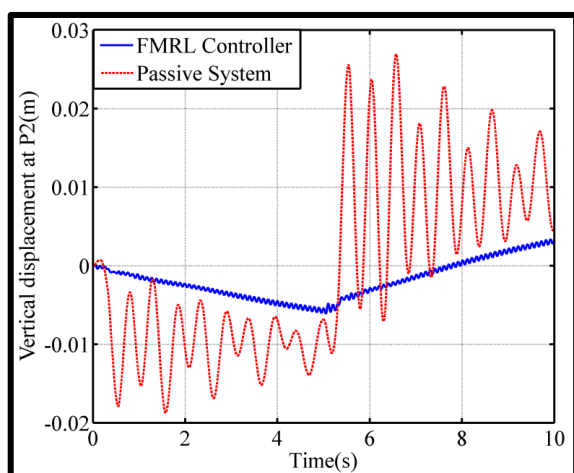


(a)

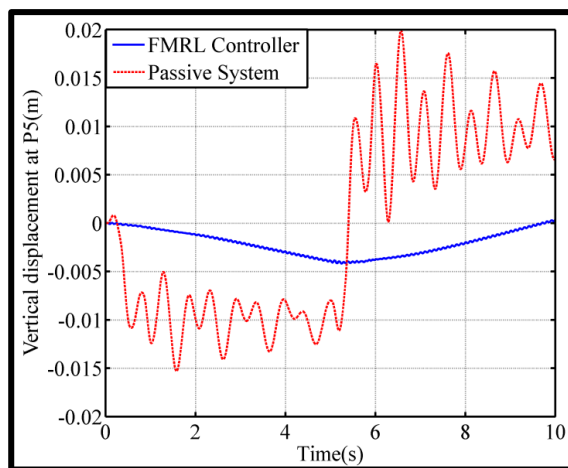


(d)

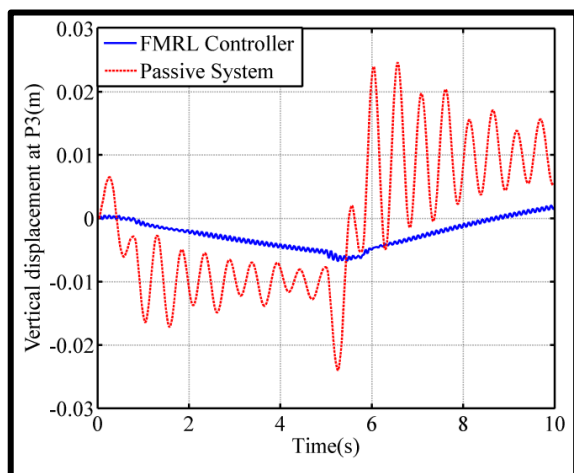
Fig11: Time response of vertical displacement at (a) P1; (b) P2; (c) P3; (d) P4



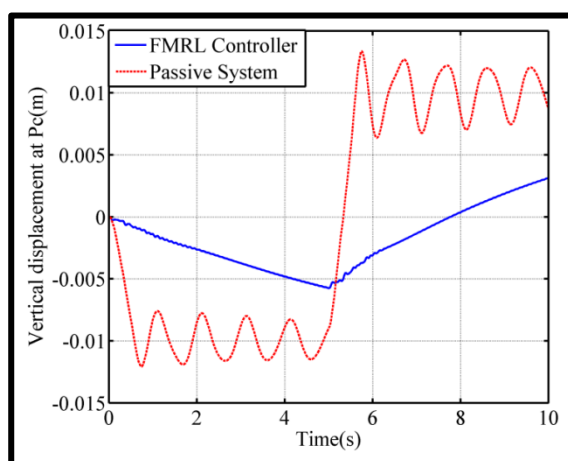
(b)



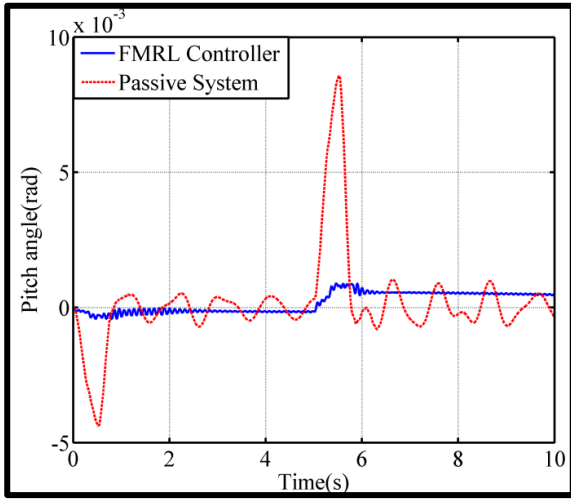
(a)



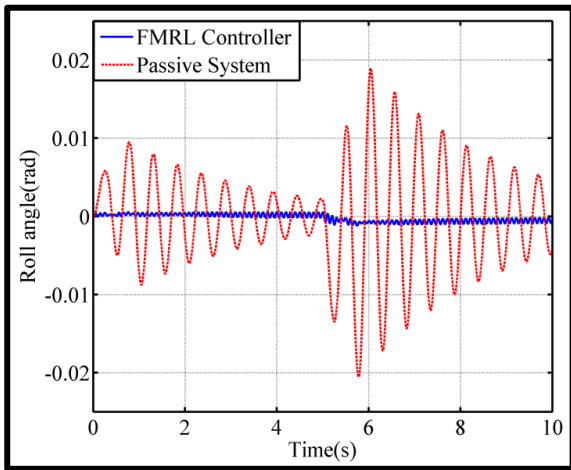
(c)



(b)



(c)



(d)

Fig 12: Time response for (a) vertical displacement at P5; (b) vertical displacement at Pc (c) Pitch angle; (d) Roll angle

IV. CALCULATION OF CONSUMPTION POWER

The j^{th} consumption power by i^{th} hydraulic actuators can be calculated from the following equation:

$$P_{ci}(j) = F_i(j) * ((\dot{z}_{si}(j) - \dot{z}_{usi}(j)) - (\dot{z}_{si}(j-1) - \dot{z}_{usi}(j-1))) \quad (18)$$

The total consumption power by the i^{th} hydraulic actuator can be calculated from the following equation:

$$P_{ti} = \sum_j F_i(j) * ((\dot{z}_{si}(j) - \dot{z}_{usi}(j)) - (\dot{z}_{si}(j-1) - \dot{z}_{usi}(j-1))) \quad (19)$$

The power generated from the i^{th} electromagnetic actuator can be calculated from Eq.(14).

Figures 13-16 show the power generated from the DC motors of the electromagnetic active suspension device. These figures have shown that the DC motors operate as a generator only because the power generated is only negative. The energy will contribute to drive the pumps of the hydraulic actuators to generate damping forces as part of the effort of improving the vehicle performance. It means that the energy consumption by the active suspension systems has been reduced and the problem of the energy consumption resulting for driving the actuators in the active suspension has been solved.

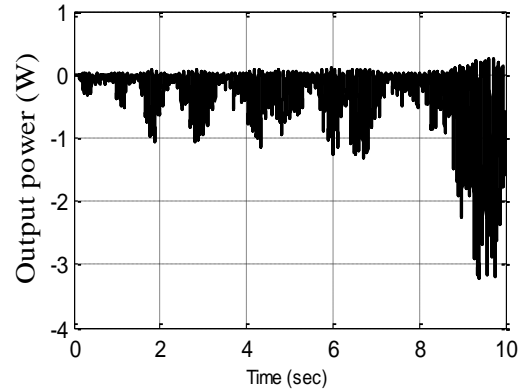


Fig. 13 Output power from front-right suspension

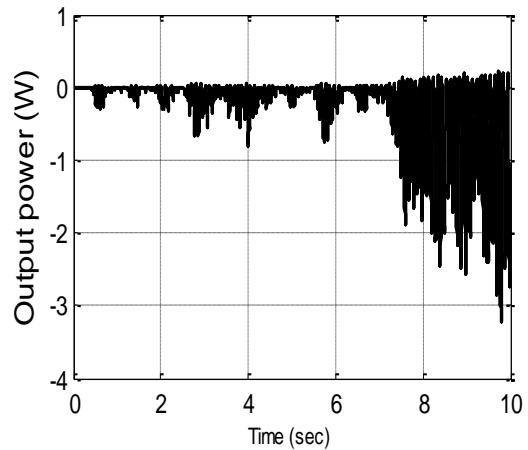


Fig. 14 Output power from front-left suspension

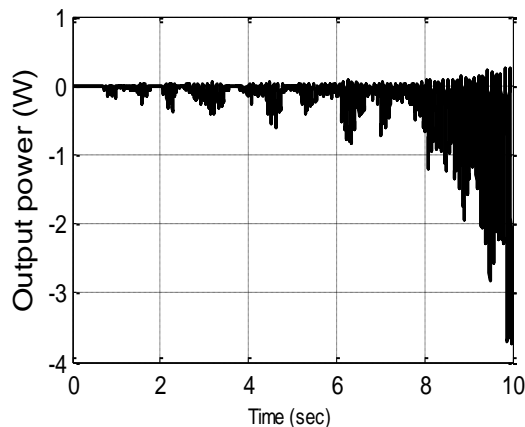


Fig. 15 Output power from rear-right suspension

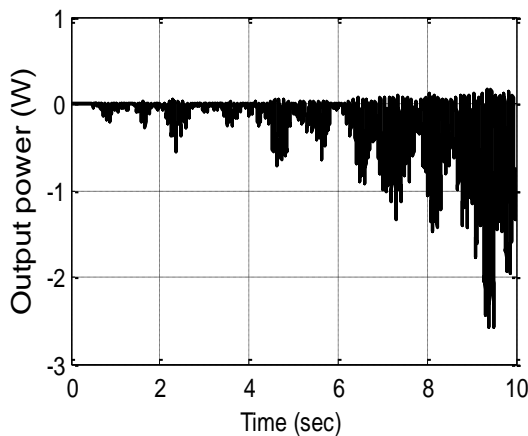


Fig. 16 Output power from rear-left suspension

IV. CONCLUSIONS

In this study, FMRL technique is proposed to improve the performance of full active suspension system and the results have been presented. The motivation of utilizing the proposed FMRL controller is to improve the vehicle suspension system and overcome the drawback of utilized the fuzzy system as a controller, where it is hard to justify the selection of fuzzy controller parameters.

The suggested controller method have the ability of tuning some of its parameters depending on the errors between the system outputs and the desired outputs to generate a suitable control signals to modify the hydraulic actuators forces to reduce the tendency of vehicle to rollover during sharp maneuvers such as cornering and breaking and to minimize the vertical displacements at each suspension when travelling on rough roads achieve the objectives control.

Five FMRL controllers have been designed, one for each suspension system. The centers parameters of the output membership functions, obtained from

used the FMRL controller approach during the training phase, are set as parameters of the output membership functions of the fuzzy controller during the working phase. The results of proposed model are compared with the passive system. According to the results of the computer simulation when only the square input has been applied as road profile the suspension system with the FMRLC given the superior performance than the passive system.

The electromagnetic actuator has been used in this paper to reduce the consumption power of the active suspension system by converting the vibration energy which comes from rough road to electrical energy. The results show that, the DC motor will be act as generator to convert the vibration energy to electrical energy. The generated power is stored in a battery. This power is used to run the pump of hydraulic actuators to generate appropriate damping forces to improve the riding comfort and road handling.

Reference

- [1] Shian, C., Ren, H., and Senlin L. (2007). "New Reclaiming Energy Suspension and its Working Principle " Chines Journal of Mechanical Engineering, 13(11), 177-182.
- [2] Ren, H., Shian, C., and Senlin, L. (2005). "A Permanent Magnetic Energy Regenerative Suspension." ZL 200520072480.9.
- [3] Shian, C., Ren, H., and Senlin L. (2006). "Operation Theory and Structure Evaluation of Reclaiming Energy Suspension." Transactions of the Chinese Society for Agricultural Machinery, 37(5), 5-9.
- [4] Yong-chao, Z., Fan, U., Yong-hui, G., and Xue-chun, Z. (2008). "Isolation and Energy regenerative Performance Experimental Verification of Automotive Electrical Suspension." Journal of Shanghai Jiaotong University, 42(6), 874-877.
- [5] Zheng, L., Li, Y. N., Shao, J., and Sun, X. S. (2007). "The Design of a Fuzzy-sliding Mode Controller of Semi-active Suspension Systems with MR Dampers " IEEE International Conference on Fuzzy Systems and knowledge Discovery., 4, 514-518.
- [6] Karnopp, D. (1978). "Power requirements for traversing uneven roadways." Vehicle System Dynamics, 7, 135-152.
- [7] Karnopp, D. (1989). "Permanent Magent Linear Motors used as Variable Mechanical Dampers for Vehicle Suspensions." Vehicle System Dynamics, 18, 187-200.
- [8] Sada, Y., and Shiiba, T. (1996). "A New Hybrid Suspension System with Active Control and



- Energy Regeneration " Vehicle System Dynamics, 25, 641-654.
- [9] Velinsky, S., and White, R. (1980). "Vehicle Energy Dissipation due to Road roughness." *Vehicle System Dynamics*, 9, 359-384.
- [10] Martins, I., Esteves, J., Marques, G., and Silva, F. (2006). "Permanent-Magnets Linear Actuators Applicability in Automobile Active Suspensions." *IEEE Transaction on Vehicular Technology*, 55(1), 86-94.
- [11] Montazeri, M., and Soleymani, M. (2010). "Investigation of the Energy Regeneration of Active Suspension System in Hybrid Electric Vehicles." *IEEE Transaction on Industrial Electronics*, 57(3), 918- 925.
- [12] Xu, L., Guo, X., and Liu, J. (2010). "Evaluation of Energy-regenerative Suspension Structure Based on Fuzzy Comprehensive Judgment." *Advanced Material Research*, 139-141, 2636-2642.
- [13] Zuo, L., Scully, B., Shestani, J., and Zhou, Y. (2010). "Design and Characterization of an Electromagnetic Energy Harvester for Vehicle Suspensions." *Smart Mater. Structure.*, 19, 1-10.
- [14] R. Guclu, K. Gulez, "Neural network control of seat vibrations of a non-linear full vehicle model using PMSM", *Journal of Mathematical and Computer Modeling*, Vol. 47, No. 11, pp.1356-1371, (2008).
- [15] R. Güçlü, "Active control of seat vibrations of a vehicle model using various suspension alternatives", *Turkish Journal of Engineering and Environmental Sciences*, Vol. 27, No. 6, pp.361-374, (2003).
- [16] S. Lajqi, S. Pehan, "Designs and optimizations of active and semi-active non-linear suspension systems for a terrain vehicle", *Strojniški vestnik Journal of Mechanical Engineering*, Vol. 58, No. 12, pp.732-743, (2012).
- [17] J. Lin, R. J. Lian, "Intelligent control of active suspension systems", *IEEE Transactions on Industrial Electronics*, Vol. 58, No. 2, pp.618-628, (2011).
- [18] F. A. Ansari, R. Taparia, "Modeling, analysis and control of active suspension system using sliding mode control and disturbance observer", *International Journal of Scientific and Research Publications*, Vol. 3, No. 1, pp.1-6, (2013).
- [19] N. G. Jabson, K.G. B. Leong, S. W. Licarte, G. M. S. Oblepias, E. M. J. Palomado, E .P. Dadios, "The Autonomous Golf Playing Micro Robot: With Global Vision And Fuzzy Logic Controller", *International Journal On Smart Sensing And Intelligent Systems*, Vol. 1, NO. 4, DECEMBER 2008
- [20] C. C. Lee, "Fuzzy logic in control systems: Fuzzy logic controller-Part1", *IEEE Transactions on Systems, Man and Cybernetics*, Vol. 20, No. 2, pp.404-418, (1990).
- [21] L. j. Yue, C. y. Tang, H. Li, "Research on vehicle suspension systems based on fuzzy logic control", *Proceedings of the IEEE International Conference on Automation and Logistics(ICAL) Qingdao, China*, pp. 1817-1821,(2008).
- [22] T. R. Rao, P. Anusha, "Active suspension system of a 3 DOF quarter car using fuzzy logic control for ride comfort" , *IEEE International Conference on Control, Automation, Robotics and Embedded Systems (CARE)*, pp. 1-6, (2013).
- [23] T. K. Dakhllallah, M. A. Zohdy, "Type-2 Fuzzy Kalman Hybrid Application for Dynamic Security Monitoring Systems based on Multiple Sensor Fusion" *International Journal On Smart Sensing And Intelligent Systems* Vol. 4, NO. 4, DECEMBER 2011
- [24] J. R. Layne, K. M. Passino, "Fuzzy model reference learning control for cargo ship steering", *IEEE Control Systems*, Vol. 13, No. 6, pp.23-34, (1993).
- [25] J. R. Layne, K.M. Passino, "Fuzzy Model Reference Learning Control", *Journal of Intelligent and Fuzzy Systems*, Vol. 4, No. 1, pp. 33-47, (1996).
- [26] B. I. Saeed, B. Mehrdadi, "Zero overshoot and fast transient response using a fuzzy logic controller", *IEEE 17th International Conference on Automation and Computing (ICAC) London*, ISBN: 9781467300001, pp. 116-120, (2011).
- [27] S. Ramesh, S. A. Lincon, "Fuzzy Model Reference Learning Control for Non-Linear Spherical Tank Process", *International Journal of Engineering Trends and Technology*, Vol.1, No. 4, pp.4459-4465, (2013).
- [28] O. Cerman, P. Husek, "Fuzzy model reference learning control with convergent rule base", *Proceedings of the International Federation of Automatic Control*, Vol. 43, No. 4, pp.282-286, (2010).



[29] A. Kharola, "A Pid Based Anfis & Fuzzy Control Of Inverted Pendulum On Inclined Plane (IPIP)" International Journal On Smart Sensing And Intelligent Systems Vol. 9, NO. 2, JUNE 2016

[30] G. Kopasakis, "Nonlinear performance seeking control using Fuzzy Model Reference Learning Control and the method of Steepest Descent", National Aeronautics and Space Administration Lewis Research Center, (1997).

[31] S. Riaz, L. Khan, "Adaptive soft computing strategy for ride quality improvement with anti-lock braking system", Proceedings of the IEEE International Bhurban Conference on Applied Sciences and Technology (IBCAST), pp. 280-285, (2016).

[32] Zheng, L., Li, Y. N., Shao, J., and Sun, X. S. (2007). "The Design of a Fuzzy-sliding Mode Controller of Semi-active Suspension Systems with MR Dampers " IEEE International Conference on Fuzzy Systems and knowledge Discovery., 4, 514-518.

[33] R. Rajamani, J. k. Hedrick, "Adaptive Observers for active automotive suspension: Theory and experiment", IEEE Transaction on control system technology, Vol.3, No. 1, pp.86-92, (1995).

[34] R. Ghazali, Y. M. Sam, M. F. Rahmat, K. Jusoff, Zulfatman, A. W. I. M. Hashim" **Self-Tuning Control of an Electro-Hydraulic Actuator System**" International Journal on Smart Sensing And Intelligent Systems Vol. 4, NO. 2, JUNE 2011.

Nomenclature

M_s is the sprung mass (Kg)

M_{us5} is the passenger seat mass (kg)

M_{us1}, M_{us2} is the front left and front right side unsprung mass respectively (kg)

M_{us3}, M_{us4} are the rear left and rear right side unsprung mass respectively (kg)

k_{s5} is the passenger seat stiffness (N/m)

k_{s1}, k_{s2} is the front left and front right side spring stiffness respectively (N/m?)

k_{s3}, k_{s4} are the rear left and rear right side spring stiffness respectively (N/m)

k_{t1}, k_{t2} are the front left and front right side tire stiffness respectively (N/m)

k_{t3}, k_{t4} are the rear left and rear right side tire stiffness respectively (N/m)

c_{s5} is the passenger seat damping coefficient (N/m)

c_{s1}, c_{s2} are the front left and front right side damping coefficient respectively (N/m)

c_{s3}, c_{s4} are the rear left and rear right side damping coefficient respectively (N/m)

c_{t1}, c_{t2} are the front left and front right side tire damping coefficient respectively (N/m)

c_{t3}, c_{t4} are the rear left and rear right side tire damping coefficient respectively (N/m)

$l_1 \& l_2$ are the distance between the center of gravity of the sprung mass and center of front and rear wheel axle respectively (m)

l_s is the distance of passenger seat position from the center of gravity (m)

b is the distance between the front or rear wheels (m)

b_s is the distance of passenger seat position from the center of gravity of the vehicle (m).

Appendix

Variable design parameters values of nonlinear active suspension system are shown in Table A1.

The design parameters of the electromagnetic actuator are listed in Table A2.



Table A1: parameters values of nonlinear

| parameters | values | Unit |
|----------------------------------|--------|-------------------|
| k_{s1}, k_{s2} | 19960 | N/m |
| k_{s3}, k_{s4} | 17500 | N/m |
| k_{s5} | 100000 | N/m |
| $k_{t1}, k_{t2}, k_{t3}, k_{t4}$ | 175500 | N/m |
| c_{s1}, c_{s2} | 1290 | N.s/m |
| c_{s3}, c_{s4} | 1620 | N.s/m |
| c_{s5} | 500 | N.s/m |
| $c_{t1}, c_{t2}, c_{t3}, c_{t4}$ | 14.6 | N.s/m |
| M_s | 1460 | Kg |
| M_{us1}, M_{us2} | 40 | Kg |
| M_{us3}, M_{us4} | 35.5 | Kg |
| M_{us5} | 100 | Kg |
| J_x | 460 | Kg.m ² |
| J_y | 2460 | Kg.m ² |
| l_s | 0.234 | M |
| l_1 | 1.011 | M |
| l_2 | 1.803 | M |
| b_s | 0.375 | M |
| b | 1.51 | M |
| ζ | 0.1 | - |

Table A2: parameters of the electromagnetic

| parameters | values | Unit |
|------------|--------|--------|
| C_m | 200 | N.s/m |
| Φ | 0.0759 | V.s |
| P_h | 0.2 | M |
| r | 0.008 | M |
| φ | 21.95 | degree |

Numerical Investigation of The Effect of Gaseous and Diesel Fuel Under Dual and Tri-mode on The Combustion and Exhaust Emissions in a CI Engine

Hayder A. Alrazen*

Technical Institute/Qurna
Southern Technical University
Qurna, Basra, Iraq
alrazan.h@stu.edu.iq

Saadoon F. Albahadili

Fuel & Energy Dep., Technical Engineering
collage/Basra
Southern Technical University
Basra, Iraq
drsadoun2@gmail.com

K. A. Ahmad

Department of Aerospace Engineering
Universiti Putra Malaysia
43400 UPM Serdang, Selangor, Malaysia
aekamarul@upm.edu.my

*Corresponding author at: E-mail address: hayderalrazen@yahoo.com, Phone NO. 009667731378400

Abstract- In this study, the engine was employed under dual-fuel and tri-fuel mode. The effect of hydrogen, methane and their mixtures on the combustion and emissions characteristics of a CI diesel engine under gas-diesel tri-fuel or dual-fuel operation was investigated at 1.4 exceed air and five mixing ratios of fuels at 2000 rpm. For CFD solver, the FLUENT code was used. The addition of gases fuels increases the peak temperature and peak in-cylinder pressure. The advantages of hydrogen addition in methane will enhance methane's combustion operation and make it further suitable for application of diesel engine. With Diesel-H₂ dual mode there is more reduction in CO₂ emission compared with Diesel-CH₄ mode. However, Diesel-H₂-CH₄ operations decrease the CO emission compared with the Diesel-CH₄ operation and decrease the NO emission compared with the Diesel-H₂ operation.

Key Words- Fluent, CFD, IC Engines, Combustion.

I. INTRODUCTION

High emissions of nitrogen oxide, smoke and particulate matter are products by diesel engines. The challenges of researchers now are to reduce exhaust emissions but without making any change on their mechanical configuration. Alternative fuel is one of new technologies to reduce emissions in CI engine. Natural gas, propane, and methanol were used in 2000 as alternative fuels for vehicles. Due to their clean burning nature and their ever-increasing employ in automobile industry, alternative fuels might be termed as future fuels. Hydrogen, methane and mixtures of methane and hydrogen were taken into consideration as alternative fuels in recent years in order to reduce the pollution of vehicles [1].

The researchers discovered that the gaseous fuel can be utilized in diesel engines as substitute fuel. For using CH₄-Diesel mode, it was observed that there is extension in the ignition delay compared with normal diesel mode. However it was found that H₂-Diesel operation produced many of the unwanted effects such as rapid burning rate, increased diffusivity and reduced ignition energy of hydrogen that

may lead to knocking. Methane addition has the ability to make hydrogen combustion stable and smoother which can avoid abnormal combustion [2,3]. Moreover, adding hydrogen can enhance methane's combustion process making it extra convenient in diesel engine application [4].

This work confirmed the worth of employing the Computational Fluid Dynamics (CFD) procedure in analyzing the dual fuel and tri fuel diesel engine and associated phenomena. The usage of GAMBIT software was chosen to create the entire computational domain of the engine. The effects of number of cells on the expected result were employed in order to examine the more accurate one. For CFD solver, the FLUENT code was used. The intake, compression, combustion, and expansion were studied in the simulation of engine cycle. The simulation data appears to obtain a well agreement with the data of experimental. The effect of hydrogen, methane and their mixtures (H₃₀-M₇₀, H₅₀-M₅₀, and H₇₀-M₃₀) on the combustion and emissions characteristics of a CI diesel engine under gas-diesel tri-fuel or dual-fuel operation was investigated at 1.4 exceed air and five mixing ratios of fuels at 2000 rev min⁻¹.

II. DATA AND INITIAL CONDITIONS

The engine simulation in this study is derived from the research which has been conducted by [5]. The engine details and properties of the gaseous fuels are shown in Table 1. In the present study, the engine was operated under dual-fuel and tri-fuel modes with different cases. Torque (20.18 N.M), intake temperature (330 K), excess air (λ) 1.4, and engine speed (2000 rpm) were taken constantly at an atmospheric pressure. Natural gas was assumed to be 100% methane as established in the literature [6,7]. Diesel-CH₄, diesel-H₂ dual-fuel operation, and diesel-CH₄-H₂ tri-fuel operation were employed in this work. H₃₀-M₇₀, H₅₀-M₅₀ and H₇₀-M₃₀ were designed for the mixtures percent of hydrogen to methane which are 30:70, 50:50 and 70:30 %, respectively based on [4], and were used in the simulations. Because of knocking, the maximum quantity addition by hydrogen was limited to 50% [8,9]. Therefore, the quantity of diesel was employed 50 percent by mass from the total fuel at diesel mode and the other 50 percent was substituted

by the methane and hydrogen as shown in Tables 2 and 3. The input power is employed to be the same for diesel, dual, and tri modes because the engine was running under the same statuses.

TABLE 1. Engine Specification [5].

| Subjects | Description |
|-----------------------------------|---|
| Model | Ricardo Hydra |
| Engine Type | DI diesel |
| Number of cylinder | 1 |
| Number of valve | 2 |
| Swept volume (lit) | 0.45 |
| Bore (mm) | 80.26 |
| Stroke (mm) | 88.9 |
| Compression ratio | 20.36: 1 |
| Combustion chamber shape | bowl in piston |
| Injector operating pressure (bar) | 250 |
| Valve timings | IVO 8 BTDC, IVC 42 ATDC EVO 60 BBDC, EVC 12 ATDC |

TABLE 2. Fuels Ration

| Total fuel at diesel mode | Ration fuel of diesel at dual and tri mode | Ration fuel of gaseous at dual and tri mode |
|---------------------------|--|---|
| 1.11 kg/h | 50% of total fuel | 50% of total fuel |

Table 3: Definition of percent for methane and hydrogen

| Cases | Hydrogen | Methane |
|----------|----------|---------|
| Methane | 0% | 100% |
| H30-M70 | 30% | 70% |
| H50-M50 | 50% | 50% |
| H70-M30 | 70% | 30% |
| Hydrogen | 100% | 0% |

In this study, the gaseous fuel was naturally aspirated along with air into the intake port, and diesel which was injected directly into the cylinder. Therefore, the gaseous fuels were defined as a mass fraction with air in FLUENT.

This work assumes that the fresh air into the cylinder was composed of O₂ and N₂ their mass fraction were 23.2% and 76.8% respectively [10], then to present the mass fraction of hydrogen in methane and air, the following expression is used:

$$X_{H_2} = \frac{m_{h_2}}{m_{h_2} + m_{ch_4} + m_{air}} \quad (1)$$

Where, \dot{m} was the mass flow rate of gaseous and \dot{m}_{air} can be calculated here by:

$$\dot{m}_{air} = \lambda \cdot AFR_{D,st.} \cdot \dot{m}_D + \lambda \cdot AFR_{st.gaseous} \cdot \dot{m}_{gaseous} \quad (2)$$

Where, λ was the exceeding air and $AFR_{st.gaseous}$, corresponding to the stoichiometric air-fuel ratio (by mass) for gaseous fuels which can be obtained from Table 4, and $AFR_{D, st.}$, corresponding to the stoichiometric air-fuel ratio (by mass) for diesel.

TABLE

| | Methane | M70-H30 | M50-H50 | M30-H70 | Hydrogen |
|--|-----------|---------|---------|---------|-----------|
| Density/(kg/m ³) | 0.65 | 0.48 | 0.37 | 0.25 | 0.0837 |
| LHV/(MJ/kg) | 50.02 | 53.57 | 57.79 | 65.81 | 119.93 |
| Stoichiometric AFR/(kg/kg) | 17.25 | 22.39 | 25.82 | 29.25 | 34.39 |
| Flammability limits/(Vol.% in air) | 5.0-15.0 | - | - | - | 4.0-75.0 |
| Flammability limits/(AFR) | 11.2-37.7 | - | - | - | 5.1-369.9 |
| Thermal conductivity/(10 ⁻² W/mK) | 2.42 | - | - | - | 4.97 |
| Laminar burning velocity/(m/s) | 0.27 | - | - | - | 2.8 |
| Auto ignition temperature/(K) | 813 | - | - | - | 858 |

Gaseous Fuel Properties (20 C, 1 Bar) [4].

III. CFD MODELING

This study has used the RNG k- ϵ turbulent model as the most appropriate turbulent model according to [6,11]. This method applies 2 model transport equations in form of differentials to control the amount of turbulent kinetic energy, k , as well as its dissipation rate, ϵ [12]. for incompressible flow, were solved numerically by finite volume method to obtain velocity, temperature and pressure distribution along the domain.

Continuity equation

$$\frac{\partial}{\partial x_i} (\rho U_i) = 0 \quad (3)$$

$i=1,2$ (equivalent to x, y, z direction)
 $U_i = U, V$

Where the instead velocities in 2D turbulent flow defined as :

$$u(t) = U + u, \quad v(t) = V + v$$

Where:

U, V , steady mean velocities in the x, y , direction respectively .

u, v , fluctuating velocities in the x, y , direction respectively.

For fluid passing an infinitesimal control volume that is fixed in space, the general form of the momentum equation yield by conservation of momentum is given as :

$$\frac{\partial}{\partial x_j}(\rho U_j U_i) = -\frac{\partial P}{\partial x_i} + \frac{\partial}{\partial x_j} \left[\mu \left(\frac{\partial U_i}{\partial x_j} + \frac{\partial U_j}{\partial x_i} \right) - \rho \overline{u_i u_j} \right] + F_i \quad (4)$$

Where: F_i : the bodyforces in the x, y, z direction. $j : 1, 2, 3$

The body forces are explicitly accounted in the source term, for example the body force per unit volume due to gravity is equivalent to $SMX=0, SMZ=0, SMY = -\rho g$.

$\overline{u_i u_j}$: represents the Reynolds stresses.

$$\overline{u_i u_j} = \frac{2}{3} k \delta_{ij} - \mu_t \left(\frac{\partial U_i}{\partial x_j} + \frac{\partial U_j}{\partial x_i} \right) \quad (5)$$

Where δ_{ij} : Kronecker delta , $\delta_{ij} = 1$ if $i=j$, $\delta_{ij} = 0$ if $i \neq j$ and k : kinetic energy, μ_t : eddy viscosity

The First Law of Thermodynamics is applied to the fluid passing an infinitesimal control volume fixed in space to obtain the energy equation.

$$\frac{\partial}{\partial x_j}(\rho U_j T) = \frac{\partial}{\partial x_j} \left[\frac{\mu}{Pr} \frac{\partial T}{\partial x_j} - \rho \overline{u_j t} \right] \quad (6)$$

Where the instead temperature $T(t) = T + t$

T : steady mean temperature , t : fluctuating temperature .

$$\overline{u_j t} = -\frac{\mu_t}{\sigma_T} \frac{\partial T}{\partial x_j} \quad (7)$$

$$Pr = \frac{\mu c_p}{k} \quad (8)$$

Pr : Prandal number, σ_T : Turbulence model constant

Species:

$$\text{div}(\rho \Phi U) = \text{div}(\Gamma \text{grad } \Phi) + S\Phi \quad (9)$$

For turbulent kinetic energy (k)[17]:

$$\frac{\partial}{\partial x_j}(\rho U_j k) = \frac{\partial}{\partial x_j} \left[\left(\mu + \frac{\mu_t}{\sigma_k} \right) \frac{\partial k}{\partial x_j} \right] + G_k - \rho \epsilon \quad (10)$$

For energy dissipation rate (ϵ):

$$\frac{\partial}{\partial x_j}(\rho U_j \epsilon) = \frac{\partial}{\partial x_j} \left[\left(\mu + \frac{\mu_t}{\sigma_\epsilon} \right) \frac{\partial \epsilon}{\partial x_j} \right] + C_{1\epsilon} \frac{\epsilon}{k} G_k - \rho C_{2\epsilon} \frac{\epsilon^2}{k} \quad (11)$$

G_k : Production term of turbulence

$$G_k = -\rho \overline{u_i u_j} \left(\frac{\partial U_i}{\partial x_j} \right) \quad (12)$$

$$\mu_t = \rho C_\mu \frac{k^2}{\epsilon} \quad (13)$$

$C_{1\epsilon} = 1.44, C_{2\epsilon} = 1.92, C_\mu = 0.09, \sigma_k = 1.0, \sigma_\epsilon = 1.3$

The pressure-based solver and implicit method were used in accordance to previous studies [7,13]. The second order segregated solver is employed to solve continuity, momentum, energy, k- ϵ equations for this research. This study makes use of the Pressure-Implicit with Splitting of Operators (PISO) pressure-velocity coupling scheme as also employed by [7]. The Wave model is used to show both the liquid atomization/primary breakup and the secondary breakup/drop breakup processes. In this model, the recommended value for Bo is for diesel sprays whilst breakup up time constant is depend on wall impingement effects and to the initial disturbance grade in the process of breakup. The advisable values are $B1 = (10-60)$ [12]. The constants in this work were $B_0 = 0.61$ and $B_1 = 30$, depend on size of nozzle and diesel mass flow rate. There were two known mechanism as stated by [14] that form nitric oxide during the process of combustion: Prompt NO_x and Thermal NO_x .

IV. CHEMICAL REACTIONS MODELING

In this research, the Finite-Rate/Eddy Dissipation Model was used to simulate the turbulent combustion based on literature [6]. As per [15,16] diesel combustion was modelled, and the process of methane combustion with a 2 stage mechanism has been modelled according to [6,17]. The single step reduced mechanism, that is $2\text{H}_2 + \text{O}_2 \rightarrow 2\text{H}_2\text{O}$, gives considerable predictions of limits for lean deflagrations and good results for deflagration velocities for near the lean flammability limit conditions. Therefore, one-step mechanism is employed in this study according to [18].

V. GRID GENERATION

Since there is very little gap between the head of the cylinder and the piston of the Direct Injection Ricardo Hydra engine [5]; it is a complex task to generate calculations for the moving mesh in that area. The geometric configuration of the 2D simulation model can be instituted in the early phase of Gambit geometry design. During that

phase, the main fluid and solid areas of the interface can be identified. Fig. 1 shows the mesh generated by the Gambit 2.4.6 of Ansys containing both quadrilateral and triangular elements. It is important to apply these elements in order to provide the needed conditions for the moving valves and deforming zone like the combustion chamber [12]. The top center of Fig. 1 denotes the location of the coordinate system origin in the middle of the cylinder head.

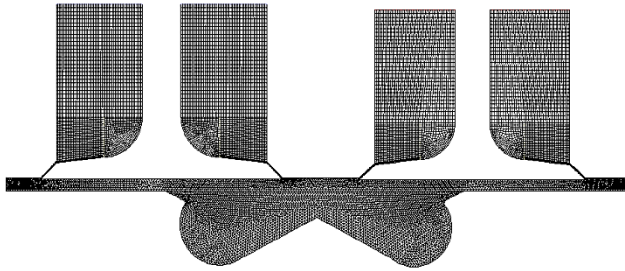


Fig. 1. Geometry and Mesh at TDC

The Fluent software uses a particular technique to simulate the closing and opening of the valve. Fig. 2 shows the interface between the combustion chamber and the valves layer. Only the intake valve has been used for reason simplicity.

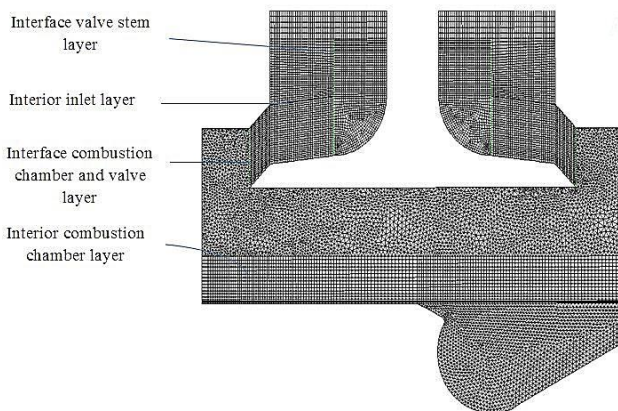


Fig. 2. Interface of computational grid

VI. RESULTS AND DISCUSSIONS

A. In Cylinder Pressure

Fig. 3 indicates the pressure cycles calculated in different numerical test cases. The result in the figure was depicted with the crank angle degree. The solid black line is a symbol for the first case without the hydrogen supply, when the engine works in the Diesel-CH₄ dual fuel mode. When the

quantity of hydrogen is increased from 30 to 100 percent, the peak pressure positions and levels as well as the shape of pressure cycles have to be altered because of the different combustion developments. As has already been demonstrated, when the hydrogen content increases, higher flame speeds take place in the gases/air mixture and this discloses the faster pressure rise. Therefore, When value of hydrogen fraction was increased, peak in cylinder pressure was also increased that due to higher in-cylinder gas temperature and pressure. As shown in Fig. 3, at 1.4 exceed air, as compared with dual and tri fuel operations, the peak in-cylinder pressure increases from 4.55 to 6.97, 7.43, 7.81 and 7.98 MPa for adding CH₄, H30-M70 H50-M50, H70-M30 and H₂, respectively.

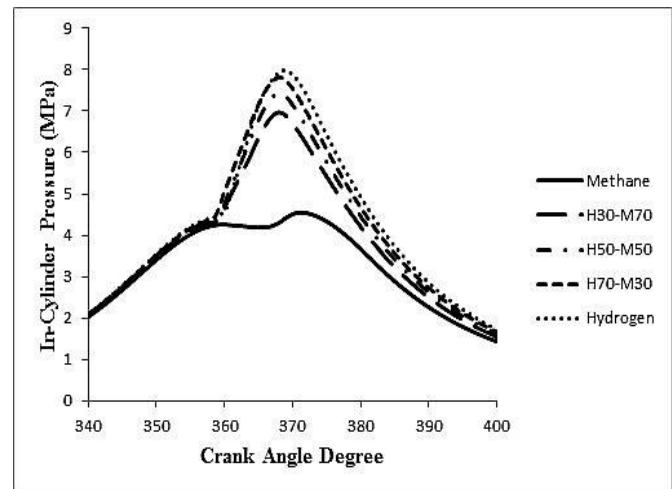


Fig. 3. In-cylinder pressure curves at different ratio of gaseous addition and 1.4 exceed air.

B. Temperature

At 1.4 exceed air (λ) for different gaseous fuel additions, the in-cylinder temperature histories are presented in Fig. 4. For the Diesel-H30-M70 operation, a temperature was lower than Diesel-H50-M50, Diesel-H70-M30, and Diesel-H₂ operations. In the figure illustrated that when adding hydrogen fraction to methane the peak temperature was increased from 1397.64 to 1804.69, 1959.2, 2096.89, and 2238.58 K for adding CH₄, H30-M70, H50-M50, H70-M30 and H₂, respectively. The increment in in-cylinder temperature here is firstly because of the burning of the premixed mixture and secondly concerned to burning of fuel mixture in diffusion phase and the flame propagation as mentioned by [10]. Table 5 illustrates that the temperature of combustion and its formation region increased with the enhancement of H₂ addition to methane and it reached its maximum rate in the Diesel-H₂ operation.

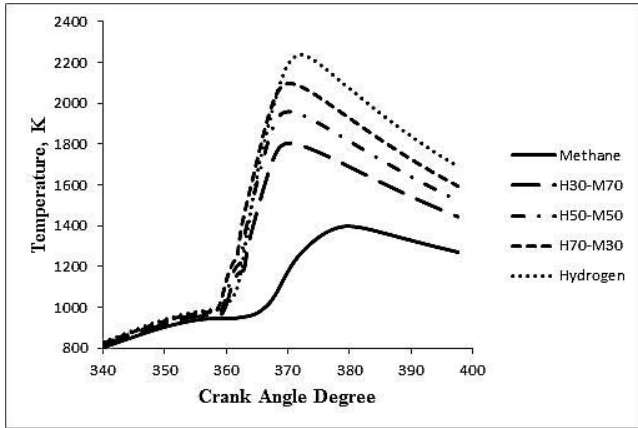


Fig. 4. Temperature curves under different ratio of gaseous addition and 1.4 exceed air.

TABLE 5. The development of average temperature under different ratio of gaseous addition and 1.4 exceed air

| | Methane | H30-M70 | H50-M50 | H70-M30 | Hydrogen | | | | | | | | | | | | | | | | | | | | | |
|--|----------|----------|----------|----------|----------|----------|----------|----------|----------|----------|----------|----------|----------|----------|----------|----------|----------|----------|----------|----------|----------|----------|----------|----------|----------|----------|
| 365 CAD | | | | | | | | | | | | | | | | | | | | | | | | | | |
| 375 CAD | | | | | | | | | | | | | | | | | | | | | | | | | | |
| 385 CAD | | | | | | | | | | | | | | | | | | | | | | | | | | |
| 395 CAD | | | | | | | | | | | | | | | | | | | | | | | | | | |
| Temperature | | | | | | | | | | | | | | | | | | | | | | | | | | |
| | | | | | | | | | | | | | | | | | | | | | | | | | | |
| <table border="0"> <tr> <td>5.77e+02</td> <td>6.69e+02</td> <td>7.62e+02</td> <td>8.55e+02</td> <td>9.47e+02</td> <td>1.04e+03</td> <td>1.13e+03</td> <td>1.23e+03</td> <td>1.32e+03</td> <td>1.41e+03</td> <td>1.50e+03</td> <td>1.60e+03</td> <td>1.69e+03</td> <td>1.78e+03</td> <td>1.87e+03</td> <td>1.97e+03</td> <td>2.06e+03</td> <td>2.15e+03</td> <td>2.24e+03</td> <td>2.34e+03</td> <td>2.43e+03</td> </tr> </table> | | | | | | 5.77e+02 | 6.69e+02 | 7.62e+02 | 8.55e+02 | 9.47e+02 | 1.04e+03 | 1.13e+03 | 1.23e+03 | 1.32e+03 | 1.41e+03 | 1.50e+03 | 1.60e+03 | 1.69e+03 | 1.78e+03 | 1.87e+03 | 1.97e+03 | 2.06e+03 | 2.15e+03 | 2.24e+03 | 2.34e+03 | 2.43e+03 |
| 5.77e+02 | 6.69e+02 | 7.62e+02 | 8.55e+02 | 9.47e+02 | 1.04e+03 | 1.13e+03 | 1.23e+03 | 1.32e+03 | 1.41e+03 | 1.50e+03 | 1.60e+03 | 1.69e+03 | 1.78e+03 | 1.87e+03 | 1.97e+03 | 2.06e+03 | 2.15e+03 | 2.24e+03 | 2.34e+03 | 2.43e+03 | | | | | | |

VII. EMISSIONS

A. Nitric Oxides (NO) Emission

In this study, three mixtures of hydrogen-methane fuel were used. The lowest hydrogen content or the highest methane content results in the best effect in decreasing NO emission. For the Diesel-H30-M70 operation, nitric oxides emission was lower than Diesel-H50-M50, Diesel-H70-M30, and Diesel-H₂ operations. Fig. 5 displays nitric oxides variations with crank angle degree for exceed air of 1.4. When the hydrogen fraction rises, the combustion temperature is frequently high, this leads to increase the peak NO emission. As shown in the figure, when adding hydrogen fraction to methane the NO mass fraction was increased from 2.19×10^{-7} to 8.12×10^{-5} , 0.0005, 0.0021, and 0.0036 for adding CH₄, H30-M70, H50-M50, H70-M30 and H₂, respectively. Table

6 represented that the NO mass fraction of pollutant and its formation region increased along with the enhancement of H₂ addition to methane and it reached its maximum rate at the Diesel-H₂ operation.

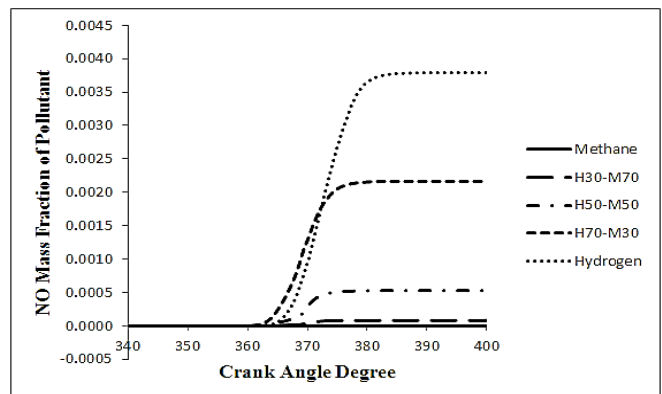
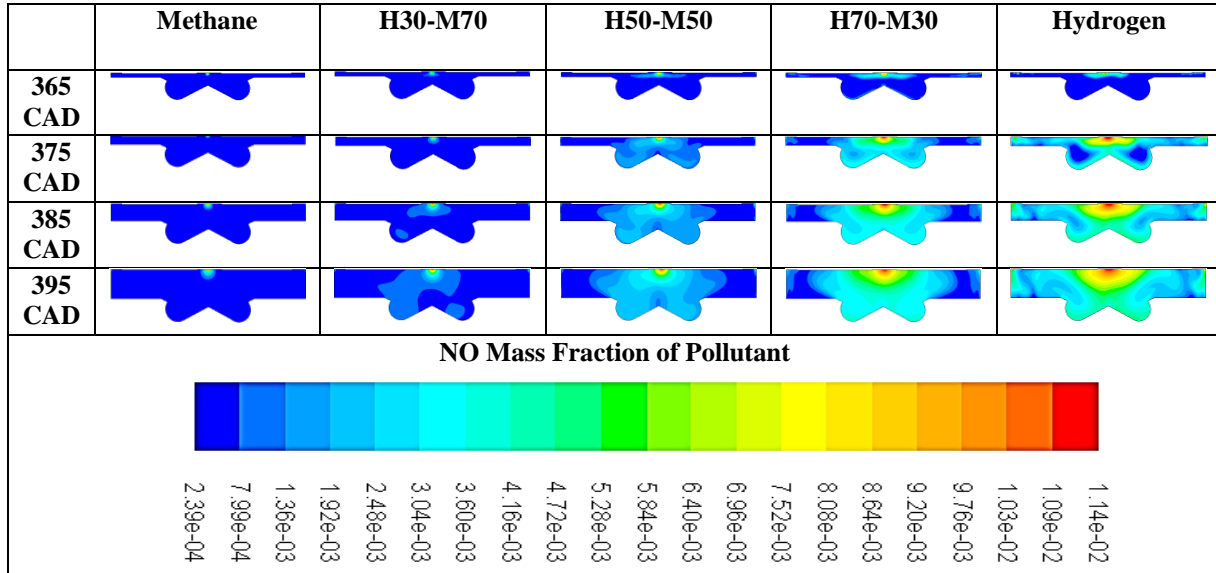


Fig. 5. NO emissions curves under different ratio of gaseous addition and 1.4 exceed air.

TABLE 6. The development of (NO) mass fraction of pollutant under different ratio of gaseous addition and 1.4 exceed air



B. CO Emission

Fig. 6 shows the CO emissions under dual-fuel and tri-fuel operations at 1.4 exceed air. For the addition of methane, H30-M70, H50-M50, H70-M30 and hydrogen in diesel fuel, the CO mass fraction reductions are 0.033, 0.0207, 0.0136, 0.0077, and 0.00032, respectively. It is noted that the CO emission was gradually reduced with hydrogen addition and employing H70-M30 can be realized to lower the CO emission than other two hydrogen-methane mixtures. Schefer et al. [19] stated that adding hydrogen into methane increased the quantity of OH, H and O radicals which enhanced certain crucial reaction rates, thus resulting in the enhancement of methane’s lean burn stability and thus lowering the CO emission. Table 7 respectively showed that the CO mass fraction and its formation region decreased along with the enhancement of H₂ addition to methane and it reached its maximum rate at the Diesel-CH₄ operation.

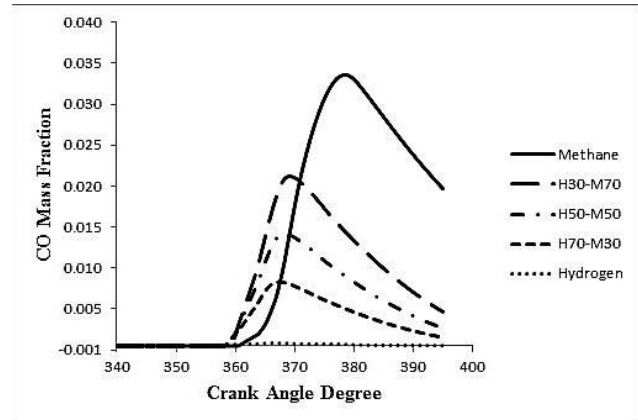
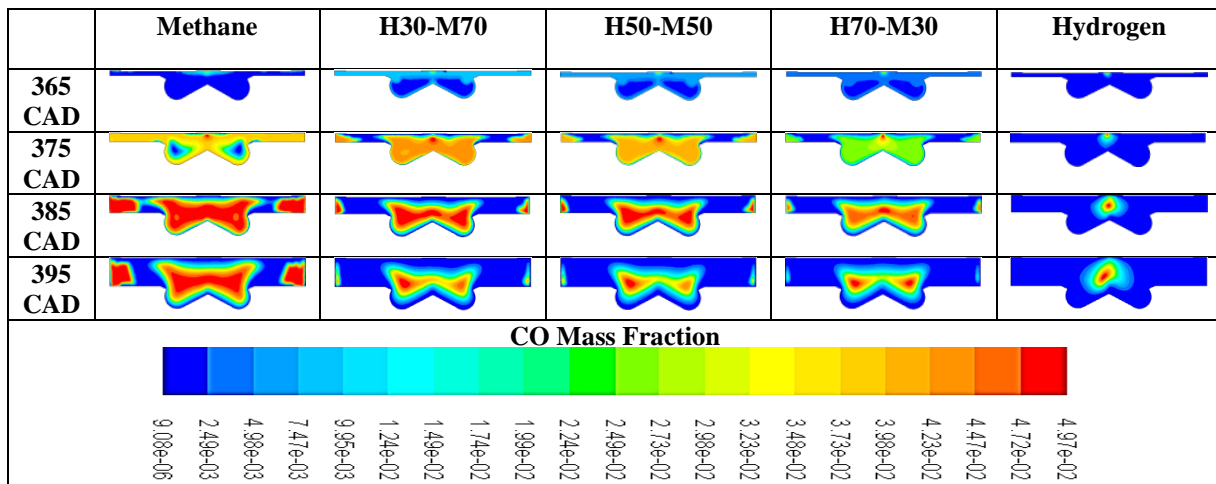


Fig. 6: CO emissions curves under different ratio of gaseous addition and 1.4 exceed air.

TABLE 7. The development of CO mass fraction under different ratio of gaseous addition and 1.4 exceed air



C. CO₂ Emissions

Fig. 7 shows the CO₂ emissions under dual-fuel and tri-fuel operations at 1.4 exceed air. For Diesel-CH₄ operation, CO₂ is one of the byproducts of incomplete combustion of methane. For the addition of methane, H30-M70, H50-M50, H70-M30 and hydrogen in diesel fuel, the CO₂ mass fraction reductions are 0.06, 0.037, 0.024, 0.0136, and 0.0005, respectively. It is noted that CO₂ emission was gradually reduced with hydrogen addition and employing H70-M30 can be realized to lower CO₂ emission than other two hydrogen-methane mixtures. Table 8 illustrated that with the enhancement of H₂ addition to methane, the CO₂ mass fraction and its formation region were decreased and it reached its maximum rate at the Diesel-CH₄ operation.

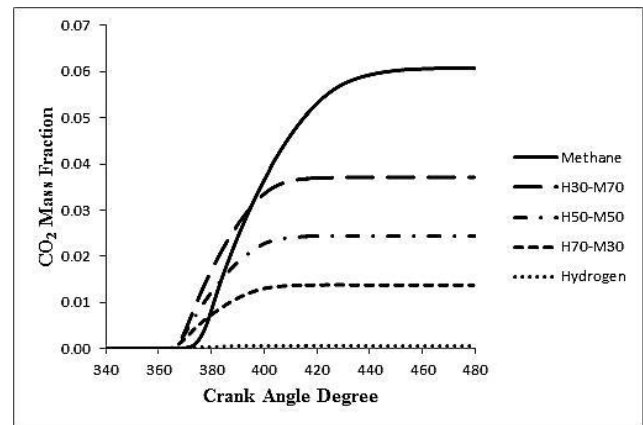
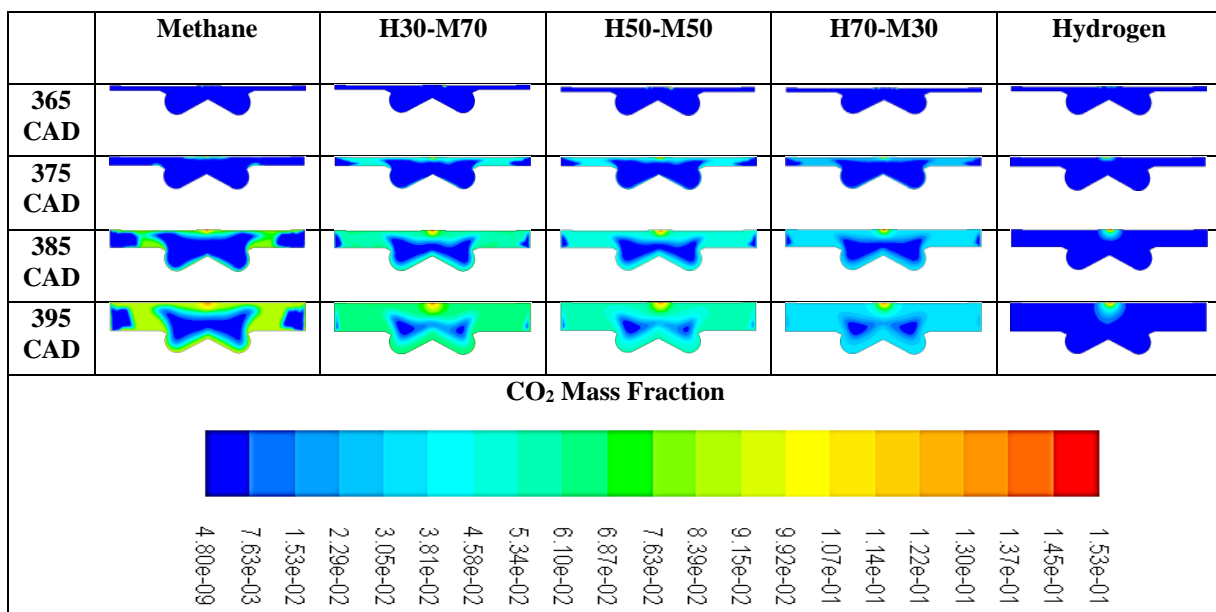


Fig. 7. CO₂ emissions curves under different ratio of gaseous addition and 1.4 exceed air.

TABLE 8. The development of CO₂ mass fraction under different ratio of gaseous addition and 1.4 exceed air



VIII. CONCLUSION

The current study proposes that by adding hydrogen into CH₄ fuel and diesel it can improve velocity of combustion and therefore enhancing the combustion characteristics. Mix of methane with hydrogen is required to increase the lean-burn attributes as well as minimize the actual engines emissions (mainly CO₂, HC as well as CO), but the possibility involving greater NO_x emissions will be involving concern. This helps combustion behaviour of action with the possibility to formulate engines with increased performance and lower environmentally friendly impact. Hydrogen itself provides the possible to be an alternate to be able to regular fuel, since it is absolutely carbon-free along with not too difficult to make but high pricey.

The major conclusions are summarized as following:

- Successfully developed a CFD simulation was obtained for predicting combustion characteristics and emissions on the diesel engine.
- Comprehension of using the dual and tri fuel in diesel engine and knowing the appropriate values of the mixture to give the best results.
- The addition of gases fuels increases the peak temperature and peak in-cylinder pressure. The advantages of hydrogen addition in methane will enhance methane's combustion operation and make it further suitable for application of diesel engine.
- Tri-fuel and dual-fuel modes have a similar suppression effect on CO₂ emission but with hydrogen there is more reduction in CO₂ emission compared with methane. However, Diesel-H₂-CH₄ operations decrease the CO emission compared with the Diesel-CH₄ operation and decrease the NO emission compared with the Diesel-H₂ operation. High hydrogen fraction in methane (H70-M30) is suggested in order to reduce CO/CO₂ emissions, whereas low hydrogen fraction in methane (H30-M70) can suppress the uncontrolled hydrogen combustion and limit the increment of the NO emission.

IX. REFERENCES

- [1] Sahoo, B., Sahoo, N., & Saha, U. (2009). Effect of engine parameters and type of gaseous fuel on the performance of dual-fuel gas diesel engines—A critical review. *Renewable and Sustainable Energy Reviews*, 13(6), 1151-1184.
- [2] Bose, P. K., & Banerjee, R. (2012). An experimental investigation on the role of hydrogen in the emission reduction and performance trade-off studies in an existing diesel engine operating in dual fuel mode under exhaust gas recirculation. *Journal of Energy Resources Technology*, 134(1), 012601.
- [3] Liew, C., Li, H., Nuszowski, J., Liu, S., Gatts, T., Atkinson, R., & Clark, N. (2010). An experimental investigation of the combustion process of a heavy-duty diesel engine enriched with H₂. *International Journal of Hydrogen Energy*, 35(20), 11357-11365.
- [4] Zhou, J., Cheung, C., & Leung, C. (2014). Combustion, performance and emissions of a diesel engine with H₂, CH₄ and H₂-CH₄ addition. *International Journal of Hydrogen Energy*, 39(9), 4611-4621.
- [5] Wannatong, K., Akarapanyavit, N., Siengsanorh, S., & Chanchaona, S. (2007). *Combustion and Knock Characteristics of Natural Gas Diesel Dual Fuel Engine*.
- [6] Abagnale, C., Cameretti, M., De Simio, L., Gambino, M., Iannaccone, S., & Tuccillo, R. (2014). Numerical simulation and experimental test of dual fuel operated diesel engines. *Applied Thermal Engineering*, 65(1), 403-417.
- [7] Abdullah, S., Kurniawan, W. H., & Shamsudeen, A. (2008). Numerical analysis of the combustion process in a compressed natural gas direct injection engine. *Journal of Applied Fluid Mechanics*, 1(2), 65-86.
- [8] Lata, D., Misra, A., & Medhekar, S. (2012). Effect of hydrogen and LPG addition on the efficiency and emissions of a dual fuel diesel engine. *International Journal of Hydrogen Energy*, 37(7), 6084-6096.
- [9] Saravanan, N., & Nagarajan, G. (2008). An experimental investigation of hydrogen-enriched air induction in a diesel engine system. *International Journal of Hydrogen Energy*, 33(6), 1769-1775.
- [10] Yang, Z., Chu, C., Wang, L., & Huang, Y. (2015). Effects of H₂ addition on combustion and exhaust emissions in a diesel engine. *Fuel*, 139, 190-197.
- [11] Ng, H. K., Gan, S., Ng, J., & Pang, K. M. (2013). Simulation of biodiesel combustion in a light-duty diesel engine using integrated compact biodiesel-diesel reaction mechanism. *Applied Energy*, 102, 1275-1287.
- [12] Fluent, F. (2006). 6.3 user's guide. *Fluent Inc*.
- [13] Shojaeefard, M., & Noorpoor, A. (2008). Flow simulation in engine cylinder with spring mesh. *American Journal of Applied Sciences*, 5(10), 1336.



- [14] Jayashankara, B., & Ganesan, V. (2010). Effect of fuel injection timing and intake pressure on the performance of a DI diesel engine–A parametric study using CFD. *Energy Conversion and Management*, 51(10), 1835-1848.
- [15] Jones, W. P., & Tyliczszak, A. (2010). Large eddy simulation of spark ignition in a gas turbine combustor. *Flow, Turbulence and Combustion*, 85(3-4), 711-734.
- [16] Jones, W., & Lindstedt, R. (1988). Global reaction schemes for hydrocarbon combustion. *Combustion and Flame*, 73(3), 233-249.
- [17] Selle, L., Lartigue, G., Poinso, T., Koch, R., Schildmacher, K., Krebs, W., . . . Veynante, D. (2004). Compressible large eddy simulation of turbulent combustion in complex geometry on unstructured meshes. *Combustion and Flame*, 137(4), 489-505.
- [18] Fernández-Galisteo, D., Sánchez, A., Liñán, A., & Williams, F. (2009). One-step reduced kinetics for lean hydrogen–air deflagration. *Combustion and Flame*, 156(5), 985-996.
- [19] Schefer, R. W., Wicksall, D., & Agrawal, A. (2002). Combustion of hydrogen-enriched methane in a lean premixed swirl-stabilized burner. *Proceedings of the Combustion Institute*, 29(1), 843-851.

Power Quality Improvement for Grid-connected Solar Plant Using Intelligent Decision Support System

Dr. Ali Hadi Abdulwaid¹ & Dr. Diyah Kammel Sharry² & Dr. Mohammed Al-Mumin³

Electrical Power Engineering / Southern Technical University

Dr_ali_h@hust.edu.cn¹, diahpower@stu.edu.iq², Mohammed_almumin@yahoo.com³

Abstract- The demand for electricity as an economical source of energy is growing rapidly. Hence, renewable energy sources are being widely used. Solar energy systems are important for system engineers. To meet international demand, system engineers have introduced solar energy into electrical networks. Along with the increase in power, energy injection from solar power plants is problematic. Hence, the power quality of current power lines fails to meet standards.

This study introduces the use of a fuzzy system with rapid control features on the basis of the continuous compensation method. In the field of power engineering, static VAR compensator devices are studied and applied. Using a Fixed Capacitor Thyristor Controlled Reactor (FC-TCR) is advantageous because it can increase dynamic stability, load transmission line capabilities and the quality of electricity. Simulation results indicate the effectiveness of the proposed compensation strategy in improving the quality of electricity and the stability of system.

Index Terms— Power Quality, Renewable Energy Sources, FC-TCR, PV Array

I. INTRODUCTION

The demand for electric power is continuously increasing. To meet this demand, the entire energy system is operated at its maximum capacity, thereby potentially generating problems of stability, voltage collapse and network failure. Controllers of flexible AC transmission systems are used to improve the stability and security of power systems along with their main application of power flow control for end users and efficiently use the available transfer capabilities. Compensating reactive power through a static VAR compensator (SVC) leads to the following benefits:

A high level of voltage in the Busbar:

- reduction of energy losses
- reduction of consumption

Improvement of the power factor:

- efficient use of existing power plants
- low plant losses

Traditional energy is often used to generate electricity. Typical sources of such energy are fossil fuels, including oil, natural gas and coal. Generation capacity must be

increased and loss should be reduced to meet the increasing power demand and optimise the transfer of energy at different levels. Thus far, traditional energy sources play an important role in generating electricity. However, engineers are now attempting to find alternative energy sources to address the increasing demand for electricity while reducing the pressure on the availability of conventional energy because of the negative environmental impacts, such as greenhouse gas emissions and detrimental effects on animals and plants, of traditional energy sources.

This search for alternative energy has led engineers to discover renewable energy sources. Solar energy, wind energy, tides, waves and geothermal energy are the main sources of renewable energy. Wind energy and solar energy are emerging renewable energy sources that provide a backup for power generation and rural (off-grid) energy services. However, these renewable energy sources are more expensive than conventional ones, and their long-term availability is uncertain. These shortcomings open up new areas of engineering and research with the goal of identifying the most cost-effective energy sources. As users of energy, we are responsible for realising such objective and promoting the use of alternative power.

II. SOLAR PHOTOVOLTAIC (PV) CELL

At present, we rely mostly on non-renewable energy, which continues to be an important cause of pollution and other types of natural corruption. Finding viable alternatives is becoming progressively crucial as a result of these problems and the diminishing oil supply. The best test is to project a reasonable future, which depends on the incorporation and control of renewable energy sources in the generation. After hydroelectric and wind energy, solar photovoltaic (PV) energy is the third most important source of renewable energy in terms of universally introduced capacity.

Solar PV systems use solar panels to convert solar energy to electrical energy (Fig. 1). These solar panels comprise PV cells. PV cells (photovoltaic cells) are composed of semiconductor materials that show PV impact. PV impact is a phenomenon in which electrons are energised in a high-energy state by means of photons. These photons lead to the electrons functioning as charge carriers for the current flow.

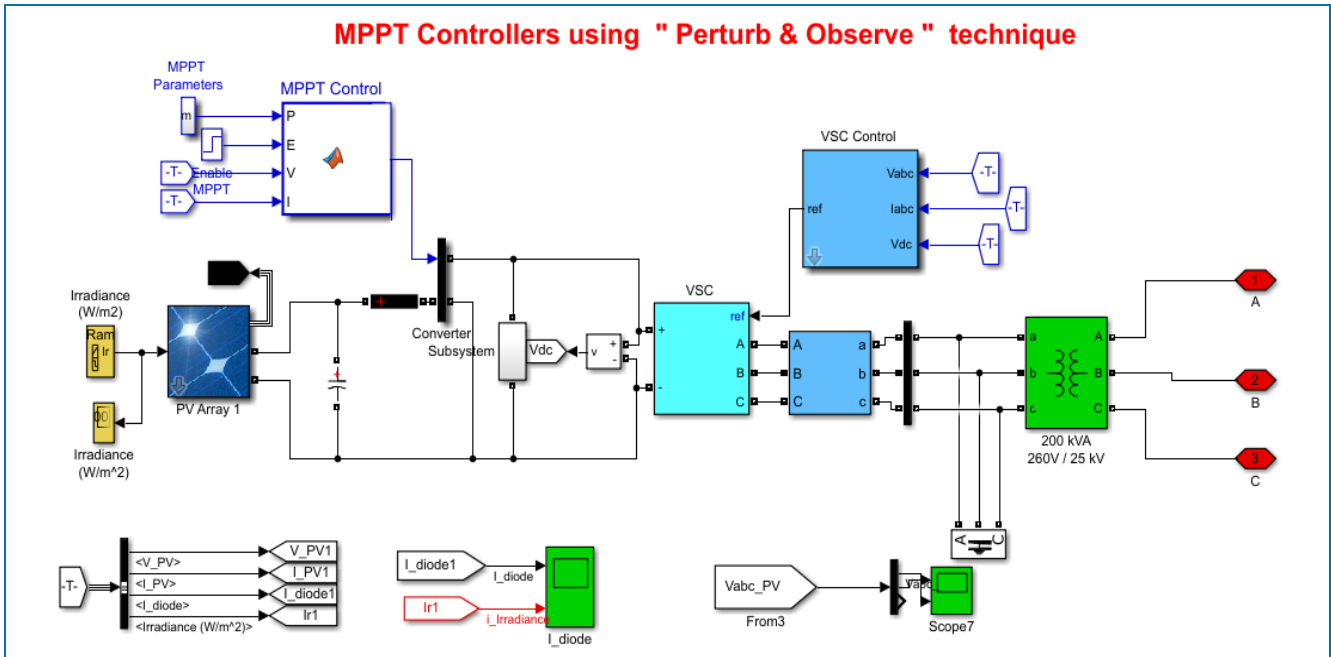


Fig. 1 Solar photovoltaic system.

From a mathematical point of view (Fig.2), the output current of a PV module can be displayed as

$$I = n_p I_{pv} - n_p I_o \left[\exp\left(\frac{V + IR_s}{aV_t}\right) - 1 \right] - \frac{V + IR_s}{R_p} \quad (1)$$

where

I = current

V = voltage of the PV module

I_{pv} = photocurrent

I_o = reverse saturation current

n_p = number of cells connected in parallel

n_s = number of cells connected in series

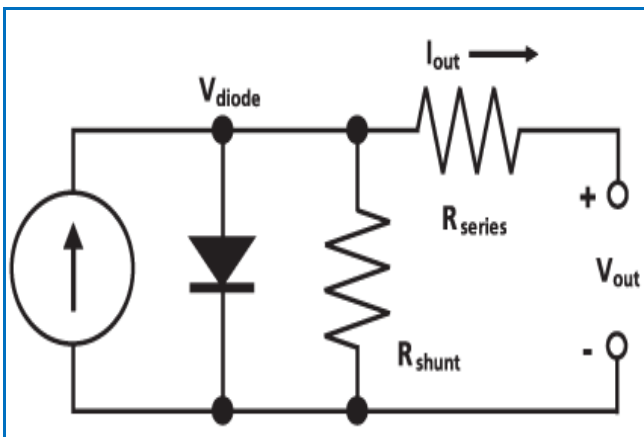


Fig. 2 Electrical circuit of PV cell.

III. STATIC VAR COMPENSATOR (SVC)

Static VAR systems are used in transmission systems for various applications. The main function is the rapid control of the voltage in a transmission network. The device can be installed in the middle or end sections of transmission lines. SVCs are static generators/absorbers connected in shunt that can be changed to control system voltage.

SVCs can improve transmission and distribution performance in many ways. Providing SVCs in one or more locations in a network can increase transmission capacity, reduce losses, maintain an even voltage profile in various operating situations, improve the dynamic stability of the system and soften fluctuations in active power.

SVCs are high-voltage systems that dynamically control network voltage at their coupling points. The main task of an SVC is to keep the network voltage constant on the Busbar of a set reference value. An SVC usually consists of a thyristor-controlled reactor (TCR) parallel to a bank of capacitors. From an operational point of view, SVCs behave like a shunt-connected variable reactance that generates or absorbs reactive power to adjust the voltage at points connected to the AC network (Fig.3).

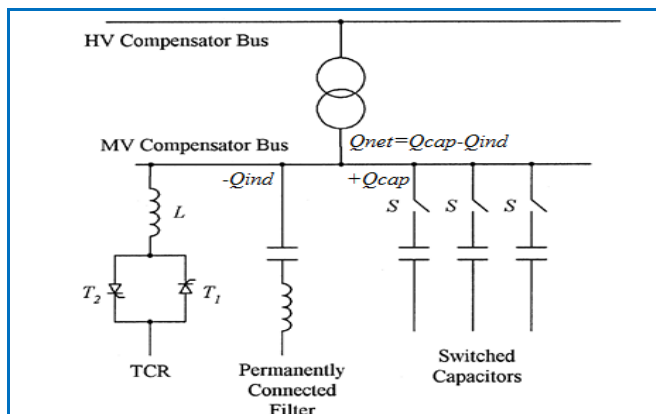


Fig. 3 Fixed capacitor–Thyristor-controlled reactor.

The bank of fixed capacitors is connected in shunt with the TCR to extend the controllable range to the main power factor region. The TCR MVAR has a greater capacity than the fixed capacitor to compensate for the capacitive MVAR and provide inductive reactive net power if a lagged power factor operation is desired.

PF is defined as the ratio of KW to KVA extracted by the load where KW describes the real power flowing to the load and KVA mentions the apparent power of the circuit . The reactive power in the AC power system is the phase angle between the current and voltage waveforms. This is a reason for a low PF. This small PF increases loads of energy consumption and also leads to equipment damage. It is efficient to maintain the ideal value of PF near the unit to avoid losses and improve the efficiency of the source. The operational flow of the methodology to improve the FP is shown in (Fig.4). If $PF = 1$, it means that the waveform of the current is in perfect synchronization with the voltage waveform, so the full power It is transferred to the load.

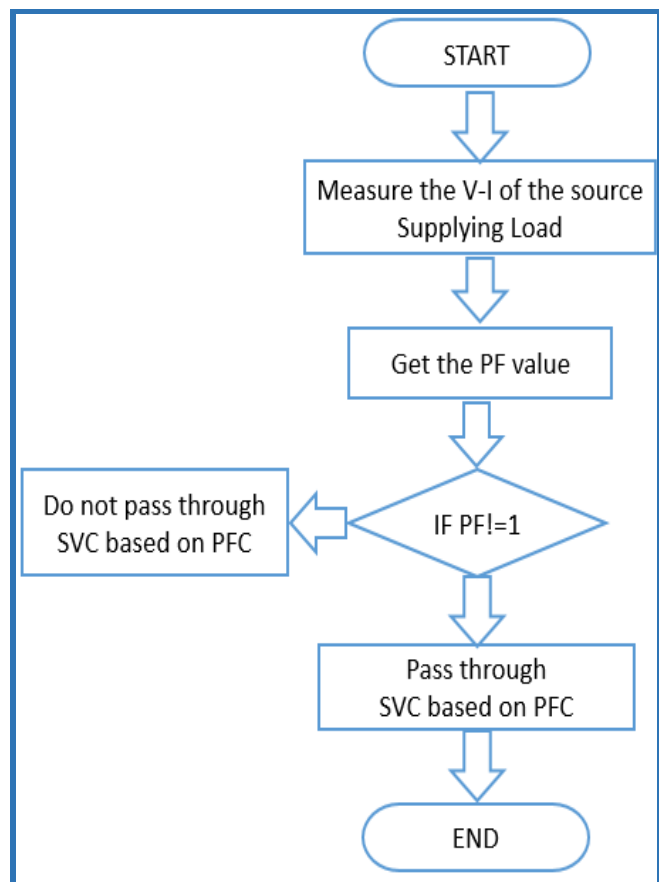


Fig. 4 Operational Flow of PFC Methodology

IV. CONTROL CONCEPT OF SVC

The SVC control strategy has been studied in terms of enhancing dynamic and transient stability, improving disturbance transmission capacity and damping power oscillation. The SVC control concept is based on the control shunt of the susceptance (B), which can be controlled by changing the working angle of the thyristor. The goal of SVC control is to maintain the desired voltage in the high-voltage bus. In constant mode, SVCs provide a certain level of stationary voltage control to keep the high-voltage bus at a predefined level. If the load suddenly increases, the high-voltage bus starts to fall under its specified value. In such condition, then the SVC injects the reactive power (Q_{net}), thereby increasing the bus voltage and returning it to the net-desired voltage level. If the load suddenly drops, then the bus voltage increases and the SVC (TCR) absorbs the reactive power. Consequently, the required bus voltage is reached.

As shown in Fig. 3, $+Q_{cap}$ is a fixed value of capacitance. Therefore, the value of the reactive power inputted into the system is controlled by the quantity $-Q_{ind}$ power absorbed by the TCR.

The SVC is modelled using a stationary capacitor–thyristor-controlled reactor (FC-TCR). The TCR can be varied by means of a variable susceptance B_{SVC} . The

equivalent of susceptance B_{equ} can be determined by the firing angle α of the thyristor.

$$B_{EQU} = B_L(\alpha) + B_C, \quad (2)$$

where:

$$B_L(\alpha) = \frac{1}{\omega L} \left(1 - \frac{2\alpha}{\pi} - \frac{1}{\pi} \ln(2\alpha)\right) \quad (3)$$

$$B_C = \omega c \text{ and } \alpha \text{ varies from } 0^0 \text{ to } 90^0$$

If the real power consumed by the SVC is zero, then $P_{SVC} = 0$

$$Q_{SVC} = V^2 B_{SVC}, \quad (4)$$

where V is the value of the bus voltage.

V. FUZZY LOGIC INTERFACING

Fuzzy logic is an important part of artificial intelligence where algorithms are designed to mimic human thinking. It also makes perfectly valuable decisions. Fuzzy logic interprets statements that are not clear to provide meaning. The process necessary for the system to work is stored in a fuzzy system. The diffuse primary system. The model accepts the input and the information is processed producing the output. The main function of the fuzzy logic controller includes the conversion of the input data to a fuzzy form called fuzzification. The fuzzification process is followed by processing according to the rules framed IF ... THEN. Finally, the fuzzy output is converted into actual output data, and the process is referred to as defuzzification. All system parameters must be properly evaluated when choosing the input and output membership functions, and the decision rules must be configured to produce the required result. The fuzzy logic controller provides the firing angle obtained from the angle PF of the load to FC-TCR.

The Mamdani rule based on fuzzy logic is adopted for the correction of the power factor. Complex power is obtained from the power measurement block, in which the angle of power is used as the input from the fuzzy controller.

In accordance with the power angle control output (firing angle), it is provided by the fuzzy controller. When the power angle is large, the firing angle is also large. The controlled output is fed to the variable delay circuit and the thyristor.

According to the variable delay circuit output, the firing angle of the thyristor is changed. When the power angle is good, the firing angle is extremely small. When the power angle is moderate, the firing angle is also moderate. When the power angle is large, the firing angle is also large (Figs. 5_6).

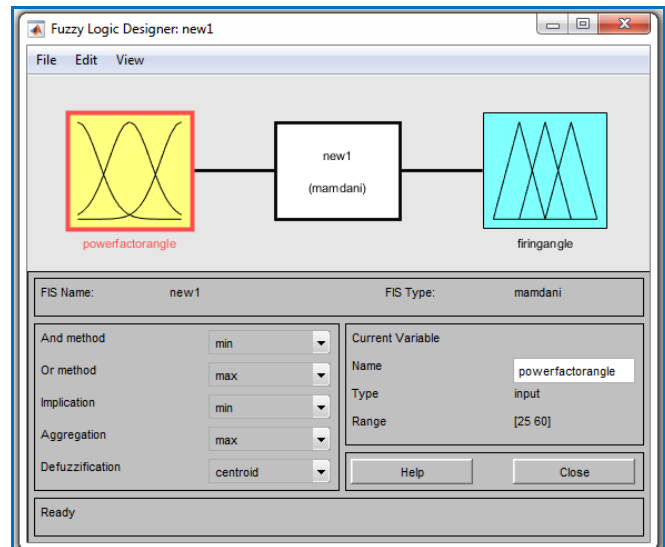


Fig. 5 Membership function plot for input variable.

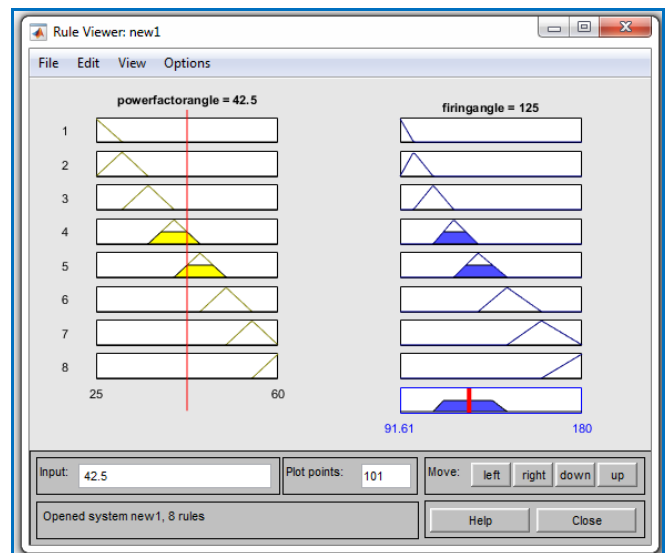


Fig. 6 Rule viewers for fuzzy controller.

VI. SIMULATION MODEL AND RESULTS

In this simulation FC-TCR is used as a compensation device and its excess amount of reactive power is absorbed by the reactor. Further, the detail controlling of the reactor in the simulation is addressed by the firing angle control of thyristor. The simulation is performed for a system with RLC load connected to the line supplied by the source. This load is connected to the source using a step signal that is used as enabling signal to connect or disconnect the load. The load chosen is highly inductive. Then we make use of designed PFC circuit and evaluate the design. This PFC circuit can be connected or disabled by setting the value of step signal. In this work, the FC-TCR circuit is connected to a PV system. MATLAB simulation is performed for various inductive loads.

Fig. 7 shows the V-I characteristics and functioning of the FC-TCR area. The maximum inductive and capacitive

admission are achieved by the voltage and rated current of the main components.

Fig. 7 Operating characteristics of FC-TCR

This study proposes a strategy that applies FC-TCR, excluding the compensator, in a renewable energy-fed grid. The grid has a PV machine and different sources, which are linked by transmission lines. The accurate tracing and compensating capacitive current automatically (Fig. 8_9).

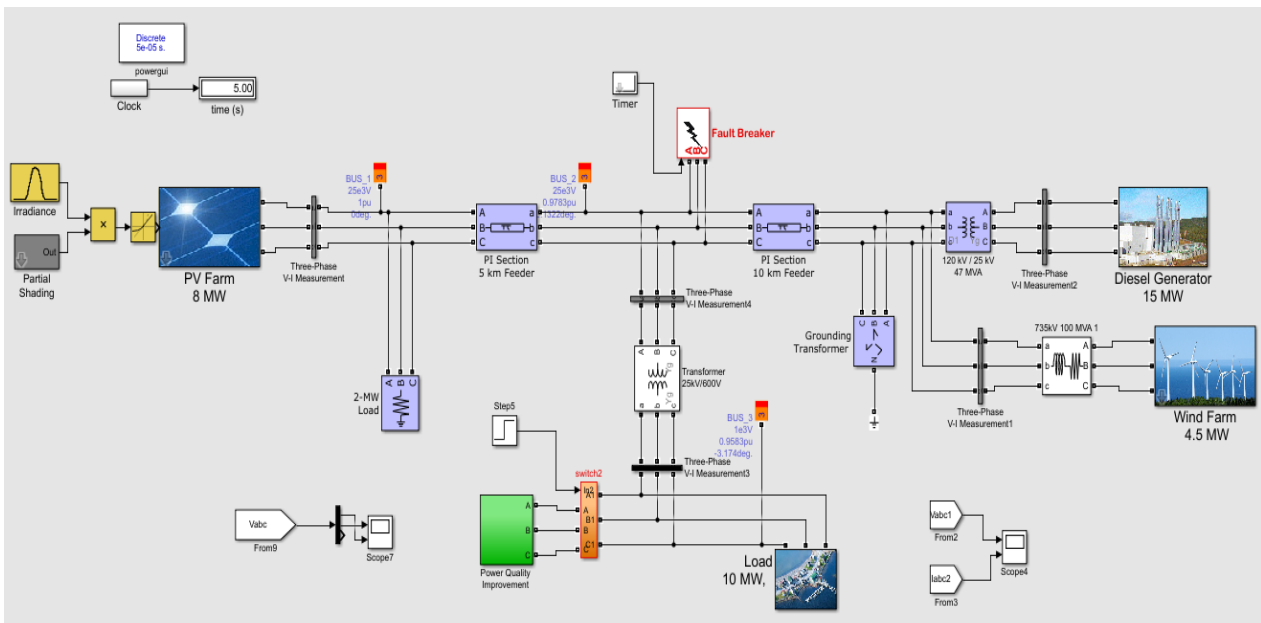
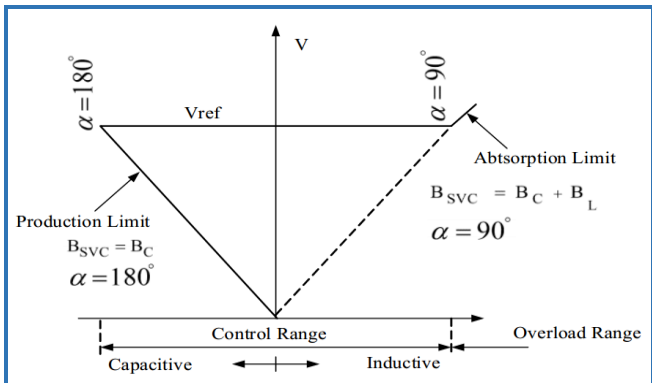


Fig. 8 Simulation model of distribution system with Fuzzy Logic Controlled FC-TCR

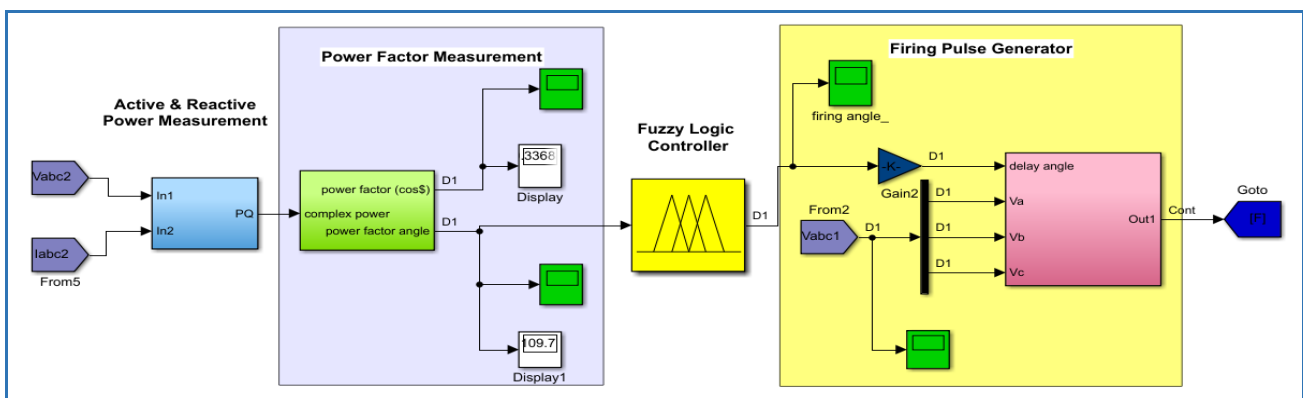


Fig. 9 Design of FC-TCR

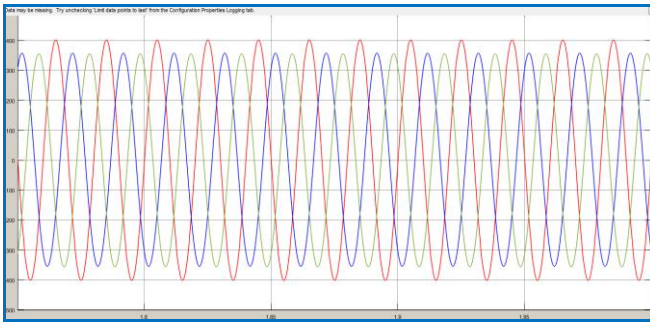


Fig. 10 Output waveform PV system without compensator.

Figs. 10_11 show the arrangement of the PV array with FC-TCR. The PV array is designed according to its characteristic equation. Therefore, the boost converter is used to raise the voltage to the desired value.

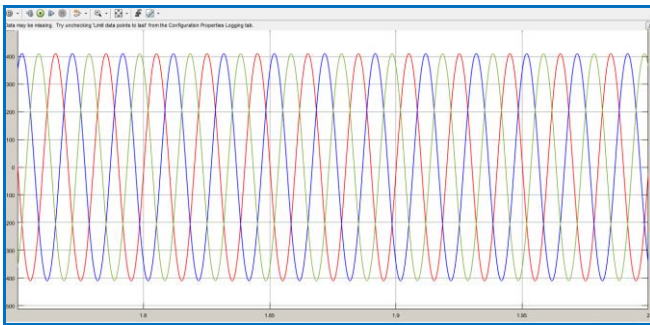


Fig. 11 Output waveform with FC-TCR compensator.

To obtain the output, we connect the output of the inverter to the 100 kVA transformer. The feeder size is 10 km. To provide reactive power compensation, we design the FC-TCR and connect it to the grid. We then design the assist switch with a transformer to analyse the impact of FC-TCR.

VII. CONCLUSION

Results of the simulation show a good fuzzy controller performance in the power factor correction and the reactive power of compensation. It is noted that the FC-TCR device is able to compensate for both over and under voltage. The use of Fuzzy logic has facilitated the closed-loop control of the system, by designing a set of rules, which decides the firing angle given to the Thyristors to reach the required voltage.

The FC-TCR with a fuzzy controller is able to maintain a constant power factor at the end of the transmission line under abnormal conditions and the changes in load show no effect.

The FC-TCR is also a cost-effective solution for maintaining constant voltage and power under load changes. An analysis of FFT with non-linear load can reduce harmonics to the desired limit. In MATLAB modelling, the SVC (FC-TCR) provides an effective control of reactive power regardless of load variation and offers voltage stability.

VIII. ACKNOWLEDGMENT

We would like to express our deep gratitude to our dear advisers, Ms. Janan Al-Hajji and Dr. Shaorong Wang, for motivating and inspiring us as we completed this research work.

IX. REFERENCES

- [1] M. Liserre, R. Cardenas, M. Molinas, and J. Rodriguez, "Overview of multi-MW wind turbines and wind parks," *IEEE Trans. Ind. Electron.*, vol. 58, no. 4, pp. 1081–1095, 2011.
- [2] G. Vishwakarma and N. Saxena, "Enhancement of voltage profile using fixed capacitor thyristor controlled reactor (FC-TCR)," *International Journal of Electrical, Electronics and Computer Engineering*, pp. 18–22, 2013.
- [3] M. Molinas and F. W. Fuchs, "STATCOM control at wind farms with fixed speed induction generators under asymmetrical grid faults," *IEEE Transactions on Industrial Electronics*, vol. 60, no. 7, 2013.
- [4] A. R. Boynuegri, B. Vural, A. Tascikaraoglu, M. Uzunoglu, and R. Yumurtac, "Voltage regulation capability of a prototype static VAR compensator for wind applications," *Applied Energy*, 93, pp. 422–431, 2012.
- [5] C. Wessels, F. Fuchs, and M. Molinas, "Voltage control of a STATCOM at a fixed speed wind farm under unbalanced grid faults," in *Proc. 37th IEEE IECON*, pp. 979–984, 2011.
- [6] A. Ortiz, T. Ostrem, and W. Sulkowski, "Indirect negative sequence voltage control for STATCOM supporting wind farms directly connected to the grid," in *proc. IEEE 37th IECON*, pp. 1903–1908, 2011.



Evaluation Of An Off-grid Photovoltaic Technology For Household Application In Iraq

Mohammed.H.R.Alktranee¹& Qudama Al- Yasiri²

1)Asst. Lec. At Dept. of Mechanic, Technical Institute Of Basrah, Southern Technical University , Basrah, Iraq

2) Asst. Lec. at Petroleum Engineering Dept, College of engineering, Misan university, Amarah, Iraq

(1)E-mail: mohammed.hr@stu.edu.iq Tel.: 009647703224065

(2)E-mail: qudamaalyasiri@uomisan.edu.iq Tel.: 00964770550008

ABSTRACT

Diversity of energy sources become an imperious need for the sustainable energy utilization and provision of alternative sources to fossil fuels. The rapid growth in renewable energy uses encouraged numerous to invest and research in different fields of renewable energy. Using of Photovoltaic (PV) technology to generate electricity was one of the most advanced technologies that attracted the attention of companies and researchers to focus on especially in the applications that touches people's life. In this study, off-grid PV system was suggested as an alternative source supplying electricity to a typical household located at latitude (30.5° N) and longitude (47.8° E) in the capital Baghdad, Iraq. The electrical power consumption compared with the electricity providing by the national grid using of design and simulation software (sunny design. 3). Electricity demand of the house was estimated based on the daily electricity usage in summer season, assessed taking the cost of electricity and environmental impact into considerations. The outcomes demonstrated that the PV system can handle more than (77.3%) of the apartment electricity within a year, while, the rest electrical shortfall compensates using genset system (local diesel generator). Moreover, the generated CO₂ emissions from traditional electrical power source was reduced to approximately (22.7%) when PV technology introduced. The study also evident the feasibility of using such system by comparing the price of total power consumption in kWh/month with the national grid price for the same power consumed where was very competitive.

Keywords: Photovoltaic system, off-grid PV systems, Storage battery, Sunny design.3.

I. INTRODUCTION

Improving the performance of photovoltaic systems have become essential to achieve wide utilization in the area of

energy planning, taking cost reduction of PV module manufacturing into consideration, which allows the consumer to compare the energy price produced from PV system with traditional systems [1]. PV systems are not used only for producing power, it can be used in other aspects as an external wall in buildings, roof, window, facade and shading while retaining greater efficiency for photovoltaic module [2]. Recently, solar energy utilization has been growing as an alternative to existing power generation systems which depends on fossil fuel, with expect to improve the efficiency of solar power generation at a sensible cost [3]. Using of renewable energy will contribute to reduce environmental degradation, such as CO₂ emissions by relying on the most reliable energy conversion systems which helpful maintain the

sustainable energy system [4]. After choosing the type of PV module and solar cells, there are many factors control in produce energy of solar power which lead to raise yield energy such as radiation intensity, surrounding temperature of PV module and load resistance [5], and, to provide the maximum energy from the photovoltaic system several methods have been used that may contribute to a large scale in develop solar systems operation during climatic changes such as high temperatures and various solar radiation.

Usually, the photovoltaic operation which extract energy from the sun and form it as a direct current (DC) electricity will be influenced by some factors such as shading and operating temperature, that will affect the performance ratio for PV system which will be clear during system outputs and the efficiency as well [6]. A statistics analysis used some photovoltaic simulation programs showed that a PV system improved significantly using interconnection model and the equation of photovoltaic in both winter and summer season depends on various combinations of tilted surfaces [7]. Moreover, it is necessary to know the path of maximum power point of photovoltaic and achieve maximize efficiency of PV system which associated with changing environmental

conditions such as quantity of solar radiation and solar cell's temperature [8]. To provide a dependable services able to meet the consumers' needs with sufficient way - especially at populated rural areas, photovoltaic Off-grid system can be helpful to meet the electricity energy demand in an efficient and sustainable method [9].

II. METHODOLOGY

This study conducted using of sunny design-3 software package. This software provided and developed by a German company called SMA (System, Mess and Anlagentechnik). SMA is a producer and manufacturer of solar inverters for photovoltaic systems with grid connection, off-grid power supply and backup operations. The software uses for planning and designing PV systems and PV hybrid systems. it gives PV system recommendations and proposes a combination of PV array(s) and inverter(s) which meet, as closely as possible, with house requirements regarding power class, energy yield and efficiency. In addition, it has the option of determining and optimizing the potential self-consumption, sizing the cables, evaluating efficiency.

PV module data that used in the study were provided from the datasheet specifications of the manufacturer where some technical, operational and economic advantages were taken into consideration. The software dealt with data of 4-people house located at latitude (30.5° N) and longitude (47.8° E) in the capital Baghdad in Iraq. The necessary metrological data were included in the software such like latitude, longitude, ambient temperature, solar irradiation etc., see Fig. 1, where those data reflect the feasibility of selecting the proper PV modules according to the Iraqi weather conditions. SMA has integrated the other available data into the software with the greatest care possible.

III. PV SYSTEM CONFIGURATION

1. PV module

To achieve highest power extraction from the PV modules requires selecting of good sort of solar cell in the system which can operate efficiently under different conditions. In this study, the polycrystalline module was selected based on technical, operational and economic considerations. This type of PV modules is available in the Iraqi market, and has an outstanding performance especially at low solar radiation and different temperatures as well as a good performance under standard test conditions (STC), as it shown in Table 1, from the manufacturer's datasheet. All PV modules used of the same type and they have connected identically in series taking into consideration the case study household area and all modules were installed at one tilt angle (37°) with an orientation toward the south in mounting type. It is worth to mention that the case study house is not surrounded by trees or

high buildings in all respects, which ensures the successful installation of PV system on its 150 m^2 roof.

The location is Baghdad in Iraq (Asia)

The annual total of global irradiation equals $1,967.45 \text{ kWh/m}^2\text{a}$

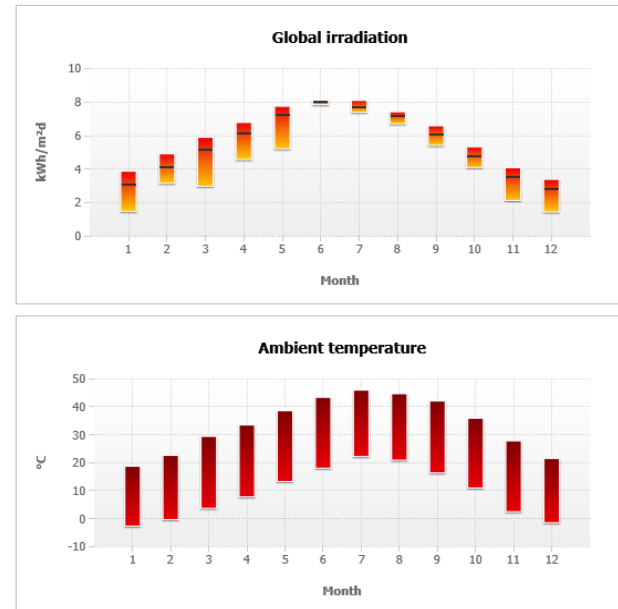


Fig. 1 The annual solar irradiation and ambient temperature variation of Baghdad 2018.

Table 1
The properties of PV module.

| Manufacturer | Canadian Solar Inc. | Cell technology | Poly |
|----------------------------|------------------------------------|------------------------------|----------|
| PV module | CS6X-320P Maxpower (05/2017) | Certification | EU |
| Electric properties | | | |
| Nominal Power | 320.00 Wp | Mechanical Properties | |
| Performance tolerance | -0.00/+5.00 W | No. of cells in PV module | 72 |
| MPP voltage | 36.80 V | Width | 982 mm |
| MPP current | 8.70 A | Length | 1954 mm |
| Open-circuit voltage | 45.30 V | Weight | 22.00 kg |
| Short-circuit current | 9.26 A | connector | Andere |
| Permissible system voltage | 1000.00 V | | |
| PV module efficiency (STC) | 16.68 % | | |

2. Battery-Storage System

Power generation and power load produced from photovoltaic off-grid system are not similar. Therefore, it became necessary to control on the variation of solar power-the fluctuation of solar radiation during the day - using storage system with different sizes as a suitable solution to reduce this issue [10].

Some important factors have been taken into consideration when we have select the type and size of battery such as night hours when the sun goes down, cloudy days, load profile, etc. it is necessary to know the time period that battery can supply the load just from the battery and planned at least for two days for bridging time. It is also important to select the battery that has the ability to charge and discharge depending on battery capacity. In our study, 16 storage batteries of 200 A were used in the system to maintain energy requirements and load demand at different situations .

3. PV inverter

The inverter plays an important role to regulate energy balancing of the supplied and consumed energy by house load. The inverter is regulating voltage and frequency of an off-grid PV system and conserve the input DC voltage of the battery at fixed value for better stability. Moreover, the average lifetime of inverter is long compared to the other parts of system, where contribute to reduce cable losses and has a significant role on the system performance especially when the connection between components of PV systems is robust.

Type of the two inverters selected for the study has the characteristics shown in Table 2 where they are appropriate for installation at extreme climate conditions in Iraq.

Table 2
Characteristic of PV inverter.

| Inverter | | Input data | |
|----------------------|---------|---|-----------|
| SB5.0-1AV-40 | | | |
| General data | | Max. DC power | 5.35 kW |
| Degree of protection | IP65 | Max. input voltage | 600 V |
| Width | 435 mm | Rated input voltage | 365 V |
| Height | 470 mm | Min. input voltage | 100 V |
| Depth | 176 mm | Start voltage | 125 V |
| Weight | 16.0 kg | Max. MPP voltage | 500 V |
| Efficiency | | Max. operating input current per MPPT | 15 A/20 A |
| Max. efficiency | 97 % | Max. input short circuit current per MPPT | 20 A/20 A |

| | | | |
|--------------------------------|----------|--------------------------|-----------|
| European Weighted efficiency | 96.5 % | Strings per MPP input | 2 / 2 |
| Output data | | | |
| Max. AC apparent power | 5.00 kVA | Rated power | 5 Kw |
| Min. displacement power factor | 0.8 | Nominal AC voltage range | 180-280 V |
| AC Power frequency | 45-65 Hz | Feed-in phases | 1 |

4. Power consumption

The photovoltaic off- grid system designed to supply electricity to 4-people house. The amount of electricity consumption is unstable within the year where electricity demand maximizes during summer period due to the temperature rising and the consumption will reduce to a certain extent throughout the winter.

A diesel genset (local diesel generator) can be used as an external electrical power source to meet the power shortage during cloudy days or to keep continuous energy supplied during the night. Using of diesel generator will provide the energy when the batteries drop or when the PV array unable to meet the energy consumption in the house sometimes. For eco-protection considerations, It is worth to mention that the use of genset will be seasonal (often during the peak period in summer) as the PV system will be sufficient in the transition period between summer and winter where the electrical load is relatively low.

The total electrical power assumed as an input to the software which consumes by the house was estimated based on the typical house (4-people) usage of electrical devices. The family is consuming about 1 329.25 kWh per month which is equal to 15,951 kWh per year, see Table 3, where the total peak load has estimated during summer season.

Table 3
Typical electrical power consumption values according to MOE of Iraq.

| Elec. Device | No. | PWR Cons. (watt) | Work hrs./day | No. of days | PWR Cons. (W/month) |
|---------------------------|-----|------------------|---------------|-------------|---------------------|
| Economic lamp 20 W | 10 | 20 | 12 | 30 | 72 000 |
| Fridge | 1 | 250 | 12 | 30 | 90 000 |
| Freezer | 1 | 300 | 12 | 30 | 108 000 |
| TV + Satellite | 1 | 250 | 6 | 30 | 45 000 |
| Dishwasher | 1 | 1250 | 0.5 | 30 | 18 750 |

| | | | | | |
|-----------------------------------|---|------|------|----|---------|
| Fan | 3 | 200 | 10 | 30 | 180 000 |
| Water pump | 1 | 800 | 0.5 | 15 | 6000 |
| Iron Washing machine | 1 | 400 | 0.5 | 10 | 2 000 |
| | 1 | 1200 | 1 | 8 | 9 600 |
| Computer | 1 | 100 | 4 | 20 | 8 000 |
| Microwave oven | 1 | 1200 | 0.25 | 15 | 4 500 |
| Vacuum cleaner | 1 | 1250 | 0.5 | 12 | 7 500 |
| Kettle | 1 | 1000 | 0.25 | 30 | 7 500 |
| A/C(1.5 tone) | 2 | 2000 | 6 | 30 | 720 000 |
| Total power consumption (kWh/yr.) | 1 329 250 Watt.h * 12 /1000 = 15 951 | | | | |

5. The cost

The cost of PV modules is the most important problems facing this technology at the beginning of its development. However, it has become somewhat stable in the last few years because of the reduction in price of manufacturing and increasing number of competitors in the market. The price of electricity generated from the PV system depends largely on its size, the large system size the lower price and viseversa. So, it is normal to conclude that small PV systems at the household level are the highest price.

Generally, the cost of PV systems can be calculated from the initial cost plus the operational cost. Total initial cost depends on the type of PV module(s) used and other system parts which include the storage battery, PV inverter, frame, electrical and electronic accessories as well as the cost of transportation, installation and maintenance. Table 4, contains the initial cost of PV system used in the study based on the Iraqi market where the prices are a little bit high because of the lack of companies deal with such systems.

The operational cost is the other significant part of photovoltaic off-grid system total cost with an operating lifetime ranged from (20 – 25) years. This cost is what makes such systems a good competitor to the traditional systems and worth to invest in addition to being an environmentally friendly technology.

Table 4
Typical prices of PV system parts. [11]

| PV system component(s) | No. in use | Component Cost (\$) |
|--------------------------------------|------------|---------------------|
| PV module 320 Watt (polycrystalline) | 21 | 190/ module |
| Storage battery 200 A | 16 | 250/ battery |
| PV inverter 8000 VA | 2 | 2000/ inverter |

| | | |
|---|-------|--------|
| Frame, cables, wires, transportation, installations | ----- | 1 500 |
| Total PV system cost | ----- | 13 490 |

IV. RESULTS AND DISCUSSION

In Iraq, it is locally known that energy consumption is variety within the day during the summer period where the peak load is associated with the human activities and the need to use electrical devices. Air-conditioning systems and cooling devices are the most which consume electric power due to the hot summer season in Iraq that requires such devices for long time hot weather during the day.

Fig. 2 and Fig. 3 show the variation during the day where the peak load can be noticed from the first hours in the morning to the late afternoon, and the variety of power consumption per each month within the year, respectively.

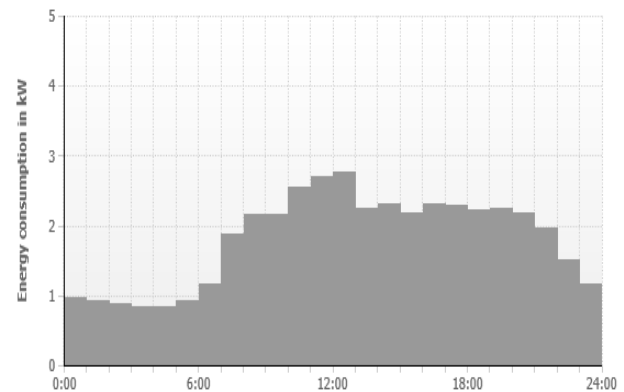


Fig. 2 Peak load variation during the day of study.

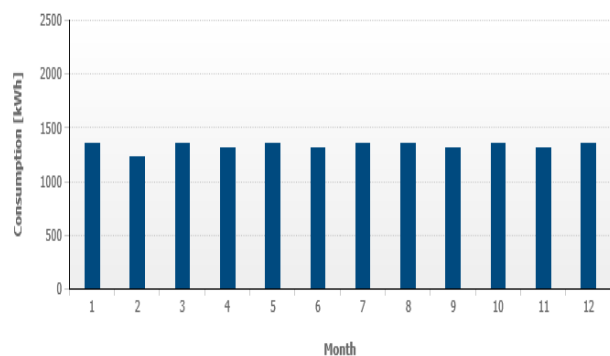


Fig.3 Power consumption of PV system per month

Table 5, and Fig. 4 detailed the power analysis and operating results generated by the software where they conducted that

off-grid photovoltaic system can produce (12 332 kWh/yr.) out of (15 951 kWh/yr.) the total electrical power demand of the house during peak load and the rest can be maintained using the genset system.

Table 5
Annual power analysis of the system

| Operating Parameter | Value (kWh) |
|--|-------------|
| Annual energy consumption | 15 951 |
| Max. available PV energy | 12 332 |
| Used PV energy | 12 332 |
| Directly consumed PV energy | 7 936 |
| Intermediately stored PV energy | 4 396 |
| Annual energy generation of the genset | 5 697 |

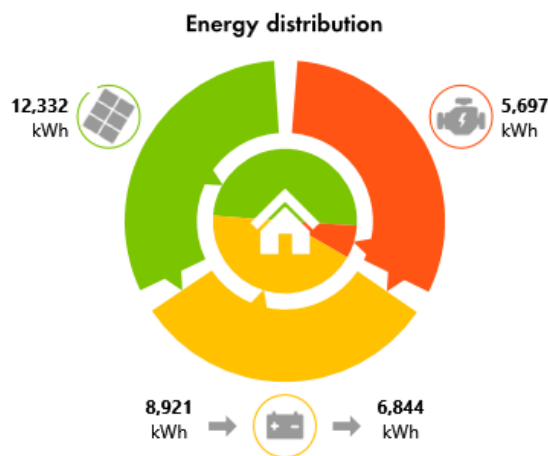


Fig. 4 Energy distribution of PV system

For the environmental point of view, Table 6, evidences that the use of PV system reduces CO₂ emissions generated from the power plants used to provide electricity to the national grid. According to the International Energy Agency IEA, Iraq is one of the countries that has a high CO₂ emissions ratio (about 1002.8367 gms./kWh) due to the use of petroleum products (gasoil, natural gas etc.) to generate electricity [12].

Table 6
Annual reduction of CO₂ emissions

| Power (kWh) | CO ₂ grammes/ kWh | CO ₂ kg emissions |
|-------------|------------------------------|------------------------------|
| 12 332 | 1002.8367 | 12 366.9822 |

Finally, It is very important to know the economic feasibility of using such system and compare the cost of each kWh produced with the official price of the governmental national grid. As it mentioned before, the total initial cost of the PV system is (13 490 \$) with operational lifetime up to 25 years. It means that it costs (540 \$) yearly, and (45\$ ≈ 56 250 ID) for each operating month which represent the approximate cost of total electrical power consumed per each month (1 329.25 kWh). On the other hand, the same total consumption costs about (44 230 ID/ month) according to the new prices of Iraqi ministry of electricity [13].

V. CONCLUSIONS

The study indicates that PV system could be a suitable alternative to traditional systems that rely on fossil fuel sources to produce electricity, especially in areas away from national power transmission lines or that do not have at all. The study also pointed out the importance of this system in terms of protecting the environment from CO₂ emissions associated with the production of electricity in conventional ways. Economically, the evaluation of such systems comparing with the new governmental electric power price is important and necessary in the study, in addition to suitability of the application and its ability to supply electricity efficiently. There is no doubt that there are other aspects that were not considered in the study, which may constitute an important reason for not using this technology in Iraq including: high initial cost, complex maintenance of the system, lack of expert hands in this area, Iraqi weather conditions especially when it comes to dust which negatively affects the efficiency of the system, etc.

The proposed system has proven successful where it produces about (77%) of the total house power consumption during peak period, and this amount is sufficient during other times when the need for electricity is low. On the other hand, since the most important characteristic of these systems is that they are environmentally friendly, so the percentage of CO₂ emissions decreased to about (23%), which is associated with the operation of the diesel generator to maintain the shortage of energy supplying.

The fact that Iraq is one of the oil-producing countries and depends on petroleum products in power generation does not mean that these systems are not feasible economically when compared to national networks. The study concluded that the monthly cost of power consumed by the house increases by only (12 000 ID ≈ 10 \$) using PV system compared to the cost of the national network which present a few cost taking other benefits into consideration.



VI. REFERENCES

- [1] G.C. Bakosa, M. Soursosb, N.F. Tsagasa. "Technoeconomic assessment of a building-integrated PV system for electrical energy saving in residential sector," Greece. Energy and Buildings, 35, pp. 757–762, (2003).
- [2] Jong-Ho Yoon a, Jonghwa Song b,c., Sung-Jin Lee b. "Practical application of building integrated photovoltaic (BIPV) system using transparent amorphous silicon thin-film PV module. Korea," Solar Energy, 85, pp. 723–733, (2011).
- [3] Kwangsun Ryu a, Jin-Geun Rhee a,b, Kang-Min Park c, Jeong Kim d. "Concept and design of modular Fresnel lenses for concentration solar PV system. Korea," Solar Energy, 80, pp. 1580–1587, (2006).
- [4] I. Nawaza, G.N. Tiwarib." Embodied energy analysis of photovoltaic (PV) system based on macro - and micro-level," India. Energy Policy, 34, pp. 3144–3152, (2006).
- [5] Ali Reza Reisi a,n, Mohammad Hassan Moradi b, Shahriar Jamasb b. "Classification and comparison of maximum power point tracking techniques for photovoltaic system," A review. Renewable and Sustainable Energy Reviews, 19, pp. 433–443, (2013).
- [6] S. Lalounia, D. Rekiouaa, T. Rekiouaa, E. Matagneb. "Fuzzy logic control of stand-alone photovoltaic system with battery storage," Algeria. Journal of Power Sources, 193, pp. 899–907, (2009).
- [7] Jayanta Deb Mondol a, Yigzaw G. Yohanis a, Brian Norton b. "Comparison of measured and predicted long term performance of grid a connected photovoltaic system," Northern Ireland, UK. Energy Conversion and Management, 48, pp. 1065–1080 , (2007).
- [8] D. Rekioua , A.Y.Achour, T. Rekiouaa. "Tracking power photovoltaic system with sliding mode control strategy," Algeria. Terragreen13 International Conference. Energy Procedia, 36, pp. 219 – 230, (2013)
- [9] Rohit Sen a, Subhes C. Bhattacharyya b." Off-grid electricity generation with renewable energy technologies in India,"An application of HOMER. India. Renewable Energy, 62, pp.388-398, (2014).
- [10] Andreas Jossen a, Juergen Garche a , Dirk Uwe Sauer b. "Operation conditions of batteries in PV applications," Germany. Solar Energy, 76, pp. 759–769, (2004).
- [11]<https://www.facebook.com/1767714390168183/photos/a.1767714740168148.1073741826.1767714390168183/1869562359983385/?type=1&theater>.
- [12] <https://www.sunearthtools.com/tools/CO2-emissions-calculator.php>.
- [13]https://l.facebook.com/l.php?u=https%3A%2F%2Fmoelc.gov.iq%2Findex.php%3Fname%3DPages%26op%3Dpage%26pid%3D269&h=ATPKNb-YxJ9YxbMaHaCDI5VNnqOyvaaT72Vb9DXESfeCPYHokybfFbnll4uwgSLoQ2LitaxD_DCpb8A_1BPJ0asM5OQyWp5Jb6Zh4qXvU2HrQRSPJj_A2RW_H_jmBRCAC0s-U-QIZUrdas.

Effect The Change of Absorber Length on Thermal Performance of Parabolic Dish Solar Collector

Ahmed. W. Hamed

Master student, Department of mechanical,
college of engineering
Wasit university
E mail: ahmedalmhnds222@yahoo.com

Ali A. F. Al-Hamadani

Ass. Prof., Department of mechanical,
college of engineering
Wasit university
E mail: aalhamadani@uowasit.edu.iq

Mahmmod aziz muhammed

Ass. Prof., Technical Institute
Amarah
Southern Technical University
E mail: mahmmodaziz@stu.edu.iq

Abstract:- The parabolic dish solar collector with a dual-axis tracking system is a good type of focus system to overcome the problem of energy sources. It generates large amounts of heat because of the high concentration ratio compared with other solar technologies. A diameter of dish 2 m was used with a two-axis tracking system and two types of absorbers: 3 m spiral coil and 4 m spiral coil with the same geometric concentration ratio (100). Experimental test has been done in Wasit university, Al-Kut city, Iraq at 32.5° latitude and 45.82° longitude. The data was taken at September 2017 with four examined day for each absorber. It has been used tonatiuh software to compare between theoretical diameter of heat flux over absorber area and experimental diameter of this flux. Theoretical diameter was 8 cm and experimental was 18 cm of this heat flux. This difference because the optical losses in practical. Water was used as a working fluid in the system. Inlet and outlet water temperatures, absorber temperature, ambient temperature, beam solar intensity, wind speed and volumetric flow rate are the parameters were measured during the test. At 1 L/min flow rate the maximum of outlet temperatures, absorber temperatures, useful energy and instantaneous efficiency of 4 m spiral absorber were as follows: 61.43 °C, 290 °C, 861.15 W and 0.366 respectively. This values of 3 m spiral absorber was 69.1 °C, 425 °C, 1012.9 W and 0.449 respectively. The direct steam was generated at low flow rate with high temperature which was maximum at 12 am 113.7 °C for 4 m and 119.32 °C for 3 m at low flow rate 0.25 L/min. From these results showed that the spiral absorber with 3 m length has performance higher than 4 m length.

Keyword :- Solar dish , Tracking system , 4 m Spiral absorber , 3 m Spiral absorber

I. INTRODUCTION

Renewable energy has become an important role at present as a result of increased demand for energy, depletion in fossil fuel as well as pollution resulting from fossil fuel combustion. This increase in energy demand has made solar energy, which is one of the most important types of renewable energies, a wide range of uses in the current [1]. Solar energy is one of the means to address the problem of lack of energy sources and thus give effective economic solutions [2]. Solar collectors are the devices that convert solar energy into thermal

energy and are on several types, each of which is used according to the required application. Flat plate solar collector used for low temperatures up to 100 °C applications [3]. Some of low concentration solar collector and evacuated tube solar collector used for temperatures level up to 200 °C [4]. Fresnel lens collector (FLC), parabolic trough solar collector (PTSC), solar tower and parabolic dish solar collector (PDSC) used for high temperatures level [5]. PDSC is an efficient device for medium and high levels of temperature [6]. Abid et al. [7], Compared between PDSC and PTSC and the results showed that the solar dish has performance better because it has high concentration ratio and low thermal losses compared with parabolic trough. There are two major groups of PDSC applications which are thermal energy applications and electrical applications. Thermal energy applications is used to generate hot water, steam, water desalination and solar cookers etc. [8-9]. Electrical applications is generate by use micro steam turbine, stirling engine and dish / alkali metal thermal to electric converter (AMTEC) system. Dascomb [10] used micro steam turbine to generate 1kW electrical power by generate 6.67 kW thermal power but the maximum thermal power generated was 5.46 kW. Reddy et al. [11], made a simulation of 50 MW power plant consist of 200 units of (dish _ Stirling engine). Hafez et al. [12] also made a simulation of (parabolic dish - stirling engine) system to generate 10 kW power output. It has been found the maximum conversion thermal efficiency occurred when used polymeric film nonmetal reflector. Most of the researches attempt to reduce the cost and increase in thermal efficiency of the collectors. Other researchers focused on the thermal applications and studied different parameters which effect on thermal performance of PDSC. Mohamed et al. [13] studied experimentally the effect of tracking system on thermal efficiency of PDSC and they found the increased in thermal efficiency was about (20 - 30) % more than the fixed collector. Daabo et al. [14] studied three types of receiver geometries: a sphere, a cone and cylinder. In each case it has been used a helical tube. It was found that the conical shape is the best choice. Sup et al [15] used "tonatiuh" software to showed the effect of rim angle of

dish on focal point diameter and distributed heat flux. They concluded that the increasing in rim angle increase in imaging and non-Imaging diameter of heat flux distribution at focal point. Mohand et al., [16]. Compared numerically between 15 turns and 20 turns of helical coil absorber. that when water entered into two types of coil in same temperature, mass flow rate and heat flux, then the outlet water in 20 turns coil heated more than in 15 turns because of heat transfer rate increases in 20 turns coil.

In this research it has been compared experimentally between three meter and four meter of spiral coil absorber used with PDSC. The comparisons included outlet water temperature, useful heat energy and efficiency. Another aspect was achieved in the present work, namely, generate steam. Also, it has been used tonatiuh software to find the diameter of heat flux at focal point and compared with experimental diameter of this heat flux.

II. DESCRIPTION OF COLLECTOR

It has been used 2 m diameter of dish with two axis tracking system. It has been used aluminum foil as a reflective material because it cheap, availability and simplicity to paste. Reflectivity for it was 0.76. The PDSC used in this research can be shown in Fig.1.



Fig. 1: The PDSC used

It has been used cavity type of receiver shell with spiral copper coil as absorber. Two different lengths of spiral absorber were used four meter and three meter as shown in Fig.(2.a-b). The absorbers were coated by mat black paint to decrease the emissivity and increase in absorptivity. Absorbers housed in a galvanized steel shell of the receiver. The shell of receiver was insulated with glass wool insulation to prevent the conduction heat losses. Cavity type of receiver is more efficient than volumetric receiver (external receiver) because the first it has low heat losses compared with volumetric receiver [10]. The properties and characteristics of PDSC used can be shown in table.1.



Fig. 2.a: Four meter spiral absorber



Fig. 2.b: Three meter spiral absorber

Table. 1: Properties and characteristics of PDSC used

| Parameter | Value | Unit |
|------------------------------------|-------|----------------|
| Diameter of parabolic dish (d) | 2 | M |
| Depth of concentrator dish (h) | 0.20 | m |
| Focal length of dish (f) | 1.25 | m |
| Aperture area of dish (A_a) | 3.141 | m ² |
| Rim angle of dish (Ψ_{rim}) | 43.6 | Deg |

| | | |
|---|-------------|----|
| Geometric concentration ratio | 100 | - |
| Absorbers coil length | 4 and 3 | m |
| Cavity diameter of receiver | 20 | cm |
| Inner Pipe diameter | 6 | mm |
| Thickness of pipe | 2 | mm |
| Absorptivity- transmissivity product of copper | 0.7 | - |
| Emissivity of copper | 0.725 | - |
| Absorptivity- transmissivity product of coating | 0.94 | - |
| Emissivity of coating | 0.10 - 0.14 | - |
| Reflectivity of aluminum foil | 0.76 | - |

III. PDSC PERFORMANCE ANALYSIS

The performance of PDSC has included the following: useful energy, the thermal efficiency of the collector and heat losses. The useful heat energy can calculate as follows equations. [14]

$$Q_u = Q_{abs} - Q_l \quad (1)$$

$$Q_u = I_a A_a \rho \tau \alpha \gamma - A_{abs} \times U_l \times (T_{abs} - T_{amb}) \quad (2)$$

The heat losses conduction, convection and radiation are happening in the absorber. Conduction heat losses can be neglected on the basis of all surface of absorber was insulated except for the exposed part of the reflected radiation [17]. Thus, the overall heat losses coefficient can be determine as following equation [18]:

$$U_l = \left[\frac{1}{h_{total} + h_r} \right]^{-1} \quad (3)$$

The total convection heat transfer coefficient is a sum of two coefficients natural convection and wind or forced convection as following equation:

$$h_{total} = h_{wind} + h_{nat} \quad (4)$$

Ma R. Y. [19] proposed a mathematical model to calculate the

forced heat transfer coefficient at any wind speed and any inclination angle of receiver.

$$h_{wind} = f(\theta) V^{1.401} \quad (5)$$

where;

$$f(\theta) = 0.1634 + 0.7498 \sin(\theta) - 0.5026 \sin(2\theta) + 0.3278 \sin(3\theta) \quad (6)$$

Where; θ is inclination angle of receiver

Prakash et.al. [18] are putted a correlation to calculate the heat losses by natural convection (no wind) for cavity receiver.

$$h_{nat} = \frac{Nu_{h,nat} K_{air}}{D_r} \quad (7)$$

$$Nu_{h,nat} = 0.21 Gr^{1/3} \left(\frac{T_{abs}}{T_a} \right)^{-1.5} \quad (8)$$

Where;

$$Gr = \frac{g \beta (T_{abs} - T_f) L^3}{\nu^2} \quad (9)$$

$$T_f = \frac{T_{abs} + T_{amb}}{2} \quad (10)$$

The useful energy can be obtaining by measurement of inlet and outlet temperature of water and select the specified mass flow rate as following equation [6]:

$$Q_u = \dot{m} \times C_{p_w} \times (T_{out} - T_{in}) \quad (11)$$

The instantaneous thermal efficiency of PDSC can be calculated from following equation [13].

$$\eta_c = \frac{Q_u}{Q_s} \quad (12)$$

Where Q_s is the beam solar radiation falling on aperture area of dish which equal :

$$Q_s = I_a \times A_a \quad (13)$$

IV. OPTICAL ANALYSIS OF PDSC

The purpose of this analysis to find the diameter of distributed heat flux over the absorber and compare with experimental diameter of this flux. It has been used "tonatiuh" software to simulate the optical behavior of PDSC used. Reflectivity of reflective material was 0.76 as in practical. The same dimensions of dish and absorber in practical have been implemented into the program. The absorber into program was as a flat disc with same diameter of receiver cavity 20 cm. The incidence angle of solar light was considered as 0°. Fig.3 shows window (picture) of this program during the simulation with four side view.

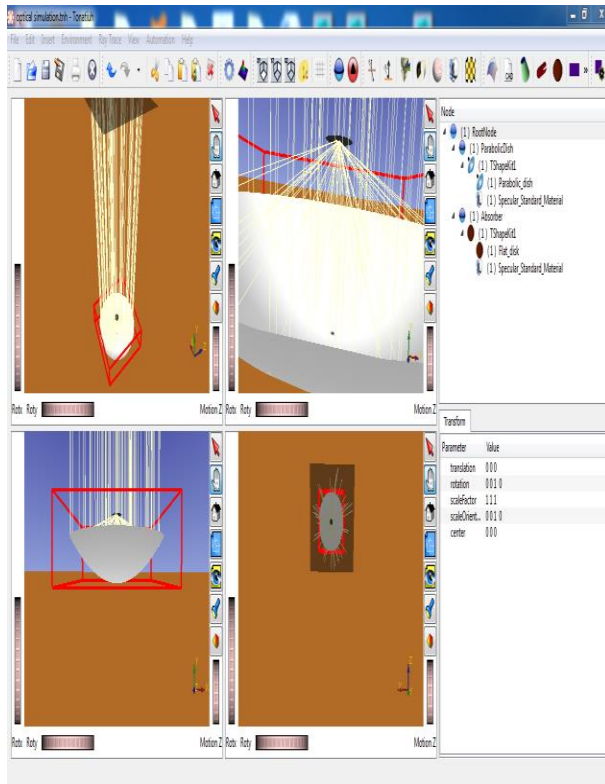


Figure (3): tonatiuh software used for optical simulation

V. EXPERIMENTAL SETUP AND TEST PROCEDURE

Experimental test has been done in Wasit university, Al-Kut city, Iraq at 32.5° latitude and 45.82° longitude. The data was taken at September 2017 with four examined day for each absorber. The schematic of PDSC used in this research with main parts can be shown in Fig.4. The water is supply into the absorber from tank putted at high building. Inlet valve to control of water flow rate which is measured by an enclosed flask as a flow meter and a stopwatch to adjust the desired volumetric flow rate per minute. Then the water exit directly from absorber to produce direct steam. Inlet and outlet water temperatures and absorber temperature have been measured by using K-type thermocouples with omega data acquisitions device connected with laptop. The beam solar intensity measured by using solar power meter device. The wind speed and ambient temperature measured by using hot wire anemometer device. Each device read has been taken after each hour with the same water flow rate throughout the examined day from 9 am to 3 pm. An automatic two axis tracking system used to make the solar radiation falls directly on aperture area of the dish. Two electrical circuits used for tracking system IC LM 339 and L293D with four LDR sensors.

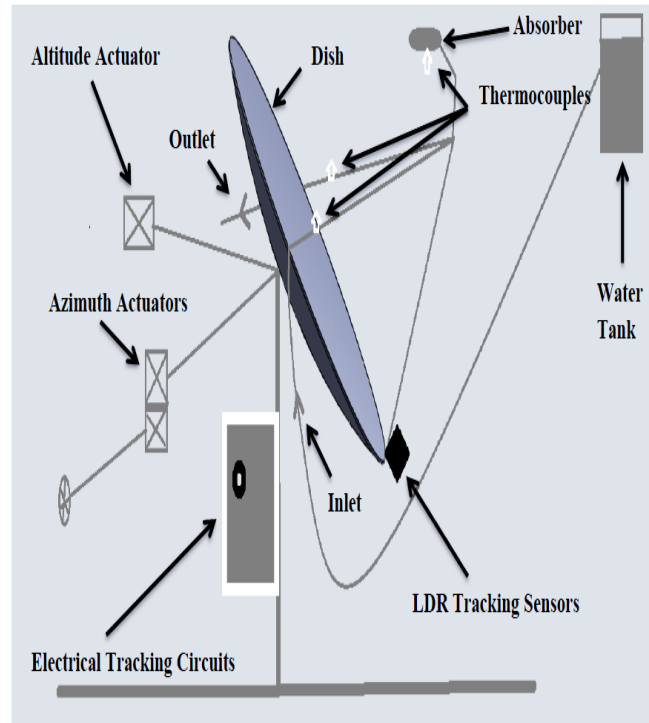


Figure (4): schematic diagram of PDSC used

VI. RESULTS AND DISCUSSIONS

1. Optical Results

The theoretical diameter of heat flux distributed on absorber area was about 8 cm as shown in Fig.. The simulation also showed that average the heat flux of reflected radiation was 47603.3 W/m^2 when the beam solar radiation was 800 W/m^2 and 0.5472 optical efficiency.

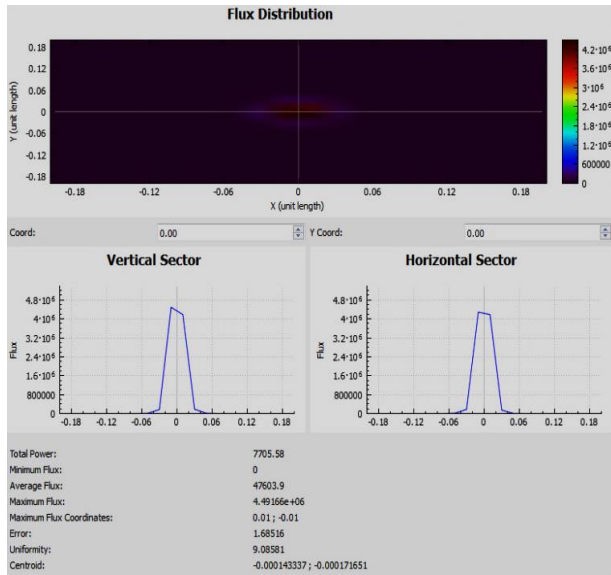


Figure (5): diameter of heat flux by optical simulation.

The experimental diameter of this flux was measured about 18 cm as shown in Fig.6. Theoretical heat flux calculated from the equation (1) and (2) by calculate Q_{abs} and dividing on absorber area which was 43776 W/m^2 at the same condition in program. This difference because the optical losses in practical such the error in tracking system and the dust on reflective material.



Figure.6: experimental diameter of heat flux distributed

II. Thermal Results

Experimental tests were conducted at four clear sky day in September, 2017 for each absorber. A period of (7th, 8th, 9th and 10th September) was chosen to test four meter spiral absorber with four different volumetric flow rates (

0.25 L/min , 0.5 L/min , 0.75 L/min and 1 L/min). One flow rate was tested throughout the day. Beam solar intensity varied between 439 W/m^2 as minimum at 9 am and 748 W/m^2 as maximum at 12 am and then decreased gradually with 1 L/min flow rate at 10/9/2017 as shown in Fig.7. Maximum temperatures of absorber and water outlet were occurred at 12 am which were $290 \text{ }^\circ\text{C}$ and $61.43 \text{ }^\circ\text{C}$ respectively.

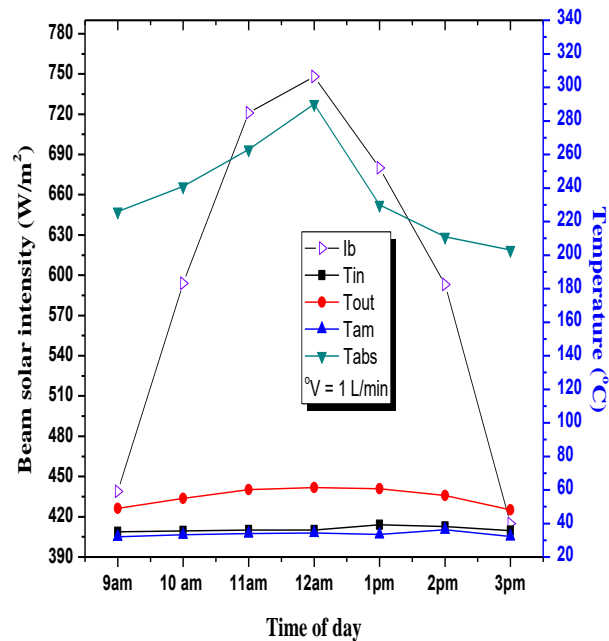


Fig. 7: Beam solar intensity and temperatures of PDSC with 4 m spiral absorber at(10/9/2017)

Other Four days (12th, 13th, 14th, 15th September) have been chosen to test the PDSC with three meter absorber with same volumetric flow rates for four meter. Also, minimum beam solar radiation was 383 W/m^2 at 9 am and 717 W/m^2 at 12 am with 1 L/min flow rate at 15/9/2017. Although, the beam solar radiation was decreased with same flow rate 1 L/min but the maximum absorber and outlet water temperatures of 3 m spiral absorber was higher than 4 m spiral absorber which were $69.1 \text{ }^\circ\text{C}$ and $425 \text{ }^\circ\text{C}$ at same time 12 am as shown in Fig.8. This is due to the reflected radiation don't fall on the entire length of the 4 m absorber and the presence of a cool part in it unlike 3 m absorber where the radiation covered the whole coil. All values of these tests for both types of absorber can be shown in table. 2 and table. 3.

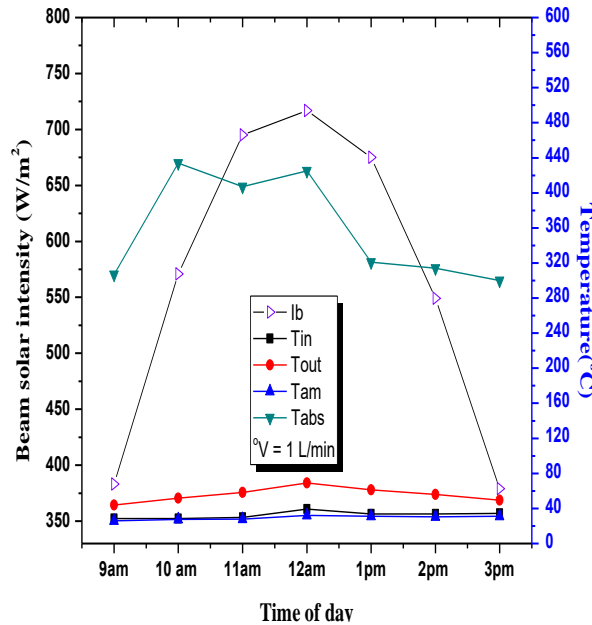


Fig. 8: Beam solar intensity and temperatures of PDSC with 3 m spiral absorber at(15/9/2017)

Table. 2: Variation of temperatures, beam solar intensity and air velocity of PDSC with 4m spiral absorber at 10/9/2017

| Time | I_b (W/m ²) | T_{in} (°C) | T_{out} (°C) | T_{am} (°C) | T_{abs} (°C) | V_{air} (m/s) |
|-------|---------------------------|---------------|----------------|---------------|----------------|-----------------|
| 9am | 439 | 35.1 | 48.95 | 32.1 | 226 | 3 |
| 10 am | 594 | 35.6 | 55 | 37 | 241 | 1.5 |
| 11am | 721 | 36.13 | 60.1 | 39.7 | 263 | 2.4 |
| 12am | 748 | 36.05 | 61.43 | 44.1 | 290 | 0.3 |
| 1pm | 680 | 39.2 | 60.78 | 44 | 230 | 1.35 |
| 2pm | 593 | 38.19 | 56.69 | 44.9 | 211 | 2.6 |
| 3pm | 415 | 35.7 | 48.2 | 45.7 | 203 | 1.6 |

Table. 3: Variation of temperatures, beam solar intensity and air velocity of PDSC with 3m spiral absorber at 15/9/2017

| Time | I_b (W/m ²) | T_{in} (°C) | T_{out} (°C) | T_{am} (°C) | T_{abs} (°C) | V_{air} (m/s) |
|-------|---------------------------|---------------|----------------|---------------|----------------|-----------------|
| 9am | 383 | 28.6 | 43.95 | 35.3 | 307 | 0.7 |
| 10 am | 571 | 28.65 | 51.8 | 37.1 | 434 | 0.6 |
| 11am | 695 | 29.82 | 58.2 | 38.8 | 407 | 2 |
| 12am | 717 | 39.19 | 69.1 | 41.5 | 425 | 2 |
| 1pm | 675 | 33.6 | 61.1 | 44.3 | 321 | 2.5 |
| 2pm | 549 | 33.84 | 56.12 | 43.5 | 314 | 3 |
| 3pm | 379 | 34.3 | 49.45 | 44 | 300 | 3.1 |

This flow rate was chosen to compare between these type of absorber. The direct steam was generated at low flow rate with high temperature which was maximum at 12 am 113.7 °C for 4 m and 119.32 °C for 3 m at low flow rate 0.25 L/min. Thus, it must the water inter into the absorber at low flow rate to generate direct steam with high temperatures.

Useful heat energy of 4 m spiral absorber was varied between 471.1 W at 9 am and 861.17 W at 12 am as maximum with 1 L/min at 10/9/2017. Maximum useful energy of 3 m spiral absorber was increased to 1012.9 W at 12 am as shown in Fig.9 although the beam solar radiation was decreased in 15/9/2017 with same flow rate. This because the high difference of temperatures between outlet and inlet which effect on useful energy with same flow rate as shown in equation (11).

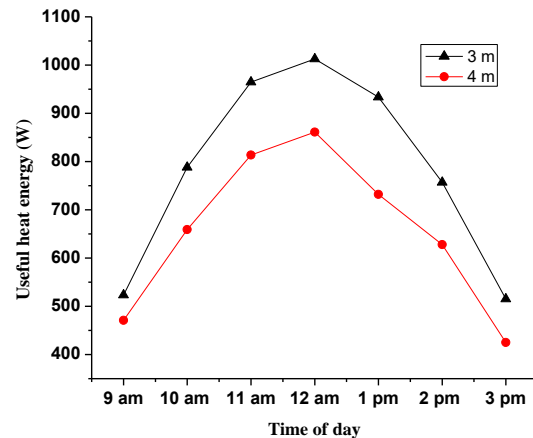


Figure (9): Variation of useful energy for two types of absorber with same volumetric flow rate 1 L/min.

Fig.10 shows the instantaneous thermal efficiency of two types of absorbers. The efficiency for 4 m spiral absorber varied between minimum and maximum value between

0.326 to 0.366 respectively when the beam radiation varied between 415 to 748 W/m². The maximum efficiency of 3 m spiral absorber was increased to 0.449 at maximum beam solar radiation 717 W/m² and with same volumetric flow rate 1 L/min. Three-meter absorber is more efficient than four-meter absorber. This increased in efficiency of 3 m absorber because the increase in useful energy which effect greatly on instantaneous efficiency as shown in equation 12.

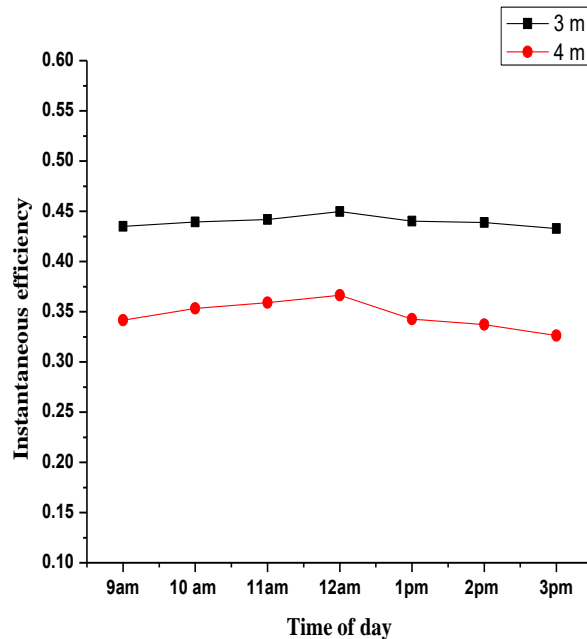


Figure (10): instantaneous efficiency for 3m and 4 m spiral absorbers

The heat losses of PDSC increased with wind speed (air velocity) increased because the forced convection increased which increased in cooler of absorber surface. Fig.11 shows the effect of wind speed on PDSC losses with 3 m absorber at 1 L/min flow rate . It shows that the variation in wind speed make a fluctuation in heat losses. The wind speed is an effective parameter on efficiency but not controlled.

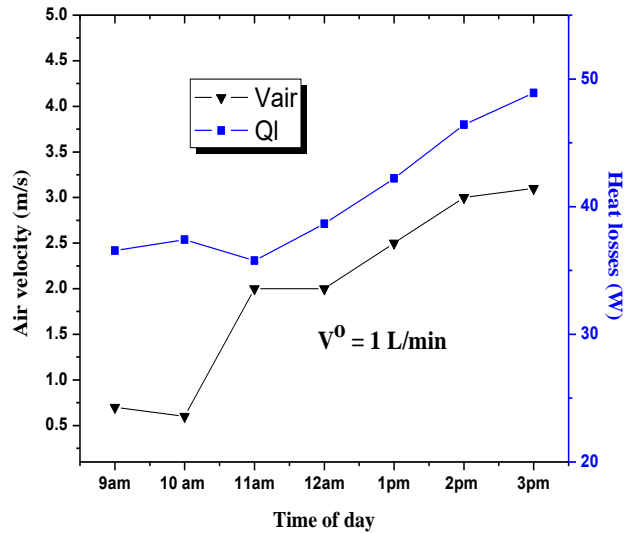


Figure (11): effect of air velocity on heat losses of PDSC with 3 m spiral absorber at (15/9/2017)

VII. CONCLUSIONS

The simulation and experimental work to compare the performance of the PDSC with two different lengths of spiral absorber four meter and three meter. It concluded from this work:

- Diameter of theoretical heat flux distributed on absorber area was about 8 cm but was 18 cm in practical because the optical losses.
- Also, the theoretical heat flux in program was 47603.3 W/m² and in theoretical calculations by equations was 43776 W/m².
- At 1 L/min volumetric flow rate, two types was compared thermally.
- Maximum outlet water temperature and absorber temperature of 3 m was 69.1 °C and 425 °C respectively which were higher than 4 m which were 61.43°C and 290 °C respectively at the same flow rate 1 L/min.
- The direct steam was generated at low flow rate with high temperature which was maximum at 12 am 113.7 °C for 4 m and 119.32 °C for 3 m at low flow rate 0.25 L/min
- With same flow rate 1 L/min of two types, maximum useful energy of 3 m was 1012.9 W higher than 4 m which was 861.17 W
- Maximum instantaneous efficiency of 3 m was 0.449 higher than 4 m which was 0.366 with same flow rate 1 L/min

| | | |
|------------------------|---|---------------------|
| Q_l | Heat losses energy | W |
| η_c | Collector thermal efficiency | - |
| U_l | Overall heat transfer coefficient | W/m ² .K |
| T_{amb} | Ambient temperature | °C |
| T_{abs} | Absorber temperature | °C |
| T_f | Film temperature | °C |
| $Nu_{h,nat}$ | Nusselt number of natural convection | - |
| Gr | Grashof number | - |
| G | Gravitational acceleration | m/s ² |
| L | Characteristic length | m |
| β | Thermal expansion | - |
| T_f | Film temperature | °C |
| h_r | Radiation heat transfer coefficient | |
| h_{wind} | Heat transfer coefficient of forced convection | W/m ² K |
| h_{nat} | Heat transfer coefficient of nature convection | W/m ² K |
| h_{total} | Total heat transfer coefficient | W/m ² K |
| K_{air} | Thermal conductivity of the air | W/m K |
| n_c | Collector efficiency | - |
| \dot{m} | Mass flow rate | Kg/s |
| Cp_w | Specific heat of water vapor | KJ/Kg.K |
| $\rho\tau\alpha\gamma$ | Reflectivity, transmittance, absorptivity and Intercept factor respectively | - |
| θ | Inclination angle of receiver | Deg |

| | | |
|-------|--|------------------|
| A_a | Aperture area of dish | m ² |
| I_a | Solar heat flux on aperture area of dish | W/m ² |
| A_r | Receiver or absorber area | m ² |
| Q_a | Radiation absorbed by receiver | W |
| Q_u | Useful energy | W |

- From results showed that the three-meter spiral absorber more efficient than four meter because the reflected radiation not falls on entire length of four-meter contrast of three meter.
- The heat losses from absorber increased with air velocity increased.

IX. Nomenclature

| Symbol | Description | Units SI |
|--------|-------------|----------|
|--------|-------------|----------|

X. References

- [1] Sánchez, D., Bortkiewicz, A., Rodríguez, J. M., Martínez, G. S., Gavagnin, G. and Sánchez, T. 2016. "A methodology to identify potential markets for small-scale solar thermal power generators." *Applied Energy*, 169, 287-300.
- [2] Bellos, E., Tzivanidis, C., and Antonopoulos, K. A. 2016c. "Exergetic, energetic and financial evaluation of a solar driven absorption cooling system with various collector types." *Applied Thermal Engineering*, 102, 749-759.
- [3] Bellos, E., Korres, D., Tzivanidis, C. and Antonopoulos, K. 2016a. "Design, simulation and optimization of a compound parabolic collector." *Sustainable Energy Technologies and Assessments*, 16, 53-63.
- [4] Kalogirou, S. A. 2004. "Solar thermal collectors and applications." *Progress in energy and combustion science*, 30(3), 231-295.
- [5] Pavlović, S. R., Bellos, E. A., Stefanović, V. P., Tzivanidis, C. and Stamenković, Z. M. 2016. "Design, simulation and optimization of a solar dish collector with spiral-coil thermal absorber." *Thermal Science* (00), 104-104.
- [6] S. Pavlovic, E. Bellos, G. Le Roux, V. Stefanovic, C. Tzivanidis, "Experimental investigation and parametric analysis of a solar thermal dish collector with spiral absorber" *Applied Thermal Engineering*, 2017.
- [7] Abid, M., Ratlamwala, T. and Atikol, U. 2015. "Performance assessment of parabolic dish and parabolic trough solar thermal power plant using nanofluids and molten salts." *International Journal of Energy Research*.
- [8] E. Bellos, C. Tzivanidis, and K. Antonopoulos, "Design and simulation of a new solar paraboloid dish collector," 2015.
- [9] H. G. Hameed and H. A. Neema, "Experimental Study for Productivity Enhancement of A parabolic Solar Concentrator System", *Al-Qadisiya Journal For Engineering Science*, Vol. 4, 2011.
- [10] J. Dascomb, "Low-cost concentrating solar collector for steam generation," 2016.
- [11] V. Siva Reddy, S. C. Kaushik, and S. K. Tyagi, "Exergetic analysis and performance evaluation of parabolic dish Stirling engine solar power plant," *ER International Journal of Energy Research*, vol. 37, pp. 1287-1301, 2013.
- [12] A. Hafez, A. Soliman, K. El-Metwally, and I. Ismail, "Solar parabolic dish Stirling engine system design, simulation, and thermal analysis," *Energy Conversion and Management*, vol. 126, pp. 60-75, 2016.
- [13] Fareed .M. Mohamed , Awatif .S. Jassim, Yaseen. h. mahmood, " Design and study of two axis tracking system," *Tikrit Journal of Pure Science*, 2012.
- [14] Daabo, A. M., Mahmoud, S., and Al-Dadah, R. K. 2016. "The effect of receiver geometry on the optical performance of a small-scale solar cavity receiver for parabolic dish applications." *Energy*, 114, 513-525.
- [15] B. A. Sup, M. F. Zainudin, T. Z. S. Ali, R. A. Bakar, and G. L. Ming, "Effect of rim angle to the flux distribution diameter in solar parabolic dish collector," *Energy Procedia*, vol. 68, pp. 45-52, 2015.
- [16] Mohand Mosa Mohammad and Mr.G.Narendar, " Design and Heat Transfer Analysis of a Parabolic Shaped Solar Dish Collector," *International Journal & Magazine of Engineering, Technology, Management and Research* , Vol. 2 , 2015.
- [17] L. Zhou, Y. Li, E. Hu, et al., Comparison in net solar efficiency between the use of concentrating and non-concentrating solar collectors in solar aided power generation systems, *Appl. Therm. Eng.* 2015;75:685-691.
- [18] Prakash, M., Kedare, S.B. and Nayak, J.K. 2009 "Investigations on heat losses from a solar cavity receiver", *Solar Energy*, December, 2009, Vol. 83, No. 12, pp.157-170
- [19] R. Y. Ma "Wind Effects on Convective Heat Loss From a Cavity Receiver for a Parabolic Concentrating Solar Collector", Sandia report contract SAND 92-7293, 15 (1993).

Evaluation the effect of wastewater conductivity on the final stable voltage applied to electrocoagulation reactor

Forat Yasir AlJaberi

Chemical Engineering department- College of Engineering-University of AlMuthanna:
furat_yasir@yahoo.com (corresponding author)

Wadood T. Mohammed

Chemical Engineering department- College of Engineering-University of Baghdad: wadood.taher@gmail.com

Abstract- The aim of the present study is to investigate the effect of the operational variables and the conductivity of the simulated wastewater on the performance of the electrocoagulation reactor, i.e. the values of the voltage applied and the consumption of the electrical energy. Aluminum concentric tubes were used in a parallel-monopolar arrangement to remove lead from the simulated wastewater. The operational variables studied in this research were the initial concentration of lead (10-300)ppm, contact time (5-60)minutes, applied current (0.5-2.5)Amps., pH (2-12), and the stirring speed (0-300)rpm. It was found that the value of the solution conductivity, as well as the studied variables remarkable, minimize the value of the final stable voltage applied that required to complete the treatment operation and also minimizing the energy consumed consequently. Response surface methodology (RSM) was used to evaluate the required response mathematical correlation and to analyze the results via statistical software programs.

Index Terms— wastewater; electrocoagulation; conductivity; stable voltage applied

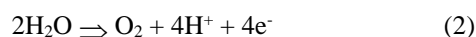
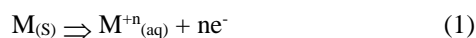
I. INTRODUCTION

Numerous techniques are presented in the modern world to treat the pollution in the aquatic environments such as chemical precipitation, ion exchange, membrane filtration, adsorption, and electrochemical methods [1], [2], [3], [4], and [5]. The most practical type of electrochemical technique is the electrocoagulation process [6] which associated with adsorption phenomenon in its work because of the production of coagulants (adsorbent) in situ [7] depending on the applied voltage to the cell by an external power supply [8].

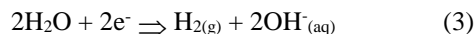
Electrocoagulation method is accomplished according to the following three successive consecutive steps [1]:

- 1- Formation of flocs as a result of the oxidation and reduction operations on anode and cathode respectively as follow:

- At the anode electrode with metal M:



- At the cathode electrode:

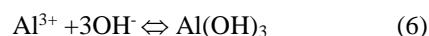
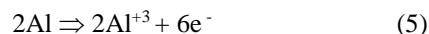


- 2- Destabilization of the pollutants, particulate suspension, and breaking of emulsions. At the cathode surface:



- 3- Aggregation of the destabilized phases to form flocs.

Therefore, electrocoagulation method involves two essential processes, the first one is the electrodeposition of aluminum electrodes and formation of flocs due to the polymerization of aluminum oxy-hydroxides as shown in the following equations:



While the second essential process is the simultaneous production of hydrogen at the cathode electrode [9] as shown in equation (3).

Conductivity is an important issue in such electrochemical process for the enhancing of the efficiency of heavy metal removal, minimizing the formation of an oxide layer on the cathode electrode using metal salt such as sodium chloride or sulphate and reducing the value of voltage required to accomplish the suggested required operation [1]. Moreover, energy consumption aimed to be minimized and also the cost-effective from the economic view. RSM method is used to design experiment via Box-Wilson technique and analysis the result using statistical software programs such as Minitab-17.

II. MATERIALS AND EXPERIMENTAL WORK

A. Apparatus

Three concentric aluminum tubes electrodes with different diameters and thicknesses were used in the batch electrocoagulation reactor as shown in Fig. 1 with an active area equals approximately 285 cm². The outer and inner tubes classified as the anode electrode and the mid tube as

the cathode electrode and they were connected in a monopolar arrangement.

B. Chemicals

Simulated samples of wastewaters according to the design of the experiments were prepared by dissolving the required amount of an initial concentration of lead nitrate $Pb(NO_3)_2$ (99.99% purity; B.D.H- England) weighed by a digital balance (500g x 0.01g) (PROF company), in distillate water belongs to the Eq. (7) [10]:

$$W = V \times C_i \times (M / mA) \quad (7)$$

Where: W is the weight of salt (grams); V: Volume of solution (liter); C_i : Initial concentration of lead ions in solution (ppm); M: M.wt of the lead nitrate; mA: Atomic weight of lead.

The value of acidity was measured by pH meter (ATC company) and adjusted by hydrochloric acid (0.1 N) and sodium hydroxide (0.1 N). While 100ppm of NaCl was added to prevent the formation of an oxidation layer on the electrode and to enhance the conductivity of the simulated solution.

Digital DC- power supply (SYADGONG company-305D) model; 0-30 volt and 0-5 Ampere was used to supply the designed voltage to the electrodes immersed in the simulated wastewater. Samples were collected from the treated solution, filtered using cellulose Glass-Microfibre discs (Grade: MGC; pore diameter is 0.47 micrometre-MUNKTELL). The value of the new conductivity of the treated wastewater sample and the stable value of the voltage applied for each experiment were recorded. At the end of each experiment, electrodes were washed one time with 0.1N HCl and several times with distillate water to ensure it was cleaned well. The same procedure was repeated for the next experiment according to the designed schedule shown later.

The energy consumption (kWh/m^3) in the electrocoagulation cell is calculated according to the following equation:

$$E = (U \cdot I \cdot t) / (1000 \cdot V) \quad (8)$$

where: U is the applied voltage (volt), I: applied current (Amps.), t: contact time (h), and V is the volume of the simulated wastewater (m^3).

The ranges of the operational parameter are listed in Table 1 shown below.

TABLE 1
OPERATIONAL VARIABLES

| Parameters | Range or fixed value |
|----------------------------------|----------------------|
| Initial lead concentration (ppm) | 10-300 |
| pH | 2-12 |
| Electrical current (Amps.) | 0.5-2.5 |
| Stirring speed (RPM) | 0-300 |
| Contact time (min) | 5-60 |

C. Statistical analysis

The empirical correlations of the final stable voltage applied variation which relates the operational variables that listed in Table 1 and the specified conductivity is studied using the response surface methodology (RSM) method via rotatable central composite design uniform- two level factorial-half fraction. The mathematical model could be achieved according to the following quadratic Eq.(9) [11]:

$$Y = B_0 + \sum_{i=1}^q B_i X_i + \sum_{i=1}^q B_{ii} X_i^2 + \sum_{i=1}^q \sum_{j=1}^q B_{ij} X_i X_j + \varepsilon \quad (9)$$

X_1 , X_2 , and X_q denote the independent variables that are continuous and a controllable with negligible ε error; where B_0 , B_i , and B_{ij} are called the regression coefficients which are unknown and to be estimated and ε is a random error (or residual) which is the amount of variation in Y.

Thirty-two experiments are designed as cube points:16, center points in the cube:6, axial points:10, the center points in axial is none, and the rotatability α is 2. Table 2 lists the natural and coded value of operational parameters. Statistical software programs are used such as Statistica-10 and Minitab-17 to estimate the regression coefficients and graphical analysis of the results obtained.

III. RESULTS AND DISCUSSION

Statistical design of experiments is performed to investigate the effect of the operational variables and solution conductivity on the voltage variation response. Table 3 shows the initial and the final values of the solution conductivity (k) for each designed experiment, the final stable value of the voltage applied (V_{FSV}), and the value of energy consumed ($E_{cons.}$) belongs to the final stable value of the voltage applied.

TABLE 2
NATURAL AND CODED OPERATIONAL VARIABLES

| Natural Variable (X_i) | Coded Variables | | | | |
|------------------------------|-----------------|----|-----|-----|-----|
| | -2 | -1 | 0 | 1 | 2 |
| X_1 = time (min.) | 5 | 19 | 33 | 46 | 60 |
| X_2 = concentration (ppm) | 10 | 83 | 155 | 228 | 300 |
| X_3 = pH | 2 | 5 | 7 | 10 | 12 |
| X_4 = current (Amps.) | 0.5 | 1 | 1.5 | 2 | 2.5 |
| X_5 = stirring speed (rpm) | 0 | 75 | 150 | 225 | 300 |



TABLE 3
VALUES OF SPECIFIED VARIABLES

| Run No. | κ (μS/cm) | | V _{FSV} (Volt) | E _{cons} (kWh/cm ²) |
|---------|-----------|-------|-------------------------|--|
| | Initial | Final | | |
| 1 | 889 | 1120 | 5.10 | 3.19 |
| 2 | 889 | 1128 | 4.40 | 6.78 |
| 3 | 1727 | 1189 | 5.10 | 3.19 |
| 4 | 1727 | 1190 | 4.60 | 7.09 |
| 5 | 889 | 1245 | 4.70 | 2.94 |
| 6 | 889 | 1192 | 4.40 | 6.78 |
| 7 | 1727 | 1329 | 4.50 | 2.81 |
| 8 | 1727 | 1270 | 4.10 | 6.32 |
| 9 | 889 | 1057 | 7.80 | 9.75 |
| 10 | 889 | 1140 | 7.10 | 21.89 |
| 11 | 1727 | 1224 | 7.30 | 9.13 |
| 12 | 1727 | 1178 | 7.40 | 22.82 |
| 13 | 889 | 1178 | 7.80 | 9.75 |
| 14 | 889 | 1183 | 7.00 | 21.58 |
| 15 | 1727 | 1298 | 7.20 | 9.00 |
| 16 | 1727 | 1280 | 7.00 | 21.58 |
| 17 | 1369 | 1308 | 7.10 | 1.78 |
| 18 | 1308 | 1147 | 5.90 | 17.70 |
| 19 | 471 | 1130 | 6.60 | 10.73 |
| 20 | 2145 | 1325 | 6.00 | 9.75 |
| 21 | 1308 | 1355 | 5.80 | 9.43 |
| 22 | 1308 | 1576 | 5.30 | 8.61 |
| 23 | 1308 | 1183 | 2.80 | 1.52 |
| 24 | 1308 | 1131 | 8.60 | 23.29 |
| 25 | 1308 | 1149 | 7.60 | 12.35 |
| 26 | 1308 | 1171 | 6.30 | 10.24 |
| 27 | 1308 | 1155 | 6.20 | 10.08 |
| 28 | 1308 | 1153 | 6.30 | 10.24 |
| 29 | 1308 | 1148 | 6.40 | 10.40 |
| 30 | 1308 | 1150 | 6.60 | 10.73 |
| 31 | 1308 | 1151 | 6.50 | 10.56 |
| 32 | 1308 | 1153 | 6.30 | 10.24 |

Fig. 2 explains clearly the effect of the operational variables on the final conductivity is minimized along the period of the experiment due to the consumption of sodium chloride for enhancing the electrochemistry issue. While it rises directly with the increasing of lead nitrate doses. The decreasing and then the increasing of its value with pH of the simulated solution was presented obviously because of the variation of coagulants formation belongs to the degree of acidity and alkalinity of the polluted solution. The value of conductivity value has the similar behavior related with applied constant current and the value of stirring speed, it maximized slowly then minimized like so as a reason of the consumption of sodium chloride through the duration of the experiment. Therefore, the conductivity of wastewater affects the Faradic yield, final stable voltage applied to the cell at constant current value, and energy consumed via electrocoagulation [12].

Fig. 3 shows the efficient design and the specific effects of operational variables on minimizing the voltage required to operate the electrocoagulation cell. These variables incorporate with the effect of solution conductivity lead to get an economic design and procedure to minimize energy consumption consequently.

The mathematical correlations of the final value of the conductivity and the final stable value of the applied current that relate these responses with the operational parameters are described below:

Final conductivity ($R^2= 0.9048$):

$$Y_k = 1372 - 0.93 X_1 + 0.06 X_2 - 106.6 X_3 + 50 X_4 + 0.640 X_5 + 0.0323 X_1^2 + 0.00116 X_2^2 + 10.50 X_3^2 - 46.1 X_4^2 - 0.00192 X_5^2 - 0.0110 X_1 X_2 - 0.331 X_1 X_3 + 1.25 X_1 X_4 - 0.0018 X_1 X_5 + 0.0186 X_2 X_3 + 0.203 X_2 X_4 + 0.00094 X_2 X_5 - 4.00 X_3 X_4 - 0.0427 X_3 X_5 + 0.160 X_4 X_5 \quad (10)$$

Final stable applied voltage ($R^2= 0.9820$):

$$Y_{V_{fsv}} = 0.65 - 0.039 X_1 + 0.00434 X_2 + 0.411 X_3 + 5.085 X_4 - 0.0079 X_5 - 0.000024 X_1^2 - 0.00001 X_2^2 - 0.0387 X_3^2 - 0.818 X_4^2 + 0.00019 X_5^2 + 0.000094 X_1 X_2 + 0.00018 X_1 X_3 + 0.0027 X_1 X_4 + 0.000018 X_1 X_5 - 0.000379 X_2 X_3 - 0.00086 X_2 X_4 - 0.00001 X_2 X_5 + 0.0450 X_3 X_4 + 0.000433 X_3 X_5 - 0.00083 X_4 X_5 \quad (11)$$

Fig. 4 represents the relation between the final stable values of voltage applied and the final conductivity according to the following predicted equation:

$$V_{FSV} = 25.303 - 0.027 \kappa + 9.364 * 10^{-6} \kappa^2 \quad (12)$$

Figures (5, 6, 7, 8, and 9) represent the mathematical correlation of the final stable voltage applied related with each one of operational variables individually when others at their mean values where their correlations are listed in Table 4 which show higher values of R^2 .

Moreover, Fig. 10 relates the energy consumption with the final stable value of the voltage applied belongs to the following equation:

$$E_{cons.} = -3.457 + 1.332 V_{fsv} + 0.145 * V_{fsv}^2 \quad (13)$$

A. Effect of initial lead concentration

As shown in Fig. 11, the voltage applied keep minimizing along the duration of the experiment for all values of initial lead concentration due to the continuous releasing of coagulants via the dissolution of aluminium electrodes which work together with sodium chloride for enhancing the conductivity of the simulated solution that leads to minimize the voltage required then less energy consumed relatively. Higher concentration solution required

more voltage applied than the dilute solution because of the requirement of more amount of aluminium ion that must be released enough as possible to be applicable to form more of coagulants then adsorbed the excess amount of pollutant in the concentrated wastewater sample.

TABLE 4
FINAL APPLIED VOLTAGE CORRELATIONS VIA EACH ONE OF VARIABLES WHILE OTHERS AT MEAN VALUES

| X | Y: Final stable applied voltage |
|----------------------------|---------------------------------------|
| Time (min.) | $Y = 6.8046 - 0.0253x + 0.0001x^2$ |
| Conc. (ppm) | $Y = 6.2026 + 0.0005x - 6.0246E-6x^2$ |
| pH | $Y = 4.8379 + 0.4673x - 0.0371x^2$ |
| Electrical current (Amps.) | $Y = 0.375 + 5.075x - 0.7667x^2$ |
| Stirring speed (rpm) | $Y = 6.7875 - 0.0089x + 2.5185E-5x^2$ |

B. Effect of solution pH

The variation of the final stable voltage applied with several designed value of pH along the period of the experiment is explained in Fig. 12. In general, the voltage applied is slightly minimized along the contact time of each experiment but it's different belongs to pH value. As seen the alkalinity medium is more efficient for economical view in this kind of wastewater treatment technique. This could be interpreted by the continuous rising of conductivity at high pH as a result of rapid dissolution of anode electrodes and by releasing of OH ions.

C. Effect of electric current supplied

Fig. 13 shows the directly proportional of the voltage applied to all values designed of current supplied to the electrocoagulation reactor. But, they are slightly minimized during the experiment contact time which leads to minimizing the value of energy consumption and the required cost as consequence.

D. Effect of stirring speed

The behavior of the voltage applied to each value of stirring speed it seemed to be similar to that with current discharged to the electrochemical cell. They are starting from the higher value of voltage then minimizing to a relatively lower value and that is noticed for all intervals of speed as shown in Fig. 14 but, the zero value of the stirring speed leads to the consuming of a higher value of the voltage applied due to the semi-stagnant solution which affects the cooperation of different ions to complete the aim of this technique efficiently.

reactor, i.e. the values of the voltage applied and the consumption of the electrical energy which seems to be an important issue for the electrochemical treatment techniques of wastewaters due to the environment and economic view that required to be the cost-effective design which leads to low cost consuming in wastewater treatment methods. Results showed that the conductivity is an essential parameter which highly affects the value of the voltage applied until this voltage reaches the final stable case. Other operational variables are different in their effects on responses but they have a very important impact on the gain of an economic value of the voltage applied then energy consumption value. Several equations were found depending on the RSM method and using the statistical soft programs, i.e. Statistica-10 and Minitab-17.

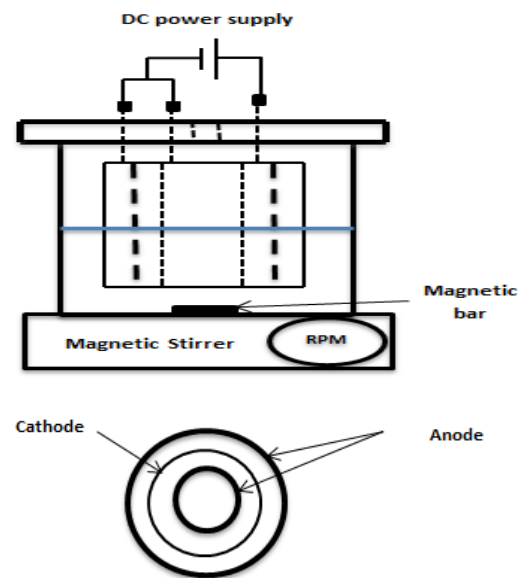


Fig. 1 Schematic of the electrocoagulation cell and the electrodes configuration

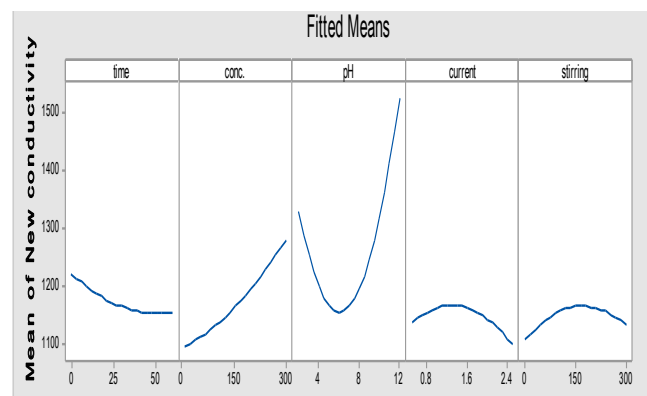


Fig. 2 Main effects plot of variables for the final conductivity

IV. CONCLUSIONS

The present study has focused on the effect of the operational variables and the conductivity of the simulated wastewater on the performance of the electrocoagulation

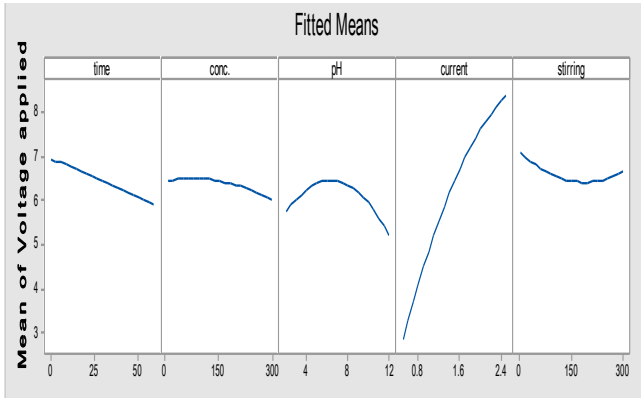


Fig. 3 Main effects plot of variables for the final stable voltage applied

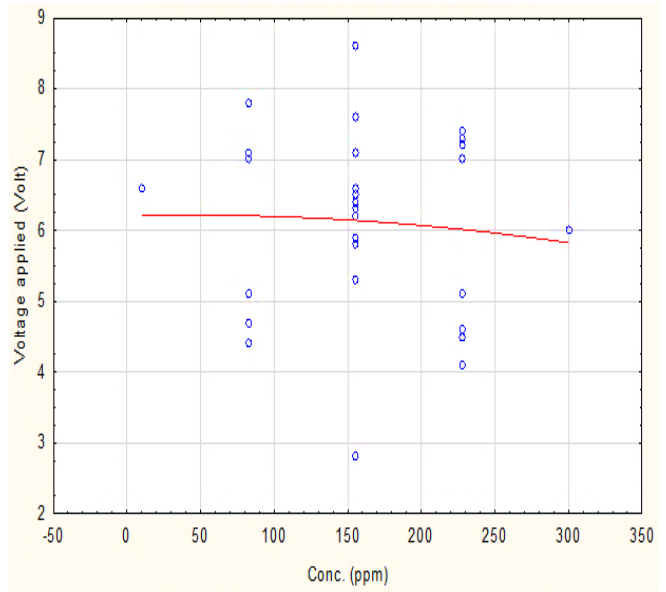


Fig. 6 Final stable voltage applied vs. conc. at mean values of other variables

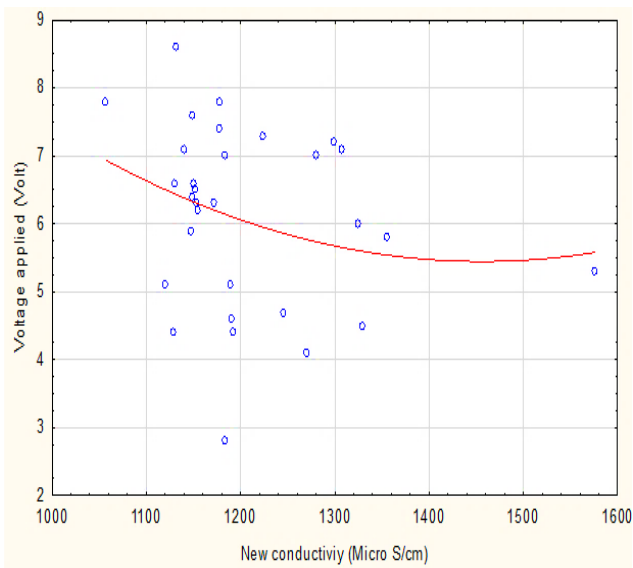


Fig. 4 Final stable voltage applied vs. final conductivity at mean values of other variables

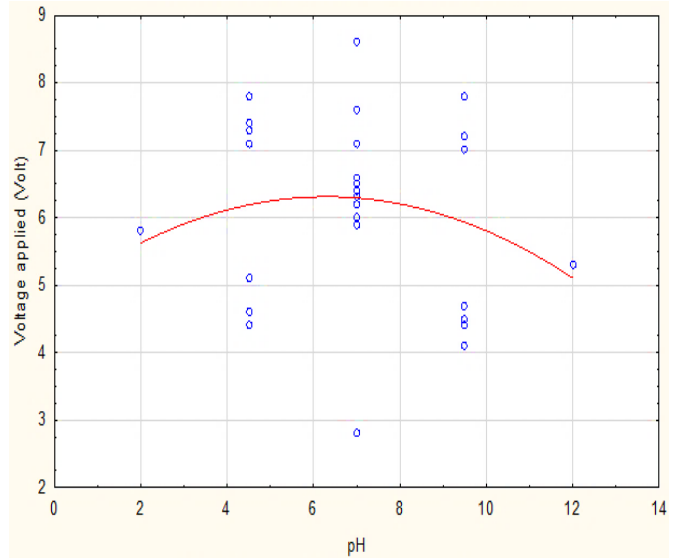


Fig. 7 Final stable voltage applied vs. pH at mean values of other variables

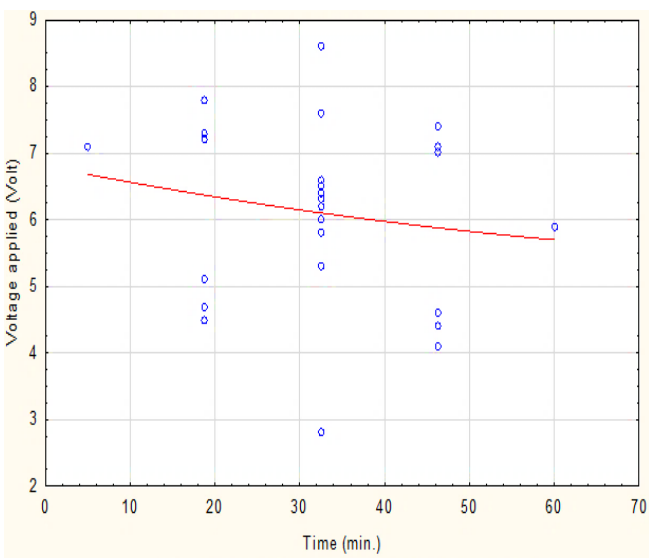


Fig. 5 Final stable voltage applied vs. time at mean values of other variables

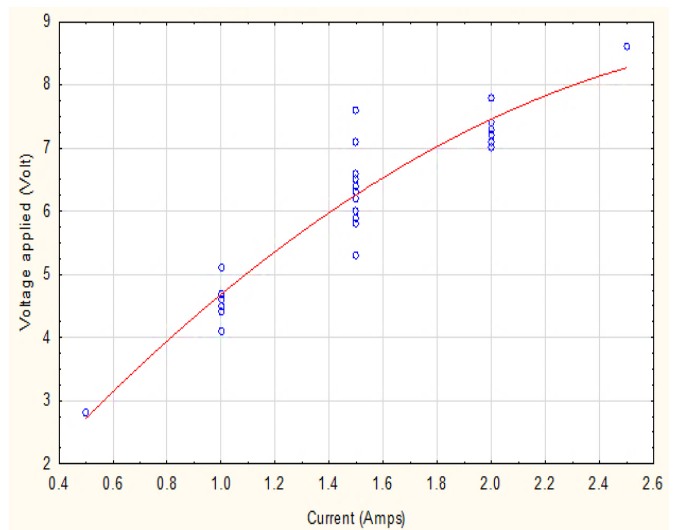


Fig. 8 Final stable voltage applied vs. current at mean values of other variables

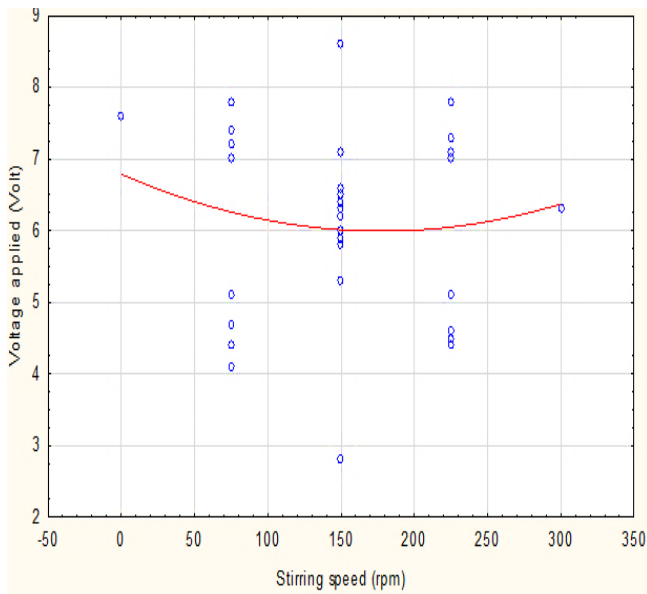


Fig. 9 Final stable voltage applied vs. the stirring speed at mean values of other variables

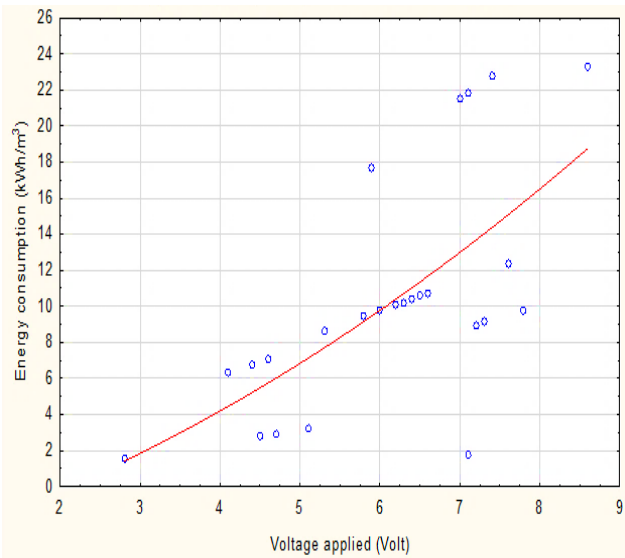


Fig. 10 Final stable voltage applied vs. energy consumption at mean values of other variables

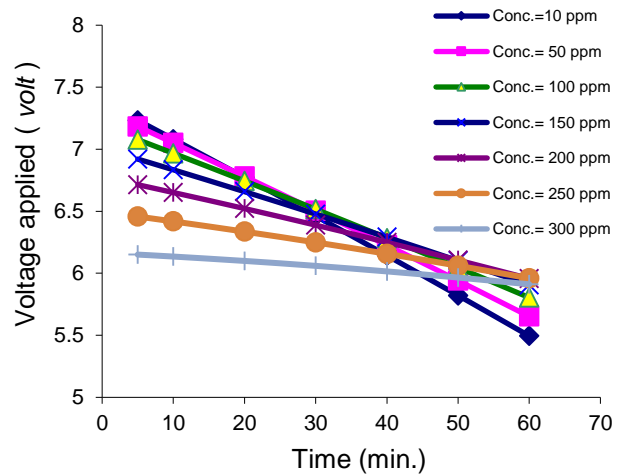


Fig. 11 Final stable voltage applied vs. time with several constant conc. at mean values of other variables

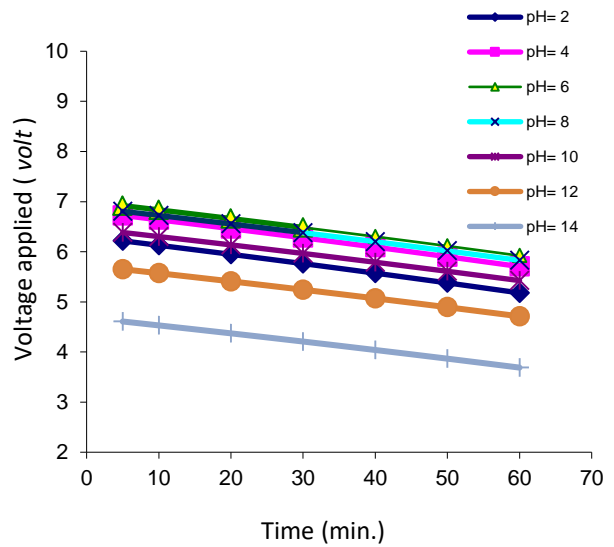


Fig. 12 Final stable voltage applied vs. time with several constant pH at mean values of other variables

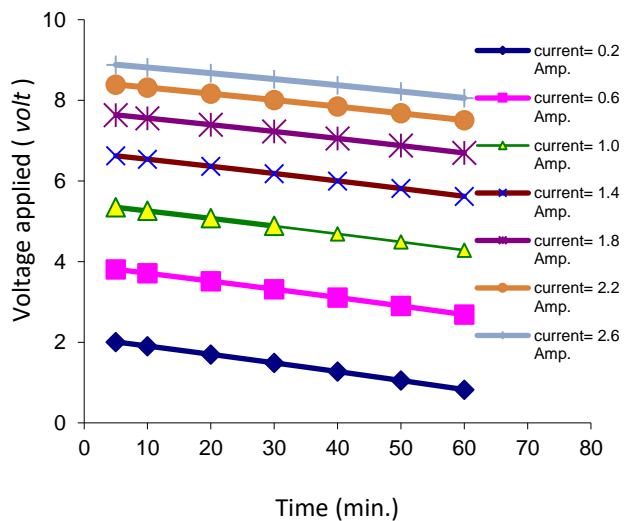


Fig. 13 Final stable voltage applied vs. time with several constant current at mean values of other variables

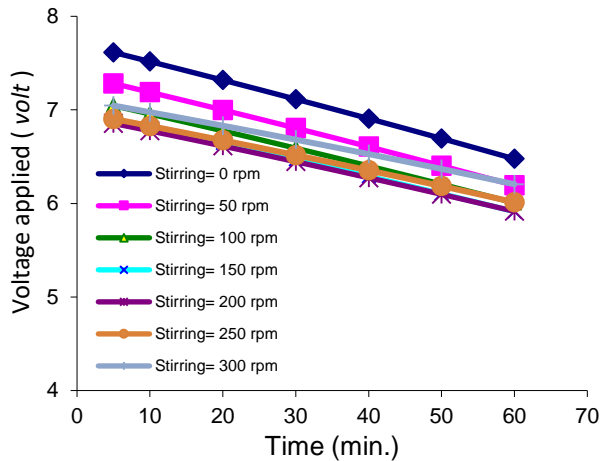


Fig. 14 Final stable voltage applied vs. time with several constant stirring speed at mean values of other variables

- [9] Ch. An, G. Huang, Y. Yao and S. Zhao, "Emerging usage of electrocoagulation technology for oil removal from wastewater: a review", *Science of the Total Environment J.*, vol.579, pp.537-556, 2017.
- [10] A.A. Mohammed and M. D. Al-Mureeb, "Removal of lead from simulated wastewater by electrocoagulation method", *Journal of Engineering*, vol.16, pp. 5811-5821, 2010.
- [11] F. Y. Al-Jaberi, W. T. Mohammed " Novel method for electrocoagulation removal of lead from simulated wastewater by using concentric tubes electrodes reactor ", *Desalination and Water Treatment*, 2018.
- [12] I. Kabdaşlı, I. Arslan-Alaton, T. Ölmez-Hanc and O. Tünay, " Electrocoagulation applications for industrial wastewaters: a critical review", *Journal of Environmental Technology Reviews*, vol.1, No.1, pp. 2-45, 2012.

V- REFERENCES

- [1] E. Bazrafshan, L. Mohamadi, A. A. Moghaddam and A. H. Mahvi, "Heavy metals removal from aqueous environments by electrocoagulation process- a systematic review", *Journal of Environmental Health Science and Engineering*, vol.13, No.74, pp. 2-16, 2015.
- [2] S. K. Gunatilake, "Methods of removing heavy metals from industrial wastewater", *Journal of Multidisciplinary Engineering Science Studies*, vol. 1, No.1, pp. 12-18, 2015.
- [3] M. A. Barakat, "New trends in removing heavy metals from industrial wastewater", *Arabian Journal of Chemistry*, vol. 4, pp. 361-377, 2011.
- [4] B. Lekhlif, L. Oudrhiri, F. Zidane, P. Drogui and J. F. Blais, "Study of the electrocoagulation of electroplating industry wastewaters charged by nickel (II) and chromium (VI)", *J. Mater. Environ. Sci.*, vol.5, No.1, pp.111-120, 2014.
- [5] Riyanto and A. Hidayatillah, "Electro-coagulation of detergent wastewater using aluminium wire netting electrode (AWNE)", in *Proc. 2014 Research, Implementation and Education of Mathematics and Sciences Conf.*, pp. 151-158.
- [6] É. Fekete, B. Lengyel, T. Cserfalvi and T. Pajkossy, " Electrocoagulation: an electrochemical process for water clarification ", *J. Electrochem. Sci. Eng.*, vol.6, No.1, pp.57-65, 2016.
- [7] B. Al Aji, Y. Yavuz and A. K. Koparal, "Electrocoagulation of heavy metals containing model wastewater using monopolar iron electrodes", *Journal of Separation and Purification Technology*, vol.86, pp. 248-254, 2012.
- [8] C. Zhang, Y. Jiang, Y. Li, Z. Hu, L. Zhou and M. Zhou, "Electrocoagulation of heavy metals containing model wastewater using monopolar iron electrodes", *Journal of Separation and Purification Technology*, vol.86, pp. 248-254, 2012.



Experimental Study the Effect of Ambient Temperature on the Performance of Photovoltaic System Work with MPPT Charge Controller in Technical Engineering College of Najaf

Dhafer Manea Hachim AL-Hasnawi

Technical Engineering, College of Najaf

Al-Furat Al-Awsat Technical University, 31001 Najaf, Iraq.

E-mail: Dhafeer_manee@yahoo.com Mobile 07809787897

Abstract- Solar energy is generated when energy from the sun (sunlight) is converted into electricity or used to heat air, water, or other fluids. Solar photovoltaic (PV) converts sunlight directly into electricity using photovoltaic cells. The ambient temperature one of the important parameter effect on the efficiency of PV system. In the present work, study the effect of ambient temperature, wind speed and solar radiation on the performance of PV system experimentally. Where the experimental work consists of experimental measurement the efficiency of standalone 3 KW PV system with variations the ambient temperature and solar radiation installed in jabir Ibn Haiyan building. AS well as data recording ambient temperature, solar radiation and wind speed, from the weather station located in the Alternative and Renewable Energy Research Unit. The effects of solar radiation, wind speed and ambient temperature were studied on the performance of PV system. During the process of conducting experiments on the PV system in a building (Jabir Ibn Haiyan) show that the ambient temperature effects on the efficiency of the solar system (voltages and power), whereas the higher ambient temperature lesser solar cell efficiency.

Index Terms— Meteorological Information, Solar energy, PV system

I. INTRODUCTION

As a great potential renewable energy source, solar energy is becoming one of the most important energies in the future. Recently, there has been an enormous increase in the understanding of the operational principle of photovoltaic devices, which led to a rapid increase in the power conversion efficiencies of such devices. Solar cells vary under temperature changes; the change in temperature will affect the power, output from the cells.[1] Used many different PV modules to simulate nominal Operation Cell Temperature (NOCT)for building integration applications, where the yearly modules temperature and performance for different orientations and tilted angles were presented. [2] conducted a study to show that Abu Dhabi has a strong potential for solar energy capture by measuring the solar radiation and surface temperature for one year. [3] Used Fuzzy logic and GIS-based spatial multi-criteria evaluation to conduct an investigation on siting large PV power plant to

study the effects of temperature and dust on the performance. [4] Investigated the change on PV panels temperature by the influence of natural wind cooling and showed that including wind data in the analysis leads to better results and prediction. [5] Presented a study addresses statistical and experimental investigation dealing with the effect of temperature within range of 15-60 °C and intensity levels of 200-500 W/m². The author showed that the current has a proportional relationship to the intensity, whereas the voltage decreases when the temperature increases.

[8] similar study is presented by [5] with different ranges, namely 25-60 °C for temperature and intensity levels of 215-515 W/m². Experimental study the effect of cell temperature in the range 25-60 C at constant light intensities 215-515 W/m² on the photovoltaic parameters of mono-crystalline silicon solar cell. The results show that the open circuit voltage, maximum power, fill factor and efficiency are decreased with cell temperature.

[6] Conducted an experimental investigation to study the effect of dust density, high humidity, rain and snow on the performance of PV panels in the town of Brighton in UK, and showed that these parameters have significant effect and could annihilate any system output.

[7] Proposed numerous models that can be used to predict the relationship between performance of PV system and solar radiation, ambient temperature and wind. Where they showed that the performance is better when the wind speed and solar radiation increase and poor performance when ambient temperature increases.

[9] conducted a study for temperature effect on performance of solar cells that made of silicon thin-film and found that the performance decreases as the ambient temperature increases. [10] Presented a 3D dynamical model to simulate the steady-state dynamic regimes of PVT collector. [11] Used support vector regression (SVR) to study various methods of PV power output prediction. [12] Analytically investigated the effect of ambient temperature on set of PV panels under high solar radiation. [13] investigate the dust accumulation on the PV panels performance in Baghdad-Iraq. [14] A recent work which is presented by [14] investigated the effect of dust and dried mud of the PV modules in the area of Kingdom of Saudi Arabia-Dhahran. [15] They work experimentally to measure the weather ambient temperatures (DBT), solar intensity and wind speed



in Najaf city (Iraq 44 oE, 31o N) over a period of one year from April 2015 to March 2016.

In this paper, experimental investigation the effect the weather conditions (the ambient temperature, wind speed and solar radiation) on performance of photovoltaic system (PV system) over one year in the city of Najaf in Iraq (Longitude 44 oE, Latitude 31o N).

II. EXPERIMENTAL SETUP AND PROCEDURE

In this work, the experiment includes two main parts. First, the implementation of Davis weather station to collect data over one year. Second part is investigating the performance of photovoltaic system (PV system) under the effect of various parameters over a period of eight months.

A. Weather Station

The weather station (Davis) is installed at 10 m from the ground in the building of Engineering Technical College in the city of Najaf in Iraq (Longitude 44 oE, Latitude 31o N), where the data was collected over a period of year starting from April 2015 to March 2016. The Davis weather station is shown in Fig. 1 and the specifications of Davis weather station are shown in table (I). All the date recorded

B. Photovoltaic system

The standalone 3 KW PV panels system is installed at the same location and level, of the weather station, to steady the effect of collected parameters on the PV system performance. The PV system consists of the following main components:

1. Solar PV panels: which includes an array of the thirty mono crystalline silicon solar modules where it is connected in series and parallel configuration. Each module provides 125 watts and the total power supply is 3.75 KW. The panels are inclined with an angle of 30o to the direction of south as shown in Fig.2 (a).
2. Charger Controller: it is (FLEXmax 80) model which is manufactured by OutBack Power company , as shown in Fig.2 (b) and operates with Maximum Power Point Tracking (MPPT) algorithm . The charger controller operates with 12, 24, 36, 48 and 60 VDC battery voltage and equipped with Backlit LCD display screen with 80 characters (4 lines, 20 character per line). Charger controller is accessible and able to store data up to 128 days of operation.
3. Inverter: which is (VFX3048E model, manufactured by OutBack Power) that works as, a DC-to-AC sine wave inverter, battery charger and an AC transfer relay housed within a die-cast aluminum chassis as shown in Fig. 2 (b). Moreover, the inverter is equipped with communication technology that connects the device with other OutBack Power devices to establish a network controlled system.

4. Battery: this system consists of eight Gel types (150 Ah 12 VDC), where two groups of four batteries each are connected together to provide 48 VDC as shown in Fig. 2(b)

TABLE I
SPECIFICATION OF THE WEATHER STATION DAVIS

| Item | Specifications | Details |
|---------------------|-------------------------|--|
| Barometric Pressure | Resolution and Units | 1 W/m2 |
| | Range | 0 to 1800 W/m2 |
| | Range | 410 to 820 mm Hg |
| | Update Interval | 50 seconds to 1 minute (5 minutes when dark) |
| | Temperature Coefficient | -0.12% per oC; reference temperature = 25 oC |
| Solar Radiation | Resolution and Units | 0.01” Hg, 0.1 mm Hg, 0.1 hPa/mb (userselectable) |
| | Range | 410 to 820 mm Hg |
| | Accuracy | ±0.3% |
| Wind | Resolution and Units | 0.4 m/s |
| | Range | 0 to 89 m/s |
| | Update Interval | 2.5 to 3 seconds |
| | Accuracy | ±0.5% |
| Temperature | Resolution and Units | 0.1 oC |
| | Range | -40 o to +65 oC |
| | Update Interval | 10 to 12 seconds |
| | Accuracy | ±0.3% |

TABLE II
UNCERTAINTY FOR EXPERIMENTAL RESULTS.

| Measured parameters | Mean value | Total uncertainty value | Total uncertainty (%) |
|------------------------------|------------|-------------------------|-----------------------|
| Ambient DBT, °C | 45 | ±0.8 | ±0.12 |
| Ambient relative humidity, % | 10 | ±0.5 | ±1.6 |
| Solar radiation, W/m2 | 1000 | ±5 | ±6.5 |
| Wind speed, m/s | 1.3 | ±0.6 | ±7.2 |

III. RESULTS AND DISCUSSIONS

The results obtained in this study include the following: Analysis of the data recorded by the photovoltaic system. It also takes data that includes solar radiation, temperature and wind speed from the weather station. All this information is



drawn and studied its effect on the performance of the photovoltaic system. In the same time period.

1. Effect of Ambient Temperature on Peak Power and Peak Voltage

The effect of ambient temperature on peak power and peak voltage output from standalone 3 KW PV system from August 2015 to March 2016. Figs. 3 to 18 shows the variation of peak power and peak voltage for eight months. Where note, that the maximum peak power and peak voltage during January month while the average ambient temperature reaches minimum value, also the minimum peak power and peak voltage during august month while the average ambient temperature reach maximum value. The results also show that with average ambient temperature decrease the peak power and peak voltage increase.

2. Effect of Average ambient temperature on Average Peak Power and Average Peak Voltage

A Fig. 19 and Fig. 20 show the variation of average peak power and average peak voltage respectively, with average ambient temperature during the eight months. This study indicates that with increasing the ambient temperature the average peak power and average peak voltage decrease, especially in August month while the solar radiation in this month is higher than the other month, because the effect of temperature negatively on the efficiency of PV cells.

3. Effect of Average Wind Speed on Average Peak Power and Average Peak Voltage

Fig. 21 and Fig. 22 Shows the change in the average peak power with an average wind speed during the eight months. Where we note that much higher energy is the least in the August month, although the average wind speed is 2.6 m/s, while reaching the highest value in the March month, where the average wind speed of 2.3 m/s by comparing the findings to the influence of wind speed is dramatically impressive compared the effect of temperature

4. Effect of Average Solar Radiation on Average Peak Power and Average Peak Voltage

Fig. 23 illustrates the change in rate of solar radiation with peak power where we notice that the highest rates of solar radiation is within the summer but peak power will be less. Fig. 24 illustrates the change in solar radiation rate with peak voltage so note that solar radiation rates are considerably higher in the summer and higher voltage being less as possible during the summer while up the peak voltage to the highest value in winter though low amount of solar radiation, this happen the influence of ambient temperature.

IV. CONCLUSIONS

During the process of conducting experiments on the solar system in a building (Jabir Ibn Haiyan) show that the ambient temperature affects significantly on the power output of PV system (peak voltages and peak power), whereas the

power output drops in summer season camper with winter season. While the maximum average solar irradiation reaches in summer camper with winter season. From that conclude the efficiency of PV system the go down at higher ambient temperature.

Also, the Iraqi weather very hot and dusty, especially in summer season and this significantly affects the efficiency of PV system, this is what made the use of PV systems is unsuccessful in Iraq.

While The the influence of wind speed on the power output from PV system is law compared the effect of ambient temperature. The results show that at august month average wind speed reach to 2.8 m/s put the peak power and peak voltage output is law comparing with January month average wind speed reach to 1.9 m/s.

V. REFERENCES

- [1] M.C. Alonso Garca, J.L. Balenzategui "Estimation of photovoltaic module yearly temperature and performance based on Nominal Operation Cell Temperature calculations" Renewable Energy, Volume 29, Issue 12, 2004, Pages 1997-2010.
- [2] M.D. Islam, I. Kubo, M. Ohadi, A.A. Alili "Measurement of solar energy radiation in Abu Dhabi, UAE" Applied Energy, Volume 86, Issue 4, 2009, Pages 511-515.
- [3] Yassine Charabi, Adel Gastli "Integration of temperature and dust effects in siting large PV power plant in hot arid area, Renewable Energy, Volume 57, 2013, Pages 635-644.
- [4] C. Schwingshackl, M. Petitta, J.E. Wagner, G. Belluardo, D. Moser, M. Castelli, M. Zebisch, A. Tetzlaff "Wind Effect on PV Module Temperature: Analysis of Different Techniques for an Accurate Estimation" Energy Procedia, Volume 40, 2013, Pages 77-86.
- [5] Erdem Cuce, Pinar Mert Cuce, Tulin Bali "An experimental analysis of illumination intensity and temperature dependency of photovoltaic cell parameters" Applied Energy, Volume 111, 2013, Pages 374-382
- [6] Sanaz Ghazi, Kenneth Ip "The effect of weather conditions on the efficiency of PV panels in the southeast of UK, Renewable Energy" Volume 69, 2014, Pages 50-59.
- [7] Hans Goverde, Dirk Goossens, Jonathan Govaerts, Vikas Dubey, Francky Cathoor, Kris Baert, Jef Poortmans, Johan Driesen "Spatial and temporal analysis of wind effects on PV module temperature and performance" Sustainable Energy Technologies and Assessments, Volume 11, 2015, Pages 36-41.
- [8] Subhash Chander, A. Purohit, Anshu Sharma, Arvind, S.P. Nehra, M.S. Dhaka "A study on photovoltaic parameters of mono-crystalline silicon solar cell with cell temperature" Energy Reports, Volume 1, 2015, Pages 104-109

[9] Yun Da, Yimin Xuan "Effect of temperature on performance of nanostructured silicon thin-film solar cells" Solar Energy, Volume 115, 2015, Pages 109-119.

[10] Haurant Pierrick, Mnzo Christophe, Gaillard Leon, Dupeyrat Patrick "Dynamic numerical model of a high efficiency PVT collector integrated into a domestic hot water system" Solar Energy, Volume 111, 2015, Pages 68-81.

[11] Bjrn Wolff, Jan Khnert, Elke Lorenz, Oliver Kramer, Detlev Heinemann " Comparing support vector regression for PV power forecasting to a physical modeling approach using measurement, numerical weather prediction, and cloud motion data" Solar Energy, Volume 135, 2016, Pages 197-208.

[12] Firoz Khan, Seong-Ho Baek, Jae Hyun Kim " Wide range temperature dependence of analytical photovoltaic cell parameters for silicon solar cells under high illumination conditions" Applied Energy, Volume 183, 2016, Pages 715-724.

[13] Motasem Saidan, Abdul Ghani Albaali, Emil Alasis, John K. Kaldellis " Experimental study on the effect of dust deposition on solar photovoltaic panels in desert environment" Renewable Energy, Volume 92, 2016, Pages 499-505

[14] Umer Mehmood, Fahad A. Al-Sulaiman, B.S. Yilbas " Characterization of dust collected from PV modules in the area of Dhahran, Kingdom of Saudi Arabia, and its impact on protective transparent covers for photovoltaic applications" Solar Energy, Volume 141, 2017, Pages 203-209.

[15] Dhafer Manea Hachim , Assaad Alsahlani, and Adel A. Eidan "Measurements of Wind and Solar Energies in Najaf, Iraq", Advances in Natural and Applied Sciences, Vol. 11, No. 8 (June), 2017



Fig. 2-b Stand Alone 3 KW PV system



Fig. 2-a Stand Alone 3 KW PV system.



Fig. 1. (a) Davis weather station and (b) Vantage Pro2

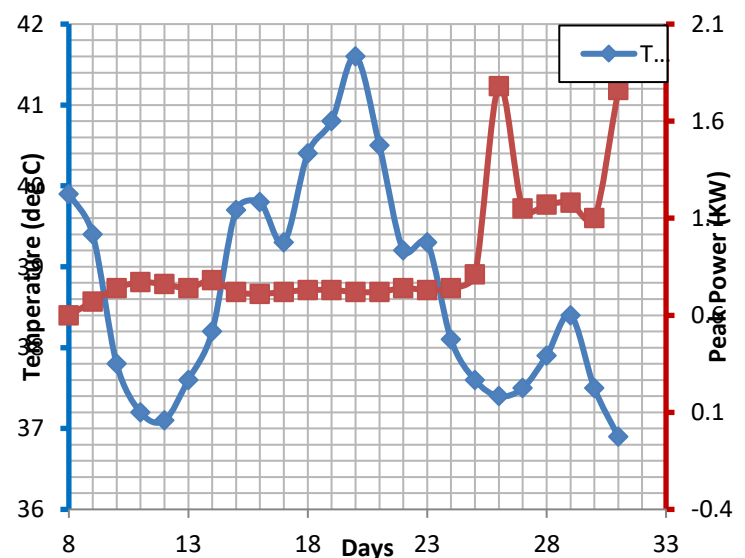


Fig. 3: Variation of the Temperature and Peak power during august month 2015

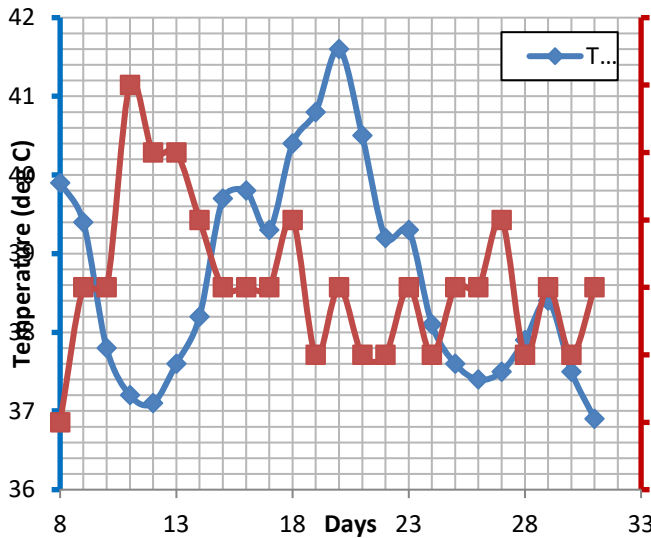


Fig. 4: Variation of the Temperature and Peak voltage during august month 2015

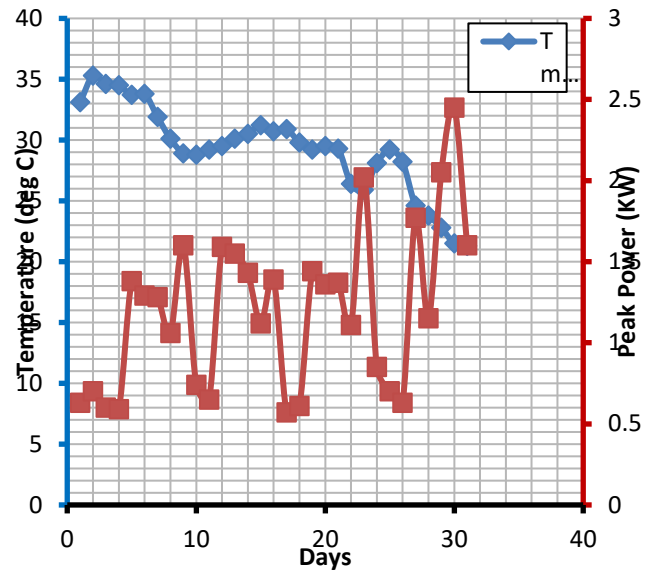


Fig. 7: Variation of the Temperature and Peak power during October month 2015

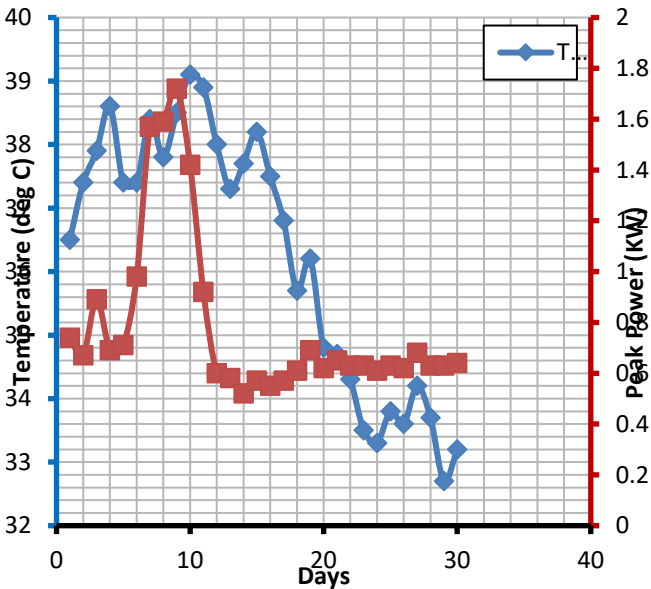


Fig. 5: Variation of the Temperature and Peak power during September month 2015

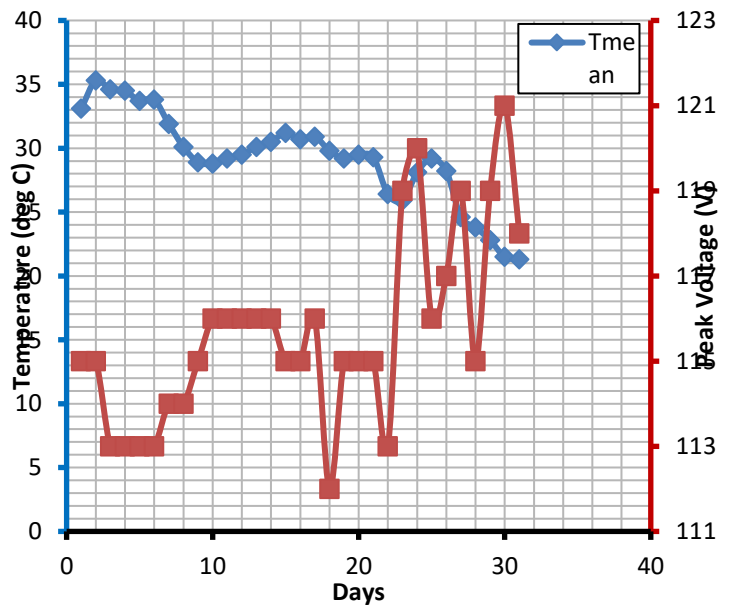


Fig. 8: Variation of the Temperature and Peak voltage during October month 2015

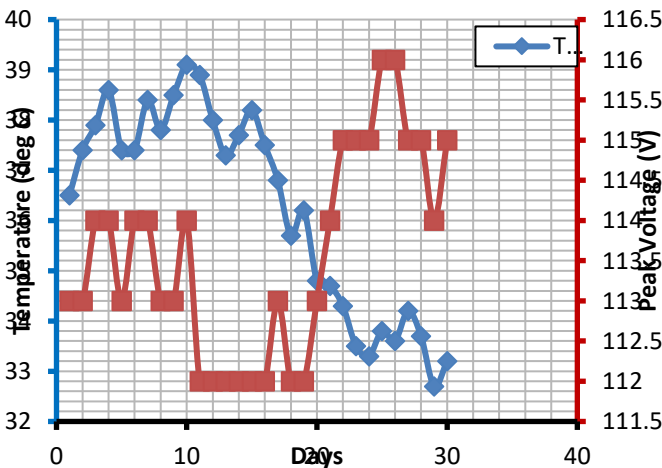


Fig. 6: Variation of the Temperature and Peak voltage during September month 2015

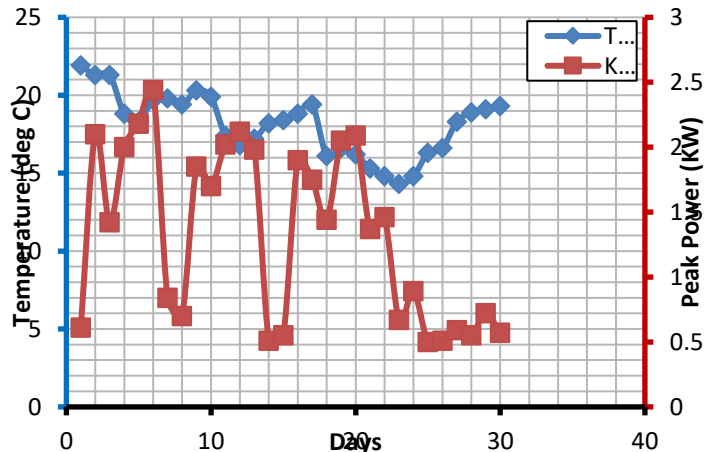


Fig. 9: Variation of the Temperature and Peak power during November month 2015

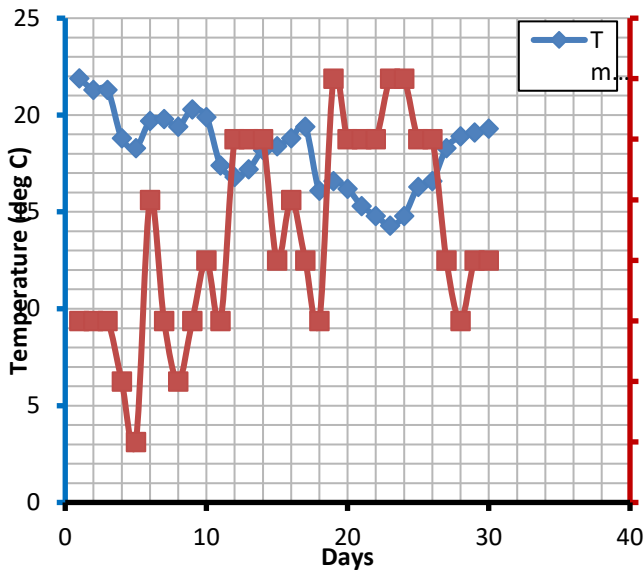


Fig. 10: Variation of the Temperature and Peak voltage during November month 2015

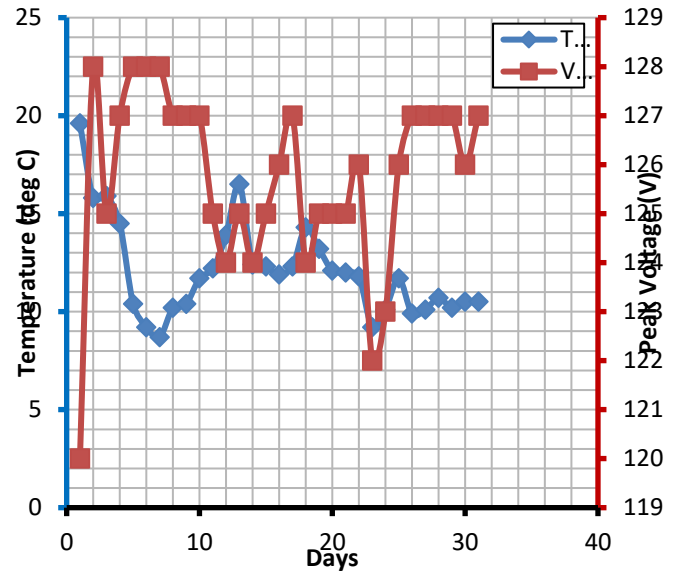


Fig. 12: Variation of the Temperature and Peak voltage during December month 2015

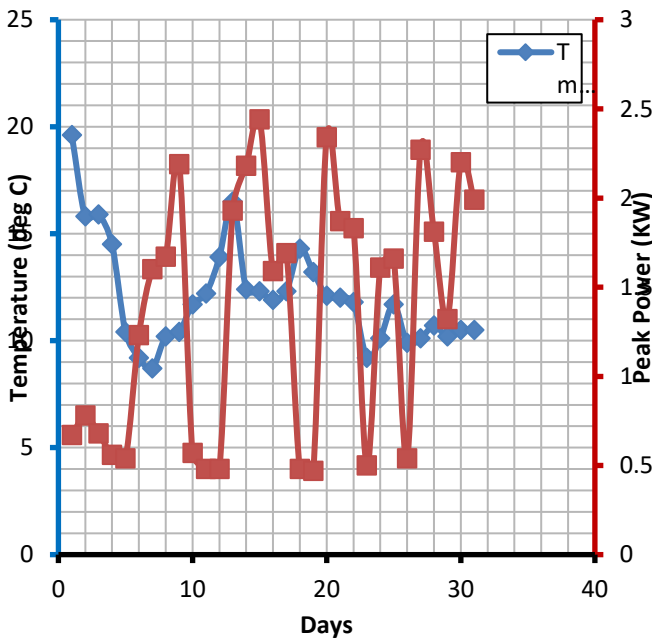


Fig. 11: Variation of the Temperature and Peak power during December month 2015

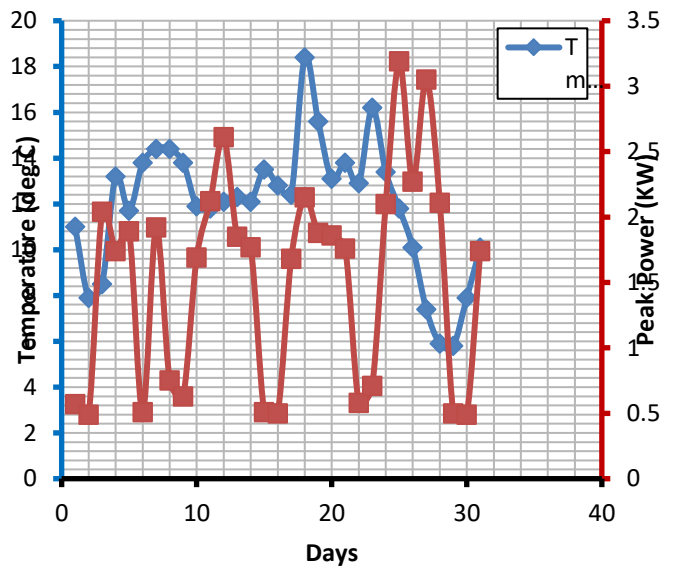


Fig. 13: Variation of the Temperature and Peak power during January month 2016

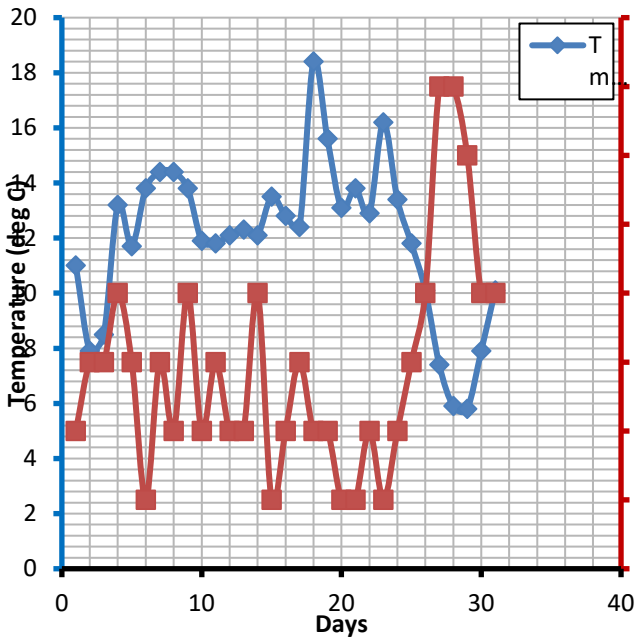


Fig. 14: Variation of the Temperature and Peak voltage during January month 2016

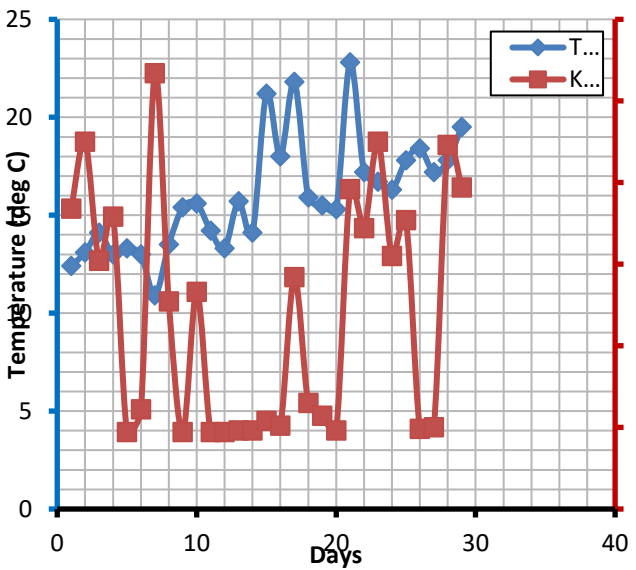


Fig. 15: Variation of the Temperature and Peak power during February month 2016

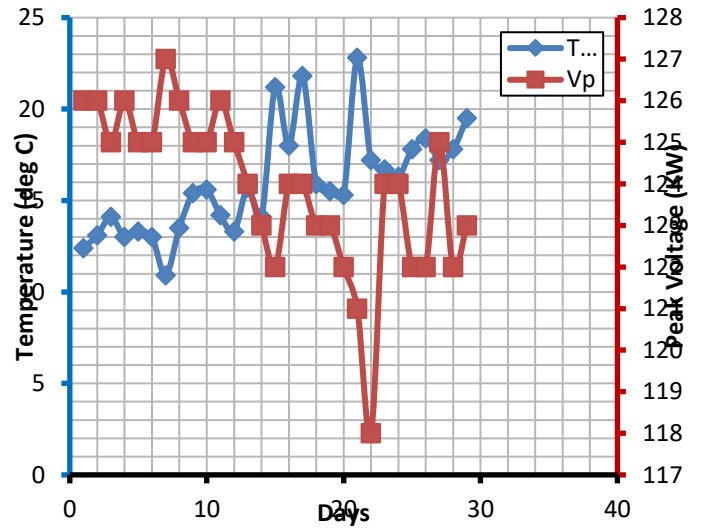


Fig. 16: Variation of the Temperature and Peak voltage during February month 2016

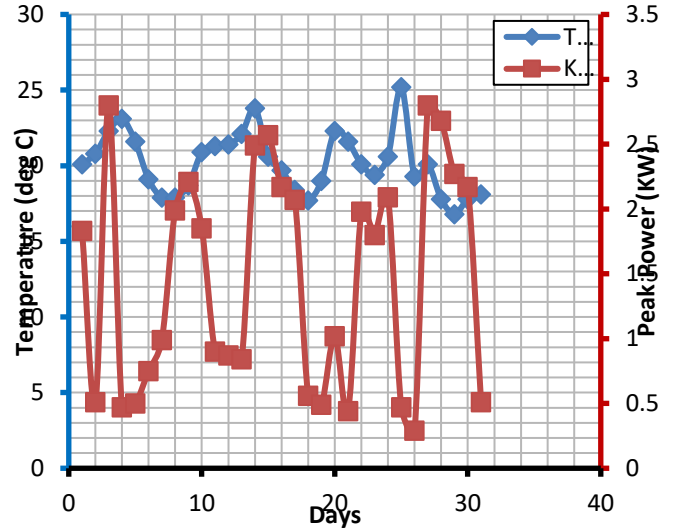


Fig. 17: Variation of the Temperature and Peak power during March month 2016

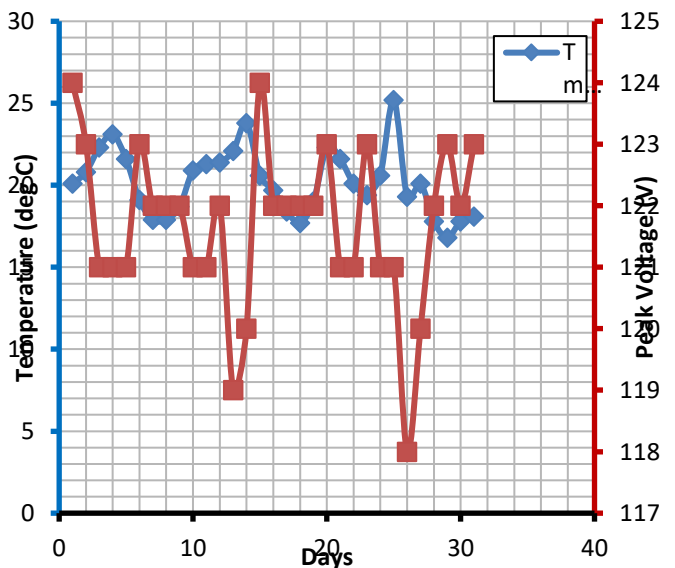


Fig. 18: Variation of the Temperature and Peak voltage during March month 2016

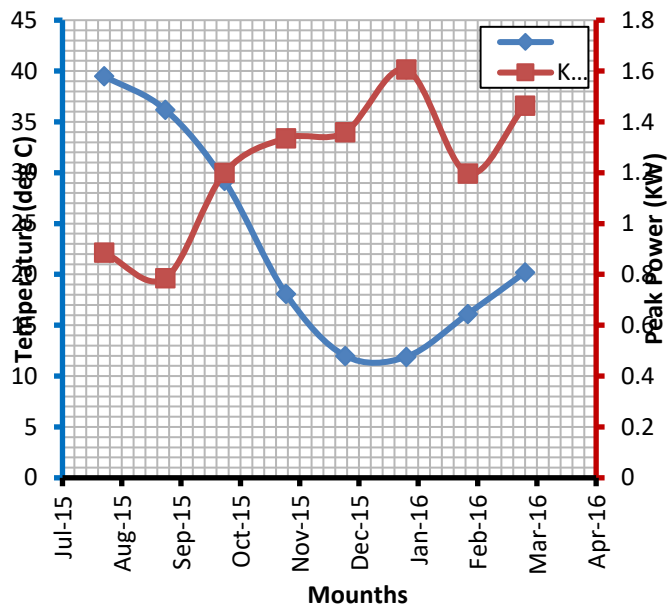


Fig. 19: Variation of the Average Ambient Temperature and Peak Power during Eight Months

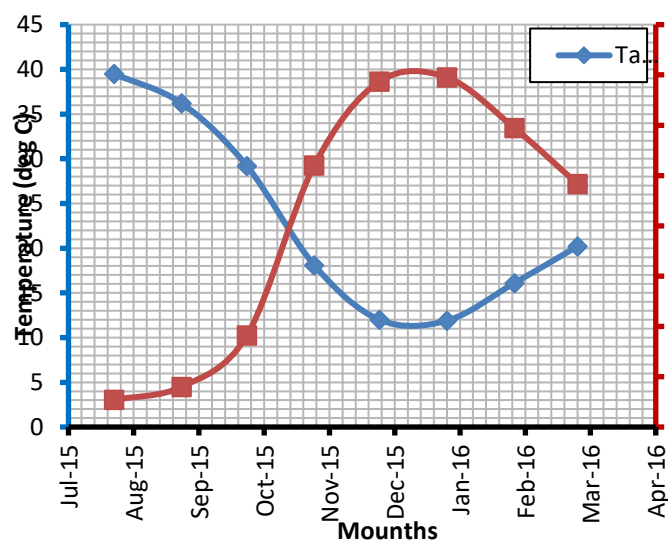


Fig. 20: Variation of the Average Ambient Temperature and Peak voltage during Eight Months

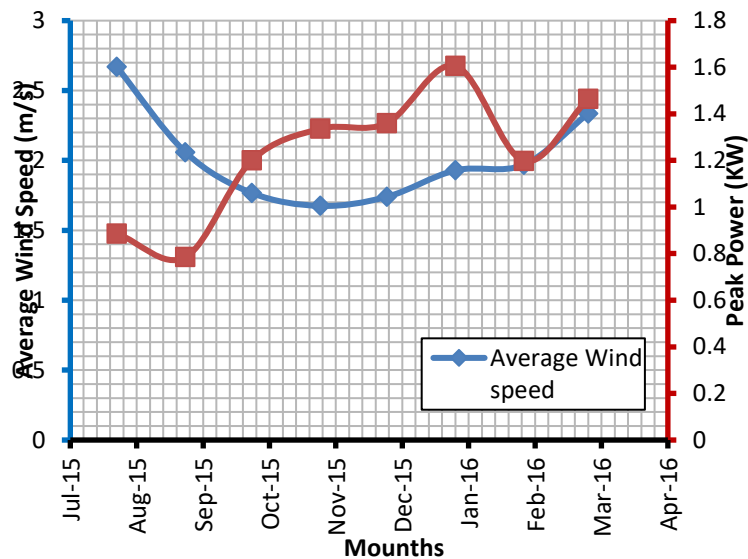


Fig. 21: Variation of the Average Wind Speed and Peak Power during Eight Months

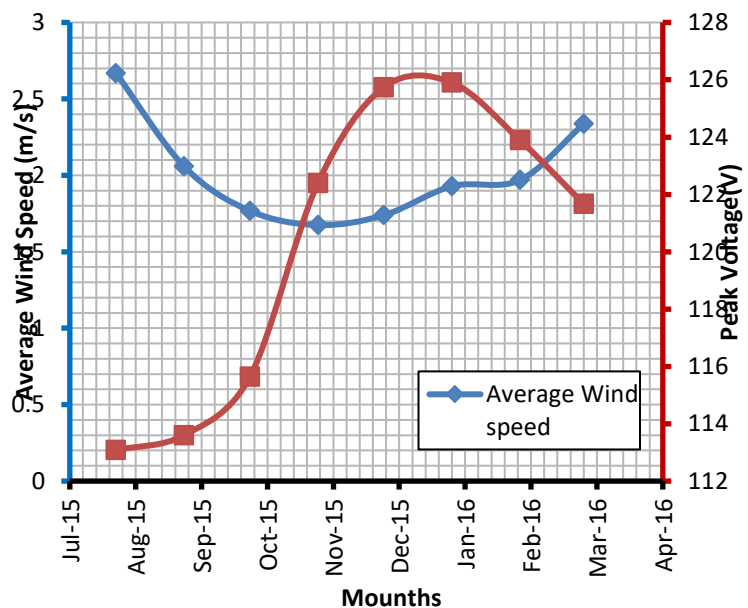


Fig. 22: Variation of the Average Wind Speed and Peak voltage during Eight Months

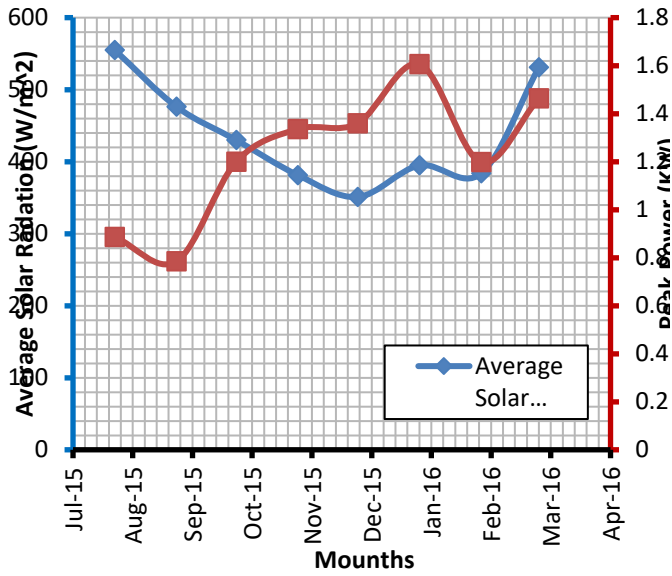


Fig. 23: Variation of the Average Solar Radiation and Peak Power during Eight Months

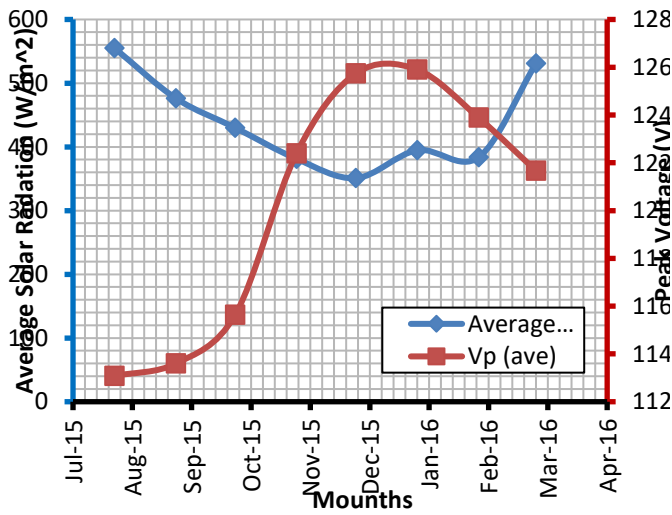


Fig. 24: Variation of the Average Solar Radiation and Peak voltage during Eight Months

Effects of substrate temperature on optical constants of CdS thin films produced by a thermal vacuum evaporation technique for solar cells application

Salah Abdul-Jabbar Jassim
Physics Department, Faculty of
Applied Science, Tamar University
Tamar, Yemen

Email- salahjassim@live.com

A.M. Abdulwahab
Physics Department, Faculty of
Applied Science, Tamar University,
Tamar, Yemen.

Abstract :- CdS thin films were prepared by thermal vacuum evaporation method at vacuum of 10^{-5} torr on glass substrates at different substrate temperatures (20 °C, 100 °C , 200 °C). UV-VIS spectra of the films were studied using the optical transmittance spectra, $T(\lambda)$, and reflectance spectra $R(\lambda)$ measurements which were taken in the spectral region from 250 nm to 2500 nm at room temperature. From the transmission spectra the films thickness and the optical constants such as: refractive index (n), absorption coefficient (α) and extinction coefficient (K), were calculated using Swanepoel's (envelope) method. The optical band gap energy of the films was found to be in the range 2.28 – 2.4 eV. Optical conductivity (σ_{op}) has been determined using transmission and reflectance spectra at different substrate temperature. The dispersion of the refractive index is discussed in terms of the single-oscillator Wemple and DiDomenico model. The substrate temperature plays an important in significant changes of optical constants.

Keywords: Vacuum evaporation CdS thin films; UV-VIS analysis; Swanepoel's (envelope) method.

1- INTRODUCTION

Cadmium sulfide (CdS), is one of the metal chalcogenide semiconductors in group (II–VI) used in solar cells due its wide and direct band gap transition (2.42 eV), high electron affinity, high index of refraction (2.4) and n- type conductivity .It is a very desirable window layer for many photovoltaic solar cells[1,2,3]. The importance of wide band gap materials is related to the possibility of fabricating light emitting diodes or laser heterostructures for emission in the visible spectral range. These devices are important for many applications. For example, they are widely used in medical diagnosis and red-green-blue display [4]. The CdS film can be grown in two crystalline forms, namely, hexagonal and cubic phases accurate knowledge of the refractive indices and absorption coefficients of semiconductors are indispensable for the design and analysis of various optoelectronic devices. Only few reports are available on the optical constant of CdS thin films [5-8].The CdS thin films have been deposited by various methods such as, successive ionic layer adsorption reaction (SILAR) [9], spray Pyrolysis [10] , dc-sputtering[11],chemical bath deposition(CBD) [12],hydrothermal method [13] ,close spaced sublimation[14]and vacuum evaporation [15]. In this paper, the effect of the substrate temperature on optical constants of cadmium sulfide thin films fabricated by vacuum evaporation method at different substrata temperatures was studied. To calculate the optical constant of the deposited film samples, UV-VIS-NIR, and Swanepoel's (envelops) methods are used

2 – Experiment

Cadmium sulfide thin films were prepared by thermal vacuum evaporation method at vacuum of 10^{-5} torr on glass substrate. The films were grown at substrate temperature of 20 °C , 100 °C and 200 °C and the details were described elsewhere (16). The structural properties have been examined by the X-ray diffraction method (XRD) (Diano PW 1370), $\text{CuK}\alpha$ radiation, $\lambda = 0.1793$ nm) The structure of the films is polycrystalline in nature with hexagonal structure. The structures and the morphology of the films were described in the earlier report [16]. The optical properties were measured by the (UV-VIS-NIR) double beam spectrophotometer (JASCO-V570 model) in the wavelength range of 250 to 2500 nm at room temperature .Films thickness were measurement by using Swanepoel's (envelops)methods

3 –Results and discussion

3.1. UV–VIS analysis

The spectral distribution of transmittance $T(\lambda)$ and reflectance $R(\lambda)$ in the wavelength range (250-2500) nm were measured at room temperature for CdS thin films deposited at different substrate temperature (20 °C, 100 °C and 200 °C). Figs. 1 and 2 show $T(\lambda)$ and $R(\lambda)$ values for CdS thin films it is shown that there are many interference fringes. The interference fringes indicate that all the CdS films had optically smooth surfaces. It provides us to apply Swanepoel's (envelops) method for the calculation of optical constant parameter such as, refractive index (n), absorption coefficient (α) and extinction coefficient (K)). The transparent region of the spectrum is useful because the interference of light give periodic variations including peak maximum points T_{max} and peak minimum points T_{min} as shown in Fig. 3. The values of T_{max} and T_{min} for all films are listed in table 1.

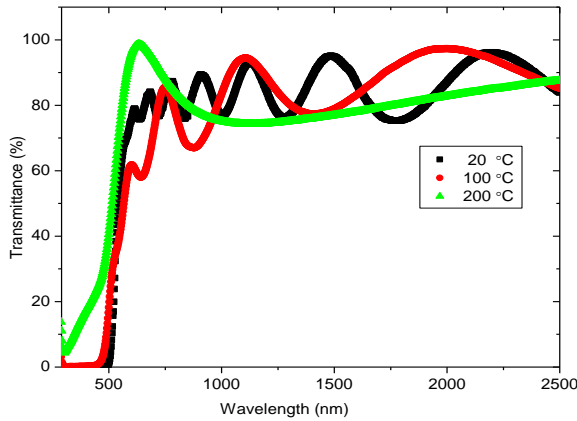


Fig. 1. Transmission spectra of CdS thin films deposited at different substrate temperatures.

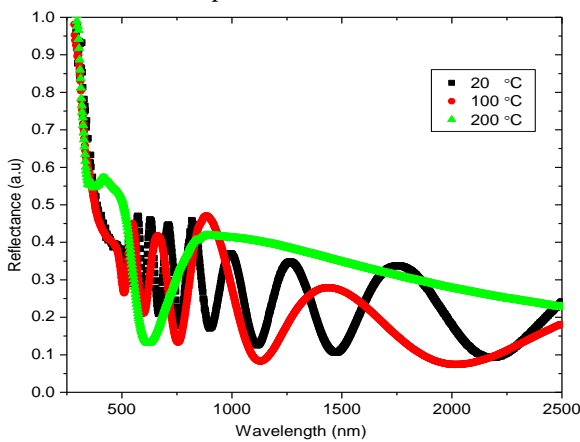


Fig. 2. Reflectance spectra of CdS thin films deposited at different substrate temperatures

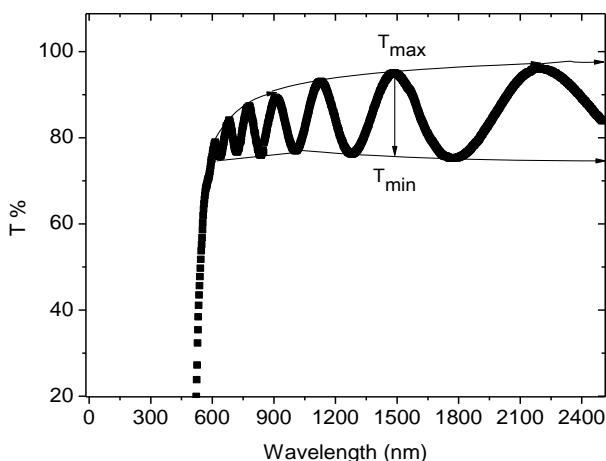


Fig. 3. Transmission spectrum of CdS thin film deposited at 20°C and envelopes for calculations of T_{max} and T_{min}

Table 1 Values of λ, T_{max}, T_{min}, A and B (Cauchy parameters) of CdS thin films deposited at different substrate temperatures, and the calculated values of refractive index obtained from the envelope method

The thickness (t) of the films can be calculated using Transmission spectrum from two maxima T_{max} or minima T_{min} using the following equation[1]

| Sup.T | λ (nm) | T _{max} | T _{min} | n | A | B |
|--------|--------|------------------|------------------|--------|-------|---------|
| 20 °C | 912 | 0.8926 | .7654 | 1.9417 | 2.172 | -188577 |
| | 1007 | 0.9139 | .7665 | 1.9853 | | |
| | 1124 | 0.9334 | .7654 | 2.0283 | | |
| | 1278 | 0.9425 | .7608 | 2.059 | | |
| | 1487 | 0.955 | .7554 | 2.0973 | | |
| | 1776 | 0.9585 | .7505 | 2.1173 | | |
| | 2201 | 0.962 | .7517 | 2.1199 | | |
| 100 °C | 743 | 0.8584 | .6219 | 2.3449 | 1.922 | 238513 |
| | 874 | 0.8934 | .6644 | 2.264 | | |
| | 1096 | .9473 | .7125 | 2.13 | | |
| | 1422 | 0.9618 | 0.777 | 2.0488 | | |
| | 2011 | 0.9744 | 0.81 | 1.989 | | |
| 200 °C | 633 | 0.994 | 0.61 | 2.59 | 1.979 | 261524 |
| | 822 | 0.968 | 0.653 | 2.429 | | |
| | 1146 | 0.986 | 0.717 | 2.199 | | |
| | 2000 | 0.982 | .816 | 2.03 | | |

$$t = \frac{\lambda_1 \lambda_2}{2(\lambda_1 n_2 - \lambda_2 n_1)} \quad (1)$$

Where (n₁) and (n₂) are refractive indices at two adjacent maxima (or minima) at (λ₁) and (λ₂) wavelengths respectively. Fig. 4 shows the variation of the films thickness versus substrate temperature .It is noted from this figure that the thicknesses decrease with the increases in substrate temperature. The thickness of the film decreases because the substrate is warmer and energetically atoms prefer to stick to cold surfaces more than warm surfaces

3-3 Reflective index

The index of refraction (n) in weak and medium absorption regions at different wavelengths was calculated using Swanepoel s envelope method from T_{max} and T_{min} in the transmission spectra. The real part of refractive index (n) is estimated using relation [18]

3-2 Thickness Measurement

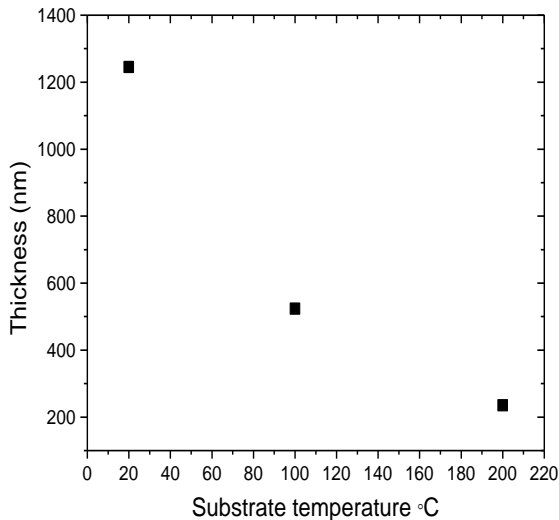


Fig.4. Variation of the films thickness with substrate temperature for CdS thin films

$$n = [N + (N^2 - n_s^2)^{1/2}]^{1/2} \quad (2)$$

Where

$$N = \frac{2n_s(T_{max} - T_{min})}{T_{max}T_{min}} + \frac{n_s^2 + 1}{2}$$

Where (n_s) is the refractive index of glass substrate (1.50), T_{max} , T_{min} are maximum and minimum transmittance at the same wavelength in the envelope curves, respectively. To determine the refractive index in the strong absorption region (Eq. (2) is no longer veiled) where the transmittance is strongly reduced by absorption, the values of (n) can be fitted by means of the two-term Cauchy dispersion relation[19]

$$n(\lambda) = A + \frac{B}{\lambda^2} \quad (3)$$

where A and B are the fitting parameters constants which are obtained from fitting the transmission spectra and their values are listed in table 1. Fig. 5 shows the experimental data of refractive index (the circular) and the Cauchy function values (the solid line). It is clear that it gives good fitting in all regions for the three samples. The refractive index values increase with increasing the substrate temperature. The increase in refractive index with increasing substrate temperature may be attributed to increasing in crystallites size. The refraction index (n) of the film deposited at 20°C increases rapidly with increase of the wavelength up to a point of critical wavelength (λ_c) and above this value it is varied slowly showing the anomalous dispersion. The initial sharp increases of (n) with (λ) indicated a rapid change in the absorption of the film below (λ_c). While the films deposited at substrate temperature (100°C and 200°C) the refraction index of the films decrease rapidly with increase of the wavelength showing the normal dispersion. The variation of the refractive index up to wavelength (λ_c) and above this value it is varied slowly. The initial sharp decrease of (n) with (λ) indicated a rapid change in the absorption of the films.

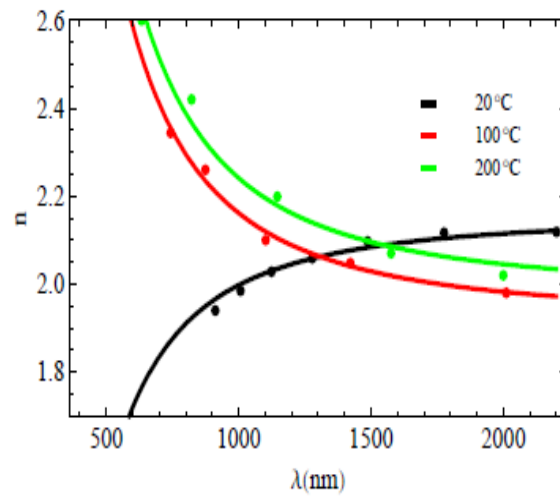


Fig (5) Refractive index of CdS thin films deposited at different substrate temperature

The dispersion data of the refractive index have been analyzed using the concept single oscillator expressed by the Wemple - DiDomenico model. The model suggests that the refractive index (n) of the films could be correlated to the oscillator energy, E_o and the dispersion energy (E_d), which is a measure of the intensity of inter-band optical transitions. it is calculated by using following formula [20].

$$(n^2 - 1) = \frac{E_d E_o}{E_o^2 - (h\nu)^2} \quad (4)$$

where ($h\nu$) is the incident photon energy .Fig. 6 shows the relation between $(n^2 - 1)^{-1}$ and $(h\nu)^2$ for prepared CdS thin films. The values of E_o and E_d are directly determined from the slope of the linear portion of the curves and it is intercept with the vertical axis. The values of (E_o) and (E_d) are listed in table 2 .It is found that the values of E_o are related empirically to the direct band gap by $E_o \approx 1.5 E_g$

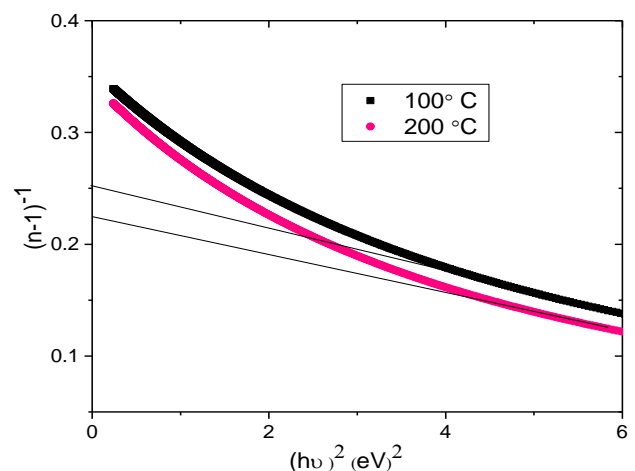


Fig. 6. Variation of $(n-1)^{-1}$ vs. photon energy $(h\nu)^2$ for CdS thin films at different substrate Temperatures.



n transparent region, the obtained data of reflective index can be analyzed to obtain the high frequency lattice dielectric constant, ϵ_L , via a procedure that describes the contribution of the carriers and the lattice vibration modes of the dispersion. The relation between the real dielectric constant, ϵ_L , and wavelength [21]:

$$n^2 = \epsilon_L - \frac{e^2 \lambda^2 N}{4 \pi^2 c^2 \epsilon_0 m^*} \quad (5)$$

Where e is the elementary charge, ϵ_0 is the permittivity of free space ($8.854 \times 10^{-12} \text{ C}^2/\text{N.m}^2$) and N/m^* is the ratio of free carrier concentration to the effective mass. Fig. 7 shows the relation between n^2 and λ^2 for CdS thin films deposited at different substrate temperature. The extrapolating of the linear parts of these curves to zero wavelength gives the values of ϵ_L and from the slopes the ratios N/m^* are obtained. The estimated values of ϵ_L and N/m^* for the CdS films are shown in Table 2.

The variation of refractive index with wavelength can be expressed by the following relation [22]

$$n^2 - 1 = \frac{S_0 \lambda_0^2}{1 - (\frac{\lambda_0}{\lambda})^2} \quad (6)$$

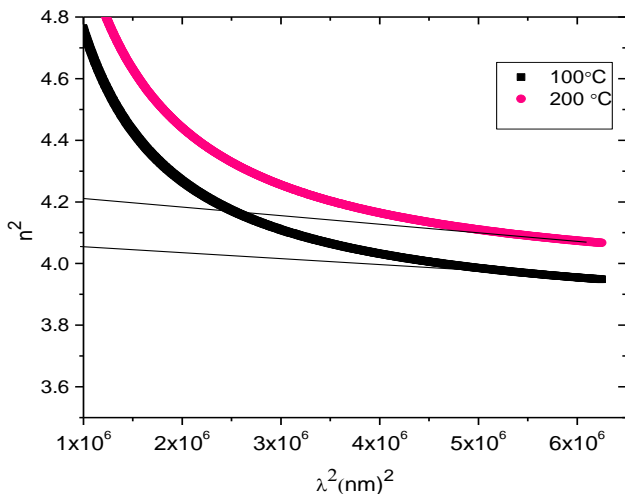


Fig.7. The relation between (n^2) and (λ^2) for CdS thin films deposited at different substrate temperatures

where λ is the wavelength of incident light. S_0 is the average oscillator strength given by

$$S_0 = (n_\infty^2 - 1)/\lambda_0^2 \quad (7)$$

And λ_0 is an average oscillator wavelength. Eq. (7) also can be converted as,

$$\frac{n_\infty^2 - 1}{n^2 - 1} = 1 - \left(\frac{\lambda_0}{\lambda}\right)^2 \quad (8)$$

where n_∞ is refractive index at infinite wavelength. The parameters S_0 and λ_0 were obtained from the slopes ($1/S_0$) and intercepts ($S_0 \lambda_0^2$)⁻¹ of the plotted curves ($n^2 - 1$) vs. λ^{-2}

as shown in figure 8 and the refractive index at infinite wavelength (n_∞) can be obtained from the relation [7].The

| Sub .temp. | E_d (eV) | E_0 (eV) | S_0 (nm) ⁻² | λ_0 (nm) | n_∞^2 | N/m^* (kg ⁻¹ .m ⁻³) |
|------------|------------|------------|--------------------------|------------------|--------------|--|
| 100°C | 15 | 3 | 3.2×10^{-5} | 361 | 2.27 | 4×10^{57} |
| 200°C | 13 | 2.87 | 3.8×10^{-5} | 356 | 2.4 | 5.3×10^{57} |

values of these parameters are given in Table 2.

Table 2 optical parameters for CdS films at different substrate temp.

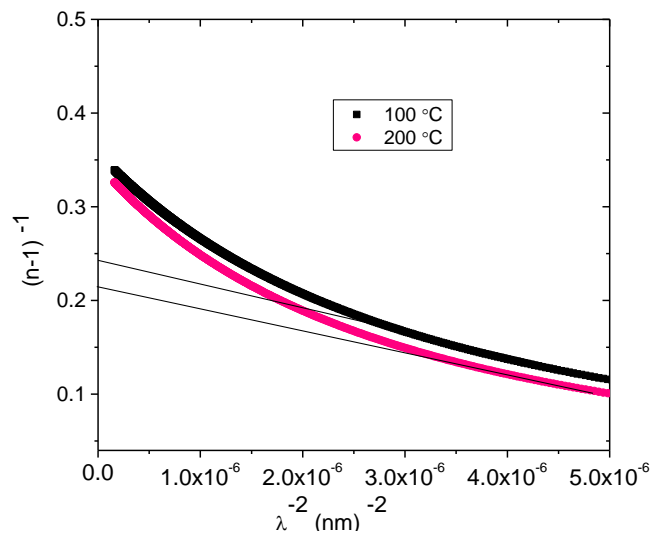


Fig. 8. The variation of ($n-1$)⁻¹ vs. λ^{-2} for CdS thin films at different substrate temperature.

3-4 Asorption and extinction coefficient

The absorption coefficient in weak and medium absorption regions is calculated by the following equation [17]:

$$\alpha = \frac{1}{d} \text{Ln} \left[\frac{E_m - [E_m^2 - (n^2 - 1)^3 (n^2 - s^2)]^{1/2}}{(n-1)^3 (n-s^2)} \right] \quad (9)$$

Where

$$E_m = \frac{8n^2 s}{T_{\text{Max}}} + (n^2 - 1)(n^2 - s^2)$$

The extinction coefficient indicates is the amount of absorption loss when electromagnetic wave propagates through a material .Extinction coefficient (k) can be evaluated as follows [23]

$$k = \alpha \lambda / 2\pi \quad (10)$$

Fig. 9 illustrates the dependence of k on the wavelength for CdS thin films deposited at different substrate temperatures, It is seen that the values of extinction coefficient decreases with increasing wavelength for samples deposited at 100 °C and 200 °C, due to light scattering and decrease of

absorbance, while increasing for film deposited at 20°C due to increase in absorbance.

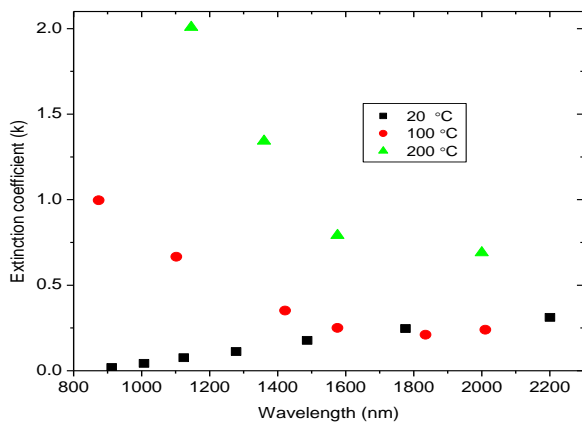


Fig. 9. Extinction coefficient versus λ for CdS thin films at different substrate temperature

3-5 Optical band gap and Urbach energy

The optical absorption coefficient (α) in the strong absorption region was computed from the experimentally measured values of transmittance $T(\lambda)$ and reflectance $R(\lambda)$ according to the following relation [24]:

$$\alpha = \left(\frac{1}{t}\right) \ln \frac{(1-R)^2}{T} \quad (11)$$

The optical energy band gap (E_g) of the semiconductor materials is related to the absorption coefficient (α) in the strong absorption region by the relation [25]

$$\alpha(h\nu) = C(h\nu - E_g)^m \quad (12)$$

Where C is an energy-independent constant, $h\nu$ the incident photon energy and m is a number which characterizes the optical transition process in the semiconductor materials. It takes the values $1/2$, $3/2$, 2 and 3 for direct allowed, direct forbidden, indirect allowed and indirect forbidden transitions, respectively., the plot of $(\alpha h\nu)^2$ versus $h\nu$ in the high absorption region for CdS thin films, shown in Fig. 10 The linear part in this figure indicates the presence of direct transition. The extrapolation of the linear portion of the plot on the energy axis determines. The energy gap of the film. the energy band gap values measured for CdS films were varied between 2.4 and 2.28 eV, These results are in a good agreement with the previous works (26,27,28). The dependence of band-gap on the substrate temperature is shown in Fig. 11 it is seen that the band –gap values decreases with increasing substrate temperature. The absorption coefficient near the fundamental absorption edge is exponentially dependent on the incident photon energy

and obeys the empirical Urbach tail relation, which can be expressed as follows (29):

$$\alpha = \alpha_0 \exp\left(\frac{h\nu}{E_u}\right) \quad (13)$$

Where (α_0) is a constant which is known as band tailing parameter, E_u is Urbach energy which indicates the band tails of the localized states in the gap region and ($h\nu$) is the energy of the incident photon, Usually , E_u depend on temperature and describes the width of the localized states and could be function of the structural disorder [30] . From the curves $\ln\alpha$ vs. $h\nu$ as shown in Fig.12, the Urbach energy is calculated taking the reciprocals of the slopes of linear portion of these curves. Fig. 11 shown relation of the optical gap and Urbach energy with the variation of substrate temperature. From this figure it is observed that E_g values decreases and increase in the Urbach energy valus with increases the substrate temperature. The increase of E_u with increases substrate temperature could be due to an increase of defects in the tail states and/or the production of the surface dangling bonds around the crystallites during the process of crystallization

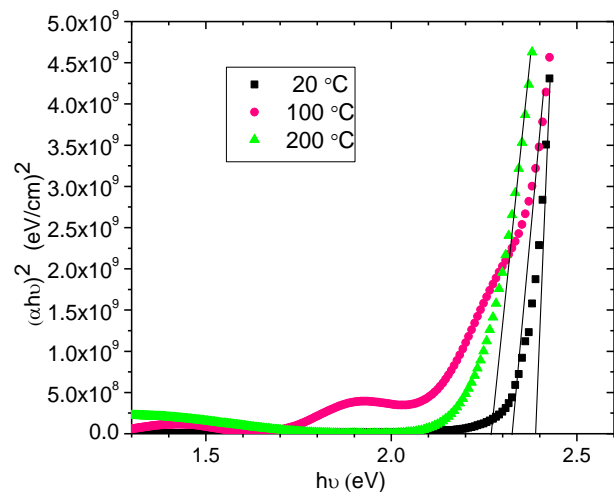


Fig. 10. Plot of $(\alpha h\nu)^2$ vs $h\nu$ for CdS thin films to estimate optical band gap

3.6. Optical conductivity

The optical conductivity is one of the important tools for studying the electronic states in materials. The optical conductivity (σ_{op}) is calculated from the equation [31]:

$$\sigma_{op} = \frac{\alpha n c}{4\pi} \quad (13)$$

where c is the velocity of light. The behaviors of optical conductivity of CdS thin films with photon energy for different substrate temperatures are shown in Fig. 13. These spectra show that the optical conductivity increases with increasing substrate temperature. The optical conductivity directly depends on the absorption coefficient and is found

to increase sharply for higher energy values due to large absorption coefficient for these values.

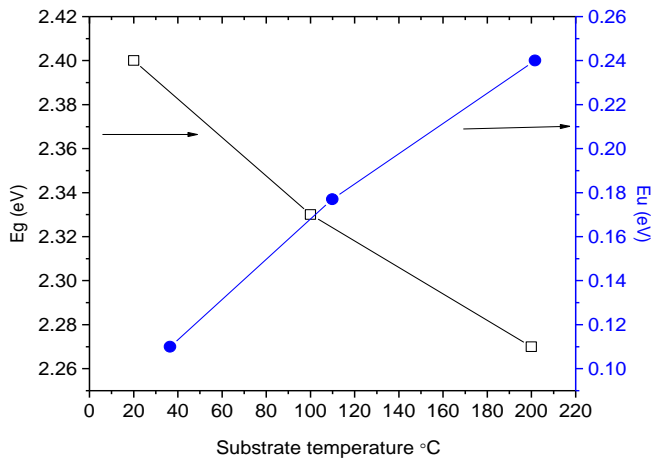


Fig. 11. Variation of the optical gap and Urbach energy as a function of the substrate temperature

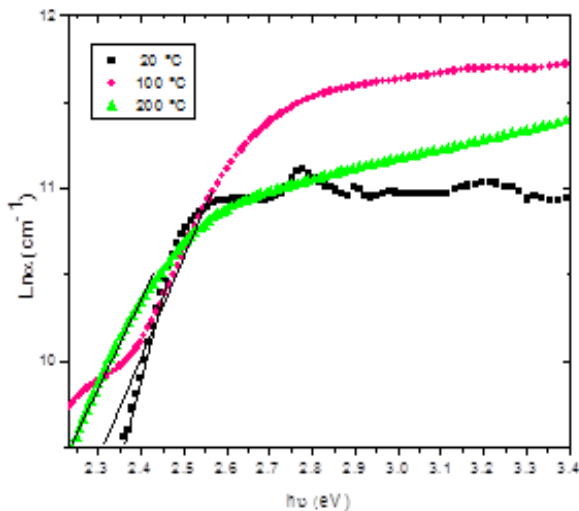


Fig. 12. The variation of $\ln \alpha$ vs. photon energy for CdS thin films at different substrate temperature

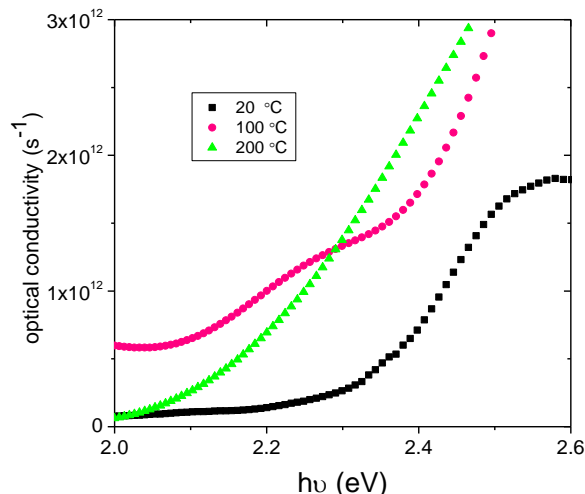


Fig. 13. Optical conductivity vs. photon energy for CdS thin films at different substrate temperature

4- Conclusion

CdS thin films were prepared by the thermal evaporation technique on glass substrates at different substrate temperature. The films were characterized by investigating their transmittance and reflectance curves. By using the envelope method proposed by Swanepoel we have calculated the thickness of the films and the optical constants such as index of refraction, extinction coefficient, and optical conductivity. The thickness of CdS films is found to be in the range (1256-233 nm) which was found to be decreasing with increasing the substrate temperature. The refractive index of the films deposited at 100 °C and 200 °C showed a normal dispersion while the film deposited at 20 °C showed anomalous dispersion. The optical band gap of the films decreases while Urbach energy E_u increases with increasing substrate temperature. The single oscillator parameter values were obtained from Wemple–Didomenico model. It is found that the optical constants increased with increasing substrate temperature.

5- References

- [1] A. Romeo, D.L. Bätzner, H. Zogg, C. Vignali, A.N. Tiwari, *Solar Energy Materials & Solar Cells* 67 (2001) 311-321.
- [2] N. Romeo, A. Bosio, D. Menossi, C. Catellani, R. Dharmadasa, A. Romeo, *High efficiency Cu(In,Ga)Se₂/CdS thin film solar cells obtained with precursors sputtered from InSe, GaSe and Cu targets*, *Thin Solid Films* 535 (2013) 88-91.
- [3] R. Mendoza-Perez, J.Sastre-Hernandez, G.Contreras-Puente, O.Vigil-Galan, *Solar Energy Materials & Solar Cells* 93 (2009) 79-84.
- [4] P.P. Hankare, P.A. Chate, D.J. Sathe, *Solid State Sciences* 11 (2009) 1226-1228
- [5] K. Senthil, D.Mangalaraj, Sa. K. Narayandass, Sadao Adachi, *Materials Science and Engineering B* 78 (2000) 53-58.
- [6] F. Yakuphanoglu, C. Viswanathan, P. peranantham, D. Soundarrajan, *J. Optoelectronics and Advanced Materials*, Vol. 11, No. 7 (2009) 945 – 949.
- [7] S. Mathew, P. S. Mukerjee, K. V. Vijayakumar, *Thin Solid Films* 254 (1995) 278-284.
- [8] A. Abdolazadeh Ziabari, F.E. Ghodsi, *Solar Energy Materials & Solar Cells* 105 (2012) 249-262.

- [9] V. Senthamilselvi, K.Ravichandran, K.Saravanakumar, Influence of immersion cycles on the stoichiometry of CdS films deposited by SILAR technique, *Journal of Physics and Chemistry of Solids* 74 (2013) 65-69.
- [10] S. J.Ikhamyies, Hassan K.Juwhari, Riyad N.Ahmad-Bitar , NanocrystallineCdS:Inthin films preparedbythe spray-pyrolisistechique , *journal of Luminescence* 41(2013) 27-32.
- [11] P. K. Ghosh, U.N. Maiti, K.K. Chattopadhyay, *materias Letters* 60 (2006) 2881-2885.
- [12] J. K. Dongre, Vikas Nogriya, M. Ramrakhiani, *Applied Surface Science* 255 (2009) 6115–612.
- [13] A.M. Abdulkarem, E.M. Elssfah, Nan-Nan Yan, G. Demissie, Ying Yu, *Journal of Physics and Chemistry of Solids* 74 (2013) 647-652.
- [14] S. Butt, N, Abbas Shah, A. Nazir, Z.r Ali, A. Maqsood, *Journal of Alloys and Compounds* 587 (2014) 582–587.
- [15] M. Tomakin , M. Altunbaş, E. Bacaksiz, Ş. Çelik , *Thin Solid Films* 520 (2012) 2532–2536.
- [16] S.A. Jassim, A.A.R.A. Zumaila, G.A.A.A. Waly, *Results in Physics* 3 (2013) 173 – 178.
- [17] R. Swanepoel, *Journal of Physics E* 16 (1983) 1214-1222.
- [18] R. Swanepoel, *J. Phys. E: Sci. Instrum.* 17 (1984) 896-903.
- [19] F. Hajakbari, M.M. Larijani, M. Ghoranneviss, M. Aslaninejad, A. Hojabri, *Jpn. J.Appl. Phys.* 49 (2010) 95802-95807.
- [20] S.H. Wemple, *Phys. Rev. B* 7 (1973) 3767-3777
- [21] S, k. Ahmmada, M.A. Samee, A. Edukondalu, S. Rahman, *Results in Physics* 2 (2012) 175–181.
- [22] F. Yakuphanoglu, Synthesis and electro-optic properties of nanosized-borondoped cadmium oxide thin films for solar cell applications, *Solar Energy* 85 (2011) 2704 -2709.
- [23] N.Koteeswara Reddy,K.T.Ramakrishna Reddy, *Materials Research Bulletin* 41(2006) 414-422.
- [24] M. Caglar, S. Ilican, Y. Caglar, *Thin Solid Films* 517 (2009) 5023 -5028.
- [25] Tauc, T., Abeies, F., 1970. *Optical Properties of solids.* IOP Publishing Ltd, North Holland, Amsterdam, p. 903.
- [26] H. Moualkia, S. Hariech, M.S. Aida, *Thin Solid Films* 518 (2009) 1259 -1262.
- [27] S. Prabahar, M. Dhanam, *Journal of Crystal Growth* 285 (2005) 41 – 48.
- [28] M. Tomakin, M.Altunbas, E.Bacaksız, I. Polat, *Materials Science in Semiconductor Processing* 14 (2011) 120 -127.
- [29] J. Tauc, *Amorphous and liquid semiconductors*, in: J. Tauc (Ed.), Plenum, New York, 1974, p. 159.
- [30] J. Olley, *Solid State Commun.* 13 (1973) 1437-1440.
- [31] S. H. Chaki, M.P. Deshpande, Jiten P. Tailor, *Thin Solid Films* 550 (2014) 291-297.

Synthesis and enhancement efficiency of organic solar cell device

Abdullah A. Hussein

*Department of Material Science
Polymer Research Centre
University of Basrah
amanar_2005@yahoo.com*

Rajaa M. Abdullah

*Department of Material Science
Polymer Research Centre
University of Basrah*

Abdullwahab A. Sultan

*Southern Technical College
Basrah, Iraq*

Abstract- The first part in this work, a thin film of Poly(3-hexylthiophene) (P3HT) has been synthesis from chloroform solvent and deposited by spin coating method on glass substrates. The second part, we have investigated thin film blend produced from P3HT and 6,6-phenyl-C61 butyric acid methylester (PCBM) bulk heterojunction (BHJ) with 1:1 weight ratio materials. This photoactive layer is sandwiched between an anode composed of ITO/poly(3,4 ethylenedioxythiophene):poly(styrenesulfonate)(PEDOT:PSS) silver nanoparticles (AgNPs)/Al as the cathode layer. We find that, absorption spectrum of the blend becomes broad with ratio varying, which is highly desirable for an organic solar cell devices. Film morphology is evaluated by atomic force microscopy (AFM). XRD patterns Measurement is also performed for the device. With a PEDOT:PSS: AgNPs film, the solar cells give Power Conversion Efficiency (PCE) of 2.06%.

Keywords: Poly(3-hexylthiophene), [6,6]-phenyl-C61 butyric acid methylester, Power Conversion Efficiency.

I. INTRODUCTION

In the context of technological applications, among many conjugated polymers, poly(3-alkylthiophenes) P3HT have been found to be a special class of polymers with good solubility, processability and environmental stability. Generally this class of materials exhibits an optical band gap $\sim (1.7-2.1)$ eV [1, 2]. P3HT is the most widely used conjugated polymer for organic material optical and electronics applications due to of their high solubility in organic solvents, high mobility, high crystallinity, acts as the light absorbing, hole transporting material excellent thermal stability, and high electrical conductivity. Considerable effort has been made to improve the intrinsic characteristics of P3HT (p-type, as the donor material) to enable their use in organic solar cells, organic field-effect transistors, acts as the light absorbing and hole transporting material [2, 3].

Photovoltage (PV) solar cells have attracted considerable interest over the last three decades due to their unique advantages which include low processing cost alternative to the traditional inorganic based solar cells, versatility of chemical structure, mechanical flexibility substrates, potential for large scale and offer easily manufactured [1,2]. Recently high PCE of about 8% has been reported for devices based on BHJ solar cells of donor-acceptor materials [3-5]. Significant work was focused on the use of polymeric systems comprising poly (3-hexylthiophene) (p-type) and [6,6]-phenyl C61- butyric acid methylester (n-type) (P3HT:PCBM) blends for the fabrication of BHJ solar cells [6-9].

To significantly enhance the photovoltaic efficiency is still one of the most important tasks for the polymer photovoltaic cells. The light to electricity conversion process involves the light absorption and exciton formation, exciton dissociation, charge transport, and charge collection. These four steps are affected by the chemical structure of active materials, that is, the donor and the acceptor, and the morphology of the active polymer film [8-12]. P3HT and PCBM become popular polymer donor and organic acceptor for polymer photovoltaic cells due to their easy availability, excellent solubility in common organic solvents, and high mobility. Great progress has recently been made on P3HT:PCBM BHJ photovoltaic cells.

Although many reports on the metallic NPs enhanced PSCs the exact understanding on the photovoltaic performance changes remains inconclusive. On one hand, several studies have shown that the absorption of photoactive conjugated polymer in the active layer can be enhanced due to the plasmonic scattering or near-

field enhancement caused by localized surface plasmon resonant (LSPR) effect of the metallic NPs (mainly enhance the optical property) [13,14]. The modern reports indicated that the strong near field around NPs due to LSPR effect mainly distributes laterally along the intermediate layer, leading to minimal enhancement of light absorption in the active layer. Thus they contributed to the improvement of PCE to the enlarged interfacial area between active layer and PEDOT: PSS intermediate layer as well as the improved PEDOT: PSS conductivity (mainly improve the electrical property) [15]. Organic solar cells are very important and promising because of their high absorption coefficient, their compatibility with low manufacturing cost and their flexible substrates. Some disadvantages such as their short lifetime due to instability in contact with oxygen molecules or humidity [16,17] and their poor efficiency need to be improved. Our work aims to improve efficiency by increasing the absorption inside an organic material. We do so by incorporating metallic NPs inside the absorbing layer, thus generating surface plasmon (SP). These SP produce evanescent waves by a strong coupling between an incident electromagnetic wave and the electrons of the conduction band of a metal occurring when the frequency of an incident wave is equal to the frequency of the plasmon resonance.

This effect leads to a strong increase in the electromagnetic field around metallic particles, which makes it possible to improve absorption in the surrounding medium. It is known that the resonance frequency varies according to the form and the diameter of the NPs, the period of the considered grating, the material composing the NPs and the optical constants of the surrounding medium [18]. Gold, silver and metal oxide NPs placed in air have their resonance frequencies in the visible spectra. Here, we used metal oxide NPs. The inclusion of these NPs also enables light to be scattered, which is especially useful in the intermediate layer.

2. Experiment

2.1 Materials

Synthesis of P3HT was achieved by a route, using Iron Chloride (FeCl_3) as catalyst [22]. FeCl_3 (1 gm, 6.15 mmol) was added to dry Chloroform CHCl_3 (~6 mL) and stirred for 15 min at room temperature. The monomer 3-Hexylthiophene (3HT) (0.25 gm, 1.5mmol) in dry CHCl_3 (~6 mL) was then added drop-wise to the FeCl_3 solution and the reaction mixture was stirred overnight under Ar at room temperature. The polymerization reaction was then terminated by pouring the reaction mixture into excess Methanol MeOH (~25mL). The crude polymer precipitate was filtered using a PTFE membrane filter (1 μm , Millipore) and washed with ethanol (100mL), a distilled water (150 mL) and acetone (150 mL) mixture, finally with acetone (125mL). The dark brown solid product obtained was dried under vacuum for 48h to afford P3HT (0.20 gm, 90%). The P3HT solution were deposited on a thoroughly cleaned glass substrates in a nitrogen atmosphere of a glove box, to obtain thin films by spin coating method.

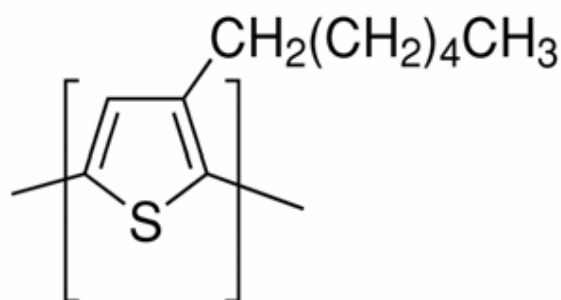


Fig. 1 The polymer poly (3-hexylthiophene) (P3HT).

2.2 Sample preparation

Pre-patterned indium tin oxide (ITO) coated glass slides (15 Ω /sq, 120nm thick sheet resistance, Sigma-Aldrich) were used as substrates and to act as transparent anode contact. The ITO-coated slides substrates were cleaned by ultrasonic treatment in washed thoroughly in acetone, isopropyl alcohol, and de-ionized water for 15 min, and finally heat dried under heating in an oven at 120 $^{\circ}\text{C}$. The silver nanoparticles AgNPs (~ 2nm diameter), from Sigma-Aldrich were added to linear polystyrene (as a inert host) in order to inhibit the wetting in the spun-cast films [10]. The AgNPs solution was prepared

by mixing with polystyrene using toluene as solvent. A film of poly(3,4-ethylenedioxythiophene) poly(styrenesulfonate) and silver nanoparticles (PEDOT:PSS:AgNPs) (1:4w/w) was spun onto the ITO substrates with a spin speed of 2000 rpm for 40 s to form the hole-transport layer (buffer layer), and was dried for 15 min at 140°C. Afterwards, mixed solutions consisting of polymer P3HT (5mg mL⁻¹) an p-type donor and PCBM fullerene (5mgmL⁻¹) PCBM, an n-type acceptor, as (1:1w/w), is prepared in chlorobenzene(CB). The obtained polymer blend (P3HT:PCBM) solutions were spun onto the PEDOT:PSS:AgNPs film at 1100 rpm for 30sec. to form the active layer. The thickness of the active layer is ~155 nm and that of the PEDOT:PSS layer is 40 nm, both measured using spectroscopic ellipsometry. Finally, a cathode consisting of 100 nm Al was thermally evaporated under vacuum of ~ 10⁻⁶ Torr with a rate of deposition of 0.2 nm/s onto the active layer surface. The devices produces have an active area of 9 mm² defined by the shadow mask used to deposit the cathode. The final device structure is ITO/PEDOT:PSS:AgNPs/P3HT:PCBM/Al,. Finally the post-annealing of the completed photovoltaic cells was carried out at 120°C for 30 min.

2.3 Characterization and Measurement

The FT-IR spectra were acquired in reflection mode at room temperature using an evacuated (type PerkinElmer Inc.- Spectrum 100 FT-IR Spectrometer). Potassium bromide (KBr) disk was used as beam splitter in wavenumber region 4000-400 cm⁻¹. Films was prepared by spin coating P3HT:PCBM solution on glass substrates for UV-vis absorption spectra of P3HT was recorded in range 300 – 800 nm wavelength by using M2000V (J.A. Woollam Co., Inc.) spectroscopic ellipsometer and Raman spectroscopy using a Horiba Jobin Yvon HR800 micro-Raman spectrometer. X-Ray Diffraction was performed using (multi-purpose X-ray diffractometer is a Philips X'Pert MPD system). Atomic Force Microscopy (AFM)

images of the polymer films were acquired using a BRUKER Nano-Scope IV Multi- Mode Adapter AFM with the tapping mode, and the film thickness was measured by spectroscopic ellipsometry (M-2000). The current density–voltage (J–V) characteristics of devices were measured with a computer-programmed Keithley 2400 source/meter, which simulated the AM1.5 sunlight with energy density of 100mWcm⁻². The PCE (η) is described by

$$\eta = FF \times (V_{oc} \times J_{sc}) / P_{light} \quad (1)$$

$$FF = (I_{max} \times V_{max}) / (I_{sc} \times V_{oc}) \quad (2)$$

where the FF is defined as, I_{max} and V_{max} are the current and voltage at the maximum power point, and the P_{light} is the power of incident light.

3. Result and Discussion

Figure (2) shows the measured Fourier transform infrared (FTIR) spectrum of P3HT film. It can be seen be that, the absorption peaks at 3419 and 2923-2443cm⁻¹ are assigned to the CH₂ out-of-phase stretching, CH₃ asymmetric stretching vibrations on the thiophene ring and the CH₂ in-phase stretching, respectively. The C=C asymmetric stretching vibration and the C–C symmetric stretching modes represented by peak at 1652–1291cm⁻¹, respectively. The peak at 1073 cm⁻¹ to the CH₂ stretching vibration. The peak at 668cm⁻¹ was the characteristic peak for the absorption of sulfate atom (S-atom) on the polythiophene ring.

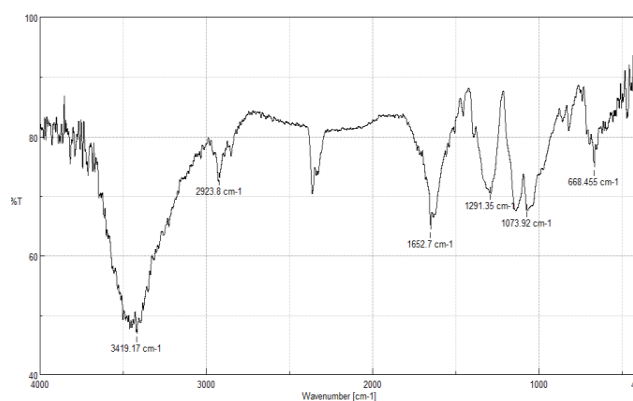


Fig. 2 (FTIR) absorption of P3HT film.

The optical absorption spectra of P3HT film deposited

onto glass substrate after annealing at 125⁰C for 15 min in the wavelength between 300-800 nm, are shown in figure (3). The UV-visible spectrum of the P3HT film showed two peaks at $\lambda = 520$ and 554 nm and one shoulder at $\lambda = 610$ nm. The three bands are also called vibronic absorption shoulders. These three bands can be attributed to the $\pi-\pi^*$ transition in crystalline $\pi-\pi$ stacking structure of polymer P3HT chains (conjugated polymer), [4]. The higher the P3HT order the more interdigitation and stacking occurs, the more pronounced are the vibronic shoulders.

The absorption coefficient, α was calculated by using Beer-Lambert's law: ($\alpha = 2.303A/d$) where, A is the absorbance. Figure (3) shows the absorption coefficient spectra of P3HT film. The spectra reveal all the films exhibit low absorption in the visible and NIR region but high absorbance in the UV range. High absorption characteristics in the UV range are due to melanin wide band gap properties. The band gap energy E_g which is associated with HOMO to LUMO electron transitions between the π and π^* molecular orbitals [5], were estimated using Tauc's approach $\alpha hv = A(hv - E_g)^{1/2}$ of direct band-gap energy (where, hv is the incident photon energy) by extrapolating the linear curve to the photon energy axis, we found that the band gap energy of P3HT as a function of film thickness are ~ 1.9 eV, which were close to the reported values of synthetic P3HT [6-8].

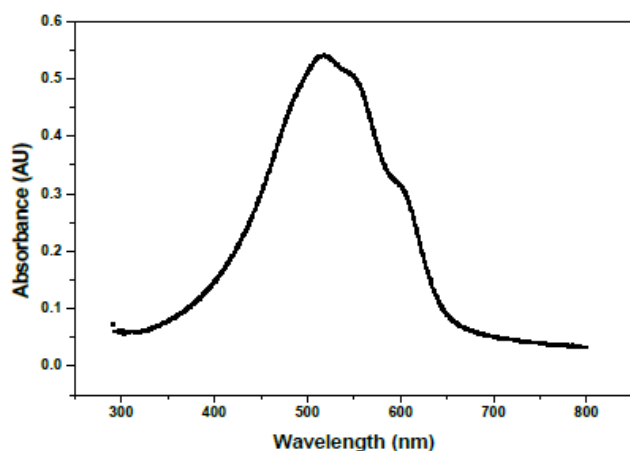


Fig. 3 UV-vis absorption spectra of P3HT film.

The energy gap values depend in general on the films crystal structure, and the arrangement and distribution of the

atoms in the crystal lattice. Also it is affected by crystal regularity. The energy gap can be calculated from the classical relation for near edge optical absorption in semiconductors [9, 10]; the relation is drawn between $(\alpha hv)^2$ and photon energy (hv), as shown in Figures (4&5) for P3HT. The determined band gap values is obtained by extrapolating the linear region of the plot $(\alpha hv)^2 = 0$. The allowed direct transition optical gap is found 1.92. This downshift is attributed to the thiophene ring in the polymer P3HT [10].

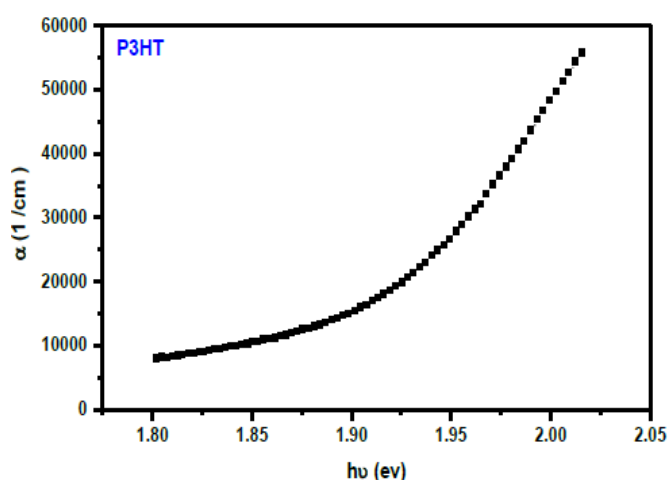


Fig. 4 The relationship between absorption coefficients (hv) versus Photon energy of P3HT.

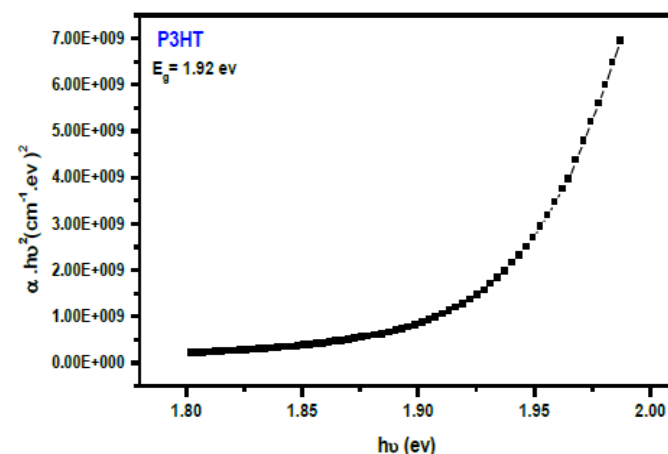


Fig. 5 The relationship between absorption coefficients $(\alpha hv)^2$ versus Photon energy of P3HT.

Figure (6) displays the Photoluminescence spectra of P3HT film under excitation by using an excitation wavelength of 430 nm in the range from 400 to 800 nm. It can be seen that the P3HT solutions had the maximum photoluminescence peak at 594 nm. The high intensity of

photoluminescence emission from the polymer P3HT film can be due to the surface oxidation defects of the exposed film. The degree of photoluminescence quenching is related to possible structural order of the polymer film on the substrate or on the oxygen adsorbed on surface active sites [11,13]. Among the several conjugated polymers, P3HT which is known to be one of region-regular polymers which have various characteristics according to self-organization [14]. The highly regular chain structure of P3HT facilitates their self-organization into two-dimensional sheets by means of inter-chain stacking and shows highly crystalline property [15]. The degree of self-organization can be varied by controlling the film growth rate or by controlling the time to solidify from a wet film [16,17]. The slow growth will assist the formation of self-organized ordered structure and give high crystallinity in the P3HT. The presence of P3HT polymer was observed by XRD analysis.

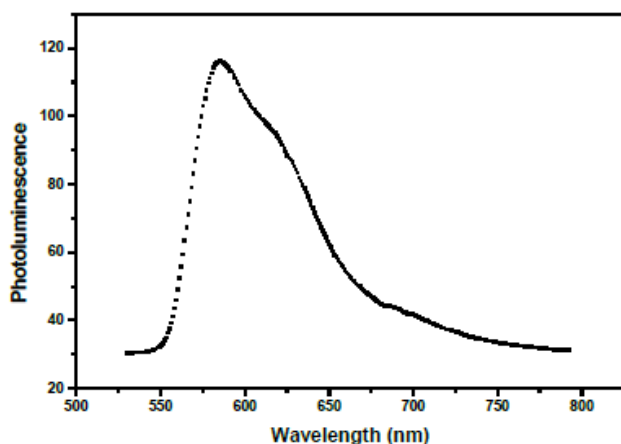


Fig. 6 Photoluminescence spectra of P3HT solution.

Figure (7) shows the X-ray diffractograms of polymer. P3HT film has a peak at $2\theta \sim 5.4^\circ$ with a full width at half maximum (FWHM) of ~ 0.25 (degree) corresponding to d_{100} -spacing, attributed to an inter-chain lamella peak. These peaks are possibly related to crystalline orientations of the thiophene units with respect to the substrate, which is similar with the literature reports [18, 19].

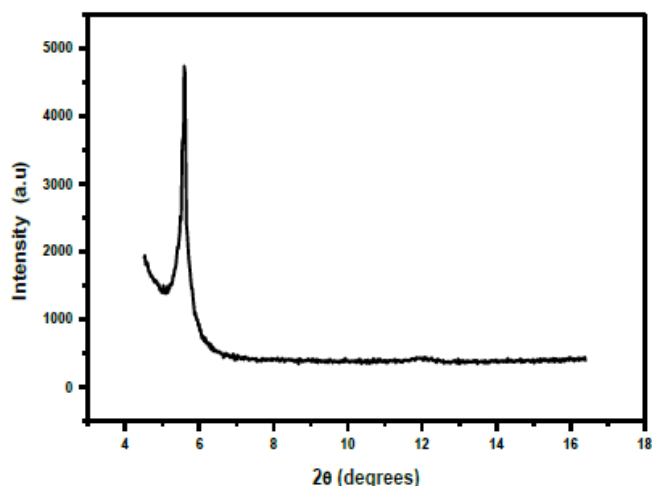


Fig. 7 X-ray diffraction of P3HT:PCBM film.

Figure (8) displays Raman spectroscopy of P3HT film in the range $200\text{-}2000\text{ cm}^{-1}$. There are several Raman modes in the range $600\text{-}1600\text{ cm}^{-1}$ [20, 22]: the main in-plane ring skeleton modes at 1452 cm^{-1} (symmetric C=C stretching mode) and at 1380 cm^{-1} (C-C intra-ring stretching mode), the inter-ring C-C stretching mode at 1208 cm^{-1} , the C-H bending mode with the C-C inter-ring stretch mode at 1180 cm^{-1} , and the C-S-C deformation mode at 728 cm^{-1} . We focus on the two main in-plane ring skeleton at ~ 1450 and $\sim 1380\text{ cm}^{-1}$ in figure (8) because they are supposed to be sensitive to π -electron delocalization (conjugation length) of P3HT molecules as well as to crystallinity extent [20-22]. Figure (9) shows image of Atomic Force Microscopy (AFM) topography measurements (surface morphologies) of P3HT film. From analyzing and the extracted data, It can be seen that, the (R.M.S) surface roughness for P3HT film was found to be 4.37 nm, mean roughness of film (R_a) is 4.12 nm, and the maximum height of the film (R_{max}) is 35.8 nm.

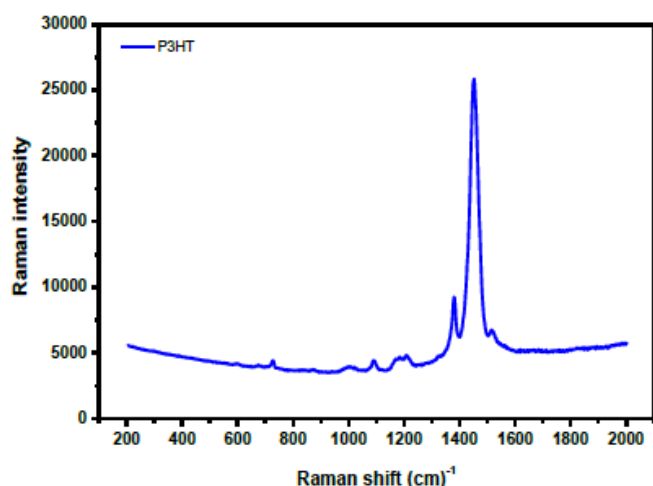


Fig. 8 Raman shift of P3HT film.

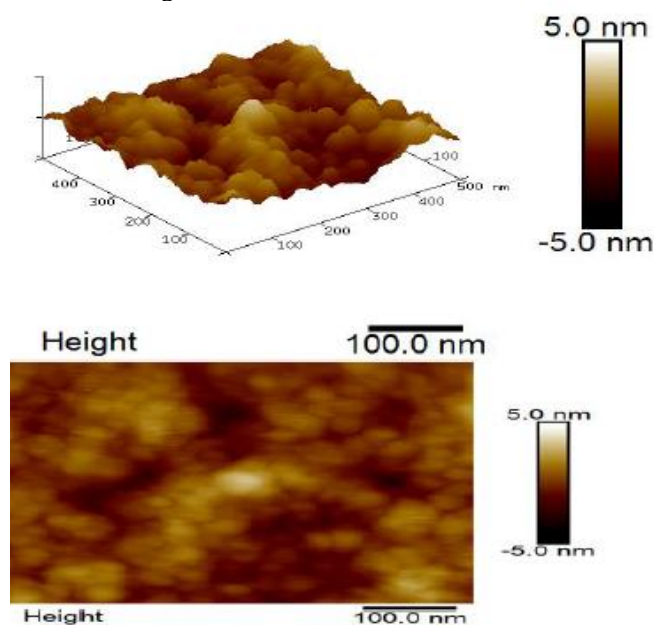


Figure (10) shows the current density versus voltage J - V characteristics of the device with the structures of PEDOT:PSS:AgNPs/P3HT:PCBM bulk heterojunction. The device fabricated shows J_{sc} , V_{oc} , FF , and PCE are 4.2 mA/cm², 0.62 v, 0.60 , and 2.06%, respectively, films show the best performance. The good value of power conversion efficiency of device can be attributed to the increases in the interfacial contact area between the P3HT:PCBM BHJ and intermediate layer (PEDOT:PSS), which allowing more efficient hole collection at the anode, i.e, AgNPs can scatter the incident light into waveguide modes in the bulk heterojunction of the organic solar cell device, increasing the optical path distance and improving absorption [18-22], and hence increases J_{sc} and FF .

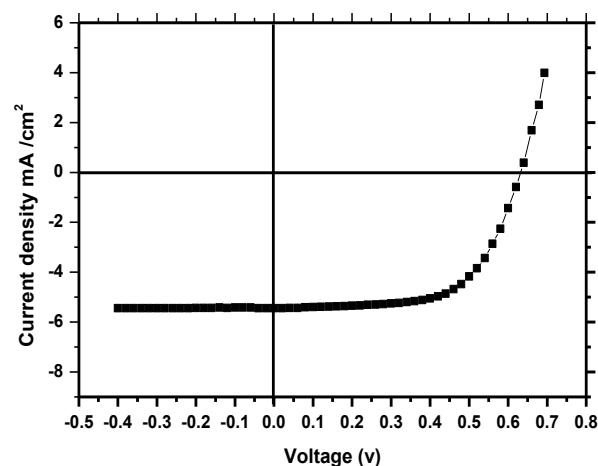


Fig.10. J-V characteristics for PEDOT:PSS:AgNPs /P3HT:PCBM thin films

Table 1: PV- parameters of the organic solar cell device

| PEDOT:PSS:AgNPs | |
|---------------------------------------|------|
| V_{oc} (v) | 0.62 |
| J_{sc} (mA/cm ²) | 4.2 |
| FF | 0.60 |
| PCE (%) | 2.06 |
| R_s (Ω cm ²) | 15.3 |
| R_{sh} (Ω cm ²) | 724 |

4. Conclusions

We have successfully synthesis P3HT polymer solution by using Iron Chloride (FeCl₃) compound as catalyst, and prepared the film by using spin coating method. The optical parameters such as absorbance, refractive index and extinction coefficient as well as FTIR spectrum, PL spectra, Raman shift, surface morphology of the P3HT film have been investigated. XRD results showed film have (100) preferred orientation. The optical band gap values of P3HT was found 1.92 eV.

Organic Photovoltage (PV) with high efficiencies were fabricated using P3HT:PCBM/PEDOT:PSS:AgNPs

structures. The inclusion of silver nanoparticles in PEDOT:PSS buffer layer is thought to enhance light harvesting for the OSCs of P3HT:PCBM. the solar cells give Power Conversion Efficiency (PCE) of 2.06%.

الخلاصة

تم في الجزء الاول من هذا البحث تحضير بوليمر البولي هكساتايوفين (P3HT) من مذيب الكلوروفورم وبطريقة الطلاء اليرمي. اما الجزء الثاني فتناول تحضير خلية شمسية عضوية من البولي هكساتايوفين المحضر ومزجه مع الفوليرين (C61) وبنسبة (1:1). حضرت الخلية الشمسية من تركيب (ITO/PEDOT:PSS:AgNPs/P3HT:PCBM/Al).

من النتائج المختبرية حصلنا على طيف امتصاص واسع يعمل بالطيف المرئي وهو مرغوب في عمل الخلايا الشمسية، كذلك تم اجراء فحوصات (AFM) و (XRD). النتائج النهائية اعطنا كفاءة خلية شمسية مقدارها (2.06%)

Acknowledgements

This work was supported by Department of Material Science, Polymer Research Centre, University of Basrah.

REFERENCES

- [1] D. Chirvase, Z. Chiguvare, M. Knipper, J. Parisi, V. Dyakonov, J.C. Hummelen, Electrical and Optical design and characterisation of regioregular poly(3-hexylthiophene-2,5diyl)/fullerene-based heterojunction polymer solar cells, *Synthetic Metals* 138, 299–304, (2003).
- [2] El. Jeffries, M., and R. D. McCullough, , Conjugated polymers theory, synthesis, properties, and characterization, in regioregular polythiophenes, T.A.S.a.J.R. Reynolds, Editor., CRC Press, Taylor & Francis Group, (2007).
- [3] Reyes, M., Kim, K., and Carroll, D., High- efficiency photovoltaic devices based on annealed poly(3-hexylthiophene) and 1-(3- methoxycarbonyl)-propyl-1- phenyl- (6,6) C61 blends. *Applied Physics Letters*, 2005. 87(083506).
- [4] T. A. Chen, X. Wu, R.B. Rieke, Regio controlled Synthesis of Poly(3-alkylthiophenes) Mediated by Rieke Zinc: Their Characterization and Solid-State Properties, *J. Am. Chem. Soc.* 117, 233, (1995).
- [5] M. A. Green, "Third generation photovoltaics: solar cells for 2020 and beyond", *Physica E- Low-Dimensional Systems & Nanostructures*, 14 (1-2), 65-70, (2002).
- [6] C. J. Keavney and M. B. Spitzer, Indium- Phosphide Solar-Cells Made By Ion- Implantation, *Applied Physics Letters* 52 (17),1439-1440 (1988).
- [7] D. E. Carlson and C. R. Wronski, Amorphous silicon solar cell, *Applied Physics Letters* 28 (11), 671-673, (1976).
- [8] Y. Ohtake, K. Kushiya, M. Ichikawa, A. Yamada and M. Konagai, Polycrystalline Cu(InGa)Se-2 thin-film solar cells with ZnSe buffer layers, *Japanese Journal of Applied Physics Part 1- Regular Papers Short Notes & Review Papers* 34 (11), 5949-5955, (1995).
- [9] V. Shrotriya, J. Ouyang, and R. Tseng, Absorption spectra modification in poly(3-hexylthiophene):methanofullerene blend thin films, *Chemical Physics Letters* 411, 138–143, (2005).
- [10] O. Ourida and B. Mohammed, Influence of the BlendConcentration of P3HT in the Performances of BHJ Solar Cells, *Science Academy Transactions on Renewable Energy Systems Engineering and Technology (SATRESET)*, 1, 3, (2011).
- [11] U. Zhokhavets, T. Erb, H. Hoppe, G. Gobsch, and S. Sariciftci N , Effect of annealing of poly(3-hexylthiophene)/fullerene bulk hetero - junction composites on structural and optical properties ,*Thin Solid Films* 496(2):679–682, (2006).
- [12] G. Li, V. Shrotriya, Y. Yao, J. Huang, and Y. Yang, Manipulating regioregular poly(3-hexylthiophene): [6]-phenyl-C61-butyrac acid methyl ester blends-route towards high efficiency polymer solar cells, *J Mater Chem* 17(30):3126–3140, (2007).
- [13] H. Shen, P. Bienstman, and B. Maes, Plasmonic absorption enhancement in organic solar cells with thin active layers, *J Appl Phys*106 (7):073109, (2009).
- [14] H. Sirringhaus, P. J. Brown, R. H. Friend, M. M. Nielsen, K. Bechgaard, B. M. W. Langeveld-Voss, A. J. H. Spiering, R. A. J. Janssen, E. W. Meijer, P. Herwig and D. M. de Leeuw, Two-dimensional charge transport in self-organized, high-mobility conjugated polymers, *Nature*, 401, 685-688 (1999).
- [15] B. Grevin, P. Rannou, R. Payerne, and A. Pron, J.P. Travers, Multi-scale scanning tunnelingmicroscopy imaging of self-organized regioregular poly (3-hexylthiophene) films, *J. Chem. Phys.* 118, 7097, (2003).
- [16] G. LI, V. Shrotriya, J. Huang, Y. Yao, T. Moriarty O, K. Emery, and Y. Yang, High-efficiency solution processable polymer photovoltaic cells by self-organization of polymer blends, *nature materials*, 4, (2005).
- [17] M. Al-Ibrahim, and O. Ambacher, Effects of solvent and annealing on the improved performance of solar cells based on poly (3- hexylthiophene): fullerene, *Appl. Phys. Lett.* 86, 201120, (2005).
- [18] B. Kippelen, and J.L. Bredas, *Organic photovoltaics*, *Energy Environ. Sci.*, 2, 251, (2009).
- [19] M. Grätzel, *Photoelectrochemical cells*, *Nature*, 414, 338, (2001).
- [20] Y. Gao, and J. K. Gery, *J. Am. Chem. Soc.*, *Resonance Chemical Imaging of Poly thiophene/Fullerene Photovoltaic Thin Films:*



Mapping Morphology-Dependent Aggregated and Unaggregated C=C Species, J. Am Chem Soc. 131, 9654–9662, (2009).

- [21] S. Wood, O. Garnett, N. Tokmoldin, W. C. Tsoi, Saif A. Haque and J. Kim, *In situ* formation of organic–inorganic hybrid nanostructures for photovoltaic applications, Faraday Discuss, 174, 267-279, (2014).
- [22] G. Louarn, M. Trznadel, J.P. Buisson, J. Laska, A. Pron, M. Lapkowski, and S.J. Lefrant, Raman spectroscopic studies of regioregular poly (3-alkylthiophenes), Phys. Chem. 100, 12532, (1996).

A Probabilistic Finite State Machine based Residential Environment for Obligation Agent Development

Wasan A. Jwad¹ & Kasim A. Al-Salim²

(1) College of Technical engineering - University of Southern Technical Basrah/ Basrah, Iraq

(2) College of Computer Science and Information Technology- University of Basrah / Basrah, Iraq

wasancsp@gmail.com¹ Kasim.alsalim@gmail.com²

Abstract- Covering the continuous growth in residential demand needs generating an adequate amount of power to cover usage of modern appliances. With the penetration of renewable distributed energy resources and the emergence of decentralized control systems new control methods emerges to the surface, one of such distributed control mechanisms is multi agent systems (MASs). Agents are the key elements in any MASs usually works and interact with each other in certain targeted environments in which they are embedded, from which they are getting their data through sensing, and on which they are influencing. Due to the complicated nature of distributed solutions, developing real-time distributed solution, such as agent-based ones, is complicated. This complication urges the need to develop software-based Integrated Development Environments (IDEs). One of the key beneficiaries of such IDEs is Demand Side Management (DSM) strategies which needs, among many other things, statistical power consumption data which is scarce in many countries. This paper focuses on developing an Integrated Agent Development environment System (IADS) that reflects the social relationships between families lining in its domain in addition to other key factors such as houses, families and appliances. The proposed system uses a probabilistic finite state machine to represent human behaviours. IADS provides an agent-based DSM solution situated in an environment and that aims at reducing residential demand taking into account the social relationships and priorities among families to coordinate agent interaction and behaviour.

Index Terms— residential demand, human behaviour, multi agent system, obligation agent, probabilistic finite state machine.

I. INTRODUCTION

The escalating residential, commercial and industrial electrical demand caused by the growth in economic activities, the continuous introduction of new appliances, and the increase in daily dependence on such devices have introduced a need for building more energy generation facilities used to cover such rocketing demand. On the other hand, the slow yet continuous spread of renewable energy such as solar, wind and hydro-electric sources [1] have introduced a scattered energy generation streams and changed the old centralized ones into just a node in

distributed energy pumping and absorbing community of nodes.

The distributed, cheap, and less labor-intensive nature of such energy renewable resources are the key factors for their penetration to the power grid [2].

These factors have mapped the power management from traditional centralized mode such as Supervisory Control and Data Acquisition Systems (SCADA) to the decentralized distributed electrical power management ones. SCADA manage power plant control, power transmission switching and communication protocols, thus SCADA needs more time to offer detail information about power system and sources [3] that is not feasible with recent requirements caused by deployments of controllable devices in smart grids. A distributed power management system and methods are thus needed to manage the ever-increasing population of distributing electrical power generation and consuming elements. Due to all that distributed power management and control methods and systems have proved themselves as the appropriate alternatives for modern power management systems. One of the key technologies of such distributed power management and control strategies is Multi Agent Systems (MAS) due to the intelligent, autonomous, modularity and social ability of agents.

This paper introduced building an environment for agents used to develop and run agent-based residential electrical power control and management strategies. the paper introduces a new type of agents called the 'Obligation agent' which mimics more accurately the social bonds, relationships, and interaction of human beings. It is aimed that such agent can produce more realistic representation of human behavior that can be used to develop more accurate power management strategies.

The paper is divided into several parts; after this introduction, part II introduces a brief introduction is given to the power shortage crisis while in part III MASs are briefed. Part IV discusses agent environments, while part V explains the developed integrated development model. In part VI the residential demand generation steps are introduced, and in Part VII the system model implementation is discussed. In part VIII the proposed systems is revealed. Finally, in part IX conclusions are drawn.

II. POWER SYSTEMS AND POWER CRISIS

A. Electrical Power System:

Electrical power system contains three elements: generation, transmission, and consumption.

- Generation station is an industrial facility for electric power generation; most power stations in the world have fossil fuels such as coal, gas, and oil to generate electricity. Others own nuclear power, but recent tendencies is to use renewable resources such as solar, wind and hydroelectric.
- Transmission lines are used to carry power from supplying sources and the distributed consumers.
- Consumption units mean end users who consume power.

B. Electrical Crisis:

Electrical crisis occurred in many countries due to two reasons: (i) Capacity constraints where electrical power generation and transmission is not enough to satisfy peak demand), (ii) Energy constraint in which consumer demand exceeds the supply levels over a period of time. To manage electricity crisis researchers worked in two streams: Demand Side Management (DSM) and Supply Side Management (SSM), their efforts have produced measures in both streams which aimed at providing a balance between supply and demand requirements [4].

One of such researchers is [5], who discussed the design of MAS and introduced what he called the Intelligent Distributed Autonomous Power System environment (IDAPS) to facilitate seamless transition from grid connected mode to an islanded one when detecting upstream outages. IDApS researchers have focused on introducing agent-based DSM solution using 4 basic types of agents which are: control agent, DER agent, user agent, and database agent. Control agents are responsible for monitoring voltage and frequency and responsible for isolate microgrid from the utility when upstream outage is detected. Authors in [6] present model of smart home involve 5000 homes using average UK consumption, they demonstrate that peak demand can be reduced by up to 17% and carbon emissions to 6%, the authors developed model to coordinate agents representing individual smart meters. In [7], a simulation of MAS proposed to reduce peak demand by shifting demand from peak hours to off-peak hours to minimize the operational cost of the system using DSM load shifting technique.

III. MULTI AGENT SYSTEM

A. Multi Agent System (MAS):

A MAS is a system which consists of entities called agents, each has the ability to work and perform the delegated tasks, they can interact with each other to achieve whole task [8]. MAS can solve large problem in a complex domain due to their modularity property, which means decomposing the large problem and delegating particular task to each entity (agent) who uses the most appropriate efforts to solve the targeted problem. These agents will coordinate and cooperate with each other in peer-to-peer interaction to complete problem solving; such functions will require techniques based on negotiation and cooperation. In addition to modularity,

other advantages of MAS are necessary in power application [3]:

- Local view of agents and limited knowledge about only neighboring agents reduce the severity of the expected intensive communication among agents, this is useful to apply MAS to grid or micro grid power system serving houses with an agent for each house, thus they need to know only about neighboring agents and their environment.
- Flexible and fault-tolerant: any changes of MAS structure or its environment will not produce high functional consequence, just its acknowledges about the changing factors that it needs to take into account without need to redesign structure, fault-tolerant means if any part (or agent) fail in doing its job, a MAS has the ability to continue working.
- Extensibility: easily add new functionalities by adding new agents with delegated tasks without need to redesign system. This offers convenient work when for example new houses or appliances are added or new tasks are scheduled.

So, a MAS can solve the complex problem that cannot be solved by a single centralized control entity, MAS decompose a complex problem into smaller simpler problems handled by several entities specially useful if they are recruited in a distributed system.

B. Agent Definition:

An agent is considered as anything that can be viewed as perceiving its environment through sensors and acting upon objects in that environment through actuators [9]. An agent is an entity situated in environment with the ability to affect it through actions and in turn affected by the environment by reshaping agent's behavior and the outcome of its decision making.

Agent has behavioral characteristics make it suitable for solve problems like [10]:

- *Autonomous*: the agent capability to make intelligent decision without external intervention.
- *Reactivity*: agents perceive their environment and provide stimuli in response to changes that occur in timely fashion,
- *Pro-activeness*: agents do not simply act in response to their environment in a reactive fashion, in addition to that they are able to exhibit goal-directed behaviour by taking the initiative.
- *Social ability*: agent's capabilities to cooperate and coordinate with each other (and possibly humans) to complete their own problem solving and to help others with their activities where it is appropriate.

So, all these properties inspire researchers to apply MAS in electrical grid control. McArthur et al. [11], find that MAS can be applied in some aspects of power engineering like: diagnostics, distributed control, modelling and simulation, protection. In case study we focus on distributed control.

IV. AGENT ENVIRONMENT

Analysis, design and operation of MAS require modeling a software integrated development environment comprises everything around agent, this environment must enable agent to interact and communicate with other entities and objects.

A. What is an Environment?

Environment is anything that can be observed by agent except the agent itself, an agent environment contains all objects or entities and their attributes. An agent can perform actions that effect its environment which in turn affect the agent in bidirectional interactive matter. Figure (1) shows the interaction between agent and environment.

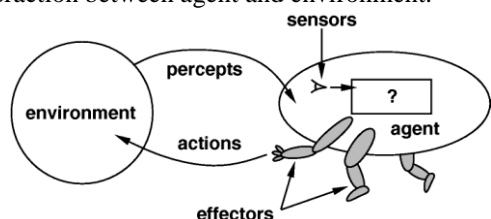


Figure 1: interaction between agent and environment [5]

B. Environment characteristics:

Agent’s environment can be classified into different categories such as [9]:

- Fully observable vs. partially observable (Accessible vs. non-accessible environment): In the first the agent’s sensors can obtain all the environment states in time. While in partially observable, the sensors cannot percept all the states of environment.
- Deterministic vs. Stochastic Environment: When the current behavior of the agent can determine the next state of the environment completely, called deterministic environment. Otherwise it is stochastic.
- Episodic vs. sequential: Episodic environment: in which the agent’s experience is divided into episodic, for each the agent take one action regardless of previous decisions. While Sequential environment: in which the agent take a decision that can affect all the future decisions.
- Dynamic vs. Static environment: Dynamic environment: in which the agent continuously need to look at environment to make decision because the environment may change with the passage of time.
- Discrete vs. Continuous: Discrete environment: has a finite number of states, the agent has a discrete set of percepts and actions, otherwise the environment is continuous.

V. THE INTEGRATED ENVIRONMENT MODEL

The proposed environment model has been built to simulate residential areas in Iraq, it is called the Integrated Agent Development System (IADS) and it is designed to generate and configure the demand profile of residential areas depending on the interaction between families

according to their social relationships, distributed appliances in each house, occupancy patterns of dwellers of each house, their behaviors and habits, financial status that impacts appliances number, types and usage pattern. These elements and factors are aggregated to configure the demand profile of residential dwellings.

A. Environment’ objects and attributes:

The integrated development environment that has been designed to support the targeted MAS, has all he necessary means to complete its services such as:

- Supply generation level: using fuel station or/and renewable distributed resources.
- Houses: number of houses in grid, with consideration the expansibility of MAS there is no problem for adding or removing any house from the grid.
- Rooms: room’s type and the number of each type.
- Family size and individual type, number of inhabitants in house and their types.
- People daily activities: the routine activities on individuals.
- Residential appliances: all appliances devices in house, which consume power especially HVAC. Comprises device type, device number each room, lower and higher power consumption per device, room in which device exist. Table.2 shows some appliances and their consumption.
- The social relationships among neighbors.

Table.1 shows objects and attributes of the proposed system.

Table 1: Objects and attributes in the environment

| Attribute \ Object | Number | Type | People actions | age | Occupation | Lower power | Higher power | Relationship type |
|--------------------|--------|------|----------------|-----|------------|-------------|--------------|-------------------|
| House | x | | | | | | | |
| Family | x | | | | | | | x |
| Individual | x | x | x | x | x | | | |
| Rooms | x | x | | | | | | |
| Appliances | x | x | | | | x | x | |
| Supply-power | | | | | | | | |
| agents | x | x | | | | | | |

Table 2: Household appliances and their power consumption

| Appliance | Lower power | Higher power | Appliance | Lower power | Higher power |
|---------------|-------------|--------------|-----------------|-------------|--------------|
| Lights | 20 | 100 | Air conditioner | 1500 | 3500 |
| Geyser | 2000 | 3000 | Air cooler | 300 | 1000 |
| Heater | 1000 | 1800 | TV | 200 | 350 |
| Fan | 50 | 100 | Hair dryer | 1000 | 2000 |
| Refrigerator | 100 | 730 | Iron | 1000 | 2200 |
| Freezer | 100 | 800 | Stereo | 70 | 400 |
| Cloth washing | 350 | 930 | Laptop | 50 | 80 |
| Dish washer | 1200 | 1500 | Printer | 30 | 50 |
| Oven | 1500 | 2000 | Water pump | 250 | 380 |
| Blender | 100 | 800 | Boiler | 1200 | 3000 |

such as power consumption and usage pattern. All these parameters affect the shape of the overall demand curve.

C. Family members

The family is described as a groups of individuals having different types, number, jobs and behavior, all that can influence the configuration of appliances’ usage patterns, which in turn shapes the power demand of each family which is when aggregated affects the overall power demand.

- **Individual types:** proposed model classify people into eleven categories shown in table 6 based on the information gathered from the conducted survey of the 168 families, other members and their types can be added flexibly.

B. House characteristics and ownership of Appliances:

In Iraq, People live in apartments and houses having different size, number of rooms and having different number and types of household appliances reflecting their financial level and amount of income. This variation leads to shape different demand profiles of dwellings that is taken into account in the proposed IADS to agree with various size and economic situations of different families. In the proposed system it is assumed that each house has at least one bathroom, one kitchen, one living room, one guests room, and a number of bedrooms ranging from 1 up to 4. Also it is assumed that similar rooms in different families have similar appliances.

Appliances means all household appliances distributed in the rooms of the house according to human needs, desires, and requirements. These appliances differ in their size, models, manufactures, operating modes, and power consumption. In order to have a realistic picture of what Iraqi families have a survey was conducted to show what appliances the survived families have among other things. The survey included 168 Iraqi families consisting of 1135 individuals. Figure (2) shows the appliances ownership according to conducted statistical questionnaire.

Table 3: Proposed people categories

| | Person | Gender | Age | Occupation |
|----|----------|--------|----------|---------------------|
| 1 | Man | Male | 19 - 60 | Government Employed |
| 2 | | | | Private employed |
| 3 | | | | Unemployed |
| 4 | Woman | Female | 19 - 60 | Housewife |
| 5 | | | | Government employed |
| 6 | | | | Private employed |
| 7 | | | | Unemployed |
| 8 | Elder | both | > 60 | Unemployed, Retired |
| 9 | Teenager | both | 13 - 18 | Student |
| 10 | Child | both | >6, < 13 | Student |
| 11 | Baby | both | < 6 | Baby |

- **Human Daily Activities:** In order to configure the appliances usage pattern and shape dwelling demand the interaction among house, families and appliances usage patterns is an affecting factor when representing certain realistic energy consumption. The relation between family and appliances is configured as a result of human activities throughout the day. Human activities comprise what people do along day such as physical needs (e.g. sleeping, studying, eating, going out, taking a bath, etc.) follow appliances operation to perform the targeted human tasks. Based on causal model [12], the proposed model was illustrated in Figure (4).

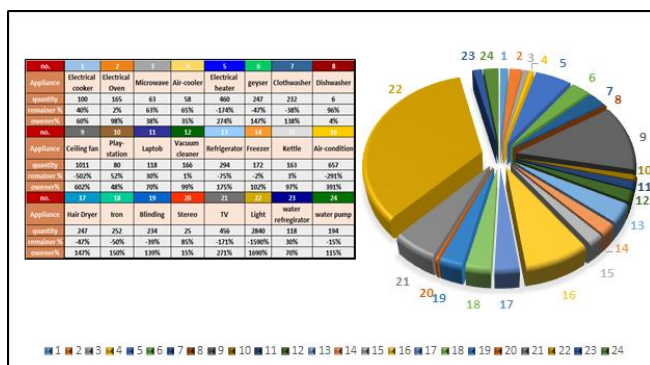


Figure 2: Iraqi owner appliances according to questionnaire

Appliances are distributed in house in a diversity manner depending on family needs, requirements and tendencies. The proposed distribution of appliances in rooms is shown in Table 3. All these appliances differ in some attributes

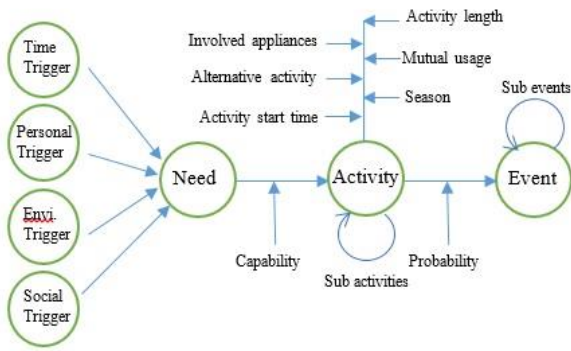


Figure 3: IADS causal model

Nature of human daily activities are repeated throughout daily life and configure daily routine for each type of inhabitants in state diagram may be represented by using a finite state machine for all family members such as in [13], or Hidden Markov model [14]. A Probabilistic Finite state machine (PFMS) [15], [16] is proposed in IADS model to schedule daily routines with probability of activity occurrence. If current activity does not have full probabilistic to occur, it will not happen and a different activity is triggered. Figures 4 to 11 show each state as an activity of certain individual starting from sleeping state and then ranging through daily hours. If probability of certain activity is 100 % , that means there is only one path to pass through it, otherwise if the probability is 50% then there are two path to choose between them, select one and follow the same process.

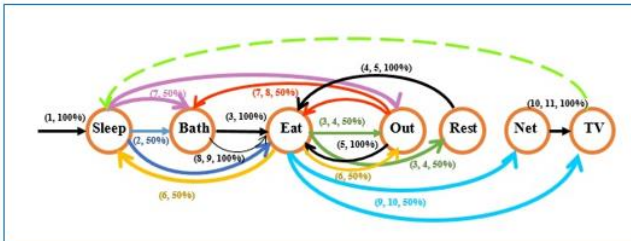


Figure 4: Unemployed man daily activities

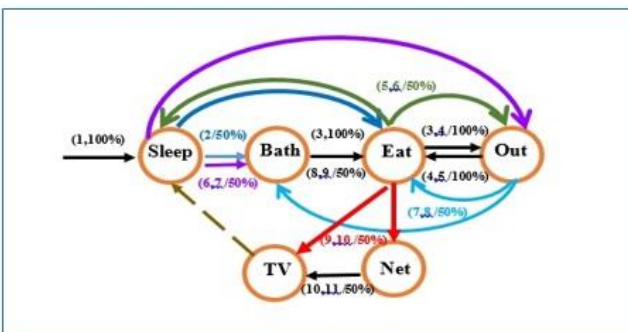


Figure 5: Government employed man activities

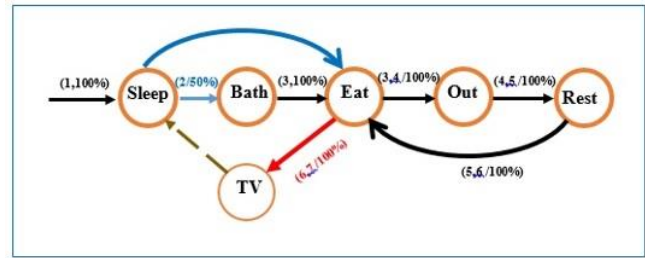


Figure 6: Private employed man / woman daily activities

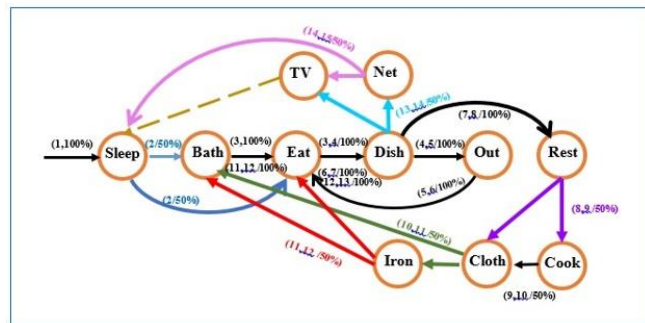


Figure 7: Government employed woman daily activities

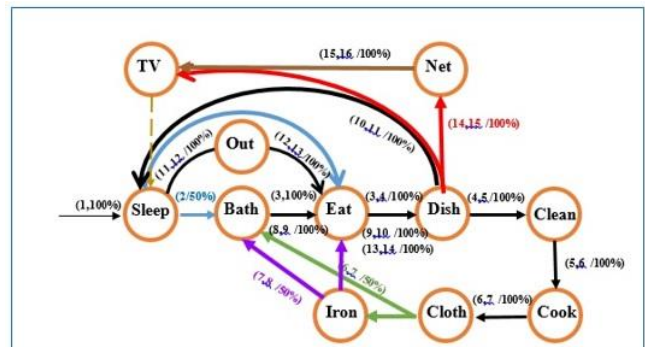


Figure 8: Housewife, Unemployed woman daily activities

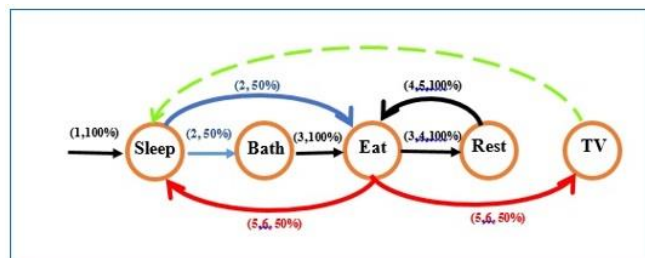


Figure 9: Elderly man / woman daily activities

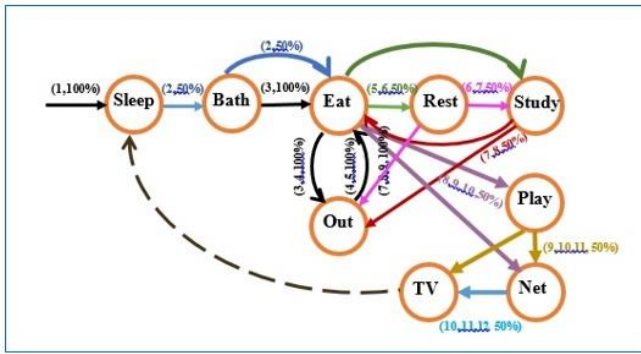


Figure 10: Teenager, Child male/ female daily activities

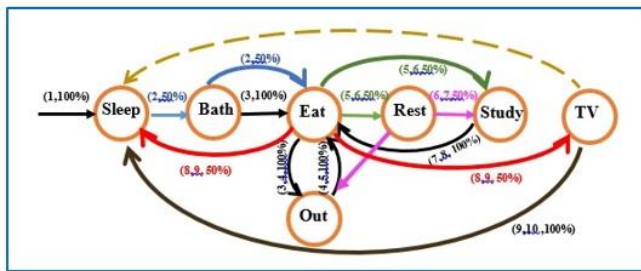


Figure 11: Baby activities

As described earlier in causal model, shown in Figure (3), inhabitants needs causes to do a certain activity that lead to triggering events such as operate appliances (open, close, turn on, turn off, etc.) to meet human requirements. Therefore, relation between activity profiles and appliances usage can shape the power consumption of each individual at time when regarding the presence and absence of family' members each time. Figure (12) shows the number of present individuals in two different families living in two separated houses in one day, we can notice the variation of presence and absence among individuals according to their types (specially if they are employed, students and child when they are sometimes go out the house).

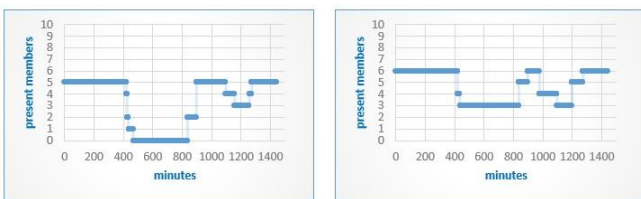


Figure 12: Occupancy patterns for two families living in two houses.

VI. THE RESIDENTIAL DEMAND GENERATION STEPS

In the real-life, residential power consumption is different from one family to another even though they live in adjacent houses under equal external conditions such as weather. A vast diversity of demand models for families

follow the occupancy patterns of houses, their characteristics, appliances specifications (number, types, locations, and power consumption), and family size. All these factors define different shapes of residential demand. IADS generate demand by aggregate knowledge of:

- Members' categories, their occupation, and their daily schedules.
- Human activities along day and related factors have been considered such as the different activities and the probability of their occurrences, alternative activities if original one has not been occurred, activity duration, start and end time for each activity, sub related activities, and the required appliances for activity.
- For each time slot, the needed appliances for each activity of individuals present in the targeted dwelling have been set and the power consumption for each device has been generated.
- After that the aggregate total demand for each time slot is produced by aggregating the demand of each participating family. Figure (13) shows total demand of four houses in 24 hours.
- The total residential demand for all houses can be obtained through aggregating single residential demand along day hours for each time step. Figure (14) shows the aggregation total demand for 10 houses in one day.

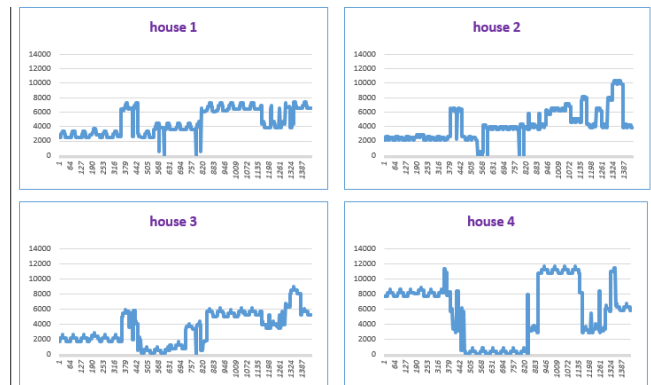


Figure 13: power demand for four families living in four dwellings, Y-axis represent the value of power consumption, X-axis represent minutes slots for one day.



Figure 14: Total aggregated demand for 10 houses

Figure (14) illustrate the demand of ten houses inhabited by different people in gender, age, and job. In addition, human occupancy, appliances usage pattern, and activities differ among individuals. The total demand of all families

configures the curve. As it can be seen the consumption on early hours is almost constant, this is true since these hours are sleeping hours for the majority of families. After that people wakes up and start waking up and moving through the rooms to perform their activities, some of them go to school or work, while others stay at home. In Iraqi summer air conditioning is considered the dominate appliance of power consumption, other devices are found according to family financial situations and the types available in local markets.

VII. SYSTEM MODEL IMPLEMENTATION

IADS provide a typical environment for electrical demand that can be used to exhibit power systems and solve energy problems such as peak load clipping that is occurred when demand exceed supply level. Figure (15) shows the total demand for ten houses in one day where the supply power covered 70% of consumers demand, we see peak loads in some daily hours such as in 4,6,7,,8 am. ,14-21 o'clock, this problem cause shortfall and may lead to blackout.



Figure 15: : total demand of ten houses, red line represent the supply threshold which covered 70% of consumer demand.

VIII. THE PROPOSED SOLUTION

To solve peak demand shortage problem, the proposed system IADS provide decentralized autonomous solution based on multi-agent system to reduce demand in peak hours autonomously without external intervention.

In case study, a newly proposed agent, called the obligation agent, look at the relationships between families when making decision. Obligation agent can perceive all objects in surrounding environment and consider the relation types among neighboring such as parents, sons, friends, relative, and unknown families, and using this information when there is a need to reduce demand for a certain house instead of other to cover the power shortage. Figure (16) shows the result after reducing power consumption of ten houses in peak hours with autonomous social strategy.



Figure 16: Demand after applying MAS based on Obligation agent.

IX. CONCLUSION

This paper presents an Integrated Agent Development System (IADS) capable of building integrated residential environment that takes into account the interaction between houses and their characteristics, types of families and individual behaviours, and available appliances to perform human activities.

IADS generate the demand profile depending on human daily life and their activities to satisfy their needs, the proposed system is based on a probabilistic finite state machine to generate individuals' activities throughout the day. It then finds the related appliances to achieve daily activities. Other essential factors influence of aggregate residential demand is human occupancy and appliances properties.

This environment has been built to generate a residential demand of neighboring dwellings by aggregate demand of each one of them. After assembling this environment it is possible to observe power shortage problems and other demand side management issues such as peak hours in day, and it will try to find an accepted solution to achieve supply-demand balance for all types of power generation sources whether they were fossil fuel or renewable resources generated power.

IADS provide a demand side management based solution using obligation multi-agent system situated in environment and work autonomously to reduce demand from houses with consideration of the social relationships and priorities among families to coordinate working and meet human behaviour.

X. REFERENCES

- [1] Fang. and et al. "smart grid – the new and improved power grid: a survey". 2012 - ieeexplore.ieee.org.
- [2] G. Heal, " the economics of renewable energy " NBER Working Paper No. 15081, 2009.
- [3] Robin Roche, et al. "multi-agent systems for grid energy management: a short review," France, 2010.
- [4] Pierre Audinet, and et. al, "managing an electricity shortfall," the world bank, Latin America, 2010. The world bank



- [5] M. Pipattanasomporn, et al. "multi-agent systems in a distributed smart grid: design and implementation," Proc. IEEE PES 2009 Power Systems Conference and Exposition (PSCE'09), Washington, USA, 2009
- [6] Sarvapali D. Ramchurn, et al. "agent-based control for decentralised demand side management in the smart grid," UK, 2011.
- [7] T. Logenthiran, et al. "Multi-Agent System for Demand Side Management in Smart Grid," IEEE PEDS Singapore, 5 - 8 December 2011 IEEE, Singapore, 2011.
- [8] M. Wooldridge, an Introduction to multiagent systems, Book.2009.
- [9] Stuart J. Russell and Peter Norvig," artificial intelligence: a modern approach", library of congress cataloging-in-publication data new jersey, 1995
- [10] M. Wooldridge, Nicholas R. Jennings "agent theories, architecture, and languages," 1994.
- [11] Stephen D. J. McArthur, et al. "multi-agent systems for power engineering applications—part I: concepts, approaches, and technical challenges," IEEE Transactions on Power Systems, vol. 22, no. 4, November 2007
- [12] Ayesha Kashif, "Simulating the dynamics of occupant behaviour for power management in residential buildings," Energy and Building, vol.65,p. 85-93, 2013.
- [13] Kasim AL Salim, et al. "A Finite State based Residential Demand Generator for Scare Statistical Data Scenarios," 2015.
- [14] M. Humayun Kabir, "two-layer hidden markov model for human activity recognition in home environments," international journal of distributed sensor networks volume 2016, Article ID 4560365, 2016.
- [15] Enrique Vidal, et al. "probabilistic finite-state machines—part I," IEEE Transactions on Pattern Analysis and Machine Intelligence, vol. 27, no. 7, 2005.
- [16] Enrique Vidal, et al. "Probabilistic finite-state machines - Part II," IEEE Transaction PAMI, 2008.

Simulation of Wind-Diesel Hybrid Power System for Fuel and Energy Department Building

Bahiya Abdulla Jabbar¹ & Hiba Abdulkareem Khamis²

Fuel and Energy Technical Engineering Dept. Electric Power Technical Engineering Dept.

Basra Eng. Technical College / Basra-Iraq

Bahia.abdalla@stu.edu.iq¹ hibakareem84@yahoo.com²

Abstract-Energy is the key factor and wheel of the development. In the shadow of the rapid depletion of fossil fuel resources on a worldwide basis and the highly concerned about the environmental issues, efforts elaborate to find an alternative energy source to meet the present day's demands. One of these promising alternatives is the hybrid energy system. In this research, hybrid energy system consisting of two elements is studied: Wind turbine and, Diesel Engine to supply energy for Fuel and Energy department classrooms at BETC. Wind speed measurement, forecast wind profile for city of Basra, and design calculation has been used in this study. The wind turbine chosen based on the sensitivity analysis through ranges of the factors that affect power generation such as wind speed, turbine's height, tip speed ratio and other variables. The Diesel engine is selected based on the cost, weather condition, and availability in the local market. MATLAB program is used as simulator for the hybrid system optimization. The suggested system found to be more affordable and flexible than the on grid-diesel engine system. The hybrid system generates 41000 W at wind speed peak. The wind turbine could cover the power demands expect at peak operation hours. The system contributes in lowering the cost of energy required to power the classrooms by reducing the diesel engine operation hours. In addition it reduces the dependency on the General Power Grid by generate an independent eco-friendly power. Moreover, the system reduces exhaust gases emission to the surrounding areas.

Index Terms— Diesel engine, Hybrid system, Renewable energy, Wind Turbine, Off-grid system

I. INTRODUCTION

Wind energy development is consumer and environment friendly, it requires shorter construction time compared to thermal, nuclear generation and it is cost competitive. It becomes one of the most competitive sources of renewable energy. However, wind power has some disadvantages. For example, wind power is considered an intermittent power supply because wind does not blow 100% of the time [1]. Today, in many parts of the world, the decisions for new capacity installation become complicated because finding new sites for generation and transmission facilities of any kind are difficult. Particularly rural areas in the developing world where most of the population is located, most people lack the essential energy services to satisfy most of their basic needs. [7].

The cost of grid connection in these rural areas is very high due to a low density of population. [9]; therefore, a various

organizations have turn to explore alternative solutions. One of the most economical and reliable alternatives is to use diesel power generation, but diesel power generation is very inefficient when the load is a small percentage of the rated power of the engine.[10]

As a result, wind energy system has been suggested to provide a good solution to supply energy loads in these rural areas. Hence, the role of hybrid power system comes into focus. Hybrid systems offer different penetration levels, Low wind penetration, and High penetration level both with reduction of the diesel generator rating. This paper presents the simulation of a hybrid Wind-Diesel System. Combining one generating technologies such as wind and diesel creates a hybrid power system. The system will be used to supply the electricity for the classrooms of fuel and energy departments. It will work as a self-sufficient power supply off the public power grid.[4]

II. WORK LOCACTION SPECIFICATION

Basra has a hot dry climate characterized by long hot dry summer and short cold winter. The climate is influenced by Iraq's location between the subtropical aridity of Arabian Desert areas and subtropical humidity of Arabian Gulf. It locate between latitudes (29.5-37.22) north[2]. In general, Iraq occupies the seventh place among Arab countries in the wind speed ranking. Wind speed is affected by the terrain effect, the presence of water bodies, the highlands aerobic, and solar radiation angel.

All the factors mentions above give an advantage to Basra city location as potential site for wind energy generation. Table I shows the ratio repeats quarterly wind direction in Basra. The annular average wind speed =4m/s and the annual wind energy density in Basra =41.3 watt/m²/h [3].

TABLE I
RATIO REPEATS QUARTERLY WIND DIRECTION IN BASRA (NATIONAL OCEAN AND ATMOSPHERIC ADMINISTRATION, NOAA)

| Forward | winter | summer | Spring | Autumn |
|-----------|--------|--------|--------|--------|
| Southeast | 0.08 | 0.1 | – | 0.07 |
| South | 0.01 | 0.05 | – | – |
| West | 0.26 | 0.02 | 0.07 | 0.05 |
| Northwest | 0.65 | 0.76 | 0.9 | 0.84 |
| North | ----- | 0.07 | 0.03 | 0.03 |

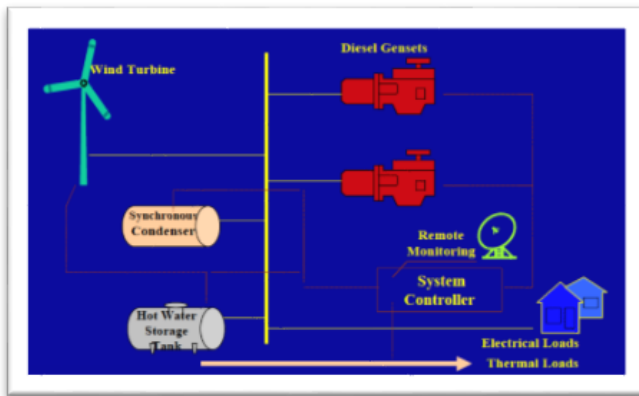


Fig. 1 Hybrid wind turbine-diesel engine system

TABLE II

Quarterly average wind speed in Basra Weather (National Ocean and atmospheric administration, NOAA)

| Autumn | Summer | Spring | Winter |
|--------|--------|--------|--------|
| 3.3 | 5.13 | 4.07 | 3.33 |

TABLE III

Wind energy density in Basra Weather (National Ocean and atmospheric administration, NOAA)

| Autumn | Summer | Spring | Winter |
|--------|--------|--------|--------|
| 23.2 | 85.6 | 44.5 | 23.2 |

III. ENERGY STORAGE SYSTEM

There are many possible techniques for energy storage, using practically all forms of energy. Mechanical, electrical, potential, chemical, and thermal. These all have been explored, leading to the birth of the techniques that will be cited herein [10]. The storage technologies that answer to specific technical and economic criteria, which vary considerably as a function of the applications and needs, will obviously be of different types. According to their applications, the storage systems can be divided into four categories:

- 1-Low-power application in isolated areas, essentially to feed transducers and emergency terminals.
- 2- Medium-power application in isolated areas (individual electrical systems, town supply).
- 3- Network connection application with peak leveling.
- 4- Power-quality control applications.

The first two categories are for small-scale systems (case of remote areas) where the energy could be stored as kinetic energy (flywheel), chemical energy, compressed air, hydrogen (fuel cells). [5]

IV. METHODOLOGY

A wind turbine can only convert a certain percentage of the captured wind power. This percentage is represented by C_p which is a function of the wind speed v , the turbine speed and the pitch angle β of any specific wind turbine blades.

The mechanical power P_{mec} extracted from the wind is mainly governed by three quantities namely: the area swept by turbine blades S , the wind speed v and the rotor power coefficient C_p . To calculate P_{mec} we use as shown in equation(1).

$$P_w = 0.5 \rho A v^3 C_p \dots\dots\dots(1)$$

Where, A is the cross section area and ρ is the density of the air.

In this paper, C_p is the power coefficient of rotor has been defined by Eq. (2). Power coefficient is a function of tip speed ratio (TSR) λ which is defined by Eq. (3) and pitch angle β . Pitch angle is kept constant.

$$C_p = \frac{2\lambda T}{\rho A v^2 r} \dots\dots\dots(2)$$

Where r is the radius of turbine and n is the number of the blades.

$$\lambda = \frac{2\pi r n}{v} \dots\dots\dots(3)$$

$$\rho = \frac{353.049}{T} e^{-\frac{0.0342z}{T}} \dots\dots\dots(4)$$

Where z is the height of the tower and T is the Temperature. The energy required to power the classrooms of fuel and energy department is the key factor in turbine choose and optimization process. The loads in three classrooms that intend to power by the system are shown in the table below.

TABLE IV

Total loads in three classrooms at F&E departments

| Devices | Number | Load(watt) |
|-----------|--------|------------|
| AC. unit | 8 | 24600 |
| Lamps | 22 | 1320 |
| Air Fan | 6 | 360 |
| Data show | 3 | 150 |
| Total | 37 | 28230 |

The next step is to inter data into MAT LAB Program and conduct the sensitivity analysis. After the sensitivity analysis has done, we chose the wind turbine type, number of blades, height and other design consideration. Then we run the hybrid wind turbine-diesel engine MATLAB simulator to calculate the power generated by the new hybrid system. We should mention that the diesel engine that combined with wind turbine in order to cover the lack in the electricity generation has power of 25 Kw and 30KVA. The other specifications of the diesel engine are shown in table V.

TABLE V

Diesel engine specifications

| Engine brand | Perkins |
|------------------------|-------------------|
| Engine model | 404A-22G1 |
| Alternator model | PI144D |
| Control system | DSE6020 / DSE7320 |
| Standard noise | 65 db |
| Frequency and Phase | 50 Hz & 3 PH |
| Engine speed RPM | 1500 |
| Fuel tank capacity (L) | 54 |

| | |
|-----------------------------------|-------------|
| Fuel consumption (l/h) (100%)load | 5.4 |
| Lubricant | 15W40 |
| Total lubricant capacity | 10.6 |
| Generator Standby Power | 25 KW/30KVA |
| Fuel | Diesel |
| Output Type | AC |

V. RESULTS

After applying the matlab program analysis, we choose the wind turbine that will used. The properties of this turbine is shown in table VI below:

TABLE VI
Wind turbine Specification

| | |
|-------------------------------|----------------------------------|
| Rotor | |
| Diameter | 7.1 m |
| Swept Area | 20 m ² |
| Rotational Speed | 9–19 rpm |
| Direction of Rotation | Clockwise |
| Blades | |
| Quantity | 3 |
| Length | 8.72m |
| Aerofoil's | Delft University and FFA-W3 |
| Material | epoxy glass fiber + carbon fibre |
| Rotor Weight | 144 kg |
| Other information | |
| Cut in Wind Speed | 2.5 m/s |
| Maximum wind speed withstand | 100m/s |
| Maximum rpm | 130 |
| Maximum operation temperature | 60C ⁰ |

The energy demands for 12 hours started from 6 am to 6 pm for the three classrooms at fuel and energy is calculated and are shown below in Fig.2:

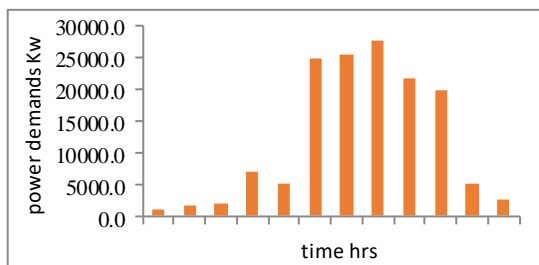


Fig. 2 Power demands for three classrooms in 12 hours

The amount of power generated by wind turbine mainly depended on the wind speed and temperature. As shown in Fig.3.

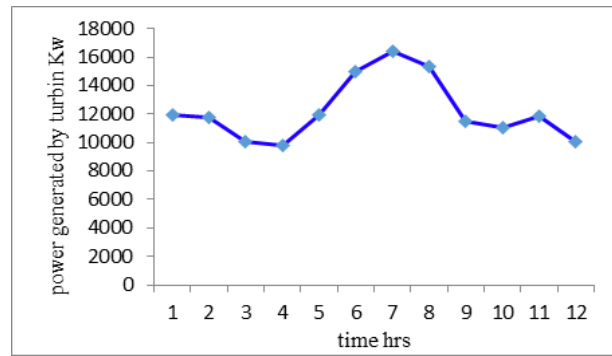


Fig. 3 Power generated by wind turbine for 12 hours

In fig.3 the wind turbine generates the maximum energy at 12 p.m. because of the high wind speed. At that time, the wind turbine generates 16439 W. wind turbine power could cover the energy demands from (6am to 11 am). However, at peak hours (11am to 3pm) the hybrid system covers up the lack in the required power.

A comparison between energy demands and power generated by wind turbine shown in Fig.4. The power generated by the wind turbine is not enough to cover the demands at the peak hours. Thus, in this case the combined system put on operation to cover the lack in the power generation. The maximum power demands is at 1pm (27690W) that is because of that the temperature reaches its highest value at that time. Thus, the classrooms have to be cooled by split units, which consume (24600W)

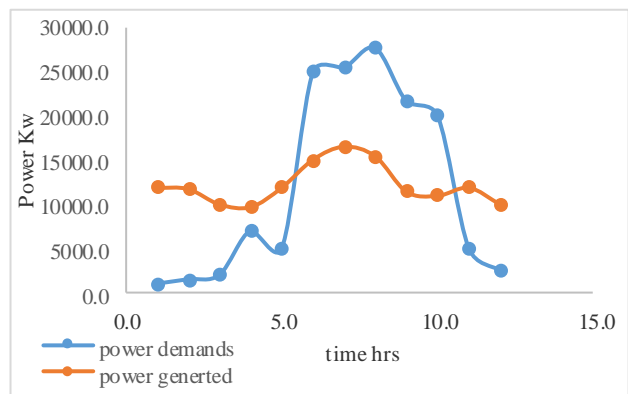


Fig. 4 Comparison between the power demands and the power generated by the wind turbine in 12 hours

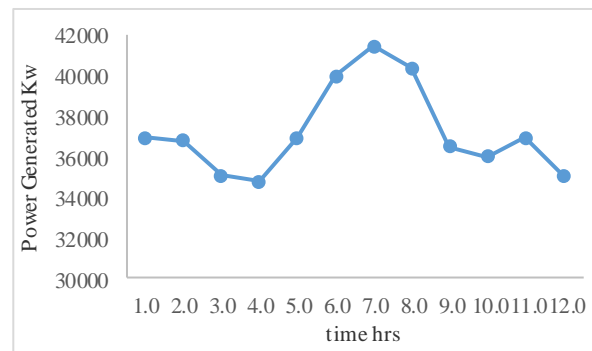


Fig. 5 The power generated by hybrid system for 12 hour

Fig.5 shows the amount of power generated by hybrid system. The maximum power generated by the hybrid system is at 12 pm due to the high wind speed and

temperature. The hybrid system generates more power than normal system and easily covers the power demands for the three classrooms. In addition, extra-generated power could be save in the storage system for further use.

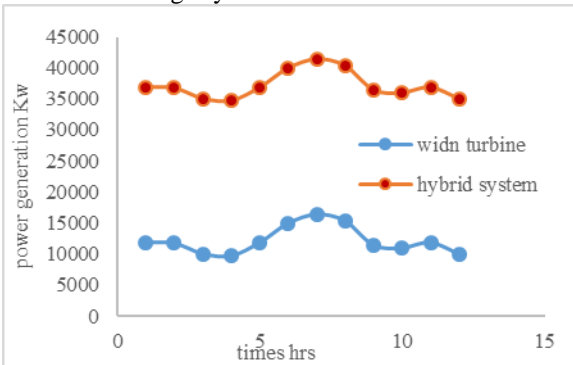


Fig. 6 Comparison between power generated by hybrid system and the power generated by the wind turbine in 12 hour

To show the advantage of the hybrid power system a comparison between the power generation by wind turbine and diesel engine shown in Fig.6. The system covers the power demands at peak hours as well as the power demands when there is no wind or low wind speed.

Finally, Fig.7 (the appendix) shows the wind speed at Basra Technical College location over 12-hours. The measurement shows the maximum wind speed for the chosen day is at 12 pm as well as the maximum wind power generation we could get from the turbine is at 12 pm at the specified day as it shown in figure.

VI. CONCLUSION

In this paper, simulations by using of Matlab for a wind-diesel hybrid system is presented. The results of simulation show the importance and flexibility of hybrid diesel generator and wind turbine system to reduce the dependency on General Power grid and diesel engine. Another benefit of this system is the proportional reduction in toxic emissions and greenhouse gas emissions mainly, due to the reduction in diesel engine operation hours. In addition, the results show that location of Basra Technical College could serve as potential site for a hybrid wind turbine – diesel engine power system. The hybrid system generates enough energy to power three classrooms and save the excess energy generated. The wind turbine itself could power the classrooms from 6am to 11am without use of the diesel engine. The analysis shows also in the case of very low or no wind speeds the system will use the saved energy to cover the lack in the power. However, the CO₂ emissions in both cases is still very low[1]. The case of very low or no wind speeds have a 3.98% probability of occurrence in the city of Basra annually [1].

VII. APPENDIX

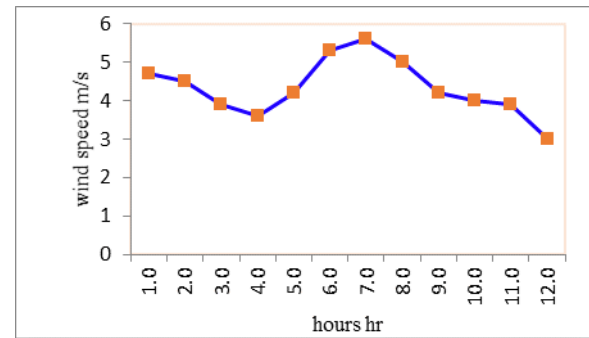


Fig. 7 Wind speed average during 12 hours under study

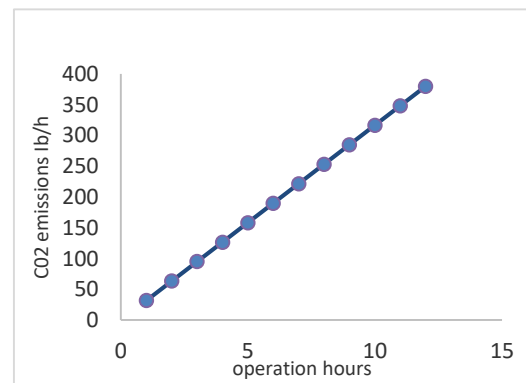


Fig. 8 CO₂ emissions form diesel engine during 12 hours under study

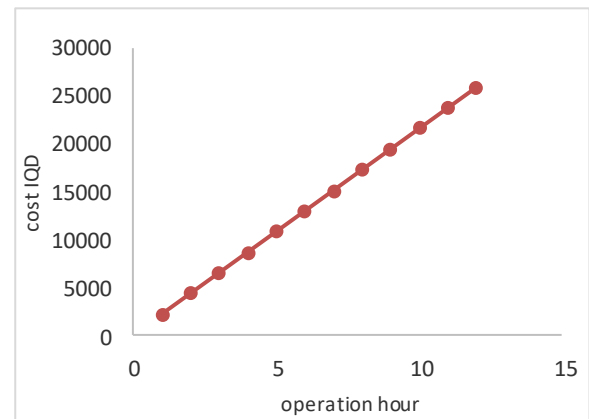


Fig. 9 The cost of diesel during 12 hours under study

TABLE VII

The power generated by wind turbine in 12 hour

| hours | wind speed average | power |
|-------|--------------------|-------|
| 1.0 | 4.7 | 11895 |
| 2.0 | 4.5 | 11750 |
| 3.0 | 3.9 | 10050 |
| 4.0 | 3.6 | 9750 |
| 5.0 | 4.2 | 11900 |
| 6.0 | 5.3 | 15000 |
| 7.0 | 5.6 | 16439 |
| 8.0 | 5 | 15369 |
| 9.0 | 4.2 | 11453 |
| 10.0 | 4 | 11000 |
| 11.0 | 3.9 | 11893 |
| 12.0 | 3 | 10050 |

TABLE VIII

The power generated by hybrid system

| hours | Wind turbine power | Hybrid power | Saving power |
|-------|--------------------|--------------|--------------|
| 1.0 | 11895 | 36895 | 35895.0 |
| 2.0 | 11750 | 36750 | 35250.0 |
| 3.0 | 10050 | 35050 | 33050.0 |
| 4.0 | 9750 | 34750 | 27750.0 |
| 5.0 | 11900 | 36900 | 31900.0 |
| 6.0 | 15000 | 40000 | 15000.0 |
| 7.0 | 16439 | 41439 | 15939.0 |
| 8.0 | 15369 | 40369 | 12679.0 |
| 9.0 | 11453 | 36453 | 14783.0 |
| 10.0 | 11000 | 36000 | 16000.0 |
| 11.0 | 11893 | 36893 | 31893.0 |
| 12.0 | 10050 | 35050 | 32550.0 |

TABLE IX

The power demands

| hours | Power demands |
|-------|---------------|
| 1.0 | 1000.0 |
| 2.0 | 1500.0 |
| 3.0 | 2000.0 |
| 4.0 | 7000.0 |
| 5.0 | 5000.0 |
| 6.0 | 25000.0 |
| 7.0 | 25500.0 |
| 8.0 | 27690.0 |
| 9.0 | 21670.0 |
| 10.0 | 20000.0 |
| 11.0 | 5000.0 |
| 12.0 | 2500.0 |

VIII. REFERENC

- [1]A. Rashem., "Analysis of Wind Speed Data and Annual Energy Potential at Three locations in Iraq", *International Journal of Computer Applications*, vol. 137, no. 11, pp. 5-16, 2016.
- [2]*Catalog of European Urban Wind Turbine Manufacturers*. European commission of energy, 2016.
- [3]"Climate of the World: Iraq | weatheronline.co.uk", *Weatheronline.co.uk*, 2018. [Online]. Available: <https://www.weatheronline.co.uk/reports/climate/Iraq.htm>. [Accessed: 03- Mar- 2018].
- [4]D. Documents, F. Data and I. Data, "Iraq Climate Data | NOAA Central Library", *Library.noaa.gov*, 2018. [Online]. Available: <http://library.noaa.gov/Collections/Digital-Docs/Foreign-Climate-Data/Iraq-Climate-Data>. [Accessed: 08- Jan- 2018].
- [5]K. Allali, E. Azzag and N. Kahoul, "Modeling and Simulation of a Wind-diesel Hybrid Power System for Isolated Areas", *International Journal of Computer Applications*, vol. 116, no. 23, pp. 18-23, 2015.
- [6]"Performance Analysis of Hybrid Renewable Power System with Simulation", *International Journal of Science and Research (IJSR)*, vol. 6, no. 7, pp. 1438-1445, 2017.
- [7]P. Schubel and R. Crossley, "Wind Turbine Blade Design Review", *Wind Engineering*, vol. 36, no. 4, pp. 365-388, 2012.
- [8]S. Rashid, S. Rana, S. Shezan, S. A.B. Karim and S. Anower, "Optimized design of a hybrid PV-wind-diesel energy system for sustainable development at coastal areas in Bangladesh", *Environmental Progress & Sustainable Energy*, vol. 36, no. 1, pp. 297-304, 2016.

[9]S. Schreck, *Wind energy aerodynamics*. [Golden, Colo.]: National Renewable Energy Laboratory, 2010.

[10]W. Lee and V. Cho, *Handbook of sustainable energy*. New York: Nova Science Publishers, 2010.

Effect of location and direct solar radiation on the performance of electric power transformer

Rafid M. Hannun

Assist. Prof.Dr. Mechanical Eng., College of Eng., Thi -Qar University, Iraq

company

rafid.alsaleh@gmail.com

Salmaan H.Hammadi

Assist. Prof.Dr. Mechanical Eng., College of Eng., Basra University, Iraq

slmnhm@yahoo.com

Mohammed H. Khalaf

MSc. Mechanical Eng
Ministry of oil, Thi-Qar oil

mohammedhamedkhalaf@gmail.com

Abstract- In this paper, a theoretical study was carried out to represent a mathematical model for the electric power transformer (250 kVA) for finding the effect of solar radiation on transformer and how its location affected the temperature of the oil cooling and internal parts of the transformer. The (ANSYS17.1/FLUENT) code program was used to simulate the electric transformer with the real dimensions of the transformer. The results showed that the solar radiation falling directly on the external surfaces body of the electric transformer has a significant effect on increasing the temperature of the oil, coils, and core. In this study, the site of the Nasiriya city was adopted and its weather conditions at the first day of August and full electrical load for power transformer were done. The study concluded that the transformer location facing the south is the best location because it gives the lowest temperature of oil, iron core, and coils while the coverage of the transformer body is the best to maintain the least impact of thermal losses and thus increase the work efficiency and the operational life of the electric transformer.

Keywords — transformer, cooling, solar radiation, core, coil, oil, heat transfer.

I. INTRODUCTION

An electrical power transformer is a main item for the dispensation of electrical power in transmission and distribution grid systems for restricted and global power to many metier applications. In this power transformer, a quantity of energy is missing through transformation into heat inside the power transformer. The core and coils raise temperature of interior parts of power transformer . The oil usually used to cool internal parts of power transformer. The oil generally used to cool the interiors of power transformer. Numerical study proposed by Zhang et al. [1] for an oil natural (ON) cooling mode of disc-type of power transformer. Their study included the temperature distribution and oil stream of power transformer by using Boussinesq approximation, for coils geometry, volumetric stream fraction in each horizontal cooling channel and the dimensionless temperatures in the coils, they showed that in a comparatively small and constant range(from 0.4 to 0.6) of Ri in spite of the values of Re and Pr in their experimental ranges. A case study has been achieved which explained the apparition of reverse stream and hot-plumes.

In this case, the hot-spot temperature was 141.6 °C. Another case study has been attained on the standard coils with Ri being relocated from 1.46 to 0.6. The new oil stream and temperature distribution became much more eminent, with the hot-spot factor and the hot-spot temperature being 1.13, 77.4 °C respectively. Garelli et al. [2] showed analytic and imitation the behavior of thermos fluid dynamic for power transformer (ONAF cooling mode) in an oil natural air force. The heat convection in power transformer transferred by two processes one by the oil inside the power transformer which rejected the heat by natural convection while other by radiator in outer walls of power transformer which rejected the heat losses by forced convection. The small model can be estimate with appropriate precision the value of the most salient design variables like temperature of oil, velocity of oil, and temperature of air. The experimental and theoretical study presented that the velocity of air along the outer walls of power transformer by using fan is not energetic as about half of transformer radiator were not puffed. Fernández et al.[3] presented an experimental study for insulation paper (Kraft paper) by using two kinds of dielectric oil, a mineral oil and vegetable oil by simulate it in scientific laboratories to remark the hot-spot of oil temperature in electric power transformer. The experimental results showed the difference of hot-spot temperatures of mineral oil reduced about 20 oC than the ones on record with vegetable oils type since increase the thermal stress suffer by Kraft (insulation paper) within electric power transformers when utilized vegetal oil. Kondrashova et al.[4] introduced a new calculation of thermal modes for the life of electric power transformer and dielectric paper. The results explained the thermal mode, the weather parameters, and nonlinearity of the thermal property were empirical. The structure of algorithm for calculating temperature charts as in the load factors with regard to the influence of the parameters was suggested. Kim. et al. [5] worked on the process life of electrical power transformer which consisted on cooling modes that caused fall down of insulations. The study introduced the planning of cooling mode was very significant to increasing the reliability and lifetime for internal parts of electrical power transformer. The work included two kinds of stream in channels, the direct oil flow for (ODAN) type and non-direct oil flow for (ONAN) type. The results explained that preference in cooling was by using (ONAN) type which increased by 20.1% more than (ONAN) type. A numerical model of thermal behaviour suggested by Gastelurrutia et al. [6] for electrical power transformer. This numerical model expected oil flow and the temperature distribution within

electrical power transformer for ONAN (Oil Natural - Air Natural). This model was employed to study the natural convection of oil stream inside electrical power transformer and best design for parts inside the transformer. Taghikhani et al. [7] introduced a numerical simulation of a 32 MVA electrical power transformer with two types of thermal modes cooling: directed oil-forced(DOF) and non-directed oil-forced (NDOF) by using (FEM) the finite element method. Their work suggested new technique to increase accuracy of the value of (HST) hottest spot temperature and its location. The results were similar compared with practical data tests. Hosseini et al. [8] studied a simulation for electrical power transformer by thermal modeling with kind of disk winding and with several geometrical factors of coils to correct the best cooling system for coils in electrical power transformer and decreased the heat losses. Some theoretical models of winding planed by using software programs, it helped to guess the site of oil (HS) hot spot. The present study aims to model the electrical power transformer to calculate the effect of oil, coils, core transformer temperature especially at hot surrounding temperature to beat low electrical efficiency and transformer damage in hot ambient season by different locations and directions of power transformer with and without solar radiation.

II. PROBLEM DESCRIPTION

The electrical power transformer (250kVA) with Turkish Transformer type is theoretically analyzed in this study by using (MATLAB) and (ANSYS17.1/FLUENT) code program. Fig.(1) exemplifies electrical power transformer which studied in this work. The electrical power transformer contains (three coils, tank, and core). Power transformer tank keeps the oil inside the power transformer which it connected to 44 fins to refuse the heat losses in windings and core to ambient as illustrated in fig.2. The windings (three coils) are copper wire wrapped as cylindrical form and iron core is magnetic iron flakes are joined together. For full electrical load, the heat generation in winding (for three coils)are 3000W and iron core is 500 W[9]. To reduce damage caused by operation of an electric transformer, the heat generation inside power transformer should be decreased.

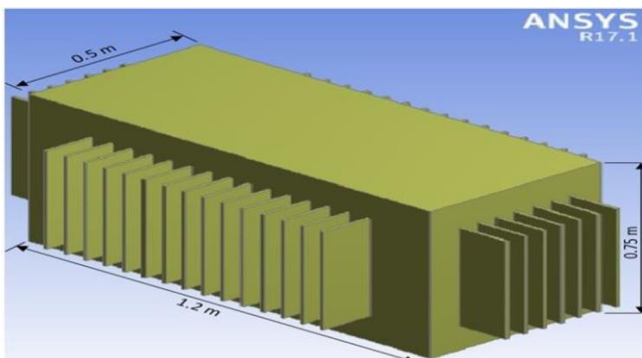


Fig. 1 The(250KVA) power transformer model.

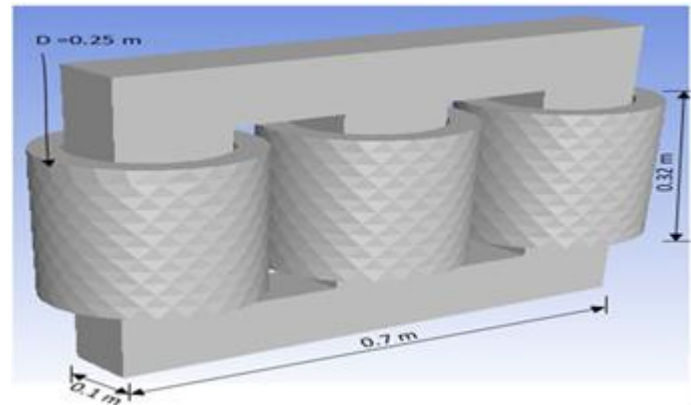


Fig. 2 The core and coils of power transformer.

III. MATHEMATICAL FORMULATION

The boundary conditions of case study can be resolved in present case study by using the following equations:

A. Calculations of directs solar radiation on a surfaces:

If the strength of frontal solar event radiation on a surface vertical to the beam of sun rays is I_b , so the value of this flux in any direction can be evaluated as[10]:

$$I_b = A_b \times e^{\left(\frac{-B}{\sin A'}\right)} \quad (1)$$

Where (La) Latitude angle : is the angular displacement above or below the plane of the equator, measured from the center of the earth.

Declination angle (δ) is the angle between the sun ray and the equator plane (directly overhead) at noon on the earth's equator. Declination angle (δ) given by [12] :

$$\delta = 23.45 \sin \left[\frac{360}{365} (284 + n) \right] \quad (2)$$

where n is day number (n=212).

Hour angle (h') is the angular displacement of the sun from noon, solar noon (h') being zero (i.e. 1 hour corresponding to (15°) of angular displacement of longitude, with morning positive and afternoon negative). Hour angle (h') given by [12]:

$$h' = (12 - \text{solar time}) \times 15 \quad (4)$$

1) Calculation of Radiation Intercepted by Surface (Beam Component):

The component of beam radiation (I_{bc}) intercepted by the surface is given by [13] :

$$I_{bc} = I_b \cos(i) \quad (5)$$

2) Incidence Angles for Fixed Surfaces :

The incidence angle (i) is defined as the angle between the perpendicular to a surface and a line collinear with the sun's rays.

3) South-Facing Tilted Surfaces can be found as [10]:

$$\cos(i) = \sin(L_a - \Sigma) \sin(\delta) + \cos(L_a - \Sigma) \cos(\delta) \cos(h') \quad (6)$$

Where (Σ) Surface tilt angle.

4) Non-South-Facing Tilted Surfaces [10]:

If a tilted wall faces a direction other than due south, then:

$$\cos(i) = \cos(a_s - a_w) \cos(A') \sin(\Sigma) + \sin(A') \cos(\Sigma) \quad (7)$$

Where (a_w): wall azimuth angle, (a_s): Solar azimuth angle: is the angle in the horizontal plane measured from north to the horizontal projection of the sun's rays. Solar azimuth angle can be found [10] :

$$\sin(a_s) = \frac{\cos(\delta) \sin(h')}{\cos(A')} \quad (8)$$

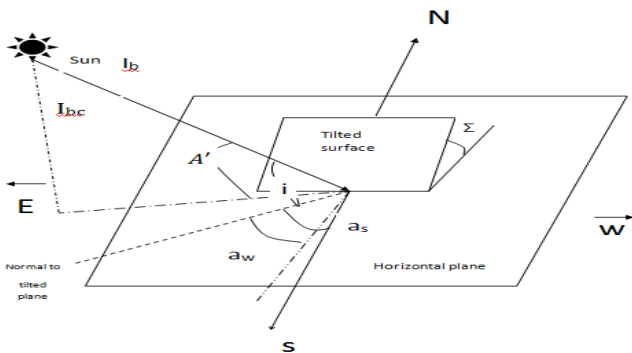


Fig. 3 The solar radiation component

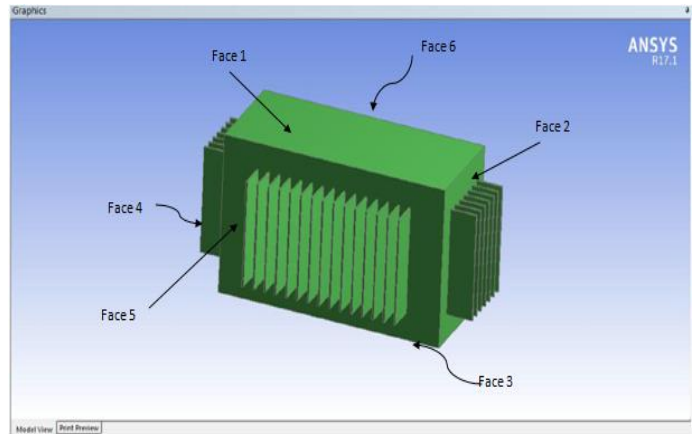


Fig. 4 The power transformer with faces.

TABLE I
THE FACES OF POWER TRANSFORMER WITH THE INTENSITY OF DIRECT RADIATION (FOR A AND B LOCATIONS)

| face | Surface area (m ²) | Direct radiation (W/ m ²) | |
|------|--------------------------------|---------------------------------------|------------------|
| | | The location (a) | The location (b) |
| 1 | 0.6108 | 872.7452 | 872.7452 |
| 2 | 0.35025 | 219 | 38 |
| 3 | 0.6108 | 0 | 0 |
| 4 | 0.35025 | 0 | 38 |
| 5 | 0.8325 | 38 | 219 |
| 6 | 0.8325 | 38 | 0 |

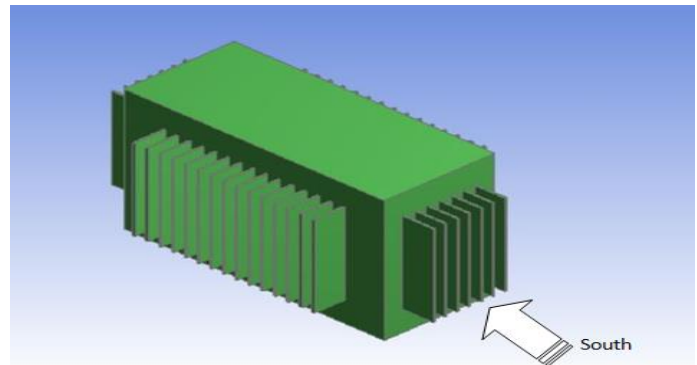


Fig. 5 The location (a) of power transformer.

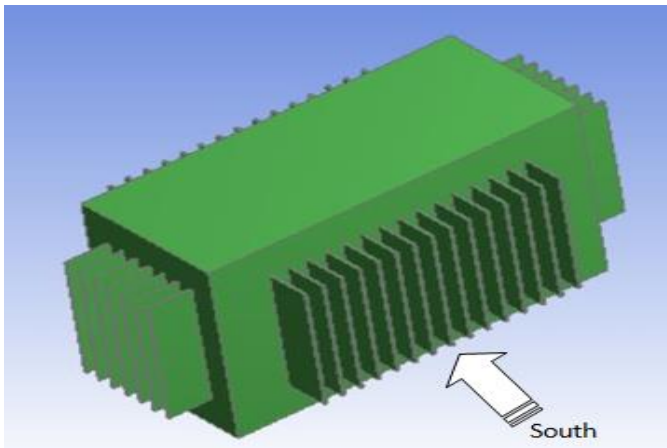


Fig. 6 The location (b) of power transformer.

B. Mathematical formulation of power transformer model:

The heat generated within the electrical power transformer is by windings (coils) and iron core due to power transformer load which transferred to the inner tank walls of power transformer by oil surrounded the interior parts of power transformer (natural convection) and then the created heat discarded from outer tank walls to ambient by radiators (convection and radiation).

The dominant equations (9, 10, and 11) for incompressible oil (constant oil density), steady state, and 3D, [14] and [15] are:

$$\nabla \cdot \vec{V} = 0 \quad (9)$$

$$\rho c_p (V \cdot \nabla T) = k \nabla^2 T \quad (10)$$

$$\rho (V \cdot \nabla \cdot \vec{V}) = -\nabla P + \nabla \cdot (\mu \nabla \cdot \vec{V}) + \frac{\rho - \rho_\infty}{\rho_\infty} g \quad (11)$$

The properties of the dielectric oil transformer can be computed as function to temperature in the relationships below [16]:

$$\rho(T) = 1098.72 - 0.712T \quad (12)$$

$$K(T) = 0.1509 - 7.101 \times 10^{-5}T \quad (13)$$

$$C_p(T) = 807.163 + 3.58T \quad (14)$$

$$\mu(T) = 0.08467 - 0.0004T + 5 \times 10^{-7}T^2 \quad (15)$$

IV. NUMERICAL MODEL

The numerical analysis used by using (FVM) finite volume method solved theoretical model by using (ANSYS17.1/FLUENT) code program. After that, the dominant equations (9, 10, and 11) are resolved. The governing equations can be solved by using the first order

upwind scheme while using the algebraic form to solve the segregation. The SIMPLE algorithm used to solve the continuity equation and analyzed velocity- pressure coupling case.

The convergence criterion utilized for the energy and momentum equation solution residuals to be less than 10^{-6} to guarantee a high precision in similes to power transformer actual specification.

The outer walls of electric power transformer are assumed to expose to coefficient of heat convection ($2 \text{ W/m}^2\text{K}$) and emissivity of 0.9 and the weather conditions and solar radiation of Nasiriya city in 1 August.

Table 2 shows the results of theoretical model mesh to obtain improved results from (ANSYS17.1/FLUENT) code program. The meshing number 8 is the better for accumulating the results because it come up to values of actual temperature.

TABLE 2
ATTEMPTS OF MESH TO ACCURACY OF THE RESULTS

| Attempt | No. of nodes | No. of elements | The value of max. oil temperature(OC) |
|---------|--------------|-----------------|---------------------------------------|
| 1 | 211885 | 139632 | 100.2 |
| 2 | 156365 | 101919 | 101.7 |
| 3 | 145106 | 99854 | 102.3 |
| 4 | 120056 | 91577 | 102.5 |
| 5 | 116345 | 88633 | 102.8 |
| 6 | 97579 | 70601 | 103.0 |
| 7 | 91866 | 62044 | 103.2 |
| 8 | 85215 | 53960 | 103.3 |

(11)

V. RESULTS AND DISCUSSION

The effect of solar arrays supplied directly on the electrical transformer body will affect the performance because it leads to raise the temperature of coils, core, oil, and body.

Fig.(7) shows the effect of solar radiation on power transformer in comparison with no-solar energy incident on two locations (transformer position direction).

These location are placed according to its direction to south-north or west-east which affect the solar intensity exerted on transformer. There is average difference between the maximum oil temperature without solar radiation and that for location (a) to be 4oC and 1.5 oC between the two locations (a and b) that due to the effect of solar radiation on the transformer. The ambient temperature is not affecting the oil temperature average difference among the three curves but the oil temperature increased with increasing ambient temperature proportionally ($26\text{-}54\text{ oC}$) where the maximum oil temperature for transformer without solar radiation at location a and b are:($123,127,$ and 128 oC respectively). While Fig.8 indicates the maximum temperature of coils and core of transformer for the same



three locations above without solar radiation at location a and b where the temperature difference is larger than that for oil because the oil dissipates the heat to outside quickly than the core and coil that are at the core of transformer (distance from atmosphere). The average temperature difference between (without solar radiation and location a) be 6oC, but between (location a and b) be 3oC. The effect of solar radiation on transformer core and coils temperature is very high 6oC for location a and 9oC for location b because of its direction. This ratio of increment is the same as that for oil ratio of positions. This increase in coils temperature may be leads to failure or damage to transformer especially at hot places or hot seasons which reaches to 158oC (fusion of many coils insulators).

Fig.9 depicted the effect of ambient temperature on oil thermal conductivity for the same previous locations. The thermal conductivity axiomaticly decrease with increasing the ambient temperature so the lower oil temperature has high thermal conductivity and vice-versa since the oil particles has short distance between them at low temperature which result high conductivity than that of wide distance at high temperature.

Fig.10 shows the variations of oil dynamic viscosity with and without solar radiation under effect of ambient temperature for both locations a and b. It is seen that the oil dynamic viscosity become identical at 54oC even there is a different in values of it. Therefore, the ambient temperature has a big effect on oil dynamic viscosity.

Fig.11 explained example of the work by using (ANSYS17.1/FLUENT) code program for section distribution of oil temperature and internal parts of power transformer.

By comparing the present work with Hasan's work, it will find that there are similarity in our findings with his results. However, the results of present work showing that temperature is less than the other researcher results for same software program as shown in fig.12.

Fig. 7 The maximum temperature of oil with and without solar radiation for location (a and b) with ambient temperature

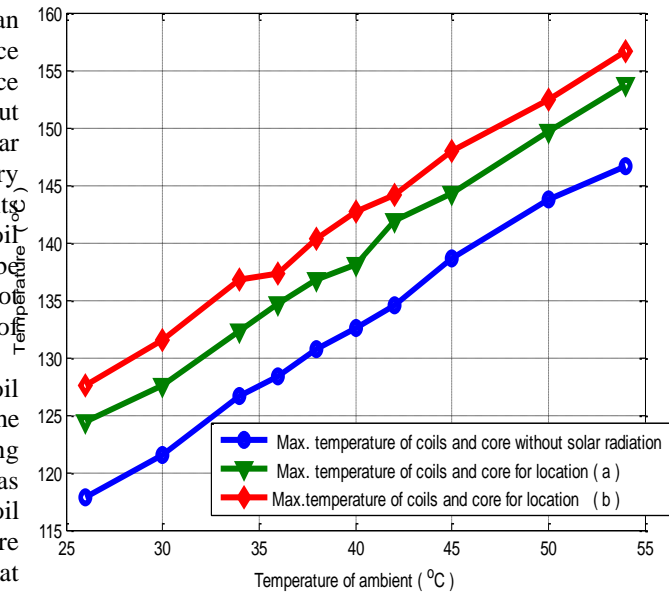


Fig. 8 Maximum temperature of coils and core with and without solar radiation for location (a and b) with ambient temperature.

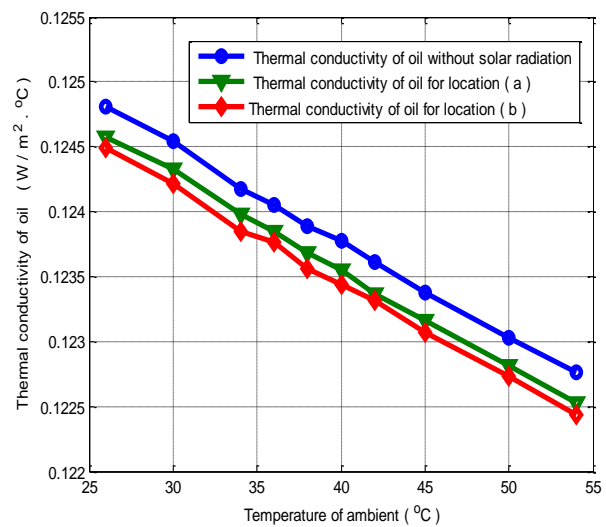


Fig. 9 Thermal conductivity of oil with and without solar radiation for location (a and b) with ambient temperature.

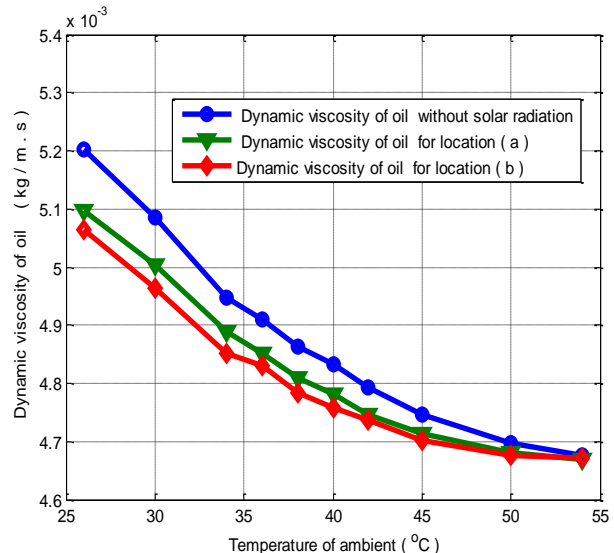
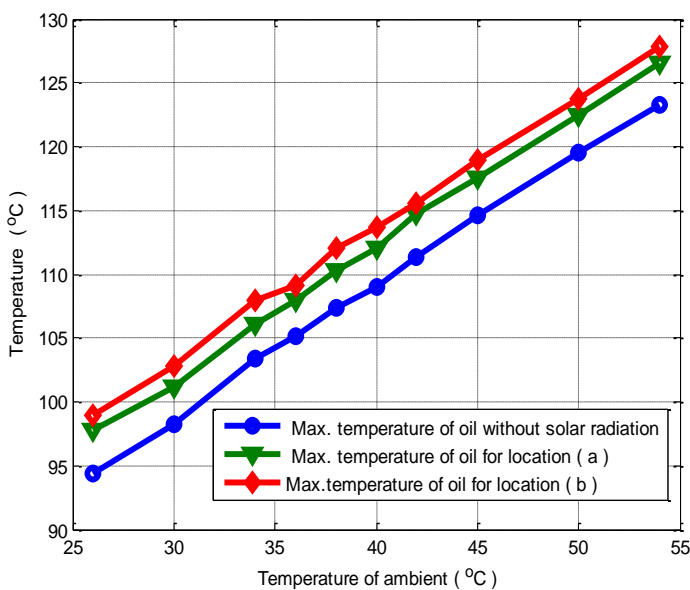


Fig. 10 Dynamic viscosity of oil with and without solar radiation for location (a and b) with ambient temperatur

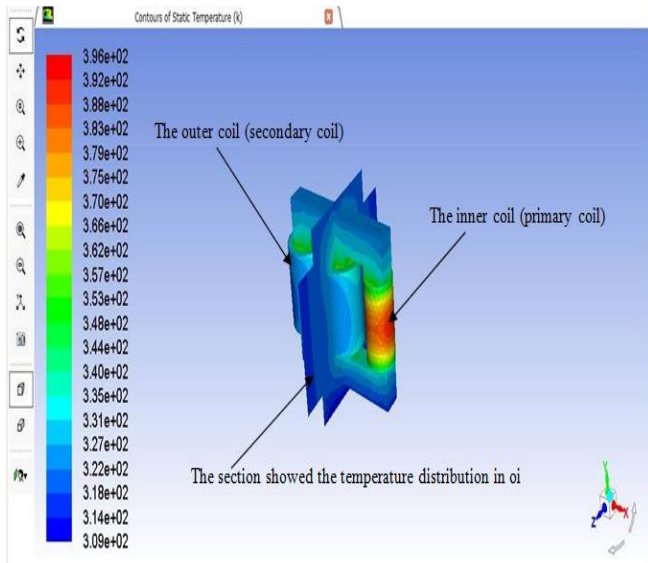


Fig. 11 internal parts of transformer and section of temperature distribution by using (ANSYS 17)

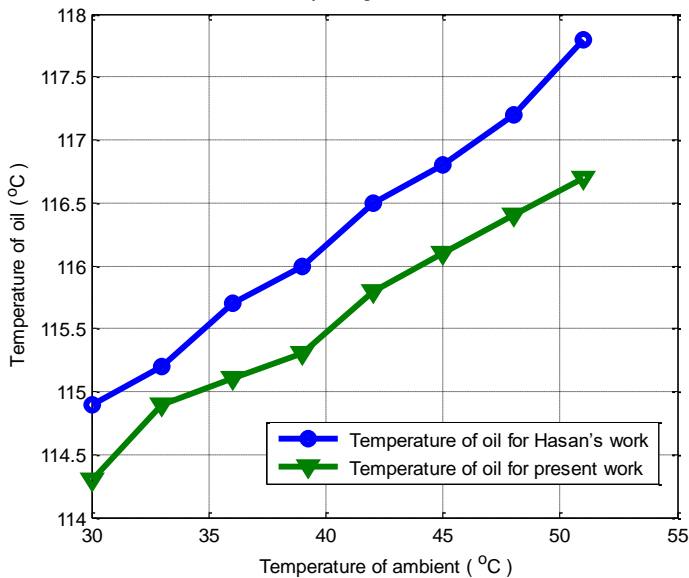


Fig. 12 The temperature of oil for Hasan's work [17]without solar radiation and temperature of oil for present work without solar radiation.

VI. CONCLUSION

The important conclusions by the previous results of paper are:

- 1) The location and direction of power transformer is very important.
- 2) The intensity of direct solar radiation affects the increasing temperature of the oil, coils, and core and oil thermal properties.
- 3) It is very important to take in to take in consideration the position and direction of electrical transformers at erecting them.

VII. REFERENCES

[1] Zhang, X., Wang, Zh., Liu, Q., Jarman, P., and Negro, M., "Numerical investigation of oil flow and temperature distributions for ON transformer windings", *Applied Thermal Engineering*, 130(2018), pp.1-9.

[2] Garelli, L., Rodriguez, G.R., Storti, M., Granata, D., Amadei, M., Rossetti, M., "Reduced Model for the Thermo-Fluid Dynamic Analysis of a Power Transformer Radiator working in ONAF mode", *Applied Thermal Engineering*, 124(2017), pp. 855-864.

[3] Fernández, I., Delgado, F., Ortiz, F., Ortiz, A., Fernández, C., Renedo, C.J., Santisteban, A., "Thermal degradation assessment of Kraft paper in power transformers insulated with natural esters", *Applied Thermal Engineering*, 104 (2016), pp. 129–138.

[4] Kondrashova, Yu.N., Khrumshin, R.R., Nikolaev, A.A., Shurygina, G.V., "Analysis of thermal state of power transformer of captive power plant", *International Conference on Industrial Engineering, Procedia Engineering* 129 (2015), pp. 832 – 838.

[5] Kim, M.g., Cho, S.M., Kim, J.K., "Prediction and evaluation of the cooling performance of radiators used in oil-filled power transformer applications with non-direct and direct-oil-forced flow", *Experimental Thermal and Fluid Science*, 44 (2013), pp. 392–397.

[6] Gastelurrutia, J., Ramos, J. C., Larraona, G. S., Rivas, A., Izagirre, J., and Río, L., "Numerical modelling of natural convection of oil inside distribution transformers", *Applied Thermal Engineering*, 31 (2011), 4, pp. 493-505.

[7] Taghikhani, M.A., and Gholami, A., "Prediction of hottest spot temperature in power transformer windings with non-directed and directed oil-forced cooling", *Electrical Power and Energy Systems*, 31 (2009), 7-8, pp. 356–364.

[8] Hosseini, R., Nourolah, M., and Gharehpetian, G.B., "Determination of OD cooling system parameters based on thermal modeling of power transformer winding", *Simulation Modelling Practice and Theory*, 16 (2008), 6, pp. 585–596.

[9] Practical specification of JOYSAN TURKISH TRANSFORMER .transformer final report. Power: 250KVA, serial number 14148, Date 14.01.2014. www.joysantransformator.com.

[10] Rai G.D. , "Solar Energy Utilization" (1987), Copyright by Khanna Publishers, Delhi , p. 295-309.



- [11] Anderson E.E., "Fundamentals of Solar Energy Conversion" 1983, Addison – Wesley Publishing Company , California, USA, 1983,p. 90-200.
- [12] Agnihotri O.P. and Gupta B.K. "Solar Selective Surfaces " , (1981), Awiley – Inter science Publication , New York, p. 58-115.
- [13] Sayigh A.A.M., "Solar Energy Engineering ",(1977),Academic Press, New York, p.p. 5-218.
- [14] Pop,I. I., Ingham,D. B., Convective Heat Transfer: "Mathematical and Computational Modelling of Viscous Fluids and Porous Media", Elsevier Science& Technology Books, Pergamon, 2010.
- [15] Inaba, H.,Zhang, Y.,Horibe, A., and Haruki,N., "Numerical simulation of natural convection of latent heat phase-change-material microcapsulate slurry packed in a horizontal rectangular enclosure heated from below and cooled from above", Heat Mass Transfer, 43 (2007),5,pp.459–470.
- [16] El Wakil,N.,Chereches,N.C., and Padet,J., "Numerical study of heat transfer and fluid flow in a power transformer", International Journal of Thermal Sciences, 45 (2006),6,pp. 615–626.
- [17] Hasan, M. I., "Using the transformer oil-based Nano fluid for cooling of power distribution transformer", International Journal of Energy and Environment,8 (2017), 3, pp.229-238.

A Novel Dual Injection Strategy to Improve the Performance of Ethanol Small Spark Ignition Engine

Nizar F.O. Al-Muhsen, Guang Hong

School of Mechanical and Mechatronic Engineering, University of Technology Sydney
15 Broadway, Ultimo, NSW, 2007, Australia

Abstract- Ethanol dual injection (DualEI) is a novel technology under development to maximize the benefits of ethanol fuel on spark ignition engines. In this study, the direct injection to port injection ratio was changed from DI0% (port injection only) to DI100% (direct injection only). Two engine speeds 3500 and 4000 were tested at light engine load. The maximum engine's output power and thermal efficiency of spark and direct injection timings (MBT) were experimentally investigated and determined at the light and medium engine loads. The results showed that the MBT timing for direct injection was 300 CAD bTDC, and for the spark timing was 30 CAD bTDC at the light load respectively. The IMEP was approximately constant when the DI ratio increased from DI0% to DI100%. The IMEP slightly increased from 0.47 to 0.50 MPa when the direct injection ratio is changed from DI0% to DI100%. However, the maximum combustion pressure was decreased by 8.32%, and volumetric efficiency was increased by 4.04%. This could be attributed to the combustion temperature reduced by the cooling effect enhanced by direct injection. The indicated specific carbon monoxide and hydrocarbons significantly increased due to the poor mixture quality caused by severe fuel impingement to combustion chamber walls. However, the indicated specific nitric oxides significantly decreased due to the cooling effect caused by the DI injection strategy. Results showed the potential of DualEI to increase the compression ratio and consequently to increase the engine thermal efficiency without any risk of knock and/or hardware limitations.

Index Terms— DualEI engine, DualEI Combustion, DualEI Emissions

I. INTRODUCTION

Emissions reduction and fuel economy improvement are the most common drivers of the internal combustion engine development. Moreover, the ever increasingly tightened regulations are enforced to reduce emissions produced by internal combustion (IC) engines. Compared to Euro 3, Euro 6 lowered the nitric oxide (NO), carbon monoxide (CO) and hydrocarbon (HC) emission limits by 60%, 57% and 50% for light-duty cars respectively [1]. These legislations are evident instances that highlight the significance of environmental protection. Ethanol fuel has been used widely as an alternative fuel to fossil fuel in engines to address the issue of sustainability [2]. Ethanol is a renewable fuel produced from a variety of bio-resources. Compared to gasoline, ethanol has a greater flame speed, octane number, and heat of vaporisation, and it provides a cleaner combustion [3]. Furthermore, the lower adiabatic flame

temperature and the greater cooling effect could result in lower combustion temperature and thus less convective heat losses [4]. Nevertheless, ethanol has lower heating value, which consequently increases the fuel consumption compared to gasoline. Slow evaporation rate is also reported to ethanol fuel at low ambient temperature [5].

Injection strategy is an important parameter to control the mixture formation processes inside the combustion chamber before combustion starts. Injecting fuel directly into the combustion chamber is an approach to improve the engine performance and reduce the pollutant emissions. The number of gasoline direct injection (GDI) engines in vehicles production continuously increase worldwide [6]. However, GDI technique comes with some drawbacks such as particular matter (PM) and greater hydrocarbon (HC) emissions due to fuel impingement [7]. Wang et al. [8] investigated the effect of fuel type and injection strategy on PM emissions produced from a GDI engine. They concluded that both the fuel type and direct injection (DI) conditions could affect the PM emissions. Using high DI pressure and ethanol fuel could potentially reduce the PM emissions. Greater injection pressure could produce finer droplets and less fuel impingement. Compared to gasoline, ethanol fuel could produce better combustion quality due to its greater combustion speed and oxygen content.

Blended fuels (e.g., ethanol-gasoline and ethanol-diesel blends) were extensively used in engine research [9, 10]. Bielaczyc et al. [10] tested a spark ignition (SI) engine under a wide range of ethanol-gasoline blending ratios from 5% to 85%. Their results showed that blended fuels had a significant effect on the engine performance and emissions. The combustion quality was enhanced due to the greater combustion speed combined with the oxygen component of ethanol fuel. The higher self-ignition temperature of ethanol associated with the greater latent heat of vaporisation of ethanol and research octane number could mitigate the engine knock. Greater ethanol percentages were commonly used in Brazil and United States aiming to reduce the depletion of fossil fuels and improve the engine performance [11, 12]. The effect of E85 on the SI engine performance was investigated [13-16]. Although ethanol is considered as an environmentally safe fuel due to its green production to consumption cycle, adopting ethanol fuel as an alternative fuel to fossil fuel such as gasoline could come with significant challenges [17]. Lower vapor pressure and heating value of ethanol are possible challenges for implementing ethanol fuel to SI engines [18]. As a result, flex-fuel systems were widely used as an auxiliary system to help engine cold starting by using gasoline fuel [19]. Nakata et al. and Taniguchi et al. [20, 21] from Toyota Motor Company investigated the feasibility of running the SI engine with ethanol fuel only. They concluded that ethanol



could improve the engine thermal efficiency due to the greater octane number and cooling effect compared to the standard unleaded gasoline. It was reported that 100% ethanol direct injection (EDI) could significantly improve the engine performance and reduce the NO emission [11, 22]. However, the over cooling effect and high fuel impingement of pure EDI were represented as possible issues to the SI engines [23].

Zhuang et al. [24, 25] investigated the merits of the EDI on a gasoline port injection (GPI) engine. It was reported that the combustion performance was significantly improved when EDI was used. Huang et al. analysed the combustion process numerically to the same project [5, 23]. Their results showed that the engine performance slightly improved due to injecting a certain amount of ethanol directly into the combustion chamber. Further increase in the EDI ratio over 60% could deteriorate the combustion quality due to the ethanol impingement and the over cooling effect. The greater laminar flame speed combined with oxygen content helped in enhancing the combustion quality. A significant reduction in the NO_x emission occurred due to the ethanol lower adiabatic flame temperature and the cooling effect of the EDI. However, HC and CO emissions increased considerably. This was because the rich mixture regions created inside the combustion chamber when the EDI was used. This was attributed to the ethanol film formed on the combustion chamber walls caused by the ethanol impingement. Zhu et al. [26] tested the effect of different ethanol-gasoline dual-injection techniques on the combustion characteristics. GPI plus EDI and ethanol port injection plus gasoline direct injection (EPI+GDI) strategies were included. The best combustion performance was recorded at GPI+EDI that the indicated mean effective pressure (IMEP) increased by 2% at light engine load.

As discussed above, adopting biofuel such as ethanol presents new challenges to the engine development. Although different technologies have been used recently to exploit the benefits of ethanol, the fossil fuel like gasoline is still the main fuel for internal combustion engines. Dual ethanol injection (DualEI) is a new technology under development aiming to exploit the benefits of using pure ethanol to SI engines. This paper aims to investigate the combined effect of DI and spark timings on the engine performance and fuel economy of a naturally aspirated SI engine equipped with a DualEI system.

II. EXPERIMENTAL SETUP AND PROCEDURE

A. Engine Setup

The experiments were performed on a modified Yamaha YBR250 motorcycle engine as shown in Figure 1. The YBR250 engine is a single cylinder four-stroke air-cooled naturally aspirated SI engine. Table 1 shows the major specifications of the research engine. The engine was originally equipped with a GPI system before it was modified to be equipped with a DualEI system by Hents Technology to meet the research needs. The engine modification included the installation of a direct fuel injection system and an electronic control unit (ECU) which was used to control the throttle position, spark timing, DI

timing and pressure and the quantity of fuel injected per cycle. The direct fuel injection system comprised of a returnless high-pressure pump and a six-hole high-pressure injector [27]. The injector was side mounted between the intake valve seat and the spark plug [25]. The slope angles of the injector are 15° from the horizontal surface of the cylinder head to the axis of the injector and 12° from the vertical surface of the cylinder head. Table 2 shows the major specifications of the injector. More details about the nozzle plume bend angles and their distribution can be found in [18]. A super-micro oval fuel flow meter with ±5 ml accuracy was used to measure the ethanol fuel flow rates of port and direct injections. An eddy current dynamometer was used to control the engine speed and measure the torque. A Kistler 6115B spark plug pressure transducer and a Kistler 5011 charge amplifier were used to recording the in-cylinder pressure. K-type thermocouples were used to measure the cylinder head temperature and exhaust gas temperature with a resolution of 0.1 °C and uncertainty of 0.35%. A MEXA-584L Horiba exhaust gas analyser was used to measure the exhaust gas emissions of CO, CO₂, HC, NO and lambda (λ). The H/C and O/C ratios were manually set in the exhaust gas analyser to be 3.0 and 0.5 respectively. The intake airflow was stabilised in an 80L intake buffer tank, and the intake air flow rate was measured using a ToCeil20N thermal air-mass flow meter.

Table 1. Specifications of the Dual Ethanol Research Engine

| | |
|---------------------------|---------------------------------|
| Engine Type | Single Cylinder, 4-stroke, SOHC |
| Displacement | 249.0 cc |
| Bore | 74.0 mm |
| Stroke | 58.0 mm |
| Compression Ratio | 9.8:1 |
| Intake Valve Open (IVO) | 382.2 CAD bTDC |
| Intake Valve Close (IVC) | 126.2 CAD bTDC |
| Exhaust Valve Open (EVO) | 594.6 CAD bTDC |
| Exhaust Valve Close (EVC) | 340.7 CAD bTDC |

B. Experimental Procedure

The research engine was started and warmed up using gasoline fuel port injection (GPI) until the cylinder head temperature became stable at around 200 °C. Then GPI was switched to ethanol port injection, and the air/fuel ratio was kept at the stoichiometric point. Table 3 shows the tested engine operating conditions. The volumetric ratio (DI%) of the ethanol DI to ethanol port injection was changed from DI0% (port injection only) to DI100% (100 direct injection) at light load (20% throttle position). The DI timing and spark timing were experimentally investigated and set at the maximum output power [28]. The spark timing was set at 30 CAD bTDC, the DI timing was set at 330 CAD bTDC.

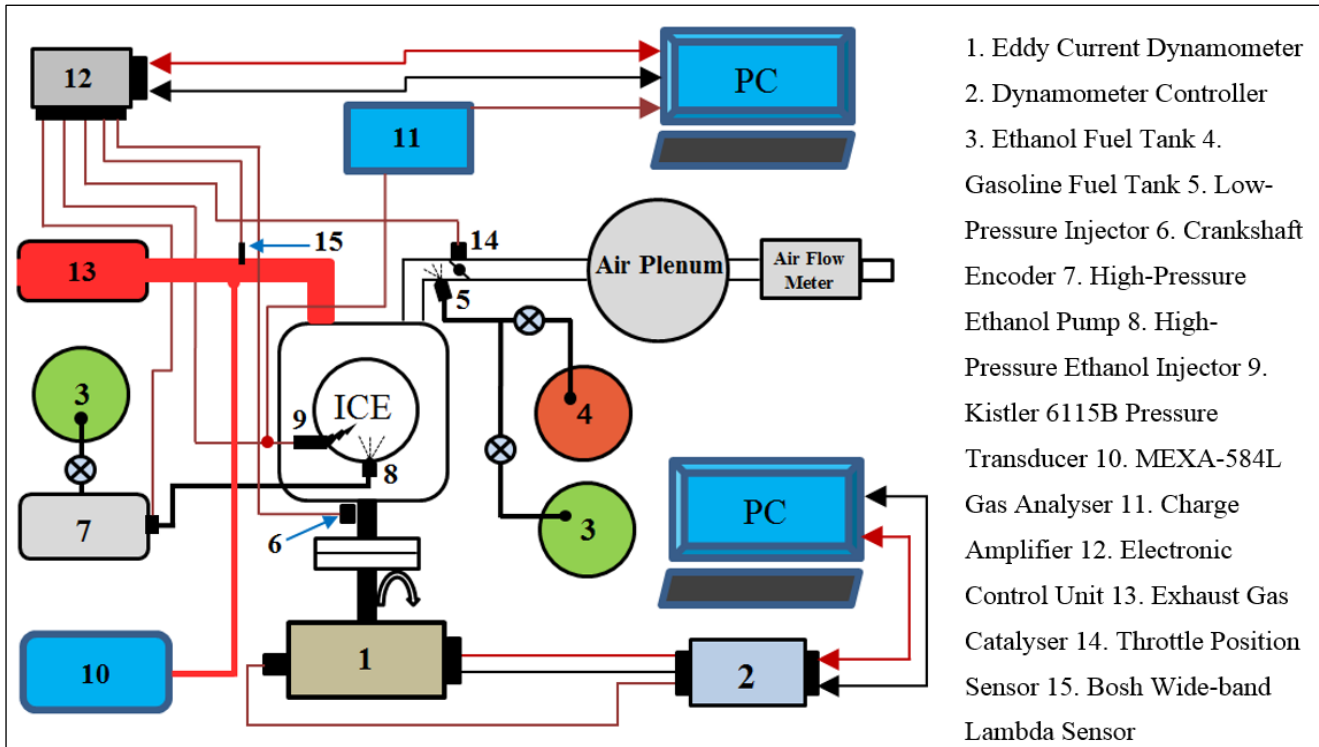


Figure 1. Dual Ethanol Research Engine.

The air/fuel equivalence ratio (λ) was kept at around the stoichiometric condition ($\lambda=1$) and the engine speed at around 3500 and 4000 RPM. A LabVIEW code was home-developed to record the engine data at each tested engine operation condition. Five samples were recorded at a sample rate of 1 Hz, and the average values were used in the calculations and analyses. The in-cylinder pressure data was recorded independently at 0.5 crank angle degree resolution with 100 consecutive cycles in each sample. The ensemble average of the cylinder pressure data was used in analysing the engine performance, and the combustion characteristics. The maximum standard deviations of the measurements were 6.8% for ISCO, 7.1% for ISNO and 3.7% for ISHC, which showed an acceptable quality of the experimental data.

Table 2. Experimental Operating Conditions

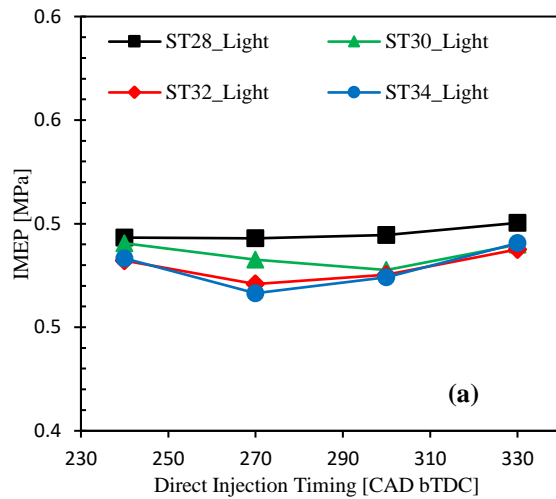
| | |
|----------------------------|------------------------------|
| Engine Loads | Light (20% throttle opening) |
| Engine Speed | 3500 and 4000 (RPM) |
| Spark Timing | 30 CAD bTDC |
| DI% (Volumetric ratio) | From DI0% to DI100% |
| Port Fuel Injection Timing | 410 CAD bTDC |
| Direct Injection Timing | 330 CAD bTDC |

III. RESULTS AND DISCUSSIONS

The experimental results will be presented and discussed as follows. Section 3.1 reports the optimum DI and spark timings to the IMEP and indicated thermal efficiency of the DualEI engine. The combustion characteristics will be analyzed and discussed to understand the mechanism behind the change in the engine performance. In Section 3.2, the results of the optimized DI and spark timings to emissions

will be discussed and analyzed. Sections 3.3 and 3.4 will analyze and discuss the effect of DI ratio on the engine performance, combustion and emissions.

A. Effect of DI timing on engine performance



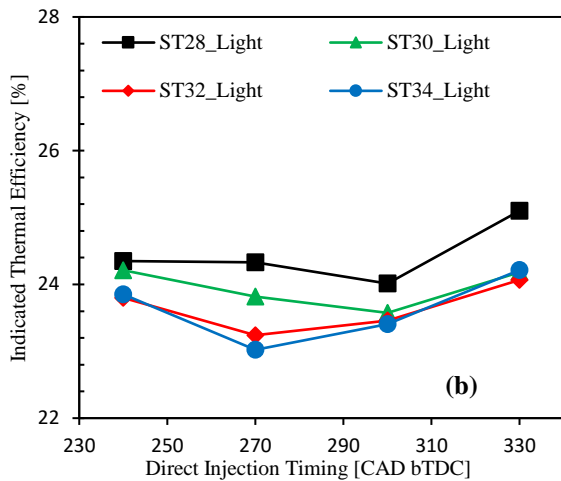


Figure 2. Variation of IMEP (a) and indicated thermal efficiency (b) with the DI and spark timings.

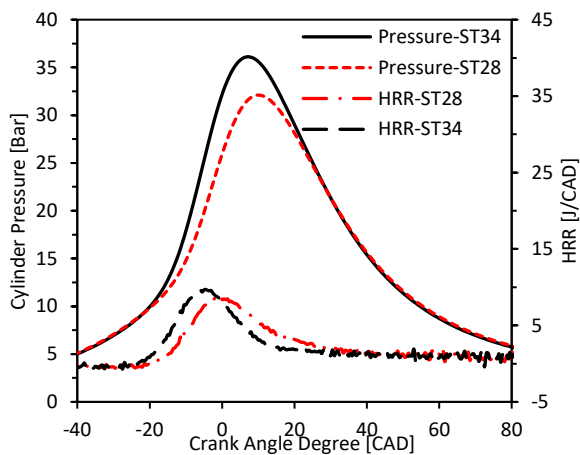


Figure 3. Cylinder pressure and HRR vs. spark timing at DIT330.

Figure 2 (a) shows the effect of the DI timing on the IMEP of the DualEI engine at different spark timings and two engine loads. The fuel heating value per cycle was fixed at around 420 J/cycle, and the load was light load. As shown in Figure 2 (a), except ST28, the IMEP slightly decreases when DI timing is advanced from DIT240 to DIT300 due to the greater fuel impingement caused by smaller cylinder volume when DI timing is advanced. Further advance to the DI timing to DIT330 slightly increases the IMEP. Although, at ST28, the IMEP increases with the advanced DI timing from DIT240 to DIT330, the emissions are greater than the ST30 which is selected to be MBT timing. This performance could be attributed to the longer time available for ethanol-air mixture to mix before the combustion start. The maximum increment of IMEP is 1.43% at spark timing of ST28 when the DI timing is advanced from DIT240 to DIT330. The small percentage of improvement might be attributed to the greater fuel impingement at the DIT330 caused by the smaller volume of the combustion chamber compared to that at DIT240. However, the hot residuals and combustion chamber walls might significantly enhance the evaporation rate resulting in this slight improvement in the IMEP. It was reported that the DI and spark timings worked interactively together on enhancing the mixture quality and then combustion quality [28]. As shown in Figure , advancing the spark timing increases the in-cylinder

pressure and then the temperature, which could promote the evaporation rate of ethanol spray droplets, leading to the improved ethanol/air mixture quality [29].

Figure 2 (b) shows the effect of the DI timing on the engine thermal efficiency at different spark timings and two engine loads. As shown in Figure 2 (b), the indicated thermal efficiency decreases with the advanced DI timing from DIT240 to DIT300 at different spark timings. This may be attributed to the rich air/fuel regions created by the ethanol fuel impinged on the combustion chamber walls, increasing the ethanol film formation on cylinder walls [23]. However, the engine thermal efficiency increases with the DI timing further advanced from DIT300 to DIT330. This may be because advancing the DI timing to DIT330 provides more time for the fuel to be evenly mixed with air. Moreover, injecting fuel directly after the exhaust valve closed might help ethanol fuel to utilise the high temperature of the cylinder walls and the residual burnt gases. This may promote ethanol's evaporation rate inside the cylinder and thus enhance the mixture's and combustion's quality. Furthermore, at DIT330, the fuel is injected at the beginning of the intake stroke when the intake valve is almost fully opened, and flow velocity of inlet air-fuel mixture is faster compare to DIT240. This may enhance the vapor pressure of ethanol, and thus promote the mixing process with air. In addition, as a result of a cooling effect caused by DI strategy, the fresh mixture temperature can decrease significantly due to early DI timing, resulting in greater engine's volumetric efficiency and consequently greater engine's thermal efficiency [24].

B. Effect of DI Timing on Emissions

The effect of DI timing on the ISCO at different spark timings is shown in Figure 4 (a). As shown in Figure 4 (a), the ISCO increases when the DI timing is advanced from DIT240 to DIT300. This could be attributed to the sever fuel impingement to the combustion chamber walls caused by smaller combustion chamber volume when the DI timing is advanced. Strong fuel impingement could result in fuel film regions which are rich, and have a slow vaporisation speed [31]. However, the ISCO emission sharply reduces when the DI timing is further advanced to DIT330. This might be because the directly injected fuel is taking the advantages of the hot residuals and hot combustion chamber walls since the DI takes place just 10.70 CAD after exhaust valve closed. This might increase the fuel vapor pressure, and accelerate the evaporation rate of ethanol droplets inside the cylinder [30-32]. Compared to DIT240, the ISCO is increased by up to 100% at DIT300, but it significantly decreases by 50% at the DI timings of DIT330 for the ST30. The ISCO results could partly explain the IMEP and indicated thermal efficiency improvement improvement, as shown in Figure 2. Similarly, the ISHC increases when the DI timing is advanced from DIT240 to DIT300, and then it slightly decreases when the DI timing is further advanced to DIT330 , as shown in Figure 4 (b). The ethanol fuel film formation caused by fuel impingement due to DI strategy is possibly the main reason behind this increment. The wall wetting effect becomes more significant when the DI timing is advanced to the CAD where the combustion chamber volume is relatively smaller at DIT330 compared to that at

DIT240. Nevertheless, the early DI timing provides more time for the spray's droplets to complete the evaporation process before the ignition timing. Moreover, the recycled hot residuals might increase the vapour pressure of the droplets, which is helping in completing of air-fuel homogenization. In addition, the combustion chamber walls, which is still warm, could enhance the evaporation of the impinged fuel. Consequently, better mixture quality can be achieved and thus better combustion performance. This might partly explain the significant reduction in the ISCO emission and the increment in the ISNO emission when DI timing was swept from DIT300 to DIT330 as shown in Figure 4 (a) and (c). Although advanced spark timing may remarkably accelerate the rate of evaporation due to greater cylinder pressure and HRR, as shown in Figure 3, it significantly reduces the time available for mixing process to be completed before the combustion starts. Consequently, the ISCO, ISHC and ISNO increase with advanced spark timing as shown in Figure 4. At DIT330, the ISCO, ISHC and ISNO increase by ??%, ??% and ??% respectively when the spark timing is advanced from ST19 to ST25. Similarly but with less significant, at light load, the ISCO, ISHC and ISNO slightly increase with advanced spark timing.

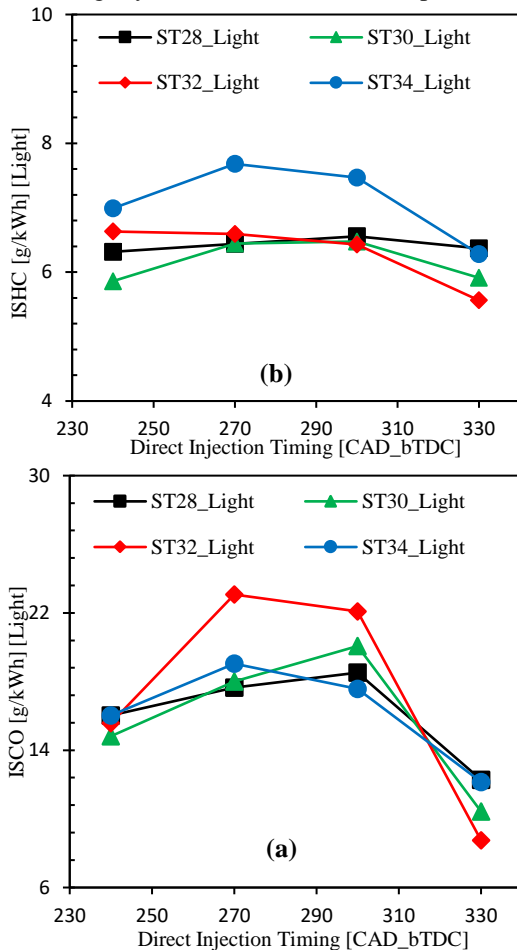


Figure 4. Variation of ISCO (a), ISHC (b) and ISNO (c) with an early DI and spark timings.

C. DualEI Engine Performance at the MBT timing

The experimental results and analysis in Sections 3.1 and 3.2 show that DI and spark timings significantly affect the DualEI engine performance, combustion and emissions characteristics. It was found that the DIT330 show superior engine performance than that of DIT240 at the same engine operating conditions and input heating value. The best possible output power for the minimum produced emissions are recorded at DI timing of DIT330 CAD bTDC and spark timing of ST30 , (MBT timing), for the light engine load. This section will evaluate the engine performance at that MBT timing.

Figure 2 (a) shows the effect of DI ratio on IMEP of the DualEI engine at the MBT timing. As shown in Figure 2 (a), the IMEP is slightly affected by the ratio of DI. The IMEP increases from 0.47 to 0.50 MPa when DI ratio is changed from DI0% (100% port injection) to the DI100% (100% direct injection). This is possibly because a constant heating value is provided at all DI ratios. Moreover, ethanol fuel properties might have a significant role in the IMEP improvement rather than the DI strategy in the DualEI engine [22]. On the other hand, the Pmax significantly reduces by about 8.32% when DI ratio increases from DI0% to DI100%, as shown in Figure 2 (b). Furthermore, the engine volumetric efficiency increases by about 4.04% when DI ratio is increased from DI0% to DI100%, as shown in Figure 2 (c). These results might be attributed to the cooling effect of the DI strategy associated with the great latent heat of vaporisation of ethanol fuel. Injecting fuel directly into the cylinder might allow the fuel droplets to absorb more heat from the gas inside the combustion chamber instead of the intake port, and thus reduces the mixture temperature significantly. This can be shown in Figure 2 (b) when the combustion pressure significantly reduces with the DI ratio while the IMEP remains almost the same, as shown in Figure 2 (a). The combustion pressure reduction might significantly reduce the combustion temperature when the DI ratio is increased. The mechanism behind the combustion temperature reduction caused by ethanol DI strategy was numerically investigated and explained in reference [5]. As a result, a significant Pmax reduction at approximately constant IMEP could provide more room to increase the intake pressure and thus improve the engine output power. Moreover, a great possibility of

implementing the engine downsizing concept to the DualEI engine with less possible hardware limits caused by high combustion pressure, temperature and knock. Furthermore, as shown in Figure 2 (d), the coefficient of variation of IMEP for all conditions is less than 4%, which is in the accepted range of the combustion stability [33].

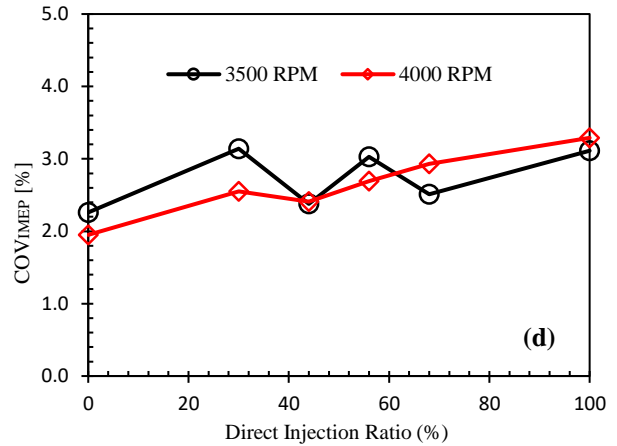
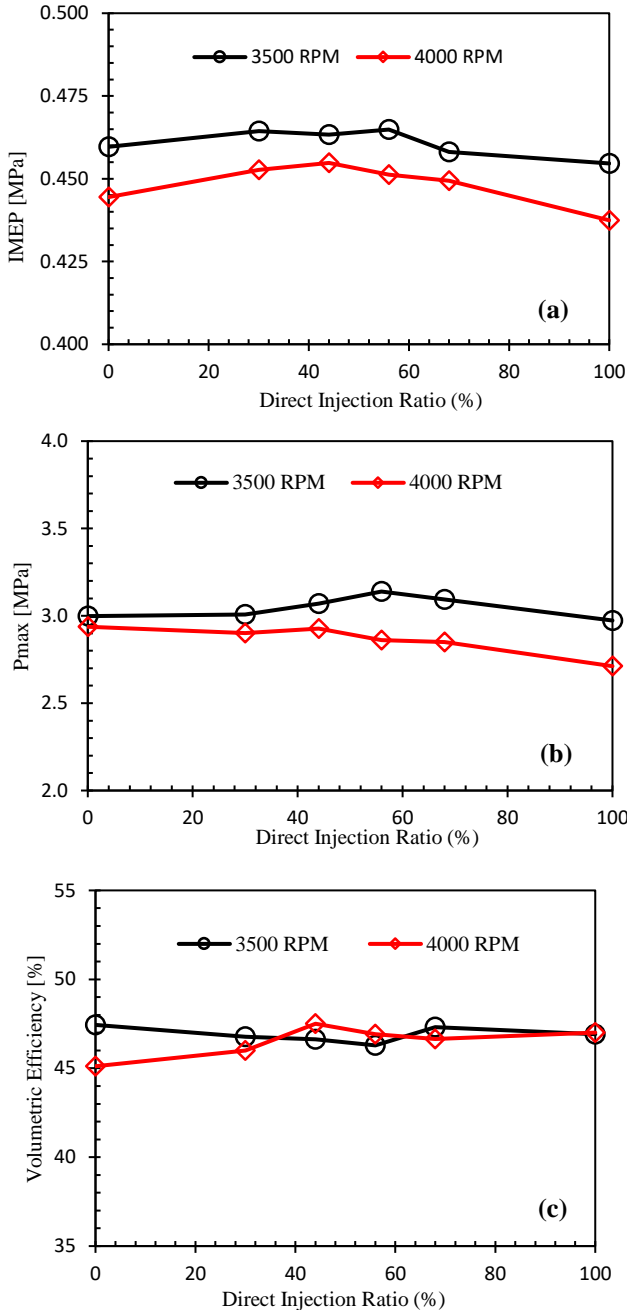


Figure 2. The IMEP (a), Pmax (a), Volumetric Efficiency (c) and COV_{IMEP} (d) variation with the DI ratio.

The ISCO and ISHC emissions results show that they are much smaller in the early DI timing than that of the late DI timing. On the other hand, late DI timing shows better ISNO performance than that of early DI timing. The emissions reduction might be attributed to three main reasons. Firstly, at early DI timings, the first DI (DIT330) is started at 52.2 CAD after the inlet valve is opened. Consequently, the intake flow rate is fast contributes significantly to accelerating fuels' evaporation and mixing processes. Secondly, the sufficient time available to fuel at early DI timing to be evenly mixed with air. Lastly, early-injected fuel might take the advantages of the high exhaust gas temperature that internally recycled. Figure 3 (a) and (b) show the variation of the ISCO and ISHC with the DI ratio from DI0% to DI100% at MBT timing. The fuel impingement becomes noticeable when DI ratio is increased from DI0% to DI100%. This might be attributed to greater penetration of the DI spray caused by greater DI width. [34]. Consequently, the poor air-fuel mixture distribution, sever fuel impingement and overcooling effect might lead to increase the ISCO and ISHC emissions when the DI ratio is increased from DI0% to DI100%. Figure 3 (c) shows the potential ISNO reduction with increased DI ratio from port injection only to 100% DI operating condition. The significant reduction in combustion pressure and temperature contributes considerably to the ISNO decrement when the DI ratio is increased to DI100%.

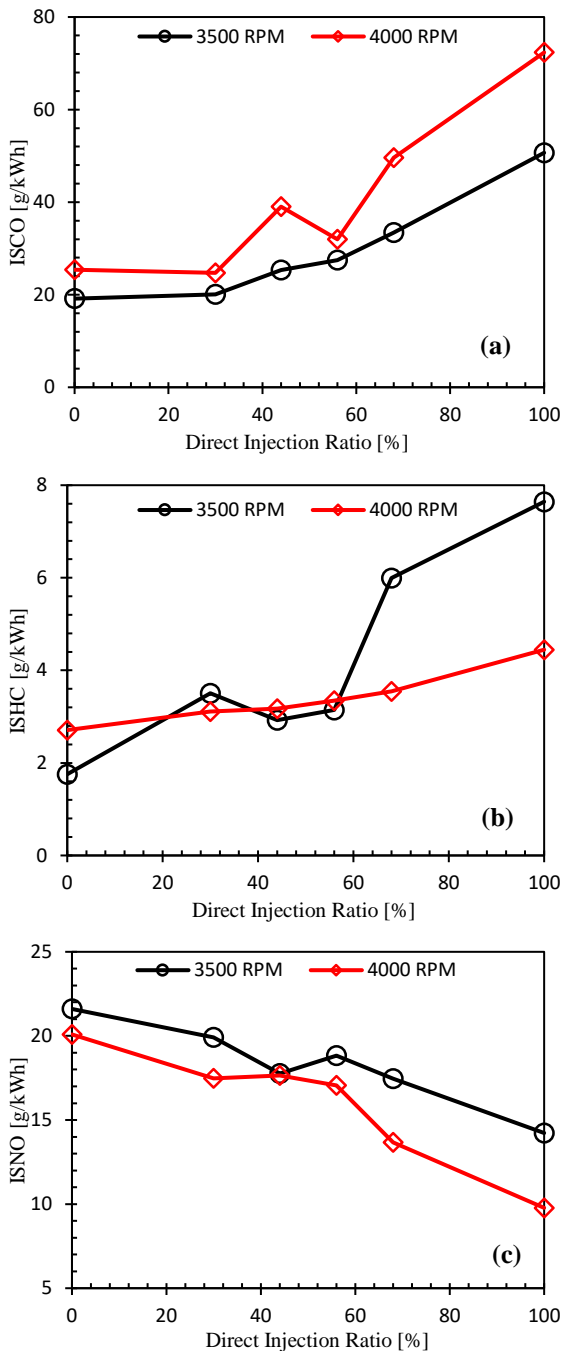


Figure 3. The ISCO (a), ISHC (b) and ISNO (c) variation with the direct injection ratio.

IV. CONCLUSIONS

Experiments were carried out to investigate the effect of DI timing on the performance of a naturally aspirated SI engine equipped with a DualEI system. At 3500 RPM, DI timing was varied from DIT60 to DIT120 as a late DI timing and from DIT240 as an early DI timing. At each DI timing, the spark timing was varied from ST28 to ST34 for the light load and from ST19 to ST25 at the medium load. The effect of the DI and spark timings on the combustion and emissions characteristics was presented and analysed. The DI timing and the spark timing (MBT timing) that produce the maximum output power while the minimum emissions were used to investigate the effect of DI ratio on

the DualEI engine. The results of this study can be concluded as follows.

- (1) The engine performance was improved with early DI timing compared to late DI timing for most of the spark timing and both engine loads. The IMEP was slightly affected when the early DI timing was advanced from DIT240 to DIT330. However, the combustion phasing (CA50) was significantly enhanced with the advanced DI timing. On the other hand, at the late DI timing, IMEP and engine thermal efficiency were significantly affected when DI timing was advanced from DIT60 to DIT120. Moreover, the combustion duration (CA0-10% and CA10-90%) significantly reduced, and the HRR (J/CAD) noticeably increased with advanced DI timing.
- (2) The spark timing interactively worked with DI timing in improving the DualEI engine performance. Correspondingly, Pmax [MPa] and HRR [J/CAD] increased with advanced DI and spark timings, but this increment is more noticeable at an early DI timing than late DI timing.
- (3) The emissions were significantly affected by the early and late DI timings. The ISCO and ISHC emissions were remarkably increased when DI timing was advanced from DIT240 to DIT330 and from DIT60 to DIT120. These results were mainly attributed to the increase of the fuel impingement of advanced DI timing.
- (4) The maximum output power for the minimum emissions was recorded at DI timing of DIT330 CAD bTDC and spark timing of ST30 and ST23 for the light and medium engine load respectively.
- (5) At the MBT timing, the IMEP was approximately constant when the DI ratio was increased from DI0% to DI100%. However, the combustion pressure was decreased when the DI ratio was increased. These results showed that there is a great possibility to implement the engine downsizing concept to the DualEI engine with fewer hardware limits caused by high combustion pressure, temperature and knock.
- (6) The ISCO and ISHC were significantly increased when the DI ratio was increased from DI% to DI100%. However, the ISNO was decreased with increased DI ratio caused by the increased DI ratio.

V. ACKNOWLEDGMENT

The scholarship provided by the Iraqi Ministry of Higher Education & Scientific Research is gratefully appreciated.

VI. REFERENCES

- [1] E.-L. A. t. E. U. law. (2007). *Regulation (EC) No 715/2007 of the European Parliament and of the Council of 20 June 2007 on type approval of motor vehicles with respect to emissions from light passenger and commercial vehicles (Euro 5 and Euro 6) and on access to vehicle repair and maintenance information (Text with EEA relevance) (OJ L 171, 29.6.2007, p. 1–16 (BG, ES, CS, DA, DE, ET, EL, EN, FR, GA, IT, LV, LT, HU, MT, NL, PL, PT, RO, SK, SL, FI, SV) Special edition in Croatian: Chapter 13 Volume 030 P. 284 - 299 ed.)*. Available: <http://data.europa.eu/eli/reg/2007/715/oj>



- [2] P. Bajpai, *Advances in Bioethanol*, 2013 ed. India: Springer New Delhi Heidelberg New York Dordrecht London, 2013.
- [3] B. M. Masum, H. H. Masjuki, M. A. Kalam, I. M. Rizwanul Fattah, S. M. Palash, and M. J. Abedin, "Effect of ethanol-gasoline blend on NO_x emission in SI engine," *Renewable and Sustainable Energy Reviews*, vol. 24, pp. 209-222, 2013.
- [4] R. D. Reitz, "Directions in internal combustion engine research," *Combustion and Flame*, vol. 160, no. 1, pp. 1-8, 2013.
- [5] Y. Huang, G. Hong, and R. Huang, "Numerical investigation to the dual-fuel spray combustion process in an ethanol direct injection plus gasoline port injection (EDI+GPI) engine," *Energy Conversion and Management*, vol. 92, no. 0, pp. 275-286, 3/1/ 2015.
- [6] Q. Jiao and R. D. Reitz, "The Effect of Operating Parameters on Soot Emissions in GDI Engines," 2015.
- [7] A. Montanaro, S. Malaguti, and S. Alfuso, "Wall Impingement Process of a Multi-Hole GDI Spray: Experimental and Numerical Investigation," 2012. Available: <http://dx.doi.org/10.4271/2012-01-1266>
- [8] C. Wang, H. Xu, J. M. Herreros, J. Wang, and R. Cracknell, "Impact of fuel and injection system on particle emissions from a GDI engine," *Applied Energy*, vol. 132, no. 0, pp. 178-191, 11/1/ 2014.
- [9] D. Turner, H. Xu, R. F. Cracknell, V. Natarajan, and X. Chen, "Combustion performance of bio-ethanol at various blend ratios in a gasoline direct injection engine," *Fuel*, vol. 90, no. 5, pp. 1999-2006, 2011.
- [10] P. Bielaczyc, A. Szczotka, and J. Woodburn, "The Effect of Various Petrol-Ethanol Blends on Exhaust Emissions and Fuel Consumption of an Unmodified Light-Duty SI Vehicle," 2011. Available: <http://dx.doi.org/10.4271/2011-24-0177>
- [11] A. Boretti, "Analysis of Design of Pure Ethanol Engines," 2010. Available: <http://dx.doi.org/10.4271/2010-01-1453>
- [12] R. C. Costa and J. R. Sodr , "Hydrous ethanol vs. gasoline-ethanol blend: Engine performance and emissions," *Fuel*, vol. 89, no. 2, pp. 287-293, 2// 2010.
- [13] C. J. H. a. T. G. L. Robert A. Stein and F. M. Company, "Optimal Use of E85 in a Turbocharged Direct Injection Engine," *SAE Int. J. Engines*, 2009.
- [14] M. Koç, Y. Sekmen, T. Topg l, and H. S. Y cesu, "The effects of ethanol-unleaded gasoline blends on engine performance and exhaust emissions in a spark-ignition engine," *Renewable Energy*, vol. 34, no. 10, pp. 2101-2106, 10// 2009.
- [15] M. Sj berg, W. Zeng, D. Singleton, J. M. Sanders, and M. A. Gundersen, "Combined Effects of Multi-Pulse Transient Plasma Ignition and Intake Heating on Lean Limits of Well-Mixed E85 DISI Engine Operation," *SAE Int. J. Engines*, vol. 7, no. 4, pp. 1781-1801, 2014.
- [16] P. Aleiferis, J. Serras-Pereira, Z. van Romunde, J. Caine, and M. Wirth, "Mechanisms of spray formation and combustion from a multi-hole injector with E85 and gasoline," *Combustion and Flame*, vol. 157, no. 4, pp. 735-756, 4// 2010.
- [17] S. Kumar, N. Singh, and R. Prasad, "Anhydrous ethanol: A renewable source of energy," *Renewable and Sustainable Energy Reviews*, vol. 14, no. 7, pp. 1830-1844, 9// 2010.
- [18] Y. Huang, S. Huang, R. Huang, and G. Hong, "Spray and evaporation characteristics of ethanol and gasoline direct injection in non-evaporating, transition and flash-boiling conditions," *Energy Conversion and Management*, vol. 108, pp. 68-77, 1/15/ 2016.
- [19] C. M. Engler-Pinto and L. de Nadai, "Volumetric Efficiency and Air-Fuel Ratio Analysis For Flex Fuel Engines," 2008. Available: <http://dx.doi.org/10.4271/2008-36-0223>
- [20] K. Nakata, S. Utsumi, A. Ota, K. Kawatake, T. Kawai, and T. Tsunooka, "The Effect of Ethanol Fuel on a Spark Ignition Engine," 2006. Available: <http://dx.doi.org/10.4271/2006-01-3380>
- [21] S. Taniguchi, K. Yoshida, and Y. Tsukasaki, "Feasibility Study of Ethanol Applications to A Direct Injection Gasoline Engine," 2007. Available: <http://dx.doi.org/10.4271/2007-01-2037>
- [22] N. Al-Muhsen, J. Wang, and G. Hong, "Investigation to Combustion and Emission Characteristics of the Dual Ethanol Injection Spark Ignition Engine," in *20th Australasian Fluid Mechanics Conference*, 2016.
- [23] Y. Huang, G. Hong, and R. Huang, "Investigation to charge cooling effect and combustion characteristics of ethanol direct injection in a gasoline port injection engine," *Applied Energy*, vol. 160, pp. 244-254, 12/15/ 2015.
- [24] Y. Zhuang and G. Hong, "Effects of direct injection timing of ethanol fuel on engine knock and lean burn in a port injection gasoline engine," *Fuel*, vol. 135, no. 0, pp. 27-37, 11/1/ 2014.
- [25] Y. Zhuang and G. Hong, "Primary investigation to leveraging effect of using ethanol fuel on reducing gasoline fuel consumption," *Fuel*, vol. 105, pp. 425-431, 2013.
- [26] G. Zhu, D. Hung, and H. Schock, "Combustion characteristics of a single-cylinder spark ignition gasoline and ethanol dual-fuelled engine," *Proceedings of the Institution of Mechanical Engineers, Part D: Journal of Automobile Engineering*, vol. 224, no. 3, pp. 387-403, 2010.
- [27] Y. Huang, S. Huang, P. Deng, R. Huang, and G. Hong, "The Effect of Fuel Temperature on the Ethanol Direct Injection Spray Characteristics of a Multi-hole Injector," *SAE Int. J. Fuels Lubr.*, vol. 7, no. 3, pp. 792-802, 2014.
- [28] N. F. O. Al-Muhsen and G. Hong, "Effect of Spark Timing on Performance and Emissions of a Small Spark Ignition Engine with Dual Ethanol Fuel Injection," presented at the SAE International Conference, 2017-01-2230, 2017.
- [29] C. L. Yaws, "Yaws' Handbook of Thermodynamic and Physical Properties of Chemical Compounds," ed: Knovel.

ABBREVIATIONS

| | |
|--------------------|---|
| bTDC | Before top dead centre |
| CAD | Crank angle degree |
| CA10-90% | The major combustion duration |
| CA0-10% | The minor combustion duration |
| CA50 | Combustion phase when 50% of the fuel is burnt. |
| DI | Direct fuel injection |
| DIT | Direct injection timing |
| DualEI | Dual ethanol injection |
| EDI+GPI | Ethanol direct injection plus Gasoline port injection |
| ETI | Early direct injection timing |
| EPI | Ethanol port injection |
| GDI | Gasoline direct injection |
| HRR_{MAX} | Maximum heat release rate |
| IMEP | Indicated mean effective pressure |
| ISCO | Indicated specific carbon monoxide |
| ISFC | Indicated specific fuel consumption |
| ISHC | Indicated specific Hydrocarbon |
| ISNO | Indicated specific nitric oxide |
| LIT | Late direct injection timing |
| MBT | Minimum spark advance for best torque |
| Pmax | Maximum cylinder pressure |
| ST | Spark timing |
| λ (Lambda) | Air/Fuel Equivalent ratio |

CONTACT INFORMATION

Nizar Faisal Odah Al-Muhsen
 School of Mechanical and Mechatronic Engineering
 University of Technology Sydney
Nizar.Al-Muhsen@student.uts.edu.au
Nizar91385@gmail.com

Guang HONG
 School of Mechanical and Mechatronic Engineering
 University of Technology Sydney
guang.hong@uts.edu.au



Numerical Investigation of Earth to Air Heat Exchanger for Cooling and Heating Applications

Mushtaq Ismael Hasan & Sajad Waleed Noori

Mechanical Engineering Department

College of Engineering, Thi-Qar University

Abstract- The earth to air heat exchanger (EAHE) is effective passive cooling and heating system for buildings. This paper studied numerically the effect of pipe material and wall thickness on the overall performance of EAHE. Two materials (PVC & steel) and three thicknesses (2, 3 and 6) are selected under the climate of Nasiriyah city in southern of Iraq. First the built numerical model was validated a gainst experimental model and the results of comparison showed good agreement. After the validation the overall performance of EAHE system was analyzed with ranges of air velocity, inlet temperature, pipe length of 50 m and 4 in (0.1016 m) pipe diameter. The simulation results showed that there is a less perfect in thermal performance for steel material but this perfect can be neglected compared with prices of materials.

NOMENCLATURE:

| | |
|------------|---|
| C_p | specific heat (J/kg.K) |
| k | thermal conductivity (W/m.K) |
| \dot{v} | volumetric flow rate (m^3/s) |
| \dot{m} | mass flow rate (kg/s) |
| T | temperature (K) |
| P | total pressure (Pa) |
| Q | heat transfer rate (W) |
| $P.P$ | pumping power |
| η^* | Performance factor |
| ΔP | total pressure drop across EAHE pipe (Pa) |
| X | horizontal coordinate (m) |
| Y | vertical coordinate (m) |

Z axial coordinate (m)

Greek Symbols:

ρ density (kg/m^3)
 μ dynamic viscosity (m^2/s)

Subscripts:

i inlet
 o outlet
 s surface of soil disturbed

I. Introduction

The need to reduce the consumption of energy for cooling and heating loads increased during past years. Energy saving can be reached by relying on renewable energies such as wind, solar and geothermal energy. Geothermal energy is a huge renewable energy source which can be used in wide range of applications such as, spaces heating and cooling, heating and cooling of water and generation of electricity. For cooling and heating buildings it can be dependent on the ground as a heat sink in summer and heat source in winter, where the soil temperature at certain depth from ground surface is relatively stable during the year and called undisturbed temperature. Undisturbed temperature is lower than outside air temperature in summer and higher in winter, and this can be accomplished by using Earth – Air Heat Exchanger (EAHE) also called ground heat exchanger.

Earth – air heat exchanger is a passive cooling and heating systems and it used in wide range of application such as cooling and heating greenhouse, residential and industrial buildings. EAHE is usually consists of pipe or multi-pipes buried in the ground horizontally or vertically. One end of the pipe is connected to the delivery end of blower and the other end is open to atmosphere Fig (1). When air flows through buried pipes, the heat is transfer from air to the surrounding soil during summer season and vice versa in winter.

Several researchers have described the earth-to-air heat exchangers (EAHE) coupled with buildings as an effective

passive energy source for building space conditioning such as: Vikas et al (2009, 2010) [1, 2] studied experimentally and numerically the effect of air velocity on the performance of EAHE. Their result obtained experimentally and numerically by using computational fluid dynamic showed that during winter and summer seasons the outlet air temperature enhanced with increasing air velocity. Sehli et al. (2012) [3] proposed a one-dimensional numerical model in South Algeria to investigate the performance of EAHE system installed at different depths. They concluded that EAHE systems alone are not enough to reach the comfort conditions, but it can be used to reduce the energy consumption in buildings when it used with conventional systems air-conditioning. Woodson et al (2012) [4] studied experimentally the performance of EAHE system in Burkina Faso at the hottest day with 39 °C outside air temperature. They used for this test 0.125 m pipe diameter, 25 m pipe length, 1.5 m depth of burial and 95 m³/h volume flow rate. They concluded from their results that with passing ambient air through EAHE system its temperature decreases by 7.6 °C compared with outside air temperature. Mohamed Khabbaz et al (2016) [5] presented a numerical and experimental study of an EAHE connected to residential building located in Morocco. Their experimental results showed that EAHX is a good semi-passive system for air refreshment, as the recorded blown air temperature into the building is quasi-constant at 25°C with air humidity around 40%, even though the outside temperature reaches more than 40°C. Furthermore, the reduction of daily and annual air temperature amplitudes is characterized by an exponential drop as a function of pipe length.

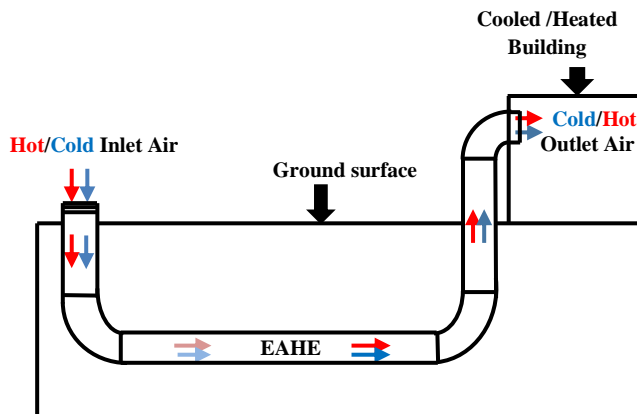


Fig. (1) schematic of EAHE system coupled with building

II. Problem description

The model studied in this paper is 3D EAHE system buried at depth of 3 m underground surface with inner pipe diameter of 4in (0.1016 m) and length of 50 m. Fig (2) shows the pipe of EAHE with thickness of disturbed soil. The materials were selected for study are steel and PVC which are available in the local market. The wall thicknesses studied were (2, 3 and 6 mm) which are selected according to the standard thickness of 4 in pipe diameter.

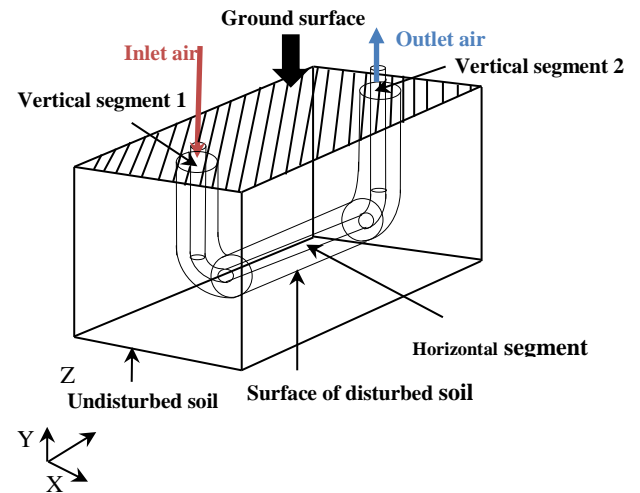


Fig. (2) schematic of the model studied of EAHE system.
A. Disturbed soil

The soil layer near surface of EAHE channel is affected by heat transfer and this soil called thermally disturbed soil Fig (3). There is no rule to calculate the thickness of disturbed soil, some researchers proposed that the thickness of disturbed soil equaled to the pipe radius [6], twice of pipe diameter [7], four times of pipe radius [8], and 10 times of pipe diameter [9], furthermore some studies found out that the effect of disturbed soil on performance of EAHE system can be decreased by running the system in summer and winter seasons [10]. In this paper the thickness of disturbed soil is equale to four times of pipe radiuse as used by [8].

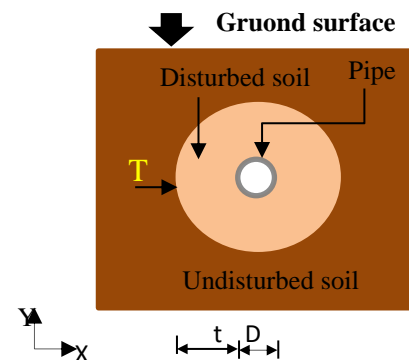


Fig. (3) Cross sections of EAHE pipe.

III. Mathematical model

The following assumptions were made during the development of mathematical model [9]:

- 1- Steady state & Turbulent flow.
- 2- Inlet velocity of flow is constant and uniform.

- 3- The soil is homogeneous and physical properties are constant.
- 4- The fluid is incompressible with constant specific heat, density and thermal conductivity.
- 5- There exists a perfect contact between the tube and the soil.

A. Governing equation

The following equations of fluid flow and heat transfer are used in this analysis [11].

Continuity equation:

$$\text{div } \vec{V} = 0 \quad (1)$$

Momentum equations

x.....dir.

$$\frac{\partial \bar{u}}{\partial t} + \text{div}(\bar{u} \bar{V}) + \text{div}(\bar{u}' \bar{V}') = -\frac{1}{\rho} \frac{\partial \bar{p}}{\partial x} + \nu \text{div}(\text{grad}(\bar{u})) \quad (2)$$

y.....dir.

$$\frac{\partial \bar{v}}{\partial t} + \text{div}(\bar{v} \bar{V}) + \text{div}(\bar{v}' \bar{V}') = -\frac{1}{\rho} \frac{\partial \bar{p}}{\partial y} + \nu \text{div}(\text{grad}(\bar{v})) \quad (3)$$

z.....dir.

$$\frac{\partial \bar{w}}{\partial t} + \text{div}(\bar{w} \bar{V}) + \text{div}(\bar{w}' \bar{V}') = -\frac{1}{\rho} \frac{\partial \bar{p}}{\partial z} + \nu \text{div}(\text{grad}(\bar{w})) \quad (4)$$

Energy equation

$$\frac{\partial uT}{\partial x} + \frac{\partial vT}{\partial y} + \frac{\partial wT}{\partial z} = \frac{k}{\rho c_p} \left(\frac{\partial}{\partial x} \left(\frac{\partial T}{\partial x} \right) + \frac{\partial}{\partial y} \left(\frac{\partial T}{\partial y} \right) + \frac{\partial}{\partial z} \left(\frac{\partial T}{\partial z} \right) \right) \quad (5)$$

For determining the overall performance of EAHE system the performance factor (η^*) is used which represents the ratio of heat transfer rate between air and soil to the pumping power required [12], [13], [14].

$$\eta^* = Q/p.p \quad (6)$$

Where:

$$Q = \dot{m} c_p \Delta T \quad (7)$$

$$P.p = \dot{v} \Delta P \quad (8)$$

Pressure drop: is the total difference in pressure between inlet section and outlet section of the channel of EAHE.

$$\Delta P = P_i - P_o \quad (9)$$

$$Re = \frac{\rho w D}{\mu} \quad (10)$$

$$Nu = \frac{h D}{k} \quad (11)$$

B. Boundary conditions

At inlet section of EAHE pipe the constant air velocity and constant inlet dry-bulb temperature (T_{in}) were used with subsonic and turbulent flow. The values of (T_{in}) which used as B.C were selected according to the Nasiriya city in south of Iraq for summer and winter seasons.

At outlet the relative pressure was taken equal to the atmospheric pressure.

At walls, the horizontal segment of EAHE pipe is in thermal contact with thickness of disturbed soil as in fig (1). At the outer surface of disturbed soil with distance ($t = 0.2032$ m) from pipe wall, the temperature is constant and equal to ($T_s = 26.3^\circ\text{C}$) which correspond to the temperature of undisturbed soil which was measured experimentally at depth of 3 m in south of Iraq [15].

While the two vertical segments were assumed thermally insulated.

IV. Numerical solution

The above governing equations are numerically solved using finite volume method. The flow is developing and the 3D continuity and 3D Navier stock equations are solved by using computational fluid dynamics modeling. To predict the turbulence inside the pipe, simple k- ϵ model with standard wall treatment is selected as turbulent model and energy equation is also solved since the computations included heat transfer. From CFD modeling the values of air flow characteristics can be obtained at large number of points in the EAHE system. These points are generally connected together in the form of numerical grid. To assess the quality of developed CFD model with high accurate solution the grid independent test was conducted. The solution is grid independent, if the mesh is refined (i.e. the cells are made smaller in size hence larger in number) and the results of solution were unchanged.

“Fig. 3,” shows that the solution is grid independent and there is no or minimum effect on the air temperature when grid size changed from mesh 1 to mesh 2 to mesh 3, therefore and for more accuracy the mesh 3 is used for all calculations.

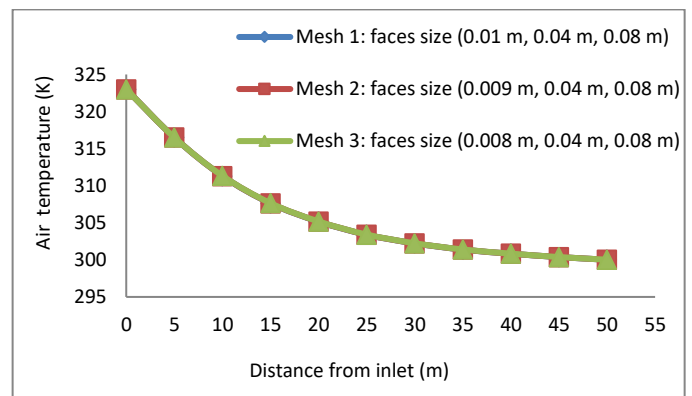


Fig. 3. Grid independent test

| | | | |
|-------|------|-----|----|
| Steel | 7833 | 465 | 54 |
|-------|------|-----|----|

V. Results and discussions

To check the validity of the built numerical model, a verification was made by solving the experimental and theoretical model presented in [2]. The same experimental and theoretical model which is presented in [2] is an EAHE system consists of a pipe with 0.15 m diameter, 23.42 m length, 2.7 m depth of burial and made up from PVC material. Air temperature of outlet EAHE system with three air velocity (2, 3 and 5 m/s) were measured with inlet air temperature of 43.7 °C and undisturbed soil temperature of 26.7 °C.

“Fig. 4,” shows the comparison between the simulation results of present model with the experimental and simulation results of [2] for variation of outlet air temperature with air velocity. From figure it can be seen that, the agreement between the simulation results of the present model with the experimental and simulation results of [2] is acceptable with the average error of 4% and 6.1% respectively. Therefore the present numerical model is reliable and can be used with adequate accuracy.

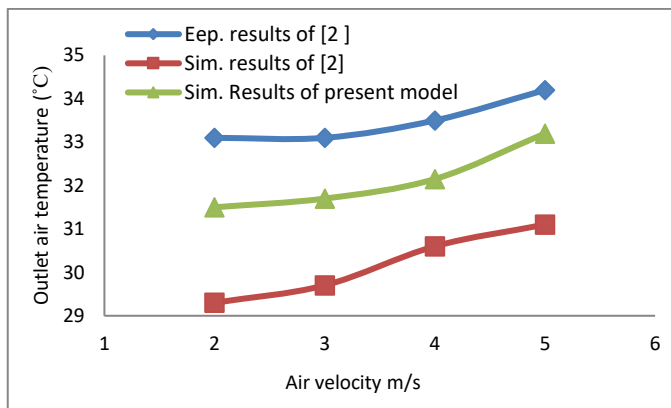


Figure 4. Outlet air temperature with air velocity as a comparison between present model with experimental and simulation results of [2].

The thermal and physical properties of air, soil and pipe material are assumed constant and their values are given in table (2).

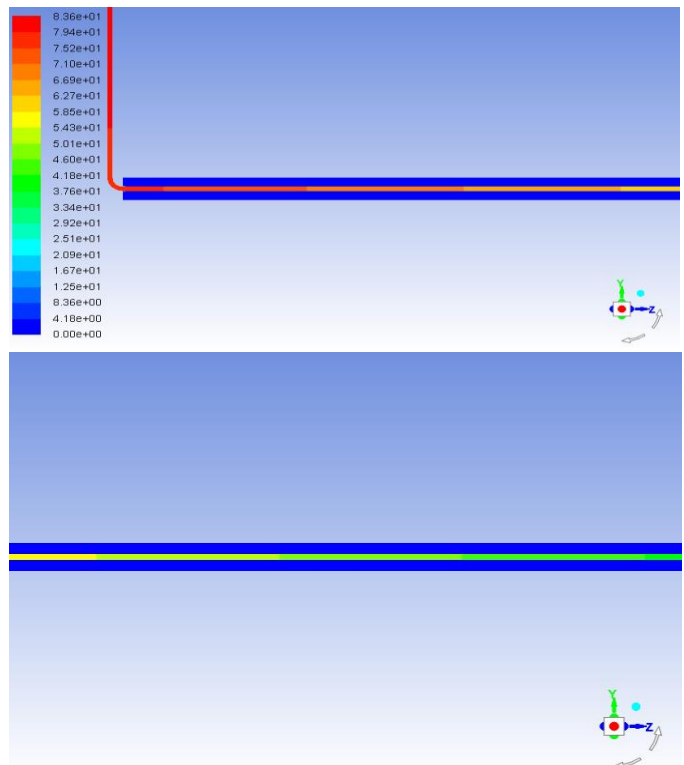
Table 2. The thermal and physical properties of the materials [15] [16].

| Material | Density (kg/m ³) | Specific heat (J/kg.°C) | Thermal conductivity (W/m.°C) |
|----------|------------------------------|-------------------------|-------------------------------|
| Air | 1.225 | 1006.5 | 0.0242 |
| soil | 1500 | 880 | 1.4 |
| PVC | 1380 | 900 | 0.16 |

A. The material effect

The simulation results of EAHE system when it is operating as a cooling system for summer seasons are presented in figures (5-17) and the results of heating are illustrated in figures (18-23). The results that show the effect of pipe material were done at 2 mm pipe wall thickness.

“Fig. 5,” indicates the pressure distribution through a pressure contour on longitudinal (y-z) plane at center of pipe (x=0) m at Reynold number of 20866.212 and inlet air temperature of 50 °C. For more clarity and to show full length of pipe this contour is divided into three parts. From this figure it can be noted that the pressure is decreased along the flow direction.



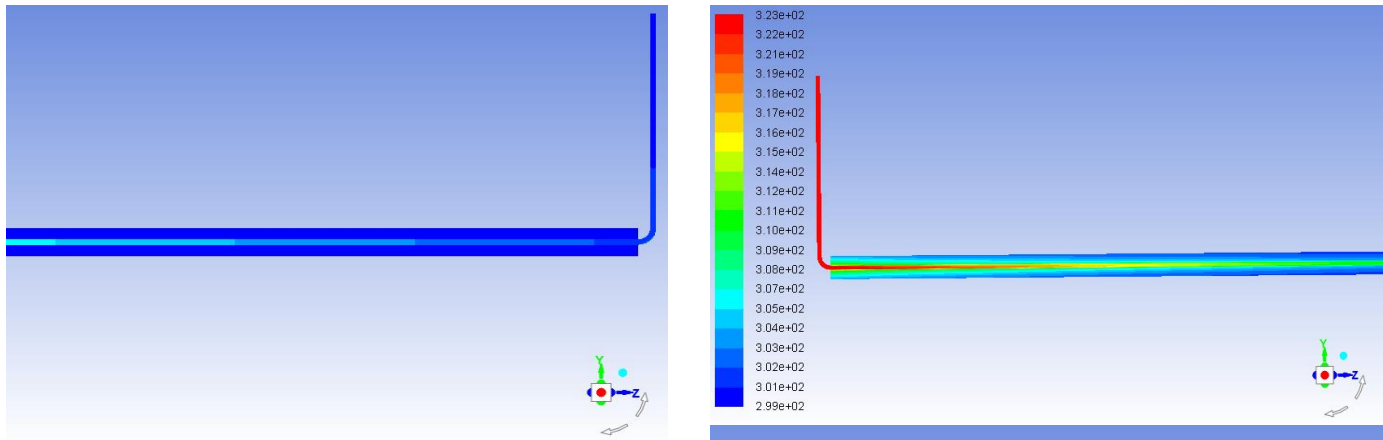


Fig. 5 pressure contour (pa) along length of EAHE pipe at Reynold Number of 20866.212

“Fig. 6,” illustrates the air temperature distribution through a temperature contour on longitudinal (y-z) plane at center of pipe ($x=0$ m) in EAHE system at Reynold number of 20866.212 and inlet air temperature of 50 °C. From this figure it can be seen that the air temperature decreased and the soil temperature increased along flow direction due to heat between pipe and soil. This decrease and increase for air and soil temperature respectively is sharp for the first 15 meters of length channel and became moderate afterword and this can be explained for the higher difference between air and soil temperature in the first meters of length channel which decreased with increasing the length.

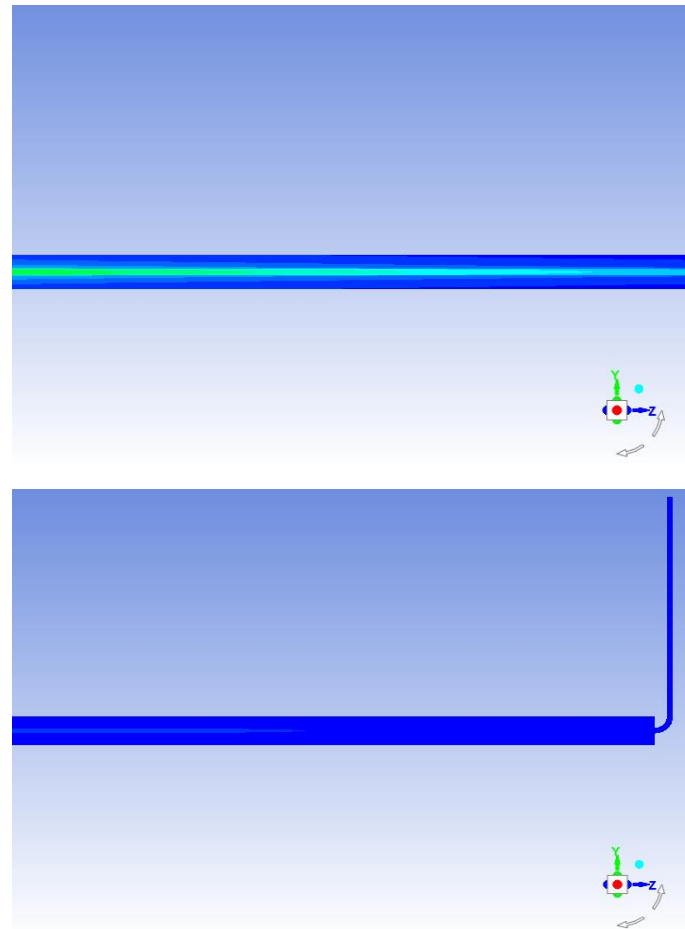


Fig. 6 Temperature contour (°C) along length of EAHE pipe at Reynold Number of 20866.212.

The variation of outlet air temperature (T_o) with Reynolds number for both studied materials at inlet air temperature of 50 °C is presented in “Fig. 7.” First from this figure it can be seen that for both studied materials the outlet air temperature increased with increasing Reynolds number due to increasing velocity of air flow and this lead to decrease residence time of heat transfer rate between air and soil. Also it can be noted that the outlet air temperature decreases with using steel material

compared with PVC material due to the effect of thermal conductivity of material.

“Fig. 8,” illustrates the variation of pressure drop (Δp) with Reynolds number at inlet air temperature of 50°C . From this figure it is easy to see that the pressure drop increased with increasing, where the air velocity increased with increasing Reynolds number and this leads to increase the pressure losses.

“Fig. 9,” shows the variation of the heat transfer rate with Reynolds number for the two studied materials at inlet air temperature of 50°C . From this figure it can be observed that the amount of heat transfer increased with increasing Reynolds number due to increasing flow rate. Also this figure illustrates that the amount of heat transfer grown with increasing thermal conductivity of pipe material, so the steel material has the maximum heat transfer rate, but this increase in heat transfer is less.

“Fig. 10,” indicates the variation of performance factor with Reynolds number for both studied materials at inlet air temperature of 50°C . From this figure it can be observed that the performance factor declined with increasing Reynolds number due to increasing the pressure drop with increasing Reynolds number and the performance factor is proportional inversely with the pressure drop. Also this figure shows that the steel material has the maximum performance factor compared with PVC material.

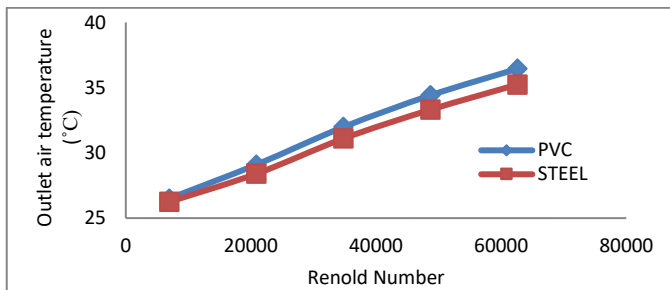


Fig. 7 the variation of the outlet air temperature of EAHE system with Reynold number for both studied materials at inlet temperature of 50°C

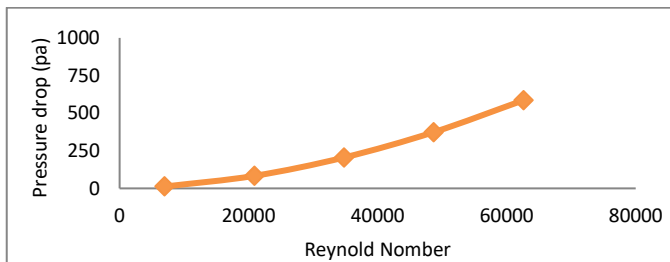


Fig. 8 the variation of the pressure drop of EAHE system with Reynold number

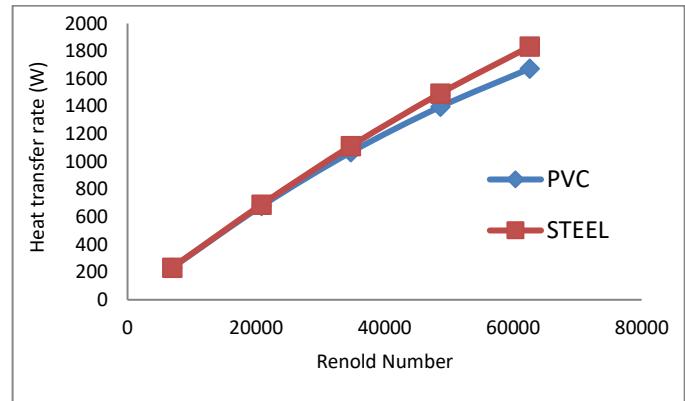


Fig. 9 the variation of the heat transfer rate with Reynold number for both studied materials at inlet temperature of 50°C .

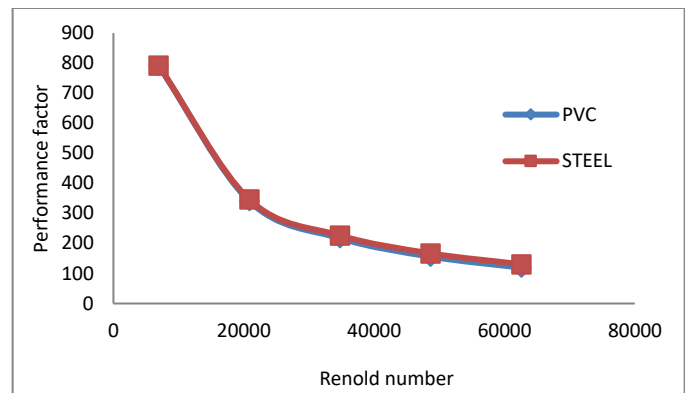


Fig. 10 the performance factor of EAHE system with Reynold number for both studied materials at inlet temperature of 50°C .

The variation of outlet air temperature with inlet air temperature the two materials are selected with Reynold number of 20866.212 is illustrated in “Fig. 11,”. From this figure it is easy to see that the outlet air temperature grown with increasing inlet air temperature. Also it seems from this figure that the outlet air temperature enhanced and declined with using steel material because the thermal resistance of PVC is high.

“Fig. 12,” shows the variation in amount of heat transfer rate with inlet air temperature for both studied materials at Reynold number of 20866.212. It is observed that the amount of heat transfer grown at high inlet air temperature due to increasing of the difference in air temperature between inlet and outlet of EAHE ($\Delta T = T_{in} - T_o$) with increasing inlet temperature and as well-known that the amount of heat transfer is proportional to the temperature difference.

“Fig. 13,” illustrates the variation of performance factor with inlet air temperature for the two studied materials at Reynold number of 20866.212. First from this figure it observed that the performance factor increased with increasing inlet temperature due to increasing rate of heat transfer. Also

this figure shows that there is a less increase in performance factor with using steel material.

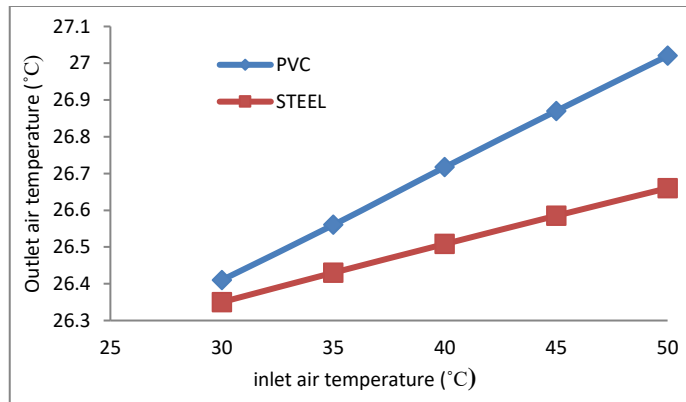


Fig. 11 The outlet air temperature of EAHE with inlet air temperature at Reynold number of 20866.212

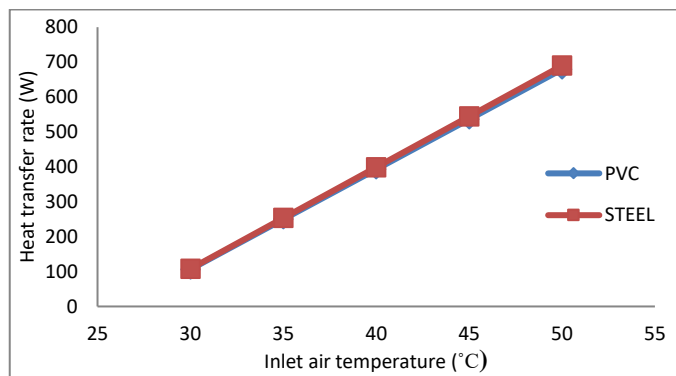


Fig. 12 The variation of heat transfer rate with inlet air temperature at Reynold number of 20866.212

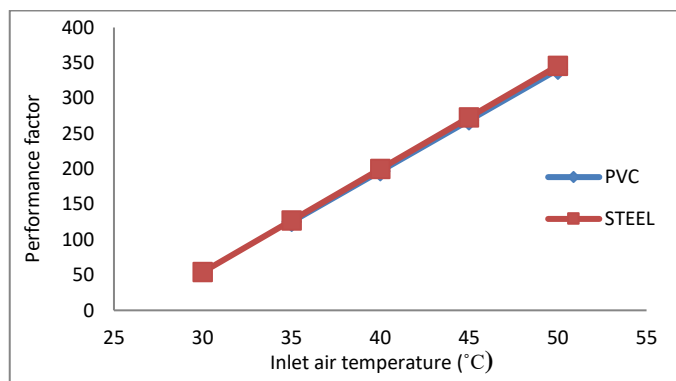


Fig. 13 The variation of performance factor of EAHE system with inlet air temperature at Reynold number of 20866.212.

The variations of local air temperature and performance factor along length of EAHE pipe for both studied materials

during summer season at Reynold number of 20866.212 and inlet air temperature of 50 °C is presented in “Fig. 14,”. From figure this figure it can be concluded that the air flows in PVC pipe has less temperature compared with steel pipe and this occurs due to high thermal resistance of PVC pipes compared with less thermal resistance for steel pipe.

“Fig. 15,” shows the variation of the pressure drop with respect to inlet ($\Delta P = P_L - P_{in}$) along EAHE pipe at Reynold number of 20866.212 and constant inlet temperature of 50 °C. It can be noted that the pressure drop increased along flow direction due to increasing the losses with increasing the length.

“Fig. 16,” illustrates the variation of heat transfer rate along EAHE pipe for the two materials are studied at constant Reynold number of 20866.212 and inlet air temperature of 50 °C where heat transfer rate is calculated up to specified section [$Q = \dot{m} c_p (T_{in} - T_L)$] to focus on EAHE pipe length. It seems from this figure that the amount of heat transfer grown along flow direction due to increasing the temperature drop (ΔT), where the period of air flow inside the pipe increased, therefore the period of the thermal exchange increase. Also this figure reveal that the amount of heat transfers with using steel material is higher than that for PVC material due to the high thermal conductivity of steel material.

“Fig. 17,” displays the variation of performance factor along length of EAHE at Reynold number of 20866.212 and inlet air temperature of 50 °C. From this figure it can be observed that for both studied materials the performance factor increased along flow direction until reach the maximum value at certain length then begins to decrease for the remaining length and this occurs due to the large increased in pressure drop with mild increasing in temperature difference after the specified value of pipe length. Also this figure shows that the steel material has the maximum performance factor compared with PVC material.

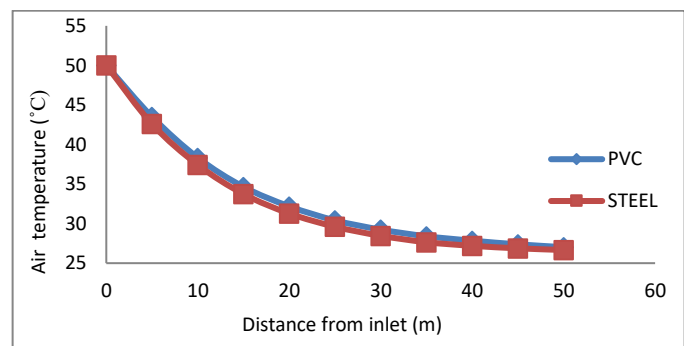


Fig. 14 Air temperature distribution along length of EAHE pipe at Reynold number of 20866.212 and 50 inlet air temperature °C.

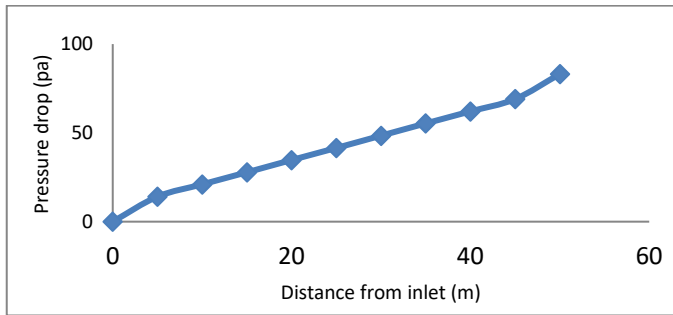


Fig. 15 The variation of the pressure drop along length of EAHE pipe at Reynold number of 20866.212 and 50 inlet air temperature °C.

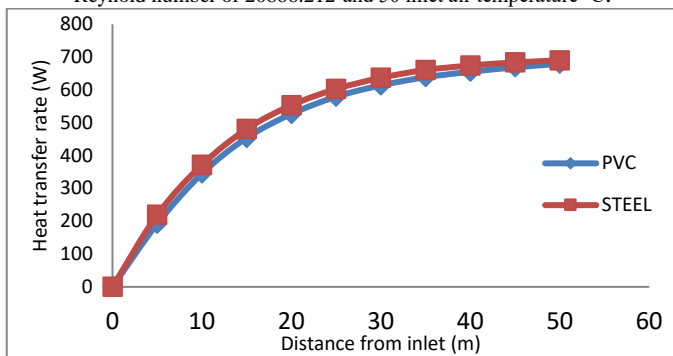


Fig. 16 The variation of the amount heat transfer along length of EAHE pipe at Reynold number of 20866.212 and 50 °C inlet air temperature.

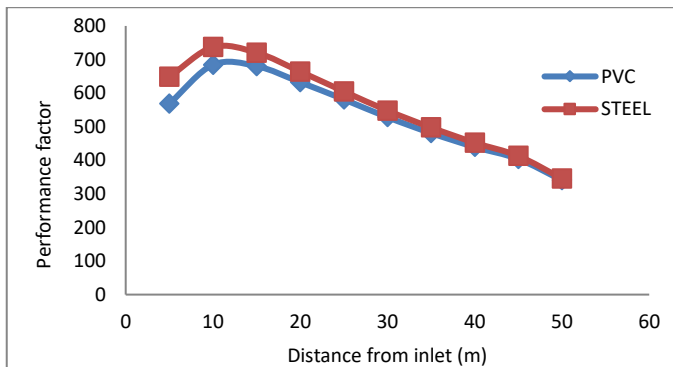


Fig. 17 The variation of the performance factor along length of EAHE pipe at Reynold number of 20866.212 and 50 °C inlet air temperature.

The variation of outlet air temperature with inlet air temperature during winter season for both studied materials during summer season at Reynold number of 20866.212 is illustrated in “Fig. 18,”. From this figure it can be seen that the outlet air temperature increased with increasing inlet air temperature at. Also it can be noted that the steel pipe gives the maximum outlet air temperature compared with PVC material.

“Fig. 19,” shows for both studied materials during winter season at Reynold number of 20866.212 the variation of heat transfer rate with inlet air temperature. It is easy to see from

this figure that the amount of heat transfer increased with increasing inlet air temperature due to the high difference in air temperature between inlet and outlet of EAHE ($\Delta T = T_o - T_{in}$) with decreasing inlet air temperature and the amount of heat transfer is proportional to the temperature difference [$Q = \dot{m} c_p (T_o - T_{in})$]. From this figure also it can be seen that the effect of pipe material on the heat transfer is less with a preference for steel.

“Fig. 20,” indicates the variation of performance factor with inlet air temperature for the two materials during summer season at Reynold number of 20866.212 for winter conditions. It can be observed that the performance factor increasing with decreased inlet temperature during winter season due to the increase in amount of heat transfer with increasing inlet temperature. Also it can be noted that the maximum performance factor can be obtain with using steel material.

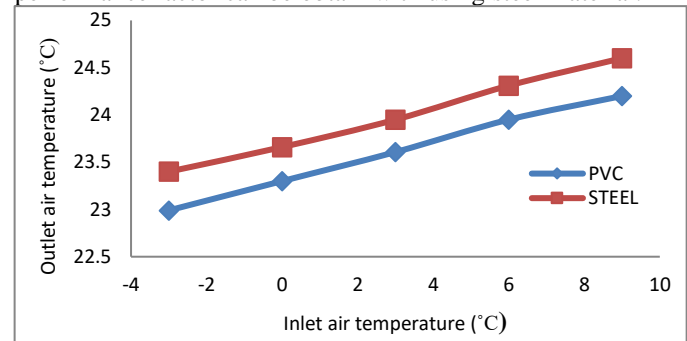


Fig. 18 The variation of outlet air temperature with inlet air temperature during winter season at Reynold number of 20866.212..

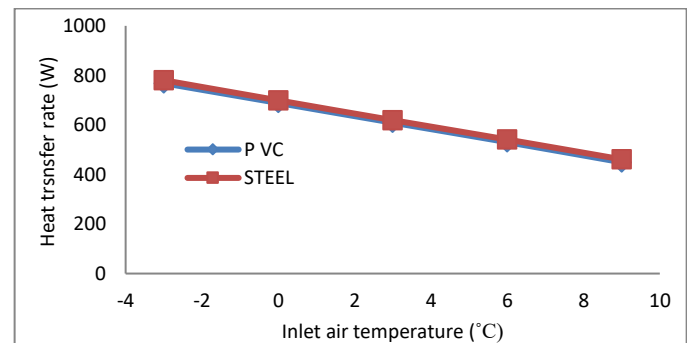


Fig. 19 The variation of heat transfer rate with inlet air temperature during winter season at Reynold number of 20866.212. .

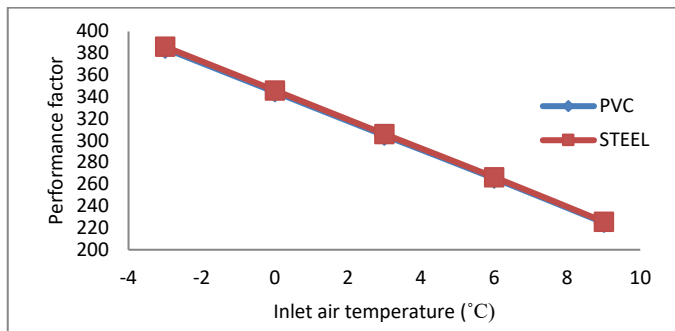


Fig. 20 The variation of performance factor with inlet air temperature during winter season at Reynold number of 20866.212.

The variation of local air temperature along the length of EAHE pipe at for both selected materials during winter season at Reynold number of 20866.212 and inlet air temperature of 3°C is shown in “Fig. 21,”. It can be seen from this figure that the local air temperature increased along flow direction and this increase is sharp at first meters of length because of the higher difference between air temperature and constant soil temperature of 26.3°C in the first meters which is decreasing along flow direction.

“Fig. 22,” indicates the variation of heat transfer rate along length of EAHE pipe for both studied materials during winter season at Reynold number of 20866.212 and inlet temperature of 3 °C where heat transfer rate is calculated up to specified section [$Q = \dot{m} c_p (T_L - T_{in})$]. It is observed that for both materials the amount of heat transfer rate increased along flow direction due to increasing the temperature difference (ΔT). Also from this figure it can be seen that the steel material gives the highest amount of heat transfer.

“Fig. 23,” indicates for the two materials during winter season at Reynold number of 20866.212 the variation of performance factor along length of EAHE pipe with inlet air temperature of 3 °C. From this figure it can be seen that both materials the performance factor increased along flow direction until reach the maximum value at certain length then begins to decrease for the remaining length and the cause of this is, the large increased in pressure drop with mild increased in difference temperature after the specified value of pipe length.

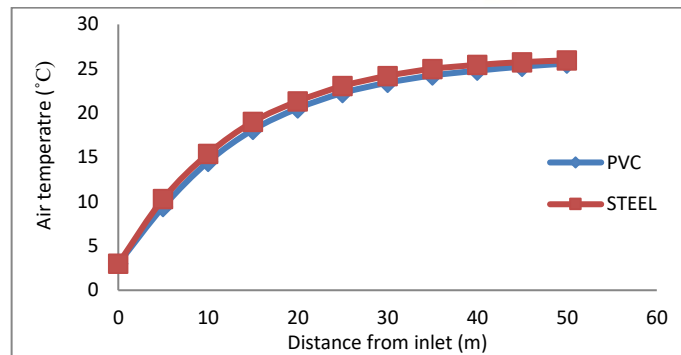


Fig. 21 Air temperature distribution along length of EAHE pipe at Reynold number of 20866.212 and 3 °C inlet air temperature.

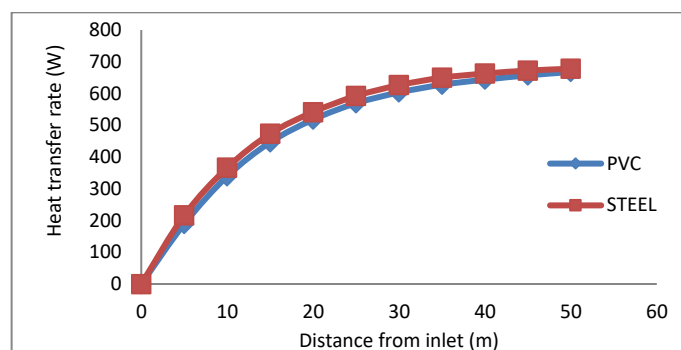


Fig. 22 The variation of the amount heat transfer along length of EAHE pipe at Reynold number of 20866.212 and 3 °C inlet air temperature.

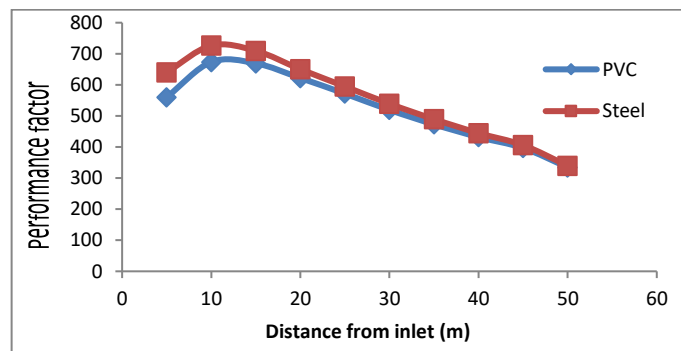


Fig. 23 The variation of the performance factor along length of EAHE pipe at Reynold number of 20866.212 and 3 °C inlet air temperature.

B. The thickness effect

The variation of outlet temperature with thickness of pipe wall for both selected materials at Reynold number of 20866.212 and inlet air temperature of 50°C is presents in “Fig. 24,”. From this figure it can be found that there is a bit increased in outlet air temperature with increasing wall thickness due to increasing thermal resistance of wall with increasing thickness. Also this figure illustrates as mentioned

previously that there is little difference in outlet air temperature between steel and PVC pipe with mild perfect for steel.

The variations of local air temperature and performance factor along length of EAHE pipe during summer season at Reynold number of 20866.212 and inlet air temperature of 50°C is illustrated in “Fig. 25,” and “Fig. 26,”. From this figures it can be observed that with increasing wall thickness the local air temperature and the overall performance decreased due to increasing thermal resistance with increasing thickness but this decrement is mild, therefore can be neglected.

The variation of outlet temperature with thickness of pipe wall for steel and PVC pipes during winter season with Reynold number of 20866.212 and inlet air temperature of 3°C is presents in “Fig. 27,”. From this figure it can be noted during winter season that the outlet air temperature decreased with increasing wall thickness, where the thermal resistance of wall increased and this lead to reduce the amount of heat transfer.

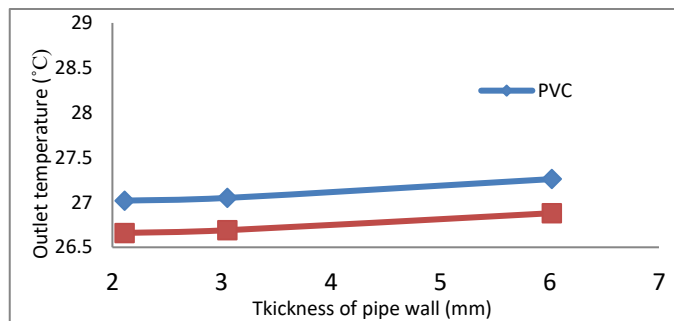


Fig. 24 the variation of the outlet air temperature of EAHE system with wall thickness for both studied materials at inlet temperature of 50°C.

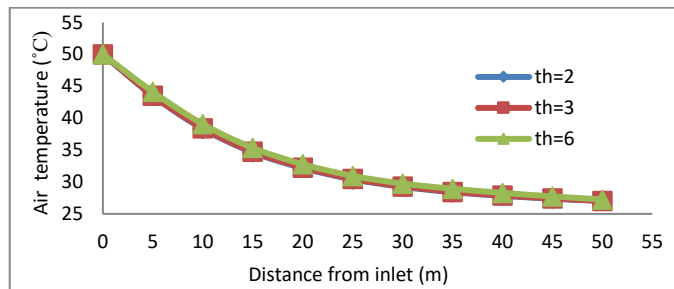


Fig. 25 Air temperature distribution along length of EAHE pipe for all selected thicknesses at Reynold number of 20866.212 and 50 inlet air temperature °C

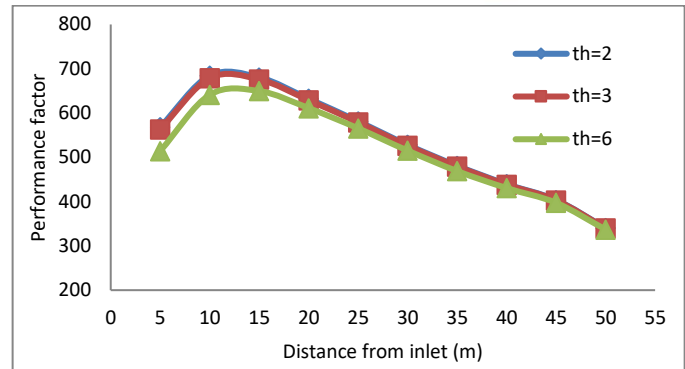


Fig. 26 the variation of the outlet air temperature of EAHE system with Reynold number for both studied materials at inlet temperature of 50°C.

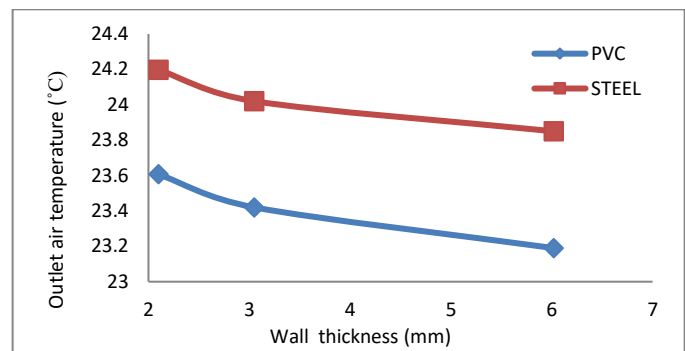


Fig. 27 the variation of the outlet air temperature of EAHE with wall thickness for both studied materials during winter season at inlet air temperature of 3°C.

VI. Conclusions

Due to the undisturbed of soil temperature at certain depth from ground surface, the earth to air heat exchanger can be used in cooling and heating the building. This paper presented a numerical study to show the effect of pipe making material and pipe wall thickness on the overall performance of EAHE system under the climatic conditions of Nasiriya city in south of Iraq. From the simulation results obtained in the present work, the following remarks can be concluded.

1. The outlet air temperature and the pressure drop for the two studied materials increased with increasing air velocity
2. For both studied materials the outlet air temperature increased with increasing inlet air temperature during summer season and decreased with decreased inlet air temperature during winter season.
3. The overall performance of EAHE system is better when it is operating as a cooling system under high inlet air temperature and heating system under low inlet air temperature.
4. With increase in length of pipe, the outlet air temperature from EAHE decrease and increases during summer and winter seasons respectively. The



decrease and increase in air temperature was sharp for the first meters length of pipe and becomes moderate afterwards.

5. There is a less improvement in outlet air temperature with using steel material compared with PVC material.
6. In spite of there is a priority in the performance of EAHE system for steel pipe but this priority is little and can be neglected compared with the prices of materials and problems of corrosion and this lead us to believe that the PVC pipe is more suitable to use because it is cheaper and non corrosive compared with steel pipe.
7. The effect of wall thickness on the overall performance is less and can be neglected.

References

- [1] Vikas B., Rohit M., Ghanshyam D. A., Jyotirmay M., "Performance analysis of earth-pipe-air heat exchanger for winter heating", Journal of Energy and buildings, 42 pp. 1151-1154, 2009.
- [2] Vikas B., Rohit M., Ghanshyam D. A., Jyotirmay M., "Performance analysis of earth-pipe-air heat exchanger for summer cooling", Journal of Energy and buildings, 41 pp. 645-648, 2010.
- [3] Abdelkrim S., Abdelhafid H., Mohammed T., " The potential of earth-air heat exchangers for low energy cooling of buildings in South Algeria", Energy Procedia, 18 pp. 496-506, 2012.
- [4] Woodson T, C. Ye'zouma, Traore' E. S, "Earth-air heat exchangers for passive air conditioning: case study Burkina Faso," Journal of Construction in Developing Countries, vo. 17(1), pp. 21-33 2012
- [5] Mohamed K., Brahim B., Karim L., Pierre H., Hassan H., Amin B., "Experimental and numerical study of an earth-to-air heat exchanger for air cooling in a residential building in hot semi-arid climate", Journal of Energy and Buildings, 125 pp. 109-121, 2016
- [6] F. Al-Ajmia, D.L. Lovedayb, V.I. Hanbyc, "The cooling potential of earth-air heat exchangers for domestic buildings in a desert climate", Journal of Building and Environment, 41 pp. 235-244, 2006.
- [7] CAROL G., MARCEL L., HERVE B., "NUMERICAL SIMULATION OF SOIL HEAT EXCHANGER-STORAGE SYSTEMS FOR GREENHOUSES", Journal of Solar Energy Vol. 60
- [8] Rohit M., Vikas B., Abhishek A., "Investigation of Thermal Performance of EATHE System under Intermittent Operation: A CFD Approach, International Journal of Engineering Technology, Management and Applied Sciences, , Volume 4, Issue 4, ISSN 2349-4476, 2016.
- [9] Fuxin N., Yuebin Y., Daihong Y., Haorong L., "Heat and mass transfer performance analysis and cooling capacity prediction of earth to air heat exchanger", Journal of Applied Energy, 137 pp. 211-221, 2015.
- [10] Anuj M., Ankit K. S., Sanjay M., "Numerical investigation of the performance and soil temperature recovery of an EATHE system under intermittent operations", Journal of Renewable Energy, 95 pp 510-521, 2016.
- [11] Guohui G., "Simulation of dynamic interactions of the earth-air heat exchanger with soil and atmosphere for preheating of ventilation air", Journal of Applied Energy, 158 pp. 118-132, 2015.
- [12] Mushtaq I. H., A. A. Rageb, M. Yaghoubib, Homayo H., "Influence of channel geometry on the performance of a counter flow microchannel heat exchanger", Journal of Thermal Sciences, 48 pp. 1607-1618, 2009.
- [13] Mushtaq I. Hasan, Hayder M. H., Ghassan A. A., "Study of the Axial Heat Conduction in Parallel Flow Microchannel Heat Exchanger", Journal of King Saud University - Engineering Sciences , 26, pp. 122-131, 2014.
- [14] Mushtaq I. H., "Influence Of Wall Axial Heat Conduction On The Forced Convection Heat Transfer In Rectangular Channels", Basrah Journal for Engineering Science, Vol. 1, p.p. 31-43, 2011.
- [15] ALAA H. M., "Theoretical and experimental study of using Earth Tube Heat Exchanger and Solar Chimney for cooling in Basrah city", PHD thesis, Mechanical Engineering Department, University of Basrah, 2015.
- [16] Engineering Consultation Office Of Thi-Qar university, <http://oce.utq.edu.iq/>.



Design And Building A Single-Phase Smart Energy Meter Using Arduino And RF Communication System

Fadhela K. Handhal & Abdulmuttalib T. Rashid
Electrical Engineering Department / University of Basrah
Basrah, Iraq Basrah, Iraq
zainabea36@gmail.com / abdturky@gmail.com

Abstract—This paper produces the design and building of system that gives a solution to the measurement of energy and helps the local customers to save the power in an efficient manner. Also, this paper introduced the design, realization, and testing a wireless monitoring system for measuring the energy consumption of electrical devices in the consumer's homes. The system consists of power consumption monitoring systems (smart meter) at customer homes and a control system for remotely reporting and handling the smart meter readings at the power distribution station. The server shows the readings from these meters system by means of a client visual interface. An Arduino kit with current and voltage sensors are used in the meter to measure the power as well as RF kit is used with a local server for communication. The client does not need to spend effort to note their power use so as to control their behavior and decrease their energy usage and costs.. The designed smart meter and a mechanical meter are compared in several experiments to indicate the differences in their features.

Index Terms—Smart meter; mechanical meter; current sensor; RF transceiver; power distribution system.

I. INTRODUCTION

In a world of rising energy cost human beings and organizations have been started for investigation for an efficient way to minimize their extended electric cost. appropriate method for decreasing these expenses is to continuously monitor the power that has being expended and from this information, comparing the available choices about how to deal with the electrical devices being controlled [1]. As more home machines and customers use electricity , residential energy consumption tends to grow rapidly [2]. A large number of home devices increase the control utilization in two ways: standby power and ordinary control. Those two types of force utilization are relative to

the quantity of home devices. Subsequently, the operational cost in homes is additionally expanding. If the users can instantly watched how much power consumes per minute, they might be more careful later on about giving devices a chance to turn off when not required. The meter that is designed aims to give a clear vision of a home's energy use. The roll-out of smart meters will necessary and important step to address the problems of energy consumption in which consumers will be able to provide real-time feedback on the effect of their energy use [3].

The present system of the energy metering has been planning to be used in Iraq, which uses electromechanical energy meter which is inaccurate and consumes more time and works for collecting the information from users' homes. In developed countries, the conventional electromechanical meters have been replaced by electronic meters to reduce efforts and to improve accuracy in meter reading. Still, the Iraqi power sector faces a serious problem of actual revenue loss of electric power processed is because of energy thefts and network losses as well as the users have another problem is the unreliable traditional billing system because the meter readings are inaccurate and leads to pay large amount of money compared to the real use [4]. One way through which today's energy problems can be tended under the reduction of energy use in households. The existing observing systems just give review toward the end of the month as kilowatt-hours (KWh) [5].

In this paper, we introduce an Arduino based power meter which objective is to give clients their consumption data that they could benefit to enhance and decrease their electricity consumption. The system was comprised of the ACS712 current sensor, AC-DC adapter with voltage divider, the main Arduino board, the wireless NRF24L01 Fro Module add-on board, 20*4 LCD and the base station computer. The comparison between electromechanical meters and smart meters is discussed in section II; the principles of measurement will be discussed in section III; Design and building of the electric smart power meter is shown in section IV. Section V shows the experimental results. Finally, the conclusion will be in section VI.

II. COMPARISON BETWEEN ELECTROMECHANICAL METERS AND SMART METERS

The operation of Energy Meters is refined by measuring the quick estimations of voltage and current continuously to get the power consumption kilowatt-hours (KWh). Single-phase KWh meters are ordered into two types: Electromechanical meters and Electronic meters [6].

A. Electromechanical meters

An electromechanical induction meter which is shown in Fig.1 counts the number of times the disc is rotated. The rotation of this disc is proportional to the power passing through the meter. Thus the energy consumption is proportional to the number of revolutions.

Electromechanical meters are extremely unreliable. Worn gears, humidity, dust, or affected by an accidental drop to floor, it can cause obstruction of work and result in an electromechanical meter that does not catch the full advantage of the reason for its manufacture [7].



Fig.1. The mechanical meter.

B. Smart meters

The smart meter is used to measure the accurate energy consumption by customers. With a flexible communication module, the meter provides varieties communication media for remote measuring and monitoring. There are two principle sorts of smart meters: Programmed Meter Reading (PMR) which utilize one-way communication and Advanced Metering Infrastructure (AMI) utilize two-way communication to both transmit use data and perform perception and maintenance tasks [8].

III. PRINCIPLES OF MEASUREMENT

Basically, a watt-hour meter is designed to measure energy or power consumed with respect to time.

$$\text{Energy} = \text{Power} * \text{Time}$$

In simple terms, the average power can be calculated by the following equation:

$$W = \frac{1}{T} \int_0^T (v * i) dt$$

Where : v = instantaneous voltage , i = instantaneous current , t = time and T = period .The method used to measure power is taken from the basic definition of power equation. The integration is performed by numerical method , where integration can be replaced by the following summation .

$$W = \frac{1}{N} \sum_{j=1}^N v_j * i_j$$

Means that taken instantaneous values and then divide it by a number of times to get the average power which equals the real power. The system can measure rms voltage and current , and real power. Measuring system can be divided into three stages :

1. Analog signal conditioning

By translating the input current and voltage to the specific range . The ACS712 current sensor used to measure current which have an inner signal condition circuit , and AC/DC adapter used to measure voltage which includes step down transformer to reduce the voltage 220 volt to 24 volt. This range is outside the analog input voltage of the microcontroller so it should be reduced to 0-5V range, this is done by the voltage divider .

2. Analog to Digital convertor (ADC)

The analog to digital convertors in Arduino converts the input signal from an analogue signal to a digital signal (zero or one logical) .where these digital information are used for several purposes in control and modification.

3. Digital measurements

The power equation is used to calculate the power consumed using the microcontroller (Arduino).

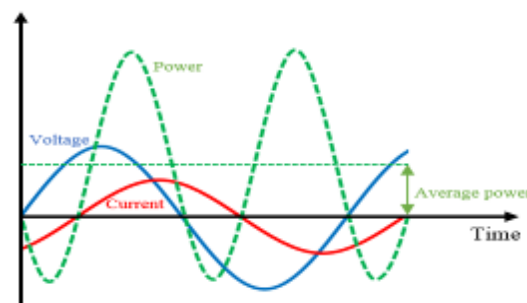


Fig. 2. The computing of the average power from the analogue voltage and current

IV. DESIGN AND BUILDING AN ELECTRONIC SMART METER

Smart Meters are electronic estimation devices used for collecting client data and transmitting their electricity use to the monitoring systems. Detecting current and voltage and energy consumption then transmission these quantities into the base monitoring station through the technology of the smart meter. Smart meters provide the advantage of saving money and saving unnecessary spending as a cost of power consumed, as well as the continuous reading of the amount of consumption and collection of this data in the electricity company also provides additional amounts instead of the previous reading through the company's officer [9]. The system proposed comprises of two fundamental parts:

- i) Hardware design
- ii) Software design

The implementation of a fundamental watt-hour meter includes four hardware modules as shown in Fig.3. These modules represent by the voltage measurement module, the current measurement module, the wireless communication module and the monitoring module.

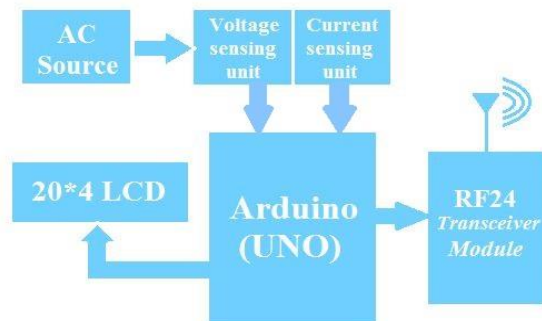


Fig. 3: Block diagram of the transmitter system

A. Voltage measurement module

To measure 220V AC, step down this voltage to AC voltage whose peak value should be less than 5V to be suitable to the voltage of the Analog to Digital converter of the microcontroller. Also, this AC voltage must convert

to DC voltage using bridge rectifier [10]. In this module, we used AC\DC voltage adapter for adapting the voltage to the microcontroller as shown in Fig. 4 (voltage measurement module). The analog voltage to be measured is connected with one of the ports of the microcontroller (A1). The microcontroller (Arduino UNO) contains a built-in ADC which changes the voltage to a computerized esteem.

The microcontroller is programmed to change over this advanced esteem again to the estimation of connected voltage. The esteem is then shown through an LCD show. ADC is determined in a number of tests. We have intended for 1024 numbers with 10mV/bit determination [11].

A. Current measurement module

The microcontroller can only sense the voltage on the analog pins, there are many ways to convert current to voltage. The choice has been used in I-V conversion is the Hall Effect current sensor (ACS712) that is connected to the analog input (Ao) of Arduino as shown in Fig. 4 (current measurement module).

The ACS712 device (Fig. 5) consists of a precise, low-offset, linear Hall sensor circuit with a copper conduction path located near the surface of the die. Applied current flowing through this copper conduction path generates a magnetic field which is sensed by the integrated Hall IC and converted into a proportional voltage[12].

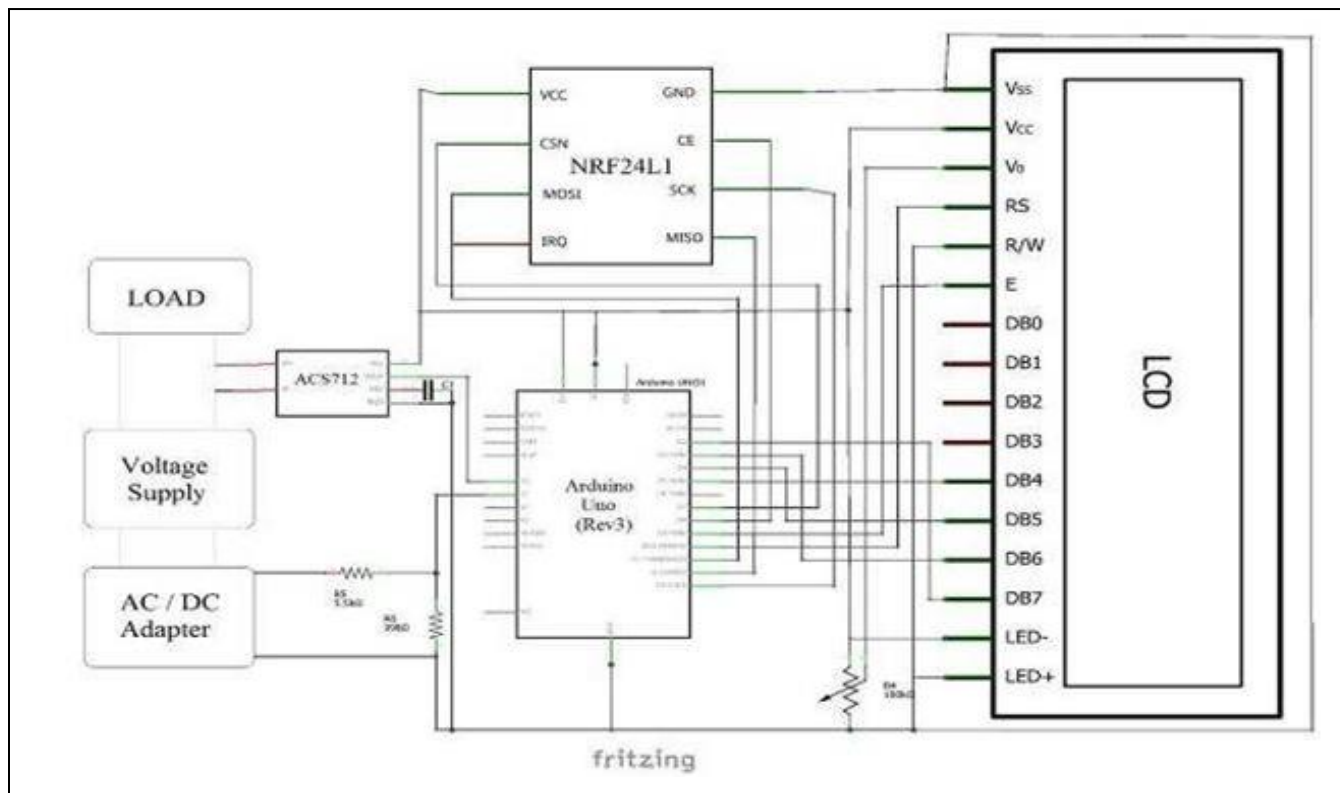


Fig. 4. The schematic diagram of electrical smart meter.

B. The wireless communication module

Arduino UNO kit does not have any wireless communication module in stock. In order to support wireless data transmission we prefer NRF24L01 RF Transceiver Module (Fig. 6) to work with the Arduino. The RF transceiver ease to use, small energy consumption, and extremely low cost. NRF24L01 supports 2.4 GHz wireless data transmission with low energy consumption [13].



Fig.5. ACS712 current sensor Fig.6. NRF24L01 RF Transceiver

C. Monitoring module

Two monitoring systems are used here : one in the transmission side (smart meter side) which are represented by Liquid crystal display (LCD) as shown in Fig. 4, while in the electricity monitoring station there is the main computer LCD which show the received information using Visual Basics program. Liquid crystal displays have an assortment of connections that can supply the client with the coveted data going from a basic clock to perusing the power consumption.

D. Receiving unit

This module is made out of an easy to use serial order set. It permits dependable and directed correspondence between microcontrollers, PCs, installed systems and so on. Basically with any system with a serial port. 2.4GHz RF24 module pack up both point and multipoint communication. In this way, it is conceivable to speak with a few remote units connected with various machines from a remote

checking unit. Special RF24 modules' setups can be used to meet different plan prerequisites, for example, remove, spending plan, arrange topology and so on. Block diagram of the receiver system is shown in Fig.7.

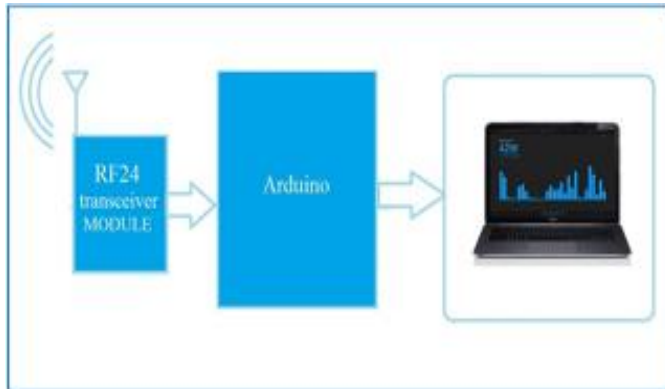


Fig.7: Block diagram of the receiver system

F. Software design

The software part of the project represents the programs written on the Arduino board and the base station PC. Current and voltage was measured from the two current conveying wires into the principle control board, tested by the Arduino board and sent as a user datagram protocol (UDP) packet over the NRF24L01 Fro Module system to the base station PC, and after that show current, voltage and power consumption to the client throw LCD. Figure 8 shows the energy monitoring software's flow chart. This software is written using C-Language for Arduino. The UDP packet that has been sent by the transmitting unit over the NRF24L01 module system is received by the base receiving unit. The receiving unit then parsed the packet, and computerized transformation into current information to the power checking base station (PC) using C-Language for Arduino placed at the receiver side and Visual Basic Language for base station PC. Figure 9 shows the receiver software's flowchart.

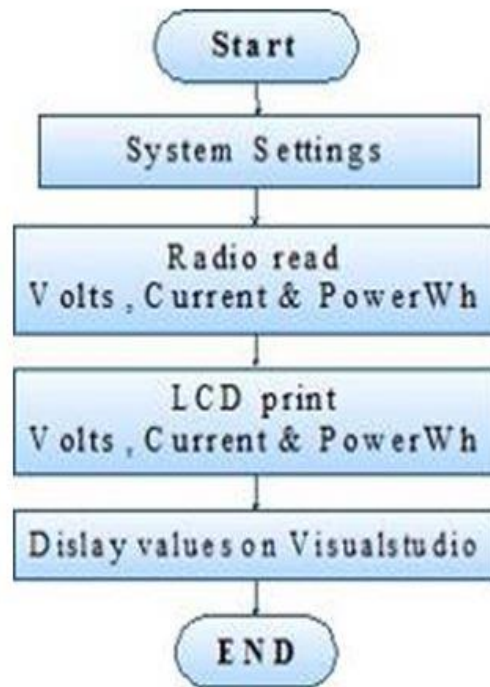


Fig. 8. Flow chart for the software of the transmitting system

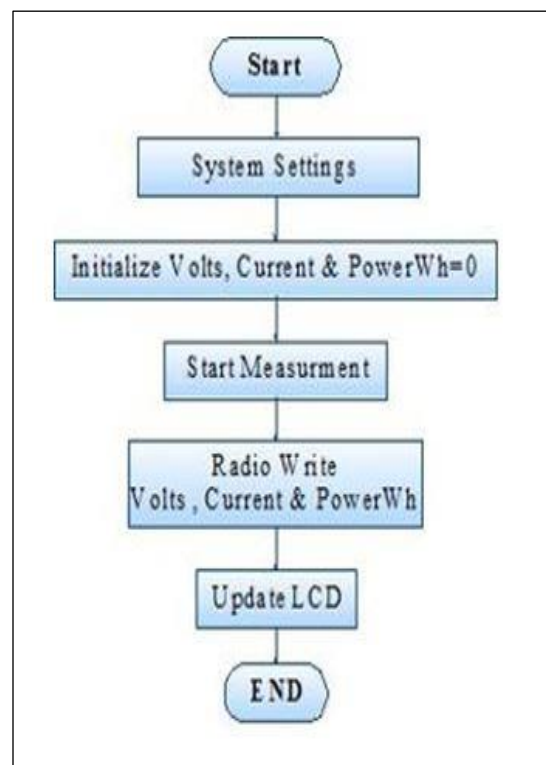


Fig. 9. Flow chart for the software of the receiving system

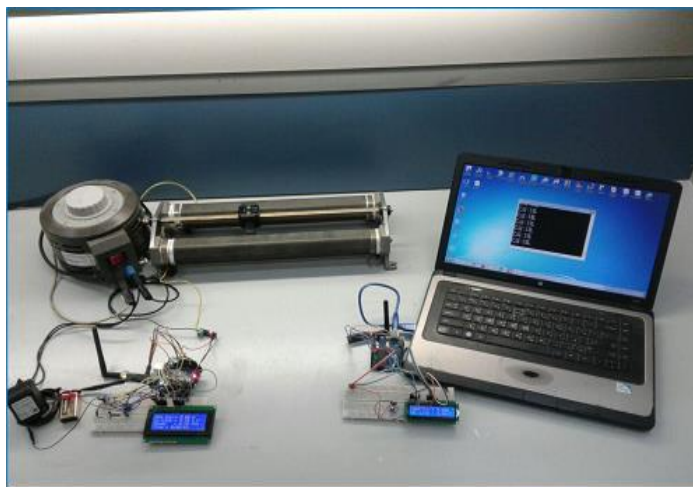


Fig. 10. First experiment: Smart power meter

V. EXPERIMENTAL RESULTS

Several experiments have been accomplished keeping in mind the end goal to imitate the operation of remote power system. Figure 10 shows the first experiment for measuring the power using the smart power meter. The measurements begin through the AC adapter as isolate and step-down

stage. Then a potential divider step which damping voltage supply to the low level voltage by utilizing voltage divider as appeared as a part of Fig. 4 where R1 and R2 are chosen ($5.5\text{ K}\Omega$ and $998\ \Omega$ respectively) to attenuate (23.48 to 3.562 V) supply voltage. The load current has been measured by using the ACS712 current sensor which converts current to the voltage suitable to the microcontroller. In microcontroller, the power consumption has been evaluated. The smart meter is connected to RF24 Transceiver, which sends the measurements to the base station. At the base station, the data has been gotten. In this venture, the ID of a client has been chosen same as RF24 Transceiver ID which communicates to the source address of RF24 Transceiver. The estimation data of electric power has been sent from END devices to the coordinator by frames incorporates source address. This information has been analyzed and displayed on the base station screen. System software has been design to show the electric power parameter of clients.

The second experiment is implemented using the mechanical meter as shown in Fig. 11. In this experiment, we used an auto transformer and thermal resistor as load and single phase mechanical meter.

The power measurements in both experiments are repeated for 12 hours to give a suitable comparison between the smart and mechanical meters.

Fig. 12 shows the results of comparison between the smart and mechanical meters with respect to actual power spent in load. From these reading, we found that the smart meter has an accurate reading with respect to the mechanical meter.

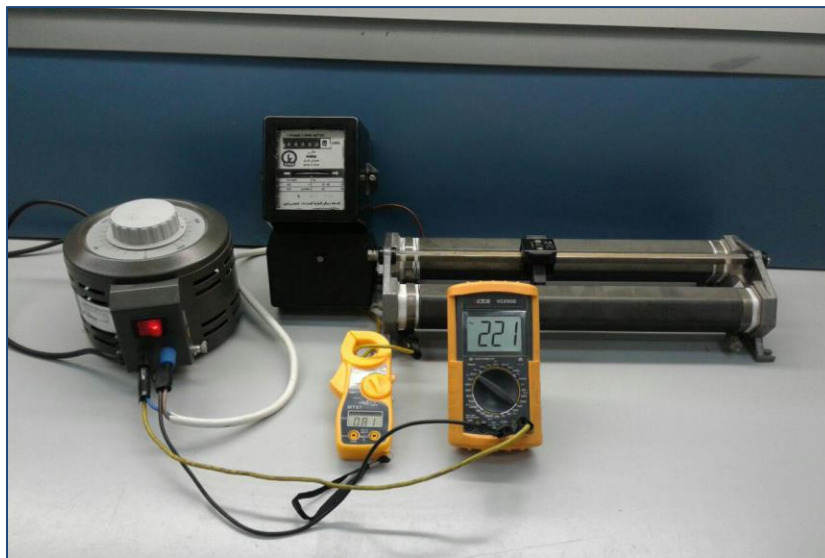


Fig. 11. Second experiment: Mechanical power meter

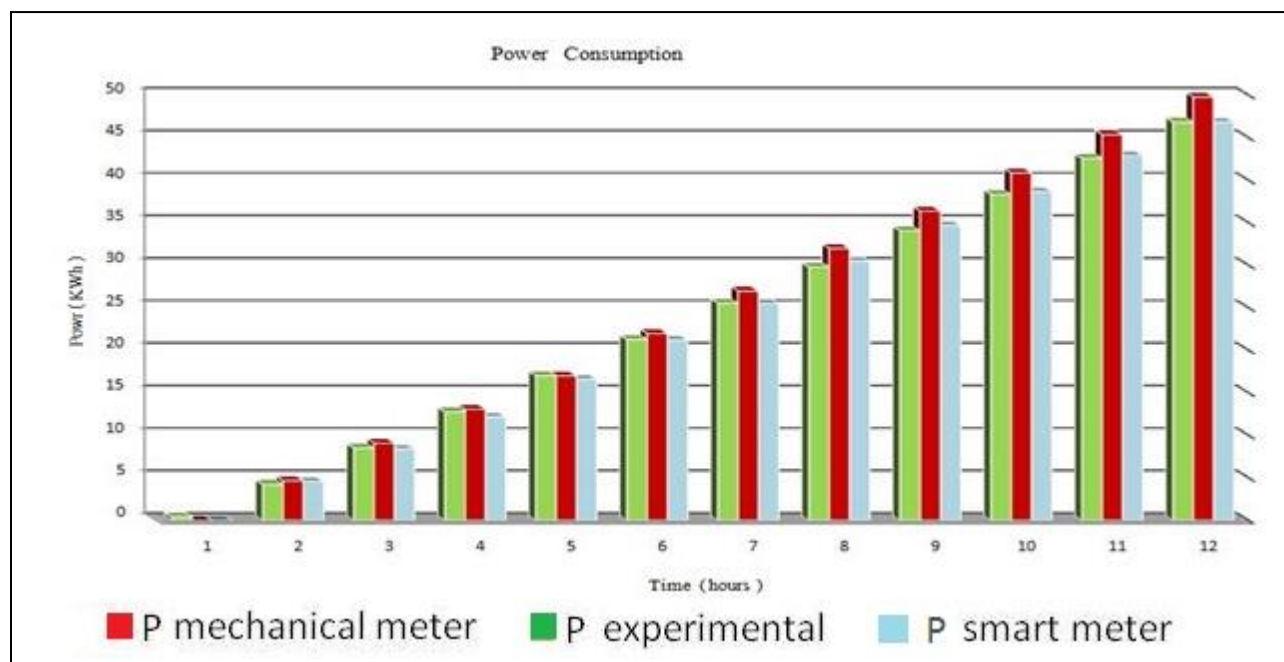


Fig. 12. Comparison among experimental, smart meter and mechanical meter readings.

| Time (hours) | 1 | 2 | 3 | 4 | 5 | 6 | 7 | 8 | 9 | 10 | 11 | 12 |
|---------------------------------|-------|------|------|-------|-------|--------|-------|-------|-------|-------|--------|--------|
| <i>P experimental (KWh)</i> | 0.426 | 4.26 | 8.52 | 12.78 | 17.04 | 21.299 | 25.56 | 29.82 | 34.07 | 38.34 | 42.598 | 46.857 |
| <i>P mechanical meter (KWh)</i> | 0 | 4.7 | 9.1 | 13.1 | 17 | 22 | 27 | 32 | 36.4 | 40.9 | 45.4 | 49.8 |
| <i>P smart meter (KWh)</i> | 0 | 4.57 | 8.4 | 12.17 | 16.6 | 21.2 | 25.51 | 30.5 | 34.69 | 38.65 | 42.9 | 46.85 |

TABEL 1. Experimental results

VI. CONCLUSIONS

In this paper, a smart energy meter system is designed and built using Arduino UNO microcontroller with current and voltage sensors. The measuring Kilowatt hours is transmitted to the base station using two RF NRF24L01 transceiver modules in both the smart meter and the base station. The smart meter is used to replace the mechanical energy meter that has several advantages over the mechanical one. Also, smart meter has the ability to give us the voltage and current reading at each instance of time.

By comparison both meters we found the proposed meter has reading approximately equal to the actual reading as shown in table 1 . The average percentage error of the smart meter is 1.86% while the mechanical meter error was 5.054%.

For future work we suggest to expand the smart meter to work with three phase system and to replace the display module with another has the ability to display the results as a graphics form.

VII. References

- [1] E. Chobot, D. Newby, R. Chandler, N. Abu-Mulaweh, C. Chen, and C. Pomalaza-Ráez , “ Design and implementation of a wireless sensor and actuator network for energy measurement and control at home,” International Journal of Embedded Systems and Applications(IJESA). vol. 3, No.1, March 2013.
- [2] B.Patil , and M. Limkar, “ Mechine to machine communication based electricity monitoring and billing system ,” International Journal of Electrical and Electronics Engineering Research (IJEEER), vol.. 6, No. 3, pp. 1-8, January 2016.
- [3] O. Letwin , G. Barker , and A. Stunell OBE , “Behaviour Change and Energy Use,” 2016.



- [4] M. T. Rashid , “Design and Implementation of Smart Electrical Power Meter System,” Iraq Journal Electrical and Electronic Engineering (IJEEE), vol. 10, No.1,2014.
- [5] C. McNally , “ Arduino based wireless power meter ,” Cornell University , Design Project Report of the Requirements for the Degree of Master of Engineering, 2010 .
- [6] K Aswathy and P. P. Narayanan , “Image Extraction-IE Approach to Extract Information from Analog and Digital KWh Meters ,” International Journal of Engineering Science and Computing (IJESC), vol. 6, No. 5, pp. 2321-3361, 2016
- [7] B.Seal ,and M. McGranaghan , “Accuracy of Digital Electricity Meters,” Electric Power Research Institute, 2010.
- [8] L. Alejandro, C. Blair, L. Bloodgood M. Khan M. Lawless, D. Meehan, P. Schneider , and K. Tsuji , “Global Market for Smart Electricity Meters: Government Policies Driving Strong Growth,” U.S. International Trade Commission (USITC), No. ID-037, June 2014.
- [9] G. Ajenikoko, and A. Olaomi , “Hardware Design of a Smart Meter ,” International Journal of Engineering Research and Applications (IJERA), vol. 4, No. 9, pp. 115-119, September 2014.
- [10] X. Jiang, S. Dawson-Haggerty, P. Dutta, and D. Culler , “Design and Implementation of a High-Fidelity AC Metering Networ,” International Conference on Information Processing in Sensor Networks, pp. 253-264, 2009.
- [11] D. Abraham1, R. Thekkekara, Sajana M S, Sandeep S ,and Sandeep T, “Development of a High Precision Digital Volt Meter,” vol. 3, No. 2, pp. 2320 – 3765, February2014.
- [12] ACS712 current sensor datasheet, Allegro Micro Systems, Inc., 2006.
- [13] NRF24L01 RF single chip 2.4 GHz transceiver datasheet, Nordic semiconductor, 2008

Experimental Investigation of a Thermally Activated Roof (TAR) for Residential Space Cooling Using Cool Water from a Low Energy Source in Iraq

Khalid A. Joudi

Professor Dr., College of Engineering,
University of Baghdad, Iraq
Address: khalidjoudi48@yahoo.com

Kamal M. Ali

Lecturer Dr., Amarah Institute of
Technology, Southern Technical University,
Maysan, Iraq
Address: al_ssafar2005@yahoo.com

Abstract- The indoor temperature and performance of a thermally activated roof (TAR) system were investigated experimentally to cool a room located at Amarah city, south of Iraq (31.83 °N, 47.15 °E), by decreasing space cooling load and circulating cool water using low energy source. The room measured 5.5 m x 4.0 m x 3.0 m with three external walls. The walls were constructed of 240 mm common brick thickness. The interior wall surfaces were covered by 20 mm Styrofoam insulation followed by a decorative PVC panel. The roof was constructed of 200 mm heavyweight concrete covered by 50 mm Styrofoam insulation and 150 mm turf. A cooling tower of 2 kW cooling capacity provided the TAR system with cool water. Water circulated through pipe coils of 13 mm galvanized steel pipes diameter embedded in the roof slab. Each coil was 5.0 m long, 170 mm spacing. The indoor temperature and the TAR system performance evaluation were achieved by studying the effect of walls insulation in the indoor conditions with and without TAR system. The indoor temperature with TAR system is found within the comfort level during April, September, most of May and August while it is above the comfort level during few days of May and August and all days of June and July. The auxiliary energy saved with TAR system for May, June, July, August and September operation was found 78.8 % based on 27 °C indoor temperature. The seasonal contribution ratio of TAR system of energy saving was found 0.68.

Index: Thermally activated building, concrete conditioning, thermal storage, thermo active structure, RC-thermal modeling.

I. INTRODUCTION

In the residential building sector in Iraq, the majority of energy consumption is used for air conditioning. The conventional constructions in Iraq show a high cooling load due to the high ambient temperature in summer. Many arrangements should be adopted in this construction to decrease the cooling load and make it suitable with renewable energy applications. Cool water produced by cooling tower which represents a low energy cooling source is the suitable energy source in Iraq.

A thermally activated roof system (TAR) is a system that integrates cooling system in the roof slab and is used for residential applications. These systems are characterized by pipes embedded in the concrete slab of the roof with water as a heat transfer medium. In the 1990s, the Swiss engineer Robert Meierhans was the first who established the practice of thermally activating buildings [1]. In 2000 Koschenz and Lehmann [2] from (Swiss Federal Laboratories for Materials Testing and Research), the German acronym for which is

EMPA, wrote a book introducing TABS in Germany. Olesen [3] stated that in central Europe (Austria, Germany, Netherlands, etc.), this type has been installed in a number of new office buildings since 1990s. He also reported that since 2005, the number of commercial floor radiant system has increased by 36% with 7% of new construction radiant system, a number expected to double by 2013. Xinhua et al. [4] presented a comprehensive review of the research and developments of the active pipe embedded system structure for space air-conditioning by using low energy cooling sources. These included the ground or the outdoor air and other sources. The norm ISO 11855-2 [5] focuses on embedded water pipe panels for heating and cooling systems and thermally activated building systems TABS. This norm distinguished 7 different types of these systems, types A to G depending on construction details. Type E TABS is most widely used in Europe and has the lowest installation and operating cost. It is also known as concrete core conditioning system CCC when pipes are embedded in the heavy weight concrete. In Type E, pipes are typically 15 mm to 20 mm in diameter and 150 – 300 mm apart are embedded near the neutral axis of the floor slab as shown in figure 1. The pipe configurations can be meander or spiral.

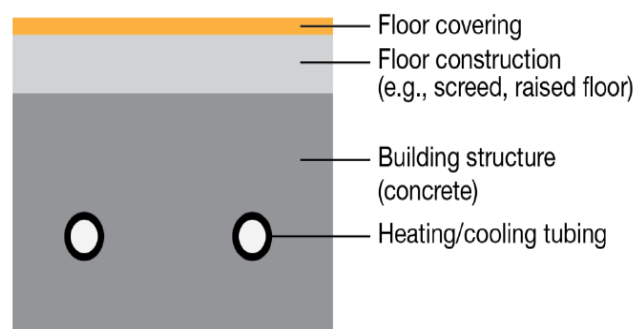


Fig. 1 Section of thermally activated building system (ISO 11855, type E).

Meierhans [6] presented a process for active cooling system using a cooling tower as shown in figure 2. At the night, the ceiling/floor slab is cooled down by the circulating cool water, and the heat is rejected by the cooling tower. At daytime, the ceiling/floor slab absorbs heat from the building envelope and from internal heat sources. For such an open system, fouling may be a big problem since it affects the heat transfer efficiency between the water and the mass of the slab. Raftery and Paul [7] presented another process of using cool water produced by a cooling tower system for slab activation.

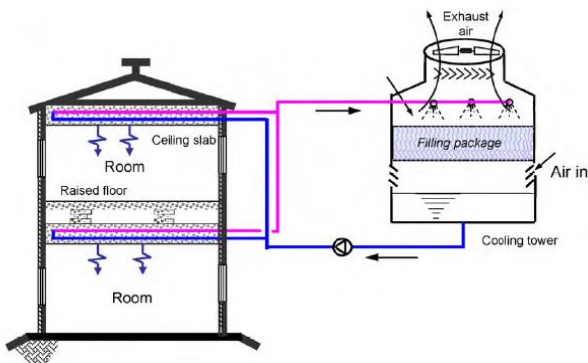


Fig. 2 Thermo-active structures coupled with cooling tower [6].

A chiller with water-cooled condenser supplies chilled water to the air handling unit AHU cooling coils during day-time while a cooling tower combined with plate heat exchanger supplies cool water to the slab during night-time and early morning hours when the outdoor wet bulb temperatures are low. A schematic of this system is shown in figure 3.

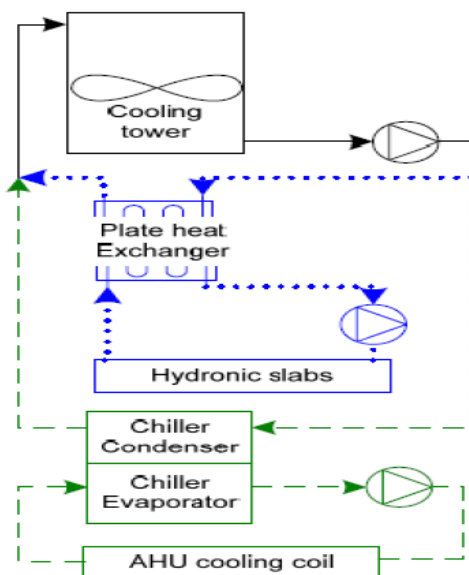


Fig. 3 Chilled water plant schematic [7].

Day operation.----

Night operation.....

Olesen [8] showed the relation between space heat gains, heat transfer on the space side, supply water temperature, heat transfer on the water side and hours of water circulation. The diagrams in Fig. 4 represent an example for these relations by Olesen. The diagram was designed for a concrete slab of resistance $R = 0.45 \text{ m}^2 \cdot \text{K/W}$, and room temperature range of $21 \text{ }^\circ\text{C}$ to $26 \text{ }^\circ\text{C}$. The upper diagram represents the maximum allowable total heat gain in space (internal sources plus solar heat gains) on the y-axis, and the required supply water temperature on the x-axis. The lines in the diagram relate to different occupation periods (8 hrs, 12 hrs, 16 hrs, and 24 hrs) and different maximum energy supplied or extracted per day ($\text{Wh/m}^2 \cdot \text{day}$). The lower diagram represents the cooling power required on the water side (to size the chiller) for thermally activated slab as a function of supply water temperature

and occupation time. Also, the amount of energy that rejected per day was indicated. It shows that, for a maximum space heat gain of 38 W/m^2 and 8 hours operation, a supply water temperature of $18.2 \text{ }^\circ\text{C}$ was circulated. Instead, for 12 hrs operation, a water temperature of $19.3 \text{ }^\circ\text{C}$ is circulated.

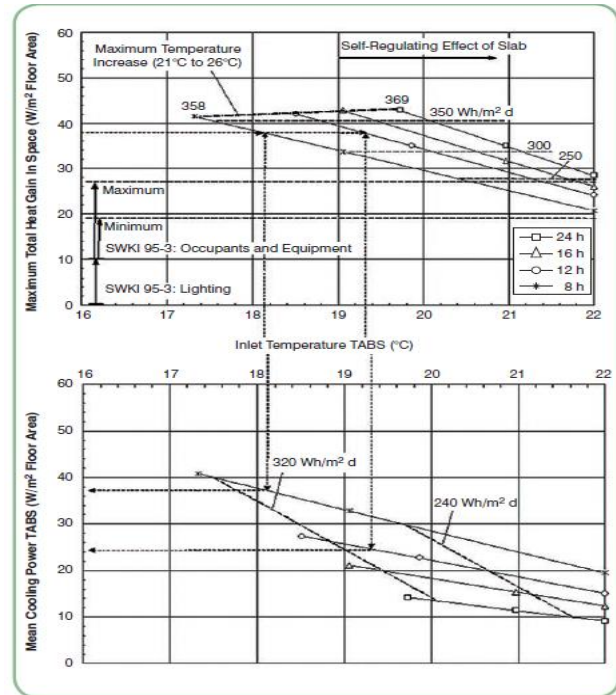


Fig. 4 Design principles of thermo-active building system [8].

Furthermore, the required cooling power on the water side is 37 W/m^2 (for 8-hours operation) and 25 W/m^2 by a 12-hours operation, respectively. Therefore, by 12-hours operation, the chiller can be sized smaller. In another study, Olesen [9] concluded that the important factors for the cooling and heating capacity of surface systems are the heat exchange coefficient between the space and the surface, the minimum and maximum surface temperatures to reach comfort condition and the heat transfer rate between the embedded pipes and the surface. Yang [10] studied numerically the effect of different thermally activated building TAB geometrical parameters on the thermal supply. The thermal demand increased when pipe diameter or pipe deepness was increased and decreased when pipe spacing was increased. The aim of this work is to provide a systematic experimental investigation for the contribution of low cooling energy source in a hot and arid climate of Iraq for cooling of a residential room by thermally activating the concrete roof and to investigate the different parameters affecting the performance of this system. This is coincident with the outlook of the government for renewable energy applications.

II. EXPERIMENTAL WORK

The experimental work consisted of four main parts which are the test room, TAR system, low grade cooling energy source unit (cooling tower) and measuring instrumentation. The room measures $5.5 \text{ m} \times 4 \text{ m} \times 3 \text{ m}$ with three exposed walls, while the 4th wall is adjacent to an interior unconditioned

space. The space below the test room is conditioned. Figure 5 shows a layout for the 1st floor and the location of the test room. Figure 6 shows a sectional view of the house illustrating the conditioned and unconditioned spaces.

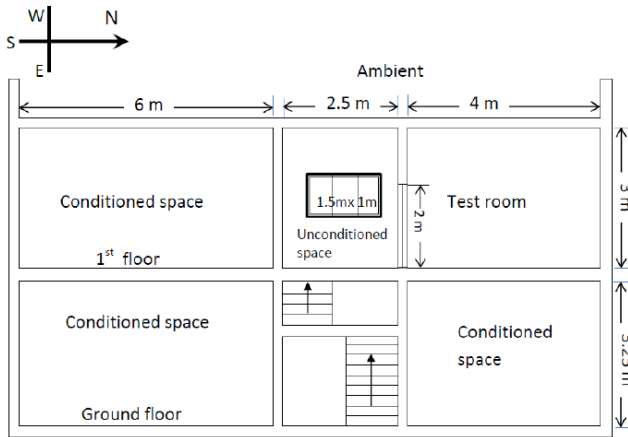


Fig. 5 Layout of the 1st floor house building illustrates the test room location.

Figure 6 shows a plan view of the test room. The roof and walls constructions details were illustrated in figure 7 and figure 8. Turf is the conventional roofing material used by people in the south of Iraq. It consists of clay, water and dry wheat stalk. It is fireproof, thermal insulator and inexpensive. It has been revitalized in recent

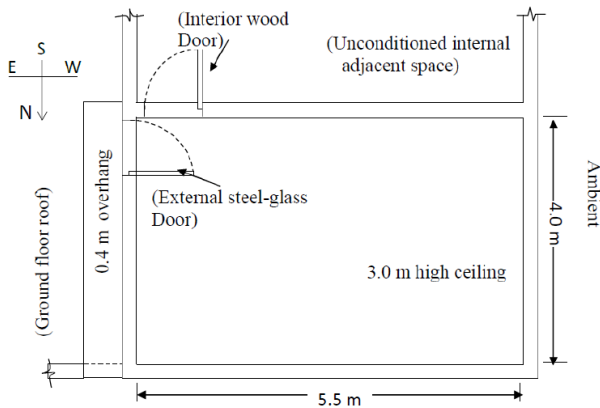


Fig. 6 A plan view of the test room.

years for green buildings and energy sustainability in Europe [10]. The outer finish of the exposed walls, west and north was painted white whereas, the east was pale purple. The inner surface finish of the walls was covered with 20 mm Styrofoam insulation and a Poly Vinyl Chloride PVC panel as an architectural wall siding material. Two doors measuring (2 m x 1 m) were installed.

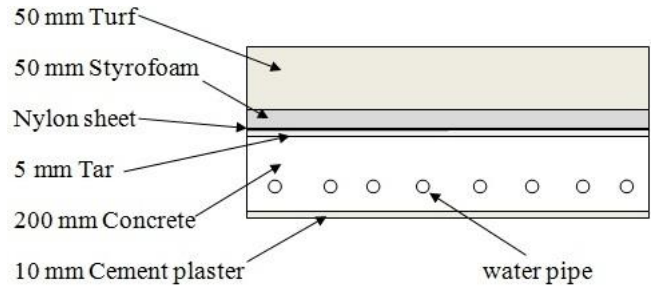


Fig. 7 Roof construction.

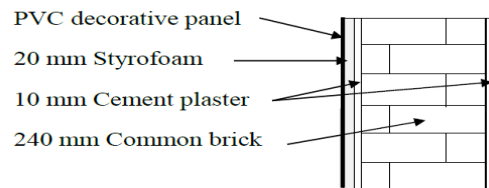


Fig. 8 Wall construction layers.

in the test room. The first is internal and fabricated of soft wood of 30 mm thickness and located at the south wall. The second is 20 mm thick double steel sheets located at the east wall leading to the roof. The lower half of this door was fabricated of 2 (1 m x 1 m) steel sheets welded to a steel frame. 20 mm glass wool insulation was placed between the two steel sheets before welding. The upper half was glazed using double glass sheets with 10 mm air space for insulation. Half of the glazed part was hinged to act as window. External opaque venetian blinds 2 m x 1 m were installed as shading for the glazed part of the steel door. The air leakage around the door and window frames was reduced using 20 mm width weather stripping gasket squeezed tight when apertures are closed. The embedded pipe loops, according to ISO 11855 type E [11], are buried in the concrete layer of the roof construction. Four loops were used in the present work to occupy the roof area with six pass each. Table I shows the concrete slab layer specifications of the TAR system. The eight loop terminals were extended from the concrete slab in order to give flexibility to study the effect of the loops parallel/series connection.

TABLE I
CONCRETE LAYER SPECIFICATIONS.

| Item | Value | Units |
|-----------------------|-------|---------------------|
| Slab length | 6 | m |
| Slab effective length | 5.5 | m |
| Slab width | 4.5 | m |
| Slab effective width | 4 | m |
| Slab area | 27 | m ² |
| Slab effective area | 22 | m ² |
| Slab height | 0.2 | m |
| Slab volume | 5.4 | m ³ |
| Thermal conductivity | 1.4* | W/m ² °C |
| Specific heat | 1* | kJ/kg. °C |
| Density | 2300* | kg/m ³ |

A cooling tower was designed and fabricated to produce cool water and equipped with filtering fittings to ensure efficient system operation with low maintenance. Water strainer was installed in the suction pipe to eliminate the insoluble matters in the circulating water. Figure 9 shows a schematic of the cooling unit used with TAR system and a detailed cooling tower which is fabricated locally.

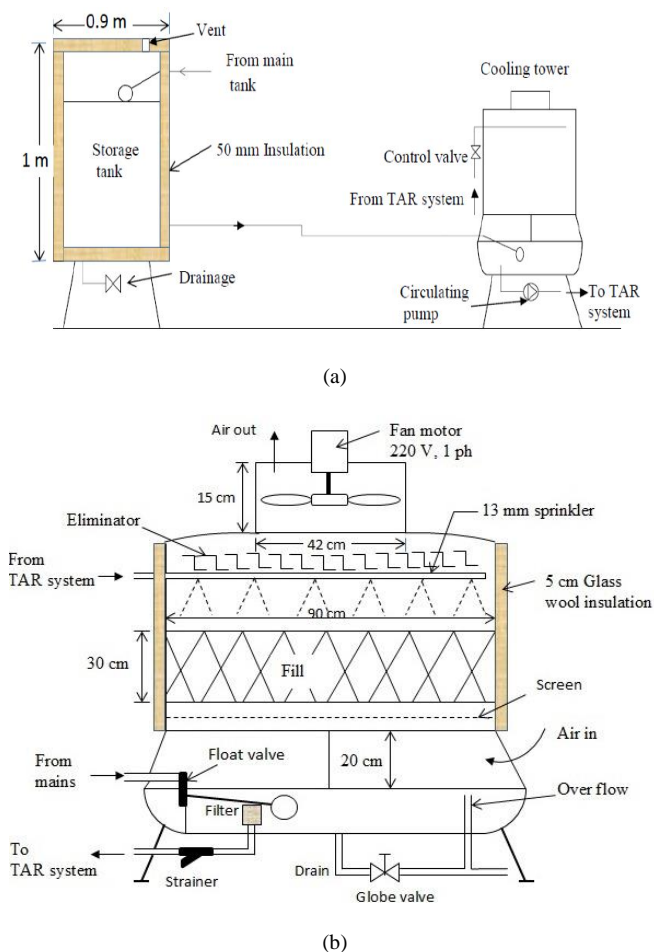


Fig. 9 (a) Cooling tower system for the TAR system.
(b) cooling tower in details.

The cooling tower is mechanical draft counter flow type of 2 kW capacities. Cooling using a TAR system was supplemented by an auxiliary energy source during high

cooling loads. One Ton domestic split unit was used in space to complement space temperature at ASHRAE comfort conditions. Measurements were achieved using 14 temperature sensors type LM 35 throughout the system. Eight sensors were buried in the roof structure as illustrated in figure 10.

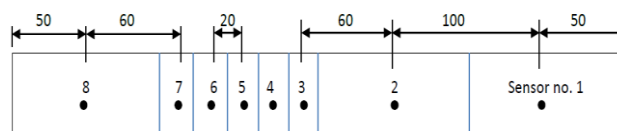


Fig. 10 Thermistors location in the concrete slab.(All dimensions are in centimeter)

● Denotes thermistor.

III. TEST ROOM COOLING LOAD

One of the main features of a typical space, cooled by a TAR system, is the moderate space cooling load (30 – 60 W/m²) [12]. Some modifications in the conventional local construction materials were made for decreasing the cooling load to be within these limits. The cooling load for the conventional construction was found as 110 W/m² which is much higher than the above limits. After walls and roof construction modifications the cooling load is becoming 51.9 W/m². Radiant time series method RTS was used to calculate the instantaneous cooling load of the space. Two persons with light works were proposed to occupy the space. The modifications include the increase of the turf thickness, increasing concrete thickness, roof and walls insulation additions, insulating glass and decreasing infiltration. A commonly used method to describe the transient heat transfer in a multi-layer material is the thermal Resistance-Capacitance or RC-thermal method. This model was used in this work to determine the hourly temperature distribution through the roof layers and to evaluate the TAR system performance and to compare with the experimental measurements. Input solar intensity and temperatures to the model were from experimental measurements of the test room for 21 July, 2013 which is shown in Fig. 11. The solar intensity incident in Amarah city can be modeled as follows:

$$I_t = 0, \quad (0 \leq t \leq 6) \quad (1)$$

$$I_t = 980 \sin\left(\frac{2\pi}{24}(t-6)\right), \quad (6 < t \leq 18) \quad (2)$$

$$I_t = 0, \quad (18 < t \leq 23) \quad (3)$$

Where, I_t is the solar intensity (W/m²), t: time (hr.)

While, the outdoor dry bulb T_{do} and wet bulb temperatures T_{wo} , indoor dry bulb temperature T_{di} and supply water temperature T_s were modeled as;

$$T_{do} = 38 + 8 \sin\left(\frac{2\pi}{24}(t-8)\right), \quad (0 \leq t \leq 23) \quad (4)$$

$$T_{wo} = 21 + 4 \sin\left(\frac{2\pi}{24}(t-8)\right), \quad (0 \leq t \leq 23) \quad (5)$$

$$T_{di} = 30.3 + \sin\left(\frac{2\pi}{24}(t+6)\right), (0 \leq t \leq 23) \quad (6)$$

$$T_s = 25 + 4 \sin\left(\frac{2\pi}{24}(t-8)\right), (0 \leq t \leq 23) \quad (7)$$

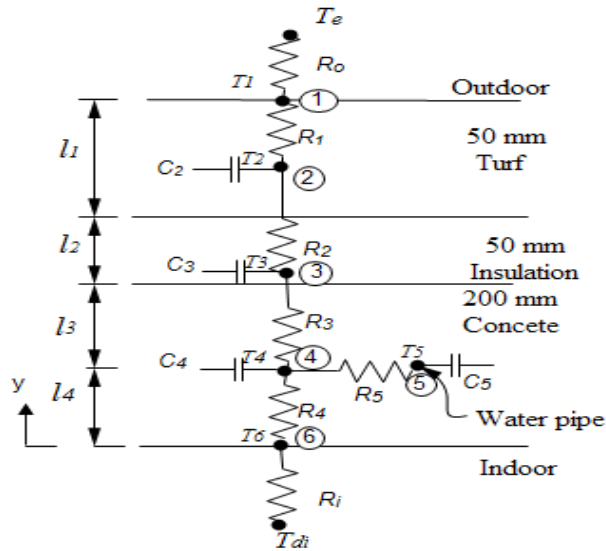


Fig.11 RC-thermal network model.

The sol-air temperature was modeled T_e as;

$$T_e = T_{do} - 4, \quad (0 \leq t \leq 6) \quad (8)$$

$$T_e = T_{do} + 25.5 \sin\left(\frac{2\pi}{24}(t-6)\right) - 4, \quad (6 < t \leq 18) \quad (9)$$

$$T_e = T_{do} - 4, \quad (18 < t \leq 24) \quad (10)$$

Six nodes were used across the roof thickness which rendered a 6th order model. The internal nodal points have thermal capacities whereas; the surface nodal point thermal capacities are set to zero. Matlab R2012a computer program was used to solve the set of six linear algebraic equations. Performance of TAR system can be evaluated once the node temperatures at each time step are determined. The heat extracted, per meter square \dot{q}_c from the concrete slab by the TAR piping system can be calculated as;

$$\dot{q}_c = \frac{T_4 - T_5}{R_5} \quad (11)$$

The heat extracted from the room by the TAR system across the lower roof surface, can be calculated as;

$$\dot{q}_i = h_i A_r (T_{di} - T_6) \quad (12)$$

Where, h_i is inside film coefficient of heat transfer ($\text{W}/\text{m}^2 \cdot ^\circ\text{C}$) and A_r is the roof area (m^2)

The rate of heat transferred to the upper roof surface from the surroundings is calculated as;

$$\dot{q}_o = h_o A_r (T_e - T_1) \quad (13)$$

Where, h_o is outside film coefficient of heat transfer ($\text{W}/\text{m}^2 \cdot ^\circ\text{C}$)

TAR system instantaneous efficiency η_{TAR} , in this work, is defined as the ratio of the heat extracted from the room by the TAR system to the heat extracted from the concrete slab by the cooled water as;

IV. RESULTS

A. The effect of wall and roof insulations

High roof mass prohibits high indoor air temperature fluctuation and sustains a steadier overall thermal environment. Figure 12 represents the concrete core temperature without turf roofing and roof insulation on 9 April, 2013 and with turf roofing and roof insulation on 15 April, 2013.

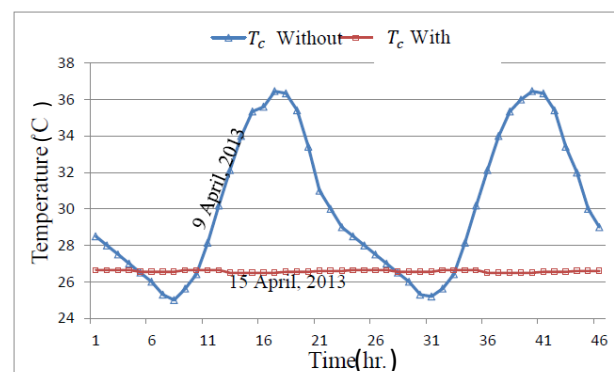


Figure 12. Concrete core temperature with and without turf roofing and roof insulation.

The mean concrete core temperature T_{cm} which covered by 150 mm turf and 50 mm insulation was greatly below that without roofing and insulation. For the present work, the following relation was found to apply;

$$T_{cm}^{with} = T_{cm}^{without} - 4.5, \quad (14)$$

According to (14), concrete core temperature reduction by approximately of 4.5 $^\circ\text{C}$ leads to a decrease in total cooling load through the roof construction by 2.25 kW.hr. This represents a decrease in total roof cooling load of 71% on 21 July. This is verified theoretically by evaluating roof cooling load with and without roofing and roof insulation which was found to be as 68.2% less on 21 July.

The turf roofing, roof and wall insulations affect the indoor approach temperature IAT parameter which is proposed in the present work and can be defined as the difference between the indoor and concrete core temperatures ($T_{di} - T_c$). This parameter represents an indicator of how close the indoor temperature is to the concrete core temperature. The IAT depends mainly on space cooling load and indoor film coefficient. For constant film coefficient, the higher the cooling load, the higher the IAT and vice versa. Figure 13 shows the IAT with and without wall insulation.

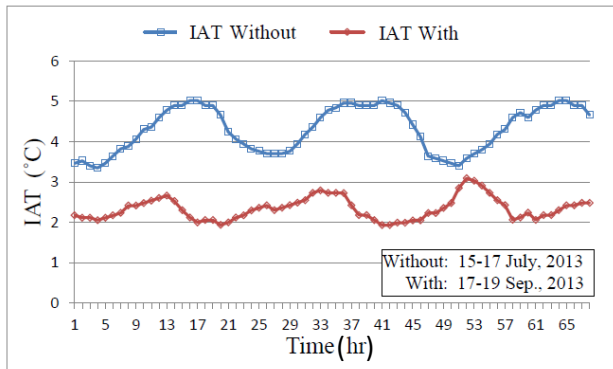


Fig.13 Indoor approach temperature with and without wall insulation.

It was found that the difference between the concrete and indoor temperatures decreased significantly with wall insulation. It is shown that the average IAT decreased from 4.3 to 2.4 °C. Consequently, from several measured results, the indoor temperature can be evaluated approximately for the present work by the concrete core temperature as;

$$T_{di} = T_c + 4.3, \quad (\text{Without wall insulation}) \quad (15)$$

$$T_{di} = T_c + 2.4, \quad (\text{With wall insulation}) \quad (16)$$

B. The effect of ambient conditions

Amarah summer is characterized by a high day time temperature, and a large difference between day and night temperatures with moderate to low humidity, high solar radiation, and little cloud cover. Amarah weather experiences high averages and extremes in temperature during the summer months. Figure 14 shows a significant increase in wet bulb temperature in July because of the humid seasonal southeasterly winds (locally called Sharji) from the Arabian Gulf and from the marshes around the city. Low ambient wet bulb temperature is observed in other summer months due to the dry northwesterly winds (locally called Shamal). From the experimental measurement, a maximum outdoor temperature of 50.7 °C was recorded on 18 July, 2013 which indicates the very hot weather the city is characterized by.

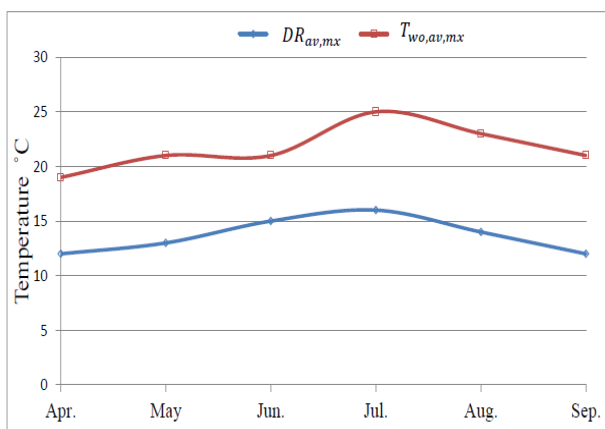


Fig. 14 Ambient wet bulb temperature and daily range for summer months of Amarah city, 2013.

Figure 15 shows the indoor temperature for different summer months before and after TAR system activation.

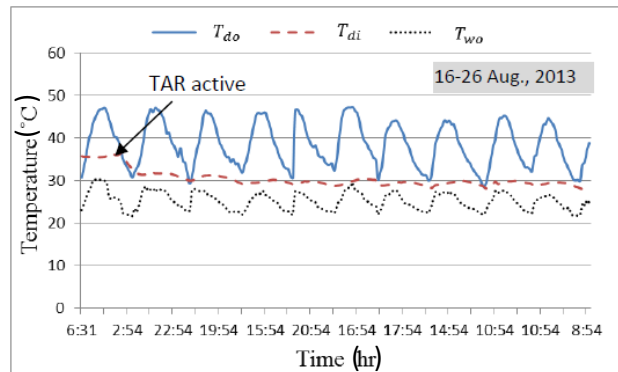
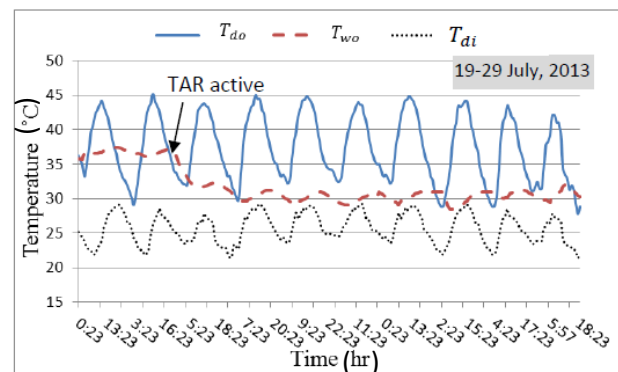
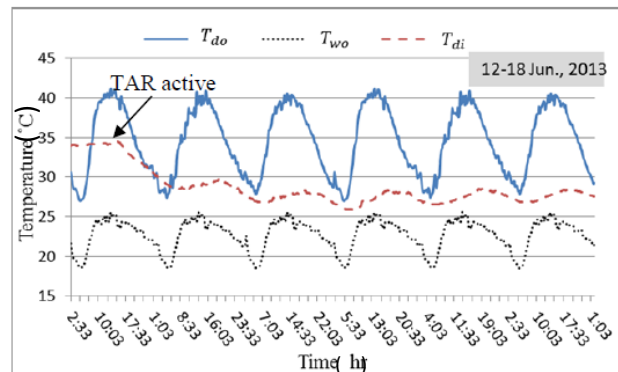


Fig. 15 The indoor temperature for different summer months before and after TAR system activation.

It was found that the indoor temperature decreased considerably with TAR system activation with a dependence on the ambient dry bulb temperature. From the experimental measurements; it was found that the indoor temperature of the test room was near the average of the minimum ambient dry bulb temperature $T_{do,mn}$ as shown in figure 15. The indoor temperature with TAR system in this work may be approximated as;

$$T_{di} = T_{do,mn,av} \quad (17)$$

This relation can be adopted as a thumb rule to estimate the indoor temperature at any time during summer months.

The hourly test room indoor temperature for a certain day was found to vary with ambient wet bulb temperature and time. The relation between the difference of indoor and wet bulb temperatures with time is shown in figure 16. This trend was observed for different temperature histories during summer operation. From these observations, the indoor dry bulb temperature at any time t may be estimated with an uncertainty of $\pm 0.5^\circ\text{C}$ as;

$$T_{di} = T_{wo} + 5 \sin\left(\frac{\pi}{12}(t + 1)\right) - 4 \quad (18)$$

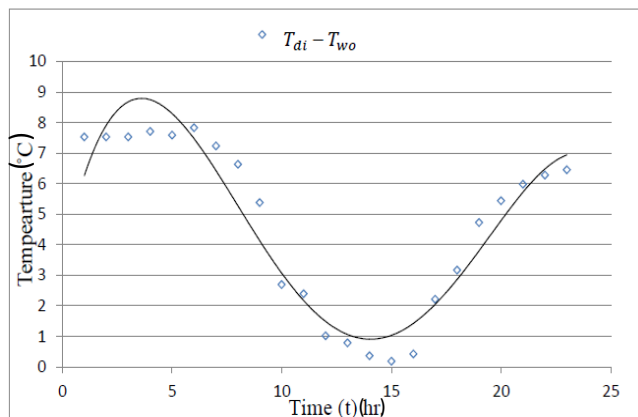


Fig. 16 The indoor temperature variation with wet bulb temperature and time.

Figure 17 shows the ASHRAE comfort zone and hourly averages of the indoor dry bulb temperature for summer months, 2013. Indoor conditions out of the comfort zone can be drawn into this zone by decreasing the temperature, moisture content or both. This can be done by using an auxiliary energy unit. Coupling auxiliary energy unit with TAR system draws the indoor conditions towards the comfort zone. Figure 18 shows the indoor condition movement towards the comfort zone. Firstly is without TAR system and no auxiliary unit operation. Secondly, only the TAR system is in operation. And finally with TAR system and auxiliary unit both in operation. The TAR system draws the indoor conditions toward the comfort zone but not inside it, while the indoor conditions are inside the comfort zone when the auxiliary unit is operated.

The auxiliary energy required for summer operation coupled with TAR system to offset the cooling load is shown in figure 19. This figure shows the TAR system contribution in balancing the space cooling load and the auxiliary energy required to complement the space cooling load for summer months. It was found that the auxiliary energy requirement is high for July, moderate for June and August, low for May and zero for April and September. The TAR system can completely balance the space cooling load during April and September. The total TAR system seasonal contribution ratio SCR in offsetting the cooling load was found 0.68 which is an energy saving during the summer season.

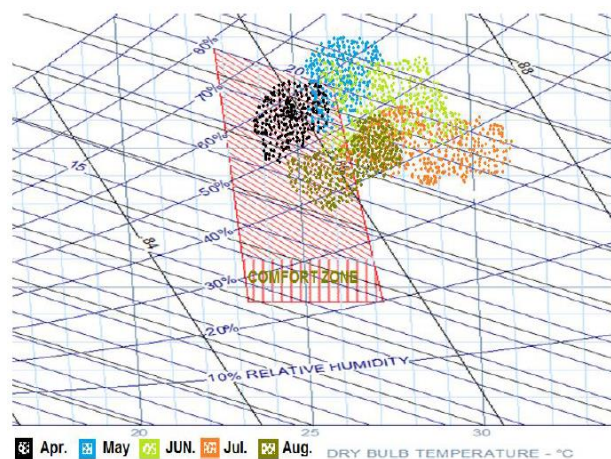


Fig. 17 Summer indoor temperature in ASHRAE comfort zone.

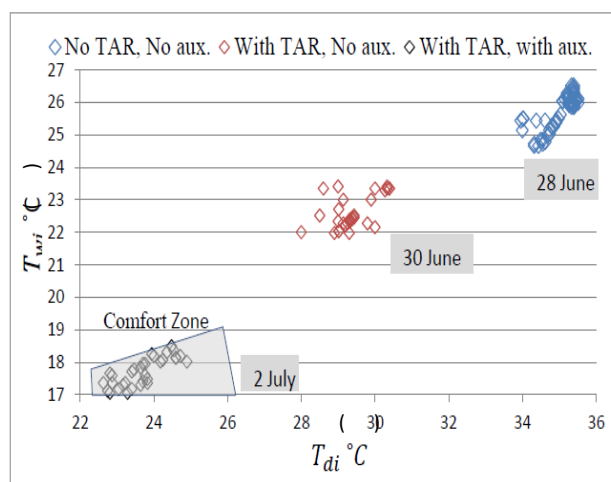


Fig. 18 Indoor conditions location related to ASHRAE comfort zone.

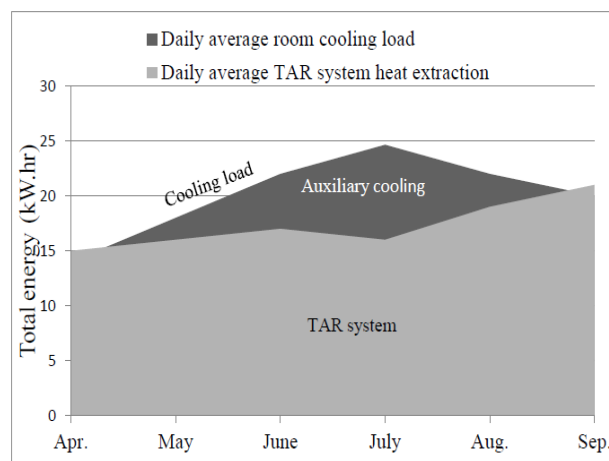


Fig. 19 The monthly average auxiliary cooling demand during summer 2013.

V. CONCLUSIONS

The following conclusions can be inferred from the present work:



- 1- Circulating cool water in a roof slab reduced the cooling load by 78.8 %.
- 2- Wall, roof, door and window insulation additions decrease the cooling load from 110 to 51.9 W/m² in 21 July.
- 3- The mean concrete temperature during cooling with TAR system decreased by 4.5 °C with turf and roof insulation addition. The indoor temperature with TAR system is ambient wet bulb temperature dependent. While it is ambient dry bulb temperature dependent without TAR system.
- 4- A rule of thumb can be used to predict the indoor temperature, for any day during summer operation with TAR system, by setting it equal to the minimum outdoor dry bulb temperature during that day.
- 5- An auxiliary energy unit is needed with TAR system for summer comfort conditions during the last days of May, all the days of June and July and during the early days of August. No auxiliary energy is needed during April and most September.

VI. REFERENCES

- [2] R.A. Meierhans, "Slab cooling and earth coupling". ASHRAE Trans., 1993; 99(2): 511-518.
- [2] M. Koschenz, B. Lehmann, "Thermo-active building system TABS. EMPA", Duebendorf Switzerland, (2000) ISBN 3-905594-19-6.
- [3] B. W. Olesen, "The history of radiant heating and cooling systems". ASHRAE journal, February 2010, 52(3): 50-55.
- [4] X. Xinhua, W. Shengwei, W. Jin, X. Fu, "Active pipe embedded structures in buildings for utilizing low-grade energy sources: A review". Energy and Buildings. 2010; 42(10): 1567–1581.
- [5] ISO 11855-2. Building Environment Design - Design, Construction and Operation of Radiant Heating and Cooling Systems. Part 2, ISO, 2012.
- [6] R.A. Meierhans, "Room air conditioning by means of overnight cooling of the concrete ceiling". ASHRAE Transactions 1996; 102 (1): 693–697.
- [7] N. Raftery, A. Paul, :Analysis of a hybrid UFAD and radiant hydronic slab HVAC system". PhD thesis, National University of Ireland Galway, Center for the Built Environment, (2014) UC Berkeley, USA.
- [8] B. W. Olesen "Cooling and heating of buildings by activating their thermal mass with embedded hydronic pipe systems". In ASHRAE, Dublin, Ireland, 2001; 158: 5-19.
- [9] B. W. Olesen, "Possibilities and limitations of radiant floor cooling". ASHRAE Transactions 1997; 103(1):42 – 48.
- [10] Y. Yang, "The role of optimization and simplified methods in the design of Thermally Activated Building Systems (TABS)". PhD thesis, Eindhoven, university of technology, unit building physics and services, 078901, 2013.
- [11] S. Clarke, "Green Building: A Complete How-to Guide to Alternative Building Methods : Earth Plaster, Straw Bale, Cordwood, Cob, Living Roofs". Sterling Publishing Company, Inc. pp. 276.(2009) ISBN 978-1-60059-534-9.
- [12] G. Hauser, C. Kempkes, B. W. Olesen, "Computer simulation of hydronic heating/cooling system with embedded pipes". ASHRAE Transactions, 2000; 106 (1): 702–71



مَدِينَة

بوقائع المؤتمر العلمي الدولي الثالث

للطاقة المتجددة / الجامعة التقنية

الجنوبية

للفترة 14 - 15 آذار 2018

مجلة علمية محكمة نصف سنوية

تصدر عن كلية الهندسة الجامعة

P – ISSN: 2415 - 4826

E- ISSN: 2523 – 2401

DOI: 10.22317. JNUC

عدد خاص بوقائع المؤتمر



J.N.U.C.

مجلة كلية النور الجامعة



العدد: 6 السنة: 2018

رئيس التحرير

أ.م.د. عبد جواد كاظم

مدير التحرير

أ.م.د. جاسم محمد سلمان

هيئة التحرير

- أ.د. بسام عباس محمد
- أ.د. نظام شيت حميد
- أ.م.د. عثمان حسين سلمان
- أ.م.د. زهير ابراهيم عبدالجبار
- أ.م.د. عبد الرضا جواد جاسم
- أ.م.د. علاء الدين محمود كريم
- أ.م.د. خالد سلمان جواد المهداوي
- م.د. مكي مهدي عبدالحسن

الهيئة الاستشارية

- أ.د. زيفرا ليرمان/ رئيسة مؤسسة مؤتمرات علمية / الولايات المتحدة الأمريكية
- أ.د. مريم بالبان / جامعة روما - ايطاليا
- أ.د. باسم حامد حميد - جامعة العلوم الماليزية - ماليزيا
- أ.د. عبد الوهاب رزوقي حمد - جامعة الزرقاء - الأردن
- أ.د. مظفر صادق الزهيري / رئيس الجامعة التقنية الجنوبية
- أ.د. فريد مجيد عبد العطار / رئاسة الجامعة التقنية الوسطى
- أ.د. عادل شريف الحسيني / جامعة سري / بريطانيا
- أ.د. اسامة سلمان عبدالرزاق - الجامعة التقنية الوسطى
- أ.د. زهير نعمان حمد - الجامعة التقنية الوسطى

عدد خاص بوقائع المؤتمر



J.N.U.C.

مجلة كلية النور الجامعة



العدد: 6 السنة: 2018

مقوم اللغة الانكليزية

أ.د. نظام شيت حميد / كلية النور الجامعة

مقوم اللغة العربية

م.د. شميم راضي عبد / كلية النور الجامعة

سكرتير التحرير

م.م. محمد عبد جواد كاظم

المتابعة

المهندسة غفران ثامر ناجي
المهندسة أرين حسن جمعة
رؤى محمد حسن محمد سعيد

P-ISSN :- 2415-4806
E-ISSN :- 2523-2401
DOI :10.22317/JNUC



J.N.U.C.



عدد خاص بوقائع المؤتمر العلمي الدولي الثالث للطاقة المتجددة
/الجامعة التقنية الجنوبية للفترة من 14 - 15 اذار 2018

مجلة كلية النسور الجامعة

مجلة علمية محكمة نصف سنوية
تصدر عن
كلية النسور الجامعة

السنة ٢٠١٨

العدد: ٦

رقم الايداع في دار الكتب والوثائق - بغداد (٢١٩١) لسنة ٢٠١٦